Fermilab

FERMILAB-TM-2136
December 2000

THE PROTON DRIVER DESIGN STUDY

Fermilab

FERMILAB-TM-2136

The Proton Driver Design Study

Edited by W. Chou, C. Ankenbrandt and E. Malamud

for the

Proton Driver Design Study Group

Russ Alber
Larry Allen
Terry Anderson
Chuck Ankenbrandt
Maurice Ball
Dave Carey
Mark Champion
Weiren Chou
Mike Church
Don Cossairt
Jim Crisp
Sasha Drozhdin
Vadim Dudnikov
Matt Ferguson
Jim Griffin
Dave Harding
Steve Holmes
Chez Jach
Rol Johnson (IIT)
Carol Johnstone
John Johnstone
Kiyomi Koba
Ioanis Kourbanis
Oleg Krivosheev
Jim Lackey
Sharon Lackey
Tom Lackowski
Jerry Leibfritz
Jim MacLachlan
Ernie Malamud
Evan Malone
Fred Mills
Nikolai Mokhov
Al Moretti
Bill Ng
Sho Ohnuma (Univ. of Hawaii)
Francois Ostiguy
Milorad Popovic
Chris Prior (RAL/England)
John Reid
Dave Ritson (Stanford Univ.)
Al Russell
Zubao Qian
Chuck Schmidt
Mike Shea
Jeff Sims
Jim Steimel
Ding Sun
Victor Terekhov (IHEP/Russia)
Ray Tomlin
Kamran Vaziri
Rod Walton
Bob Webber
Dave Wildman
Dan Wolff
Don Young
Bruno Zotter (CERN)

December 2000

Table of Contents

Executive Summary

In a 1997 summer study, a team led by Steve Holmes formulated a development plan for the Fermilab proton source and described the results in TM-2021. Subsequently, at the end of 1998, a task group was formed to prepare a detailed design of a high intensity facility called the Proton Driver to replace the Fermilab Booster. In the past two years the design effort has attracted more than fifty participants, mostly from the Beams Division. Physicists and engineers from the Technical Division and FESS as well as other institutions, including the Illinois Institute of Technology (IIT), Stanford University, University of Hawaii, CERN in Switzerland, Rutherford Appleton Laboratory in England and the IHEP in Russia also contributed heavily. The results of that effort are summarized in this document describing the design of a 16 GeV synchrotron, two new beam transport lines (a 400 MeV injection line and a 12/16 GeV extraction line), and related improvements to the present negative ion source and the 400 MeV Linac. A construction cost estimate is presented in Appendix A.

The conventional wisdom in the particle accelerator world is that high energy machines and high intensity machines furnish complementary capabilities, with high energy accelerators providing the potential for new discoveries while high intensity accelerators enable precision measurements. However, that distinction is blurring because colliders at the energy frontier, such as the Tevatron in Run II, require high intensity injectors in order to achieve the substantial integrated luminosity that is necessary to make discoveries. Moreover, neutrino factories and muon colliders, which have both attracted considerable interest in the high energy physics community, require a high intensity proton source for muon beam production. An intense proton source is also useful for the production of high-intensity secondary particle beams of pions, kaons, muons, neutrons and neutrinos. A physics study focusing on applications of the Proton Driver is underway at Fermilab, with a report due in several months.

The Proton Driver is a rapid-cycling high-intensity 16-GeV synchrotron that serves a number of purposes in the Fermilab HEP program. In the near term, it replaces the present Booster and increases the proton beam intensity in the Main Injector by a factor of four, thereby providing an upgrade path for NuMI and other 120 GeV fixed target programs. It also helps increase the Tevatron collider luminosity after the antiproton source takes necessary measures to accommodate more antiprotons. The Proton Driver also opens the avenue for new physics programs based on its stand-alone capabilities as a source of intense proton beams. In the medium term, it could serve a neutrino factory by generating intense short muon bunches from a target. These muon bunches would then be phase rotated, cooled, accelerated and stored in a muon storage ring in order to generate intense beams of muon neutrinos and electron neutrinos. In the long term, the Proton Driver could be upgraded to a 4 MW proton source (by adding a 600 MeV linac and a 3 GeV Pre-Booster) in order to serve a muon collider.

At present, the Booster is the bottleneck that limits the proton beam intensity in the Fermilab accelerator complex. Its upstream machine, the Linac, is capable of providing

3.4×10^{13} particles per cycle at 15 Hz. However, due to numerous problems, the Booster intensity is limited to 5×10^{12} particles per cycle. After some modest upgrades, the downstream machine, the Main Injector, is capable of accelerating four times more protons than the Booster can provide. The Proton Driver, as a complete functional replacement for the Booster, removes this bottleneck and makes full use of the capabilities of the Linac and Main Injector.

This report presents a staged design of the Proton Driver having two phases. Phase I, the focus of this report, provides 1 MW of beam power. Phase II, which is discussed only briefly in Appendix C, is an upgrade path to 4 MW. Furthermore, Phase I has two stages. Stage 1 provides a maximum beam energy of 12 GeV with a 53 MHz rf system, whereas Stage 2 increases the beam energy to 16 GeV with a new 7.5 MHz rf system. There are several reasons for this two-stage implementation. In Stage 1, when there is no neutrino factory for the Proton Driver to serve, the 53 MHz rf system matches that of the Main Injector. Besides, one may reuse the rf system of the present Booster (with some modifications) and thus reduce the capital cost in this stage. In order to match the acceptance of the Main Injector to that of the Proton Driver, the Main Injector injection energy is raised to 12 GeV in Stage 1. In Stage 2, it is envisioned that a neutrino factory will require a small number of proton bunches. Therefore, a low frequency (7.5 MHz) rf system replaces the 53 MHz system. Another reason for choosing 7.5 MHz is that it provides the bunch spacing (132 ns) required by the Tevatron Collider in Run IIb, thereby obviating the need for beam coalescing in the Main Injector. The maximum beam energy of the Proton Driver is increased to 16 GeV in Stage 2 in order to generate enough muons for a neutrino factory.

In order to achieve the demanding performance specifications of the Proton Driver, a number of state-of-the-art features are incorporated in its design. The guide-field magnets are arranged in a transition-free FMC (flexible momentum compaction) lattice having large momentum acceptance and dynamic aperture. The injection scheme employs transverse painting to reduce space charge effects. The power supply uses a dual-harmonic resonant system (15 Hz plus 12.5% of 30 Hz component), thereby lowering the peak rf power requirement by 25%. The 7.5 MHz rf cavities employ a new type of alloy called Finemet for their magnetic cores. The main advantages of the Finemet cores are high accelerating gradient and wide bandwidth. The magnets employ external vacuum skins like those in the Booster, have large apertures like those in the Fermilab Accumulator, and use stranded conductors for the coil in order to reduce eddy current losses. Metallic stripes or liners are used to provide a low-impedance environment for the beam. A sophisticated beam collimator system collects about 99% of the lost particles in a small area, thereby allowing hands-on maintenance in the rest of the enclosure.

In addition to high intensity, another main requirement on the Proton Driver is short (1 ns rms) bunch lengths. In order to meet this requirement, the design adopts various measures to preserve the beam longitudinal emittance and to provide large (±2.5%) momentum acceptance. Bunch compression will be used at the end of the cycle when it is necessary to shorten the bunches.

This report also includes a chapter on related improvements to the H^- source and the present Linac. The main goal of these improvements is to increase the beam current by a factor of two while reducing the transverse emittances by the same factor, thereby increasing the transverse brightness by a factor of four. These improvements are necessary not only to provide the required beam intensity but also to control the linac beam losses during high intensity operations.

A main consideration in this design study is to minimize possible interruptions to the ongoing Fermilab HEP program, specifically Run II. Therefore the Proton Driver is located on the west side of Kautz Road, where construction can proceed without interfering with the operation of the existing machines and where two new beam transport lines can conveniently connect the Proton Driver to the Linac and Main Injector. A new 400 MeV line connects the Linac to the Proton Driver, and a new 12/16 GeV line connects the Proton Driver to the Main Injector. A large portion of the MI-8 enclosure can be reused for the latter line. Only the connections between the new beam transport lines and the existing accelerators require a machine shutdown. (This is similar to how the Main Injector was integrated into the existing accelerator chain.) Space is also reserved for a future new Linac and a Pre-Booster.

W. Chou and C. Ankenbrandt

Chapter 1. Introduction

C. Ankenbrandt, W. Chou, S. D. Holmes and R. C. Webber

1.1. Overview

The Fermilab Proton Source was constructed in the early 1970's and originally consisted of a proton ion source, a 750 kV Cockcroft-Walton, a 200-MeV Linac, and an 8 GeV Booster synchrotron. Since then the facility has undergone substantial improvements including the addition of a second Cockcroft-Walton, conversion to H^- ions for acceleration through the Linac and charge-exchange injection into the Booster, and a Linac energy upgrade to 400 MeV. However the Booster itself is basically the same machine that was built three decades ago. This facility currently provides proton beams at intensities up to 5×10^{12} protons per pulse (6×10^{10} protons/bunch $\times$ 84 bunches), at 8.9 GeV/c, for injection into the Main Injector in support of Tevatron Collider and Main Injector fixed target operations. Most Proton Source hardware is capable of 15 Hz operation without beam and a few Hz with beam.

With the advent of the Main Injector, the demand for protons in support of a diverse physics research program at Fermilab is growing. The reason is that the Main Injector creates a new capability for simultaneous operation of the collider and 120 GeV fixed target programs. In parallel the utility of the Booster itself as a source of protons for fixed target neutrino experiments has also been identified. Two experiments are now under construction, the Neutrinos at the Main Injector (NUMI) project and the MiniBooNe (Booster Neutrinos), that utilize protons delivered from the Booster either via the Main Injector or directly. These experiments require not only the full 5×10^{12} protons per pulse intensity of the proton source (or more), but a 7.5 Hz repetition rate. Two experiments under consideration at the current time, Kaons at the Main Injector (KAMI) and Charged Kaons at the Main Injector (CKM), could also place demands on the proton source over the coming decade. Finally, a number of future initiatives are in various states of consideration — the BTeV experiment has stage 1 approval as a continuation of the Fermilab collider program, a neutrino source based on a muon storage ring (aka "neutrino factory") and a Very Large Hadron Collider have been identified as possible long range facilities for Fermilab. Low energy antiproton facilities also are receiving attention. Each of the near term activities would benefit from an improvement in the per pulse and per hour intensities delivered from the existing Proton Source, while the longer term possibilities would demand performance beyond the capabilities of the existing proton source, even with substantial additional improvements.

The purpose of this study is to outline a possible design of a new Proton Source that could satisfy the demands of the future Fermilab research program for the next several decades. The goal is to outline a staged plan, with significant enhancements to the Fermilab research program evident at each step, with minimal disruption to the ongoing program from required construction activities, and with maximal flexibility in meeting

future demands. As will be described in this document, we believe that such a plan would consist of some or all of the following components:

- Replacement of the Booster by a modern synchrotron of considerably greater capabilities
- Upgrading of the Linac energy and intensity
- Addition of a second synchrotron to further augment the long-term capabilities

An evolutionary implementation of these improvements is envisaged, with benefits accruing to the Fermilab program at each stage. The timing of these stages as well as the possible consolidation of multiple stages will presumably be dictated by the occurrence of normally scheduled program interruptions, by the availability of funding, and by the future direction of the Fermilab research program. Mostly for historical reasons, two phases of this plan have been identified, and furthermore, Phase I has two stages. Primary design criteria have been established, in chronological order, as follows:

Near term (Phase I, Stage 1)

- Replacement of the Booster by a synchrotron capable of delivering 2.4×10^{11} protons/bunch ($4 \times$ current performance) with beam delivered at a rate of 15 Hz and with a kinetic energy of at least 8 GeV and at most 16 GeV.
- Compatibility with injection of this increased bunch intensity into the Main Injector utilizing the existing 53 MHz Main Injector rf system.

Neutrino Factory era (Phase I, Stage 2)

- A capability for delivering 1 MW of protons onto a production target with a 7.5 MHz bunch structure, while maintaining compatibility with Main Injector injection.

Longer term (Phase II, Muon Collider Era)

- A capability of delivering 4 MW of protons onto a production target with a bunch structure matched to the needs of a muon collider.

This document describes a particular scenario based on the above considerations, a plan that includes a 16 GeV Booster replacement, a 1 GeV Linac upgrade, and a 3 GeV Pre-Booster. This scenario is regarded as representative but not necessarily optimal. The design described in the body of this report primarily addresses Phase I, the items listed through the "Neutrino Factory Era". The report also includes a preliminary assessment of the costs associated with that design. The cost and performance implications of choosing a different operating energy are discussed in Appendix B. Discussion of the modifications required to support the "Phase II, Muon Collider Era" are included in Appendix C. Impacts on the Fermilab program of each step are discussed, as are technical issues and areas of fruitful R&D.

1.2. Present Performance of the Proton Source

The performance of the Proton Source can be characterized by the number of protons per bunch, the number of protons per second, and the transverse and longitudinal emittances of the beam. Under current operating conditions the number of protons per bunch is fundamentally limited by the space charge tune shift achievable at the 400 MeV injection energy and the aperture of the machine, the number of protons per second by the losses during injection, acceleration, and extraction coupled with the available shielding, the

transverse emittance by the space charge forces at injection, and the longitudinal emittance by the momentum spread delivered from the Linac and our ability to control longitudinal instabilities. Figures 1.1 and 1.2 characterize current performance.

Figure 1.1 displays Booster performance, as measured by transverse beam emittance (95%, normalized), as a function of intensity. Two sets of points are included: the "200 MeV" points refer to pre-September 1993 operations when the injection energy was 200 MeV. The "400 MeV" points refer to current operations with a 400 MeV injection energy. It has long been believed that Booster performance is limited by space charge forces at injection. The straight lines through the points represent contours of constant space-charge tune shift (~0.4) as calculated at the injection energy. The data demonstrate that the improved performance attained by raising the injection energy is as anticipated based on a fixed space-charge tune shift limit. By way of reference, the Booster and Main Injector apertures are approximately 20 π and 40 π mm-mrad respectively. As can be seen from the figure, an emittance of 15 π mm-mrad from the Booster is characteristic of the nominal Main Injector operating intensity of 6×10^{10} protons/bunch.

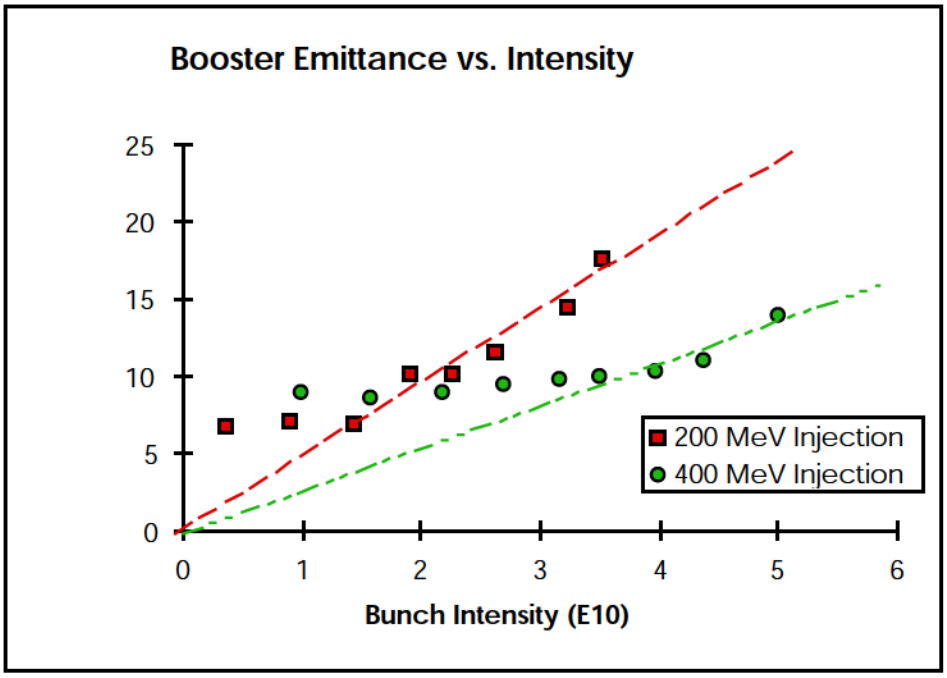

Figure 1.1 Measured transverse beam emittance (95%, normalized, in π mm-mrad) delivered from the 8 GeV Booster as a function of beam intensity

Figure 1.2 shows the performance of the Booster as measured in longitudinal emittance (95%, per bunch) during the period covered by operations with 200 MeV and 400 MeV injection energies. Based on extrapolation of the 200 MeV points, the Main Injector was designed with an acceptance of 0.6 eV-s. As can be seen, the achieved performance is dramatically better than had been assumed. This improvement comes not only from increasing the injection energy but also from the implementation of dampers to control several longitudinal coupled bunch modes. The improved performance has

created options for increased Main Injector intensities based on slip stacking, a subject that is beyond the scope of this report.

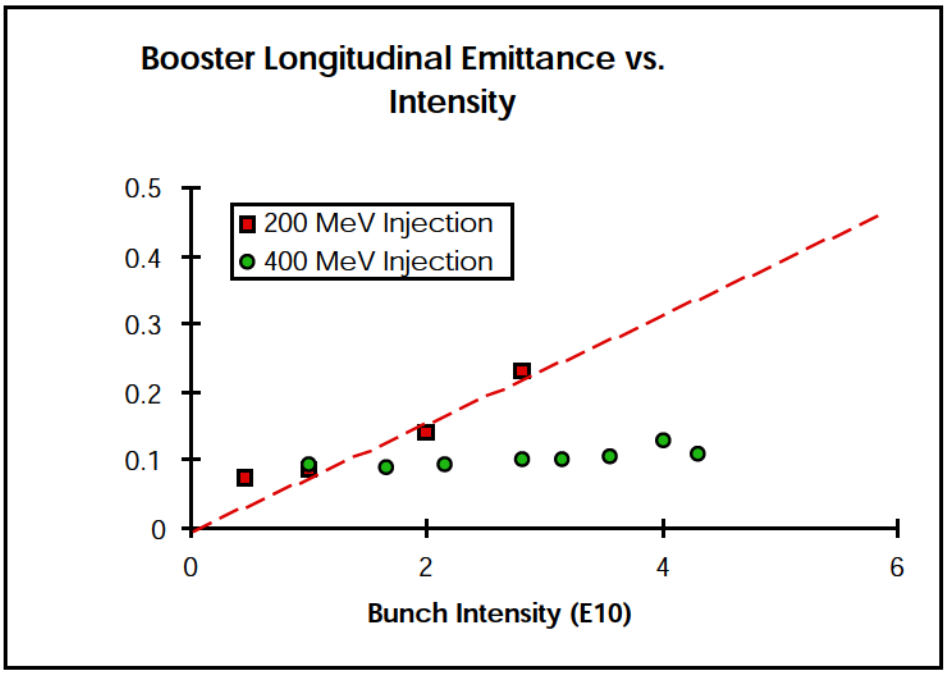

Figure 1.2 Measured longitudinal beam emittance (95%, in eV-s) delivered from the 8 GeV Booster as a function of beam intensity

The above data suggest that the Booster can produce beam pulses having intensity and emittances corresponding to Main Injector design specifications. However, beam losses in the Booster are a major problem. Passive radiation shielding of the Booster is inadequate even for present operations, and options for additional shielding in the current configuration are extremely limited. The maximum proton delivery rate is limited by the ability to fine-tune beam losses within a safety envelope enforced by an array of some fifty interlocked radiation detectors. Since the Booster was originally designed, the implications of beam-on radiation external to the enclosure have been exacerbated by the increased demand for protons, by construction of office and laboratory space in the immediate vicinity of the machine, by relocation of the extraction point to an area below an office building, and by tighter regulations on allowable radiation doses. Extrapolation of the present readings of those detectors to the intensities required by approved near-future programs (MiniBooNe and NUMI) shows that several of these interlocked detectors would exceed their allowed values by factors as large as 20.

Independent of shielding issues, maintenance of beamline components will become a significant operational problem due to component activation. Given present machine performance, activation levels may rise two orders of magnitude from present levels

based on the proton demands for approved experiments. For example, current dose rates of 20-50 mRem/hr at one foot from rf cavities will rise to 2000-5000 mRem/hr.

The current performance of the Proton Source (6×10^{10} protons/bunch with a transverse emittance of 15 π mm-mrad and a longitudinal emittance of 0.1 eV-s/bunch) is sufficient to support the goals of antiproton production for Run II, NUMI or KAMI, and the fast extracted neutrino experiment MiniBooNE — assuming the implementation of effective solutions to the beam loss problems in the Booster that will allow operations beyond 1.2×10^{16} protons per hour. Utilization of the Proton Source in support of a neutrino factory and/or a muon collider are both clearly beyond current capabilities. Support for an upgrade of the Tevatron Collider may or may not be within current capability, depending on the antiproton production strategy implemented.

1.3. Design Criteria for the Proton Driver

Support for muon facilities is by far the biggest challenge for a future Proton Source at Fermilab. The requirements for a neutrino factory based on a muon storage ring include the capability of providing, at a reference energy of 16 GeV, 3×10^{13} protons per pulse (4.5×10^{14} protons per second, 1.6×10^{18} protons per hour). In addition, the shielding requirements associated with delivering 1.6×10^{18} protons per hour are so far beyond the capabilities of the present Booster that a relocation of the Proton Source is unavoidable. These specifications correspond to a beam power of 1.2 MW. A muon collider would be even more demanding, requiring 10^{14} protons per cycle or about 4 MW of beam power.

Design criteria have been established for an upgraded Proton Source based on the requirements of the near term program and a program including support for a neutrino factory, with an auxiliary goal of defining a configuration that simultaneously enhances Fermilab's ability to support the broad scope of hadron-based capabilities described above. The design criteria so derived form the basis for choosing the major machine parameters shown in Table 2.1.

1.4. Why do we need a new Booster?

Upon hearing that we were working on the design of the Proton Driver, some of our colleagues asked “Why do we need a new Booster?” or “Why not upgrade the Booster instead of replacing it?” or some other variant of that question. Although the answers to those questions are contained implicitly in this report, it is perhaps appropriate at this point to address them explicitly because the answers will serve as a preview of the contents of this document.

For clarity in communicating with those colleagues, it was useful first to turn the question around by asking “What major Booster subsystem(s) do you think ought to be reused?” They answered that question in various ways. To give an extreme example, at least one person thought that the Booster tunnel was the only subsystem worth reusing, while at least one other colleague thought that it was the only subsystem that ought to be

replaced. It is appropriate to examine individually the major cost drivers: the tunnel, the magnets, and the rf systems.

1.4.1. Reuse the Booster tunnel?

The decision not to reuse the Booster tunnel was based on the following factors:

- Shielding problems: The existing tunnel is not deep enough to provide passive shielding against radiation problems at the surface. The losses from the present Booster are already problematical; approved near-future programs already require an "electronic berm" that may cause frequent trips unless the basic beam-loss problems are greatly alleviated. The new Proton Driver is designed to accelerate much more beam power.

- Size and shape constraints: The size and shape of the existing tunnel would have severely constrained the accelerator lattice design. The existing tunnel is a 24-sided regular polygon, almost a perfect circle. That would limit the length of straight sections and the locations of dipoles, so it would have been difficult if not impossible to design a modern lattice with space for rf cavities in dispersion-free straight sections, transition avoidance, and room for a 1 GeV H^- injection system. Of course the circumference of the new machine would have had to be very close to that of the Booster, which may or may not be optimal. The 16-GeV machine described in this report has a circumference 1.5 times that of the Booster and obviously would not fit in the existing tunnel.

- Location constraints: There is no obvious place to put a Linac energy upgrade or a Pre-Booster near the existing Booster tunnel. A new tunnel can be located optimally so as to allow space nearby on the site for the other possible new devices.

- Relative costs of civil construction: The question about reusing the Booster tunnel is of course motivated by the desire to save money, and reusing it would indeed save the cost of constructing a new tunnel. However, that saving must be weighed against the direct and indirect costs of reusing the existing tunnel. The advice from Fermilab civil construction experts was that the cost of adapting and retrofitting the Booster tunnel and galleries for the Proton Driver would be comparable to that of a new tunnel. For example, the galleries would require extensive shielding augmentations to make them usable, and then would have to be substantially enlarged to house Proton Driver components such as the massive capacitors and chokes of the 15-Hz resonant circuits. The demolition and replacement costs of buildings rendered unusable, such as the Booster towers, would also be considerable.

- HEP Downtime: Phase I would require a longer interruption in the high-energy physics program if the Booster were replaced with another machine in the same tunnel.

1.4.2. Reuse the Booster guide field magnets?

The decision not to reuse the Booster guide field magnets was based on the following factors:

- Lattice design limitations: The Booster guide field magnets are combined-function or gradient magnets. For the existing lattice the transition energy is in the middle of the operating range. It is unlikely that any new arrangement of the magnets would circumvent that problem, because in order to move transition out of the operating range the lattice designers need independent control over the location of dipole and quadrupole fields. The achievement of other desirable features of the lattice such as dispersionless straight sections and control of betatron tunes is also constrained by having only gradient magnets to work with.

- Aperture: The physical aperture of the Booster gradient magnets is about half the linear dimension needed for the baseline Proton Driver in each plane. Worse yet, field quality problems limit the dynamic aperture to a value considerably smaller than the physical aperture.

- Strength: The peak field of the gradient magnet is only about 0.8 T. The magnets have been operated at fields corresponding to a kinetic energy as high as 10 GeV, a value limited by the saturation of the backlegs.

- Beam impedance issues: The magnets have no beam pipe and no liner to carry the beam image currents. The resulting high impedances make the beam susceptible to instabilities.

1.4.3. Reuse the Booster rf cavities?

In connection with the Proton Driver design effort, there is a research and development program, detailed in this report, to upgrade the existing Booster rf cavities. The major goals are higher accelerating voltage and a larger physical aperture. Considerable mechanical renovation of these 30-year-old systems is also necessary. Besides being useful for the existing Booster, the upgraded cavities would be used in the Proton Driver for Stage 1 of Phase I. Of course, new cavities would still be needed to produce the 7.5 MHz bunch spacing required in Stage 2.

Chapter 2. Machine Layout and Performance

R. Alber, C. Ankenbrandt and W. Chou

2.1. Overview

The Proton Driver (Phase I) design includes the following items:

1. A new 16 GeV rapid cycling synchrotron (the Proton Driver) in a new enclosure.
2. A new 400 MeV beam transport line in a new enclosure.
3. A new 12/16 GeV beam transport line, of which about one third is in a new enclosure; another two thirds is in the existing 8 GeV enclosure.
4. A modest improvement of the negative ion source and the low energy part of the existing 400 MeV Linac.

The layout of this new accelerator complex is shown in Figure 2.1.

The H^- beam will be extracted from the Linac to the 400 MeV transport line via the existing Linac access way. This beam is injected into the Proton Driver in the same way as in the present Booster, namely, through a charge exchange process, in which the electrons are stripped by a foil and dumped. The H^+ (proton) beam will then be accelerated to 16 GeV (or 12 GeV in Stage 1) in about 38 ms and extracted to the 12/16 GeV transport line. It is then injected into the MI-10 section of the Main Injector.

The 400 MeV beam line is about 320 m long. It has three sections: (i) a matching section between the existing Linac and the beam line, which includes a vertical drop; (ii) a linear section about 150 m long, which is reserved for a future 600 MeV Linac; (iii) another matching section between the beam line and the synchrotron, which includes another vertical drop as well as a debunching sector.

The Proton Driver has a circumference of 711.3 m, which is exactly 1.5 times the size of the present Booster (474.2 m). It is of a triangular shape and has 3-fold symmetry as shown in Figure 2.2. It has three arcs (P10, P30 and P50) and three long straight sections (P20, P40 and P60). Each arc is about 173 m long and each straight section about 64 m long. Of the three straight sections, P20 is dedicated to injection and beam collimation, P40 and half of P60 will be occupied by rf cavities; another half of P60 is for extraction. Details of the lattice structure will be described in Chapter 3.

The extraction beam line will be at 12 GeV in Stage 1 and 16 GeV in Stage 2. The total length is about 900 m. It consists of two sections. The upstream section, which is about 335 m long, connects the synchrotron to the present MI-8 enclosure. It is followed by a 564 m long section in the MI-8 enclosure. In this section, the lattice will remain the same as that in the present MI-8 line but the magnets will be replaced so that it can transport 12 or16 GeV beams.

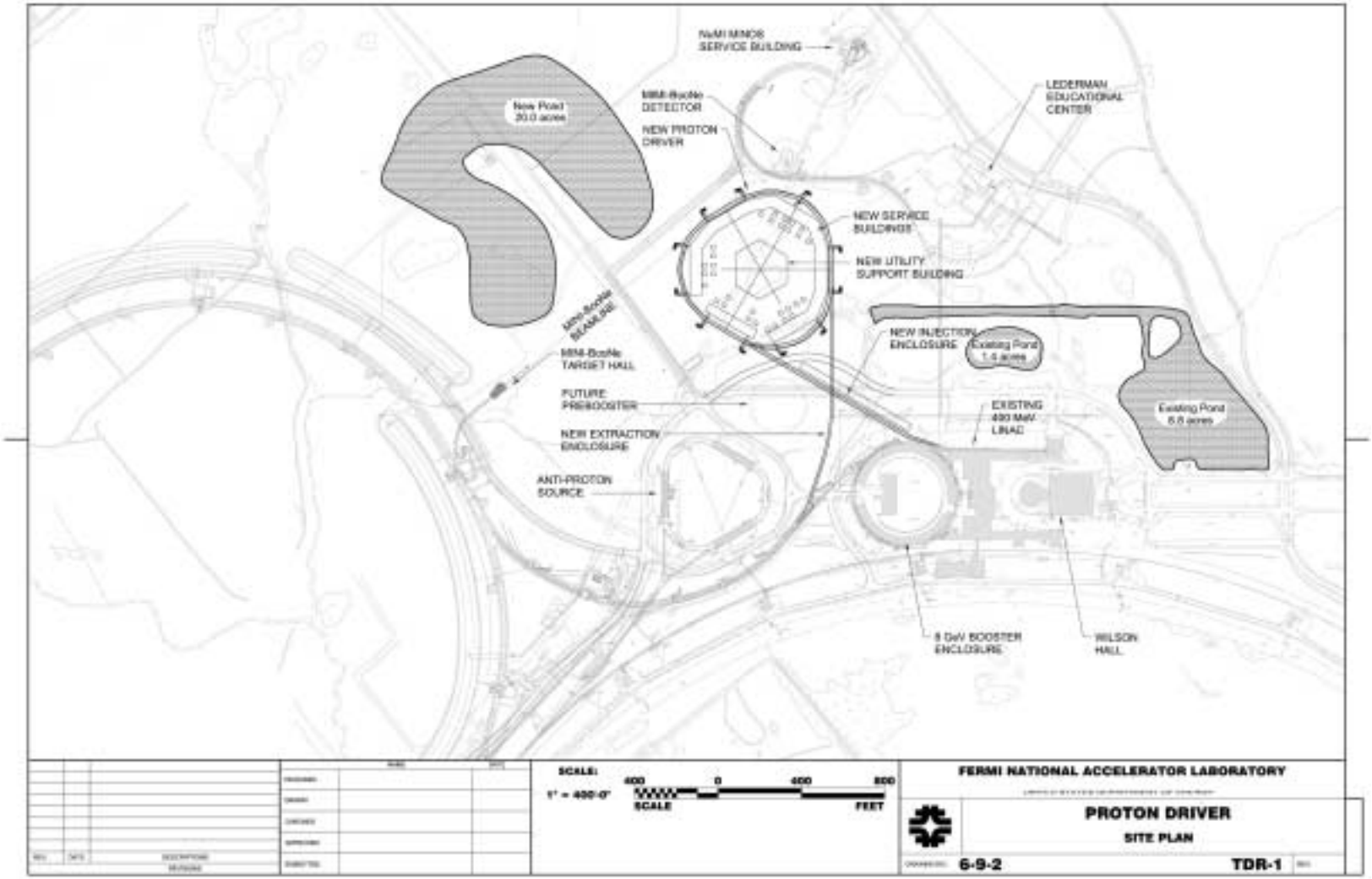

Figure 2.1. Layout of the Proton Driver Accelerator Complex

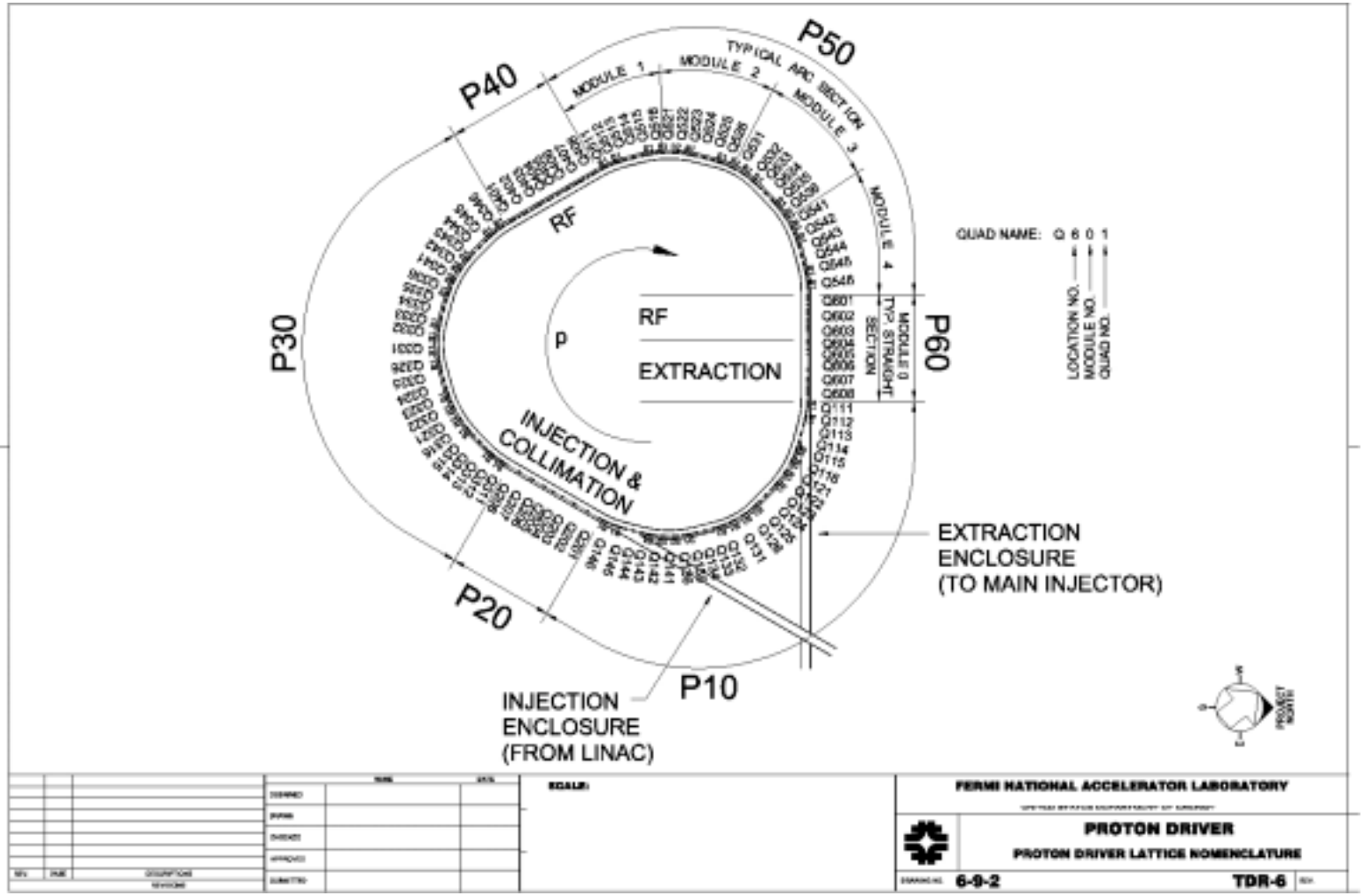

Figure 2.2. Layout of the Proton Driver Ring

2.2. Siting

The following criteria have been applied to the site selection:

- Minimize any possible interruption to the ongoing Fermilab HEP program, in particular, to Run II.
- Accommodate a triangular ring of 711.3 m, in which the injection and extraction are at two different straight sections.
- Leave enough space for a future upgrade (Phase II), i.e., space for addition of a 600 MeV Linac and for a 3 GeV pre-booster.
- Be in the vicinity of the present Linac and the Main Injector.
- Be able to reuse a large portion of the MI-8 enclosure.

Based on these considerations, the site of the Proton Driver is chosen at the west side of Kautz Road, see Figure 2.3. In this layout, the new 400 MeV beam line includes 150 m of free space for a future Linac upgrade. A future Pre-Booster can also easily fit in. The new 12/16 GeV beam line looks long, but about two thirds of it will be in the existing enclosure. The elevation of the Proton Driver is the same as that of the Main Injector. This ensures appropriate radiation shielding. The NuMI beam line is deeper. There will be no intersection between the NuMI line and the Proton Driver. Although the Proton Driver intersects the neutrino beam from the MiniBooNE target, this is not a problem.

The location of this site in a wetland area raises concerns. That will be addressed in Chapter 18.

2.3. Major Design Parameters

The Proton Driver has two distinct features:

1. It provides high beam power (about 1 MW).
2. It can produce short proton bunches (rms length about 1 ns).

While the former is a common feature of high intensity proton machines, the latter is a special feature of the Proton Driver, which could serve a future neutrino factory and/or a muon collider by generating intense short pion/muon bunches from a graphite or high Z target.

A major constraint in the design is to reuse the present Linac. The performance of this Linac has the following limits: maximum beam energy 400 MeV, maximum beam intensity 90 mA (or 60 mA after chopping), maximum usable pulse length 90 μsec and maximum repetition rate 15 Hz.

For a minimal neutrino factory, the required beam power from the Proton Driver is about 1 MW. The beam power is the product of beam energy E, number of protons per cycle N, and repetition rate f_{rep}:

$$P_{beam} = E \times N \times f_{rep} \quad (2.1)$$

The repetition rate of the Linac is limited to 15 Hz. The number of protons per cycle from the Linac is limited to 90 mA × 90 μsec (or 60 mA × 90 μsec after chopping), equivalent to 5×10^{13} (or 3.4×10^{13} after chopping) protons. Because chopping is necessary in Stage 2, we pick 3.4×10^{13} the maximum available proton intensity at the injection from the Linac to the ring. Allowing reasonable beam losses during the cycle (10% at injection, 1% during ramp and at extraction), the design value of N is chosen to be 3×10^{13}. (This is the number of protons per cycle that will be delivered to the Main Injector or the muon production target.) At this repetition rate and beam intensity, a 12 GeV beam (Stage 1) would give 0.864 MW, and a 16 GeV beam (Stage 2) 1.152 MW.

We have studied the trade off between E and N for given beam power (1 MW) and repetition rate (15 Hz) in the energy range of 8 - 16 GeV. Generally speaking, a lower E would require a higher N. This implies significant changes in the present Linac, which we want to avoid because it would lead to a major interruption to Run II. Besides, a higher E (16 GeV) also has other virtues in producing short proton bunches, namely, making the bunch compression at the end of the cycle easier. This is because: (i) The longitudinal brightness N/ε_L would be lower; (ii) The space charge tune shift $\Delta\nu$ and momentum spread $\Delta p/p$ of the beam at top energy would be smaller, which mean the η-spread (η is the slip factor) during bunch compression would be smaller. A detailed study of the cost and performance impact for different energy choices can be found in Appendix B.

A caveat in choosing 16 GeV is that the beam in the Main Injector will still cross transition ($\gamma_t = 21.6$ in the MI). However, simulation shows no particle loss nor emittance dilution would occur during transition crossing when proper measures are taken. This will be discussed in Appendix D.

Another issue related to the beam energy E is the muon yield per unit proton beam power. When a high Z target is used, this yield is almost independent of E. When a graphite target is used, however, MARS simulations indicate that the yield could be 18% higher at E = 6 GeV than at 16 GeV for the same beam power. Because there are different opinions about these simulations, a HARP (Hadron Production) experiment is being conducted at the CERN PS to measure the muon yield at different proton beam energies on a variety of targets. We will revisit the energy issue when the HARP data are available.

The major design parameters of the Proton Driver in Stage 1 and 2 are listed in Table 2.1. As a comparison, the parameters of the present Linac and Booster are also listed.

Table 2.2. is a list of parameters of the 16 GeV synchrotron.

Table 2.1. Proton Driver Parameters of Present , Stage 1 and Stage 2

Parameters	Present	Stage 1 (MI)	Stage 2 (MI + ν-fact)
Linac (operating at 15 Hz)			
Kinetic energy (MeV)	400	400	400
Peak current (mA)	40	60	60
Pulse length (μs)	25	90	90
H^- per pulse	6.3×10^{12}	3.4×10^{13}	3.4×10^{13}
Average beam current (μA)	15	81	81
Beam power (kW)	6	32	32
Booster (operating at 15 Hz)			
Extraction kinetic energy (GeV)	8	12	16
Protons per bunch	6×10^{10}	2.4×10^{11}	1.7×10^{12}
Number of bunches	84	126	18
Total number of protons	5×10^{12}	3×10^{13}	3×10^{13}
Normalized transverse emittance (mm-mrad)	15π	60π	60π
Longitudinal emittance (eV-s)	0.1	0.1	0.4
RF frequency (MHz)	53	53	7.5
Extracted bunch length σ_t (ns)	0.2	1	1
Average beam current (μA)	12	72	72
Target beam power (MW)	0.1	0.9	1.2

Note: Although originally designed for 15 Hz operation, the present Booster has never delivered beam at 15 Hz continuously. In the past it used to run at 2.5 Hz. In the near future it will run at 7.5 Hz for the MiniBooNE experiment.

Table 2.2. Parameters of the 16 GeV Synchrotron

Circumference (m)	711.3
Super-periodicity	3
Number of straight sections	3
Length of each arc (m)	173.2
Length of each straight section (m)	63.9
Injection kinetic energy (MeV)	400
Extraction kinetic energy (GeV)	16 (12 in Stage 1)
Injection dipole field (T)	0.08464
Peak dipole field (T)	1.5 (1.1445 in Stage 1)
Bending radius (m)	37.6
Maximum quad gradient (T/m)	8.7494 (6.6758 in Stage 1)
Number of dipoles	36 (long) 12 (short)
Number of quads in the arcs	72
Number of quads in the straight sections	24
Max β_x, β_y (m)	35, 38
Min β_x, β_y (m)	1.3, 2.0
Max D_x in the arcs (m)	3.0
Min D_x in the arcs (m)	-3.0
Dispersion in the straight sections	0
Transition γ_t	-j 28
Horizontal, vertical tune ν_x , ν_y	12.428, 11.380
Natural chromaticity ξ_x , ξ_y	-19.0, -18.7
Revolution time at injection, extraction (μs)	3.3, 2.4
Injection time (μs)	90
Injection turns	27
Laslett tune shift at injection	0.2
Normalized transverse emittance (mm-mrad)	
Injection beam (95%)	3 π
Circulating beam (100%)	60 π
Longitudinal emittance (95%, eV-s)	
Injection beam	0.14 (0.03 in Stage 1)
Circulating beam	0.4 (0.1 in Stage 1)
Extraction bunch length σ_t (rms, ns)	1
Momentum acceptance	±2.5%
Dynamic aperture	> 100 π

2.4. Comparison with Other High Intensity Proton Machines

Table 2.3 lists the existing as well as the planned high intensity proton machines in the world. The ISIS at the Rutherford Appleton Lab in England provides the highest beam power (160 kW) at this moment. When the SNS at the Oak Ridge National Lab becomes operational in 2004, it will provide 2 MW beam power. The SNS is an accumulator ring, as is the European ESS. Probably the closest machine to the Fermilab Proton Driver is the JHF Project in Japan. It has a rapid cycling 3 GeV Booster and a slow ramp 50 GeV Main Ring. Both are capable of delivering about 1 MW of beam power. This similarity provides the foundation of the successful US-Japan collaboration on high intensity proton facilities, in progress now for three years.

Table 2.3. High Beam Power Proton Machines

Machine	Protons Per Cycle	Repetition Rate (Hz)	Protons Per Second	Beam Energy (GeV)	Beam Power (MW)
Existing:					
RAL ISIS	2.5×10^{13}	50	1.25×10^{15}	0.8	0.16
BNL AGS	7×10^{13}	0.5	3.5×10^{13}	24	0.13
LANL PSR	2.5×10^{13}	20	5×10^{14}	0.8	0.064
Planned:					
Fermilab MiniBooNE	5×10^{12}	7.5	3.8×10^{13}	8	0.05
Fermilab NuMI	3×10^{13}	0.5	1.5×10^{13}	120	0.3
Proton Driver Phase I	3×10^{13}	15	4.5×10^{14}	16	1.2
Proton Driver Phase II	1×10^{14}	15	1.5×10^{15}	16	4
ORNL SNS	2×10^{14}	60	1.2×10^{16}	1	2
Europe ESS	2.34×10^{14}	50	1.2×10^{16}	1.334	2.5
Japan JHF	3.2×10^{14}	0.3	1×10^{14}	50	0.8

2.5. Operation Modes

There are five possible operation modes of the Proton Driver.

1. *Main Injector 120 GeV fixed target experiments: (NuMI, KAMI, Meson, etc.)*
   The Main Injector will take four Proton Driver batches to fill its ring. Each batch gives 3×10^{13} protons. So the Main Injector will operate at 1.2×10^{14} protons per cycle, a factor of four higher than its present beam intensity (3×10^{13} protons per cycle). The necessary measures for the Main Injector intensity upgrade will be discussed in Appendix D. The cycle time of the Main Injector is 2 seconds. Therefore, it will take only 2/15 of the protons available from the Proton Driver. The other 13/15 can be used for other programs (see below).

2. *Proton Driver fixed target experiments:*
   These will be new physics programs based on the stand-alone capabilities of the Proton Driver and can be carried out in parallel to the Main Injector experiments. Thirteen out of every fifteen Proton Driver cycles can be dedicated to these experiments. This gives an average proton flux of 3.9×10^{14} per second. The beam energy is 12 GeV in Stage 1 and 16 GeV in Stage 2. Therefore, the beam power available to these experiments will be 0.75 MW and 1 MW in Stages 1 and 2, respectively. The high intensity secondary particle beams produced by the proton beams will enable a rich class of physics programs based on muon, kaon, neutron, and neutrino beams.

3. *Antiproton production:*
   In this operation mode, the Main Injector will take one Proton Driver batch every 1.5 seconds. In order to fit the size of the Accumulator, the batch size will be 84 bunches (at 53 MHz operation). In other words, the batch will only occupy 2/3 of the Proton Driver. The other 1/3 will be chopped in the front end of the Linac. Each Proton Driver batch would contain 2×10^{13} protons, which is four times more than the present Booster batch (5×10^{12}). This means the antiproton production rate would be increased by a factor of four, provided that the production target and the cooling systems in the Debuncher and Accumulator would be upgraded accordingly. This mode of operation can be performed simultaneously with operation mode 1.

4. *Protons for Tevatron Collider experiments:*
   The 7.5 MHz bunch structure in Stage 2 would provide a useful feature for the Tevatron Collider experiments, namely, a 132 ns bunch spacing in Run IIb. The coalescing process in the Main Injector would no longer be necessary.

5. *Neutrino factory:*
   In Stage 2, a neutrino factory could take all the protons that the Proton Driver can provide. So there will be a competition between the experiments in operation mode 2 and a neutrino factory. However, it is conceivable that operation modes 1 and 3 would continue because they only need a small portion of protons from the Proton Driver.

Figure 2.3. Proton Driver Site Plan

Chapter 3. Beam Optics

Alexandr Drozhdin, Carol J. Johnstone, Shoroku Ohnuma, and David Ritson

3.1. Lattice Design Considerations

Requirements for high beam intensity and beam power dictate the design of the Proton Driver lattice. This is particularly true in the arc part of the lattice where optical parameters determine the beam size.

3.1.1. Requirements and desired features

1. Avoidance of transition crossing. Although there are many ways to reduce beam loss during transition crossing [1], e.g., a γ_t-jump with a special quadrupole system, it is not possible to eliminate the loss completely. Furthermore, any source of longitudinal emittance dilution of the beam should be avoided in order to achieve a short bunch length in the extracted beam. The design presented here avoids transition crossing by choosing γ_t to be imaginary or the transition energy to be much higher than the extraction energy of the beam [2,3].

2. Large momentum acceptance. In order to make the bunch length short, it is necessary to rotate the bunch in longitudinal phase space. To meet the needs of a neutrino factory and a muon collider, the lattice should have momentum acceptance of $\pm 2.5\%$.

3. Large dynamic aperture. Tune spread within the beam due to space charge may be as large as 0.3 or more if the charge distribution of the injected beam has a peak at the center. To reduce this effect, the transverse charge distribution of the injected beam will be made as uniform as possible by the "painting" technique. As a result of painting, the beam emittance will be enlarged to 60π mm-mr (normalized, 100%). The dynamic aperture of the lattice is required to be twice this value for the entire momentum spread range, $\pm 2.5\%$.

4. Long straight sections. Three long straight sections P20, P40, and P60 will be used for injection/collimation, rf cavities, and extraction. Because of the high beam power and the rapid cycling operation, rf cavities must occupy at least 60 m of free space. At the same time, it is not desirable to place rf cavities near the injection/collimation devices or downstream of extraction devices. In the present design, P20 is used exclusively for injection/collimation and P40 for rf cavities. The extraction system occupies the downstream end of P60 but the upstream end of that long straight is available for rf cavities. Specific considerations given to the design of three long straight sections are:

    a) Superperiodicity. It is always desirable to avoid structural resonances in any machine and this is especially true when large-aperture magnets may contain a significant amount of systematic nonlinear field components. Although it is sufficient to have the same transfer matrix in three long straights for this purpose, *i.e.*,

Twiss parameters matched to the arcs and the same phase advance, the design presented here utilizes the identical quadrupole arrangement in all three long straights. It may be possible to optimize each long straight for its intended use while preserving the superperiodicity. This will be studied in the future.

b) Choice of tunes. Since the phase advance in each arc is chosen to be 6π, the operating point in the tune diagram is determined by the phase advance in the long straights. Based on results from numerical studies, it has been decided to split horizontal and vertical tunes by one unit, which will avoid resonances of the type $2\nu_x - 2\nu_y = 0$. In addition, the fractional part of ν_x is larger than that of ν_y by 0.05 so that the operating point stays below the coupling resonance line. The integer part of the tunes should be chosen such that as many structural resonances as possible will be sufficiently away from the working point. The choice of (12.43, 11.38) in this design is nominal, and the performance of the real machine will eventually decide the working point.

c) Injection straight. The beam size at the stripping foil should not be too small in order to prevent an excessive temperature rise. At the same time, the large β function at the foil will contribute to emittance growth due to multiple Coulomb scattering. The compromise choice of $\beta = 10$ m in both directions satisfies these requirements. Drift spaces between the stripping foil and adjacent quadrupoles must be large enough to accommodate H^- injection and dumping of the H^0 component. The phase advance between the first and last kicker magnets for the painting, located on each side of the foil, should be close to π so that the required kicker strength is not excessive.

d) Collimation. Large dispersion and β function are necessary at the primary collimators. The phase advance over the collimation system should not be less than 180 degrees in both directions.

e) Extraction straight. The phase advance between kickers and septa as well as β functions at various extraction devices should be chosen carefully in order not to make excessive demands on magnets. The system should be able to accommodate at least twice the expected beam emittance, $120\,\pi$ mm-mr (normalized), so that there is no halo scraping in any of the extraction magnets.

f) RF straight. Although it has not been observed in proton machines, it is prudent to avoid any possibility of synchro-betatron coupling resonances [4], especially in view of a relatively large value of ν_s (≈ 0.1) at low energies. The choice of a multiple of 2π as the arc phase advance assures zero dispersion in all long straights.

3.1.2. Constraints

Because of the large aperture in dipoles and quadrupoles, saturation at high field is a serious issue when they are in the same resonant circuit. Degradation of field quality is another concern. Based on experience gained in building and operating the Antiproton Accumulator, it has been decided to limit the peak dipole field to 1.5 T and the peak gradient of the quadrupoles to 8.9 T/m. The actual peak gradient is slightly less than this value for the chosen winding ratio of dipoles and quadrupoles. Expected performance of the magnets is discussed in Chapter 6 and the system requirements for the quadrupole tracking are presented in Chapter 7.

3.1.3. Other considerations

In an early stage of the design study, a lattice using combined function magnets was considered as a possible choice. It has been found that, with the requirements listed in Section 3.1.1, a lattice with combined function magnets cannot provide the needed flexibility. For one thing, the dispersion was too large to be usable for this machine. If one is to avoid transition crossing from 400 MeV (injection kinetic energy) up to 16 GeV (extraction kinetic energy), a lattice based on simple FODO cells in the arcs will not work. Instead, it is necessary to have cells with missing dipoles, or cells with doublets or triplets. Such lattice structures are often called "FMC" (flexible momentum compaction) [2].

3.2. Lattice Design

3.2.1. Lattice layout and nomenclature

The lattice layout is shown in Figure 2.2**.** It is composed of three arcs (P10, P30, P50) and three long straights (P20, P40, P60) with superperiod three. Each arc has four modules while each module is made of three different cells:

Cell_a: FODO (with different QF and QD) with two regular dipoles,
Cell_b: FODO (with different QF and QD), no dipoles,
Cell_c: mirror image of Cell_a but with one regular and one short dipole.

module = (a)(b)(c), half_arc = (module, –module), arc = (half_arc, –half_arc)

Note that arc can also be regarded as (half_arc, half_arc) since –half_arc (mirror image of half_arc) is identical to half_arc.

Three long straights, each approximately 64 m long, are identical and their structure is essentially of the FODO type except that distances between quadrupoles are varied according to the requirements of injection/collimation and extraction.

Nomenclature

The beam direction in the ring is clockwise. Starting from the arc (P10) upstream of the injection/collimation long straight (P20), arcs and long straights are arranged in a triangular shape: P10, P20, P30, P40, P50, and P60. Each item in the ring is referred to the quadrupole that is located immediately upstream of that item. Quadrupole names are "Q" followed by three numbers to identify their locations:

First number: section number, 1 to 6 (1 for P10, etc.).
Second number: module number, 1 to 4 in arcs, and 0 in long straights.
Third number: quadrupole ID, odd for QF and even for QD.

Examples: Arc P10: module 1: Q111, Q112, …, Q116
module 2: Q121, Q122, …, Q126, etc.

Long straight P20: Q201, Q202, …, Q208, etc.

Sextupoles are all in Cell_b so that in module 1 of Arc P10, they will be designated as (HS113, VS113, VS114, HS114). Note that VS113 is closer to Q114 and HS114 closer to Q115. As explained above, however, the convention is to refer to the upstream quadrupole.

3.2.2. Space allocations

The circumference of the ring is exactly 3/2 of the present Booster, namely, $(3/2) \times 474.203$ m = 711.304 m. Three arcs occupy 3×173.18 m = 519.54 m and three long straights 3×63.92 m = 191.76 m. Spaces allocated to dipoles and quadrupoles are:

dipoles, regular (36):	186.0 m	
dipoles, short (12):	50.3 m	
quadrupoles in arcs (72):	102.7 m	
quadrupoles in long straights (24):	29.7 m	
free space in long straights:	147.6 m	(total for 24 locations)
short straights in arcs (24):	77.8 m	
mini straights in arcs (24):	11.5 m	

Note that the lengths of dipoles given here are the path length of the beam within the dipoles and not necessarily their physical length. There are altogether four types of quadrupoles in the arcs and five types in the long straights. These nine types are different only in their lengths. It is hoped that this number will be reduced in future improvement of the lattice design. It should be noted also that a substantial amount of space is allocated to the magnet ends. For example, between a quadrupole and a dipole, 0.8 m is necessary to accommodate magnet ends and vacuum ports. Consequently, there is no space for sextupoles or trim dipoles in Cell_a. Sextupoles will be installed in the short straights of

Cell_b, altogether 48 of them occupying 14.4 m. Mini straights in Cell_c are for vertical steering magnets.

3.2.3. Various types of arc lattices and their comparisons

Several different candidates for the arc lattice, all satisfying the requirements of no transition crossing and zero dispersion in long straights, have been studied to see their relative merits and possible defects.

a) Doublet [5]. The merit of this choice is its simplicity. Only two types of quadrupoles are needed in the arcs. It has been found that, for reasonable values of dispersion and β function, the required quadrupole strength, 20 T/m, is far above a realizable value. Perhaps the most serious defect of this lattice is the lack of suitable locations for sextupoles. For our case, because of the large momentum range, chromaticity sextupoles are essential components of the ring.

b) Racetrack. It is possible to design a racetrack ring with the same modules as in a triangular ring. The superperiod of two may be less advantageous but this should not be a major concern. A triangular lattice has been chosen for the present design over a racetrack lattice for two reasons. 1) In a racetrack lattice, it is necessary to put injection/collimation and extraction in the same long straight, thereby complicating the design of this section. 2) For reasons explained in the next section, 3.2.4, the phase advance in each module is 270° and the total phase advance in each arc is a multiple of 2π. For a triangular lattice, there will be altogether $3 \times 4 = 12$ modules but $2 \times 8 = 16$ modules for a racetrack lattice. The total length of long straights will then be reduced.

c) Various choices of phase advance in FODO or DOFO modules. There are two ways to suppress dispersion in long straights. One is to introduce a special dispersion suppressor section, which usually requires dipoles of different lengths in order to reduce the maximum dispersion in the arc, and the other is to rely on a $(2n\pi)$ horizontal phase advance in each arc, which automatically assures zero dispersion at both ends of the arc. Although a dispersion suppressor provides more flexibility in choosing the phase advance per module, it has been decided to achieve zero dispersion in long straights by choosing the horizontal phase advance to be a multiple of 2π. After several combinations of horizontal/vertical phase advances per module were studied, 270°/270° has been selected as the best in overall performance.

3.2.4. Arc design: 270°/270° FODO modules

In selecting the phase advance per module, the overriding concerns have been the momentum aperture and the dynamic aperture. They are both determined essentially by the effects of chromaticity sextupoles as long as nonlinear field components of magnets are not excessive. This is particularly true when dispersion in the arc is not allowed to go above 3 m or so in order to limit the increase in beam size, $D_x (\Delta p/p)$. The choice of 270° as the horizontal phase advance per module is natural since four modules provide 6π. It

also cancels all the driving terms of the third-integer resonances. For the vertical phase advance per module, choices other than 270° are possible. For example, either 135° or 180° will also cancel all the resonance driving terms arising from sextupoles. It has been found out, however, that there are no suitable locations for sextupoles with the choice of 135°. As a consequence, the sextupole strength becomes large and their higher order effects reduce the momentum aperture as well as the dynamic aperture. The choice of 180° has an advantage in reducing the higher order effects of sextupoles. However, it produces a large amount of β beat, which is obvious from the relation $2\psi_y = 360°$. Another case that has been studied is 270°/270° but in DOFO. This is as good as FODO of the same phase advance giving good momentum and dynamic aperture. It has, however, a large maximum dispersion, 4 to 5 m, compared with 2.5 to 3 m for FODO.

3.2.5. Straight section design

Three straight sections P20, P40, and P60 are identical in beam optics to insure periodicity three. The structure is FODO but the cell lengths are varied according to the requirements of injection/collimation as well as of extraction. At present, there are five different types of quadrupoles but it may be possible to reduce this to two or three. Injection and collimation systems are located in P20 and the detailed description is given in Chapters 9 and 11. In Stage 1 of Phase I (see Chapter 5), most rf cavities will be in P40 but some will share P60 with the extraction devices. The extraction system and its hardware components are described in detail in Chapter 12.

3.2.6. Improvements

Work to improve the present lattice is still in progress. The dependence of zero dispersion in long straights on $(2n\pi)$ horizontal phase advance in each arc may not be as robust as a standard dispersion suppressor. For example, the horizontal closed orbit for $\Delta p/p = 2.5\%$ oscillates between –4.5 mm and +3.7 mm in long straights where rf cavities are placed. When the beam intensity is high, this may cause longitudinal emittance dilution or even some beam loss. The dependence of residual dispersion in long straights on the horizontal phase advance in the arc is another concern. If the horizontal phase advance in an arc is changed by $\pm 0.05 \times (2\pi)$, the maximum residual dispersion may become as large as 0.15 m.

Lack of space for vertical steering magnets in Cell_a is another concern. In the middle of each arc, two vertical steering magnets are located side-by-side covering a phase advance of more than 180°. As more space is needed for rf cavities in Stage 2, it may be necessary to redesign the long straights for a more efficient use of available free space.

With the present arc design, transition gamma is always either imaginary or comfortably above the extraction energy for the full range of $\Delta p/p = \pm 2.5\%$. This does not guarantee that the bunch rotation in longitudinal phase space, which is required to get a short bunch, will be free of distortion as the dependence of $\alpha \equiv 1/\gamma_t^2$ on $\Delta p/p$ is not favorable for such an operation. (See Section 3.3.1.) This defect will be taken into account in redesigning the dispersion suppression.

3.3. Lattice Analysis

Beta functions and dispersion are shown in Figure 3.1. Maximum values are:

arc: $\beta_x = 35.4$ m, $\beta_y = 34.8$ m, $D_x = 3.0$ m
long straight: $\beta_x = 35.4$ m, $\beta_y = 39.0$ m, $D_x = 0.03$ m

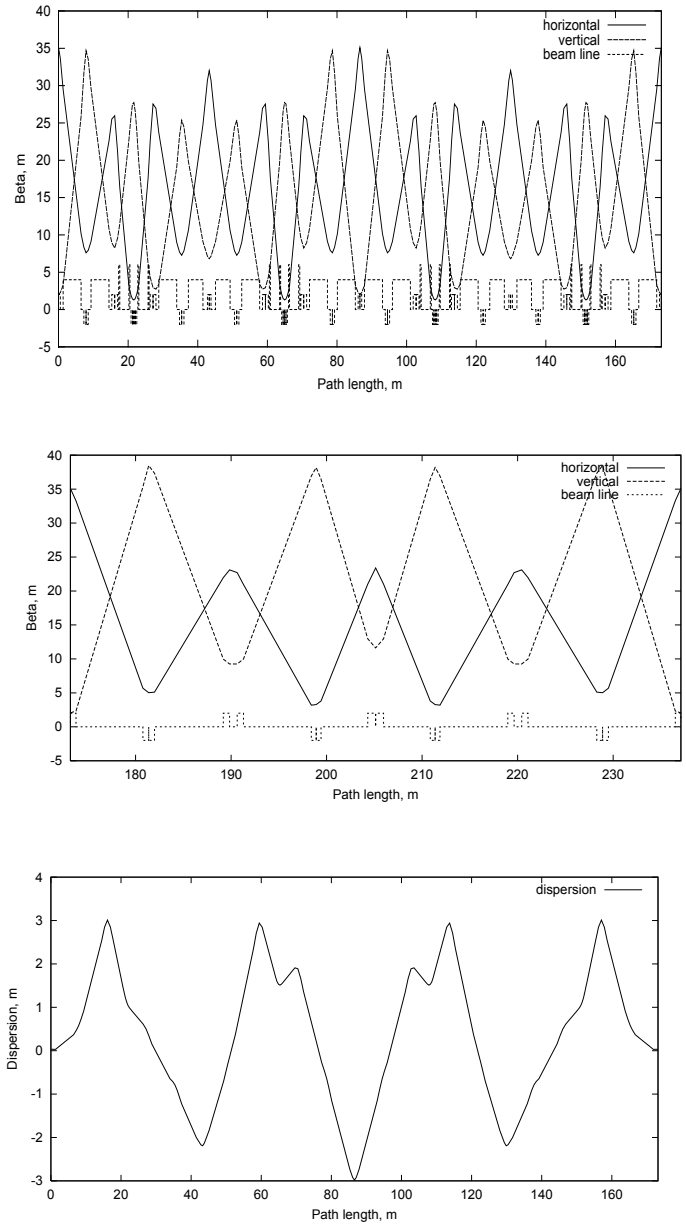

Figure 3.1. (top) β functions in the arc ; (center) β functions in the long straight; (bottom) dispersion in the arc

3.3.1. Chromatic properties

One important requirement for this lattice is the large momentum acceptance, $\Delta p/p$ from –2.5% to 2.5%. Chromaticity correcting sextupoles are therefore essential in preventing the dependence of linear optical parameters (tunes, Twiss parameters, and dispersion) on the momentum deviation. Since β functions and dispersion are not allowed to be large in the arcs, the required sextupole strength tends to be large and the higher order effects may become a source of dynamic aperture limitation. The choice of phase advance, 270˚/270˚ per module, minimizes such effects.

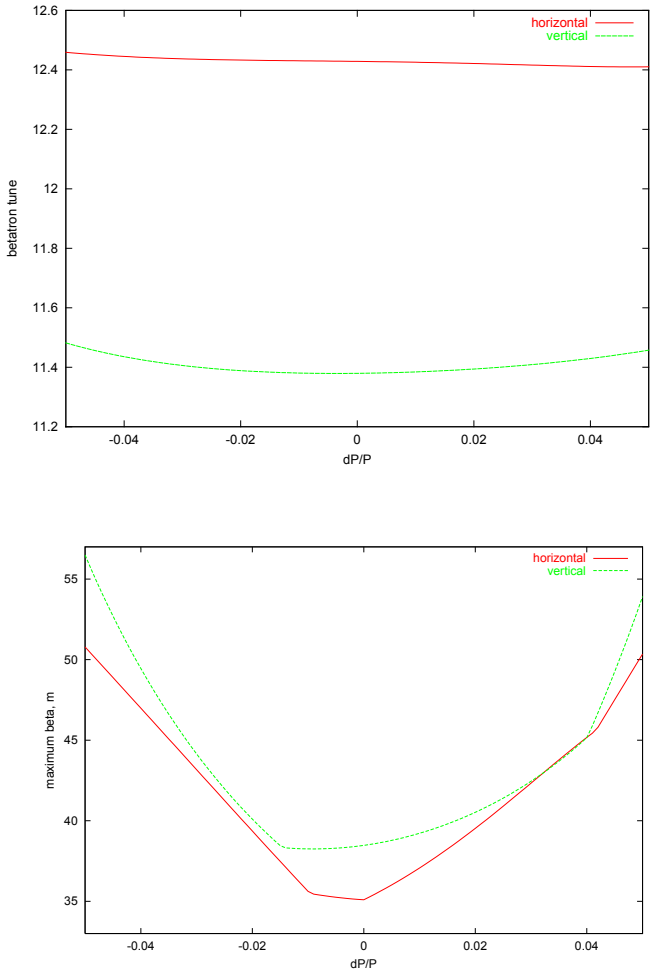

Figure 3.2. Tunes and maximum β as a function of $\Delta p/p$

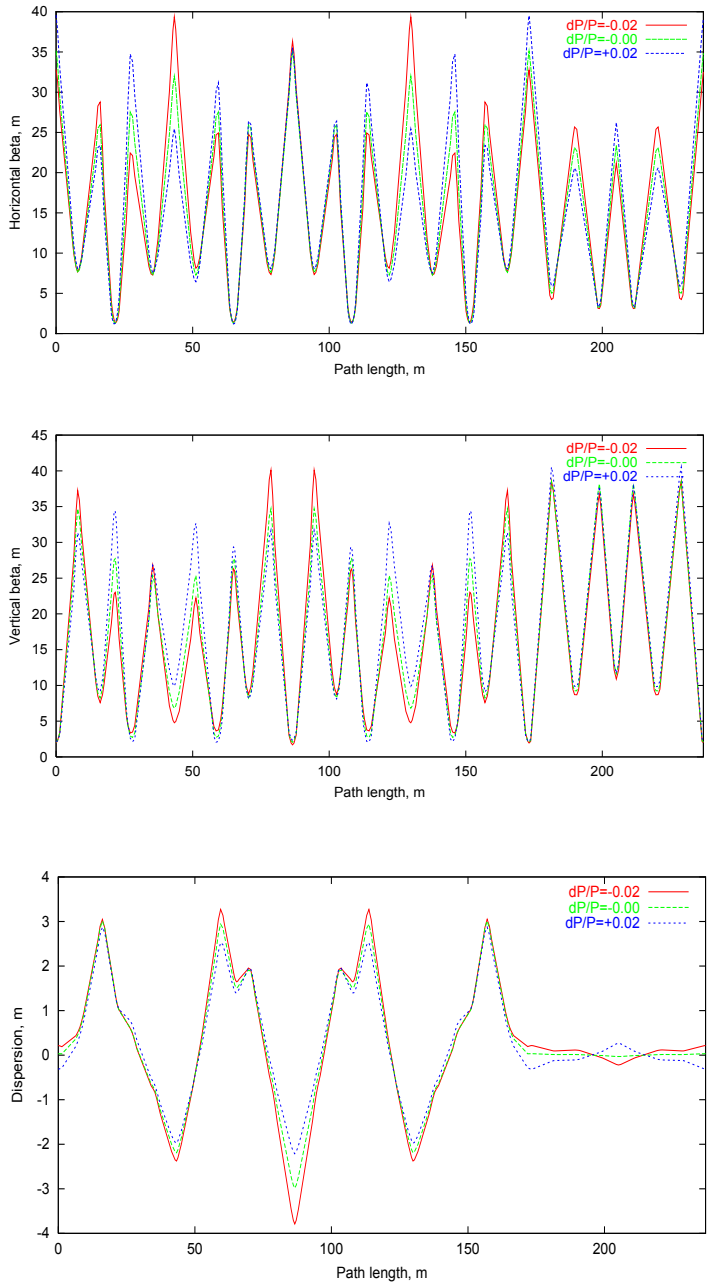

Figure 3.3. (top and center) β functions in one superperiod;
(bottom) dispersion in one superperiod

There are altogether 48 sextupoles, each 0.3 m long, located in the short straights of Cell_b where dipoles are missing. The required strengths are $B'' = 68.8$ T/m^2 for HS and –95.4 T/m^2 for VS. Tunes and the maximum β functions are shown in Figure 3.2 as a function of Δp/p while in Figure 3.3, Twiss parameters in one superperiod are displayed. Transition gamma, γ_t, and the parameter $\alpha \equiv 1/\gamma_t^2$ are shown in Figure 3.4.

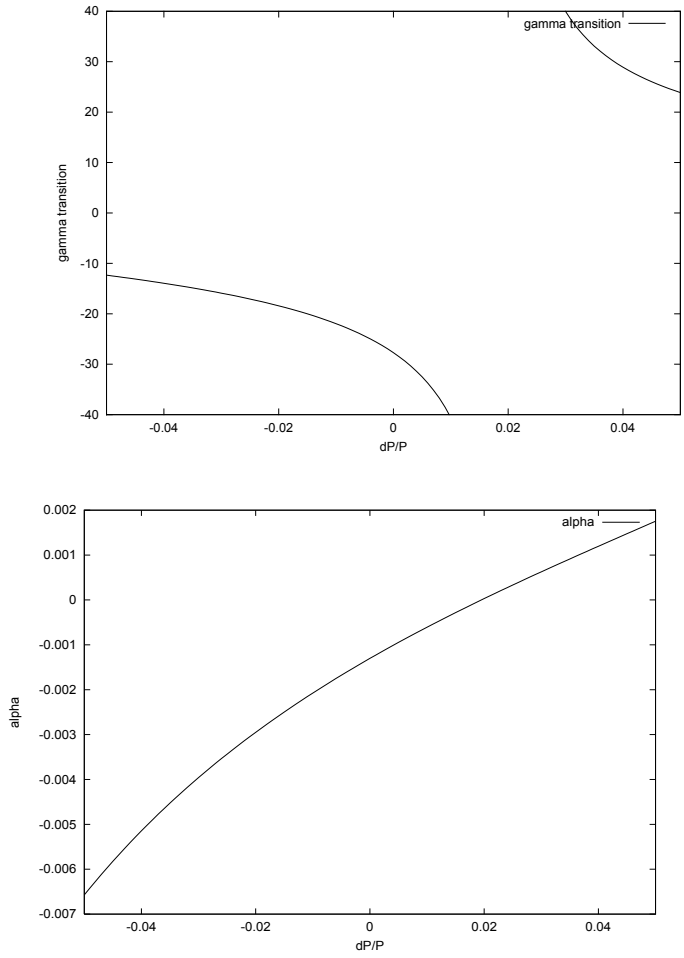

Figure 3.4. (top) transition-gamma, γ_t ; (bottom) $\alpha \equiv 1/\gamma_t^2$

In Figure 3.4, for the sake of convenience, imaginary γ_t is plotted as a negative quantity. For all values of $\Delta p/p$ under consideration, γ_t is safely away from the energy of the extracted beam, $\gamma = 18.05$ for 16 GeV (KE). For bunch rotation, the important quantity is the momentum dependence of the pathlength C,

$$(\Delta C/C) = \alpha_0 (\Delta p/p) + \alpha_1 (\Delta p/p)^2 + \alpha_3 (\Delta p/p)^3 \qquad (3.1)$$

where $\alpha_0 = -0.001302$, $\alpha_1 = 0.07302$, and $\alpha_3 = -0.3952$.

With these values, the momentum dependence of the revolution time T can be written as

$$(\Delta T/T) = -0.004370\,(\Delta p/p) + 0.07762\,(\Delta p/p)^2 - 0.4016\,(\Delta p/p)^3 \qquad (3.2)$$

shown in Figure 3.5. This relation should be used to estimate the degree of deformation when the bunch is rotated before extraction at 16 GeV. Such a study is now in progress.

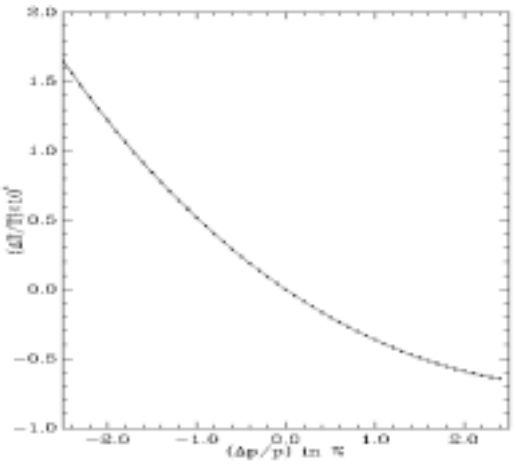

Figure 3.5 Dependence of revolution time as a function of (Δp/p)

3.3.2. Dynamic aperture

In the absence of any closed orbit distortion or magnet errors, the dynamic aperture has been found by tracking particles over 1000 revolutions and the results are shown in Figure 3.6.

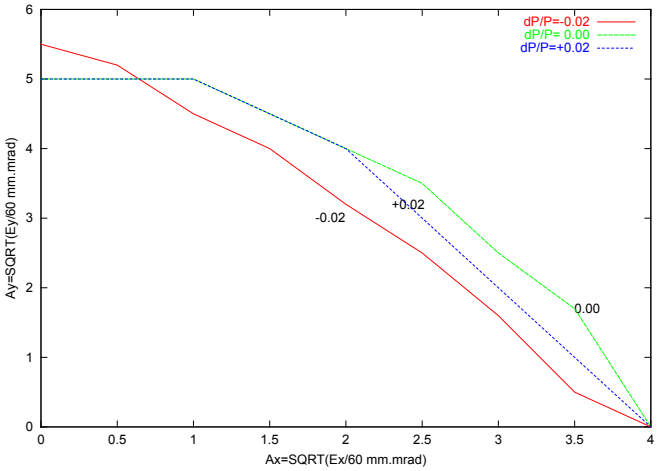

Figure 3.6. Dynamic aperture at injection

Scales used for amplitudes A_x and A_y are such that A_x or $A_y = 1$ corresponds to normalized emittance of 60π mm-mr, the design value. It is clear from Figure 3.6 that the dynamic aperture is more than five times this value in both directions, $A > \sqrt{5}$, for $\Delta p/p$ from –2% to +2%. During injection and acceleration, the momentum spread of the beam will be much less than $\pm 2\%$ until the bunch begins to be rotated immediately before extraction.

3.4. Magnet Errors and Corrections

A reliable estimate is possible for magnet field quality and alignment precision from experience gained in construction of the Accumulator. For those figures that were found to be difficult to achieve in the Accumulator, specifications will be relaxed so that the goals presented below are sound and realistic.

3.4.1. Field errors and their effects

3.4.1.1. Orbit distortions

For the Accumulator, it was possible to achieve the following alignment accuracies and dipole field uniformity [6]:

1) quadrupole misalignments: $\Delta_{rms} = 0.2$ mm in both directions.
2) dipole tilt: $\Delta'_{rms} = 0.2$ mrad; this will be relaxed to 0.5 mrad.
3) integrated dipole field uniformity: 2×10^{-4}; this will be relaxed to 5×10^{-4}.

With 90% probability and including the influence of higher harmonics [7], the expected closed orbit distortions are:

1) max $|x| = 74\ \Delta_{rms} = 14.8$ mm, max $|y| = 66\ \Delta_{rms} = 13.2$ mm.
2) max $|y| = 26\ \Delta'_{rms} = 13.0$ mm.
3) max $|x| = 29$ m $\times$ $(5 \times 10^{-4}) = 14.5$ mm.

Adding all in quadrature, one finds max $|x| = 21$ mm and max $|y| = 19$ mm.

3.4.1.2. Horizontal-vertical coupling

This will result from tilting of the quadrupoles. The figure achieved in the Accumulator is $\theta_{rms} = 0.2$ mrad. The coupling coefficient is defined by

$$k \equiv \frac{1}{4\pi}(2\theta_{rms})\sqrt{\sum \beta_x \beta_y \left(\frac{GL}{B\rho}\right)^2} \qquad (3.3)$$

where the summation is for all quadrupoles in the ring and (GL) is the integrated field gradient of each quadrupole. The amount of coupling in transverse amplitudes is

$$\frac{(2k)}{\sqrt{(2k)^2 + \Delta^2}} \tag{3.4}$$

where $\Delta \equiv$ fractional part of $(\nu_x - \nu_y)$. With $\theta_{rms} = 0.2$ mrad, $2k_{rms} = 0.0016$. If $\Delta = 0.05$, for example, the amount of amplitude coupling is 3.2% (rms). That is, if the horizontal excursion of the beam is 10 mm, the expected rms excursion of the beam in the vertical direction generated by the coupling is 0.3 mm. Correction of the closed orbit or other diagnostic procedures during commissioning will not be disturbed by this amount of coupling.

3.4.1.3. Systematic quadrupole effects

Natural chromaticity of the lattice can be found from the relations

$$\Delta\upsilon_x = 22.9\ \Delta_{QF} - 3.9\ \Delta_{QD}, \quad \Delta\upsilon_y = -5.3\ \Delta_{QF} + 23.7\ \Delta_{QD} \tag{3.5}$$

or, equivalently,

$$\Delta_{QF} = 0.0454\ \Delta\upsilon_x + 0.0074\ \Delta\upsilon_y, \quad \Delta_{QD} = 0.0101\ \Delta\upsilon_x + 0.0439\ \Delta\upsilon_y \tag{3.6}$$

where Δ_{QF} and Δ_{QD} are fractional changes in focusing and defocusing quadrupole gradients, respectively. Natural chromaticities are: $\xi_x = -(22.9 - 3.9) = -19$ and $\xi_y = -(-5.3 + 23.7) = -18.4$ for $\xi = \Delta\nu/(\Delta p/p)$. Focusing quadrupoles in arcs are important in keeping the dispersion in long straights small. If the third and the fifth quadrupoles (called QF3 in MAD input file) in all modules are changed by 0.5%, the dispersion in the long straights will be increased to 0.25 m while the same change in the first quadrupoles in all modules will cause an increase of 0.12 m. It may become necessary to depend entirely on quadrupoles in long straights to move the operating point to the optimum position. For quadrupoles in long straights alone, the natural chromaticity is given by

$$\Delta\upsilon_x = 5.0\ \Delta_{QF} - 0.68\ \Delta_{QD}, \quad \Delta\upsilon_y = -1.7\ \Delta_{QF} + 6.1\ \Delta_{QD} \tag{3.7}$$

or, equivalently,

$$\Delta_{QF} = 0.208\ \Delta\upsilon_x + 0.023\ \Delta\upsilon_y, \quad \Delta_{QD} = 0.057\Delta\upsilon_x + 0.170\Delta\upsilon_y \tag{3.8}$$

3.4.2. Specifications for magnet field quality

Specifications for magnet field quality will be similar to the ones adopted for the Accumulator magnets [8] but they will be relaxed somewhat since this machine is not a storage ring. It will not be necessary to have rotating-coil measurements of any magnet to find multipole contents. Rather, it is essential to make an accurate measurement of the integrated field covering both ends completely. For one thing, this will give a reliable value of the effective magnet length. Precise control of the integrated gradient is especially important for arc quadrupoles in order to achieve the desired phase advance per module.

The specification for magnet field quality will be in terms of "flatness", which is defined as

$$\text{flatness at } x = x_o \equiv \left| \frac{\int B_y(x_o, y = 0; z)\, dz}{\int B_y(x = y = 0; z)\, dz} - 1 \right| \tag{3.9}$$

for dipoles. Integrals are over the entire field of a magnet including the fringe field at both ends. For quadrupoles, the field gradient $G \equiv \partial B_y/\partial x$ is to be used in place of B_y. For large aperture magnets in the Accumulators, the specifications were, for dipoles: 2×10^{-4} at x = 3.75 inches; and for quadrupoles: 2×10^{-3} at x = 4 inches.

For the Proton Driver, the corresponding specifications are

$$\text{dipoles: } 5 \times 10^{-4} \text{ at } x = 4 \text{ in; quadrupoles: } 5 \times 10^{-3} \text{ at } x = 4 \text{ in.} \tag{3.10}$$

The consequence of these specification will be discussed in Section 3.4.3. It should be emphasized that these are NOT rms values but should be treated as the maximum allowed values for any magnet. If averaged over the magnet, they are equivalent to

$$\text{dipoles:} \quad |B''/B_o| = 0.10\ \text{m}^{-2} \text{ if sextupoles alone,} \tag{3.11}$$
$$|B''''/B_o| = 110\ \text{m}^{-4} \text{ if decapoles alone;}$$
$$\text{quadrupoles:} \quad |G''/G_o| = 1.0\ \text{m}^{-2} \text{ if octupoles alone,} \tag{3.12}$$
$$|G''''/G_o| = 29\ \text{m}^{-3} \text{ if dodecapoles alone.}$$

It is of course better to have a separate estimate of sextupole and decapole contents in dipoles, and of octupole and dodecapole contents in quadrupoles. It is doubtful, however that, unlike in storage rings, multipoles higher than octupole will play any significant role in this ring. In what follows, it will be assumed that the nonlinear field is all sextupole in dipoles and all octupole in quadrupoles. If needed, one can estimate these multipole contents separately by measuring the integrated bend field or the integrated gradient field at, say, $x = \pm 2$ in, ± 3 in, and ± 4 in. and fitting data by least squares. Unlike rotating coil measurements, this procedure is not exact but it is more practical. If measurements show a significant amount of decapole content, it will be necessary to evaluate its impact on the momentum dependence and amplitude dependence of tunes. This is straightforward as the needed formulas already exist [9].

In bending magnets, sextupole field in the "body" can have both systematic and random components but it is mostly systematic at magnet ends. In quadrupole magnets, octupole field is expected to be predominantly random in the "body" and systematic at ends unless there is a breakdown of quadrupole symmetry common to all quadrupoles.

3.4.2.1. Magnet end field

It has been noticed in the design of muon storage rings at Fermilab as well as at CERN [10] that the dynamic aperture of the ring is reduced drastically when the quadrupole edge field is taken into account. On close inspection, it has been confirmed that this happens when the variation of the β function is abnormally steep. One obvious cure is to lengthen the magnet and reduce the β variation. For the Proton Driver lattice, the variation of β is everywhere normal and the edge field of quadrupoles or dipoles should not affect the dynamic aperture. Nevertheless, possible effects of field fall-off have been examined using the existing measurement data on the Accumulator large aperture quadrupoles and dipoles [11,12]. The study has confirmed that indeed the effects can be ignored as long as the flatness defined by Eq. (3.9) covers the entire magnet including both ends.

For accumulator quadrupoles and dipoles, the measured field fall-off can be expressed remarkably well by the function $f(z) = \frac{1}{1+\alpha(z+6)^p}$ where z (in inches) is the distance along the magnet axis measured from the endplate. This form is chosen such that f(z) = 1 at z = –6 in., that is, 6 in. into the magnet from the endplate. Two fitting parameters are

dipoles: $\alpha = 0.0134$, $p = 3.010$
quadrupoles: $\alpha = 1.955 \times 10^{-4}$, $p = 4.55$

It is interesting to note that the effective magnetic boundary is at z = –1″ for dipoles while it is at z = +1″ for quadrupoles. If one assumes that the body field is purely dipole or quadrupole, end field can be expressed as [11]

$$\text{dipole} \qquad B_y = B_o\{f_1(z) - \frac{1}{8} f_1''(z)(x^2+3y^2)\}, \tag{3.13}$$

$$\text{quadrupole} \qquad \partial B_y/\partial x = G_o\{f_2(z) - \frac{1}{4} f_2''(z)(x^2+y^2)\}. \tag{3.14}$$

Nonlinear components arising from the field fall-off are not pure sextupole, $B_y \propto (x^2 - y^2)$, or pure octupole, $\partial B_y/\partial x \propto (x^2 - y^2)$, but their effects on the particle motion are similar to those from pure multipoles.

3.4.3. Resonances

In discussing possible resonances that may affect the beam, the major uncertainty is the amount of tune spread within the beam due to space charge. For a uniform charge distribution, the space charge tune shift varies little from particle to particle and the shift itself can easily be corrected by quadrupole trim windings. The tune spread is another matter. The core of the beam will experience the largest (negative) shift while the peripheral part

will be affected mostly by the image force on the wall. If the normalized emittance stays constant, the real emittance goes down as $1/(\gamma\beta)$ and the tune shift caused by the self field will have a $1/(\gamma^2\beta)$ dependence on beam energy. For example, with $\Delta\upsilon = -0.30$ at injection, 400 MeV(KE), the tune shift due to self field will be down to less than –0.05 at 2 GeV(KE) and –0.01 at 5 GeV(KE). Regardless of what one does with the tune correction, tunes of the core part will always be the lowest. As the beam energy increases, tune of the entire beam will approach the value determined by quadrupole settings and, for $\Delta p/p \neq 0$, by the sextupole settings.

3.4.3.1. Tune diagram

Low order resonances in the area $\nu_x = 12.0 - 12.5$ and $\nu_y = 11.0 - 11.5$ are displayed in Figure 3.7 with the nominal working point at (12.43, 11.38). If the maximum amount of tune shift is assumed to be $\Delta\nu_x = -0.2$ and $\Delta\nu_y = -0.25$ at injection, the range of ν_x is from 12.23 to 12.43 and ν_y from 11.13 to 11.38. Resonances up to the fourth order experienced by some part of the beam will be

normal sextupole: $3\nu_x = 37$, $\nu_x + 2\nu_y = 35$;
skew sextupole: $3\nu_y = 34$, $2\nu_x + \nu_y = 36$;

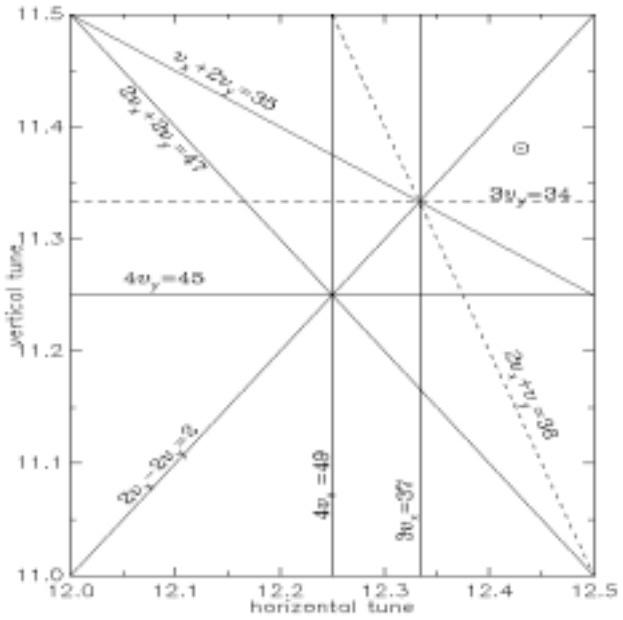

normal octupole: $4\nu_x = 49$, $4\nu_y = 45$, $2\nu_x + 2\nu_y = 47$, $2\nu_x - 2\nu_y = 2$.

Figure 3.7. Nominal working point and low-order resonances; solid lines: normal sextupole and octupole; dashed lines: skew sextupole

Difference resonances, except for $2\nu_x - 2\nu_y = 2$, are generally considered unimportant. It is also unlikely that magnets would have a significant amount of skew octupole contents unless quadrupole tilting is large. It is to be noticed that, of these resonances, only two, $2\nu_x + \nu_y = 36$ and $4\nu_y = 45$, are structural. Furthermore, there is no reason to suspect that the skew sextupole field will be systematic so that $4\nu_y = 45$ is the only structural resonance for the present lattice with three-fold symmetry. The importance of the resonance $2\nu_x - 2\nu_y = 2$ is not well understood. It is known from simulations that resonance $2\nu_x - 2\nu_y = 0$ may cause some emittance growth in the presence of a strong space charge force. Tunes are therefore split by one unit. How much split in the fractional parts is needed is not known but 0.05 for the design values should be sufficient. Because of the negative tune shifts from space charge, the working point is chosen below the diagonal line.

3.4.3.2. Low order resonances

Half-integer resonances

It is important to see how close one can place the working point to the half-integer lines. The stopband width is proportional to the deviation of the integrated gradient of each magnet from its design value:

$$|\Delta\nu|_{rms} = 6 \times (\Delta K/K)_{rms} ; \quad K \equiv (1/B\rho) \int G\, dz.$$

With $(\Delta K/K)_{rms} = 3 \times 10^{-3}$, which is achievable, the rms stopband width will be less than 0.02. The working point, which is 0.05 away from the half-integer lines, will therefore be quite safe. The nominal design values of the tune are (12.43, 11.38).

Sextupole components in dipoles: $|(B''/B_o)|_{av} = 0.10\ m^{-2}$. See Eq. (3.11).

Contributions to the chromaticity are

$\Delta\xi_x = +0.24$ and $\Delta\xi_y = -0.17$ from all regular dipoles,
$\Delta\xi_x = -0.17$ and $\Delta\xi_y = +0.12$ from all short dipoles.

These values are negligible compared with the natural chromaticities, which are approximately –20. See Eq. (3.5). Because of the phase advance per module of 270˚/270˚, there will be no contribution to any third-integer resonance driving terms from the average sextupole field in dipoles. Driving terms are cancelled in each arc separately so that the periodicity is immaterial. This is true for contributions from the chromaticity correcting sextupole magnets as well, resulting in a comfortable dynamic aperture.

Octupole components in quadrupoles: $|(G''/G_o)| = 1.0\ m^{-2}$. See Eq. (3.12).

There are three issues to be examined in the presence of octupole contents in quadrupoles: 1) momentum dependence of the tunes, 2) amplitude dependence of the tunes, and 3) fourth order resonances.

1) Tune *vs.* momentum [9]. From each quadrupole, the contribution is

$$\Delta\nu = (\frac{1}{8\pi})(\frac{GL}{B\rho})(\frac{G''}{G_0})\beta x_c^2 \tag{3.15}$$

where $x_c \approx D_x(\Delta p/p)$ is the closed orbit for $(\Delta p/p)$. From this relation, by simply adding the contribution from each quadrupole, one finds for all quadrupoles combined

$(\Delta p/p)$	$\Delta\nu_x$	$\Delta\nu_y$
– 2.5%	0.019	0.001
+2.5%	0.015	0.001

This includes contributions from body and ends. The contribution from the ends alone is $\Delta\nu_x = 0.007$ for $(\Delta p/p) = 3\%$. Since this is not a storage ring, these values should be acceptable. It is possible that the specification given in Eq. (3.10) for quadrupoles is needlessly too relaxed. If one goes back to the original specification used for the Accumulator quadrupoles, that is, the maximum flatness at 4 in. $= 2 \times 10^{-3}$ instead of 5×10^{-3}, the momentum dependence will be reduced proportionately and $\Delta\nu$ will be less than 0.008 for all values of $(\Delta p/p)$.

2) Tune *vs.* amplitudes. For amplitudes $A = \sqrt{\beta\varepsilon}$, the dependences of the tune on amplitudes are proportional to [9]

$$\Delta\nu_x \propto (3/8)\beta_x^2\varepsilon_x - (3/4)\beta_x\,\beta_y\,\varepsilon_y\,,\ \ \Delta\nu_y \propto (3/8)\beta_y^2\varepsilon_y - (3/4)\beta_x\,\beta_y\,\varepsilon_x \tag{3.16}$$

The maximum value of $\Delta\nu$ with ε_x and $\varepsilon_y = 120\ \pi$ mm-mr, twice the beam emittance at injection, is less than 0.006. The contribution from the ends alone is less than 0.0006.

3) Fourth order resonances. When the beam energy reaches 5 GeV or so, the tunes will be close to the nominal design values, 12.43 and 11.38, and the working point is safely away from all fourth order resonances. This is important. Fourth order resonances have been found to be responsible for the extraction beam loss in ISIS [13]. Below that, because of the tune spread within the beam due to space charge, a structural resonance $4\nu_y = 45$ may exist as the phase advance for the arc, 270°/270° per module, is the most unfavorable choice. The contributions from each magnet to the resonance driving term simply add up. Fortunately, the magnitude of the driving term is not excessive and the required strength for harmonic correction magnets is manageable. See Section 3.4.4.3. It is hoped that the effect of this resonance during acceleration is a minor emittance dilution and not a beam loss.

3.4.3.3. Magnet sorting

In Section 3.4.3.2, it has been emphasized that the average sextupole content in dipoles does not excite any third integer resonance because of the favorable phase advance per

module. This will not be the case if the random sextupole content is dominant. It is, however, still possible to reduce substantially the resonance driving terms of $3\nu_x$ and $\nu_x + 2\nu_y$ simultaneously by a suitable arrangement of dipoles.

In each arc, there are twelve regular dipoles and four short dipoles. For both resonances, the relevant phase distance between the first and the seventh regular dipoles, between the second and the eighth, and so on, is almost exactly 180˚. The same phase relation is true for the first and the third, and the second and the fourth short dipoles. If two magnets with similar sextupole strengths are placed as a pair at these locations, the magnitude of the resonance driving term will be reduced substantially. In general, it is not possible to achieve a perfect cancellation but the arrangement will certainly avoid the possibility of unlucky combinations. If it is necessary, mixing regular and short dipoles in this sorting scheme is worth considering.

Sorting is not practical for suppressing the driving term of the $4\nu_y = 45$ resonance since all defocusing quadrupoles have the same phase.

3.4.4. Requirements for correction systems

Requirements for correction systems are based on the analyses of magnet errors presented in Section 3.4.1. Chromaticity correcting sextupoles are considered as essential items of a synchrotron and they are not included in the discussion of correction systems.

3.4.4.1. Steering magnets

In Section 3.4.1.1, the expected closed orbit distortion has been estimated to be approximately 20 mm in both directions. Most likely, this is an overestimate and there is a definite possibility that a closed orbit would be established without any use of steering magnets. Such an orbit with large excursions will, of course, be unsuitable for stable operation of the machine, and a correction system is essential for assuring the necessary dynamic aperture.

The specification common to horizontal and vertical directions is that the maximum kick angle of each steering element should be 5 mr. The maximum horizontal and vertical deflections generated by this kick will be 65 mm and 100 mm, respectively. For horizontal kick, there will be special windings in each dipole. The required kick angle is 3.6% of the bend angle of regular dipoles and 4.5% of short dipoles. Horizontal orbit correction is then possible up to the highest energy. Vertically, the kick will be provided by 25 cm-long steering magnets. With the maximum field of 0.26 T, the required kick angle of 5 mrad will be available up to 3 GeV (kinetic energy). If it is required to correct the orbit vertically beyond this energy, it will be necessary to realign some quadrupoles. Based on the BPM readings of the established closed orbit, it is possible to select the optimum combination of a specified number of quadrupoles for realignment.

One defect of the present lattice is that, unlike a lattice composed of regular FODO cells, the phase distance between two adjacent correctors can be uncomfortably large.

Horizontally, there is no dipole in Cell_b and the phase over this cell is 163°. This can be reduced by installing in Cell_b a steering magnet similar to the vertical one but the reduction is not significant, 146° instead of 163°. At other locations, the typical phase distance is 45°. One alternative scheme is to depend on steering magnets alone located in the short straights of Cell_b and in the mini straights of Cell_c. There will be ten magnets in each arc, eight in Cell_b and two in Cell_c. Even with this arrangement, the largest phase distance between two adjacent kicks is 138°.

There will be eight vertical correctors in an arc, four each in Cell_b and in Cell_c. The same defect exists in the vertical direction as well. In Cell_a, there is no space for installing correctors. In the middle of each arc, there are two consecutive Cell_a′s and the phase distance to cover them is 230°. It is clear that the customary local three-bump algorithm will not work there and a more comprehensive means of straightening the orbit with more than three correctors may be required.

In long straights, three vertical correctors and four or five horizontal correctors are sufficient to cover the entire length.

3.4.4.2. Tune adjustment

Experience gained in Accumulator and Main Injector operation clearly indicates that if magnets are constructed carefully, it is not necessary to have the flexibility to explore a wide range of tune values. For the present machine, tune adjustment is needed primarily for three reasons: maintenance of the 270°/270° phase advance per module in arcs, compensation of space charge detuning, which is expected to be less than 0.4 even for a peaked charge distribution of the bunch, and minimization of beam loss during extraction. It has been found in ISIS that precise control of the tune is essential to reduce the beam loss to less than one part in 10^4 during extraction when an orbit bump is introduced [13]. The bump moves the beam toward the stray field of the septum magnet and also far off center in some quadrupoles.

Tune adjustment will be done by special windings in each quadrupole. At least two power supplies in each arc, one for controlling all QFs and one for QDs, are desirable so that the phase advance in each arc can be adjusted independently. Similarly, each long straight should have two power supplies, although adjustment of the phase advance in P40, where rf cavities are located, is not important. Arc quadrupoles will be responsible for maintaining the phase advance per module in arcs while quadrupoles in long straights will be used to locate the working point at the optimum position in the tune diagram. It is not possible to predict where this optimum position will be a priori. It is, however, unlikely that tunes would have to be moved by more than 0.2 or 0.3 from the nominal design values.

3.4.4.3. Harmonic corrections: sextupoles and octupoles

As has been discussed in Section 3.4.3, all structural resonances are avoided except for one fourth order resonance, $4\nu_y = 45$. The possibility of being affected by nonstructural

resonances depends primarily on the amount of tune spread within the beam. There are two third order and two fourth order resonances of this type: ($3\nu_x = 37$, $\nu_x+2\nu_y = 35$) and ($4\nu_x = 49$, $2\nu_x+2\nu_y = 47$). Nonstructural third order resonances are excited predominantly by random sextupole components in dipoles, and the sorting scheme to reduce their driving terms has been described in Section 3.4.3.3. If necessary, it is possible to install two families of sextupoles, which are identical to chromaticity correcting sextupoles but much weaker, for harmonic correction. This, however, should wait until there is a clear indication of such a resonance in the actual machine. In the Accumulator, one sextupole resonance of the type $\nu_x+2\nu_y$ has been found to affect the beam and a correction system has been installed to eliminate its harmful effect.

For fourth order resonances, magnet sorting is not available. One can estimate the required strength of correction octupoles from the expected octupole contents in quadrupoles. (See Section 3.4.3.2.) If six correctors are installed in two families at $\beta = 20$ m, for example, the required strength for each corrector is $(B''' \ell) \approx 85$ T/m^2. If $\ell = 0.3$ m, the poletip field at r =10 cm is 500 G. It is unlikely that such a system will ever be needed. In any case, these correctors should be installed in long straights where dispersion is zero or very small so that the correction of the chromaticity will not be affected by them.

References

[1] J. Wei, Handbook of Accelerator Physics and Engineering, edited by A. Chao and M. Tigner, p. 281.

[2] S.Y. Lee, et al., Phys. Rev. **E48**(1993), 3040.

[3] U. Wienands, et al., Proc. 1992 HEACC (Hamburg), p. 1070.

[4] A. Piwinski, Handbook of Accelerator Physics and Engineering, p. 72.

[5] G. Rees, private communication.

[6] F. Mills, private communication.

[7] C. Bovet, et al., A SELECTION OF FORMULAE AND DATA USEFUL FOR THE DESIGN OF A.G. SYNCHROTRONS, CERN/MPS-SI/Int. DL/70/4. 23 April, 1970. p. 24.

[8] S. Ohnuma, $\bar{p}$ Note #346 (October 24, 1983).

[9] S. Ohnuma, $\bar{p}$ Note #324 (July 1983).

[10] E. Keil, private communication.

[11] S. Ohnuma, $\bar{p}$ Note #380 (April 18, 1984) and #380A (April 5, 1985).

[12] D. Harding, private communication.

[13] G. Rees, private communication.

Chapter 4. Space Charge and Beam Stability

D. Carey, V. Dunikov, K.Y. Ng, C. Prior, B. Zotter

4.1 Space Charge and Image Effects

4.1.1 Incoherent Betatron Tune Shifts

The *betatron tunes* ν_z, $z = x$ or y, of transverse oscillations of charged particles in the beam moving with axial velocity $v = \beta c$, c being the velocity of light, are mainly determined by the applied focusing forces due to quadrupoles. With finite beam current the tunes are shifted, both by direct space charge and by "image" forces due to induced voltages in the surrounding structure impedances. At relativistic beam energies, the space charge forces are strongly reduced by a factor $\gamma^{-2} = 1 - \beta^2$ (with γ being the particle energy E in units of its rest energy) due to partial compensation of electric and magnetic forces. However, in the Proton Driver at 400 MeV injection energy, γ = 1.426 and the space charge term is then largely dominant.

The vertical *incoherent tune shift* of a transversely uniform beam of elliptic cross section, with half width a_x and half height a_y, consisting of N protons with classical radius r_p, with bunching factor B_f, the ratio of average to peak current, circulating in a vacuum chamber of half height b, inside a magnet gap of half-height g extending over a fraction κ of the machine circumference, is given by [1]

$$\Delta\nu_z = -\frac{N r_p \langle\beta_z\rangle}{\pi\beta^2\gamma}\left[\frac{\gamma^{-2}-\chi_e}{B_f\, a_z(a_x+a_y)} + \left(\beta^2 + \frac{\gamma^{-2}-\chi_e}{B_f}\right)\frac{\epsilon_{1z}}{b^2} + \kappa\beta^2\frac{\epsilon_{2z}}{g^2}\right], \qquad (4.1)$$

where $\langle\beta_z\rangle \approx R/\nu_z$ is the average value of the betatron function, R the average radius of the ring, χ_e the fractional *neutralization* which reduces the electric but not the magnetic force, thus perturbing their compensation. The *Laslett coefficients* $\epsilon_{1,2z}$ describe the strength of image forces for a particular geometry. A number are shown in Table 4.1; here we take parallel-plate values.

Except for large neutralizations at high energies (when $\chi_e > \gamma^{-2}$), the space charge tune shift is always negative. This is the first term in Eq. (4.1) and is also known as *tune depression*. Since the vertical Laslett coefficients are positive, these image terms add to the space charge tune shift, while they reduce it in the horizontal direction.

The reduction of bunch length and transverse dimensions during acceleration was obtained by computer simulation [2]. The evolution of tune shifts during an acceleration cycle has been calculated from Eq. (4.1) with the program TUNES written in MATHEMATICA [3]. The results for $\chi_e = 0$ are shown in Fig. 4.1 and Table 4.2. For small neutralizations the incoherent tune shifts are actually reduced. The parameters used

for Fig. 4.1 and Table 4.1 were ring circumference C = 711.2 m, particle kinetic energy E_{kin} = 400 MeV, betatron tune $\nu_z = 11.4$, average betatron function $\langle\beta_z\rangle$ = 9.92 m, normalized 95% emittance $\varepsilon = 60 \times 10^{-6}$ πm, full energy spread $\Delta E/E = 7 \times 10^{-4}$, average dispersion $\langle D_x\rangle$ = 1.27 m, average half beam width $a_{x,y}$ = 25.0 and 24.2 mm, beam pipe radius $b = 63$ mm, magnet half gap $g = 64$ mm covering $\kappa = 0.5$ of the ring, zero neutralization, and bunching factor at injection $B_f = 0.5$.

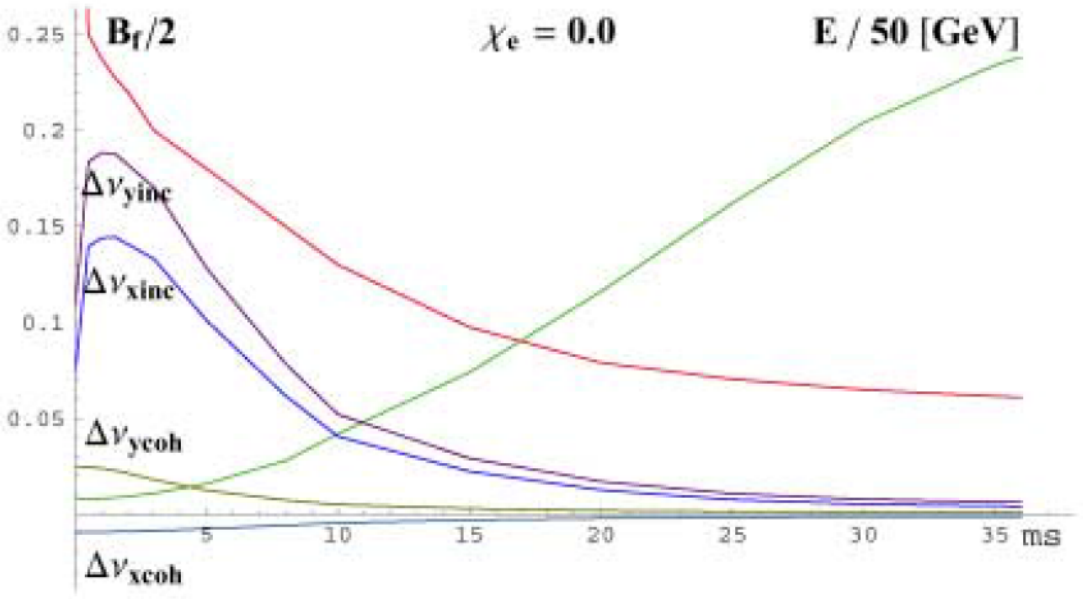

Figure 4.1. Bunching factor, energy and tune shifts during one acceleration cycle

The largest incoherent tune shifts occur 1–2 ms after injection, when the beam energy is still low, but the bunch length had decreased strongly when the protons were captured in the rf field.

Table 4.1. Laslett Coefficients at center of various cross sections

Geometry	ϵ_{1v}	ϵ_{1h}	ξ_{1v}	ξ_{1h}	$\xi_{1v}-\epsilon_{1v}$	$\xi_{1h}-\epsilon_{1h}$
parallel plate	0.205	−0.205	0.615	0.0	0.410	0.205
rectangular 5:9	0.188	−0.188	0.600	0.035	0.411	0.223
elliptic 5:9	0.162	−0.162	0.592	0.107	0.430	0.269
circular	0.000	−0.000	0.500	0.500	0.500	0.500

It is usually considered prudent to keep all tunes away from low-order resonances, in particular from integer multiples of the revolution frequency. Therefore conservative tune shift limits of 0.25 are often assumed, and it is satisfying that the estimates given above do not exceed this limit. However, if the transverse distribution of particles is not uniform but peaked, the space charge tune shift is up to 300% higher, with bi-Gaussian

distribution, for example. Values obtained by computer simulation were slightly above 0.25 in the vertical, and just below it in the horizontal direction.

However, since the dominant space charge force is generated inside a particle beam itself, it actually does not deflect the beam and thus cannot drive it into *dipole resonances* [4]. This can be seen from the equation for betatron oscillations of a particle with offset y from the center of the vacuum chamber, in the presence of (normalized) image and space-charge forces F_{im} and F_{sc}, which are

$$\frac{d^2y}{dt^2} + (\nu_y\omega_0)^2 y = F_{im}y + F_{sc}(y - \bar{y}) \tag{4.2}$$

where $\bar{y}$ is the offset of the beam center. Averaging over all particles yields

$$\frac{d^2\bar{y}}{dt^2} + (\nu_y\omega_0)^2 \bar{y} = F_{im}\bar{y} \tag{4.3}$$

i.e., the driving term for the space charge effect vanishes, while the image term causes a shift of the *coherent tune* to $\nu_{\rm coh}^2 = \nu_{y0}^2 - F_{im}/\omega_0^2$.

Table 4.2. (Negative) Space charge and Image Tune Shifts

t [ms]	$\Delta\nu_{xsc}$	$\Delta\nu_{xim}$	$\Delta\nu_{xinc}$	$\Delta\nu_{xcoh}$	$\Delta\nu_{ysc}$	$\Delta\nu_{yim}$	$\Delta\nu_{yinc}$	$\Delta\nu_{ycoh}$
0	0.089	−0.0213	0.0678	0.0156	0.092	0.0213	0.114	0.0310
1	0.163	−0.0256	0.1376	0.0154	0.169	0.0256	0.194	0.0299
2	0.159	−0.0241	0.1347	0.0148	0.164	0.0241	0.188	0.0271
5	0.113	−0.0167	0.0963	0.0120	0.116	0.0167	0.133	0.0170
10	0.045	−0.0078	0.0381	0.0069	0.047	0.0078	0.055	0.0076
20	0.015	−0.0032	0.0116	0.0031	0.015	0.0032	0.018	0.0031
30	0.007	−0.0019	0.0047	0.0019	0.007	0.0019	0.009	0.0019
38	0.005	−0.0016	0.0037	0.0016	0.005	0.0016	0.007	0.0016

4.1.2 Coherent Betatron Tune Shifts

The coherent tune shifts are given by the same equations as the incoherent ones, but without the space charge term and with the Laslett coefficients $\varepsilon_{1,2z}$ replaced by $\xi_{1,2z}$. However, for the usual case of a chamber wall thick enough that ac magnetic fields do not penetrate, the term $\beta^2\varepsilon_{1z}/b^2$ remains unchanged [5]:

$$\Delta\nu_z = -\frac{Nr_p\langle\beta_z\rangle}{\pi\beta^2\gamma}\left[\beta^2\frac{\epsilon_{1z}}{b^2} + \frac{\gamma^{-2} - \chi_e}{B_f}\frac{\xi_{1z}}{b^2} + \kappa\beta^2\frac{\xi_{2z}}{g^2}\right] . \tag{4.4}$$

In a flat chamber, $\xi_{1y} = \xi_{2y} = \pi^2/16$, while both $\xi_{1x} = \xi_{2x} = 0$. For a 5:9 rectangular chamber, $\xi_{1y} = 0.60$ and $\xi_{1x} = 0.035$, with similar values for an elliptic one.

The direct space charge force does not affect dipole oscillations, but it does change the external focusing forces. In one dimension, the evolution of the beam size a_z ($z = x$ or y) is described by the *envelope equation*

$$\frac{d^2 a_z}{ds^2} + K_z(s) a_z - \frac{\epsilon_z}{a_z^3} = \frac{4\lambda r_p}{\beta^2 \gamma^3 (a_x + a_y)} \tag{4.5}$$

where $K_z(s)$ is the external focusing strength, ε_z the unnormalized transverse emittance, λ the number of particles per unit length.

The space charge force leads to a *modulation of the beam envelope*, which reduces the tune shift of the lowest *quadrupole mode* to $\frac{3}{4}\nu_{sc}$. For the 2-dimensional case, there are 2 modes of quadrupole oscillations: the *antisymmetric mode* has its tune shift also reduced to $\frac{3}{4}\nu_{sc}$, and the *symmetric mode* even to $\frac{1}{2}\nu_{sc}$. Hence these modes are not excited when only the *incoherent tune* crosses (half-) integer resonances. Nevertheless, one has to allow for a variation of tunes during acceleration due to incomplete tracking of quadrupole and dipole strengths, and therefore one needs a certain safety margin to these resonances. In Phase I of the Proton Driver, tune shifts do not exceed 0.25, which can be safely accommodated with a properly chosen working point.

Higher order oscillations—sextupole, octupole, etc—have larger space charge tune shifts, but have not been observed in simulation nor in actual machines. They are suppressed by *Landau damping* due to the nonlinearity of space charge forces.

4.1.3 Longitudinal space charge effects

The *coherent synchrotron frequency* of a bunch is nearly constant with current since the coherent and incoherent longitudinal tune shifts cancel, $\Delta\nu_{s,coh} = -\Delta\nu_{s,inc}$. At low energies the incoherent frequency shift of Gaussian beam can be written [6]

$$\Delta\nu_{s,inc} = -\frac{3Nr_p\eta R^2}{2\beta^2\gamma^3\nu_{s0}}\frac{g_f}{L_b^3}\,, \tag{4.6}$$

where L_b is the full bunch length, and g_f is commonly known as the *g-factor*. For a circular beam of radius a in a concentric chamber of radius b, it is $g_f = 2\ln(b/a) + \frac{1}{2}$; for a rectangular chamber b should be multiplied by $4/\pi$. This expression contains both the contribution of space charge in the term $\ln a$ and that of the wall in the term $\ln b$.

The voltage induced by the bunch current creates a local *potential-well distortion*, which slides up and down the applied rf voltage when the synchronous phase angle

changes with bunch current. The (coherent) synchrotron frequency of the bunch, which depends on the derivative of the rf voltage, therefore remains constant as long as the applied voltage is sufficiently linear. However, the (incoherent) synchrotron frequency of individual particles, given by the local derivative inside the potential well, not only depends on beam current but also varies between the center and the edge of a bunch. When the (square of the) synchrotron frequency in the center of a bunch is shifted below zero, an instability may occur, hence excessive potential well deformations should be avoided.

The mainly *inductive wall impedance* reduces the tune shift of the "*capacitive*" space charge, but is insufficient to compensate it in particular at injection energy. Thus it is useful to add more inductance, which can be done e.g. with *inductive inserts*, containing ferrite (Finemet) cores (see Chapter 5). Even at higher energies the space charge tune shift may be large if the bunch length is sufficiently small, e.g. due to reduced transition energy or rotation in phase space (see below). Again inductive inserts can be helpful. However, one has to take care that the total resistive part of the impedance is not increased excessively by them, as this determines the growth-rate of instabilities (see next section).

4.1.4 Effects of space charge on bunch rotation

In Phase I Stage 2 and Phase II, it is desirable to have short proton bunches (1–2 ns) impinging on the target for efficient production of muons and hence neutrinos. Therefore it was proposed to rotate the bunches in phase space just prior to ejection, converting their small energy spread into a short bunch length.

The minimum bunch length thus achievable is restricted by distortions of the bunch during phase space rotation. The speed of rotation of individual particles is given by their synchrotron tunes:

$$\nu_s = \sqrt{\frac{-\eta h V_{\mathrm{rf}} \cos\phi_s}{2\pi E/e}} \,, \qquad (4.7)$$

where V_{rf} is the applied rf voltage at frequency f_{rf} with harmonic number $h = f_{\mathrm{rf}}/f_0$, $f_0 = \omega_0/(2\pi)$ the revolution frequency, and the synchronous phase is ϕ_s. The *slip factor* $\eta = \gamma_T^{-2} - \gamma^{-2}$ expresses the distance to transition energy, and is negative below transition (for which cos ϕ_s is therefore chosen positive). η is only a weak function of energy when γ is not too close to γ_T, and then the variation of synchrotron frequency becomes only important for beams with large momentum spreads.

In the Proton Driver, the full momentum spread is usually quite small (7×10^{-4}). However, it has been proposed to reduce transition energy prior to ejection to shorten the bunches and require only little rotation in phase space. Strong distortions may result during bunch rotation due to the increased synchrotron frequency spread [7].

Longitudinal effects

For an intense proton bunch, the longitudinal space charge force will counteract the focusing rf force, thus reducing the synchrotron tune and slowing down the rotation rate. This cancellation becomes larger and larger as the bunch becomes shorter and shorter during the rotation. Sometimes, this space charge force will even be larger than the rf focusing force, making the particles rotate in the reverse direction in longitudinal phase space. Theoretically this is an instability of the synchrotron motion, which, however, is unimportant here, because we are interested in only about $\frac{1}{4}$ of a synchrotron period. The space charge modification of the rf potential occurs only near the core of the bunch where the particle intensity and therefore space charge is most intense. Ironically, this longitudinal space charge force is actually beneficial to the bunch rotation. This is because the slowing down of the rotation near the core provides time for the particles near the separatrices to catch up. As a result, the fraction of particles in the tails of the rotated compressed bunch will be much less. Of course, when the space charge is too large, bunch lengthening dominates and bunch compression becomes impossible.

We believe that the effect of space charge distortion of the rf waveform is governed by the ratio of the space charge force to the rf force. Simulations show that bunch compression through rotation in the longitudinal phase space is feasible provided that [9]

$$\frac{\text{Sp-ch force}}{\text{Rf force}} = \frac{eN_b|Z/n|_{sc}}{\sqrt{2\pi}h\omega_0^2\sigma_\tau^3 V_{\text{rf}}} \lesssim 17 \ , \qquad (4.8)$$

where N_b is the number of particles in the bunch $(Z/n)_{\text{sc}}$ is the longitudinal space charge impedance per harmonic, and σ_τ is the desired rms bunch length after compression. From Table 4.3, it is evident that for Phase I Stage 2 of the Fermilab proton driver, the space-charge-to-rf ratio is very much less than the critical value of 17 stated in Eq. (4.8), implying that the longitudinal space charge constitute negligible influence on the bunch compression.

For Phase II operation, a compression to $\sigma_\tau = 1$ ns is still possible, because of the σ_τ^3 dependency in Eq. (4.8) and the space-charge-to-rf ratio is only slightly larger the critical value.

A shortcoming of the bunch rotation method is the possible development of microwave instability when the rf voltage is reduced adiabatically to a small value so that the bunch will fill the whole bucket prior to the rotation. This can be avoided if the synchronous-phase-shift method of compression is used instead. The synchronous phase is first shifted from the center of the bucket to an unstable fixed point. The bunch is allowed to spread out along one set of separatrices. Later the synchronous phase is shifted back to the center of the bucket. The bunch is allowed to rotate in the longitudinal phase space for about $\frac{3}{8}$ of a synchrotron period and the shortest bunch results. This method gives a theoretical linear compression ratio of $\sqrt{2}/(\sqrt{3}\sigma_\phi)$, where σ_ϕ is the initial rms

bunch length measured in rf phase. Of course, final rotation will introduce nonlinearity and tails for the compressed bunch. However, this can be alleviated by extracting the bunch immediately at the end of the drift along the separatrices. The bunch is then sheared back to an upright position in the beam line via an optical system with local momentum compaction, or the R_{56} element of the transfer matrix.

Table 4.3. Comparison of the space-charge-to-rf ratio in bunch compression through rotation for Phase I Stage 2 and Phase II of the Fermilab proton driver

	Fermilab Proton Driver	
	Phase I	Phase II
Extraction kinetic energy (GeV)	16	16
h	18	18
Number per bunch N_b	$1.7\ 10^{12}$	$2.5\ 10^{13}$
Revolution frequency (MHz)	0.40932	0.40932
$\lvert Z/n\rvert_{sc}$ (Ohms)	2.639	2.639
$V_{\rm rf}$ (kV)	1400	1400
Extraction σ_τ (ns)	3	1
Sp-ch-to-rf ratio	0.060	23.9

Transverse effects

At the end of the bunch rotation in longitudinal phase space, the bunch will be compressed to its minimum length of, for example, $\sigma_\tau = 1$ ns with half momentum spread $\delta = \pm 0.0482$, where a bunch area of 2 eV-s has been assumed. (Actually, the momentum aperture of the proton driver is less than ±0.025. Thus to compress a bunch to 1 ns, the bunch area must be tailored to less than 1 eV-s to start with.) Although the extraction energy is high, the self-field space charge tune shift $\Delta\nu_{\rm sc}$ given by the first term of Eq. (4.1) can still be appreciable. It is possible that the reduction in betatron tune can modify the effective transition γ_T to such an extent that particles find themselves near transition. Higher order momentum compaction will be needed because of the large momentum spread. This may result in ruining the whole bunch rotation procedure as a result of nonlinearity.

Notice that the self-field space charge tune shift in Eq. (4.1) is inversely proportional to $\gamma^3\beta^2$. Thus, the tune shift is momentum dependent and can be written as

$$\Delta\nu_z \approx \Delta\nu_{sc}\left(1 - 3\delta + 12\delta^2\right), \qquad (4.9)$$

where $\Delta\nu_{sc}$ is evaluated at the nominal momentum. It is evident that the last two terms represent the first two lowest orders of chromaticity generated by the transverse space-charge force. In a Hamiltonian formalism, $\nu_z = \partial H/\partial J_z$, where J_z ($z = x$ or y) is the

transverse betatron action, which is related to the transverse offset z from the off-momentum closed orbit by $z = (2\beta_z J_z)^{1/2}$, and the *unnormalized* emittance ε by $\varepsilon = 2J_z$. For the simple case of a Kapchinakij–Vladimirskij (KV) beam [10] where the transverse distribution is uniform, $\Delta\nu_{sc}$ is J_z independent. Thus, the contribution of the self-field space charge tune shift to the Hamiltonian is [9]

$$\Delta H = \Delta\nu_{sc}\,(J_x + J_y)\left(1 - 3\delta + 12\delta^2\right) - \frac{\alpha_0 R}{2}\delta^2 \ , \tag{4.10}$$

where we have added the term contributing the nominal momentum compaction factor α_0. This Hamiltonian will result in a path length difference $\Delta\ell$ given by

$$-\frac{\Delta\ell}{2\pi} = \left\langle \frac{\partial \Delta H}{\partial \delta} \right\rangle = \Delta\nu_{sc}\,(J_x + J_y)\,(-3 + 6\delta) - \alpha_0 R\delta \ . \tag{4.11}$$

Here we arrive at an up-shift in the momentum compaction ($\Delta\nu_{sc}$ is negative)

$$\Delta\alpha_0 = -6\Delta\nu_{sc}\frac{J_x + J_y}{R} \ , \tag{4.12}$$

or down-shift of the transition gamma

$$\Delta\gamma_T = 3\Delta\nu_{sc}\gamma_T^3\,\frac{J_x + J_y}{R} \ , \tag{4.13}$$

which is dependent on the betatron oscillation amplitudes.

In Phase II of the Proton Driver, the number per bunch is $N_b = 2.5 \times 10^{13}$ and the rf harmonic $h = 18$. For the $\sigma_\tau = 1$ ns compressed bunch, the bucket bunching factor is $B_f \approx (2\pi)^{1/2} h f_0 \sigma_\tau = 0.01899$. With normalized 95% emittance $\varepsilon_N = 60\times10^{-6}\pi$ m, the self-field space charge tune shift is $\Delta\nu_{sc} = -0.297$. The maximum actions for betatron motion are only $J_x = J_y = 1.66 \times 10^{-6}$ m. However, most of the transverse beam size comes from the off-momentum dispersion. With a maximum dispersion[1] of $D \sim 3$ m, there is a contribution to the equivalent action at 2% momentum offset of $J_x = (D\delta)^2/(2\beta_x) \sim 0.00018$ m, where the horizontal betatron function has been taken as $\beta_x \sim 10$ m. With the nominal transition gamma of $\gamma_T = 27.71j$, the shift is only $\Delta\gamma_T = -0.031j$, which is small, and the particles are nowhere near transition.

It is important to point out that even if the transverse space charge force is very large, the modification to γ_T can be very much reduced by correcting the two lowest orders of

[1]A more accurate derivation should take into account the modification of horizontal dispersion and the introduction of vertical dispersion by the self-field space charge tune shift. See Ref. [11] for detail.

chromaticities. Although the self-field space charge tune shift actually contributes a spread in a non-KV beam, most particles, which reside in the core, will see roughly the same linear tune depression $\Delta\nu_{sc}$ and therefore a correction of the chromaticities will remedy the situation.

4.1.5 Computer simulation of beams with space charge

A number of computer codes exist which allow simulation of space charge effects in high current machines by tracking several thousands of super-particles over many turns. They are subjected to the effect of external focusing as well as to space charge forces. Some codes also permit inclusion of image effects.

At Fermilab, the longitudinal code ESME has been developed over more than 20 years for this purpose [8]. It has been used to optimize parameters by following particles from injection, through acceleration by rf cavities to their final energy. In particular, the evolution of energy and bunch length can be studied and the effect of inductive inserts optimized to minimize the loss of particles during injection.

The code TRACK-2D, developed in the Rutherford Laboratory in England [12], also includes transverse space charge effects, making use of a nonlinear space charge solver based on finite elements. Image charges, corresponding to an elliptical vacuum chamber, are also taken into account. The code has been applied to the parameters of the Fermilab Proton Driver to study the evolution of particles in transverse phase space. The results are shown in Figure 4.2 for the transverse plane (*x, y*), in Figure 4.3 for the horizontal phase space (*x, x'*), and in Figure 4.4 for the vertical phase space (*y, y'*). Each figure shows a sequence of shots in successive revolutions. These pictures give final transverse normalized 95% emittances of $\varepsilon_x = 69.5\times10^{-6}\,\pi$ m ($12.2 \times 10^{-6}\,\pi$ m rms) and $\varepsilon_y = 82.6\times10^{-6}\,\pi$ m ($12.4 \times 10^{-6}\,\pi$ m rms). The code has also been used to minimize the loss of particles at injection and keep the stripping foil from overheating by an excessive number of traversals. The foil is depicted as a rectangle in Fig. 4.2. The average number of foil hits per particle during the 27-turn injection cycle has been 1.4, in addition to the first passage when the electrons are stripped from the H^- beam. The code contains an improved calculation of space charge forces, and its longitudinal results have been in good agreement with previous ones obtained with ESME.

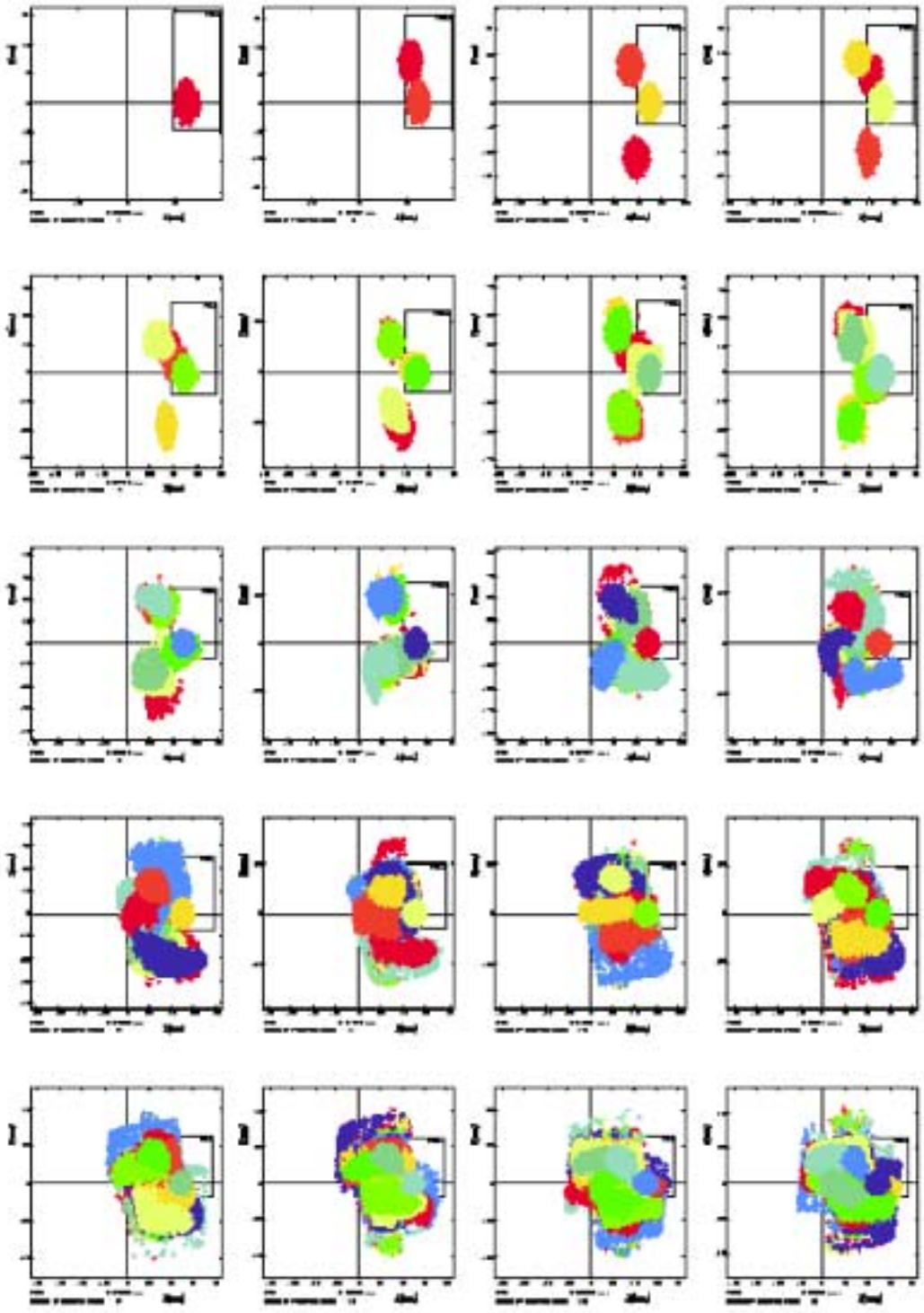

Figure 4.2. Plots of *x*-*y* at injection for the first 20 successive turns with space charge taken into consideration. The foil is depicted as a rectangle in each plot

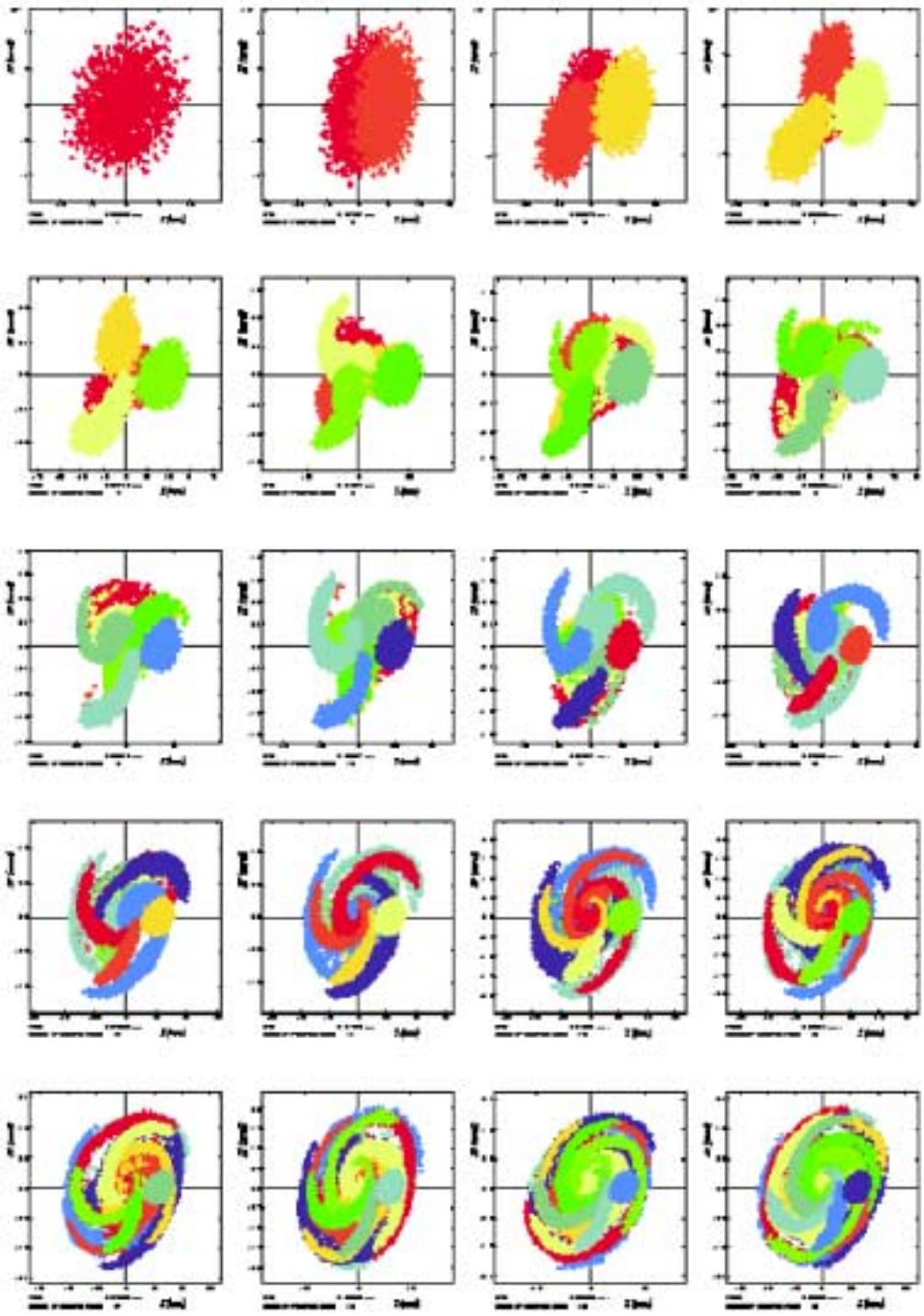

Figure 4.3. Horizontal phase space plots (x-x') at injection for the first 20 successive turns with space charge taken into consideration

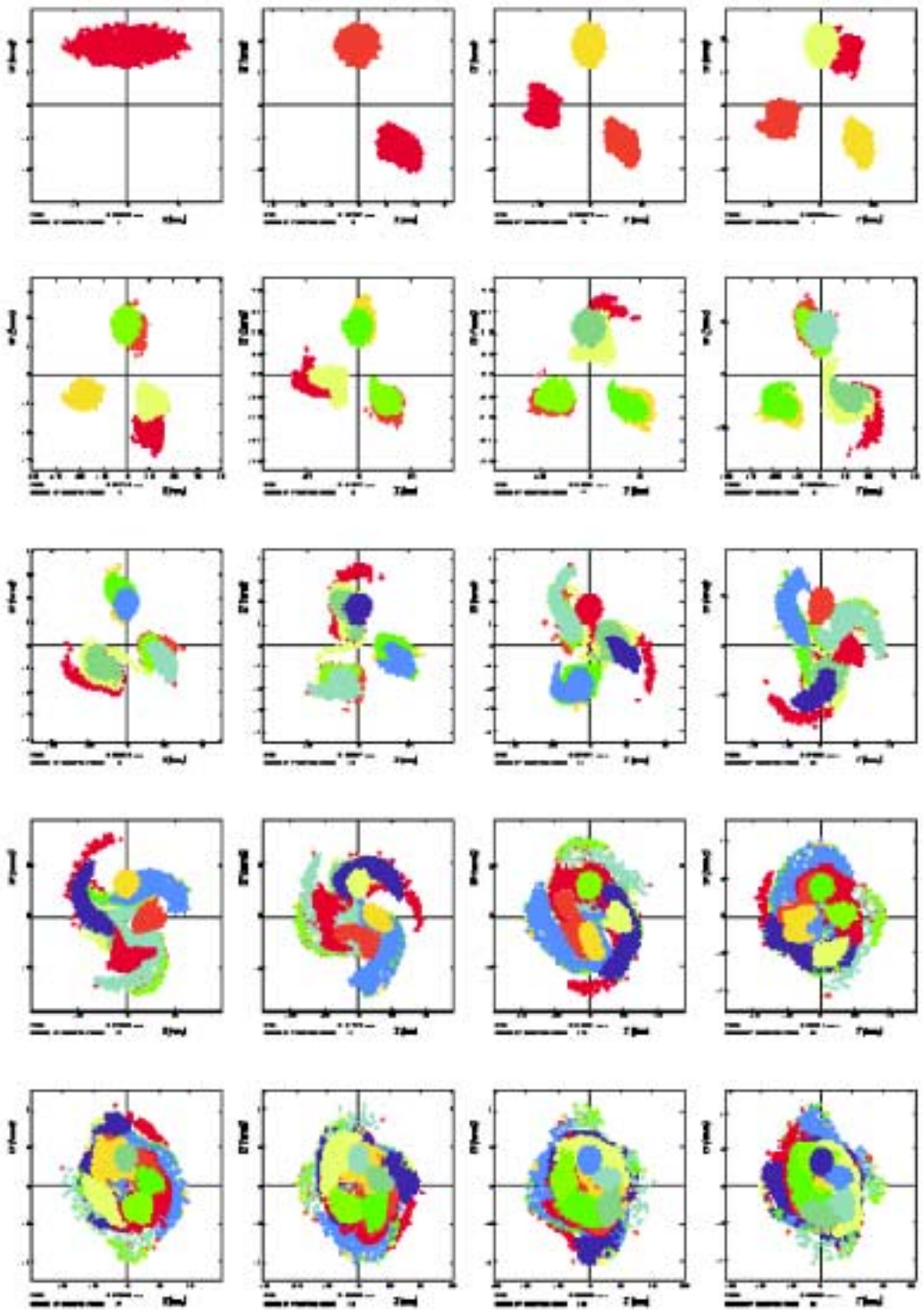

Figure 4.4. Vertical phase space plots (*y*-*y'*) at injection for the first 20 successive turns with space charge taken into consideration

4.2 Coherent Single Bunch Instabilities

4.2.1 Broad-band impedance estimates

The largest impedances in the Proton Driver, in particular at low energies, are due to space charge. They can be obtained from the last section [19]

$$\frac{Z_\parallel}{n}^{sc} = -j\frac{Z_0}{2\beta\gamma^2}\, g_f \ , \quad Z_{\perp_z}^{sc} = -j\frac{2RZ_0}{\beta^2\gamma^2}\left[\frac{1}{a_z(a_x+a_y)} - \frac{\xi_{1z}-\epsilon_{1z}}{b^2}\right] . \qquad (4.14)$$

The *g-factor* g_f was already given after Eq. (4.6). For a rectangular chamber with 5 to 9 ratio, the Laslett coefficients yield $\xi_1 - \varepsilon_1 = 0.412\,/\,0.223$ vertically/horizontally, and for an elliptic one 0.430/0.269. For a beam of radius $a = 25$ mm, in a chamber of radius $b = 63$ mm, the longitudinal impedance at injection energy is then about $-371j\ \Omega$, while the transverse impedance reaches nearly $-61j$ MΩ/m.

The finite conductivity of the vacuum chamber wall creates the *resistive wall impedance*, which contributes the largest real part to the impedance. It increases when the wall is made of high-resistance material such as Inconel or Ti alloys in order to reduce eddy currents.

For a material with conductivity σ_c, permeability $\mu = \mu_r\mu_0$, the *skin depth* at frequency ω is $\delta = \sqrt{2/(\omega\mu\sigma_c)}$. For a wall thickness larger than the skin depth, the longitudinal resistive wall impedance, divided by mode number $n = \omega/\omega_0$, of a circular cylindrical wall at radius b becomes

$$\frac{Z_\parallel}{n}^{rw} = (1+j)\beta\mu_r Z_0\frac{\delta_b}{2b} , \qquad (4.15)$$

assuming that the wall is thick compared to the skin depth. The transverse impedance is found simply by multiplication with $2R/(\beta b^2)$. The skin depths for various materials, evaluated at 300 kHz, the revolution frequency f_0 at injection energy, are shown in Table 4.4. The lowest betatron frequencies are smaller; f_0 is multiplied by the non-integer part of the tune q or $(1-q)$ if $q > \frac{1}{2}$. For simplicity, we give the skin depths and all impedances for the revolution frequency at injection energy. The transverse impedances have to be increased by the factor $q^{-1/2}$ or $(1-q)^{-1/2}$ once the exact tune is known.

Table 4.4. Resistive wall and space charge impedances at injection energy

Resistiv wall	ρ_c	σ_c	μ_r	δ	$Z_\parallel/n$	$Z_{\perp x}$	$Z_{\perp y}$
Material	$[\mu\Omega cm]$	[MS/m]		[mm]	[Ω]	[KΩ/m]	[KΩ/m]
Silver	1.59	62.9	1.0	0.12	0.247	5.53	19.7
Copper OF	1.71	58.5	1.0	0.14	0.256	5.74	20.5
Aluminum	2.91	34.4	1.0	0.30	0.337	7.49	27.1
SS Steel	57	1.75	1.001	0.4	1.48	33,2	118.4
Si-Steel 1%	23	4.34	9000	0.01	89.1	1998	7131.
Inconel	129	.775	1.002	0.92	2.22	49.9	178.0
Ti alloy	148	.676	1.0	1.07	2.38	53.4	190.5
Space charge					$-j371$	$-j60500$	$-j57200$

If the walls were made of good conductors, such as copper or aluminum, eddy current losses would be excessively high unless the metal was divided into narrow strips or wires, similar to the wire-cage used in ISIS [14]. The eddy current power loss per unit length in a metal strip of width *w*, height *h* and conductivity σ_c, at right angles to a changing magnetic field with time derivative *dB/dt*, is approximately given by $P/L = \sigma_c h w^3 (dB/dt)^2 /12$. Since this is proportional to the third power of the width, it can be reduced from over 8 kW/m for a 1.3 mm thick, 22 cm wide, elliptic Inconel chamber to a few W/m by replacing it with 2 × 50 copper strips of 4 mm width and 50-100 μm thickness. For a metal thickness *t* small compared to the skin depth δ, the impedance given by Eq. (4.15) has to be multiplied by a factor $\delta/t > 1$. For the present case, this yields an impedance increase by about 3 for strips of 50 μm thickness, still tolerable due to the higher conductivity of copper.

For vacuum chambers made of ceramics, thin metal stripes of high conductivity can be deposited on the inside to shield the high impedance of the magnetic pole pieces behind them. However, such chambers need a thickness of 5-6 mm to withstand the pressure of air and thus would require larger magnet gaps for the full aperture. *Composite chambers* can be made slightly thinner, with a thickness of 2-3 mm, and would thus be preferable if their vacuum properties are found adequate.

Other sources of broad-band impedance are the rf cavities loaded with ferrite (or Finemet). Kicker tanks may create both broad-band and narrow-band impedances. Finally, bellows and other small cross-section variations of the vacuum chamber become important when they are present in large numbers, but have essentially mainly inductive impedance at low frequencies.

4.2.2 Shielding of electromagnetic fields by liners and cages

Although the skin depth is smaller for larger permeability, the additional factor μ_r in Eq. (4.15) makes the impedance large for magnetic material such as used for iron pole pieces. In particular if the pole pieces form part of the vacuum chamber as in the Fermilab Booster, they should be shielded in the Proton Driver where higher beam currents are desired. For this purpose, a screen or liner has been proposed, similar to the one being built as radiation shield for the LHC [13]. But to minimize eddy current losses, the screen for the driver should be made as thin as possible.

Therefore it is important to estimate the minimum thickness required to effectively shield the beam from the outer region. Assuming rotational symmetry, a screen of thickness t at radius b, with skin depth $\delta_b >> t$, and an outer wall at radius d, with skin depth δ_d, the *shielding condition* in the longitudinal direction can be written [18]

$$\frac{t}{\delta_b} \gg \frac{\beta^2\gamma^2}{2\ln(d/b)}\frac{\delta_b}{b} \approx \frac{\beta^2\gamma^2}{2}\frac{\delta_b}{d-b} \qquad (4.16)$$

where the second relation holds when $d - b << b$. At low energies, when $\beta\gamma$ is small, the required screen thickness t can thus be smaller than the skin depth by the factor δ_b / b, or $\delta_b /(d-b)$ when the screen is close to the outer wall.

A similar condition has been given for a metallized ceramic wall [17], where $(d - b)$ is replaced by the thickness of the ceramic wall. In the *transverse direction*, the shielding condition under the same assumption becomes simply [18] $t/\delta_b >> \beta^2\gamma^2\delta_b / b$, similar to the longitudinal criterion but without the logarithmic term. Hence for γ not too large, shielding in the transverse direction is always achieved when longitudinal shielding is good.

For higher energies, taking into account the finite skin depth at the outer wall, the criterion becomes $t/\delta_b >> (d/b)(\delta_b / \delta_d)$, i.e., the skin depth of the screen should be less than that of the outer wall. This is difficult to fulfill when the outer wall is ferromagnetic and thus has a very small skin depth. However, at higher energies the beam is more stable and the space charge part of the impedance is strongly reduced.

4.2.3 Longitudinal stability criteria

The simplified *Keil-Schnell* or *circle criterion* is often used to estimate longitudinal stability limits, but is really not applicable for space charge dominated beams, since the actual stability limit is very large for a capacitive reactance. For bunched beams, one has to replace average current I_b by peak current by dividing it with the bunching factor B_f. One thus obtains the *Boussard criterion* for the *microwave instability*

$$\frac{|Z_\parallel|}{n} < F\frac{|\eta|B_f E_0}{e\beta^2 I_b}\left[\frac{\Delta E}{E}\right]_{FWHM} . \qquad (4.17)$$

The *form factor F*—originally assumed to be of the order of unity—is much larger for a space charge dominated impedance. In Phase I, the total beam current with 3×10^{13} protons is 1.4 A in 126 bunches and I_b only 12 mA. The bunching factor is about 0.5 near injection energy $E = \gamma E_0 = 1.3$ GeV, E_0 being the rest energy. The full energy spread is then 7×10^{-4}, and the full spread at half height about $\sqrt{2}$ smaller. Even with $F = 1$ one finds a quite comfortable limit of over 12 kΩ at injection when the particle energy is at its lowest value. The transition gamma of $\gamma_T = 27.71j$ has been used although the result is not sensitive to it at injection. For Phase I Stage 2, the same current is divided into only 18 bunches; the threshold with the same form factor of unity is still several kΩ and hence no problem is expected from microwave instability.

4.2.4 Transverse stability criteria

The situation is more critical in the transverse case. The lowest oscillation frequency is smaller than the revolution frequency, multiplied by the non-integer part of the tune $q = \nu_z - \text{int}(\nu_z)$, or its complement $(1 - q)$, whichever is smaller. This impedance is quite large at very low frequencies, but mainly on one or two narrow spectral lines. The effective broad-band impedance is obtained by integrating over the bunch spectrum. For a centered spectrum, the resistive part is thus quite small as $Z_\perp(\omega)$ has opposite signs for positive and negative frequencies. However, when the transverse bunch spectrum is shifted by chromaticity ξ_z, the real part of the effective broad-band impedance due to finite wall resistivity can become quite large.

The growth rate of the *head-tail instability* for a beam consisting of n_b equally spaced bunches, each with average bunch current I_b, can be written as [16]

$$\frac{1}{\tau} = -\frac{1}{m+1}\frac{en_b I_b c}{4\pi\nu_z E}\sum_k \mathcal{R}e\, Z_\perp(\omega_k) F'_m(\omega_k - \chi_z) , \qquad (4.18)$$

where $\chi_z = -\xi_z \omega_0 \tau_L / \eta$ is the *chromatic phase shift* across the full length τ_L of the bunch. The spectrum of frequencies for the m^{th} mode of transverse oscillations with *coupled bunch mode number n* $(0 \le n < n_b)$ is given by

$$\omega_k = kn_b + n + \nu_z + m\nu_s . \qquad (4.19)$$

The form factor $F'_m(\omega)$ expresses the cancellation occurring in the summation over both positive and negative frequencies of the real parts of the impedance, weighted by the spectrum of the m^{th} mode of oscillation. In practice, mainly mode $m = 0$ is of concern, which can be damped below transition by *negative chromaticity*. The higher modes, $m \ge 1$, are damped by a tune spread of order $1/(\omega_0 \tau_L)$ which usually occurs naturally.

Ferrite loaded cavities and inductive inserts may contribute a large broad-band impedance, with a resistive part, which becomes large at frequencies where the ferrites become lossy. Fortunately, most ferrites have low losses below 100 MHz where the resistive wall contribution is highest.

4.2.5 Cures

Inductive inserts can be effective for compensating the "capacitive" space charge impedance. However, they require considerable space around the machine. Ferrite with small losses at lower frequencies should be chosen to limit the resistive impedance.

It is further prudent to keep transition well above the highest operation energy by designing a lattice with small or imaginary momentum compaction. A reduction of transition to limit the required bunch rotation could be dangerous and should be applied only very shortly before the beam is ejected.

4.3 Coupled Bunch Instabilities

4.3.1 Narrow-band impedance estimates

We already mentioned the resistive wall impedance, which is in particular high in the transverse plane at the lowest betatron frequency qf_0, which is about 100 kHz for $q = 0.33$. For a thick Inconel wall at $b = 63$ mm, with a skin depth of 1 mm, $Z_\perp \approx 200$ kΩ/m, but for a very thin one, such as proposed for shielding the pole pieces, the value would be much higher, e.g. 40 times for a thickness of 25 μm.(1 mil). For copper, with a nearly hundred times better conductivity, all values are 10 times lower.

In addition, we have to include narrow band resonances of higher order modes (HOMs) in rf and other cavities, such as kicker tanks for injection or ejection. For Stage 2 of Phase I, the 5 MHz rf cavities will be either tuned or damped by ferrite (or Finemet) and their losses will damp most HOMs. However, for Stage 1, with a 53 MHz rf system, the cavity modes must be measured and either damped internally or coupled out to a load. Measurements should be made when a prototype of these cavities becomes available.

Also the kicker tanks should be designed to permit damping of the HOMs by similar means. Sometimes it is already sufficient to use lossy material for the insulators inside these tanks.

4.3.2 Longitudinal stability criterion

Coupled-bunch modes will become unstable in a beam of n_b equally space bunches with equal average currents I_b when the imaginary part of the complex frequency shift $\mathrm{Im}(\Delta\omega_{mk})$ exceeds the frequency spread [15]. Here $m \geq 1$ is the *azimuthal mode number*

($m = 1$ dipole, $m = 2$ quadrupole, etc.), and $0 \le k < n_b$ the *modal mode number* of an oscillation with phase shift $\Delta\phi = 2\pi k / n_b$ between adjacent bunches [15]:

$$\Delta\omega_m = \frac{2m}{m+1}\frac{E_0 I_b}{e h V_{\rm rf} cos\phi_s}\left(\frac{Z_\parallel}{n}\right)_{\rm eff}^{(m,k)} , \qquad (4.20)$$

where the *effective impedance* is defined as the (infinite) sum over the product of the impedance $Z_\parallel / n$ and the power density $h_m(\omega)$, evaluated at all spectral frequencies $\omega_{mkp} = \omega_0(pn_b + k + m\nu_s)$, and normalized by the sum over all power densities:

$$\left(\frac{Z_\parallel}{n}\right)_{\rm eff}^{(m,k)} = \sum_{p=-\infty}^{\infty} \frac{Z_\parallel}{n}(\omega_{mkp}) h_m(\omega_{mkp}) , \qquad (4.21)$$

where the power spectrum $h_m(\omega)$ of the m[th] mode of oscillation has been normalized such that $\sum_p h_m(\omega_{mkp}) = 1$.

For a single resonance at frequency ω_r, with shunt impedance R_s and quality factor Q, the growth rate of the *longitudinal coupled bunch oscillations* can be written as

$$\frac{1}{\tau} = -\frac{|\eta| n_b I_b R_s f_0}{2\pi\nu_s B_f} \mathcal{R}e[D(\alpha_d) F_m(\Delta\Phi)] , \qquad (4.22)$$

where $\alpha_d = \omega_r \tau_{sep} / (2Q)$ is the decrement between bunches separated by τ_{sep}. The function $D(\alpha_d)$ is unity for small arguments, and decreases rapidly for larger ones. The form factor F_m is a function of the phase shift across the bunch $\Delta\Phi = \omega_r \tau_L$. It has maxima for the m[th] mode when the argument is $m\pi$, decreasing approximately as $1/m$.

The required damping of the higher modes in the rf cavities, kicker tanks and other incidental cavities can be calculated only when their frequencies, shunt impedances and quality factors have been measured. Computer programs like BBI [20] or ZAP [21] can be used to perform the necessary summations over all impedances.

4.3.3 Transverse stability criterion

The criterion for stability against transverse coupled bunch modes can be written as [16]

$$|Z_{\perp z}| < F \frac{4 B_f E}{e\beta\langle\beta_z\rangle I_b}\left[\frac{\Delta E}{E}\right]_{\rm FWHM} |S_z| , \qquad (4.23)$$

where the *effective tune spread* is $S_z = (n - \nu_z)\eta + \xi_z$, with n an arbitrary integer. However, instability occurs only for *slow waves* with $n > \nu_z$. The form factor F depends on the transverse particle distribution, but is large compared to unity for a space charge dominated impedance as in the longitudinal case.

Stability becomes particularly critical when the spread $|S_z|$ is very small, which can happen when its two terms nearly cancel. For the proton driver, operating below transition energy, the slip factor $\eta = \gamma_T^{-2} - \gamma^{-2}$ is negative. If the chromaticity ξ_z also is negative, the two terms add and cannot cancel. The lowest value of the spread is obtained for n just above the tune ν_z. Since also $|\eta| \approx ½$, the first term in S_z can be neglected if the (negative) chromaticity is large enough. For $F = S_z = 1$, the transverse impedance threshold is approximately 14 MΩ/m. Hence the transverse impedance of over 50 MΩ/m could make the beam unstable. However, stability is already achieved with a form factor $F = 2$ and a chromaticity $\xi_z = -3$.

4.3.4 Cures

The design of the vacuum chamber and the choice of material for the chamber walls are most important to keep the resistive wall effect small. Sufficient shielding of the magnetic pole pieces is necessary if they form part of the vacuum chamber or are separated only by ceramic or composite walls.

The obvious cure for HOMs of the cavities is damping by lossy material inside or by coupling the offensive modes into a load. A larger energy spread would increase the safety margin for Landau damping and could be obtained simply by increasing the (negative) chromaticity. The transverse feedback system would only be required for the lowest unstable oscillation frequencies and could thus be rather inexpensive.

4.4 Electron-Proton Instability

4.4.1 Equations of motion

When a proton beam is partially neutralized, with fractional neutralization χ_e, the electrons in it will start to oscillate transversely with the so-called *bounce frequency*. For small amplitudes it is given by

$$\omega_e^2 = 4c^2 r_e n_p \,, \qquad (4.24)$$

where $r_e = 1.535 \times 10^{-15}$ m is the classical electron radius, and $n_p = N_p/(\pi a_x a_y L_b)$ is the volume density of the protons in a bunch with N_p protons, cross section $\pi a_x a_y$ and full length L_b.

The oscillating electrons will also excite the protons to oscillate with frequency

$$\omega_p^2 = 4c^2 r_p n_e = 4c^2 r_p \chi_e n_p \ . \qquad (4.25)$$

The coupled oscillations lead to a dispersion relation for the *e-p oscillation frequency* ω as a function of the azimuthal mode number *n*:

$$(\omega_e^2 - \omega^2)[\omega_\beta^2 + \omega_p^2 - (n\omega_0 - \omega)^2] = \omega_e^2 \omega_p^2 \ . \qquad (4.26)$$

The amplitudes of the lighter electrons will grow rapidly, while the oscillations of the heavier proton remain smaller. When electrons reach the vacuum chamber wall, more electrons may be generated by *secondary emission*, which can lead to an avalanche effect called *multipactoring*. This may then lead also to emittance growth or beam loss of the protons.

4.4.2 Observations

Electron-proton oscillations have been seen in a number of *proton storage rings* (PSRs), and were overcome by different means. In a small PSR at the INP in Novosibirsk, constructed mainly for the study of charge exchange injection, these oscillations could be overcome by a simple feedback system. In the CERN ISR, electrons impinging on the chamber wall caused periodic background spikes, and had to be eliminated by better clearing and pumping. However, at the PSR in Los Alamos (LANL), the e-p instability was limiting the beam current for many years to values below the design goal. All attempts to eliminate or at least reduce the number of electrons failed.

The most common method to reduce neutralization of a beam is to leave a gap in the train of bunches; this has also been foreseen for the Fermilab proton driver. A more active method is to install clearing electrodes, and eliminate the electrons by applying transverse electric fields. If the electrons are generated by vacuum, better pumping may help—but not if the electrons are coming from the H^- stripping foil. Multipactoring at the wall can be reduced by coating with a material with a low secondary emission coefficient, such as Ti-N. If nothing else helps, a feedback system can be the solution. For the case of the LANL PSR, all these methods were tried and failed, and only a combination of higher rf voltage, sextupoles, partial wall coating and finally an inductive insert permitted reaching the design current.

A particular encouraging experience comes from the spallation source ISIS, where no e-p instability has ever been seen, even when the vacuum pressure was increased by switching off several pumps. The instability did not even occur when the machine was not running as a rapid-cycling synchrotron but with stored beam. This observation is not fully understood, and further studies are being made, both theoretically and experimentally.

The main conclusion is that a very low vacuum is mainly required for storage rings, not for a rapid cycling synchrotron as the Proton Driver where the beam is present only

for a short time. Furthermore, electrons are created by many other processes in addition to residual gas ionization. A vacuum at level 10^{-7} Torr is therefore considered sufficient. This is still economically achievable even with the magnet inside the vacuum, which has a rather high out-gassing rate due to various exposed epoxy surfaces. This approach, shielding by a liner made from copper strips to reduce the impedance of the exposed ferromagnetic pole pieces while keeping eddy current losses small, is presently considered the preferred solution for the vacuum chamber of the Fermilab Proton Driver.

References

[1] J. Laslett, BNL Report 7534, (1963) p. 234.
[2] Z. Qian, private communication.
[3] S. Wolfram, MATHEMATICA, Cambridge Univ.Press (1996).
[4] R. Baartman, AIP Conf. Proc. 448 (1998) p. 56.
[5] A. Chao, M. Tigner, Handbook Accel. Physics, World Scientific (1999).
[6] A. Chao, Physics of Collective Beam Instabilities, Wiley (1993).
[7] J. Norem, et al, Proc. PAC Vancouver 1995, p. 396; D. Trbojevic, et al, Proc. PAC Vancouver, 1995, p. 1030.
[8] J. Maclachlan, et al, Fermilab Report 1650, 1990.
[9] K.Y. Ng, Fermilab Report FN-702, 2000.
[10] I.M. Kapchinakij and V.V. Vladimirskij, Proc. 2nd Int. Conf. on High Energy Accel. and Instr., CERN, Geneva, 1959, p. 274.
[11] S.Y. Lee and H. Okamoto, Phys. Rev. Lett. **23**, 5133 (1998).
[12] C. Prior, Track-2D, private communication.
[13] F. Caspers, Proc. PAC New York, 1999, p. 1408.
[14] I. Gardner et al, Part. Accel. **31**, 227 (1990).
[15] F. Sacherer, CERN Report CERN/MPS/BR 73--1, 1973; IEEE-NS **20**, 3, 825 (1973). Proc. PAC San Francisco, 1973.
[16] F. Sacherer, CERN Report 77-13, 1977.
[17] A. Piwinski, DESY Report 1978.
[18] R. Gluckstern, US Acceler. School, Phoenix, AZ, Jan. 2000, to be published as a CERN Yellow Report.
[19] D. Moehl, A. Sessler, "rf knockout," LBL Report 1970.
[20] A. Hofmann, et al, IEEE-NS **26**, 3514 (1979).
[21] M. Zisman, et al, LBL Report 21270, 1985.

Chapter 5. RF Systems

M. Champion, W. Chou, J. Griffin, K. Koba, J. MacLachlan, A. Moretti,
M. Popovic, Z. Qian, J. Reid, J. Steimel, D. Wildman

5.1. Introduction

In this section two completely separate Proton Driver rf systems are described. Because of space limitations in the lattice it will not be possible to install and/or operate the two systems concurrently. For Stage 1 operation, a 37 - 53 MHz rf system will be installed. Development for this application of a large aperture (5"), increased voltage modification of an existing Fermilab Booster rf cavity is described in Sec. 5.2.2. As an alternative, efforts have begun on modification of the TRIUMF/SSC style orthogonally biased ferrite rf cavity, cf. Sec. 5.2.3.

For Stage 2 operation the 53 MHz system will be removed, and a lower frequency, harmonic number 18, rf system will be installed. For this system, development of an rf cavity using a new nanocrystalline soft magnetic material, Finemet, is described in Sec. 5.3.2. The lower frequency cavities may use some ferrite tuner components obtained from the removed 53 MHz cavities for tuning during acceleration.

The rf parameters for the two stages are summarized in Table 5.1.

Table 5.1. Summary of RF Parameters

Stage 1 rf parameters (Section 5.2)	Stage 2 rf parameters (Section 5.3)
Harmonic number 126, with 119 occupied buckets.	Harmonic number 18, with all buckets occupied.
Extraction longitudinal emittance, (95%), 0.1 eV-s per bunch.	Extraction longitudinal emittance, (95%), 0.4 -0.5 eV-s per bunch.
Rf frequency range: 37.8 - 53 MHz.	Rf frequency range: 5.4 - 7.6 MHz.
Maximum ring voltage: 1.2 MV.	Maximum ring voltage: 1.4 MV
Average rf power to beam (66.6 ms period) ~ 835 kW	Average rf power to beam (66.6 ms period) ~1.2 MW.
Peak rf power to beam capability ~2 MW.	Peak rf power to beam capability ~ 2.9 MW.
	Extracted bunch length ~ 1 ns rms (neutrino source operation).

Section 5.2, (Stage 1), describes an rf system which is consistent with use of the Proton Driver as an injector for the Main Injector ring in "normal" operation. In this mode the ring will operate from injection energy 400 MeV to extraction energy 12 GeV with intensity ~3×10^{13} protons per cycle. The guide fields will be sinusoidal at 15 Hz, with a 12.5% second harmonic component, phased so as to optimize certain rf voltage and bucket area parameters.

Section, 5.3, (Stage 2), describes an rf system to be used in neutrino source service, but also capable of injecting widely spaced intense bunches into matched Main Injector buckets. In this mode the extraction energy will be 16 GeV with beam intensity 3×10^{13} protons per cycle. Guide field parameters will be similar to those described above.

In each case the rf accelerating voltage, $V\sin\varphi_s$, is defined uniquely by the ring circumference and the rate of rise of the magnetic guide field, dB/dt. The additional rf voltage necessary to obtain the design intensities, longitudinal emittances, and bunch configurations proposed for each of the Proton Driver stages have been elucidated through extensive simulations of rf capture, acceleration, and bunch manipulation prior to extraction, using the code ESME. In each case the effect of installation of space charge compensating inductance (see Section 5.1.1) has been included in the calculations. Also, the higher harmonic effects of frequency variation of the parameters of the introduced inductance have been simulated. Descriptions of these simulations and their results for Stage 1 and Stage 2 acceleration are presented in 5.2.1, 5.2.2, 5.3.1, and 5.3.2. For injection into the Main Injector, the rf voltage and bucket area will be adjusted during acceleration such that extracted bunches will be matched to stationary buckets in the Main Injector. In neutrino source application, the rf voltage will be manipulated prior to extraction so that the extracted bunch length will be ≤ 1 ns rms.

5.1.1 Beam Loading.

With intensity 3×10^{13} protons per cycle, design techniques for compensation of various forms of beam loading must be incorporated. This is especially true in Stage 2, where, at $h = 18$, the charge per bunch will be 1.67×10^{12} protons per bunch (0.27 μC). The amplitude and phase of the net rf voltage will be affected by cavity excitation by fundamental and lower harmonic Fourier components of the beam current. These beam loading errors are to be corrected by a global feedback system in which unwanted beam phase motion, detected by broad-band beam pick-ups, will be compensated for by correction signals delivered to each rf station. Global feedback systems are described in 5.2.4, 5.2.6, 5.3.3, and 5.3.5.

Below transition the charges in each bunch interact with the vacuum chamber conducting wall in such a way as to reduce the rf focusing force and bucket area [1]. It has been pointed out, by A. Sessler and V. Vaccaro [2], that this "potential well distortion" may be minimized by the intentional introduction of inductance into the vacuum chamber.

The effect of installed inductance has been studied in the KEK Proton Synchrotron. Because the potential well distortion moves with the charge distribution, the coherent synchrotron dipole phase oscillation frequency is not affected. Predicted changes in incoherent phase oscillation frequency, representing changes in the bucket area, were observed by measurement of the synchrotron quadrupole frequency as a function of beam intensity with fixed rf voltage [3,4].

In a Fermilab-Los Alamos collaboration experiment, inductances sufficient to cancel a large fraction of the space-charge potential well distortion were installed in the Los Alamos Proton Storage Ring (PSR). The PSR beam intensity has been limited by the onset of a transverse ep instability caused by electrons trapped in the proton beam potential well. An h = 1 rf bunching system is operated to create a gap in the proton beam to allow trapped electrons to escape. With increasing beam intensity the effectiveness of the rf system is compromised by beam induced potential well distortion, and small numbers of protons escape the rf generated potential well and drift into the gap. Initial results of the experiment indicated that the inductors increased the effectiveness of the rf bunching system such that significantly larger beam intensities could be attained [5,6].

Because of the geometry of the introduced ferrite rings and the real and imaginary properties of the ferrite permeability at high frequency, the installed inductors caused an unacceptable self-bunching (microwave-like) instability. This problem was solved by heating the ferrite in such a way that the Q and the shunt impedance of the offending resonance were reduced so that no instability occurs at the PSR design intensity. An added benefit of the heating is that the real permeability of the ferrite is increased to a level such that the installed inductors almost exactly cancel the beam-induced distortion. No additional inductance was required to reach the design intensity.

The Proton Driver design group will take advantage of the added inductance to minimize the requirement for installed rf capability in the 53 MHz Stage 1 design. It may also be useful to utilize installed inductance to enhance the performance in Stage 2 following injection capture and during bunch manipulation to create narrow bunches.

5.1.2 Direct Space Charge Compensation

As the 0.27 μC charges in each bunch (Stage 2) pass through the gap capacitance C of each rf cavity, a decelerating voltage approaching q/C may be developed, so that the charges in the bunch do not all see the same accelerating voltage. If, for instance, the effective gap capacitance were 100 pF, the voltage developed may reach 2.7 kV, a significant fraction of the design gap voltage. The developed voltage may be reduced by increasing the effective gap capacitance (effectively lowering the cavity R_s/Q). At significantly higher beam intensity (a future possibility), the effect may be countered through the addition of a second power amplifier tube with its anode connected directly to the down-stream side of the gap capacitance. This additional tube may be pulsed in a feed-forward configuration so that it delivers an electron charge to the gap capacitor approximately equal to the beam bunch charge during the bunch passage, thus minimizing the pass through charging effect of the beam.

5.1.3 Single Frequency High Gradient Burst Mode RF Cavity

Research and development for a very high gradient fixed low frequency rf cavity, (~ 600 kV per meter), is in progress here and at KEK Japan. Such a cavity could be installed to add to the rf voltage during bunch rotation for the development of narrow bunches at extraction.

5.2. Stage 1 (53 MHz) RF

5.2.1 RF Voltage, φ_s, Bucket Area, Simulations

In Phase I the Proton Driver is used with the Main Injector and possibly a neutrino factory; the defining property is a beam intensity of 3.0×10^{13} protons/pulse. In Stage 1 the Proton Driver serves only to replace the present Booster for injection into the Main Injector and possibly for low energy neutrino production. It will employ refurbished Booster rf cavities, modified to give a 5 inch aperture. The design parameters used to define the rf requirements for Phase I, Stage 1 are collected in Table 5.2.

Table 5.2. Stage 1 Proton Driver rf Parameters

E_{inj}	injection kinetic energy	400	MeV
	Beam intensity	3×10^{13}	p/cycle
	Cycle repetition	15	Hz
E_{ex}	extraction kinetic energy	12	GeV
R_{eq}	circumference/2π	113.21	m
V_{rf}	maximum rf voltage	1.2	MV
V_{acc}	accelerating voltage at dp/dt max	1.09	MV
h	harmonic number	126	
	number of populated buckets (at extraction)	119	
ε_l	longitudinal emittance at extraction	0.1	eV-s
	bunch intensity	2.5×10^{11}	
ΔE_{inj}	energy spread at injection	± 0.5	MeV
α_0	momentum compaction	-1.306×10^{-3}	
α_1	coefficient of $(\Delta p)^2$ in path length	8.252×10^{-2}	
b	vacuum chamber radius	6.35	cm
a	mean beam radius at injection	4.44	cm

The combination of performance demands with the mandated use of the 400 MeV Linac injector and modified Booster cavities calls for some unconventional measures. The specified intensity and emittance put the Proton Driver into the class of high brightness synchrotrons. The space charge impedance corresponding to the perfectly conducting wall force is $Z_{\|}/n \approx -340i\ \Omega$ at injection energy. To control the space charge defocusing, a tunable inductive insert is proposed, which will cancel this impedance throughout most of the cycle. The insert looks very attractive in the modeling; it makes the difference between 96.8 % and 99.99% for the particle transmission efficiency of the complete cycle. The idea is not new [2]; it has been tried in two different machines (Section 5.1.1). However, the studies have not been carried out over a wide range of beam energy or momentum spread and more beam studies are needed.

The next subsection gives curves for the time dependence of parameters, which change during the acceleration cycle; it is followed by a subsection with details of the

scenario, beam physics, and description of the optimization process, considerations substantially reducing the scope for arbitrary choice of the parameter curves.

5.2.1.1. Parameter Programs – Stage 1 RF Curves

The magnet ramp is driven by a 15 Hz resonant power supply plus an independent second harmonic supply that is adjusted in phase and amplitude to minimize the required peak rf voltage. The fixed parameters are those in Table 5.2. The design optimization has been carried out primarily by multi-particle tracking simulation; the results include the time curves, a demonstration of potential for low loss operation, and a demonstration that the specification for longitudinal emittance at extraction is reasonable. Because the rf voltage limit is so stringent, loss limitation naturally relates closely to longitudinal emittance preservation.

The curves in Figs. 5.1 - 5.5 present the momentum p, its time derivative dp/dt, the peak rf voltage $V_{rf,}$ the synchronous phase ϕ_s, and the h = 1 reactance of the inductive insert. In this last case, three optimum levels with optimum break times are shown. Also shown is a continuous dotted curve, calculated to just cancel the space charge force. The issues related to the optimum for this curve are examined in the following subsection.

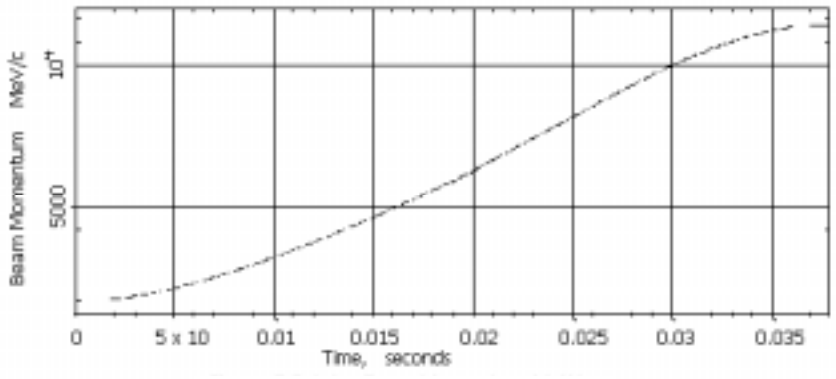

Figure 5.1. Beam Momentum, MeV/c

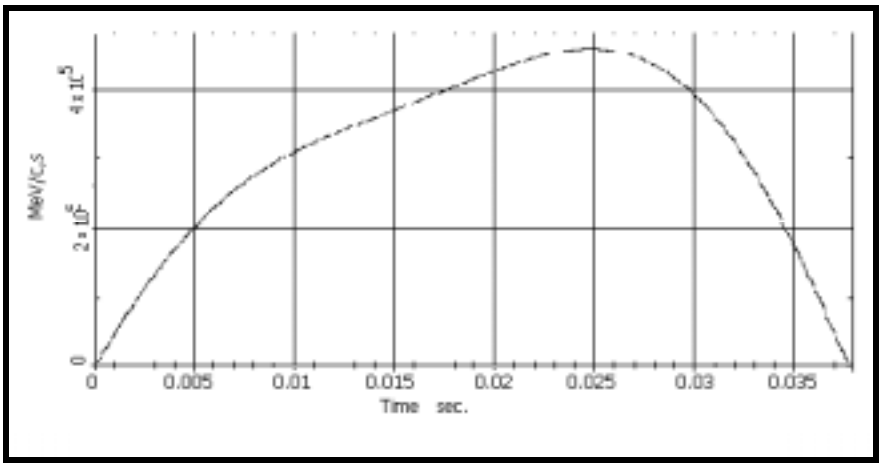

Figure 5.2. Rate of change of momentum, dp/dt vs. time, Stage 1

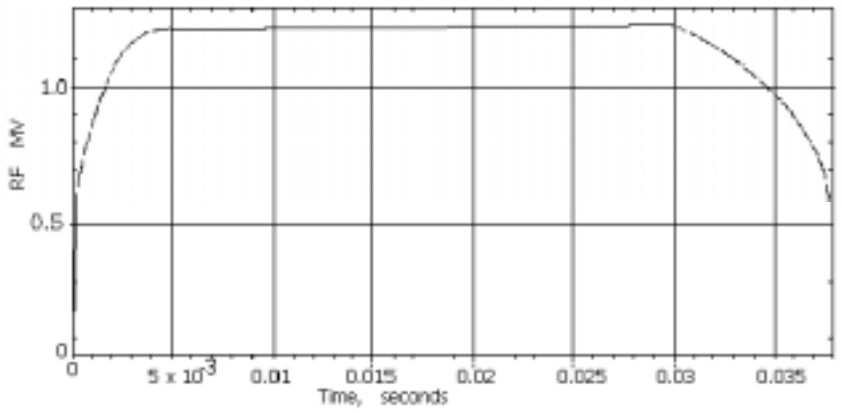

Figure 5.3. Stage 1 rf voltage in MV

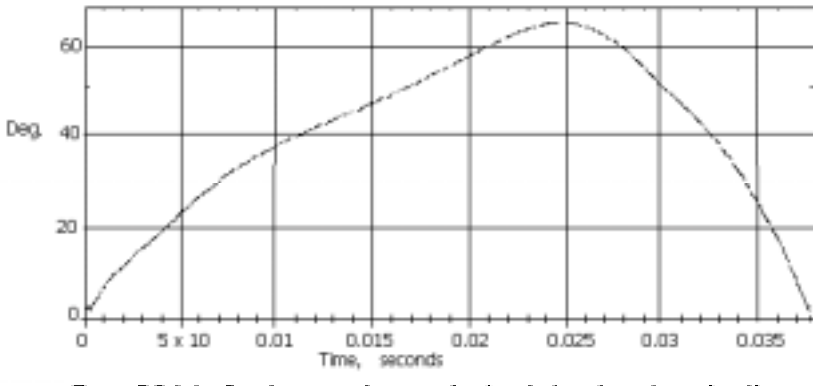

Figure 5.4. Synchronous phase angle, ϕ_s, during Stage 1 acceleration

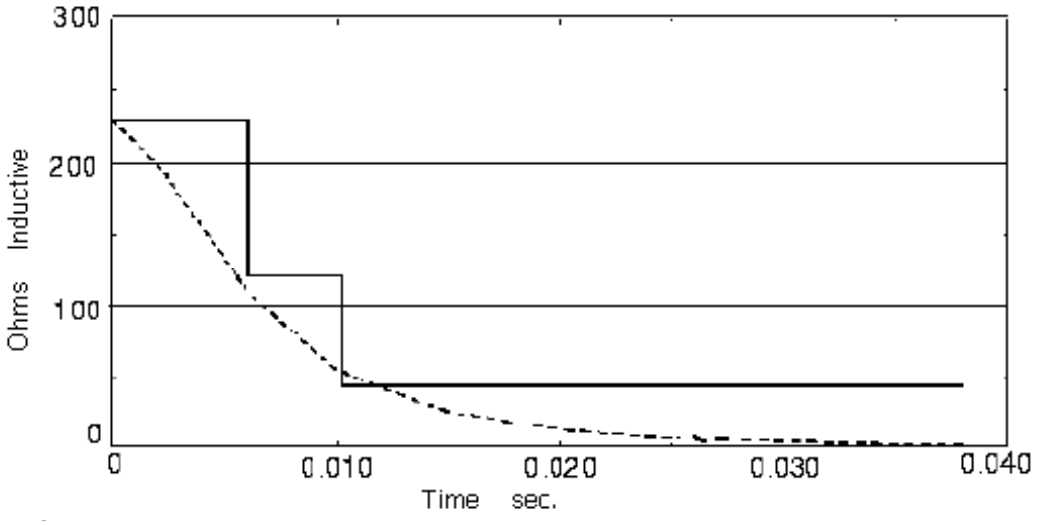

Figure 5.5. Reactance of the inserted inductor at rotation frequency (h = 1) as a function of time during acceleration

The curves in Figs. 5.6 - 5.8 present useful derived quantities, viz., synchrotron tune ν_s, bucket area S_B, and the rms longitudinal emittance per bunch ε_l.

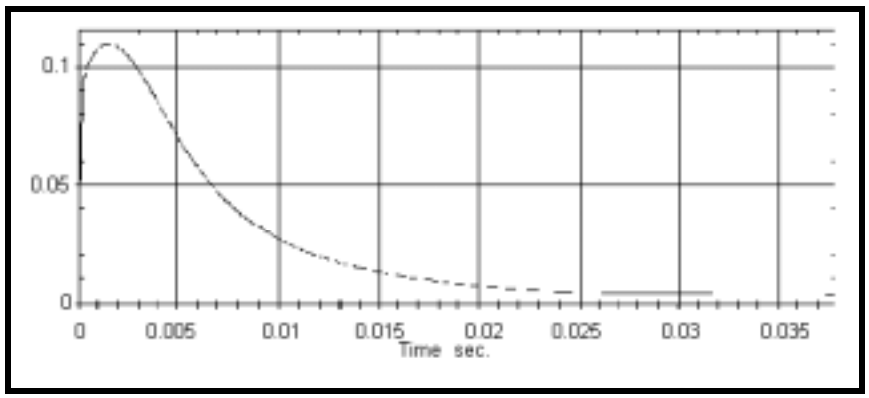

Figure 5.6. Small amplitude synchrotron tune, units of F_{rot}

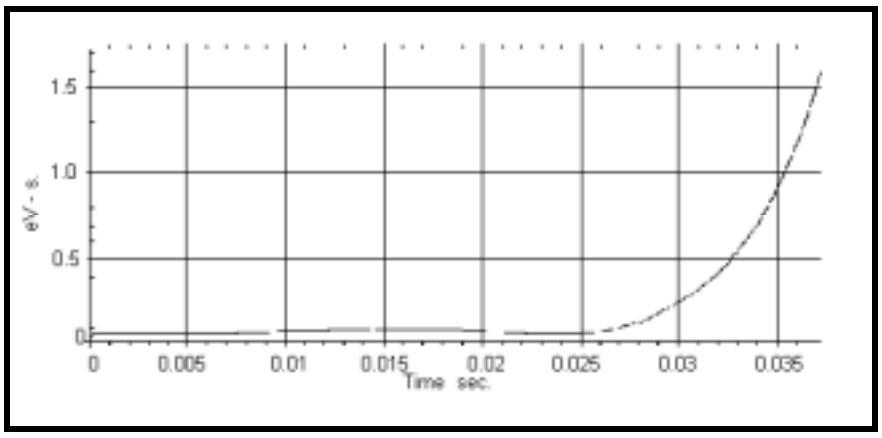

Figure 5.7. Stage 1 rf bucket area, eV-s

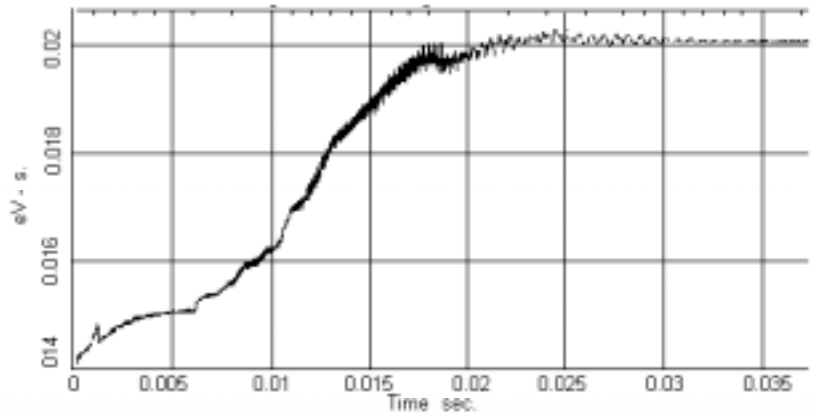

Figure 5.8. Stage 1, rms longitudinal emittance, eV-s

5.2.1.2. Capture and Acceleration – Stage 1 Scenario and Modeling

A macro-particle tracking model has been used for the entire cycle from multi-turn injection through matching to Main Injector buckets. The injected protons are assumed to be a continuous coasting beam lasting up to 90 μs, timed symmetrically about $dB/dt=0$. Other timings have been tried as well, but for an injection period this short nothing better has been found. For nominal Linac intensity, 70 μs is sufficient to give the required 3×10^{13} protons, but efficiency remains good over a longer injection time. A good approximation is to represent continuous injection by injections every other turn. The beam charge is raised in concert with the macro-particle injection; the perfectly conducting wall term and the inductive insert are the only sources of the collective potential included in these simulations.

The rf voltage is raised linearly during injection from 0 to 65 kV. Because of the large slip factor η for this machine, the particles near $\pm 180^{o}$ of rf phase are all captured in this simple maneuver. Certainly some are quite close to the separatrix and subject to later loss because of space charge and limited rf voltage, but these losses are essentially eliminated by use of the inductive insert. They could also be largely eliminated with a substantially higher rf voltage capability. After 226 μs, the voltage curve is changed to provide a bucket area that grows slowly to 0.064 eV-s at 4.96 ms. At this time the voltage has reached the design limit of 1.2 MV and it is held at that value until η has dropped sufficiently, at about 30 ms, to allow a reduction while continuing to increase the bucket area. dB/dt reaches zero at 37.93 ms. The voltage required for acceleration at maximum dp/dt is 1.09 MV, so there is little rf focusing. The synchronous phase reaches 64^{o}. Although dp/dt continues to increase, the magnet ramp has been tailored so that the bucket area does not decrease; in fact it rises slightly in the middle of the flat part of the voltage curve. Nonetheless, in the absence of the inductive insert there are losses at maximum dp/dt (about 0.025 s into the cycle). This indicates that the specified maximum rf voltage is marginal and the inductive insert could be very important.

There are three ways in which these modeling efforts have fed back to change somewhat the initial design ideas. One way is that the optimum magnet ramp has been determined as a minimum V_{rf} ramp rather than a minimum dB/dt ramp. Another change is the discovery of the apparent effectiveness of an inductive insert and its importance for low beam loss with h = 126 rf. Finally, it was noticed that the slip factor is so high at injection that the captured beam displays significant energy-phase correlation (bunch tilt). Precious bucket area is wasted; beam is lost because the momentum spread is increased by the tilt. Dividing the rf into 2 parts on opposite sides of the ring made a substantial improvement in the tilt and resulting loss. Dividing the rf into 3 equally spaced groups would make a small additional improvement. The planned configuration of the injection, extraction, and collimation systems may be inconsistent with the 3-way division.

Table 5.3 shows the injection-to-extraction transmission efficiency and emittance at extraction for different departures from the optimum modeling result. The top entry is the best result obtained, and each entry following gives the transmission when one condition is changed without attempting to re-optimize the other parameters. Possibly some of the

apparently lost efficiency could be recovered in such a re-optimization, but the intention is only to suggest the importance of various conditions to the optimum obtained. The lower final emittance for the more closely grouped cavities reflects directly the removal of halo by having the bunch tilted in the early part of cycle. The 95% emittance at extraction is 0.08 eV-s for the optimum case.

Table 5.3. RMS emittance at extraction and fractional beam loss during a complete cycle for optimum parameters and cases each differing from the optimum in a single property

Optimum case	0.0201 eV-s 0.01%
All rf clumped	0.0154 eV-s 0.21%
rf in two sets	0.0181 eV-s 0.07%
no inductive insert	0.0247 eV-s 3.19%

Clearly the inductive insert is a significant element in this scenario; a limited amount of rf focusing is supplemented with a self-excited focusing voltage. The character of the inductance curve suggests that there is room for refinement here. It is natural to consider tuning the inductance to just cancel the space charge impedance at all times, and indeed this could be a satisfactory mode. However, it is not a straightforward matter because a pure inductance will not cause instability even if it over-compensates, and extra focusing should be helpful. There are at least three sources of real impedance which could decelerate self-excited bunches out of the 53 MHz bunch at some higher frequency, i.e. the inductor could cause self-trapping instability. The impedances which should be taken into account at a minimum in constructing a good model are the resistive wall, the broadband beam pipe impedance from miscellaneous sources (the usual $Z_{\|}/n$), and the resistive component of inductor impedance. Permeability and loss factor curves for a Transtek Yttrium garnet ferrite have been used. The real impedance of the inductor is approximated by a 45 MHz Q = 50 resonance with R_{shunt} = 13 kΩ; $Z_{\|}/n$ = 5 Ω is included in the impedance tables that represent the inductance of the insert.

The resistive wall term is expected to be important only for the multi-bunch effects. The stability issues have not been adequately treated in the modeling, which is aimed at the problems of bucket distortion and bucket area loss. The charge distribution is smoothed to take out high frequency fluctuations, which are principally numerical noise. Once a realistic longitudinal impedance has been specified, it will be appropriate to track a portion of the cycle with enough macro-particles to represent the beam current Fourier spectrum up to 1 GHz or so.

The inductive insert is an important area for development in modeling and in machine studies as well. The Fermilab Booster is a suitable machine for investigating the effectiveness of an inductive insert, and it has also a reasonable prospect for obtaining an operational benefit.

5.2.2 Fermilab Booster Cavity Upgrade

A proposal [7,8] to modify the existing Booster rf cavity was made in January, 2000. In this proposal, two goals were set forth: (1) to enlarge the cavity beam pipe aperture from 2.25 to 5 inches; (2) to increase the cavity voltage by 20%, from 55 kV to 66 kV. The motivation for this effort is twofold. For the existing Booster, aperture enlargement will result in less activation of the rf cavities and power amplifiers, thereby permitting access to the cavities for regular maintenance during future high duty factor operation. Increased cavity voltage will allow for operation with fewer than 100% of installed cavities, thereby reducing downtime due to unscheduled maintenance. For the Proton Driver, aperture enlargement is necessary to accommodate the higher beam intensity with acceptable beam loss. The increased cavity voltage is required to increase the beam energy from 8 to 12 GeV without increasing the acceleration cycle time.

5.2.2.1. Overview of existing Booster rf cavities.

The Booster depends on 18 rf cavities for acceleration, each cavity providing approximately 55 kV over a frequency of 37 to 53 MHz. Hence, a ring voltage of 990 kV is achieved. (A voltage increase of 20% would raise the ring voltage to 1188 kV.) The rf cavity is a center-fed coaxial double-gap structure with an electrical length of 136 degrees, gap-to-gap, as illustrated in Figure 5.9. The 150 kW power amplifier is mounted directly to the cavity and is coupled to the center conductor via a 1200 pF anode dc blocking capacitor. The cavity frequency is controlled by three ferrite-loaded variable inductors attached at the center of the cavity in parallel. The ferrite bias windings are series connected and driven by a 2500 A programmable bias supply. Near the accelerating gaps at each end of the cavity are 12 inch o.d. conical coaxial alumina windows separating the beam vacuum from the air-filled center section of the cavity. The gap spacing is 0.9 inches and the beam aperture is 2.25 inches. The cavity anode to gap voltage step-up ratio varies from 1.2 to 1.6 over the tunable frequency range. Figure 5.10 is a photograph of the cavity.

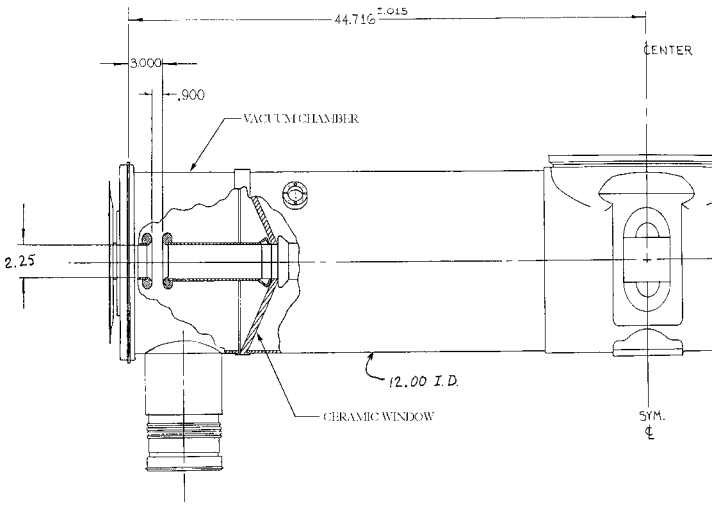

Figure 5.9. Detail of Booster cavity gap geometry

Figure 5.10. Booster cavity with ferrite tuner in foreground

5.2.2.2. Prototype large aperture Booster rf cavity; aperture enlargement and tuning.

A damaged Booster rf cavity has been the basis of the prototype work to date. Both ceramic windows, one of which was already broken, were removed to allow for extraction of the cavity center conductor. The center conductor was cut off along the taper on both sides of the center hub and new 5.5 inch outside diameter ends were attached along with variable spacing gap electrodes. The 5.5 inch diameter was chosen to allow for an inside diameter of 5 inches including the required vacuum beam tube and a high permeability cylinder intended to shield the beam from tuner magnetic fields. The end plates of the cavity were modified to match the 5 inch aperture. Gap spacing up to 3 inches can be achieved with the prototype cavity. Alumina washers were purchased to approximate the capacitive loading that will be present in a new vacuum window design.

As a first step, two standard Booster cavity ferrite tuners were mounted on the modified cavity prototype and measurements were performed with a special cut-away power amplifier that allows access to the amplifier tube anode via the screen basket. The impedance at the anode of the tube can be measured by inserting the probe of a vector voltmeter into the screen basket between the anode and screen. The ferrite tuner bias current is set and the frequency of the vector voltmeter is adjusted until a phase angle of zero, (real load), is indicated. Following this procedure, curves of anode impedance versus resonant frequency may be measured for various configurations.

Three tuner configurations were explored: two Booster tuners, three Booster tuners, and two Booster tuners with one Main Injector tuner. The resulting anode impedance versus cavity frequency is shown in Figure 5.11. For comparison, the data for a standard Booster cavity is included. Clearly the lower inductance of the Main Injector tuner is necessary to make up for the increased capacitance resulting from the cavity aperture increase. Two different gap spacings were investigated: 0.9 inch and 2 inch. As expected, the larger gap spacing results in a slightly higher upper frequency limit due to

the decrease in gap capacitance. These data do not extend to higher frequencies because the first measurements were performed using only a 1000 A bias supply.

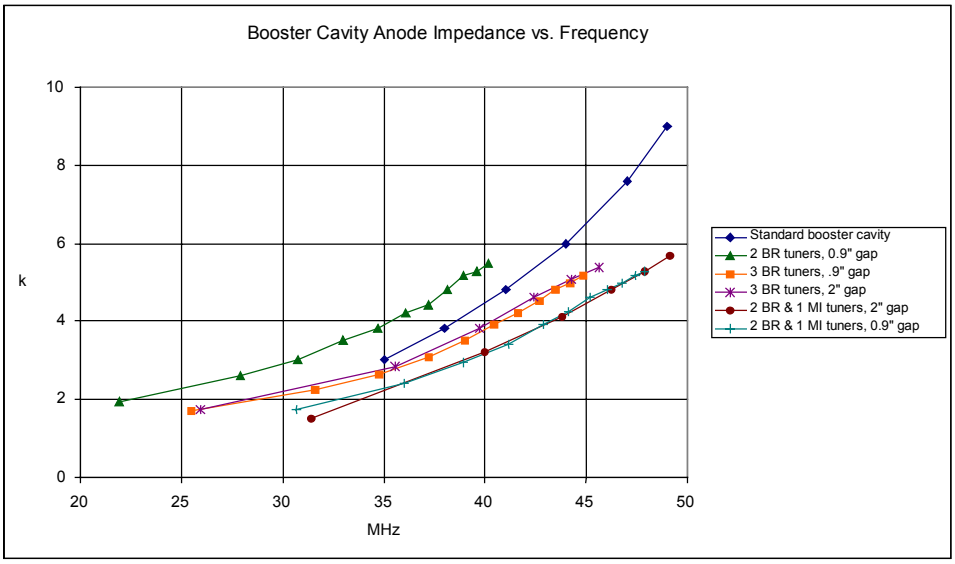

Figure 5.11. Curves of prototype cavity anode impedance versus resonant frequency for various tuner and gap configurations

Based on the foregoing results, the prototype cavity, configured with two Booster tuners and one Main Injector tuner, was moved to the MI–60 test station, where first tests with a 2500 A bias supply were recently performed. Bias currents from 0 to 2500 A provided a frequency tuning range from 29.8 to 53.4 MHz with a gap spacing of 0.9 inches. For comparison, a standard Booster cavity has a maximum frequency of 53.3 MHz. These data are shown in Figure 5.12.

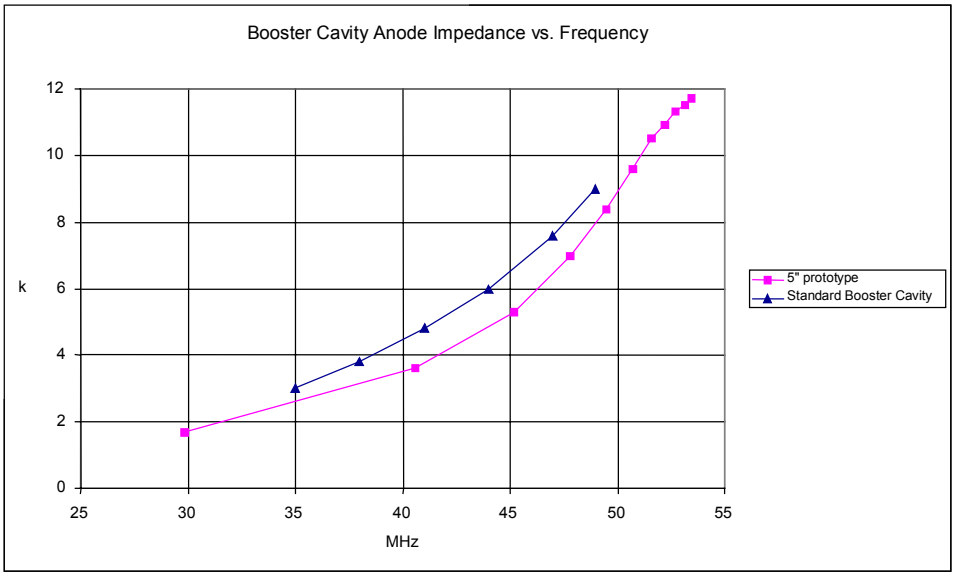

Figure 5.12. Curves of anode impedance versus resonant frequency comparing the prototype and standard Booster cavities

5.2.2.3 Cavity shunt impedance, Q, and R_s/Q

The impedance shown is the impedance presented to the power amplifier by the cavity with no beam loading. These impedances, coupled with the tube anode rf swing, can be used to calculate the dissipation in the cavity. However, they do not represent the true shunt impedance of the cavity as seen by the beam. The beam effective shunt impedance is obtained by multiplying the measured anode impedance by $4 \times S^2 \sin^2 \Delta$, where S is the voltage step-up from hub to gap and Δ is the hub to gap electrical length.

The prototype R_s varies from ~ 11 kΩ to 56 kΩ between 30 and 50 MHz. The Q of the prototype cavity has recently been measured to vary from ~230 to 900 over the same frequency range. From these data it can be inferred that the effective R/Q ranges from ~50 to ~60, reaching a maximum value ~69 at 45 MHz.

5.2.2.4 Raising the Voltage

Achieving higher ring voltage might be accomplished in several ways. One technique is to simply install more cavities. There exist enough Booster cavity components to install a total of 21 modified cavities in the Proton Driver, and sufficient rf space exists in the lattice to accommodate these cavities. With 21 cavities operating at the present voltage of 55 kV per cavity, a ring voltage of 1155 kV would be obtained. This figure is not far from the 1188 kV number derived from 18 cavities operating at a 20% higher voltage (66 kV). A second way to achieve higher voltage is to raise the anode voltage on the power tubes to approximately 30 kV. This technique will be explored on the test station at MI–60 upon completion of the high power prototype cavity. A third way to higher voltage is to decrease the capacitance of the anode blocking capacitor from 1200 pF to 400 pF, thereby increasing the step up ratio of the cavity by about 20%. A low power prototype 400 pF capacitor has been fabricated and installed on a standard Booster cavity, and indeed an increased step up ratio was achieved, as shown in Figure 5.13. It is planned to modify an existing 1200 pF blocking capacitor in a way that will allow for high power testing in the future.

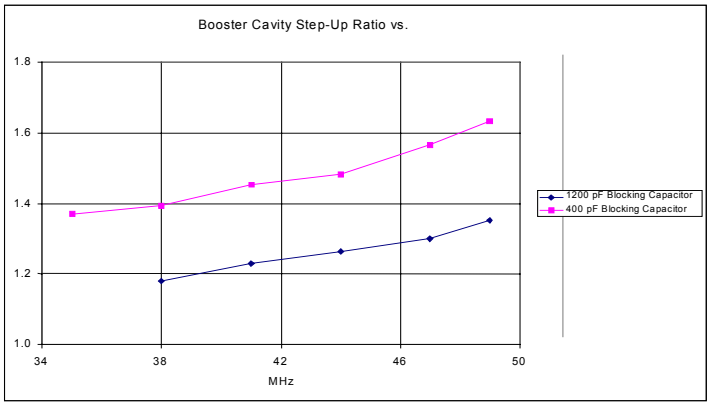

Figure 5.13 Standard Booster cavity anode-to-gap step-up ratio with 1200 pF and 400 pF blocking capacitor

One potential problem with increasing the voltage per cavity is the voltage breakdown limit of the existing ferrite tuners. The stem connection is the first place to break down when operating at high voltages. High power rf tests with the prototype cavity will confirm the maximum operating voltage as determined by this tuner limitation. This limitation might be overcome by increasing the length of the tuner stem, thereby inserting a series inductance over which some rf voltage will be dropped. This would require a somewhat different tuning inductance with which to achieve the desired frequency range of 37 to 53 MHz.

5.2.3 TRIUMF RF Cavities

An alternative to rebuilding the present Fermilab Booster rf cavities is to construct twelve new orthogonally biased rf cavities similar to the Los Alamos/SSC/TRIUMF design [9]. This type of cavity offers three clear advantages. First, higher peak accelerating voltage of 100 kV/cavity (the TRIUMF cavity has been run for several two hour intervals at 50 Hz at 62.5 kV on the gap) will require only two thirds the number of cavities in the ring. Secondly, the accelerating gradient of 94 kV/m is three times the 29 kV/m anticipated in the modified Booster cavity. This reduces the total length of the rf straight sections by a factor of three. Thirdly, the use of orthogonally biased garnets instead of the present Ni-Zn ferrites reduces the rf losses in this cavity design by at least a factor of two.

The TRIUMF prototype cavity, shown in Figure 15.14 is now at Fermilab. It has a 6 inch aperture and is tunable from 36 to 53.4 MHz. Tuning is provided by six, 60 cm OD × 30 cm ID, Trans-Tech G810 aluminum doped yttrium garnet rings. These rings are orthogonally biased by a toroidal C-magnet excited by bias current from 500 to 1050 amps. The TRIUMF cavity Q ranges from 240 to 2000 and the shunt impedance increases from 12.4 kΩ to 88 kΩ as the resonant frequency is raised. The cavity final amplifier is powered by an Eimac Y567B tetrode, identical to those used in the present Booster, Main Injector, and Tevatron rf systems.

Figure 5.14. TRIUMF Prototype Cavity

An additional six months of development work would be useful in evaluating the TRIUMF cavity. One item that needs further investigation is the cavity's

non-linear frequency response at high rf magnetic fluxes. This effect, also observed in some ferrites, is characterized by a shift in the cavity's resonant frequency to a lower frequency as the gap voltage approaches its maximum value. This frequency shifting will add an extra complication to dynamically tuning the cavity during acceleration. However, it is anticipated that a fast feedback loop around each rf station should be able to keep the cavity tuned to the correct frequency.

5.2.4 Steady State Beam Loading, Robinson Detuning.

Robinson's inequalities for maintaining longitudinal stability in the presence of beam loading are shown below. The first inequality states that the cavities must be tuned such that the fundamental frequency lies just below the resonant frequency of the cavity (below transition). The ferrite tuning loops automatically maintain this condition.

$$0 < \sin\left(2\,\Psi_z\right) < 2\,Y\cos\left(\Psi_B\right) \qquad Y := \frac{I_B}{\mathrm{Re}\left(I_T\right)}$$

The second inequality states that the cavities must deliver more power to the beam than the beam delivers to the cavity. Assuming that each cavity can deliver about 30kV to a gap with a shunt impedance of about 15 kΩ, the ratio of the beam current with respect to the in phase current of the cavity is about 1. This is still considered stable, but it is very close to becoming unstable.

The transient voltage caused by the six-bucket extraction kicker gap in the beam is less than 0.1% of the total accelerating voltage. Since transient compensation will not be necessary, only fundamental compensation is required. The same system used in the Main Injector for fundamental feedback can be modified for use in the Booster. It can provide an increase in the beam current threshold by about a factor of 14 (assuming about the same group delay from cavity drive to the gap). This will allow the RF voltage to be decreased to about 85 kV before beam loading becomes significant.

5.2.5 Stage 1 (37 - 53 MHz) RF Cavities, Power Supplies, Total Power, Water

Table 5.4 summarizes equipment and installation requirements.

Table 5.4. Equipment and installation requirements

37 - 53 MHz RF Cavities	20 Existing Booster Cavities Modified for 5 inch Aperture
High Level RF	20 High Level Booster Stations Required. Use 18 existing Ferrite Bias Supplies Use 18 existing IRM station control & data acquisition systems
New Equipment;	(20) - 200 kW Power Amplifiers. (20) - 30 kV Series Tube Modulators (20) - 6 kW Solid State Wide band Drivers. (2) - Additional Ferrite Bias Supplies (0-2500A). (2) – 35 kV Anode Power Supplies.

Existing Booster cavities will be modified to increase their aperture from 2-1/4 inch to 5 inch and gain approximately 20% in accelerating voltage over their nominal operating voltage. A large aperture prototype cavity is presently under construction. The cavity modifications are described in detail in Section 5.2.2.

Remaining components required to complete a high level station fall into two groups, one is new equipment and the other is reuse of existing equipment. Twenty rf stations are planned to meet the required 1.2 MV of peak accelerating voltage (66 kV/cavity).

A prototype 200 kW rf power amplifier is currently undergoing preliminary testing on the Booster test station at MI-60. This amplifier is a modified Main Injector amplifier with a broadband cathode drive circuit for operation over the frequency range from 37 MHz to 53.1 MHz. It utilizes the Eimac (CPI) Y567B power tetrode presently used in the Booster and Main Injector power amplifiers. This rf amplifier is grounded grid for rf but programmed dc grid bias for optimizing tube performance during the rf envelope. The amplifier will be driven by a 6 kW solid state MOSFET amplifier located in the equipment gallery.

The 6 kW wideband Solid State Driver Amplifier design is based on the Main Injector's 4 kW amplifier but with two additional 1 kW rf modules. This is a proven design with very high reliability. The 1 kW rf modules are produced by a commercial vendor.

The 30 kV Series Tube Modulator is basically a Main Injector modulator with minimal modifications. It utilizes the same Eimac (CPI) Y567B power tetrode and has a proven reliable track record. Construction drawings exist and fabrication would be straightforward.

Additional ferrite bias supplies would be exact copies of existing ferrite bias supplies presently used in the Booster. They have a proven 25-year design and are highly reliable. Construction drawings exist and fabrication would be straightforward.

Two new 35 kV 2.5 MW anode power supplies would be built. Each anode supply would supply 10 rf stations. These will be very similar to the Main Injector's anode supplies. New 13.8 kV electronic switch-gear, fused disconnect, 2 MW rectifier transformer, along with associated DC components are needed. They would be configured with an indoor DC enclosure containing the main rectifier stack, interphase reactor, capacitor bank, crowbar circuit, and high voltage disconnect switches.

Two additional IRM stations for digital I/O and analog monitoring are required. These are standard units and are widely used around the laboratory so additional units are available.

At least one and possibly two relay racks will be required per station. They will contain the station's remote controls and low level rf station control modules. Additional station control modules will have to be built since presently we are running 18 rf stations in the Booster.

To summarize, the existing equipment that will be reused consists of 18 each of ferrite bias supplies, IRM station control for digital I/O and analog monitors and control, and rf station control modules.

Overhead cable trays of standard 18 inch wide by 5 inch deep (pre-galvanized) will carry signal cables only. All rf signal cabling in trays will be HELIAX type cable. Trays will be supported approximately every 5 feet.

Since the rf system will be installed in a new building, all of the supporting utilities for the high power rf systems will be installed as part of the building construction. The LCW piping, 480/208/120 Volt AC power distribution, and cable trays will be an integral part of the construction.

Table 5.5 summarizes electrical power requirements (AC power duty factor = 50%) and Table 5.6 is a summary of cooling requirements.

Table 5.5. Summary of Electrical Power Requirements

480 Volt 3-phase		**Per station**	**20 Stations**
	Ferrite Bias Supply	105 kW	2100 kW
	Series Tube Modulator:	20 kW	400 kW
	Solid State Driver Amp	12 kW	240 kW
	RF Pump room		350 kW
120/208 volts			
	Relay racks	3 kW	60 kW
	Ion pump PS	1 kW	20 kW
	Miscellaneous	2 kW	40 kW
13.8kV			
	Anode Supply # 1		2000 kW
	Anode Supply # 2		2000 kW
Total Power			**7210 kW**

Table 5.6. Summary of LCW Cooling Requirements (duty factor = 50%)

95 Degree LCW		**Per station**	**20 Stations**
	Ferrite Bias Supply	17 gpm	340 gpm
	Series Tube Modulator:	35 gpm	700 gpm
	Solid State Driver Amp	12 gpm	240 gpm
	RF Cavity	35 gpm	700 gpm
	200 kW Power Amplifier	35 gpm	700 gpm
	Anode Supply # 1		35 gpm
	Anode Supply # 2		35 gpm
Total Flow			**2750 gpm**

The rf LCW system is a separate closed system that operates at 95 degree F with a maximum supply manifold pressure of 105 psi and a maximum return pressure of 25 psi

(ΔP = 80 psi). Conductivity must be greater than 10 MΩ cm. The heat load to the water system is approximately 5 MW.

5.2.6 Low Level RF and Global Feedback System

The purpose of the LLRF system is to develop an rf reference with the proper phase relative to the beam to maintain longitudinal stability and radial position in the presence of a varying guide field. The signals are delivered with proper phase to each rf station through a fan-out system. The LLRF system must also control the beam synchronous phase for the purpose of synchronous transfer between different accelerators and provide a beam-synchronous signal for related operations such as beam transfer, instability damping and instrumentation.

The frequency range of operation for the Proton Driver LLRF system is well within the abilities of digital signal processors (DSP) and direct digital synthesizers (DDS). A digital design makes the system very flexible. Filter parameters, gain, frequency of operation, and state machines can be modified with software parameters. This LLRF system should be able to control both the h = 126 and the h = 18 accelerators with minimal modification.

Figures 5.15 and 5.16 show the block diagrams of the phase and frequency control hardware and software.

The DSP acts as the central control processor in the system and provides the digital synthesizers with their frequency values. DDS1 provides the actual rf used to accelerate the beam. This output includes the synchronous phase angle required for acceleration. The signal is split, and each output drives half of the cavities. Each output also has its own phase shifter for counterphasing operations at injection. The DSP contains a user-defined time program that controls the values of the counterphase phase shifters.

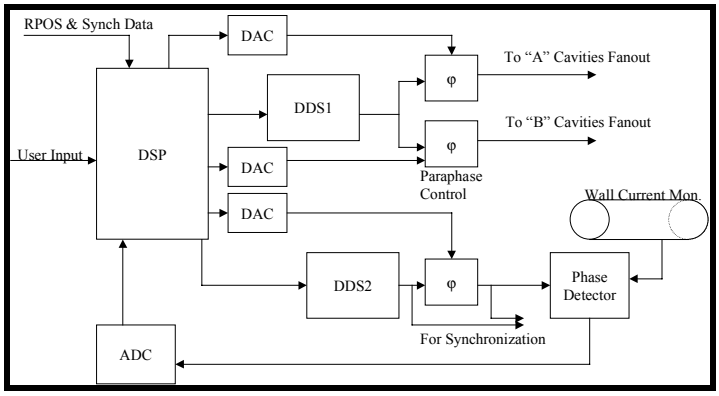

Figure 5.15. Phase and frequency control hardware

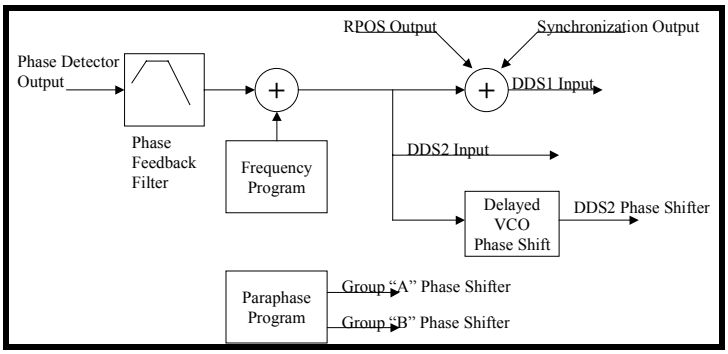

Figure 5.16. Phase and frequency control DSP function hardware and DSP function

DDS2 provides the beam synchronous rf signal. It does not contain the synchronous phase angle, so, with the proper time delay, it should always remain in quadrature with the beam signal. One of the key parameters in designing a stable LLRF feedback system is the fanout delay. The fanout delay is the time it takes for the signal from the DDS to reach each cavity gap. This delay will be about 2 μs for the Booster. It is important that the reference DDS be delayed by the exact fanout delay (plus the current monitor's cable transit time) in order to duplicate effectively the phase error as seen by the beam in the cavity. This reference delay can be generated by a long spool of cable or by an external phase shifter with a value proportional to the frequency value. The phase error is fed back into the DSP and used to adjust both the DDS1 and DDS2 frequencies to minimize the error. The DSP also contains a time table of frequency values to preempt the changing frequency and reduce phase and frequency errors.

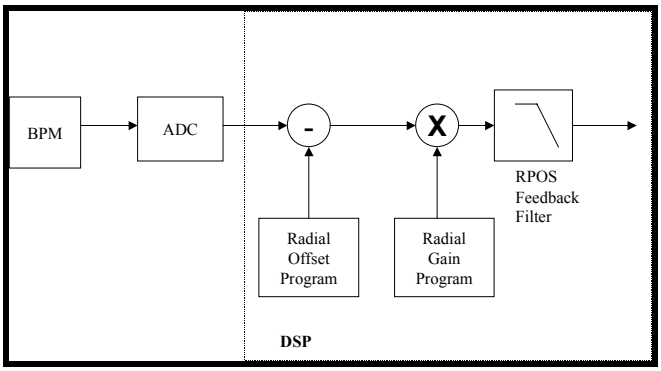

Figure 5.17. RPOS control

Figure 5.17 shows the radial position (RPOS) hardware and software functions. The position signal from a beam position monitor is sampled, and the DSP compares the value to a time-table of desired radial position values. Errors in position are filtered and summed into the DDS frequency values. The gain of the loop is controlled by another time table ramp. As the beam energy increases, the effect of frequency changes on radial position begins to increase. Also, the required bandwidth of operation begins to decrease

because of the lower synchrotron frequency. These situations make a time-varying RPOS loop gain at higher energies desirable.

Figures 5.18 and 5.19 show the block diagrams of the external synchronization control.

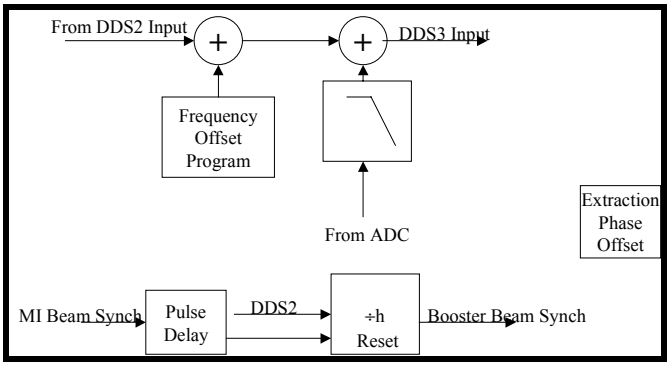

Figure 5.18. Synchronization control hardware

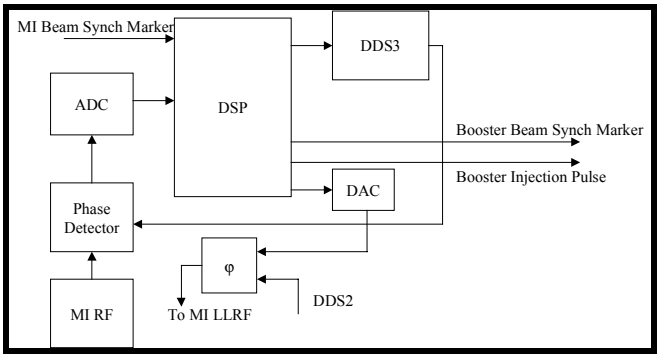

Figure 5.19. Synchronization DSP function

Maintaining phase lock to the Main Injector is the responsibility of the synchronization control. To bring the Booster beam in alignment with the proper Main Injector bucket, the synchronization control must cog the Booster beam by changing its frequency with respect to the Main Injector. The radial position of the Booster beam is not a free parameter in this process, and the RPOS loop must be disabled while attempting to phase lock to the Main Injector. The Booster lattice is designed to have a very small slip factor at extraction, which means that small changes in frequency will produce large changes in radial position. In order to keep the radial position offset to a reasonable level, phase lock to the Main Injector must start a considerable amount of time before extraction time. A 180° phase adjustment would require about 4 ms of cogging time. Cogging half the ring to line up the extraction kicker gap would require almost the entire Booster cycle.

To accommodate for the potentially long cogging periods, another DDS is used to track the Main Injector oscillator. This DDS uses the same error signal to drive its

frequency value that the beam synchronous DDS uses. The only difference between the drive of DDS3 and DDS2 is a frequency offset program that should be equal to the difference between the frequency program and the Main Injector frequency. The phase error produced by comparing this oscillator to the Main Injector oscillator is filtered and drives the fanout DDS frequency. This will produce a radial offset in the beam that will eventually bring the beam into a kind of phase lock with the Main Injector. Although the actual RPOS system is disabled during this time, it will still be possible to program a radial offset through the frequency offset program. A fixed error in this program will produce a radial offset in the beam when the synchronization loop is active. The desired radial offset can be calculated offline and loaded into the frequency offset program.

The other purpose of the synchronization control is to produce a beam synchronous pulse for generating and tracking the extraction kicker gap. Generating the pulse is quite simple; it's just a digital counter that is clocked by the rf frequency and counts up to the harmonic number. Determining when to reset the count for different injections into the Booster is rather tricky. The reset should be a function of the Main Injector beam synch marker. If a predictable relationship exists between the Main Injector markers at Booster injection and extraction, then the Booster beam synch marker could be generated by the Main Injector marker and reduce the total amount of cogging necessary to align the extraction gap. The predictability of the relationship is dependent on the accumulated RPOS error in the two machines, plus the stability of the magnetic fields. Large enough random errors in either system could eliminate the advantage to resetting the Booster beam synch marker with the Main Injector marker.

It is assumed the Main Injector will produce the extraction pulse when the phase relationship between the Booster and Main Injector rf is correct and the markers lined up appropriately. The extraction phase offset is shown as a DSP parameter controlling a phase shifter upstream of the Main Injector LLRF system. This parameter can be located and operated by the Main Injector LLRF system if necessary. The injection trigger is completely generated by the B_{min} signal from the test magnet. This signal may go through the DSP or drive the Linac chopper directly. Either way, the trigger time jitter relative to the real B_{min} must be minimized to maintain a stable magnetic field ramp for the external phase lock system to operate without large radial offsets.

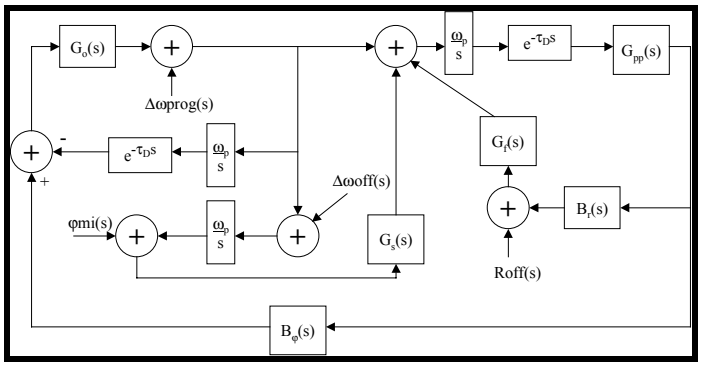

Figure 5.20. LLRF transfer functions

Figure 5.20 is the block diagram of the entire closed loop system. The transfer function equations of the phase loop and the RPOS loop are given below.

$$B_{\psi}(s) := \frac{\omega_s^2}{\omega_s^2 + .01\,s\cdot\omega_s + s^2}$$

$$B_R(s) := s\cdot B_{\psi}(s)$$

$$G_o(s) := g1\cdot\frac{\left(1 + s\cdot\tau_{dif}\right)}{\left(1 + s\cdot\tau_{o1}\right)}$$

$$G_{pp}(s) := \frac{\sigma}{s + \sigma}$$

$$G_f(s) := \frac{g_{fo}}{\left(1 + s\cdot\tau_{ri}\right)}$$

The maximum synchrotron frequency dictates the bandwidth of operation. In this case, it is about 32 kHz. This is very close to the half bandwidth of the 53 MHz cavities. An extra zero is included in the phase feedback filter in order to compensate this pole at about 40 kHz. This increases the phase margin significantly.

The transfer functions are also used to determine the errors in phase and radial position for step changes in frequency and radial position. The cascaded integrators in the RPOS loop keep the DC error at zero. The loops will still have errors for ramp inputs such as the magnetic field ramp. This ramp error can be minimized with a good frequency program. At the point of the fastest instantaneous radial offset ramp, the radial offset can be held to better than 0.1 mm by an accurate frequency program that updates at a rate close to the synchrotron frequency.

Although no detailed calculations are shown, the synchronization loop can be designed to look and operate just like the RPOS loop. It is very important, however, that the offset frequency table be very accurate (with update rates at about the synchrotron frequency) to avoid large fixed radial offsets.

5.3. Stage 2, 7.5 MHz RF System

In Stage 2 the Proton Driver is to be used to produce muons for a neutrino factory storage ring. The extraction energy is raised to 16 GeV and the rf system is replaced with an h = 18 system to provide the desired bunch spacing. A factor of four larger extracted longitudinal emittance is allowed for each of the 18 bunches compared to that for the 119 bunches of Stage 1, so the design brightness is raised by 65%. However, the larger inter-bunch gap permits chopping the Linac beam, allowing synchronous injection. The Linac beam spans 252^{o} of an approximately stationary bucket.

A major difference between operation as an injector for the Main Injector and Stage 2 operation is the requirement for ~ 1 ns rms bunch length at extraction. This requirement can be met by keeping the voltage at 1.4 MV even as dB/dt drops toward the end of the

acceleration cycle. Even narrower bunches can be obtained by a quarter period bunch rotation in a mismatched bucket. The momentum spread becomes wide enough that the contributions of the second and third order dependence of path length on momentum difference from the synchronous momentum are important. These contributions are included in the macro-particle model. The rms bunch length with no rotation (described above), is 1.55 ns. With bunch rotation the rms bunch length may be reduced to 0.64 ns. The final 95% emittances are 0.39 eV-s and 0.43 eV-s respectively.

The rf parameters of the Proton Driver for Stage 2 are collected in Table 5.7.

Table 5.7. Stage 2 Proton Driver rf Parameters

E_{inj}	injection kinetic energy	400	MeV
	Beam intensity	3×10^{13}	p/cycle
	Cycle repetition	15	Hz
E_{ext}	extraction kinetic energy	16	GeV
R_{eq}	circumference/2π	113.21	M
V_{rf}	maximum rf voltage	1.4	MV
V_{acc}	accelerating voltage at dp/dt max	1.33	MV
h	harmonic number	18	
	Bunch intensity	1.7×10^{12}	
	Momentum acceptance	2.5	%
ε_l	longitudinal emittance at extraction	0.4	eV-s
	rms bunch length at extraction	≤3	eV-s
ΔE_{inj}	energy spread at injection	±0.5	MeV
α_0	momentum compaction	-1.306×10^{-3}	
α_1	coefficient of $(\Delta p)^2$ in path length	8.252×10^{-2}	
α_2	coefficient of $(\Delta p)^3$ in path length	–0.4456	
b	vacuum chamber radius	6.35	cm
a	mean beam radius at injection	4.44	cm

5.3.1 Parameter Programs – Stage 2 RF Curves

The magnet ramp is driven by a 15 Hz resonant supply plus an independent second harmonic supply that is adjusted in phase and amplitude to minimize the maximum value of d*p*/d*t*. Because there is chopping and more adequate rf focusing in Stage 2, there is no need for an inductive insert. Thus, the model results given for Stage 2 require less in the way of cautionary disclaimers. With the model parameters used there is no loss during the cycle. However, the longitudinal emittance has been simulated with only the perfectly conducting wall impedance included.

The curves in Figs. 5.21 - 5.24 present the momentum *p*, its time derivative d*p*/d*t*, the peak rf voltage V_{rf}, and the synchronous phase ϕ_s when the bunch rotation is used.

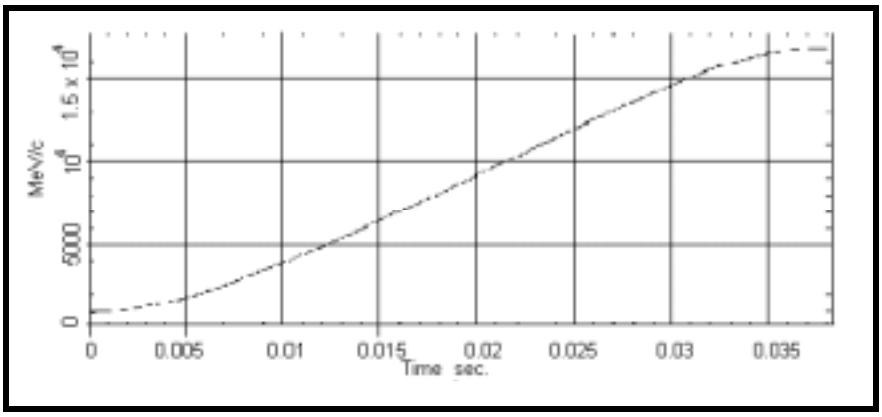

Figure 5.21. Stage 2, Beam momentum

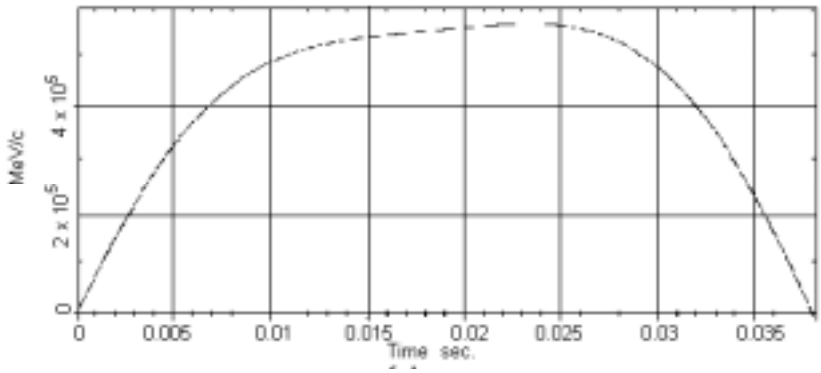

Figure 5.22. Stage 2, Rate of change of momentum, dp/dt, MeV/c/sec

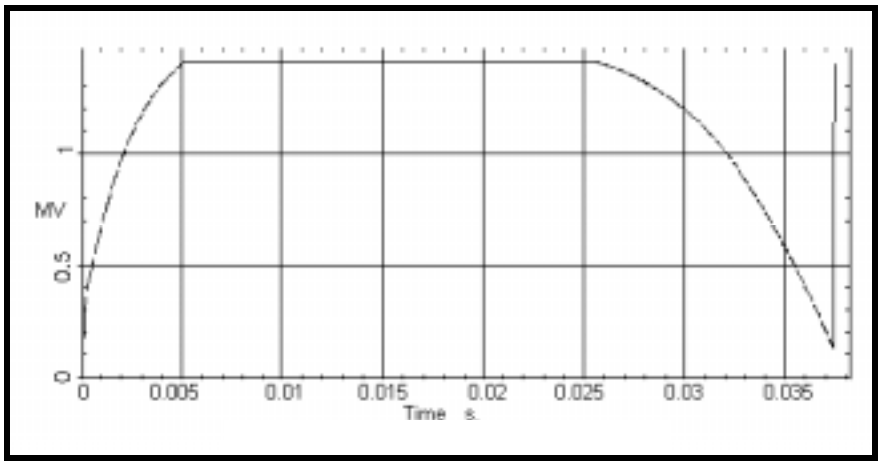

Figure 5.23. Stage 2, rf voltage

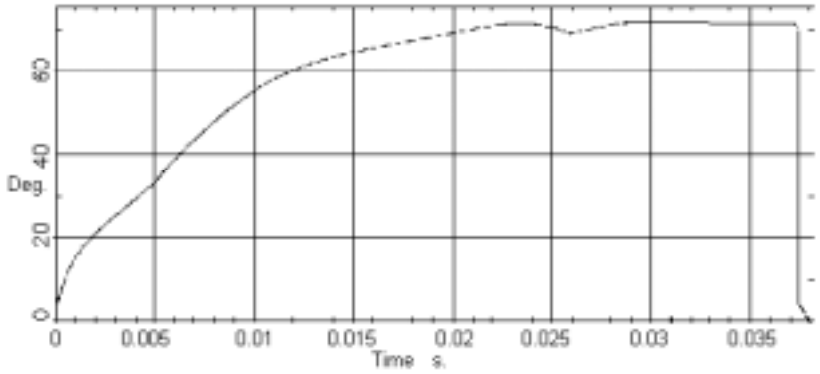

Figure 5.24. Stage 2, Synchronous phase angle ϕ_s during acceleration in degrees

The curves in Figs. 5.25 – 5.27 present useful derived quantities, *viz*., synchrotron tune ν_s, bucket area S_B, and rms longitudinal emittance per bunch ε_l. When rotation is not used, the rf voltage curve is the same through 26 ms; however it remains at 1.4 MV for the rest of the cycle.

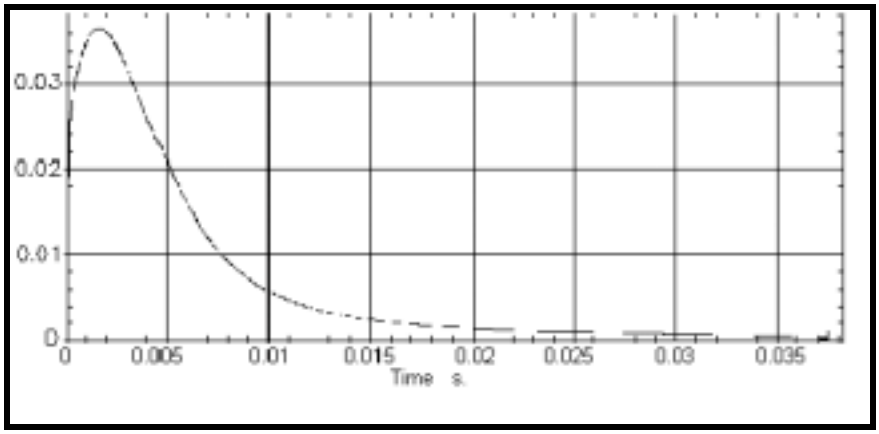

Figure 5.25. Stage 2, small amplitude synchrotron tune in units of F_{rot}

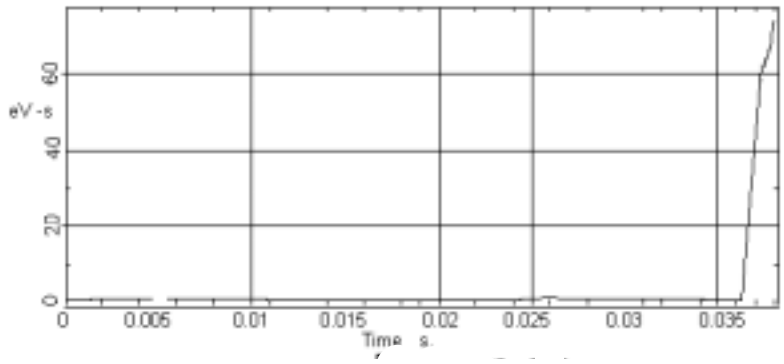

Figure 5.26. Stage 2, rf bucket area in eV-s

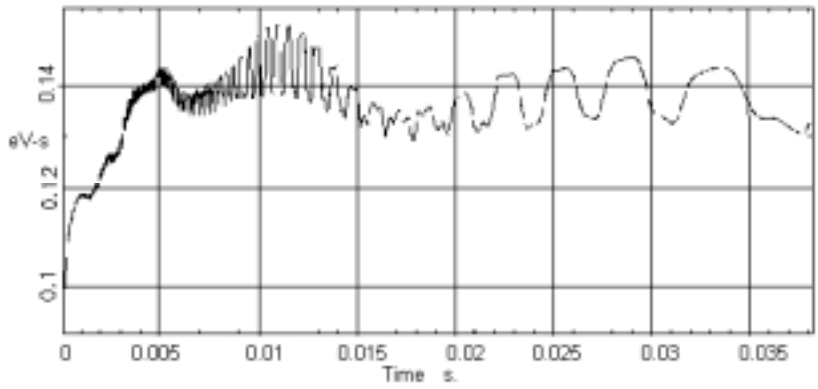

Figure 5.27. Stage 2, rms longitudinal emittance per bunch, eV-s

5.3.1.1 Capture and Acceleration – Stage 2 Scenario and Modeling

The 252^{o} chop which becomes possible with the 7.5 MHz rf system means that beam is injected into nearly stationary buckets. Therefore, losses are a much less severe problem, not only at injection, but also throughout the acceleration cycle. The voltage and magnet ramp curves are similar to those found for Stage 1, but the buckets are less full and there is no need for fine tuning of the curves to control losses.

For the narrowest bunches, mismatched bucket bunch rotation is intended. However, merely keeping the voltage at its maximum permissible 1.4 MV until the end of the cycle already gives an rms bunch length of < 2 ns, somewhat better than had been anticipated in the initial design. For injection into the Main Injector the final voltage can be set at any convenient value between 1.4 MV and ~100 kV. Fig. 5.28 shows the azimuthal projection in degrees at extraction for $V_{rf} = 1.4$ MV, where each degree of azimuth corresponds to 6.6 ns of bunch length. The rms length is 1.55 ns.

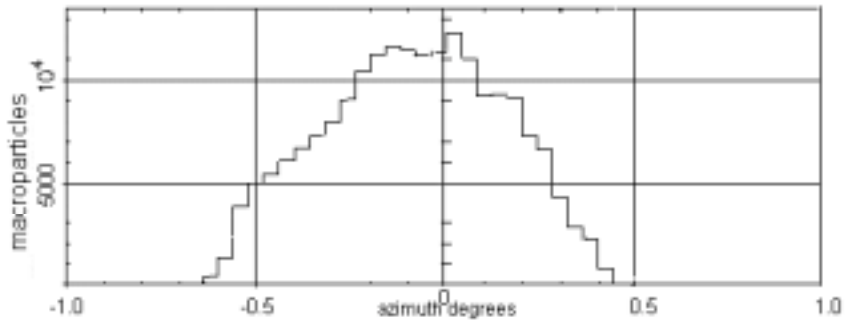

Figure 5.28. Stage 2, azimuthal charge histogram of macroparticle number in 0.02^{o} bins, at extraction without bunch rotation. Each degree represents ~ 6.6 ns.

5.3.1.2 Bunch Rotation – < 1 ns rms Bunch Length

Figure 5.29 shows the azimuthal projection of a bunch at extraction when rotated to minimum rms bunch length in a bucket produced by the maximum 1.4 MV. The rotation starts at 37.6 ms when the synchronous phase is $\phi_s = 71^o$ and V_{rf} is 124 kV. The rotated bunch has rms length 0.64 ns.

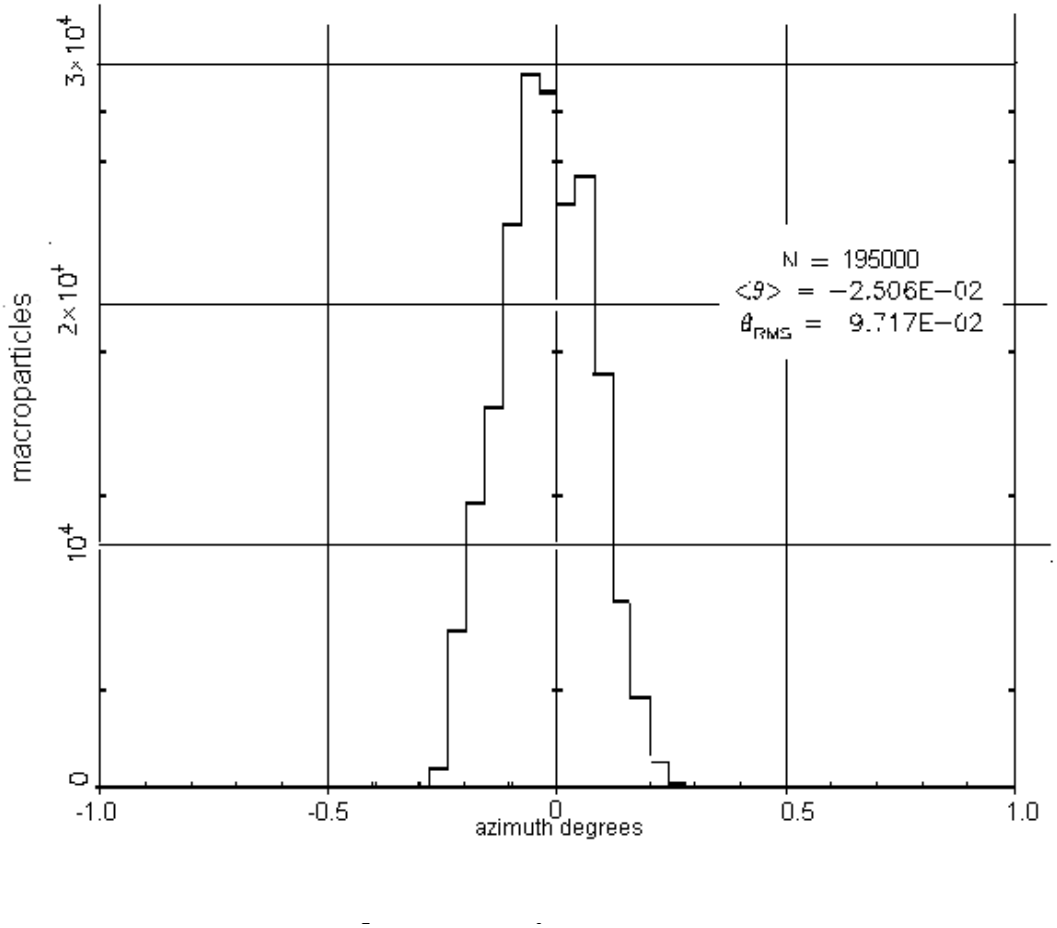

Figure 5.29. Azimuthal charge histogram of macroparticle number in 0.02^o bins at extraction with bunch rotation. One degree at h = 1 represents 6.6 ns.

5.3.2 Finemet Low Frequency rf Cavities

Stage 2 of the Proton Driver requires a large rf system operating at 15 Hz with a 60% duty cycle over the frequency range of 5.4 to 7.6 MHz. The system must be capable of producing a total peak accelerating ring voltage of 1.4 MV while delivering 3 MW of peak power to the beam. These conditions can be met with 100 rf cavities, each generating a peak accelerating voltage of 15 kV. Traditionally, rf systems operating in this frequency range have relied on nickel-zinc ferrite loaded rf cavities. However, the available tunnel space for the rf system dictates an accelerating gradient of at least 30 - 40 kV/m which is the upper limit for ferrite cavities at these frequencies.

Finemet [10], a nanocrystalline soft magnetic material, manufactured by Hitachi Metals and previously used at KEK, Japan, is a possible replacement for the nickel-zinc ferrites. Finemet has a Curie temperature of ≈ 500°C and is available in large diameter (1 meter) tape wound cores. The best available Ni-Zn ferrites can operate at a maximum rf magnetic flux, B_{rf}, between 100 and 200 Gauss. Finemet has the useful property that, unlike ferrites, it can maintain all of its normal magnetic characteristics at B_{rf} levels an order of magnitude larger (1000 - 2000 Gauss). Theoretically, this should enable an rf cavity containing Finemet cores to achieve a voltage gradient at least ten times higher than a comparable ferrite loaded cavity of the same dimensions. In practice this is probably not possible for cw operation, since the cores are very lossy at these frequencies, $Q < 1$. Under these extreme cw conditions, the Finemet cores would probably not have sufficient cooling to remain below the Curie temperature. To reduce these core losses, the Finemet cores are covered with epoxy and then cut in half to give an adjustable air gap between the two halves. Cut Finemet cores are ideally suited for use in the range of higher gradients just beyond those attainable with the Ni-Zn ferrites.

How will a Finemet cavity behave at high beam intensities under heavy beam loading? A known rf dynamics theorem is that in order to avoid Robinson type instabilities, without using rf feedback, the amount of power delivered to the beam must be equal to or less than the amount of power dissipated in the rf cavity. A lossy Finemet cavity with a shunt impedance of $R_s \approx 500\ \Omega$ provides an easy way to satisfy this stability criterion. The transient beam loading response is proportional to the ratio R_s/Q of the rf cavity. For a Finemet cavity with cut cores, R_s is relatively constant as a function of core separation while Q undergoes large changes as the core separation is adjusted. This means that once the cavity shunt impedance is fixed, the ratio R_s/Q can be lowered to suppress the transient beam loading response by simply increasing the separation between core halves to increase Q.

Early in the Proton Driver Study, it was decided to build an rf cavity using Finemet cores that could be powered by a 200 kW rf amplifier; provisions were included for adding a second power amplifier at a later date whose express purpose was to provide transient beam loading compensation. At that time in the study it was envisioned that the cavity would be used in a 3 - 16 GeV machine whose frequency sweep was only 500 kHz. For this reason the prototype cavity was designed and built to have a $Q \approx 10$ so that no dynamic tuning would be required during the acceleration cycle. During the past year, a staged approach to the construction of the Proton Driver has been developed. This led to the elimination of the original 400 MeV – 3 GeV Pre-Booster from the Stage 2 design.

Injection into the new ring at 400 MeV requires the present 5.4 - 7.6 MHz tuning range. In the next section the $Q = 10$ prototype cavity will be described, followed by two proposals on how to extend the cavity's tuning range.

As part of the US-Japan HEP collaboration, a prototype Finemet cavity has been built and tested at Fermilab. Fig.5.30 is a photograph of this Finemet cavity installed in the Main Injector tunnel.

Figure 5.30. Finemet rf cavity with attached power amplifier

The cavity is a single gap, quarter-wave coaxial structure less than 0.5 m long. It consists of five 95 cm OD × 26 cm ID × 2.54 cm thick Finemet cores cut in half and separated by 3 cm. The cores are encased in epoxy and cooled by 2.54 cm thick water-cooled copper heat sinks which are the same size as the cores (KEK is experimenting with cooling Finemet cores directly with Fluorinert FC-77). The interface between the cores and heat sinks is made using Kapton 300 CR film coated with a thermally conductive compound (Wakefield 120). The stack of cores and heat sinks is compressed together using six 1-in. fiberglass rods. The anode of the final power tetrode is capacitively coupled to the gap with a 1200 pf dc blocking capacitor. The cavity is tuned to 7.5 MHz with no additional gap capacitance. The completed cavity has $Q = 11$ and $R_s = 550\ \Omega$.

The cavity is powered by a 200 kW final amplifier which uses an Eimac Y567B tetrode. The cathode of the final tetrode is driven from the combined outputs of two Amplifier Research 3500A100 solid-state amplifiers. The prototype cavity has achieved a peak gap voltage of 17 kV for short pulses, 13.8 kV at 15 Hz with a 60 % duty cycle, and 10 kV cw. At average powers in excess of 100 kW damage has been observed after several minutes of operation on two of the corners of two of the split cores, due to the increased eddy current heating. In an attempt to alleviate this problem, rounded profiles were water-jet cut on the corners of a single core. This core has survived in the cavity without sustaining any damage. We expect that proper shaping of all of the cut core corners will eliminate this thermal heating problem and allow the cavity to achieve continuous 15 Hz operation at 15 kV with a 60% duty cycle.

Two proposals have been made as to how to obtain the required 5.4 - 7.6 MHz tuning range using a Finemet cavity. One proposal is to lower the cavity Q from 11 to 3 by decreasing the gap between the split core halves to 3 mm. Contrary to what might be

expected, lowering the cavity Q will only slightly decrease the cavity shunt impedance. However, this will increase the cavity inductance and require changing the design from a single gap cavity to a double gap cavity. The second proposal would add an external tuner (a recycled Fermilab Booster tuner) in parallel with the prototype Finemet cavity. Three of these external tuners could be run in series using one of the present Booster ferrite bias supplies. The first proposal offers the simplicity of a broadband system, but places greater demands on the power amplifier. The second proposal adds the complexity of a tuner and external bias tuning loop but gives a lower cavity R_s/Q, which will be beneficial for transient beam loading compensation. Both schemes and a combination of the two are currently under study.

5.3.3 Beam Loading and Robinson Stability

Robinson's inequalities show that fundamental beam loading is not a problem for the $h = 18$ system. Assuming 15 kV per cavity and $R_{sh} \sim 500\ \Omega$, the ratio between beam current and cavity current is about 0.066. This is well below the intensity criterion and will allow the total voltage to be lowered to 92 kV before fundamental beam loading becomes a factor. Transient beam loading is not a factor because all the buckets are full throughout the cycle.

One significant problem in the $h = 18$ system is the potential well distortion. The bunches are specified to be very narrow (1 ns) relative to the bucket size. Such a large amount of charge in a small amount of time will overwhelm the voltage gradient produced by the cavities and cause bunch spreading. One possible remedy for this problem is to install a multi-harmonic beam loading compensation system. This system would provide feedback at every rf harmonic to reduce the potential well distortion. It is important to note that for such a system to work properly the peak current delivery of the power amplifier tube must be comparable to the peak bunch current anticipated in the accelerating gap during narrow bunch passage. If the tube current capability is inadequate, the broad-band feed-back system will just drive the amplifier to saturation, resulting in inadequate compensation. A 1 ns rms bunch with total charge 0.27 μC will have peak current ~ 120 A. This is barely within the peak current capability of the Y567B tetrodes that are proposed for the system.

5.3.4 Stage 2 (5.4-7.6 MHz) Cavities, Power Supplies, LCW Water, Mains Power

In Table 5.8 are summarized equipment requirements for Stage 2. A prototype rf amplifier has been tested on the prototype Finemet cavity. This amplifier is a modified Main Injector amplifier with a broadband cathode drive circuit for operation over 5.4 MHz to 7.6 MHz. It utilizes the Eimac (CPI) Y567B power tetrode that is presently used in the Booster and Main Injector power amplifiers. This rf amplifier is grounded grid for rf but programmed dc grid bias for optimizing tube performance during the rf envelope. The amplifier will be driven by a 8 kW solid state MOSFET amplifier located in the equipment gallery.

Table 5.8. Equipment requirements for Stage 2

Finemet RF Cavities	100 cavities @ 15 kV /Cavity; prototype currently under test. One ferrite tuner per cavity may be needed (See section 5.3.2 for Cavity Details
High Level RF	100 High Level stations. If cavity tuners are required then ferrite bias supplies will be needed. 100 IRM station control & data acquisition systems
New Equipment	(100) - 200 kW Power Amplifiers. (100) - 20 kV Series Tube Modulators (100) - 8 kW Solid State Drivers. (15) - Additional bias supplies for ferrite tuners . (10) - 20 kV Anode Power Supplies.

The 8 kW wideband Solid State Driver Amplifier consists of running two commercially available 3.5 kW solid state amplifiers in parallel. An alternative would be to build a version of the Main Injector's solid state amplifier with eight 1 kW modules operating at 5.4 to 7.6 MHz.

The 20 kV Series Tube Modulator is basically a Main Injector modulator with minimal modifications. It utilizes the same Eimac (CPI) Y567B power tetrode and has a proven reliable track record. Construction drawings exist and fabrication would be straightforward. All testing of the prototype cavity and power amplifier was done with a slightly modified Main Injector modulator.

The additional ferrite bias supplies would be exact copies of existing ferrite bias supplies that are presently used in Booster. They have a proven 25-year design and are highly reliable. Construction drawings exist and fabrication would be straightforward. One supply would supply bias for multiple cavities. Depending on the final cavity design, ferrite bias supplies may not be needed.

Ten new 20 kV 2.5 MW anode power supplies would be built. Each anode supply would supply 10 rf stations. These will be very similar to the Main Injector's anode supplies. New 13.8 kV electronic switch gear, fused disconnect, 2 MW rectifier transformer, along with associated DC components are needed. They would be configured with an indoor DC enclosure containing the main rectifier stack, interphase reactor, capacitor bank, crowbar circuit, and high voltage disconnect switches.

Thirty two additional IRM station control chassis are needed. These are standard units and are widely used around the laboratory, so additional units could be purchased easily. One IRM would be required for every two stations (total 50 IRM's).

At least one and possibly two relay racks will be required per station. They will contain the station's remote controls and low level rf station control modules.

Existing equipment that will be reused are 18 each of Ferrite bias supplies, and IRM station control for digital I/O & Analog monitors and control.

Overhead cable trays of standard 18 inch wide by 5 inch deep (pre-galvanized) will carry only signal cables. All rf signal cabling in trays will be HELIAX type cable. Trays will be supported approximately every 5 feet.

Tables 5.9 and 5.10 itemize the electrical power and LCW cooling requirements. Since the rf system will be installed in a new building, all of the supporting utilities for the high power rf systems will be installed as part of the building construction. The LCW piping, 480/208/120 Volt AC power distribution, and cable trays will be an integral part of the construction. The AC power duty factor = 50%.

Table 5.9. Summary of Electrical Power Requirements

480 Volt 3-phase		**Per station**	**100 Stations**
	Ferrite Bias Supply/3 stations	35 kW	3465 kW
	Series Tube Modulator:	20 kW	2000 kW
	Solid State Driver Amp	12 kW	1200 kW
	RF Pump room		1000 kW
120/208 volts			
	Relay racks	1.5 kW	150 kW
	Ion pump PS	0.5 kW	50 kW
	Miscellaneous	1 kW	100 kW
13.8 kV			
	10 - Anode Supplies	200 kW	20,000 kW
Total Power			**27,965 kW**

Table 5.10. Summary of Cooling Requirements

95 Degree LCW		**Per station**	**100 Stations**
	Ferrite Bias Supply	17 gpm	561 gpm
	Series Tube Modulator:	35 gpm	3500 gpm
	Solid State Driver Amp	15 gpm	1500 gpm
	RF Cavity	20 gpm	2000 gpm
	200 kW Power Amplifier	35 gpm	3500 gpm
	Anode Supplies	35 gpm	350 gpm
Total Flow			**11,411 gpm**

The LCW cooling is based on a duty factor = 50%. The rf LCW system is a separate closed system that operates at 95° F with a maximum supply manifold pressure of 105 psi and a maximum return pressure of 25 psi (ΔP = 80 psi). Conductivity must be greater than 10 Ω cm. Heat load to the water system is approximately 28 MW.

5.4. R & D Plans and Proposals

5.4.1 Future Work, Booster Cavity Modification

At present the prototype cavity is installed at the MI–60 test station and is ready for high power testing. The modifications and measurements performed to date indicate the aperture enlargement goal is achievable. Upon completion of successful high power tests, the next step will be to convert the prototype cavity into a tunnel-ready model that will be high power tested at MI–60 prior to being installed in the Booster for beam tests. This step will require that all design details be addressed, including new ceramic windows, beam tubes with magnetic shielding, a rebuilt Main Injector tuner with appropriately modified inner conductors and bus bars, and myriad other details. The higher order modes of this cavity will have to be measured and compared with the existing Booster cavity. It may be necessary to develop new higher order mode couplers to damp these modes.

It is further proposed that this completed large aperture prototype become one component of a complete rf station, including a new solid state driver, power amplifier, and dc supply modulator. It is anticipated that this complete program can be completed on a two year time scale if sufficient funds and staff are made available.

5.4.2 LLRF and Beam Loading Compensation R & D

The new LLRF system should be constructed and tested on the current Booster before it is decommissioned. The current Booster already has the ability to produce an extraction kicker notch in the beam, but it does not have the ability to cog the notch for injection into a specific Main Injector bucket. Design should begin early on the new system to benefit the neutrino experiments. Tracking the extraction gap is the major non-trivial design aspect of the new Booster LLRF system. Once this is designed, built and tested, the remainder of the system construction should be straightforward.

Beam loading compensation R & D is already underway. The system that will be used for the h = 126 Booster has been commissioned in the Main Injector. Once the distributed amplifiers in the current Booster are upgraded with solid-state amplifiers, work can begin on commissioning a fundamental beam loading compensation system that will also work with the h = 126 Booster.

A multi-harmonic beam loading compensation module is also currently under construction. This module will be tested in the Main Injector for the purpose of transient beam loading compensation. The module will also be tested on the 7.5 MHz cavity that has been installed in the Main Injector. Once the cavity, power amplifiers, and beam loading modules are complete and installed, low energy and low voltage acceleration studies will be scheduled to test the systems ability to compensate the potential well distortion.

5.4.3. TRIUMF rf cavity study

In experiments at TRIUMF, SSC, and Los Alamos it has been observed that the permeability of the Yt-Garnet ferrite in the TRIUMF cavity is affected by changes in the ferrite H field due to the rf current generated by the cavity. In the Yt-Garnet case the cavity may be dynamically de-tuned by fields induced in the cavity by high beam current. It may be possible to stabilize the cavity frequency against this effect by a high gain feedback loop around the cavity. Before it is decided to augment the Proton Driver h = 126 ring voltage with TRIUMF style cavities, several months of R & D study of this problem and possible solutions would be invaluable.

5.4.4. Inductive insert study in the existing Fermilab Booster

At high beam intensity there continues to be substantial and unexplained beam loss at injection and during early phase of acceleration. There is reason to expect that introduction of space charge compensating inductors may be helpful in alleviating this loss. A detailed study of the properties of available ferrite over a frequency range spanning perhaps five Booster rf harmonics would lend strength to the argument for the usefulness of such an installation. Continued ESME simulation studies should proceed in concert with and using results of the ferrite properties study. The results of such a study may contribute to the understanding of the use of inductive compensation in a ramping synchrotron, as well as contributing to improved operation of the existing Booster.

References

[1] S. Hansen et al, "Effects of Space Charge and Reactive Wall Impedance on Bunched Beams," IEEE Trans. Nucl. Sci., NS-22 No.3, (1975).

[2] A.M. Sessler and V.G. Vaccaro, "Passive Compensation of Longitudinal Space Charge Effects in Circular Accelerators - The Helical Insert," CERN 68-1, ISR Div. (1968).

[3] K. Koba et al, "Longitudinal Tuner Using High Permeability Material," R.S.I. 70-7, (1999).

[4] K. Koba, "Longitudinal Tuner Using a New Material, Finemet," AIP Conf. Proc. 496, (1999).

[5] M.A. Plum et al, "Experimental Study of Passive Compensation of Space Charge at the LANL Proton Storage Ring," Physical Review Special Topics - Accelerators and Beams, Vol.2, 064201 (1999).

[6] J.E. Griffin et al, same title as in [5], Fermilab FN-661 (1997).

[7] W. Chou et al, "A Joint Proposal for Booster Cavity Modification," Fermilab, Jan. 12, 2000.

[8] J. E. Griffin, "Proposal to Rebuild Damaged Booster RF Cavity with Significant improvement in Aperture, Gap Voltage, and Power Delivery Capability," Draft, Nov. 1999.

[9] R.L. Poirier, "Perpendicular Biased ferrite-Tuned Cavities", Proc. 1993 PAC, 753, (1993).

[10] http://www.hitachi-metals.hbi.ne.jp/topics/prod/npo3.htm.

Chapter 6. Magnets

Frederick Mills and Jean-François Ostiguy

6.1. Introduction

To accelerate and deliver 1 MW of beam power at 16 GeV while keeping space charge induced tune shift and tune spread at acceptable levels, the Fermilab Proton driver uses rapid cycling magnets with unusually large apertures. Space charge mitigation is accomplished by spreading out the charge both transversely and longitudinally. The aperture size, which is a principal cost driver, is determined not only by the need to accommodate large transverse beam sizes to reduce the tune shift, but also to keep losses at a level compatible with safety requirements. The chosen magnet apertures should be adequate to keep the worst case injection losses below 10 %, that is 2.5 kW out of the 25 kW total beam power at injection.

Aside from the fact that large stored energy and rapid cycling lead to substantial power supply costs, many aspects of the proton driver magnets are challenging, including high voltage insulation, eddy-current power loss minimization and eddy current induced fiel errors compensation.

It is worth mentioning that because the space charge tune shift scales as $\beta^{-1}\gamma^{-2}$, increasing the injection energy – currently set to 400 MeV by the existing FNAL linac – would significantl reduce the cost of magnet and related subsystems and possibly reduce technical risks as well, at the expense of more linac rf. A detailed discussion of the trade-offs can be found in Appendix B.

The presence of large energy dependent space charge tune shift and tune spread dictates the need for tight tracking between the quadrupole and bending dipole magnets during the entire acceleration cycle. Quadrupole tracking error is effectively equivalent to momentum offset error and results in a tune shift of magnitude

$$\Delta\nu = \xi_{\text{uncorrected}} \left[\frac{\Delta G}{G} - \frac{\Delta B}{B} \right] \tag{6.1}$$

$$= \xi_{\text{uncorrected}} \left[\frac{\Delta(G/B)}{(G/B)} \right] \tag{6.2}$$

where $\frac{\Delta G}{G}$ and $\frac{\Delta B}{B}$ are respectively the relative gradient and main dipole fiel errors. Note that the tune variation is proportional to $\xi_{\text{uncorrected}}$, the *uncorrected* chromaticity because, in the context of a quadrupole tracking error, there is no closed orbit error and the chromaticity correction sextupoles have no effect.

The magnitude of the tolerable tune shift is arguable. Although tracking is expected to become less critical as energy increases, in the context of this report, we *conservatively* de-

mand that

$$\Delta\nu < 0.01 \tag{6.3}$$

during the *entire* cycle. This requirement is based on the ISIS experience, where the ability to control the tune at that level was shown to be necessary in order to avoid specifi resonances at extraction. While it is possible that the upper limit for the tolerable tracking error induced tune shift may turn out to be be larger, this report errs on the conservative side, in absence of the availability of detailed simulations.

In some machines like the Fermilab Booster, good tracking is naturally achieved by employing combined function magnets operating well below 1 T, far away from saturation. In contrast, the Proton Driver lattice is based on separate function magnets with main bending dipoles operating at an aggressive 1.5 T peak field This fiel was chosen to simultaneously make the circumference ratio between the Main Injector and the Proton Driver a simple rational fraction (for synchronous beam transfers) and minimize the space charge tune shift, which is proportional to the machine circumference. While the magnet transfer function starts deviating from linearity above 1 T, this can be compensated for by a combination of careful quadrupole and dipole saturation matching supplemented by an active quadrupole correction system. Admittedly, 1.5 T is not a very precisely define limit; however, it is fair to say that above 1.5 T, the nonlinearity becomes too substantial for active correction to be practical.

6.2. Dipoles

6.2.1. Design Considerations

The Proton Driver dipole is a conventional H-magnet design with Rogowsky profile pole edges to help maintain fiel homogeneity at higher excitations. The lamination cross-section is shown in Figure 6.1 and a list of relevant parameters is presented in Table 6.1. The dipoles are excited so as to produce a magnetic fiel strength of the form

$$B(t) = B_0 - B_1\cos(\omega t) + 0.125B_1\sin(2\omega t) \tag{6.4}$$

where B_0 is the injection field B_1 is the magnitude of the fundamental component and $\omega/2\pi = f = 15$ Hz. The second harmonic component is introduced to flatte the RF accelerating voltage, resulting in substantial RF system cost savings. Both the magnetic fiel ramp and its derivative are shown in Figure 6.3. Field homogeneity over the largest possible fraction of the physical aperture is obtained by shimming the pole pieces edges. The shim effectiveness can be estimated theoretically using formulas developed by K. Halbach [1]. Referring to Figure 6.4, assume the origin of the x-axis is situated exactly at the pole edge and that the pole continues to infinit for $x > 0$. At any fixe horizontal position x and, in particular at $x = 0$, the complex fiel is an even function of the vertical position y can be expanded in a

Table 6.1: Proton Driver Main Dipole Magnet Parameters

Max Stored Energy (5.1655 m)	0.336	MJ
Inductance (low field	3.07	mH /m
Inductance (@ 1.5 T, with saturation)	2.88	mH /m
No of Turns/pole	2(parallel) $\times$ 12 = 24	
Transfer Constant (linear, $\mu = \infty$)	2.365×10^{-4}	T/A
Peak Dipole Field	1.5	Tesla
Peak Current (M17, including saturation)	6720	A
Steel Length	5.1655, 4.1924	m
Conductor Dimensions	37×37	mm^2
Conductor cooling tube dimensions	8 ID, 10 OD	mm
Conductor Packing Fraction	80% (approx)	
Physical Aperture	5×12.5	in^2
Good Field Aperture	5×9.0	in^2
Coil Area	0.105	m^2
Lamination Area	1.109	m^2
Lamination Thickness	0.014	in
Lamination Material	M17 Steel	
Core mass (5.1655 m magnet)	44,900	kg
Coil mass (5.1655 m magnet)	10,700	kg
Maximum Terminal Voltage (16 GeV, 5.1655 m magnet)	5	kV

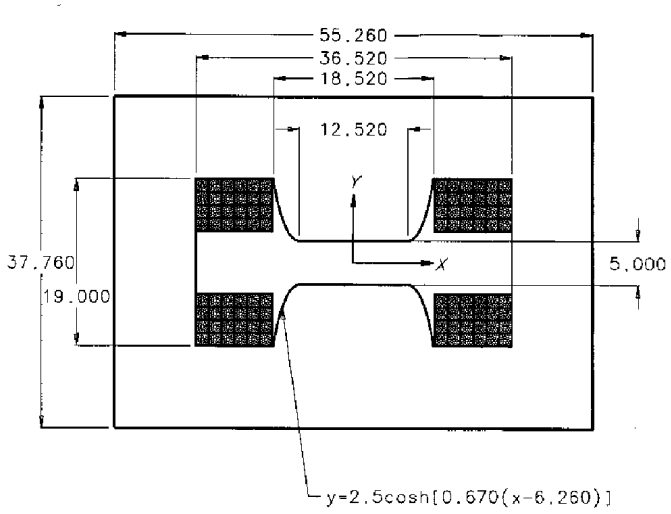

Figure 6.1: Proton Driver dipole cross-section.

Fourier series of the form

$$H_y + jH_x = \sum_{n=-\infty}^{\infty} C_n \exp \frac{n\pi jy}{g} \tag{6.5}$$

where g is the total vertical gap and the C_n are complex constant coefficients Since the two-dimensional complex magnetic fiel in the aperture region must be an analytic function, (6.5) can be analytically continued over the entire aperture region

$$H_y + jH_x = \sum_{n=-\infty}^{\infty} C_n \exp \frac{n\pi z}{g} \tag{6.6}$$

where $z = x + jy$. The coefficient C_n must vanish for $n > 0$ since

$$|\exp \frac{\pi nx}{g}| \to \infty \quad x \to \infty \tag{6.7}$$

Thus,

$$H_y + jH_x = \sum_{n=-\infty}^{0} C_n \exp \frac{n\pi z}{g} \tag{6.8}$$

Note that $C_0 = H_{y0}$ represents the fiel deep into the aperture region. Let d be the the pole overhang, as shown in Figure 6.4. Without shims, the firs few low order harmonics dominate the fiel deviation from uniformity. Considering only the firs $(n = -1)$ harmonic, the fiel error at the edge of the good fiel region is

$$\frac{\Delta B}{B} = \frac{\Delta H_y}{H_{y0}} \simeq h_1 \exp \frac{-\pi d}{g} \tag{6.9}$$

where

$$h_n = \frac{1}{H_{y0}} \Re\{C_n\} \tag{6.10}$$

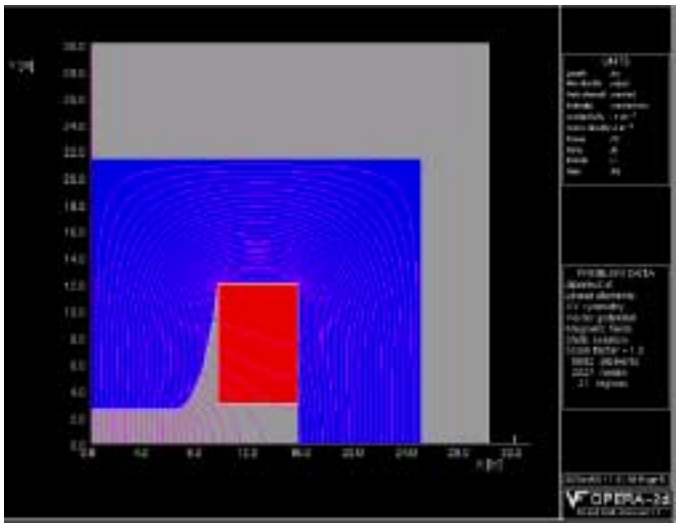

Figure 6.2: Proton Driver dipole flu lines.

A properly designed shim should suppress the firs few spatial harmonics. Assume, for simplicity, that only the the firs harmonic is suppressed. In that case, the second dominates and

$$\frac{\Delta B}{B} = \frac{\Delta H_y}{H_{y0}} \simeq h_2 \exp \frac{-2\pi d}{g} \tag{6.11}$$

In practice, one needs to consider more than one harmonic in order to accurately determine fiel homogeneity. Nevertheless, Halbach found that a simple two-parameter empirical relation of the form

$$\frac{\Delta B}{B} \simeq \lambda_1 \exp \frac{-\lambda_2 d}{g} \tag{6.12}$$

is generally adequate. The values of λ_1 and λ_2 are obtained by fittin results obtained numerically from two-dimensional calculations. In absence of shims, Halbach found that the overhang necessary to achieve a fiel homogeneity $\frac{\Delta B}{B}$ fit the relation

$$2d/g = -0.36 \log(\frac{\Delta B}{B}) - 0.9 \tag{6.13}$$

assuming that good fiel means $\frac{\Delta B}{B} < 1.0 \times 10^{-3}$, with $g = 5$ in, one gets

$$d \simeq 4.0 \text{ in} \tag{6.14}$$

Similarly, with shims, Halbach find that the amount of necessary overhang fit the relation

$$2d/g = -0.14 \log(\frac{\Delta B}{B}) - 0.25 \tag{6.15}$$

that is, once again, with $\frac{\Delta B}{B} < 1.0 \times 10^{-3}$ and $g = 5$ in,

$$d \simeq 1.8 \text{ in} \tag{6.16}$$

Note that the empirical coefficient $\lambda_2 = 1/0.36 = 2.78$ and $\lambda_2 = 1/0.14 = 7.14$ are not too different from the values π and 2π predicted by the single dominant harmonic assumption.

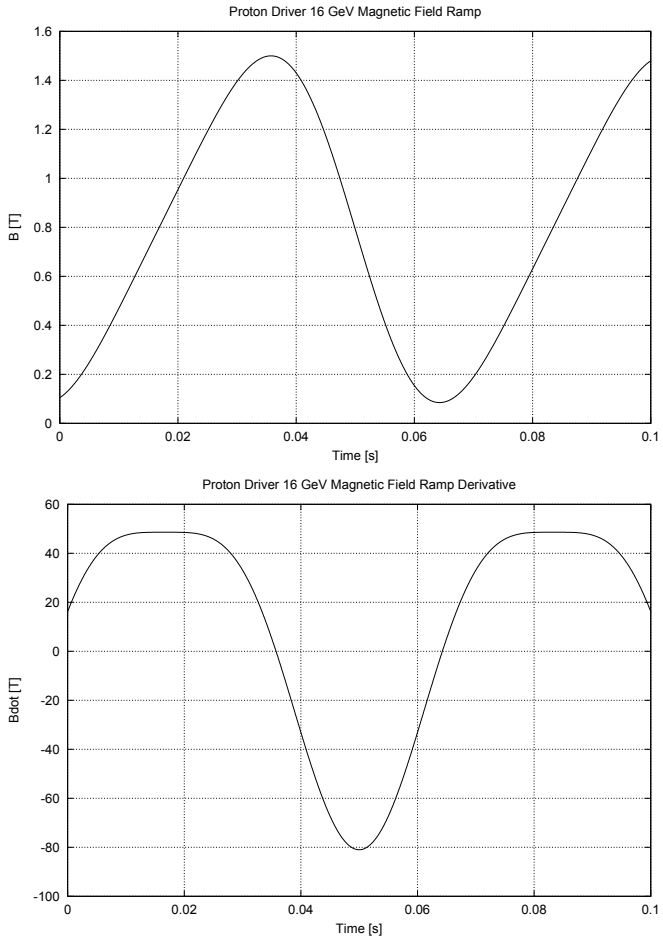

Figure 6.3: Magnetic fiel ramp and its derivative for 16 GeV operation ($B_0 = 0.7923$ T, $B_1 = 0.6876$ T). The RF accelerating voltage is proportional to the derivative of the magnetic field

Halbach's formulae predictions are approximate and in principle, it should be possible to achieve better homogeneity with a complex shim. However, they provide a safe and conservative estimate. Figure 6.5 compares calculated low excitation fiel homogeneities for shimmed and unshimmed versions of the Proton Driver dipole magnet. The shim used in this example is a simple one-parameter rectangular shim.

The magnet cores are assembled from 0.014 in (29 gage) thick Si-Fe M17 laminations, of the type used in power transformers. For Si-Fe at 15 Hz, the skin depth $\delta \simeq 1$ mm = 0.040 in. In principle, one could use even thinner laminations to further reduce losses, but they become hard to handle.

Compared to low carbon steel used in slow ramping accelerators, Si-Fe has the advantage of reduced coercivity and conductivity; this helps reduce hysteresis and eddy current losses respectively. In principle, Si-Fe should be marginally more expensive to produce than low carbon steel; in practice, economies of scale and widespread availability due to applications

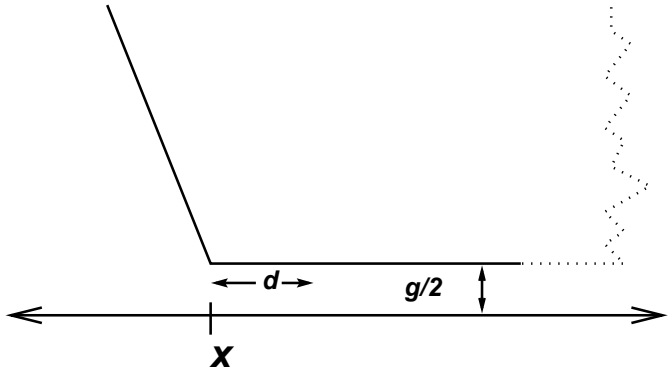

Figure 6.4: Idealized semi-infinit dipole magnet with pole overhang *d* and full gap is *g*. The horizontal origin is exactly at the outer edge of the pole and the fiel deep inside the aperture region is uniform.

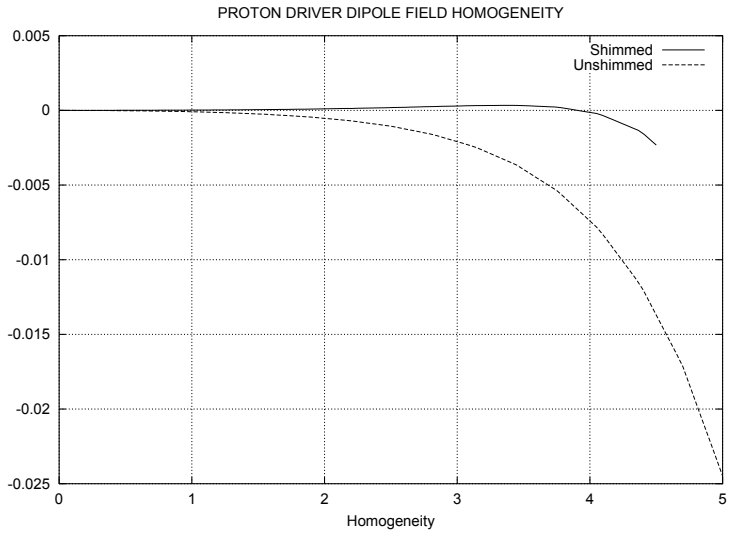

Figure 6.5: Proton Driver dipole fiel homogeneity at low excitation.

in the power industry more than compensate for this.

Virtually all manufacturer data on hysteresis and eddy current losses in Si-Fe corresponds to measurements performed at 50 or 60 Hz with a sinusoidal excitation. While simple scaling laws can be applied to estimate losses at 15 Hz, the Proton Driver magnet excitation also has a non-zero average component I_0, which corresponds to the injection energy. The presence of this component renders the hysteresis loops asymmetric. As a result, the standard scaling does not apply. To obtain a reliable estimate of the expected cyclic core losses, measurements were performed on a small core made out of M17 laminations. The results are summarized in Figure 6.6.

Macroscopic eddy current losses scale like the square of the frequency and the square of the peak field In order to keep coil losses at reasonable levels, it was found necessary to use a special water cooled stranded conductor, as illustrated in Figure 6.7. This type of

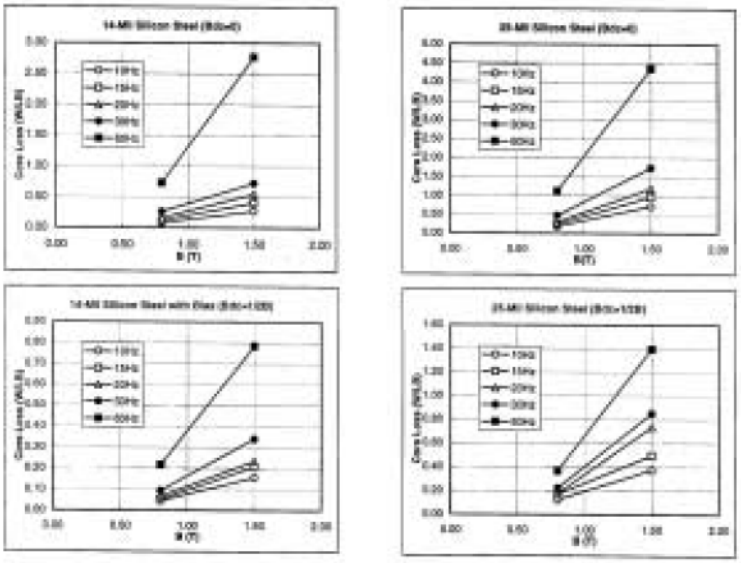

Figure 6.6: M17 Cyclic Steel loss measurements.

conductor is available commercially from at least two sources. The strands can be made out of either aluminum or copper. While for the former, inter-strand insulation is naturally provided by a layer of aluminum oxide, for the latter, a thin coat of "enamel" such as polyimide or polyamide-imide is necessary. Strands are are periodically transposed to provide uniform current distribution and lower losses. In general, the computation of conductor eddy current losses in conductors requires a self-consistent solution of Maxwell's equations (neglecting radiation). When the eddy currents induced by the quasi-statically computed field are small with respect to the externally applied currents, they can be considered as a perturbation. This is often the case for eddy currents induced in the coils of slow ramping magnets; this is also the case for stranded conductors.

A quantity of interest is the resistance ratio R, define as

$$R = \frac{R_{\mathrm{AC}}}{R_{\mathrm{DC}}} \tag{6.17}$$

where R_{AC} is the effective AC resistance, which is larger than the DC resistance R_{DC} for the same net current because of the different spatial current density distributions. Since the AC losses are proportional to R_{AC}, one can see that R is actually the ratio between the AC and the DC ohmic losses[1]. For the FNAL Booster (0.45 in $\times$ 0.45 in solid copper conductor with 0.25 in radius water cooling hole), numerical computations yield $R \simeq 2$. Assuming conductors of roughly the same type would lead to $R \simeq 8$ for the Proton Driver which is clearly not acceptable. We note in passing that there is practical limit for the size of water cooled conductor which is set by the surface to volume ratio of the cooling channel (which scales like $1/r$). While the volume of water flowin sets the water temperature rise, the

[1] In the present context, the term "AC losses" refers to the total time-averaged losses produced by a periodic current.

Figure 6.7: Stranded conductor.

surface area determines both the thermal and water flo resistance.

The eddy currents losses induced in a stranded conductor can be estimated in a straightforward manner. Consider, a circular strand of radius r immersed in a time-varying magnetic fiel $B(t)$ such as illustrated in Figure 6.8. Over the strand area, the magnetic fiel may be considered uniform. Using Maxwell's curl equation for the electric field it is easily shown that the induced eddy current is

$$J_{\text{eddy}} \simeq \sigma x \dot{B} \tag{6.18}$$

provided that is small enough to be considered as a perturbation with respect to the total current. Integrating over the entire strand cross-section, one gets, for the instantaneous power loss per unit length (for one strand)

$$\begin{aligned} P_{\text{eddy}} &= \int \rho\sigma^2 x^2 (\dot{B})^2 \, dA & (6.19)\\ &= \int_0^{2\pi} \int_0^r \sigma r^3 (\dot{B})^2 \cos^2\theta \, dr d\theta & (6.20)\\ &= \frac{\pi}{4}\sigma r^4 (\dot{B})^2 & (6.21) \end{aligned}$$

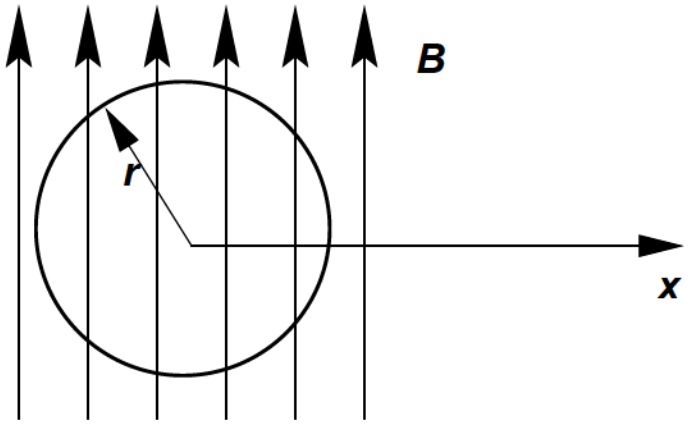

Figure 6.8: A circular strand immersed in a uniform, time varying magnetic field

Over one excitation period, the rms average of $\dot{B}$ is

$$< \dot{B} >= \frac{3}{4}\omega B_1 \tag{6.22}$$

Thus,

$$P_{\text{eddy}} \simeq \frac{9\pi}{64}\sigma r^4 \omega^2 B_1^2 \tag{6.23}$$

and the resistance ratio R is

$$R = \frac{P_{\text{eddy}} + P_{\text{DC}}}{P_{\text{DC}}} \tag{6.24}$$

$$= 1 + \frac{9\pi}{64}\frac{r^4\omega^2 B_1^2}{\rho^2 J_{\text{DC}}^2} \tag{6.25}$$

For the Proton Driver dipole, $\omega = 30\pi$, $J_{\text{DC}} \simeq 1.92$ A/mm^2. Magnetostatic calculations show that the spatial rms average of the magnetic fiel over the coil cross-section is approximately 0.27 T when the gap fiel reaches 1.5 T. Using this value as representative of B_1 (although it is an overestimation) and assuming 2 mm Cu strands ($\rho = 1.7 \times 10^{-8}$ ohm-m), we get

$$R - 1 = \frac{9\pi}{64}\frac{(2\times 10^{-3})^4 (30\pi)^2 (0.27)^2}{(1.7\times 10^{-8})^2 (1.92\times 10^6)^2} \simeq 10^{-5} \tag{6.26}$$

a result which validates the assumption that eddy currents are a perturbation under these conditions.

Although the AC resistance of the stranded cable is expected to be only slightly larger than its DC resistance, it should be noted that because of the transposition, the stranded conductor is effectively longer than a solid conductor of identical total cross-section.

In order to minimize the overall inductance of the magnet and keep the voltage to ground below 5 kV, two pairs of top-bottom pancake coils are connected in parallel to provide the total magnet excitation.

Because of the large amount of magnetic energy stored in the magnets and its impact on the power supplies, the ratio of magnetic energy stored in the aperture region as a fraction of the total stored magnetic should be maximized. While profile poles help maintain fiel homogeneity and linearity up to 1.5T, this comes at the cost of storing a substantial amount of energy in the pole fringing regions. No systematic attempt has been made to optimize the magnet in that regard. It is likely that efficienc could be improved somewhat by positioning conductors in the mid-plane; this has to be weighed against increased sensitivity of the fiel quality on coil positioning and eddy currents as well as the need for mechanically more complex saddle shaped coils.

6.3. Quadrupoles

6.3.1. Design Considerations

The Proton Driver Quadrupoles are four-fold symmetric magnets. Both the horizontal and the vertical focusing quadrupoles are identical. Large aperture iron-dominated quadrupoles become difficul to build when the pole tip fiel approaches 1.5 T. Note that the fiel is maximum not at the pole tip, but near the edges of the truncated hyperbolic pole profiles and saturation occurs in these regions first If the beam occupies a large fraction of the aperture, a four-fold symmetric quadrupole magnet has the advantage of suppressing all fiel harmonics except those of order 4n (8n-pole). Thus, the firs allowed harmonic is the 12-pole. In contrast, for an asymmetric lamination with a wider horizontal aperture, the firs allowed harmonic would be the 8-pole. When the fiel in the aperture (at least for the circular region inscribed inside the pole tips) is expanded as a power series in (r/r_0) – where r_0 is the pole tip radius – contributions from each term become rapidly less important with increasing order.

In order to allow the quadrupole and dipole strength to track each other dynamically, the quadrupoles are on the same current bus as the main bending dipoles. The number of turns and the dimensions of the quadrupole are selected to match as well as possible the saturation behavior of the dipoles. Figure 6.11 is a plot of the tracking function as a function of the excitation current. At 16 GeV, the deviation is on the order of 2.5%.

6.4. Sextupoles

6.4.1. Design Considerations

The Proton Driver sextupole magnets have, just like the quadrupoles, the symmetry of the dominant multipole in order to suppress lower order fiel harmonics. The horizontal and

Table 6.2: Proton Driver Quadrupole Magnet Parameters.

Aperture (Inscribed circle radius)	3.3541	in
Peak Gradient (16 GeV)	8.7494	Tesla/m
Peak Current (M17, including saturation)	6500	A
Steel Length	1.6824^2	m
Transfer Constant ($\mu = \infty$)	1.37865×10^{-3}	T/m/A
Stored Energy (1.6824 m)	0.052	MJ
Inductance	1.481	mH/m
No of Turns/pole	8	
Conductor Dimensions	37×37	mm^2
Conductor cooling tube dimensions	8 ID, 10 OD	mm
Conductor Packing Fraction	80%	
Lamination Area	1.095	m^2
Coil Area	0.0929	m^2
Lamination Thickness	0.014	in
Lamination Material	M17 Steel	
Core mass (1.6824 m)	14,500	kg
Coil mass (1.6824 m)	1,400	kg
Max Terminal Voltage (1.6824 m)	0.425	kV

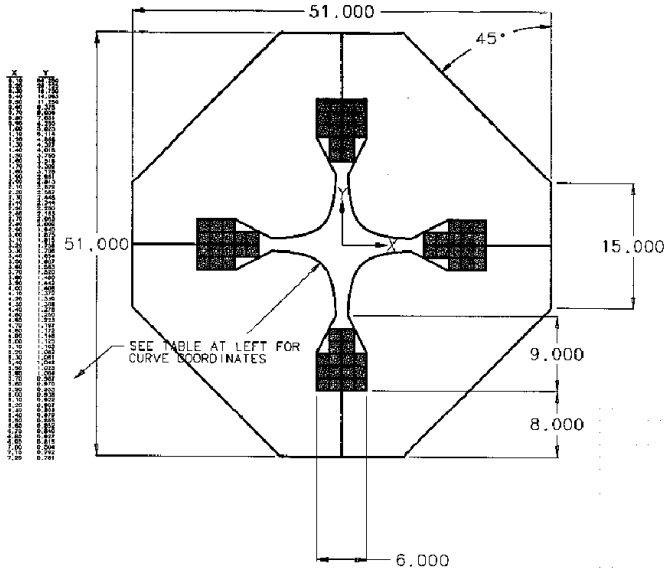

Figure 6.9: Proton Driver quadrupole cross-section.

vertical sextupoles cross-sections are identical; however, the backleg is dimensioned to accommodate the flu required by the strongest magnet. Sextupoles magnets are grouped in families; the families are powered by independent programmable supplies.

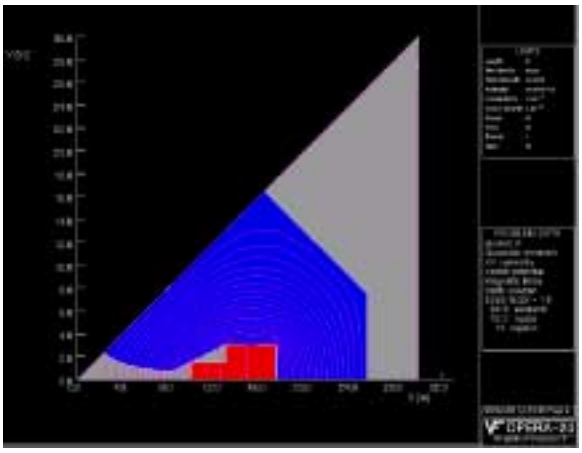

Figure 6.10: Proton Driver quadrupole flu lines.

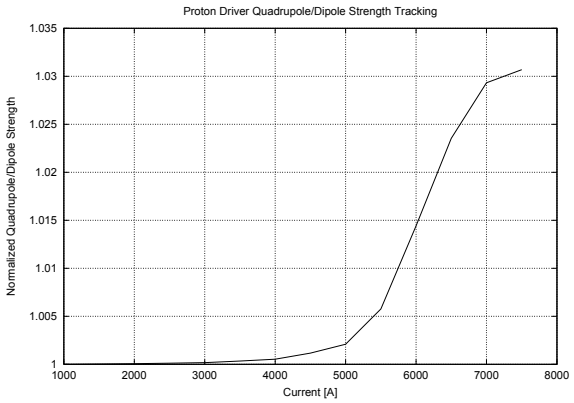

Figure 6.11: Normalized Quadrupole/Dipole strength tracking. At 16 GeV (common bus current of 6720 A), the deviation is approximately 2.5%. The residual tracking error is compensated by an active correction system.

6.5. Trim Magnets

Operational experience with ISIS has demonstrated that good orbit control during the entire acceleration cycle is one of the keys to loss minimization. This is not entirely surprising since small orbit changes typically result in small tune perturbations caused by change in overall orbit length and quadrupole feed-down in sextupoles.

6.5.1. Horizontal Dipole Correction

Due to space constraints in the lattice, all 48 main dipole bending magnets will include extra windings to integrate the function of *horizontal correctors*. Although the magnet described in this section does not include those windings, this should not pose fundamental difficul ties. Nevertheless, it will be necessary to modify the lamination profil to accommodate the

Table 6.3: Proton Driver Sextupole Magnet Parameters.

Aperture (Inscribed circle radius)	3.818	in
Peak Sextupole (H,V)	35,47.5	T/m^2
Peak Current	2850	A
Steel Length	0.3	m
Max Stored Energy	2980	J
Inductance	2.448	mH/m
No of Turns/pole	4	
Transfer Constant ($\mu = \infty$)	0.016667	$T/m^2/A$
Conductor Dimensions	1.5×1.5	in^2
Lamination Thickness	0.014	in
Lamination Material	M17 Steel	
Lamination Area	0.5676	m^2
Coil Area	0.0696	m^2
Core Mass	1,340	kg
Coil Mass	190	kg

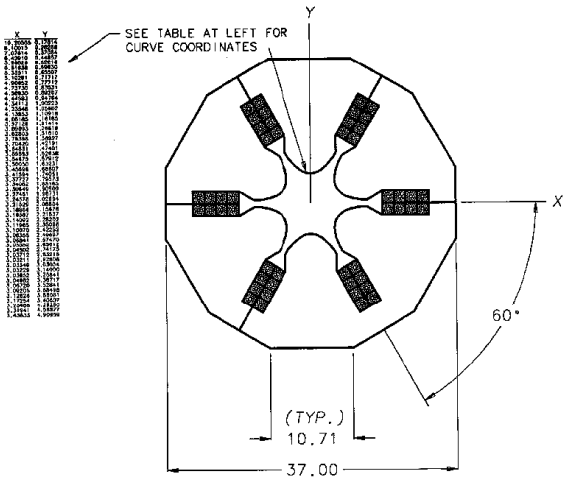

Figure 6.12: Proton driver sextupole cross-section.

correction windings. The electrical interconnections needed to suppress the large electromotive force induced by the main dipole flu are also a concern and will introduce additional complexity. The required horizontal correction is approximately 5 mrad, i.e. 3.8% of the bending angle of a dipole. Full range correction over the entire cycle requires a supplementary peak excitation of 5760 A-turn. The correction range could be reduced at high energy since it is envisioned that horizontal orbit corrections will be performed by physically moving quadrupoles.

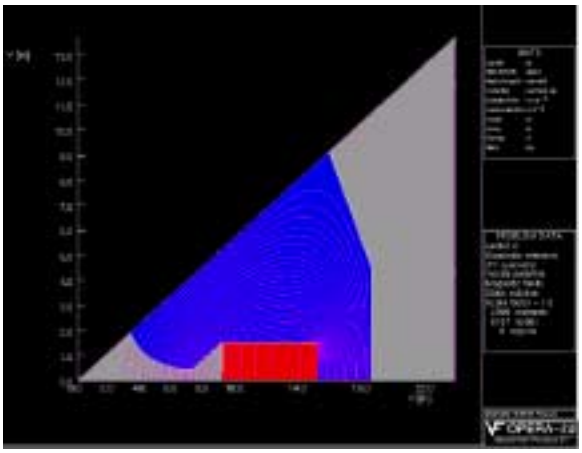

Figure 6.13: Proton driver sextupole flu lines.

6.5.2. Vertical Dipole Correction

The vertical correctors magnets are of a standard "pole-less" design, as shown in Figure 6.14. This has the advantage of providing good fiel quality even under moderate saturation levels. The two coils are excited so as to produce counter-circulating fluxes resulting in uniform horizontal fiel within the interior region, as well as a considerable amount of flu in the exterior region. The inefficienc is usually of little concern for such small orbit correction magnets although time-varying external leakage flu may affect nearby instrumentation. The vertical trims are capable of full range correction ($\pm$5 mrad) below 3 GeV. There are 8 trims per arc for a total of 24 in three arcs. Assuming another 12 in three straights, the total number of vertical trims is 36.

Table 6.4: Proton Driver Vertical Trim Parameters

No of Turns/pole	3×48	
Max Current (including saturation)	400	A
Max Field (including saturation)	0.25	T
Steel Length	0.25	m
Lamination Material	M17	
Lamination Thickness	0.014	in

6.6. Beam Pipe Induced Field Distortion

The presence of high frequency magnetic field renders difficult if not impractical, the utilization of a conventional beam chamber. The eddy currents induced in such a chamber lead to very high resistive losses and significan magnetic fiel distortion. These effects can be

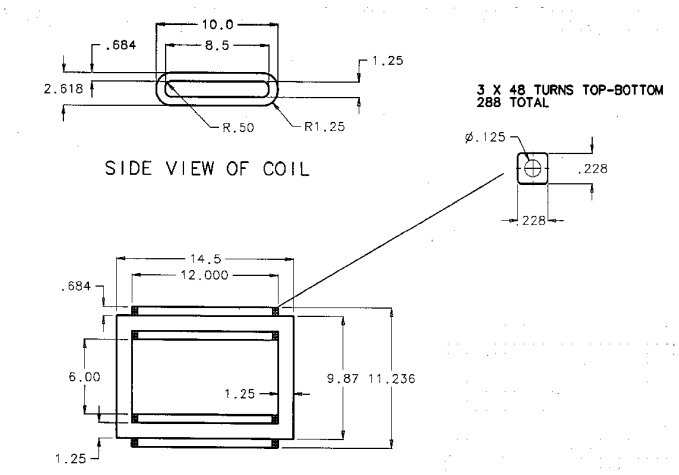

Figure 6.14: Vertical trim magnet cross-section.

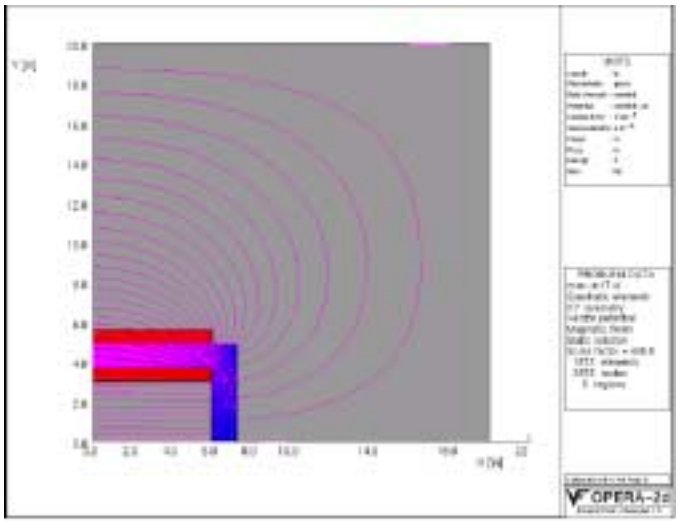

Figure 6.15: Vertical trim magnet flu lines.

reduced to a certain extent by making the vacuum chamber thinner; however, it has to be remain thick enough in order not to collapse. As described in Chapter 8, various alternatives to a conventional beam chamber have been considered. This report assumes that the beam chamber is eliminated by enclosing both the dipole and quadrupole magnets inside an external vacuum skins. While this approach results in a mechanically more complex magnet and in difficultie with out-gassing of magnet laminations and electrical coil insulation, it is a relatively well-established technology. One uncertainty, given the high beam intensity, is beam impedance minimization. It is envisioned that this will be accomplished by disposing closely spaced, thin metal strips on the pole face. To prevent eddy current flo , the strips are connected capacitively magnet-to-magnet.

While there are good reasons to be optimistic, it is possible that the strips may not provide sufficien impedance reduction. In that case, it may be necessary to resort to a "liner" similar in spirit to that proposed for the SSC or the LHC. Such a liner is basically a very thin

pipe with "random" holes to allow passage of the residual gas. The randomness of the hole pattern is necessary in order to avoid the introduction of new resonances.

Whenever a vacuum chamber or a liner is present, the time varying dipole fiel induces eddy currents within the chamber walls. As mentioned earlier, the magnitude of the induced current density is given by

$$J = \sigma E = \sigma x \dot{B} \tag{6.27}$$

These eddy currents in turn produce a magnetic fiel distortion which perturbs the fiel homogeneity. The distortion may be easily computed by subdividing the beam chamber into a number of filaments Each of these filaments assumed to be located between two infinitel permeable planes separated by a distance g, contribute a fiel

$$H_y + jH_x = \frac{I}{4g}\left(\tanh\frac{\pi(z-z_c^*)}{2g} + \coth\frac{\pi(z-z_c)}{2g}\right) \tag{6.28}$$

The total perturbation is the simply the sum of the filamen contributions. The coefficient of the multipolar expansion of the fiel about the axis can be determined by differentiating this sum term by term. Using this approach, the multipoles induced during the proton driver acceleration cycle have been computed, assuming the parameters presented in Table 6.5. These parameters correspond approximately to the thinnest elliptical chamber capable of withstanding vaccuum pressure without collapsing. Note that the multipoles scale with the chamber thickness and resistivity; therefore, a liner could easily result in a magnetic fiel perturbation a few times smaller. If the perturbation is unacceptable, it can be passively compensated using a scheme which has been successfully implemented in the Brookhaven AGS Booster [3, 4]. Basically, a few turns of wire are fixe to the vacuum chamber. and the current in these wires is driven by a small coil wrapped around the pole. The circuit is closed by a small adjustable resistor.

Table 6.5: Vacuum chamber parameters used for Eddy current fiel distortion calculations. The distortion is proportional to both vacuum chamber thickness and wall conductivity.

conductivity	0.8×10^6	mho/m	(INCONEL)
wall thickness	1.27	mm	(50 mils)
major radius	11.43	cm	
minor radius	6.35	cm	
magnet gap	12.7	cm	

6.7. Research and Development

Fermilab has limited experience with rapid cycling magnets. The Booster magnets were fabricated more than thirty years ago; because of their relatively low fiel they were built

using technology similar to other conventional slow cycling magnets. In part because of an aggressive 1.5 T field the Proton Driver magnets will need to use a special type of water-cooled stranded conductor. While this type of conductor is commercially available from the Japanese industry and has been used on a limited basis at KEK, the fact remains there is limited worldwide accumulated experience with such conductor. In particular, the following issues will require attention: (1) The minimum bending radius for cooled stranded conductor will be larger than for solid conductor of the same cross-section. Great care will be needed to engineer ends so as to minimize the longitudinal space allocated for the end region, especially in view of that fact that each magnet requires two set of coils connected in parallel in order to keep the inductance and the voltage to ground to acceptable levels. (2) The technology to make good electrical and mechanical joints in the conductor will need to be developed. (3) While it is believed that the stranded conductors described in this report would provide adequate cooling, this needs to be experimentally confirmed

Another are of concern is high voltage operation. As described in this report, the dipole magnets have a maximum terminal voltage of 5 kV, which is somewhat aggressive. Voltage to ground insulation is a very important issue for magnet reliability and Fermilab has very limited experience with high voltage magnet technology. Although trouble spots are often concentrated in the vicinity of corners, they can be difficul to anticipate because they are very dependent on details of the magnet geometry that are difficul to include in computer models. The work involved in experimentally localizing troublesome high fiel regions and subsequently modifying magnet and coil geometries to even out electric stress distribution is potentially tricky and time-consuming.

Finally, high frequency operation will introduce small fiel distortions as well as a time lag between the excitation and the fiel and the presence of metallic strips or liner to reduce high frequency impedance will also perturb the field These effects will need to be carefully measured for both the dipole and the quadrupole magnets. While the magnitudes of all these perturbations can be estimated, in view of the importance of minimizing particle losses, it would be extremely beneficia to conduct dynamic measurements of the transfer function (for dipole-quadrupole tracking) and fiel quality (including hysteresis effects) for both the dipole and quadrupole magnets. Much of the technology and expertise required could be developed by measuring an existing Booster magnet. Moreover, independently of the Proton Driver project, the information collected would be valuable to the existing program to help understand particle loss in the Booster.

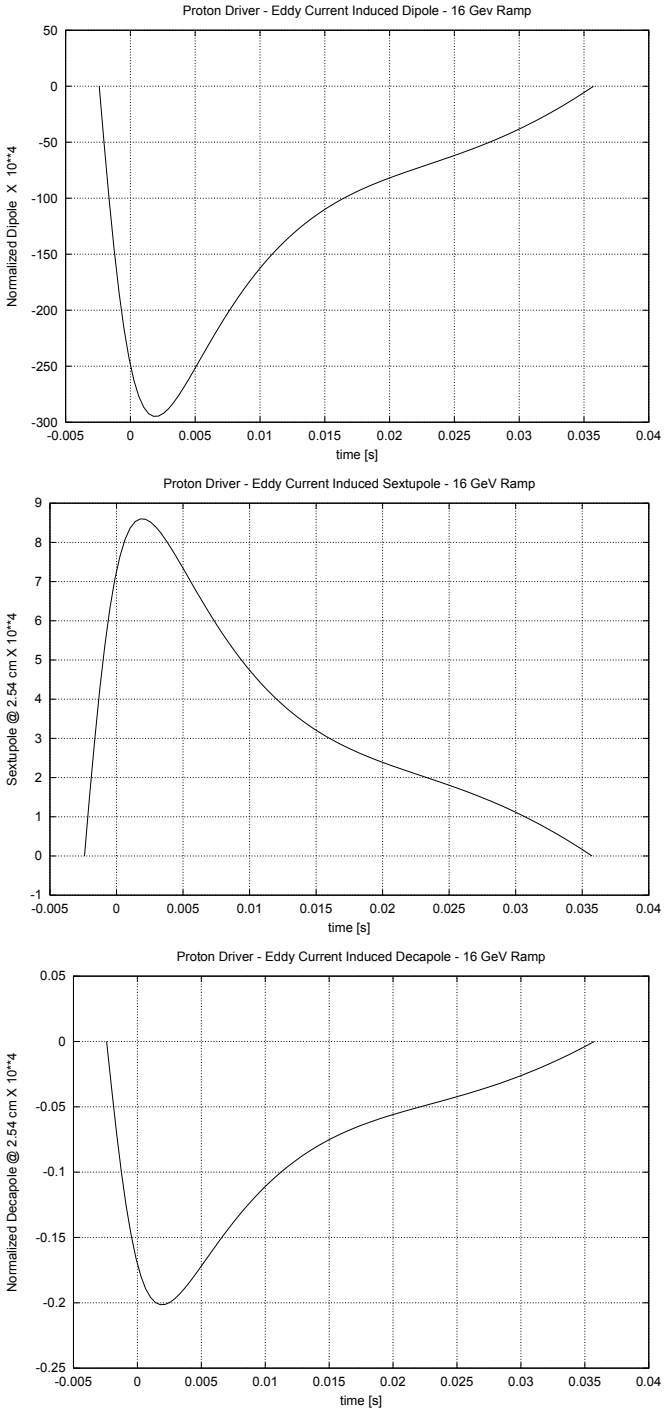

Figure 6.16: Normalized Dipole, Sextupole and Decapole variation during the acceleration cycle for 16 GeV (1.5 T peak dipole field.) The parameters in Table 6.5 have been assumed.

References

[1] A.W. Chao and M. Tigner Eds., *Handbook of Accelerator Physics and Engineering*, World Scientific 1999.

[2] S.Y. Lee *A Multipole Expansion for the fiel of Vacuum Chamber Eddy Currents*, NIM A300, pp-151-158, 1991

[3] G.T. Danby, J.W. Jackson, *Description of New Vacum Chamber Correction Concept*, Proceedings of IEEE PAC 1989

[4] G.T. Danby, J.W. Jackson, *Vacuum Chamber Eddy Current Self-Correction for the AGS Booster Accelerator*, Particle Accelerators 27, pp 33-38 (1990)

Chapter 7. Power Supplies

Cezary Jach and Dan Wolff

7.1. Introduction

The Proton Driver power supply system consists of a dipole/quadrupole power supply system, a quadrupole tracking and correction power supply system, a dipole horizontal and vertical correction power supply system and a sextupole power supply system. This Chapter also describes preliminary design of the power distribution system supplying 13.8 kV power to all Proton Driver electrical systems (in Section 7.7).

The power supply system is designed to provide current to the magnets in the form:

$$I(t) = I_{dc} - I_{ac} \cdot \cos(2\pi 15t) + 0.125 \cdot I_{ac} \cdot \sin(2\pi 30t)$$

where: I(t) is the magnet current, I_{dc} is the dc component of the magnet current and I_{ac} the a.c. component.

A second harmonic (30 Hz) is added to the fundamental to reduce dB/dt in the magnets during acceleration. A 12.5% second harmonic component results in a 25% reduction in dB/dt.

Since all Proton Driver magnets are designed to operate at 16 GeV, all magnet power supply system components have been designed to operate at this level. These include interconnecting bus, terminals, LCW water system, bucking chokes, power supplies, controls and regulation systems. Infrastructure (service buildings, equipment pads) and the 13.8 kV power distribution system are also designed to accommodate 16 GeV operation. Energy storage devices (resonant cell chokes and capacitors) for the dipole/quadrupole resonant network are designed to operate at 12 GeV and can be fully utilized in the 16 GeV configuration using the upgrade described in Section 7.2.4.

7.2. Dipole and Quadrupole Power Supply

7.2.1. System Requirements

The system requirements are listed in Table 7.1.

Table 7.1. System Requirements

	Stage 1 12 GeV Operation	Stage 2 16 GeV Operation
Repetition rate	15 Hz	15 Hz
Maximum magnet current, I_{max}	4,820 A	6,317 A
Minimum magnet current, I_{min}	356 A	356 A
I_{dc}	2,546 A	3,337 A
I_{ac} (15 Hz)	2,274 A	2,980 A
0.125 I_{ac} (30 Hz)	284 A	373 A
$\Delta I / I_{max}$	0.01%	0.01%
Dipole number of electrical turns per pole	12	12
Dipole inductance	2.88 mH/m	2.88 mH/m
Length of long dipoles	5.25 m	5.25 m
Number of long dipoles	36	36
Length of short dipoles	3.94 m	3.94 m
Number of short dipoles	12	12
Total Length of Dipoles	236.3 m	236.3 m
Total Inductance of Dipoles	680.5 mH	680.5 mH
Quadrupole number of electrical turns per pole	4	4
Quadrupole inductance	1.48 mH/m	1.48 mH/m
Total length of quadrupoles	132.4 m	132.4 m
Total inductance of quadrupoles	196.0 mH	196.0 mH
Beam pipe losses	1.10 MW	1.97 MW

7.2.2. System Design

The choice of the magnet resonant network configuration is influenced by three factors: the need to avoid drawing a large reactive power from the a.c. line, reliability, and the importance of maintaining equal currents in the magnets.

The circuit in Figure 7.1 satisfies these basic requirements. The diagram shows three typical resonant cells adjacent to the power supply. Dipoles, F-quadrupoles and D-quadrupoles are connected in series. Power supplies are inserted in series with the magnets near the virtual ground of the distributed resonant circuit. Each power supply is a source of a.c. and d.c. power (similar to the Fermilab Booster). Dividing the resonant system into 30 resonant cells permits a significant decrease in the system voltage to ground. The magnet (L_m), capacitor banks (C and C_1), and chokes (L_{ch}, and L_1), form a resonant cell. Its frequency response is shown in Figure 7.2.

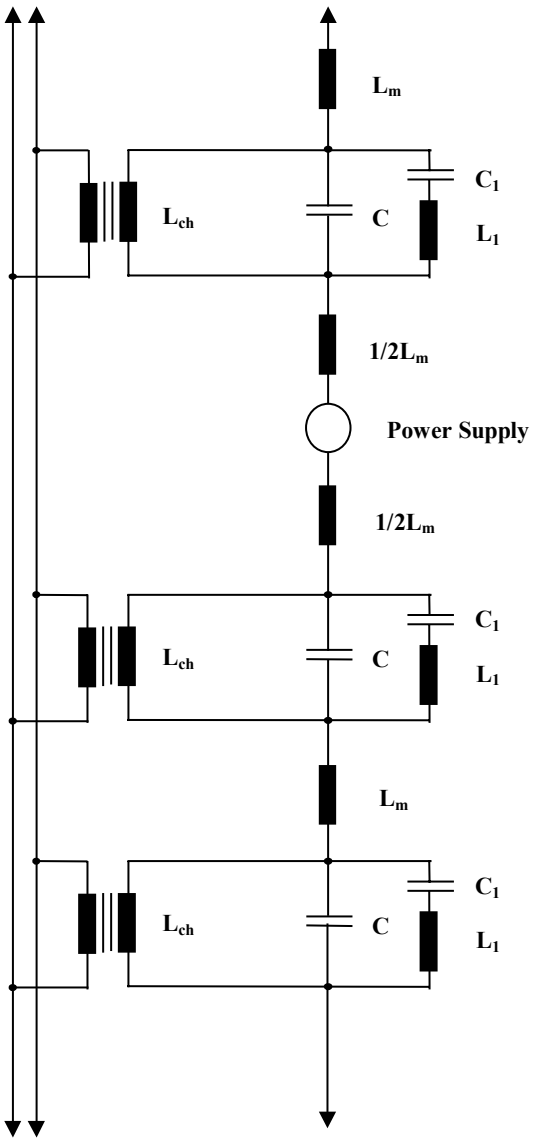

Figure 7.1. Dipole/Quadrupole Power Supply Resonant System Diagram

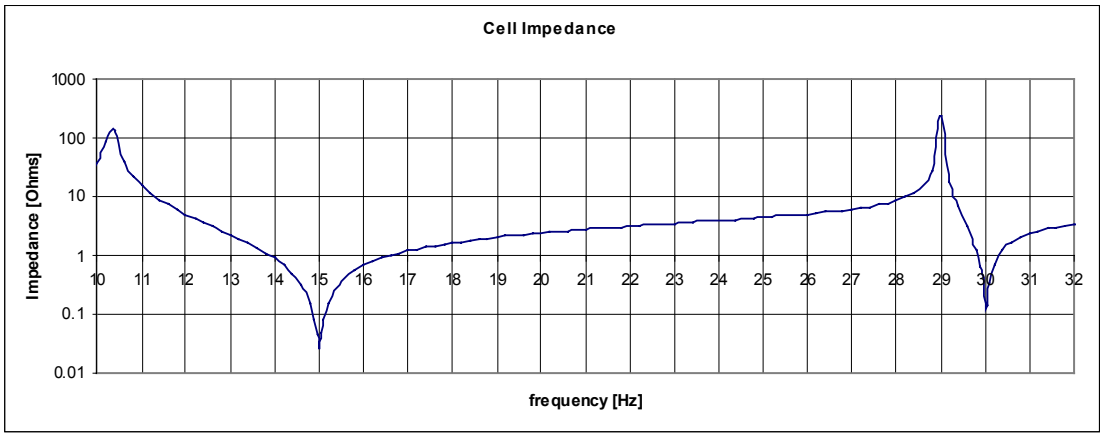

Figure 7.2. Resonant Cell Frequency Response

Although, owing to its series connection, the distributed resonance circuit provides a basic uniformity in magnet currents, the effect of leakage capacitance currents to ground can distort this current equality to a degree that is significant. Since these leakage paths are distributed around the network in a generally uniform manner, it is necessary to ensure that the a.c. potentials of the corresponding points in the network attain a similar value. This is achieved by matching equivalent cell magnet inductances, requiring close tolerances of each resonant cell component and having auxiliary windings in chokes L_{ch} connected in parallel with each other.

7.2.3. System Parameters

Calculations of d.c. resistances and d.c. losses have been done using the proposed stranded conductor described in Chapter 6; a.c. resistances and a.c. losses have been scaled from the Fermilab Booster. All system parameters will be verified when a prototype resonant cell becomes available. System parameters are listed in Table 7.2.

Table 7.2. System Parameters

	Stage 1 12 GeV Operation	Stage 2 16 GeV Operation
I_{rms}	3,018 A	3,955 A
Total a.c. induced voltage, peak	246,960 V	323,776 V
Total d.c. voltage	1,450 V	1,900 V
Number of resonant cells	30	30
Voltage to ground, peak	4,358 V	5,713 V
Total a.c. losses	1.10 MW	1.90 MW
Total d.c. losses	1.85 MW	3.17 MW
Beam pipe losses	1.10 MW	1.97 MW
Total losses	4.05 MW	8.87 MW
Number of power supplies	3	3
Power supply current, peak	4,900 A	6,400 A
Power supply voltage, peak[1]	±900 V	±1,200 V

7.2.4. 16 GeV Upgrade

The resonant cell chokes and capacitor banks are designed for full utilization when the system is upgraded to 16 GeV. Adding capacitor units and fuses to an upgrade-ready frame (Figure 7.3) increases the rating of the capacitor banks while maintaining their net capacitance.

[1] Includes 30% margin for off-resonant operation

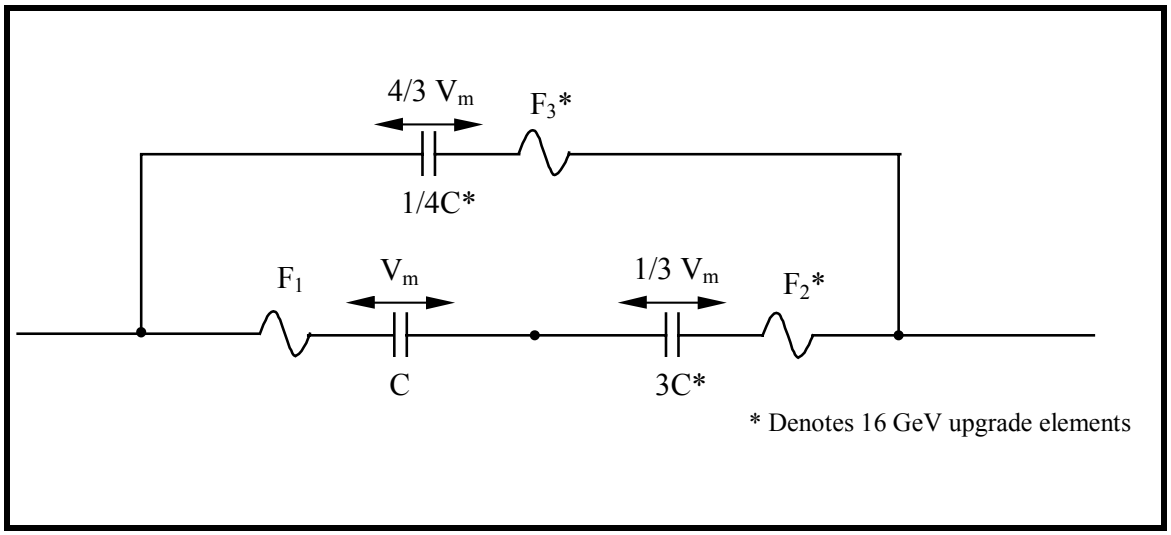

Figure 7.3. Cell Capacitor Banks Upgrade

Chokes will require a two-step upgrade. First, 12 GeV chokes are reconfigured to handle 33% higher peak current and then additional units are added in series (Figure 7.4) to arrive at the required total inductance. The 12 GeV/16 GeV convertible chokes will have multiple main and auxiliary current terminals.

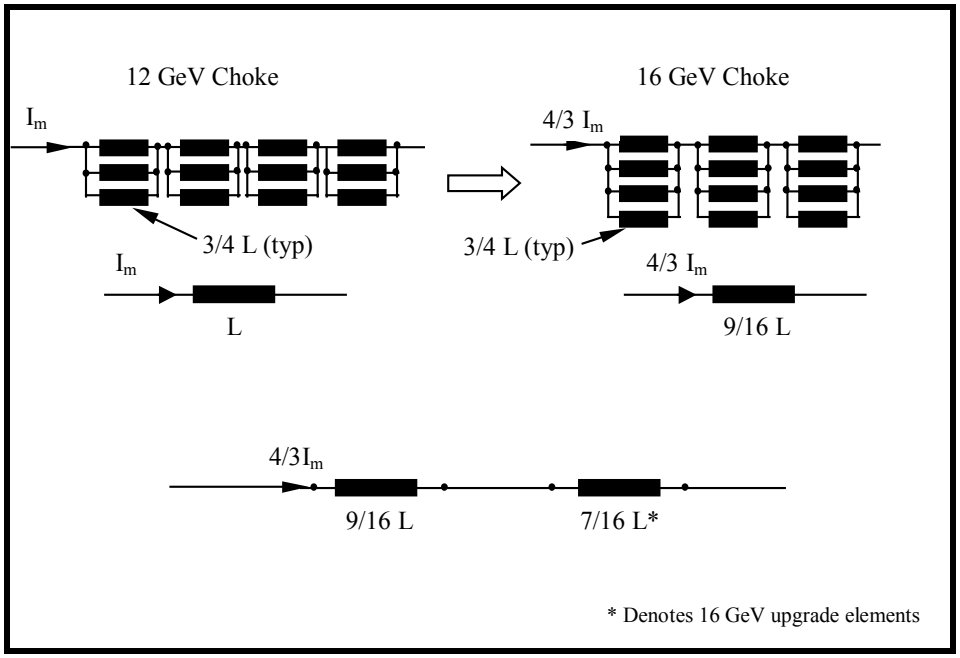

Figure 7.4. Two Step Cell Chokes Upgrade

7.3. Quadrupole Tracking and Correction Power Supply

7.3.1. System Requirements

The system peak current requirement at given frequencies is set by the required tune compensation or tracking compensation, whichever is higher. It is assumed that only frequencies up to the 7^{th} harmonic (105 Hz) will be required to provide sufficient quadrupole field gradient correction (tracking compensation and tune control). System requirements are listed in Table 7.3.

Table 7.3. System Requirements

Frequency [Hz]	Tracking Compensation [± %]	Tune Control [± %]	Power Supply Peak Current Requirement [± %]
15	0.53	2.00	2.00
30	0.36	0.20	0.36
45	0.21	0.10	0.21
60	0.09	0.10	0.10
75	0.02	0.10	0.10
90	0.03	0.10	0.10
105	0.03	0.10	0.10

7.3.2. System Design

Driving the quadrupole trim coils with currents specified in Table 7.3 provides the quadrupole field gradient correction. A bucking choke is used for each quadrupole circuit to cancel the voltage induced in the trim coil circuit caused by the main coil circuit. The estimated peak induced voltage is 8.5 kV per quadrupole family.

The primary windings of the bucking choke are connected in series with the quadrupole trim windings, while the secondary windings are connected in series with the main coils. The mutual inductance of the bucking choke must be equal in value (but opposite in sign) to the sum of mutual inductances of the quadrupole main/trim coil transformers for proper operation.

Figure 7.5 shows the principle of the system and Table 7.4 lists the system requirements.

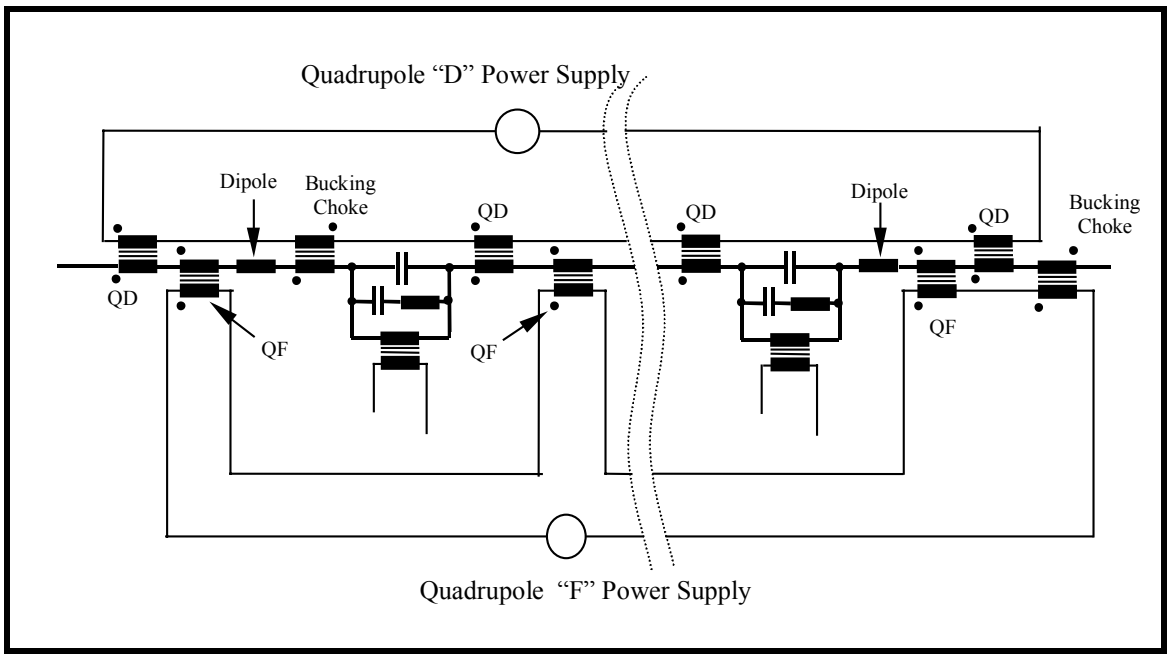

Figure 7.5. The Principle of the Quadrupole Correction System

Table 7.4. System Parameters

	12 GeV Operation	16 GeV Operation
Number of quadrupole "D" trim circuits	6	6
Number of quadrupole "F" trim circuits	6	6
Number of bucking chokes per trim circuit	1	1
Quadrupole "D" main coil inductance, per circuit total	16.33 mH	16.33 mH
Quadrupole "F" main coil inductance, per circuit total	16.33 mH	16.33 mH
Quadrupole main number of turns per pole (electrical equivalent)	4	4
Quadrupole trim number of turns per pole (electrical equivalent)	1	1
Quadrupole main-trim coil coupling coefficient	0.98	0.98
Number of bucking chokes	12	12
Bucking choke main coil inductance	3.77 mH	3.77 mH
Bucking choke turns ratio (trim coil : main coil)	25 : 27	25 : 27
Bucking choke peak stored energy	71 kJ	94 kJ
Bucking choke main-trim coil coupling coefficient	0.98	0.98
Power supply peak current	±544 A	±725 A
Power supply peak voltage	±530 V	±706 V
Trim circuit rms current	492 A	520 A
Power supply minimum bandwidth	210 Hz	210 Hz
Total number of power supplies	12	12

7.4. Horizontal Dipole Correction Power Supply

Figure 7.6 shows the required current waveform and Table 7.5 lists the system requirements.

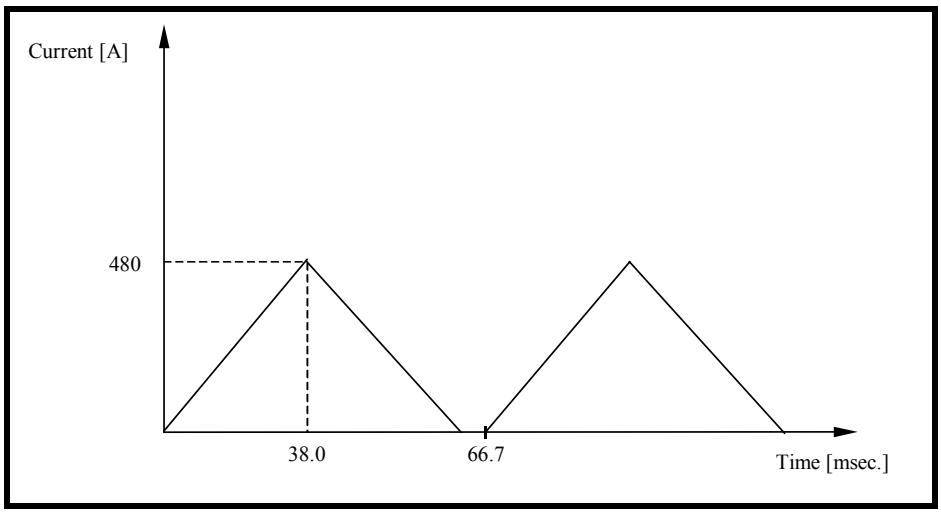

Figure 7.6. Horizontal trim required current waveform

Table 7.5. System Requirements

Parameter	12 GeV Operation	16 GeV Operation
Repetition Rate	15 Hz	15 Hz
Max. Current, I_{max}	480 A	480 A
Required current waveform	Figure 7.6	Figure 7.6
$\Delta I / I_{max}$	0.01%	0.01%
Number of turns per pole	6	6
Long Dipole Trim Coil Inductance	3.8 mH	3.8 mH
Number of Long Dipoles	36	36
Short Dipole Trim Coil Inductance	2.8 mH	2.8 mH
Number of Short Dipoles	12	12

The system is designed so that horizontal orbit correction is accomplished using trim coils wound on the dipole magnet cores. Each dipole magnet is supplied with two sets of trim coils having an equal number of turns. They are connected in series but with opposite magnetic sense so that no net voltage is induced across them by the main coil current. The common connection point between the two trim coils is then connected together with the common points between the other trim coils as shown in Figure 7.6. Each trim set is driven by an independent programmable power supply. The effect of energizing a single trim set is to cause a local horizontal orbit shift without altering the beam orbit path length and beam energy.

System parameters are shown in Table 7.6 and the principle by which the horizontal correction system works is shown in Figure 7.7.

Table 7.6. System Parameters

Parameter	12 GeV Operation	16 GeV Operation
I_{rms}	210 A	280 A
Number of Power Supplies	48	48
Power Supply Current, peak	360 A	480 A
Power Supply Voltage, peak	±40 V	±50 V

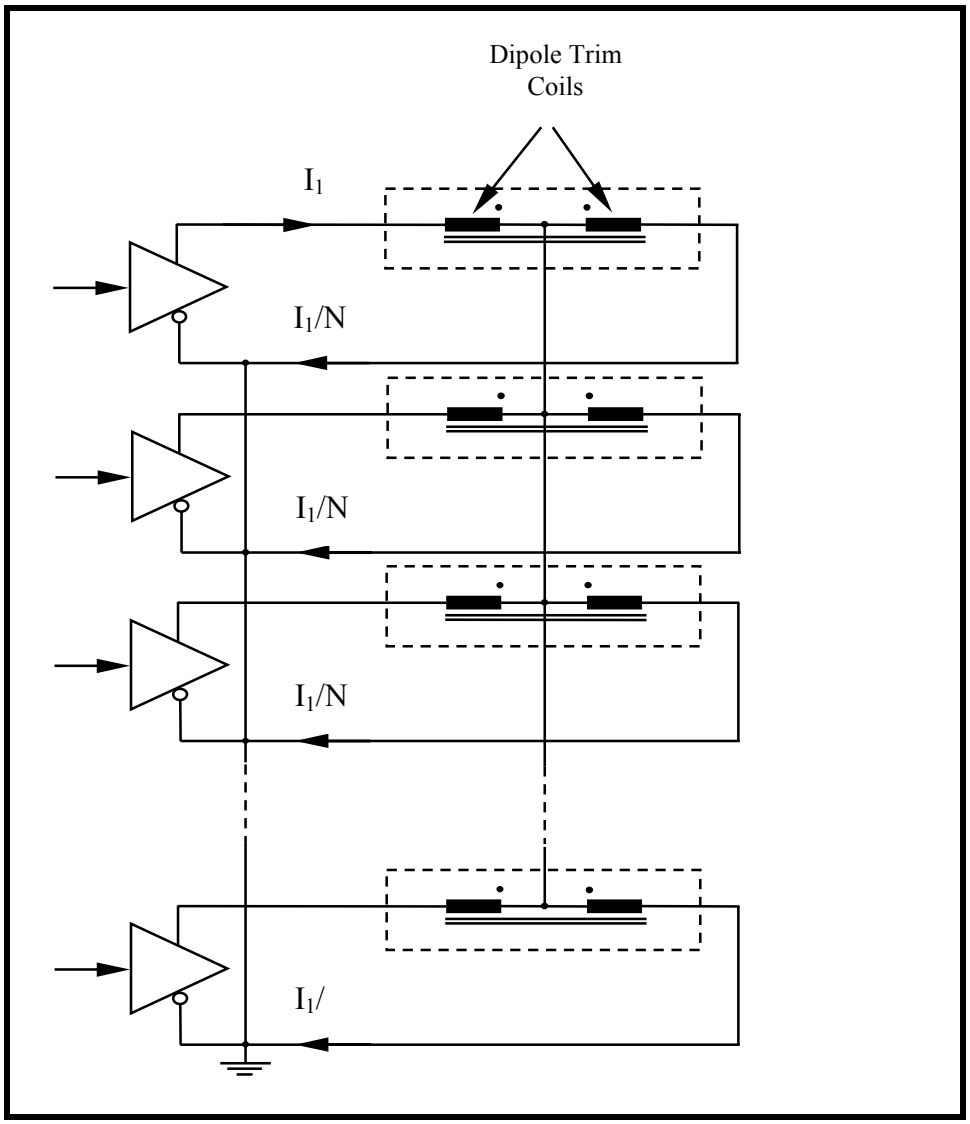

Figure 7.7. Horizontal Dipole Correction Power Supply System Principle

7.5. Vertical Dipole Correction Power Supply

7.5.1. System Requirements

The required waveform for the vertical correction system is shown in Figure 7.8 and the system requirements are listed in Table 7.7.

Figure 7.8. Vertical trim required current waveform

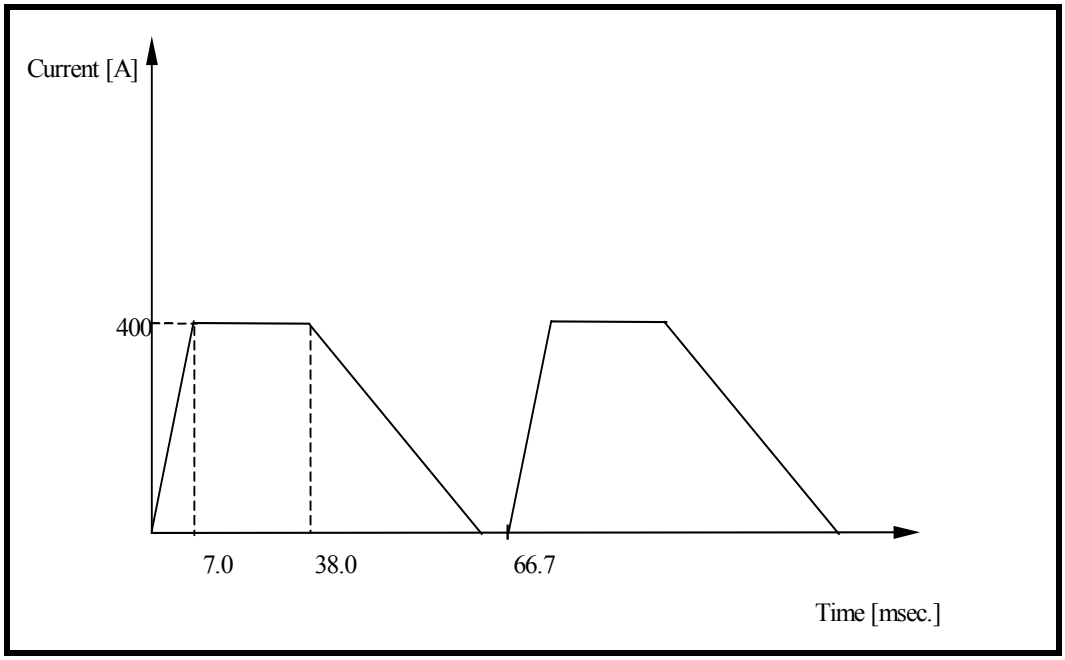

Table 7.7. System Requirements

Parameter	12 GeV Operation	16 GeV Operation
Repetition Rate	15 Hz	15 Hz
Max. current, I_{max}	300 A	400 A
Required current waveform	Figure 7.8	Figure 7.8
$\Delta I / I_{max}$	0.01%	0.01%
Dipole Trim Coil Inductance	10 mH	10 mH
Number of Vertical Trim Dipoles	36	36

7.5.2. System Design

Separate corrector magnets situated at specific points in the ring accomplish vertical orbit correction. The vertical corrector magnets are driven with programmable power supplies similar to those used for horizontal correction. Parameters are shown in Table 7.8.

Table 7.8. System Parameters

Parameter	12 GeV Operation	16 GeV Operation
I_{rms}	230 A	310 A
Number of Power Supplies	36	36
Power Supply Rated Current, peak	300 A	400 A
Power Supply Rated Voltage, peak	±450 V	±600 V

7.6. Sextupole Power Supply

The sextupole power supply system consists of 3 independent circuits with distributed power supplies: SF loop, SD loop, and a stray field compensation loop. System requirements are in Table 7.9 and system parameters in Table 7.10.

Table 7.9. System Requirements

Parameter	12 GeV Operation		16 GeV Operation	
Repetition rate	15 Hz		15 Hz	
Sextupole specific inductance	2.45 mH/m		2.45 mH/m	
$\Delta I / I_{max}$	0.01%		0.01%	
Magnet type	SF	SD	SF	SD
Max. magnet current, I_{max}	1350 A	1,965 A	1800 A	2,620 A
Min. magnet current, I_{min}	76 A	128 A	101 A	147 A
I_{dc}	713 A	1038 A	950 A	1,383 A
I_{ac} (15 Hz)	637 A	928 A	850 A	1,237 A
0.125 I_{ac} (30 Hz)	80 A	116 A	106 A	155 A
Number of sextupoles	24	24	24	24
Total length of sextupoles	7.2 m	7.2 m	7.2 m	7.2 m
Total inductance of sextupoles	17.64 mH	17.64 mH	17.64 mH	17.64 mH

Table 7.10. System Parameters

Parameter	12 GeV Operation			16 GeV Operation		
Circuit	SF	SD	Comp.	SF	SD	Comp.
Number of sextupoles per circuit	24	24		24	24	
I_{rms}	960 A	1,397 A	440 A	1,279 A	1,862 A	590 A
Induced voltage per circuit, peak	1,325 V	1,929 V	25 V	1,766 V	2,572 V	33 V
Number of power supplies	2	3	1	2	3	1
Power supply current, peak	1,800 A	2,700 A	900 A	1,800 A	2,700 A	900 A
Power supply voltage, peak	±700 V	±700 V	±30 V	±1,000 V	±1,000 V	±40 V

7.7. Power Distribution System

The existing site power distribution system is not able to meet the Proton Driver power demand. Therefore, as part of the Proton Driver Project, infrastructure upgrades will be needed. To meet the power requirements, a new substation will be installed. This will be utilized together with existing facilities. Table 7.11 gives power requirements and Figure 7.9 shows single line diagram of the power distribution system. To take advantage of the existing 345 kV equipment, the substation will be located inside Kautz Road Substation.

Table 7.11. Power distribution system requirements

Subsysem	RF system	Main PS	Sext. PS	Quad PS	Vertical corrector	Horiz. corrector	Vacuum system	Conv. power	Total
Peak MVA	40.0	18.0	11.7	5.0	10.0	0.8	1.8[2]	1.5	88.8
RMS MVA	10.0	16.1	8.5	4.4	8.9	0.7	1.8	1.5	51.9

7.8. Required R&D

The power supply system will require a substantial R&D program. Major efforts will be directed towards:

- Design and testing of high voltage magnets (dipole and quadrupole)
- Prototyping a complete resonant cell. This will include dipole and quadrupole prototypes, chokes, capacitors, power supply, regulation and control systems.
- Developing a quadrupole tracking system. This will include a prototype of a resonant cell, bucking choke, tracking power supply, regulation, and control systems.
- Development of the main dipole/quadrupole power supplies employing the newest IGBT technology.

[2] May increase to 4.0 MVA during magnet bake-out.

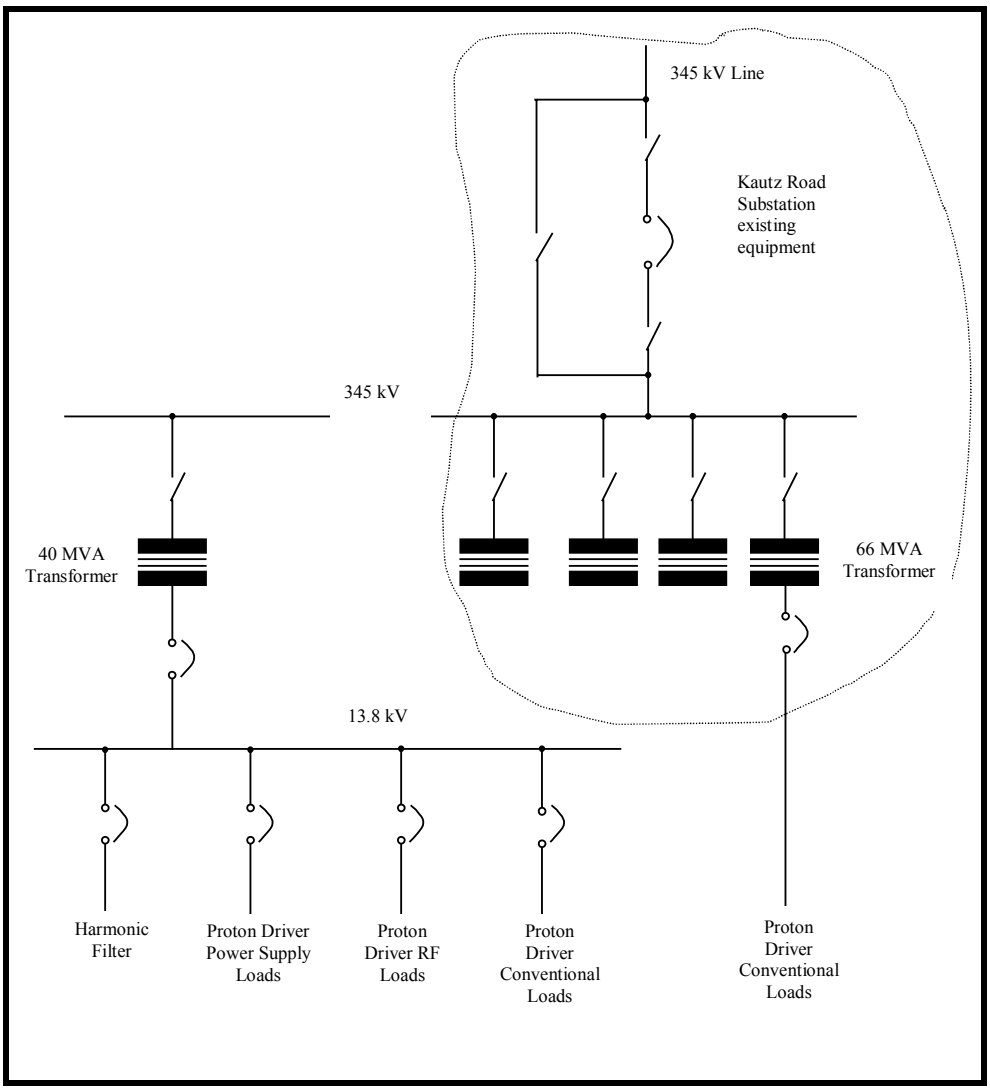

Figure 7.9. Power Distribution System Diagram

References

[1] FERMILAB-Pub-74/85 0323.000 (1974)

[2] R. Hettel, C. Jach, - "The 10 Hz Resonant Magnet Power Supply for the SSRL 3 GeV Injector," 1991 IEEE Particle Accelerator Conference.

[3] C. Jach, A. Medvedko, Y. Fishler – "Energy Storage Inductor for the Low Energy Booster Resonant Power Supply System," 1993 IEEE Particle Accelerator Conference.

Chapter 8. Vacuum

Terry Anderson and Evan Malone

8.1. Design Overview

The Proton Driver Ring Vacuum System is a 711-m continuous vacuum chamber composed of magnets, short sections of tubing, bellows, ion pumps, valves, and instrumentation. The system is divided into twenty (20) sectors, eighteen (18) ring sectors and two (2) transfer lines. The complete Proton Driver Ring layout is shown in Figure 8.1 and a detailed layout of typical sectors is shown in Figure 8.2. Table 8.1 shows the primary system design parameters used as the basis for this description.

Table 8.1. Vacuum System Design Parameters

Average Pressure Range	10^{-7} to 5×10^{-8} Torr
Total System Length	711 m
Vacuum Sector Lengths	69.3 m, 41.7 m, 36.7 m, and 29 m.
Vacuum Aperture	5" × 9"
Primary Pump Type	Ion Pump, 800 l/s.
Roughing Pump Type	Turbo Molecular (500 l/s), w/10 CFM Dry Backing Pump.
Sector Pump-down Time	12 hr to rough; 72 hr bake-out to high vacuum.
Vacuum Gauging	Pirani, Ion Gauge and Ion Pump read-back.
Beam Tube Material	Straight Sections and Magnets without eddy current heating: Stainless Steel Magnets with eddy current heating: Titanium.
Vacuum Interface Type	Flanged w/bellows.
Special Considerations	Dipoles and Quadrupoles will be of a vacuum canned design (core and coils will be in the vacuum space).
Bake-out System	Magnet vacuum chambers will have low temperature (<150 C) bake-out capability.

The primary vacuum system operating parameter for the Proton Driver is the base pressure, 10^{-7} Torr. In typical accelerator vacuum systems this is relatively easy to obtain. Most systems are limited by the aperture conductance and the specific out-gassing rate of the chamber walls. In typical systems at 10^{-7} Torr these limitations are easily overcome by reasonable spacing of relatively small pumps. Pump down times are generally on the order of several hours to one day and are for the most part determined by the time it takes for the specific out-gassing rate to reach 10^{-10} to 10^{-11} Torr-l/s-cm^2. These rates are the lower limits of metals with many monolayers of water molecules adsorbed on the surface and only improve over a long time or by baking the system. Although the Proton Driver is not limited by conductance issues it is limited by the amount of pumping available and the specific out-gassing rate due to the extremely large amount of surface area in the canned

magnets and the high out-gassing of the coil assemblies. In order for the Proton Driver to reach 10^{-7} Torr it is necessary for the out-gassing rates of the magnet laminations and the coil assemblies not to exceed 5×10^{-13} and 10^{-9} Torr-l/s-cm^2 respectively. This can only be achieved by fabricating all components that make up the vacuum system using ultra-high vacuum (UHV) practices and incorporating in a (relatively) low temperature bake-out system.

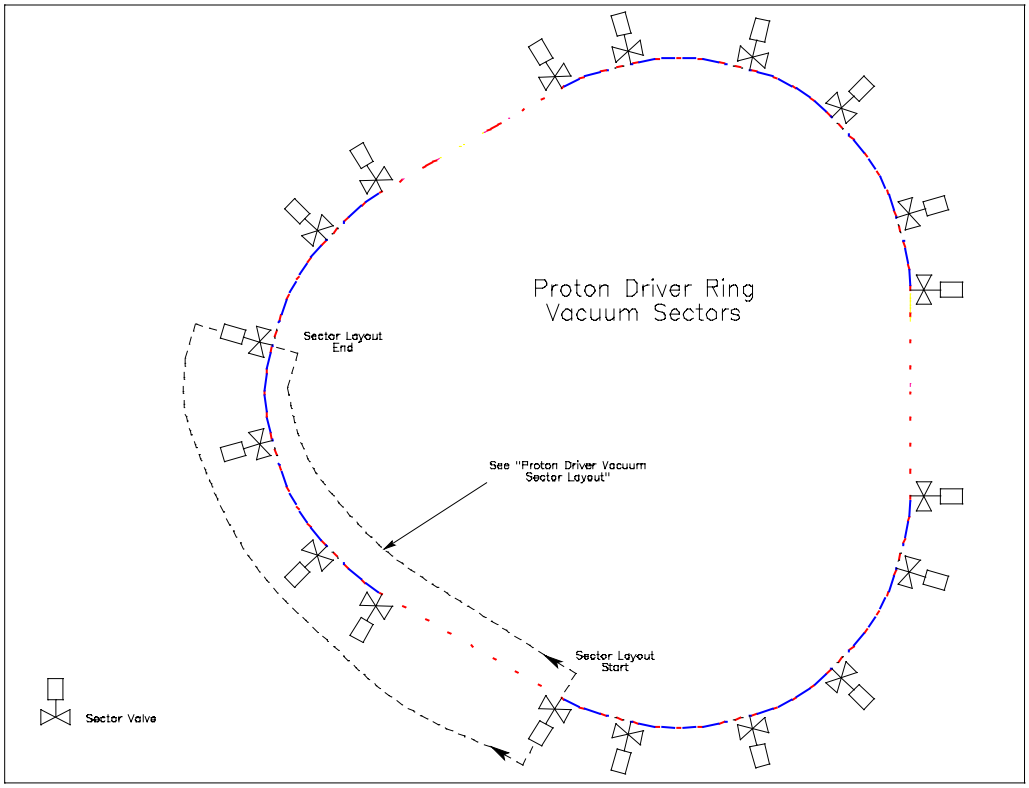

Figure 8.1. Proton Driver Ring Vacuum Sector

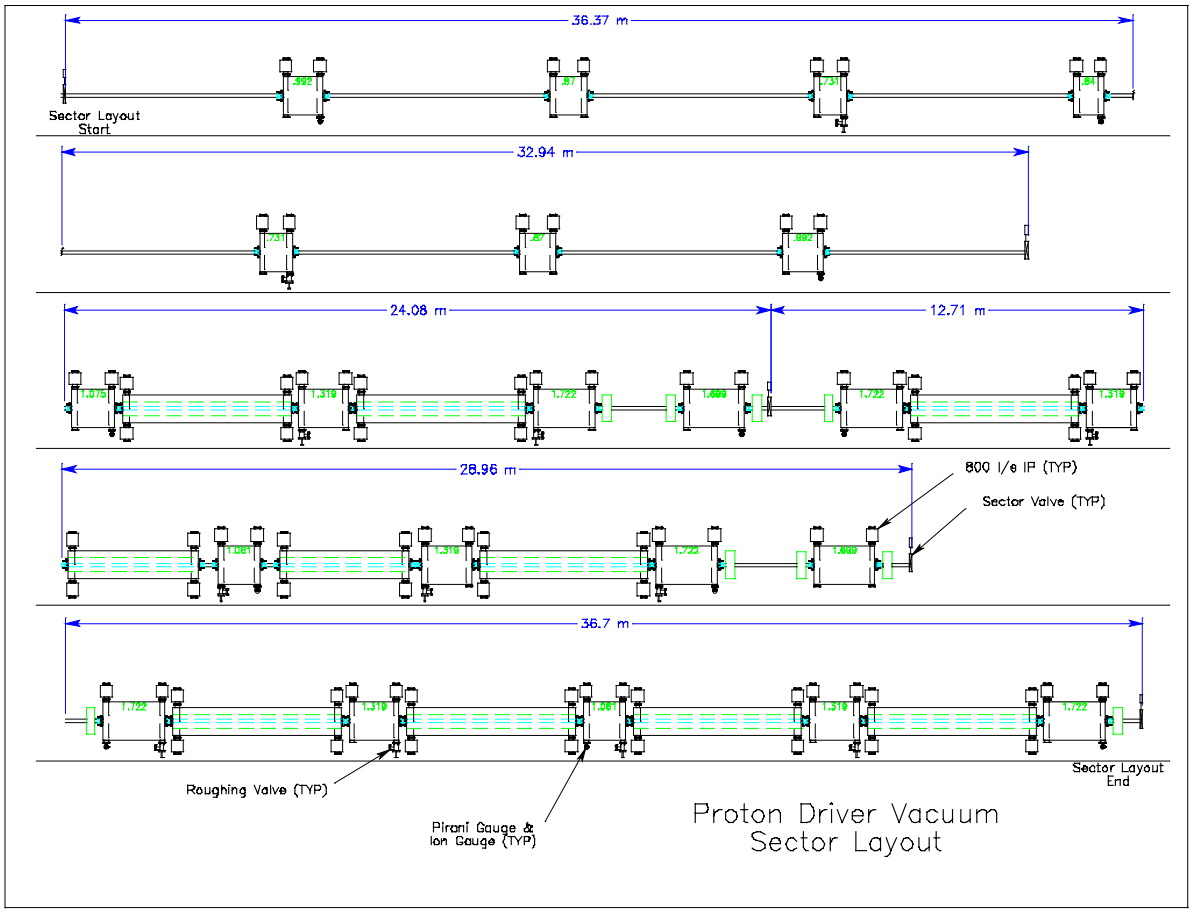

Figure 8.2. Proton Driver Vacuum Sector Layout

8.2. System Components

The vacuum system components for the Proton Driver are, with the exception of the magnets and bellows, fairly standard high to ultra high vacuum components. The magnets are discussed in Section 8.3 below and the bellows are similar to those used in the Fermilab Recycler. The concept is a round, stainless steel, formed bellow and tube section with the basic aperture cross-section. The tube sections extend into the bellow space and a thin (0.005-inch) metallic foil is allowed to slide over the two tube ends to provide rf shielding. The basic vacuum interface is shown in Figure 8.3.

The interface design uses EVAC style ISO NW 250 flanges with chain style clamps. This reduces the amount of space needed between magnet ends, as opposed to Conflat style flanges, and also reduces the exposure time during maintenance operations, thereby contributing to radiation ALARA compliance. Straight sections will be made of stainless steel tubing with a cross-section conforming to the basic aperture. Each end of the straight section will have a bellows and flange. The current design has no vacuum ports or components on the vacuum chamber in the straight sections. All ports and components are on the magnets.

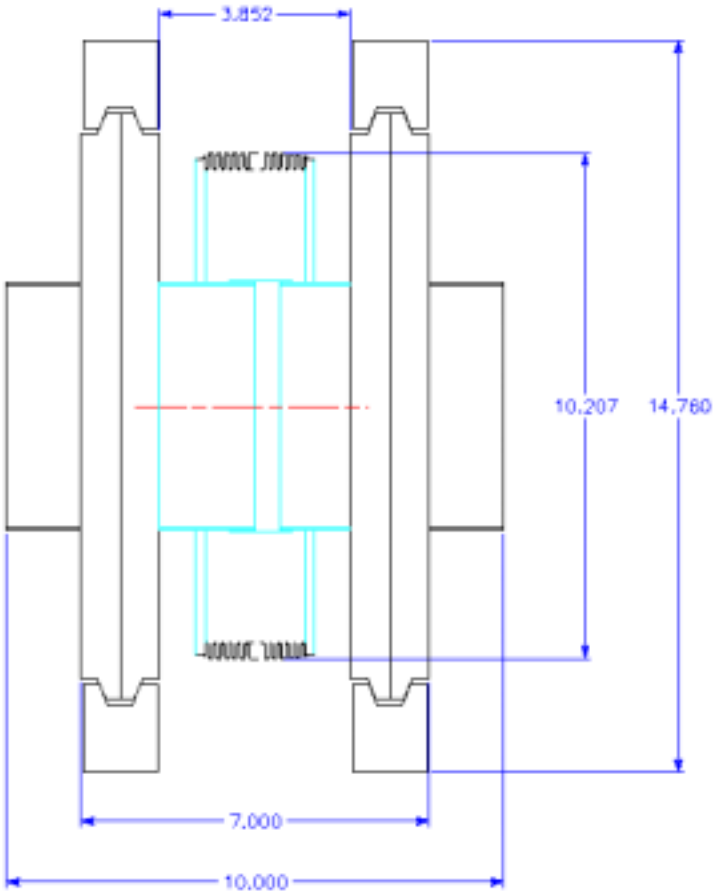

Figure 8.3. Proton Driver Quad/Dipole Interface with Bellows

The remaining basic permanently installed components are: 800 l/s ion pumps, 6 inch roughing valves, Pirani gauges, ion gauges, 10 inch rf shielded sector valves, and the control and read-back systems for each component. The basic vacuum sector configurations are shown in Figure 8.2. Portable turbo molecular roughing carts will attach to the roughing valves for pump down. Other components and systems used in the vacuum system are temperature sensors and controllers for magnet bake-out, a compressed air system for sector valve operation, and stands for valves, chambers, and ion pumps.

8.3. Magnet Vacuum

The proposed magnet design for the Proton Driver is a canned magnet with coils and core contained within the vacuum shell. With this type of design the dominant gas load for the vacuum system comes from the core and the coils, the core due to the large surface area of the laminations and the coil due to the higher out-gassing rate of the insulating material. The design is based on the out-gassing rates shown in Table 8.2.

Table 8.2. Outgassing rates

	Out Gassing Rate (Torr-l/s-cm^2)
Skin	5×10^{-13}
Laminations	5×10^{-13}
Coil	1×10^{-9}

The surface areas for the largest of the Proton Driver magnets are shown in Table 8.3 along with the calculated pressure at the pump, assuming multiple 800 l/s ion pumps for each magnet. The magnet also contains a beam tube, but the gas load contribution from the tube is negligible. A discussion of the beam tube is in Section 8.4 below.

Table 8.3. Vacuum Design Numbers for Proton Driver Magnets

Magnet	Surface Area (cm^2)			Total Gas Load (Torr-l/s)	Pump Speed (l/s)	Pump Pressure (Torr)
	Skin	Laminations	Coil			
5.25 m Dipole	2.77×10^5	2.80×10^8	1.71×10^5	3.11×10^{-4}	3200	9.71×10^{-8}
3.93 m Dipole	2.07×10^5	2.10×10^8	1.28×10^5	2.33×10^{-4}	3200	7.28×10^{-8}
1.72 m Quad	9.73×10^4	1.05×10^8	6.29×10^4	1.15×10^{-4}	1600	7.21×10^{-8}
1.70 m Quad	9.62×10^4	1.04×10^8	6.22×10^4	1.14×10^{-4}	1600	7.14×10^{-8}
1.32 m Quad	7.47×10^4	8.06×10^7	4.83×10^4	8.86×10^{-5}	1600	5.54×10^{-8}
1.06 m Quad	6.00×10^4	6.47×10^7	3.88×10^4	7.12×10^{-5}	1600	4.45×10^{-8}

To achieve the out-gassing rates in Tables 8.2 and 8.3 the magnet assembly needs to be constructed using UHV practices. Steel components will need to be hydrogen degassed prior to assembly and special care taken to insure that all materials in the assembly are free of contaminants such as oils and greases. All materials must be capable of surviving repeated low temperature (150° C) bakes.

From a vacuum standpoint, the coil pack will be especially challenging. The conductor that will be used is a square copper stranded conductor. The strands are wrapped around a stainless steel cooling tube for the LCW cooling water. In order to minimize the gas load due to this assembly, the coil pack will need to be vacuum impregnated with a low out-gassing epoxy type material (preferably polyimide) and then wrapped with a polyimide film. The film must have a near 100% bond to the coil pack to prevent local delaminating that would create unacceptable virtual leaks. The basic concept is to create a low out-

gassing surface that atmospheric gasses will not penetrate to any great degree when the system is let up to atmospheric pressure. Some R&D work still remains to be done with respect to the coil pack design, but the general consensus is that an out-gassing rate of 10^{-9} Torr-l/s-cm^2 is achievable. With considerably more R&D work it is conceivable that the outgassing rate could be reduced by an additional order of magnitude, thereby giving a factor of two decrease in operating pressure.

8.4. Beam Tubes

Besides providing an unobstructed path for the beam, the beam pipe must also control the resistive wall impedance (shielding). Typically, a simple stainless steel pipe serves both purposes, but for the Proton Driver a traditional approach is problematic. The large transverse emittance of the beam requires a large chamber aperture, and therefore large expensive magnets to provide required magnetic field properties over such a large area. Thick chamber walls would be required to support the pressure differential, but such walls would increase the magnet size and cost by consuming aperture. The 15 Hz cycling of the machine would drive immense eddy currents in a metallic chamber inside of the dipole magnets, wasting power and necessitating cooling and field correction. Nevertheless some metal is required to provide adequate shielding. The design chosen attempts to circumvent many of these constraints by segregating the functions of the beam pipe into physically distinct components. The eddy currents are minimized and the aperture maximized by moving the "vacuum skin" to the outside of the magnets. Only the amount of metal required for shielding need be placed inside.

Two methods of shielding the beam are under consideration. The preferred method nearly eliminates eddy currents by dividing the metal shield into parallel, longitudinal conductors capacitively coupled at one end to the next section of beam tube, and in electrical contact at the other end with the previous section of beam tube. This is shown in Figure 8.4. The shield thus acts as a high pass filter. The capacitors act as short circuits for the high frequency beam image currents, but present an open circuit to the 15 Hz eddy currents, confining them to within individual stripes. Because the currents circulate only within a stripe, magnetic fields of neighboring stripes largely cancel each other and Lorentz forces act only within stripes, not between them. This shielding concept was pioneered at the Rutherford Laboratory ISIS spallation source, and has been highly successful [1]. The proposed implementation of this concept for the Proton Driver was conceived of by Bruno Zotter of CERN [2].

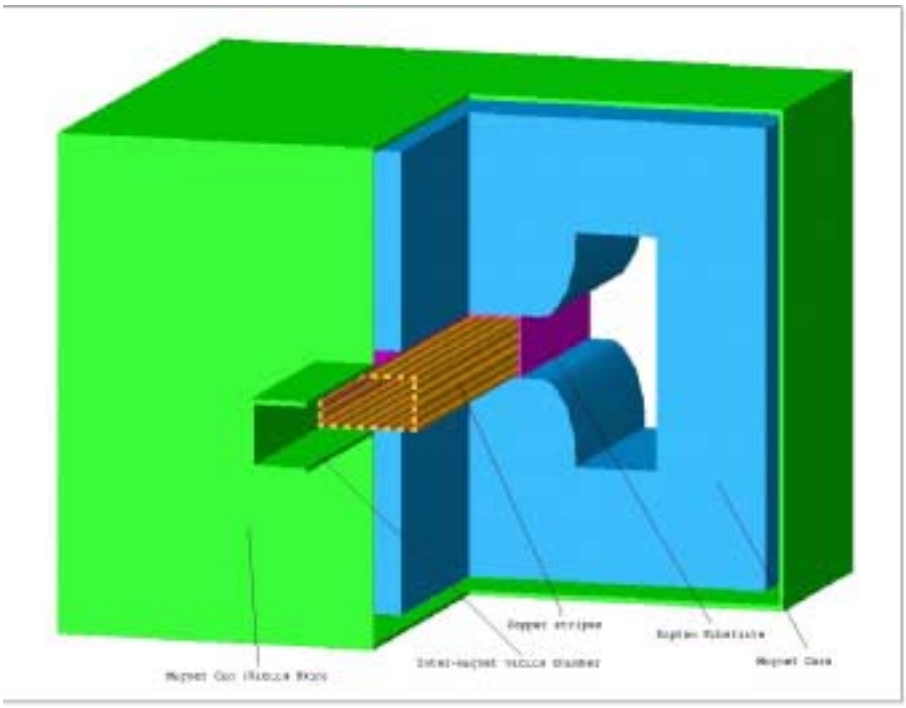

Figure 8.4. Corner Section of Canned Dipole (Striped Shield)

In the Zotter shield, closely spaced copper strips, ~ 0.1 mm thick and 4 mm wide, would be attached to a thin (~ 1 mm) insulating substrate (e.g. Kapton) of rectangular cross section. This would surround the beam supported by adhesive bonds to the magnet pole tips. The cross section of the shield and substrate would need to be contoured to accommodate the reduced diagonal dimensions available within the quadrupoles and sextupoles. There are, however, concerns about the transverse wall impedance that may result from this type of shield. Previous laboratory measurements [3] indicate strips have much larger transverse impedance than that of a uniform metallic coating. Possible resonances that may result from the gaps between strips are also concerns. [11] Currently there is no consensus of theoretical analysis on this type of shield. Technical measures, such as adding circumferential strips insulated from the longitudinal strips [4], may be able to resolve some of these concerns, but further investigation is warranted.

A second shield concept has been examined as an alternative to the Zotter design. A tube of rectangular cross-section, roughly 23 cm × 13 cm, made of an electrically resistive metal alloy, ~ 0.13 mm thick, surrounds the beam inside the magnets. The tube is perforated to permit evacuation of its interior and the perforations are randomly located to prevent electromagnetic resonances. This is shown in Figure 8.5.

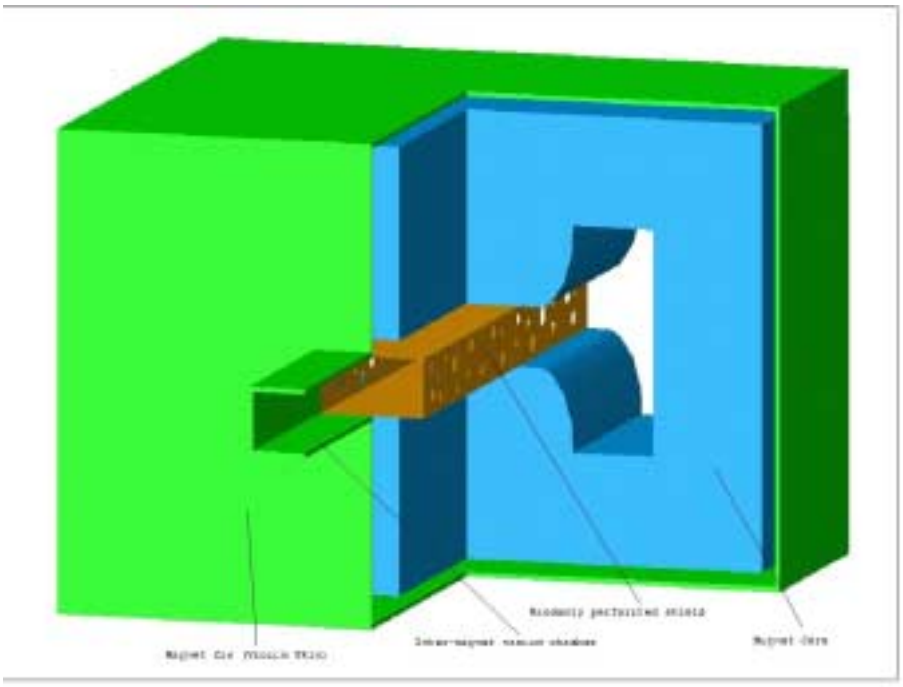

Figure 8.5. Corner section of Canned Dipole (Perforated Tubular Shield)

As in the first concept, the cross-section would need to be contoured within the quadrupoles and sextupoles to accommodate the reduced dimension. The associated resistive wall impedance has not been definitively determined and warrants further investigation. This design must cope with significant eddy currents and their consequences (Lorentz forces, resistive heating, and magnetic field distortions). Due to the thinness of the shield material a means of supporting it against the 15 Hz Lorentz forces without significantly impeding heat transfer will need to be developed. Simulations have shown that 1.2 kW/m or more of eddy current heat can be radiatively transferred to the dipole magnet core without thermal damage to the shield, the core, or the conductor insulation (Figure. 8.6).

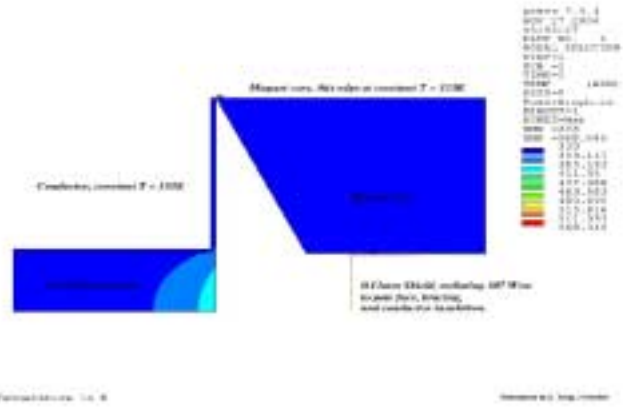

Figure 8.6. FEM of Radiative Heat Transfer from Tubular Shield to Dipole Core

The resulting non-uniform thermal expansion of the magnet core (Figure 8.7) results in substantially less pole face distortion than the 0.13 mm "maximum deviation from planarity" criterion employed during the conceptual design [5].

Figure 8.7. Plot of Vertical Component of Dipole Pole Face Thermal Displacement

A passive scheme for compensating the sextupole magnetic field resulting from the eddy currents has been investigated [6, 7] and seems very promising. Despite the additional complexity of the compensation system, and the significant eddy current heating, this shielding design is considered to be a practical alternative to the Zotter shield.

It is useful to compare the consequences of the two proposed shield designs. Let $I_{beam,RMS}$ be the RMS beam current, ω the beam angular circulation frequency, $B(t)$ the dipole magnetic field, and $B'(t)$ its time derivative. Using these variables, one can calculate $I_{eddy,}$ the induced eddy current, F_{Lor}/l, the total Lorentz force per unit length, P_{eddy}/l, the total eddy current resistive dissipation per unit length, P_{image}/l, the RMS beam image current resistive dissipation per unit length, and d_s, the longitudinal "shielding condition" shield thickness.

The formulae for each design are given in Table 8.4. Using the operating parameters from Table 8.5, results for specific implementations of these two shield designs are given in Table 8.6. It is assumed that for shields in quadrupoles and sextupoles the eddy currents and their consequences would be reduced by at least one order of magnitude; thus the emphasis is on the dipole design.

Table 8.4. Shield Design Equations

RECTANGULAR TUBE width: $2a$, meters height: $2b$, meters thickness: d, meters shortest distance shield to pole: h, meters mag permeability: $\mu = \mu_r\mu_0$, Henry per m electrical resistivity: ρ, Ohm-meters	**LONGITUDINAL STRIPES** stripe width: $2w$, meters stripe thickness: d, meters hor stripes (top + bottom surfaces): N_H vertical stripes (left + right surfaces): N_V shortest distance shield to pole: h, meters mag permeability: $\mu = \mu_r\mu_0$, Henry per m electrical resistivity: ρ, Ohm-meters
$I_{eddy}(t) = B'(t)\, a\, d\, (a + 2b)/\rho$ Amps	$I_{eddy}(t) = B'(t)\, d\, w^2/2\rho$ Amps, inside one horizontal stripe
	$I_{eddy}(t) = B'(t)\, w\, d^2/2\rho$ Amps, inside one vertical stripe
$F_{Lor}/l = B(t)I_{eddy}(t)$ $= B(t)B'(t)\, a\, d\, (a+2b)/\rho$ N/m	$F_{Lor}/l = B(t)I_{eddy}(t)$ N/m, acting only within a stripe
$P_{eddy}/l = 4B'(t)^2\, a^2\, d\, (a/3+b)/\rho$ Watts/m	$P_{eddy}/l = 2B'(t)^2\, wd\, (N_H w^2 + N_V d^2)/3\rho$ Watts/m.
$P_{image}/l \approx (I_{beam,RMS})^2 \rho\, /2d/(2a + 2b)$ Watts/m	$P_{image}/l \approx (I_{beam,RMS})^2 \rho\, /2wd/(N_H + N_V)$ Watts/m
$d_s \gg \rho/\mu wh$ m	$d_s \gg \rho/\mu wh$ m

Table 8.5. Relevant Proton Driver operating parameters

	Phase 1, Stage 1	Phase 1, Stage 2
ω (at injection)	1.88×10^6 radian/s	1.88×10^6 radian/s
$B'(t)_{RMS}$	35 T/s	47 T/s
$Max(B(t)B'(t))$	34 T^2/s	61 T^2/s
$I_{beam,RMS}$	2.69 A	7.12 A

Table 8.6. Shield Design Results

	RECTANGULAR TUBE (Inconel alloy 718) $2a = 0.2286$ meters $2b = 0.127$ meters $d = 1.27 \times 10^{-4}$ meters $h = 1 \times 10^{-3}$ meters $\mu = 1.002\ \mu_0$ Henry per m $\rho = 121 \times 10^{-8}$ Ohm-meters		LONGITUDINAL STRIPES (Oxygen Free Copper) $2w = 4 \times 10^{-3}$meters $d = 1 \times 10^{-4}$ meters $N_H = 100$ (2 sheets of 50) $N_V = 54$ (2 sheets of 27) $h = 1 \times 10^{-3}$ meters $\mu = 1.000\ \mu_0$ Henry per meter $\rho = 1.71 \times 10^{-8}$ Ohm-meters	
	Stage 1	Stage 2	Stage 1	Stage 2
$RMS(I_{eddy})$[1]	101 A	136 A	1.64 A (in one horizontal stripe)	2.20 A (in 1 one horizontal stripe)
			40.9 mA (in one vertical stripe)	55.0 mA (in one vertical stripe)
$MAX(F_{Lor}/l)$ [1]	98.4 N/m	177 N/m	1.59 N/m (in one horizontal stripe)	2.85 N/m (in one horizontal stripe)
			39.8 mN/m (in one vertical stripe)	71.3 mN/m (in one vertical stripe)
$RMS(P_{eddy}/l)$	683 W/m	1230 W/m	30.6 W/m	55.1 W/m
$RMS(P_{image}/l)$	96.9 mW/m	679 mW/m	1.00 mW/m	7.04 mW/m
d/d_s (longitudinal, at injection)	0.25		13.8	

In the course of the conceptual design of the Proton Driver, several additional vacuum chamber designs were considered. Each of the designs involved some significant drawback that made it inferior, at this stage, to the design selected. A brief description of these designs and the decisive issues associated with them follows. More detailed technical descriptions of the R&D work on those designs will be available in Fermilab technical notes.

The first design investigated was a metallic vacuum chamber 22.86 cm × 12.7 cm (9 in × 5 in) elliptical cross section, made of 1.27 mm (50 mils) thick Inconel alloy 718 (Figure. 8.8). The significant distortion of the chamber wall under vacuum required that the tube be

[1] Note: eddy currents and Lorentz forces for the striped shield are confined to the interior of each stripe. There are essentially no inter-stripe forces, and magnetic fields generated by eddy currents in one stripe are essentially cancelled by fields from neighboring stripes.

initially formed to a less eccentric cross-section than desired for the final chamber. The chamber would need to be built inside of the dipole magnets. Despite being constructed of thin, highly electrically resistive alloy, this chamber would experience eddy currents of 1370 A inside the dipole magnets. This would result in very large and difficult to correct sextupole (and higher order) fields, and nearly 8500 W/m of eddy current heating. The design therefore would require the passive sextupole compensation system mentioned above, as well as an active cooling system. Significant effort was expended on development and processing of thermally conducting, electrically insulating epoxy materials to increase thermal contact between the cooling pipes and the chamber, and promising results were obtained. However, the longevity of these materials in service, as well as the significant quantity of power wasted, the large sextupole fields, and the difficulty of building and maintaining the system make it undesirable.

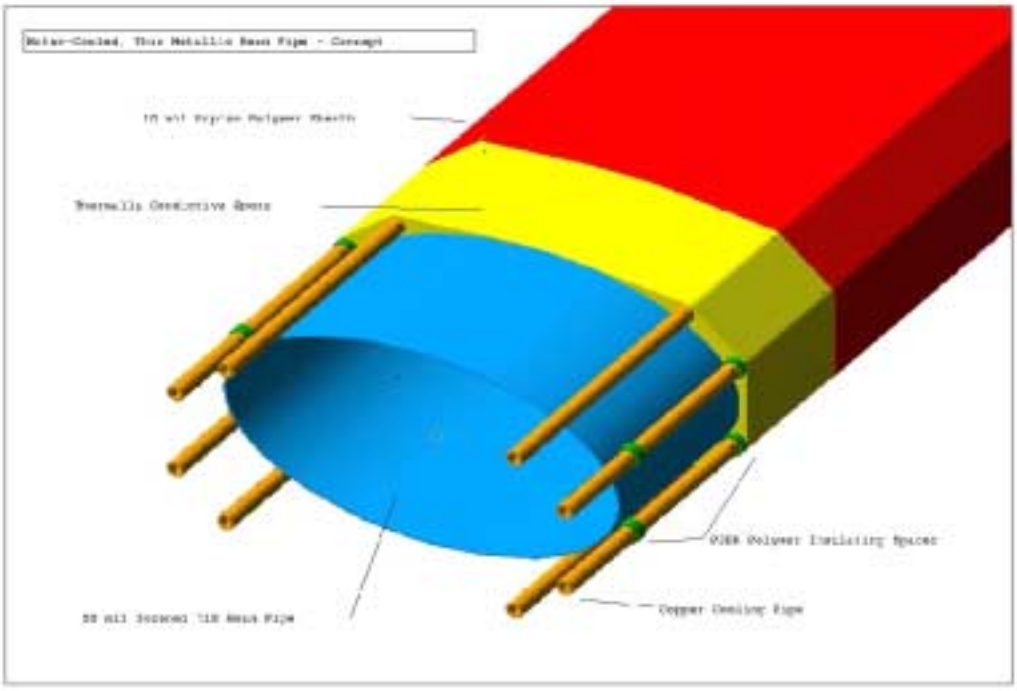

Figure 8.8. Water-cooled Vacuum Chamber Design

A second design investigated was an extrapolation of a vacuum chamber design used in the DESY III accelerator [8]. The particular implementation studied involved a metallic vacuum chamber of 22.86 cm × 12.7 cm (9 in × 5 in) elliptical cross section, made of 0.127 mm (5 mils) thick Inconel alloy 718. Reinforcing ribs of 1 mm thick alloy 718 were brazed to the outside, 75 ribs per meter of tube, to support it against atmospheric pressure. In practice, obtaining a high enough braze quality without distorting such flimsy material proved exceedingly difficult (Figure 8.9). In addition, though the eddy currents and their effects are reduced by a factor of ten from the first design described, they are still quite large. Sextupole compensation would be required, the chamber and adjacent materials inside of the dipole magnets would reach high temperatures (300° C) without active cooling, and any significant deviation of the supporting ribs from parallelism with the

magnetic fields would result in catastrophic eddy currents, probably destroying the chamber. For these reasons, this design was rejected.

Figure 8.9. Photograph of Unsuccessful Prototype of Rib-Reinforced Vacuum Chamber

A third design is based on metal foil lined, fiber-reinforced epoxy chambers built for the CERN SPS interaction region during the mid-1980's [9]. Such chambers are conceptually similar to chambers of ceramic, with an insulating external structure surrounding/supporting a metallic shield of some sort. In particular, to manufacture the composite vacuum chamber, a metal tool form of the desired cross-section would be wrapped with the desired shield material, for instance a continuous Titanium alloy foil, or longitudinal copper stripes on a Kapton polymer backing. A ceramic fiber impregnated with a bismaleimide resin would then be wound over the tool and the shield material to build up the desired thickness. The resin is cured and metal flanges would be bonded to the ends. Composite chambers can be nearly as strong and stiff as ceramic, but are less brittle, and so can be made slightly thinner. Composite chambers also can be manufactured in single units of 6 m or more in length, can be curved, and are significantly cheaper per unit. However, the durability of epoxy composite materials in accelerator service conditions of thermal and mechanical cycling, radiation, and high humidity, and the vacuum out-gassing and gas permeability of such materials need further investigation. Fermilab lacks the equipment to manufacture high-performance, filament wound composite materials, and the high cost of outsourcing the work (> K$ 100) prevented further investigation of the design at this time. Composite chambers are considered to be very promising and worthy of further R&D.

8.5. Vacuum Performance

As stated earlier, the primary vacuum system operating parameter for the Proton Driver is the 10^{-7} Torr base pressure. Because of the need to have as low as possible out-gassing rates, this can only be achieved after a low temperature bake-out for at least seventy-two (72) hours. The vacuum sectors have been made sufficiently short to minimize the number of turbo carts and to create manageable sections for bake-out operations. The longest sector is the 69.3 m straight section containing seven (7) quadrupoles. The most difficult sector to pump down is the 36.7 m arc sector that contains five (5) quadrupoles and four (4) dipoles. The performance curves for the straight section and the arc sector are shown in Figures 8.10 and 8.11, respectively.

In both charts the top curve (black) is the sector pressure profile during rough down at the end of the bake-out. The middle curve (purple) is the sector pressure profile after starting the ion pumps on the quads that the turbo carts are attached to. The bottom curve (orange) is the sector pressure profile after all ion pumps have been started and the system has cooled down to ambient conditions. In both cases the final average steady state pressure is less than 10^{-7} Torr. In the arc sector, at the center of the dipoles, the pressure does peak at 1.24×10^{-7} Torr but the average is still less than 10^{-7} Torr.

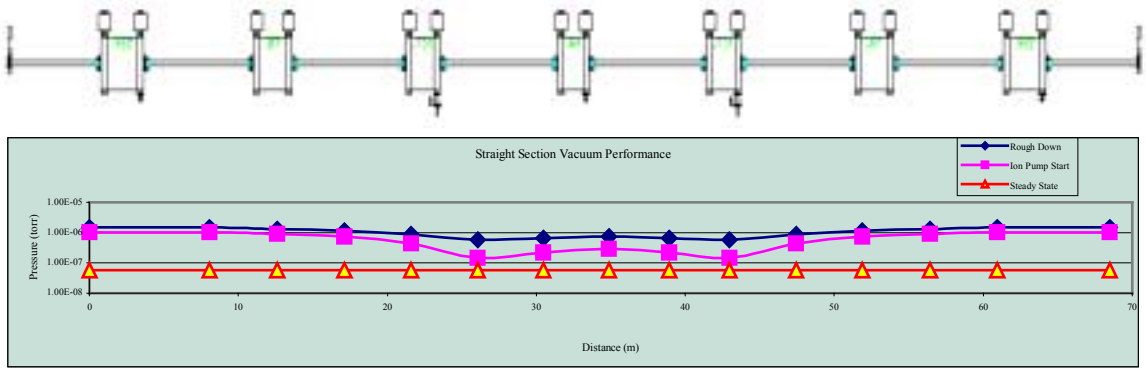

Figure 8.10. Straight Section Vacuum Performance

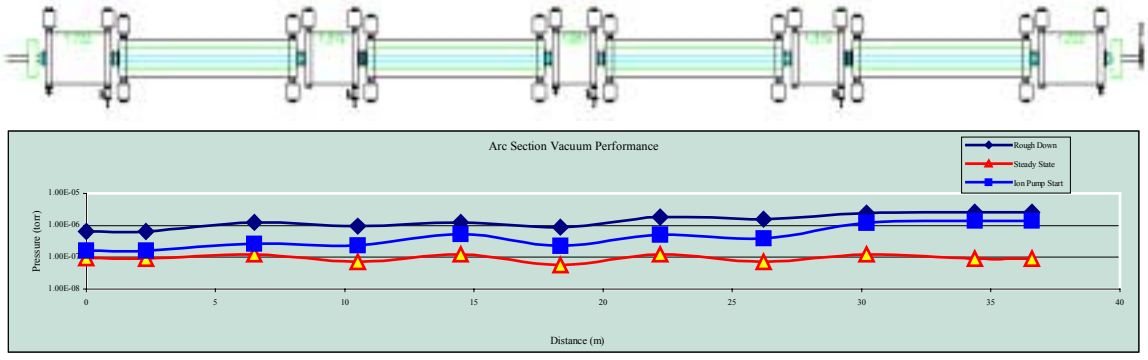

Figure 8.11. Arc Section Vacuum Performance

8.6. R&D Efforts

The main remaining vacuum issue is the outgassing rate of the coil assembly. It is believed that we can obtain a rate of 10^{-9} Torr-l/s-cm^2, but this needs to be verified experimentally. With further R&D to improve this rate it should be possible to realize a factor of two (2) or better decrease in the ultimate pressure, putting the vacuum level comfortably in the mid to low 10^{-8} Torr range.

The highest priority for research and development related to the magnet beam tubes for the Proton Driver is to establish a solid and experimentally verified understanding of the minimum beam shielding requirements for tolerable resistive wall impedance. If discontinuous shield designs (capacitively coupled stripes) provide sufficient shielding, then eddy-currents and all of their consequences are practically eliminated. Magnetic field distortion compensation becomes unnecessary. Power dissipation is minimal, and thus heat transfer, material temperature limits, and thermal stresses are of little concern and Lorentz forces are small. If a continuous shield is required, then awareness and use of the minimum shield thickness permits the minimization of eddy-currents and their consequences.

During the conceptual design of the Proton Driver, vacuum chambers made of fiber-reinforced epoxy with a continuous metal foil lining were investigated [10]. This design was extrapolated from composite chambers designed for the CERN SPS interaction region, which had significantly different design constraints [9]. The lining is intended to reduce the permeation of gases through the composite material and to provide shielding for the beam. There is consensus that this design is worthy of further investigation and prototyping, as it could provide a very thin chamber with significant cost and manufacturing advantages. There is the potential for a significant break through for the Proton Driver. Successful implementation of this design would significantly reduce the pumping and cost requirements of the vacuum system. In addition the magnet costs would be reduced due to elimination of the canned magnet design.

The following is a list of R&D activities that should be undertaken to address the issues and opportunities discussed above.

For verification of coil out-gassing rates:

1) Out-gassing tests on various coil coatings and configurations.

For understanding of the minimum shielding requirement:

1) Additional theoretical investigation of the minimum beam-shielding requirement and of the longitudinal and transverse resistive wall impedance of discontinuous (striped) shielding.
2) Laboratory and accelerator tests of resistive wall impedances of thin, metallic tubular and striped shield designs.

For evaluation of fiber-reinforced epoxy composite vacuum chambers:

1) Tests of vacuum out-gassing and permeability of gasses through candidate materials.
2) Evaluation of processes/coatings/linings to enhance vacuum properties if necessary.
3) Tests of thermal and mechanical properties of candidate materials.
4) Tests of effects of radiation exposure on vacuum and mechanical properties of candidate materials (service lifetime).
5) Small scale prototyping and testing of tubes with various interface (flange) and shielding (Kapton with copper stripes, Ti alloy foil liner, etc.) designs.
6) Prototyping and in-accelerator testing of best designs to establish manufacturing process and validate design.

Assuming that the minimum shielding requirement is well understood, and that the two shielding methods described for the proposed "canned magnet" vacuum system are still feasible in light of that understanding, practical implementations of these two designs will depend upon engineering solutions to several outstanding problems. The following is the R&D effort that will need to be conducted based on the outcome of the beam shielding assessment.

For the perforated, thin-wall tubular shield in "canned magnet" vacuum system:

1) Development of manufacturing process to produce randomly perforated thin-wall tubing.
2) Development of mechanical support structure to reinforce thin-wall shield against Lorentz forces without impeding heat flow from shield to surroundings.
3) Prototyping of eddy-current magnetic field passive compensation system.
4) In-magnet tests (comparable dB/dt to Proton Driver) to validate shield and eddy-current magnetic field compensation system designs.

For the striped shield in "canned magnet" vacuum system:

1) Evaluation of mechanical, vacuum and radiation properties of candidate substrate materials for metallic stripe shield designs.
2) Evaluation of mechanical, vacuum, and radiation properties of adhesive or other stripe-to-substrate bonding methods and substrate-to-magnet pole bonding methods.
3) Design and testing of capacitive interconnection of stripes to intermagnet vacuum chamber.

References

[1] Rees, G.H., "Aspects of Beam Stability at ISIS," in: Workshop on Instabilities of High Intensity Hadron Beams in Rings, Upton, NY, USA, June 28 - July 1, 1999, pp. 17 – 21

[2] See Ch. 4, sections 4.2.1-4.2.2 of this report

[3] Walling, L.S., et. al., "Transmission-Line Impedance Measurements for an Advanced Hadron Facility," Nuclear Instruments and Methods in Physics Research, North-Holland, Amsterdam, A281 (1989), pp. 433-447

[4] Harvey, A., "Tailored Vacuum Chambers for AC Magnets," IEEE Transactions on Nuclear Science, V. NS-32, Number 5, Oct. 1985, pp. 3815 – 3817

[5] Mills, F., personal communication, ~9/1999

[6] Danby, G., et. al., "Description of New Vacuum Chamber Correction Concept," Brookhaven National Laboratory, BNL41856, 1989

[7] See discussion in Chapter 6 of this report

[8] Kouptsidis, J., et. al., "A Novel Fabrication Technique for Thin Metallic Vacuum Chambers with Low Eddy Current Losses,"IEEE Transactions on Nuclear Science, V. NS-32, Number 5, Oct. 1985, pp. 3584-3586

[9] Engelmann, M., et. al., "Vacuum Chambers in Composite Material," Journal of Vacuum Science and Technology A, 5, Jul/Aug 1987, pp. 2337-2341

[10] Anderson, T., Malone, E., "Fermilab Proton Driver: R&D Effort for Composite Vacuum Chamber," PDF file on Proton Driver Website, http://www-bd.fnal.gov/pdriver/systems/CompositeTubeInfo.pdf

[11] W. Chou and T. Barts, "Impedance of a Perforated Liner and Its Impact on the SSC Collider," Proc. of the 1993 IEEE Particle Accelerator Conference, May 17-20, Washington, D.C., p. 3444.

Chapter 9. Beam Loss and Collimation

M. Church, A. Drozhdin, O. Krivosheev, N. Mokhov

9.1. Introduction

A very high beam power of ~1.2 MW (4 MW in Phase II) implies serious constraints on beam losses in the machine [1, 2]. As will be shown below, the main concerns are hands-on maintenance and ground-water activation. Only with a very efficien beam collimation system [3] can one reduce uncontrolled beam losses in the machine to an allowable level. Massive local shielding is needed around the collimators. The entire complex must be well shielded to allow a non-controlled access to the outside surfaces under normal operation and accidental beam loss.

There are three 63.921 meter long straight sections in the Proton Driver lattice. Thr firs of them, P20, together with 17 m of the preceding arc, called below "utility section", is used for beam injection and collimation (Fig. 9.1). The β-functions and dispersion in this region and along the ring are shown in Fig. 9.1 and Fig. 9.2.

In this study, a multi-turn particle tracking in the accelerator define by all lattice components with their realistic strengths and aperture restrictions, and halo interactions with the collimators is done with the STRUCT [4] code. Protons lost on the machine components are stored in the file for the next step of calculations with the MARS [5] code. Full-scale Monte Carlo hadronic and electromagnetic shower simulations in the lattice elements, shielding, tunnel and surrounding dirt with realistic geometry and materials and magnetic fiel are done with MARS14. This shapter summarizes the results on tolerable beam loss and on a proposed beam collimation system design.

9.2. Deduction of Tolerable Beam Loss

To determine tolerable beam loss in the arcs, MARS14 simulations are done in the arc cells. A detailed lattice description with dipoles, quadrupoles and long bare beam pipes has been implemented into a 3-D model with corresponding materials and magnetic fiel distributions (see Figs. 9.3 and 9.4). A 16-GeV proton beam is assumed to be lost on a beam pipe at a grazing angle of 1 mrad inward. It is distrubuted uniformly along the arc lattice. Results are normalized per 1 W/m beam loss rate, that corresponds to 3.9×10^8 p/(m·sec). In this simplifie model, a round 2-m radius tunnel with a 0.4-m concrete wall followed by wet dirt is assumed with the beam line in the center. Dose accumulated in the hottest spots of the coils, residual dose rates on the outer surface of the lattice elements after 30 days of irradiation and 1 day of cooling, and ground-water activation and dose attenuation in the surrounding dirt are calculated. Regulatory requirements of Section 10.2 are taken as the limits to be met.

Maximum residual dose rates calculated for the arc elements at 1 W/m uniform beam loss are shown in the third column of Table 9.1. The table gives also the peak dose ac-

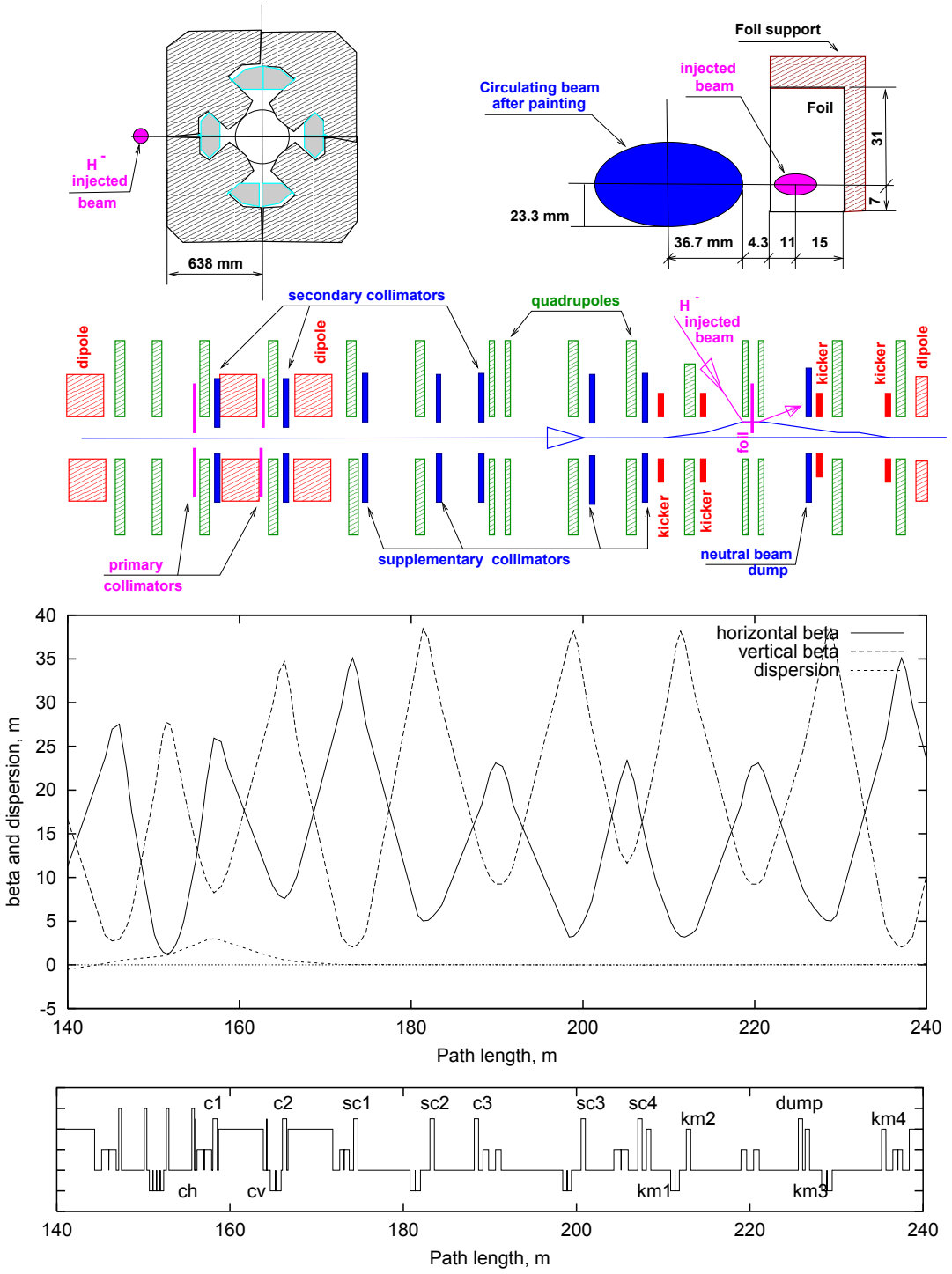

Figure 9.1. Beam collimation and beam painting systems (top) and beta functions and dispersion in the utility section (bottom).

cumulated in the coils and the parameter C_{tot} calculated according to Eq. (10.2). The last column gives corresponding beam loss rates calculated to meet the limits of Section 10.2: P_γ=100 mrem/hr, D=20 Mrad/yr and C_{tot}=1.

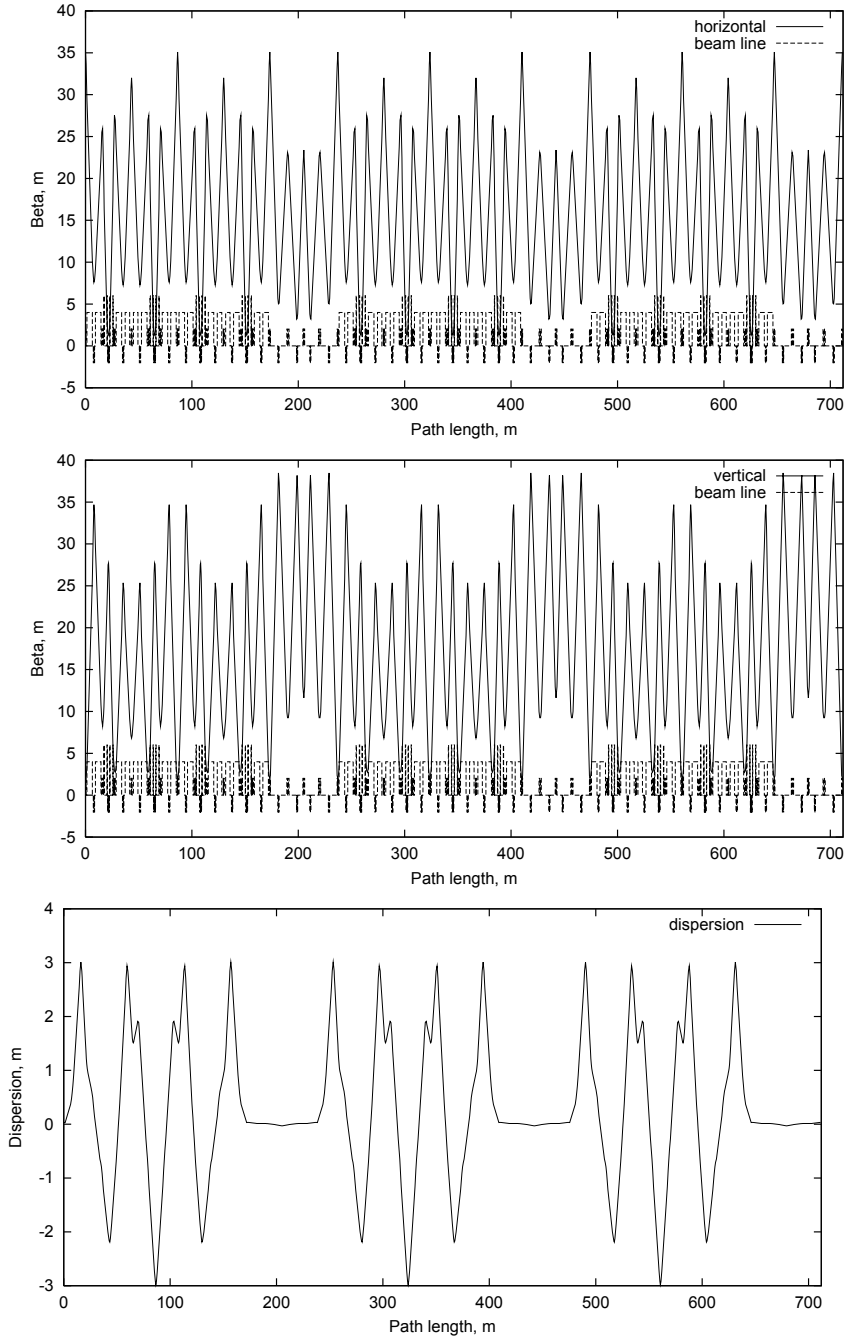

Figure 9.2. Proton Driver beta functions and dispersion.

The dose near the bare beam pipes exceeds the design goal for hot regions of 100 mrem/hr; it is noticeably lower near the magnets due to signif cant absorption of soft photons in the dipole and quadrupole materials. One sees that hands-on maintenance is a serious issue with about 3 W/m as a tolerable maximum beam loss rate in the lattice elements, except for the long bare beam pipes where one should decrease the loss rate to 0.25 W/m to reduce the dose to 100 mrem/hr. One needs further reduction to bring the dose down to a good practice value

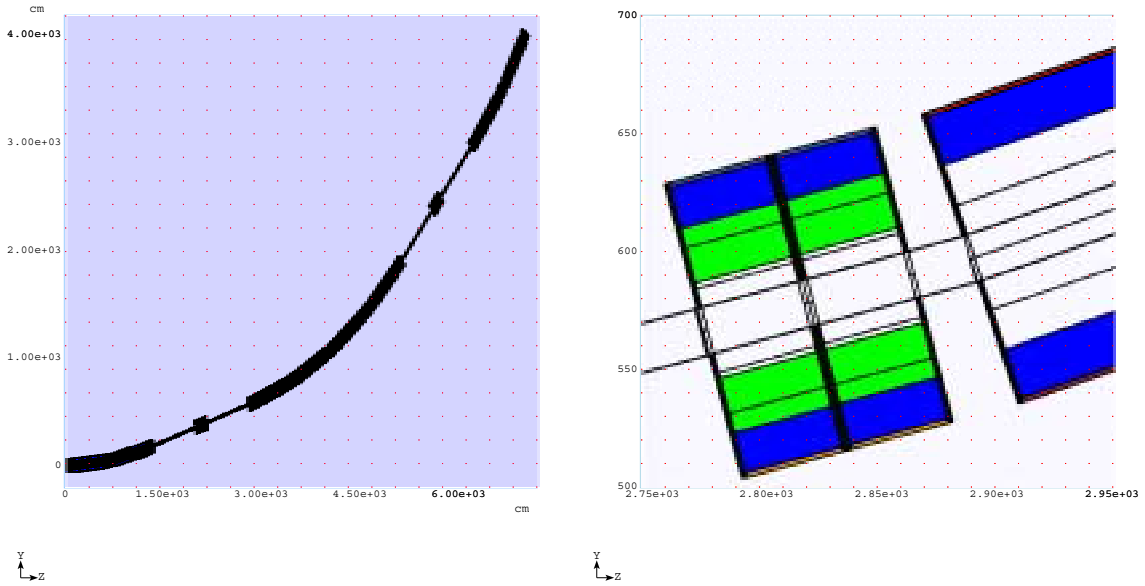

Figure 9.3. MARS model of a Proton Driver arc cell.

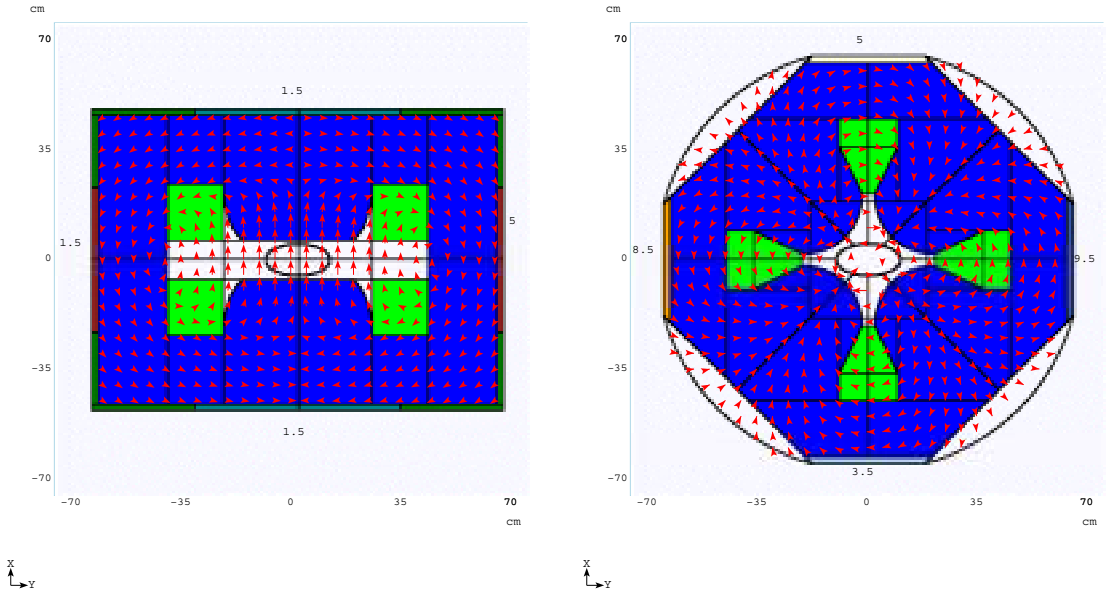

Figure 9.4. MARS model of arc dipole (left) and quadrupole (right).

of about 10-20 mrem/hr. Alternatively, one can think of providing simple shielding around the bare beam pipes. For ground-water activation C_{tot}=0.975 immediately outside the 40-cm tunnel wall (see Eq. (10.2)), that allows 1.03 W/m beam loss rate. The peak accumulated dose in the coils is about 2 Mrad/yr at 1 W/m beam loss rate which is acceptable with use of appropriate materials for insulation.

Table 9.1. Peak residual dose rate P_γ on 16 GeV lattice elements, accumulated dose D in dipole and quadrupole coils, ground-water activation parameter C_{tot} and allowable beam loss rate.

Value	Element	Peak at 1 W/m	Allowable loss (W/m)
P_γ (mrem/hr)	Long pipe	400	0.25
	Quad side	9.4	10.6
	Quad f ange	34	2.94
	Dipole side	5	20
	Dipole f ange	20	5
D (Mrad/yr)	Coil	2	10
C_{tot}	Ground water	0.98	1.03

9.3. Goals and Principles of Collimation

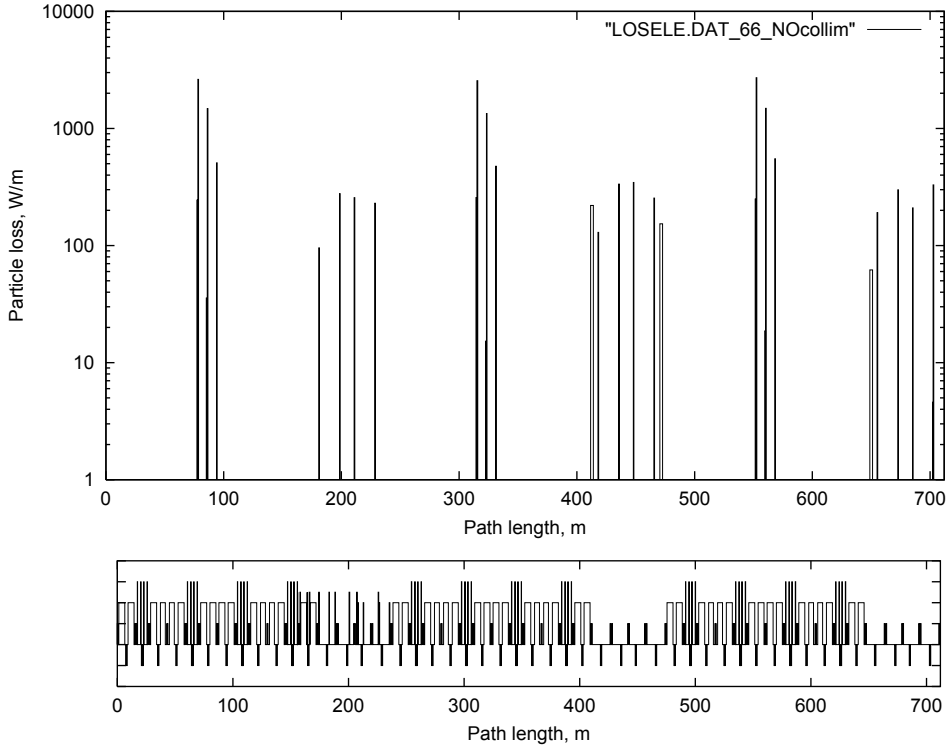

Figure 9.5. Beam loss distribution without collimators at 1% loss of intensity.

The beam power at the top accelerator energy is 1.152 MW. Assuming that 1% of the beam is lost at steady growth of the beam size and momentum spread, this amounts to 11.52 kW of beam loss distributed around the ring (Fig. 9.5) with a peak loss of up to 2 kW/m on several quadrupoles. This level is 2000 times higher than that which can be accepted in the arcs. The purpose of the beam halo cleaning system is to localize proton losses in a specially

shielded short section. This reduces irradiation of the rest of the machine to the acceptable levels described in the previous section.

A two-stage collimation is proposed [3, 8] with a set of primary and secondary collimators. At normal operating conditions, a circulating beam size grows slowly with a small step size per turn. A corresponding proton impact parameter on a collimator would be of the order of few μm. A thin primary collimator, introduced into the lattice as a limiting aperture, increases proton amplitude as a result of multiple Coulomb scattering and thus results in drastic increase of impact parameter on the downstream secondary collimators. This results in a signif cant reduction of the out-scattered proton yield and total beam loss in the accelerator, decreases collimator jaw overheating and mitigates requirements on the collimator alignment [3, 8].

9.4. Collimation System Design Analysis

9.4.1. Collimation at injection and top energy

A two-stage beam collimation system is designed using the available spaces in the utility section. It consists of horizontal and vertical primary collimators CH, CV, secondary collimators C1-C3, and supplementary collimators SC1-SC4 (Fig. 9.1 and Table 9.2).

Table 9.2. β-functions, dispersion and phase advance between the primary and secondary collimators.

Collimator	β-function (m)		Dispersion (m)	Phase advance between primary and secondary collimators (deg)	
	horizontal	vertical		horizontal	vertical
Horizontal primary CH	19.7	10.0	2.8	0	-
Secondary C1	24.8	10.4	2.8	5	-
Vertical primary CV	8.4	31.7	0.8	-	0
Secondary C2	9.6	30.7	0.4	45	4
Supplementary SC1	30.3	3.8	0.0	69	100
Supplementary SC2	6.9	31.5	0.0	125	140
Secondary C3	20.0	12.4	0.0	152	156
Supplementary SC3	7.3	30.0	0.0	253	198
Supplementary SC4	15.7	19.1	0.0	279	221
Neutral beam dump	7.7	26.5	0.0	411	283

Secondary collimators need to be placed at phase advances which are optimal to intercept most of particles out-scattered from the primary collimators during the f rst turn after the halo interaction with the primary collimator. Transverse phase space at the collimators is shown in Fig. 9.6. The optimal phase advances are around $k \cdot \pi \pm 30^{o}$. Phase advances between the primary and secondary collimators are presented in Table 9.2. The horizontal and vertical secondary collimators C1 and C2 and collimator C3 with jaws in both horizontal and

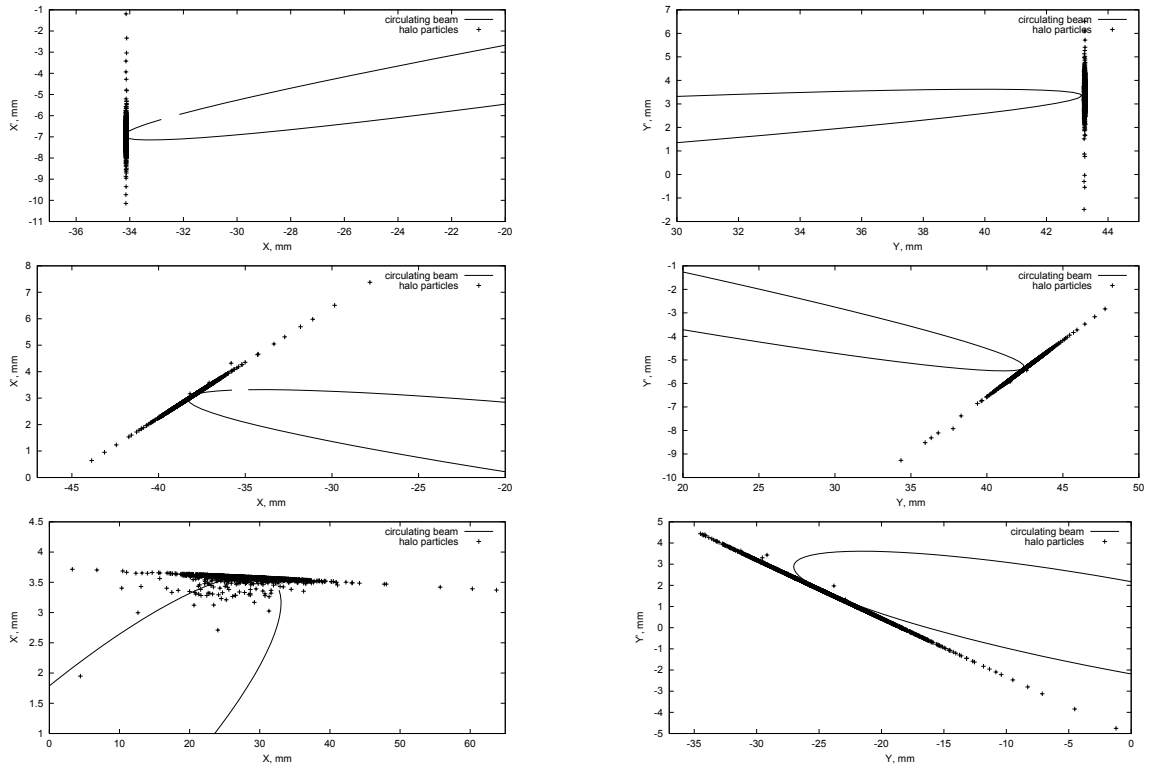

Figure 9.6. Horizontal (left) and vertical (right) phase space at the primary collimators (top), secondary collimators C1 and C2 (middle), and C3 (bottom).

vertical planes have good phase advances with respect to the primary collimator. The horizontal and vertical primary collimators are placed at the edge of the beam after painting. The beam loss distribution at the top accelerator energy with three secondary collimators located at 2 mm from the beam edge is shown in Fig. 9.7. The jaws of the secondary collimators should be made of stainless steel about 3 cm thick and 0.5 m long. It is assumed in calculations that 0.66% of the beam is lost on the horizontal primary collimator (half for off-momentum protons with $\Delta p/p = \pm 0.002$ and half for on-momentum protons) and 0.33% is lost on the vertical primary collimator.

The right side of Fig. 9.7 shows details of beam loss in the collimation region. Secondary collimators generate out-scattered particles lost later in the lattice. One can reduce this component with a *3-stage collimation system* positioning several *main* secondary collimators close to the beam to deal with protons scattered in the primary collimator and several *supplementary* collimators farther from the beam to catch particles out-scattered from the main secondary collimators. Beam loss distributions with 3 and 5 supplementary collimators 0.5 m long located at 5 mm from the beam edge are shown in the middle and bottom of Fig. 9.7. One can see signif cant reduction of beam loss rates with the proposed system. Table 9.3 summarizes results of this optimization.

The thickness and material of primary collimators affect the out-scattered proton angular distribution and nuclear interaction rate. Such a thin scatterer should give a considerable an-

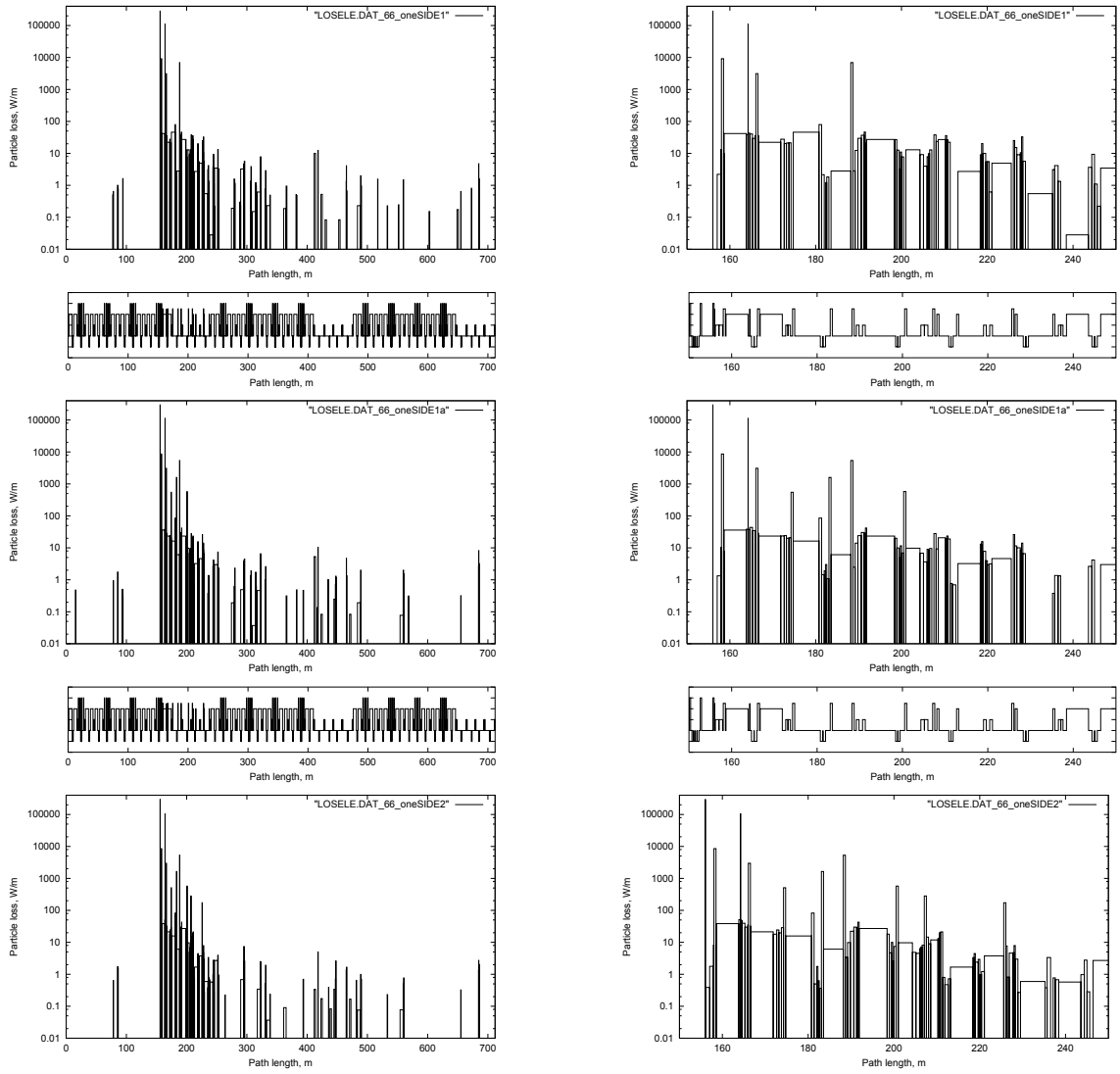

Figure 9.7. Beam loss at the top accelerator energy with secondary collimators at a 2 mm offset with respect to the primary ones (top), with three additional supplementary collimators SC1-SC3 at 5 mm offset (middle) and with f ve supplementary collimators (bottom).

gular kick to the halo particles, but their amplitude should remain smaller than the machine aperture on their way to the secondary collimators. Calculated beam losses are presented in Table 9.4 for 0.5, 1 and 1.5 mm thick tungsten collimators. A 1 mm collimator provides minimal loss rate in the ring.

The β-function varies along the length of a secondary collimator, therefore the collimator jaws are assumed to be aligned to follow the beam envelope after the painting. Longer secondary collimators reduce the punchthrough probability. We found that at 16 GeV the minimal length is 0.3 m of steel, with the optimum of about 0.5 m (see Table 9.5). The results shown are for 1 mm thick tungsten primary collimators and for secondary and sup-

Table 9.3. Beam loss in the Proton Driver. Total losses at injection (E_{kin} = 0.4 GeV) are assumed to be ∼2.88 kW, at the top energy (E_{kin} = 16 GeV) - ∼11.52 kW.

	Beam loss		
Collimation system	Utility section	Rest of the ring	Peak loss rate in the ring
	kW	kW	W/m
AT THE TOP ENERGY			
No collimators	0.470	11.050	2700
two-side collimators			
three secondary at 2 mm f ve supplementary at 5 mm	11.432	0.089	9.0
one-side collimators			
three secondary at 2 mm	11.375	0.146	13.2
three secondary at 2 mm three supplementary at 5 mm	11.422	0.098	10.4
three secondary at 2, 2 and 3 mm f ve supplementary at 5 mm	11.449	0.071	6.7
three supplementary - one-side, two others two-side			
three secondary at 1, 1 and 2 mm f ve supplementary at 3 mm	11.476	0.044	4.9
three secondary at 2, 2 and 3 mm f ve supplementary at 5 mm	11.462	0.059	6.6
three secondary at 3, 3 and 4 mm f ve supplementary at 7 mm	11.449	0.071	6.8
with bump three secondary at 2, 2 and 3 mm f ve supplementary at 5 mm	11.487	0.033	4.7
AT INJECTION three supplementary - one-side, two others two-side			
three secondary at 2, 2 and 3 mm f ve supplementary at 5 mm	2.879	0.001	0.2
at RF capture loss three secondary at 2, 2 and 3 mm f ve supplementary at 5 mm	2.877	0.003	1.0

Table 9.4. Beam loss as a function of tungsten primary collimators thickness.

Thickness	Utility section	Rest of the ring	Peak loss rate in the ring
mm	kW	kW	W/m
0.7	11.445	0.075	7.9
1.0	11.461	0.059	6.6
1.5	11.453	0.067	6.4

plementary collimators position as above.

Table 9.5. Beam loss as a function of steel secondary collimators length.

Length	Utility section	Rest of the ring	Peak loss rate in the ring
m	kW	kW	W/m
0.3	11.393	0.127	14.7
0.5	11.461	0.059	6.6
0.8	11.499	0.021	3.8

With the proposed system, ∼99% of the beam halo energy is intercepted in the 80-m long utility section. About 1% is lost in the rest of the machine along 630 m length with a mean rate of 0.12 W/m. At several locations the beam loss is noticeably higher (∼7 W/m), exceeding the tolerable rates of 0.6 W/m. The above hot locations should be taken care of via local shielding if necessary. Beam loss rates in the collimation system section itself are very high implying a special shielding design (see Section 10). Collimators, magnets and other equipment of the utility section require special cooling as well as fast disconnects and remote control.

9.4.2. Collimation during the accelerator cycle

It is assumed that 10% of the intensity is intercepted at injection, and 1% at the top energy. A practicality in a rapid cycling proton synchrotron dictates a stationary collimator approach with collimator jaws in a f xed position with respect to the beam orbit during the entire cycle. In the optimal conf guration described in the previous section, the primary collimators are positioned at the edge of the beam after beam painting in the horizontal and vertical planes with the secondary and supplementary collimators farther from the beam.

In an ideal case, the edge of the circulating beam should be kept at these conditions during the total cycle. This requires rather complicated horizontal and vertical bumps, created by at least ten fast magnets for each direction. To simplify the system, we propose to keep the beam at the edge of the primary collimators and close to the f rst secondary collimators using only three fast magnets for each direction. Most of the particles scattered out of the primary collimators are intercepted now by these secondary collimators, with other collimators intercepting the larger amplitude and off-momentum protons. Such a scheme allows to localize a majority of the beam loss in a short 35-m long region with the maximum rate of (120-50) W/m in two dipoles immediately downstream of collimator C1 and C2, and to reduce the average loss in the ring from 0.12 W/m to 0.05 W/m. Corresponding beam loss distributions at injection and at the top energy are shown in Fig. 9.8 and in Table 9.3.

9.4.3. Beam collimation at RF capture

The eff ciency of the collimation system depends on the impact parameter at the primary collimators. Particle coordinate step size at the collimator is def ned by the particle mo-

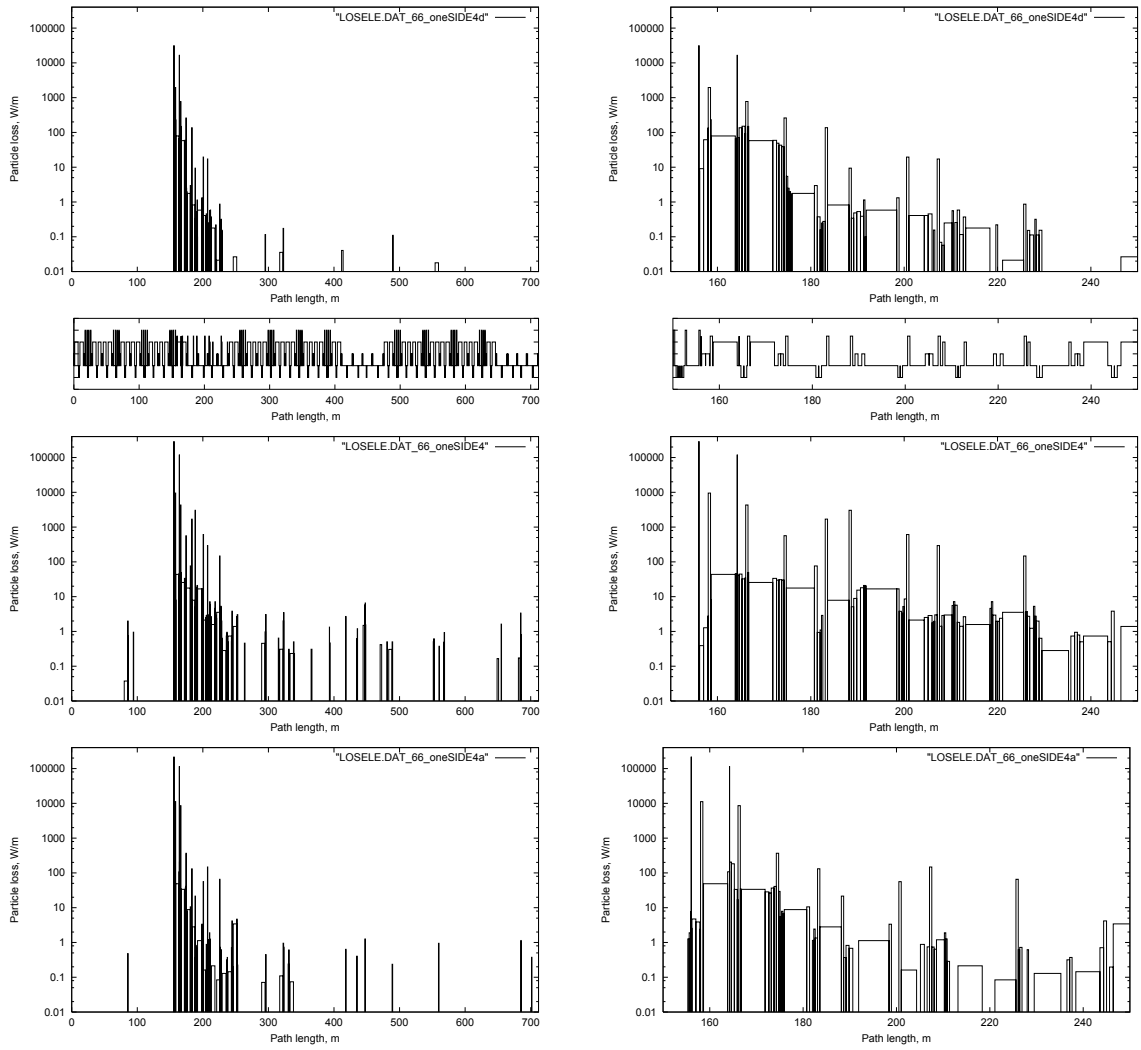

Figure 9.8. Beam loss at injection (top) and at the top energy (middle) without bump. Beam loss at the top energy with horizontal and vertical bump for keeping edge of the beam near the primary and f rst secondary collimators during the total cycle (bottom). It is assumed that 10% of intensity is lost at injection and 1% at the top energy.

mentum deviation with time and by the rate of particle betatron amplitude growth caused by the possible approach to betatron resonances, beam-gas interactions and other reasons. The f rst effect may signif cantly increase an impact parameter at the collimator if particles are lost off the separatrix at injection. The reason for simulations described here is to def ne the rate of particle energy evolution during this process and conditions for particles loss at the primary collimator, but not to investigate the RF capture itself. Because of this we did these simulations with assumptions which simplify calculations. For simulations of particle loss during RF capture the initial protons were placed in the vicinity of an unstable point. Synchro-betatron oscillations at the RF capture were simulated in the STRUCT code with longitudinal dynamics described by the difference equations for proton motion with respect to the synchronous particle [9]:

$$\varphi_i = \varphi_{i-1} - 2\pi \cdot f_{RF} \cdot f_{rev}^{-1} \left[\alpha - \frac{1}{\gamma^2}\right] \frac{\Delta E}{\beta^2 \cdot E_s}, \tag{9.1}$$

$$E_{exit} = E_{entrance} + \frac{e \cdot U}{1000} \left[\sin(\varphi_I) - \sin(\varphi_s)\right], \tag{9.2}$$

where

φ_I is the RF phase at particle pass through the cavity (radian);

φ_{I-1} is the RF phase at the previous turn (radian);

φ_s is the synchronous phase at the beginning of acceleration (radian);

E_s =1338.3 MeV is the synchronous energy;

$f_{RF} = 37.864 \times 10^6$ Hz is the RF frequency at the beginning of acceleration for the f rst stage of project;

$f_{RF} = 5.4091 \times 10^6$ Hz is the RF frequency at the beginning of acceleration for the second stage of project;

$f_{rev} = 0.3 \times 10^6$ Hz is the revolution frequency at injection;

α = -0.000744 is the momentum compaction factor; we neglect the dependence of α on proton momentum;

$\gamma = E_s/(m_o \times c^2)$ = 1.4263 is the γ factor;

U is the RF voltage at the beginning of injection.

The RF voltage, synchronous phase φ_s and longitudinal phase space at the beginning of acceleration are shown in Fig. 9.9. The maximum energy deviation from the synchronous energy in the bucket at injection is ΔE=1 MeV for f_{RF}=37.86 MHz and ΔE=2.5 MeV for f_{RF}=5.41 MHz. Fig. 9.10 shows evolution of the longitudinal phase space of particles lost from the separatrix during this process. The duration of synchrotron oscillation for particles lost from the separatrix is about 2 turns for f_{RF}=37.86 MHz and 20 turns for f_{RF}=5.41 MHz. The impact parameter at the primary collimator is def ned by the particle coordinate growth during 3-5 turns. During this time, particle momentum may change by several hundred keV (Fig. 9.10) affecting impact parameter increase at the primary collimator to 1-2 mm. Corresponding transverse distributions at the primary collimator and momentum spectrum of the lost protons are shown in Fig. 9.11. Most of halo protons on the primary collimator have $\Delta p/p \leq 1\%$. Beam losses at injection in the utility section and in the entire ring are presented in Fig. 9.12; for the beam size growing slowly, with impact parameter of 20 μm, and for beam loss at RF capture.

9.4.4. Crystal collimation

In this section we explore the possibility to use a crystal instead of an amorphous primary collimator, studied earlier for the Tevatron beam scraping system [10]. To evaluate the eff - ciency for such a collimation system, realistic simulations have been performed with CATCH

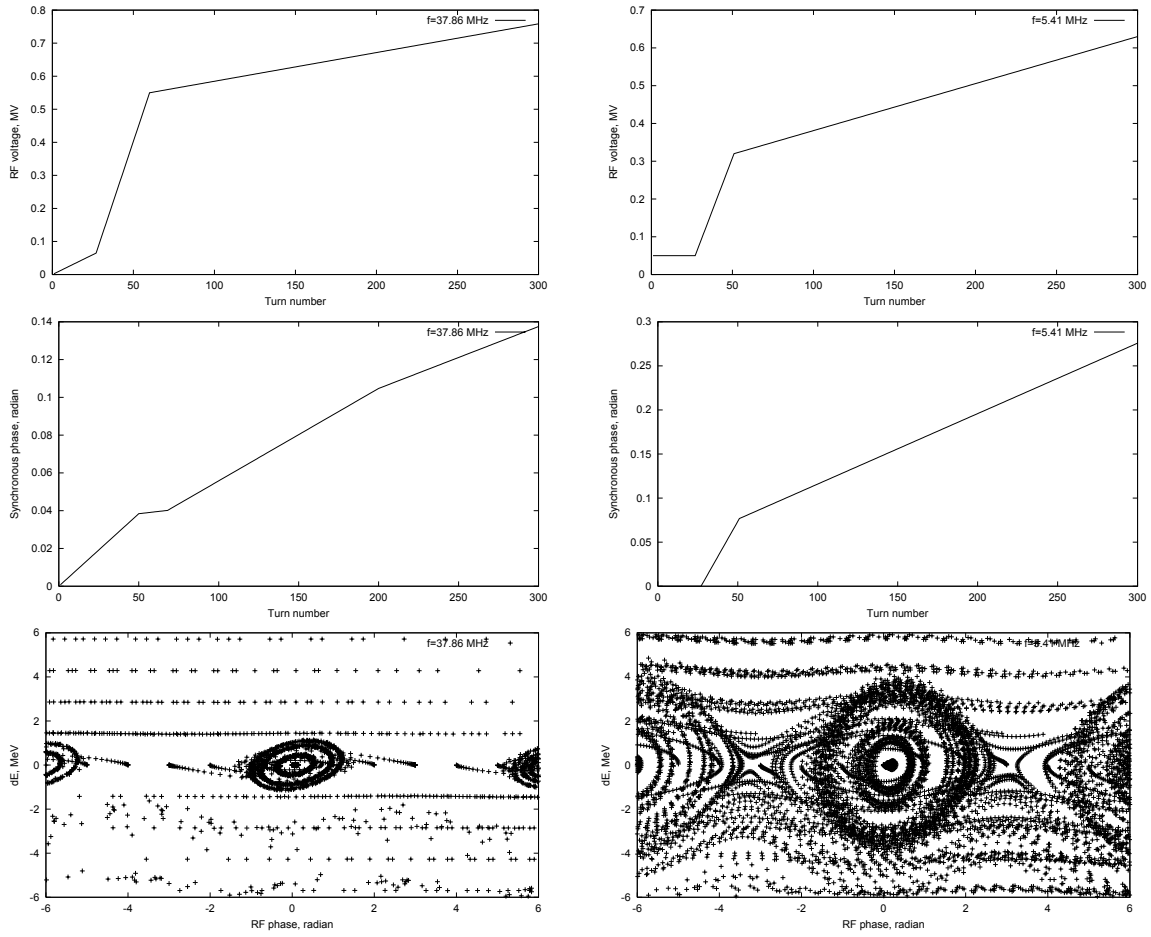

Figure 9.9. RF voltage (top), φ_s (middle) and longitudinal phase space (bottom) at RF capture for the Stage 1 f_{RF} = 37.86 MHz (left) and for Stage 2 f_{RF} = 5.41 MHz (right).

[11] linked to the STRUCT code. Crystal channeling is simulated in CATCH as described in "Crystal Channeling and its Application at High Energy Accelerators" Ref. [12]. Interactions with a crystal amorphous layer and all other near-beam interactions and tracking are performed with STRUCT.

An optimal Si(110) crystal radius is estimated as R (mm)$\approx 30 \times p\beta$, where p is proton momentum (GeV/c) and β is its velocity relative to the speed of light. Corresponding crystal length needed to def ect a proton by an angle θ is L = Rθ. A 3-mm silicon crystal def ects 16-GeV protons by 5.9 mrad. A crystal critical angle, estimated as α(mrad)$\approx 0.15/\sqrt{p\beta}$, is 0.18 mrad at injection and 0.036 mrad at 16 GeV. For channeling to occur, these angles should be larger than the beam divergence. Another parameter, especially important at low energies, is the crystal dechanneling length L_{dechan}(mm) $\approx p\beta$, that is 0.7 mm at 400 MeV and 17 mm at 16 GeV. In a rapid cycling machine the same crystal should be used both at injection and at the top energy. It is clear that the requirement L ¡ L_{dechan} is violated at injection.

In this study an attempt was made to replace the primary collimator with a silicon crystal.

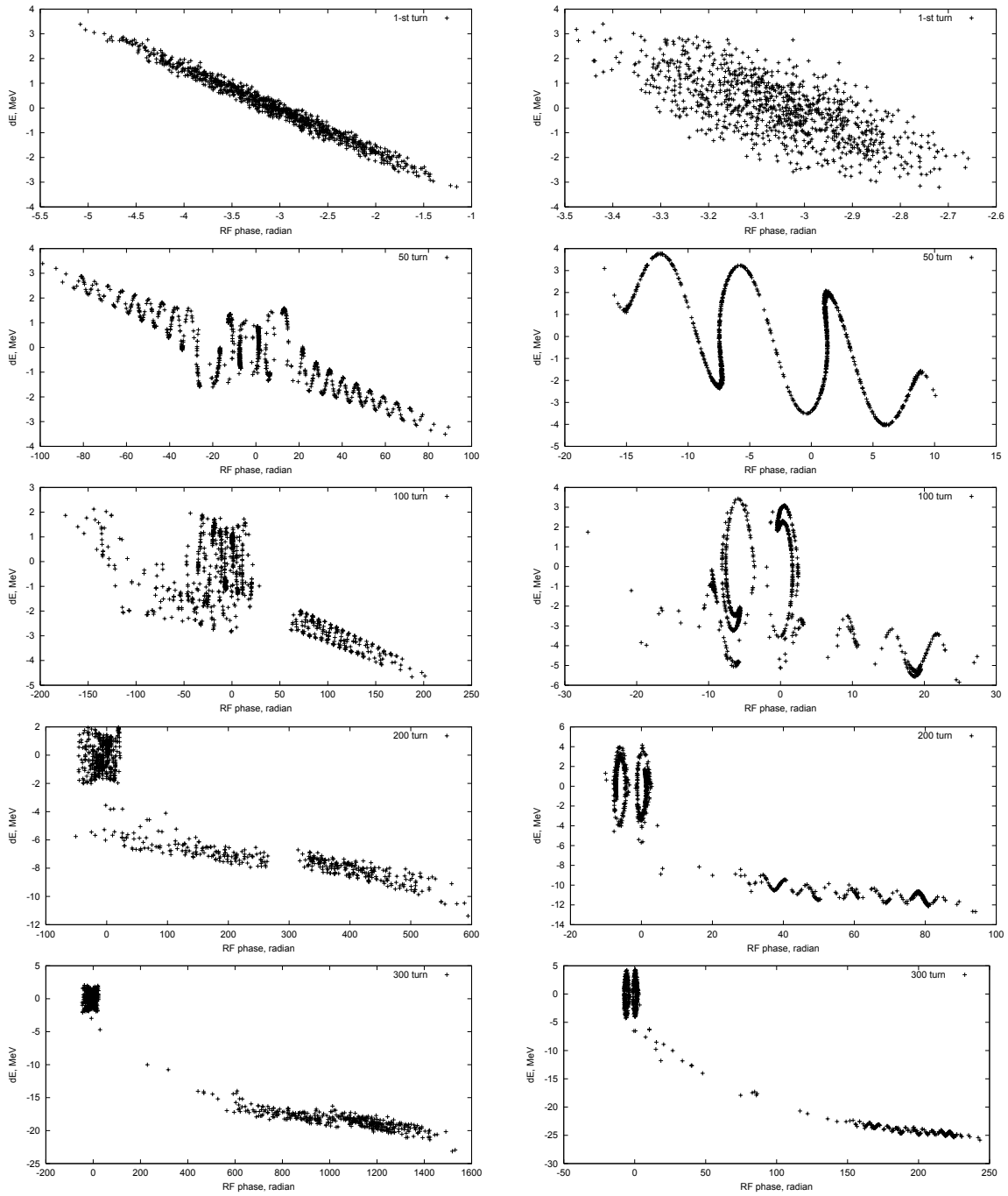

Figure 9.10. Longitudinal phase space at RF capture for f_{RF} = 37.86 MHz (left) and for f_{RF} = 5.41 MHz (right) at the f rst turn (f rst line), 50-th turn (second line), 100-th turn (third line), 200-th turn (fourth line), 300-th turn (f fth line). Initial protons are in the vicinity of the unstable point.

The crystal was assumed to have a perfect lattice and crystal surface, with a 1 μm thick amorphous layer on the beam-side of the crystal. The horizontal beam half-size at the crystal is 34.1 mm. The beam amplitude can grow fast due to the space charge effects. We assumed

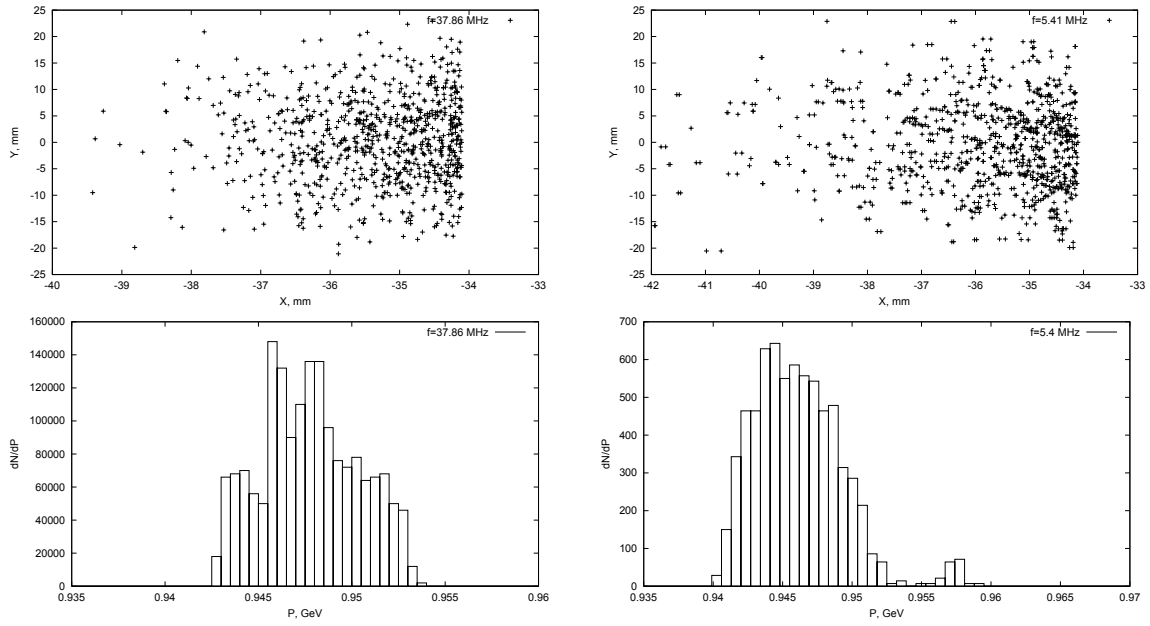

Figure 9.11. Transverse distributions (top) of halo protons on the primary collimator and momentum spectrum of lost protons (bottom) during the RF capture for f_{RF} = 37.86 MHz (left) and for f_{RF} = 5.41 MHz (right).

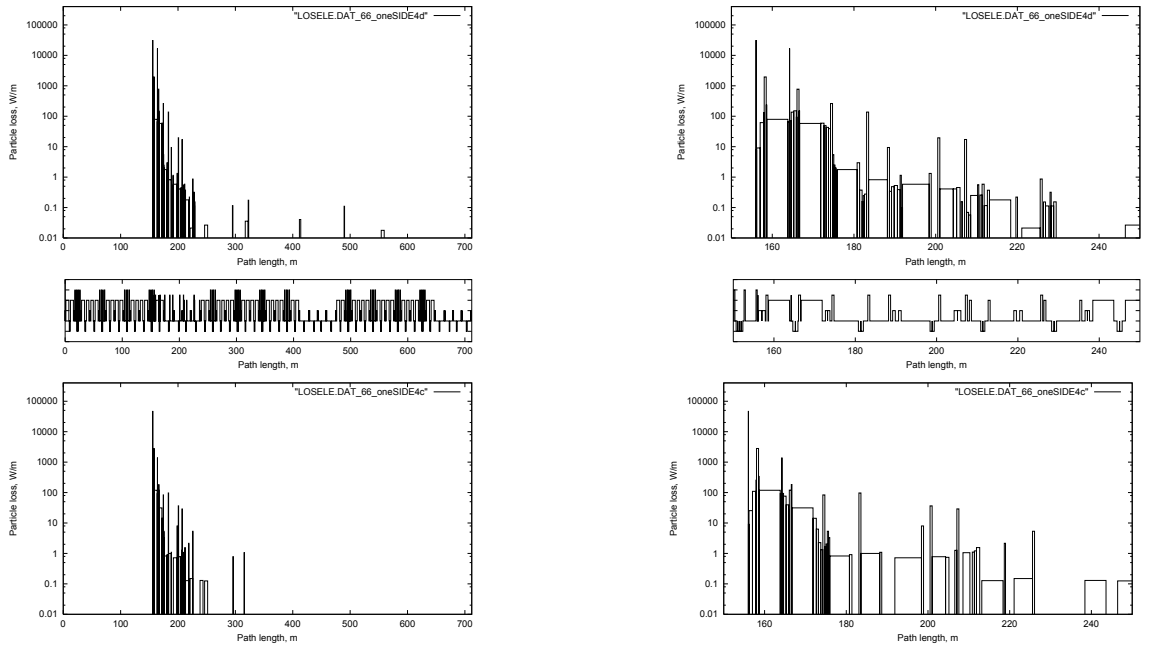

Figure 9.12. Beam losses at injection in the entire ring (left) and in the utility section (right) for the beam size growing slowly with step size of 20 μm (top) and at the RF capture loss (f_{RF} = 37.86 MHz) with a step size of about 2 mm (bottom).

a proton impact parameter at the crystal of 28 μm independent of the beam energy. Then the corresponding beam divergence at the crystal entrance (Fig. 9.13) is ±70 μrad.

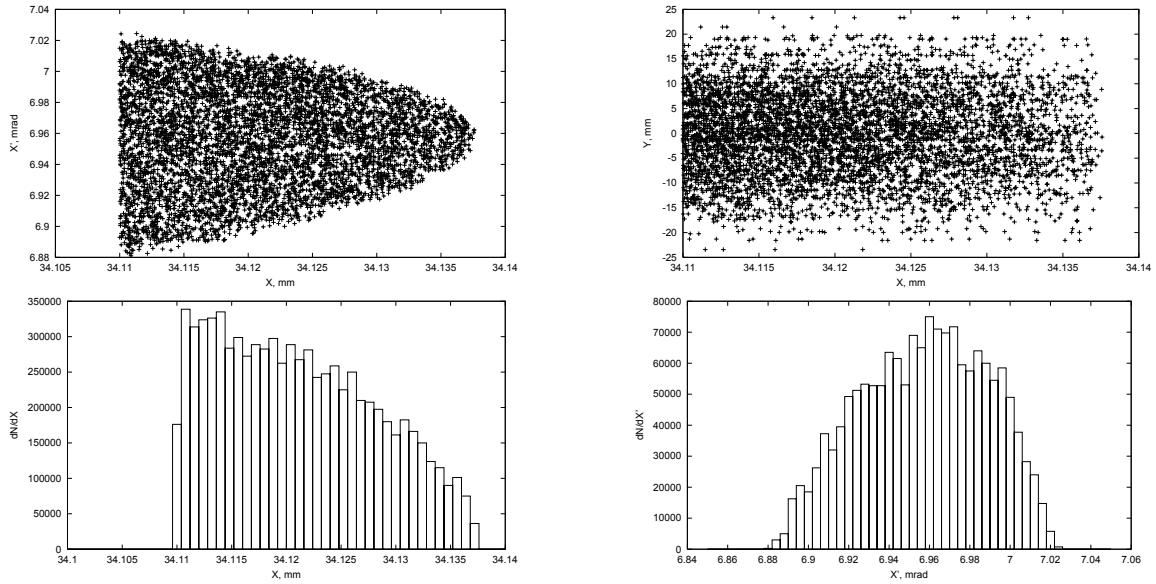

Figure 9.13. Horizontal phase space (top, left), transverse (top, right), horizontal (bottom, left) and angular (bottom, right) distributions of particles at the crystal entrance.

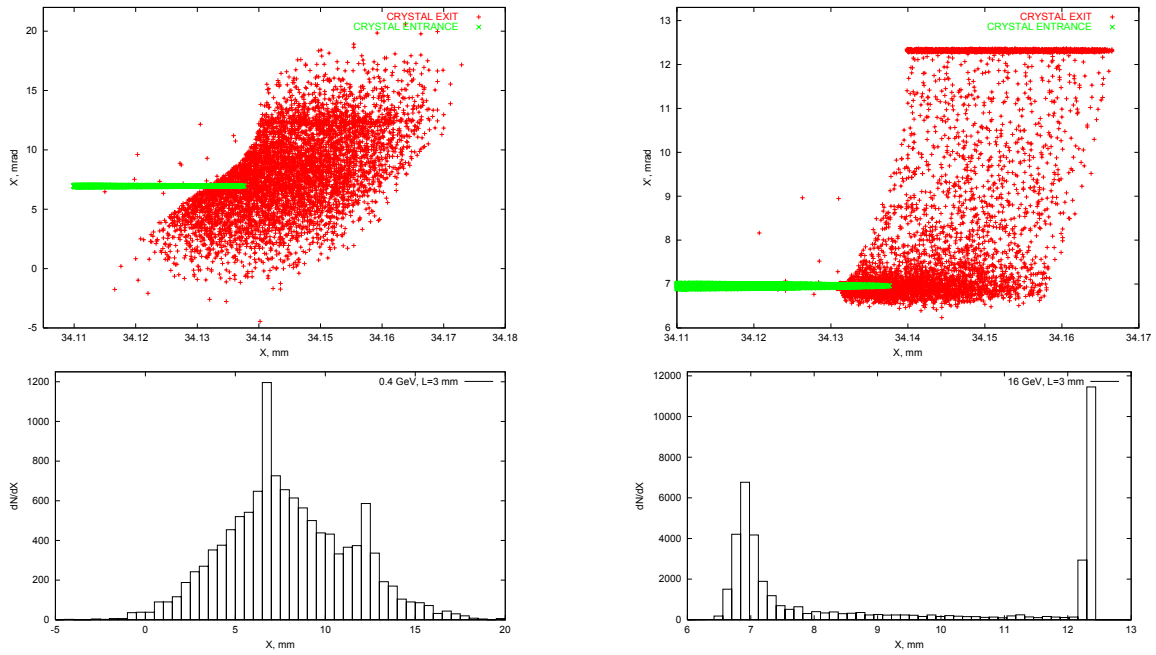

Figure 9.14. Horizontal phase space at a 3-mm crystal entrance and exit (top), and angular distribution at the crystal exit (bottom) at injection (left) and at the top energy (right).

Beam distributions upstream and immediately downstream of a 3 mm silicon crystal are shown in Fig. 9.14. With this crystal L ¡ L_{dechan} at the top energy, but the beam divergence exceeds the critical angle. Therefore, the channeling eff ciency at the f rst pass is only 15%. At injection - although a critical angle (180 µrad) is a factor of 2.6 higher compared to the beam divergence - the eff ciency is even lower (5%), because of a very short dechanneling

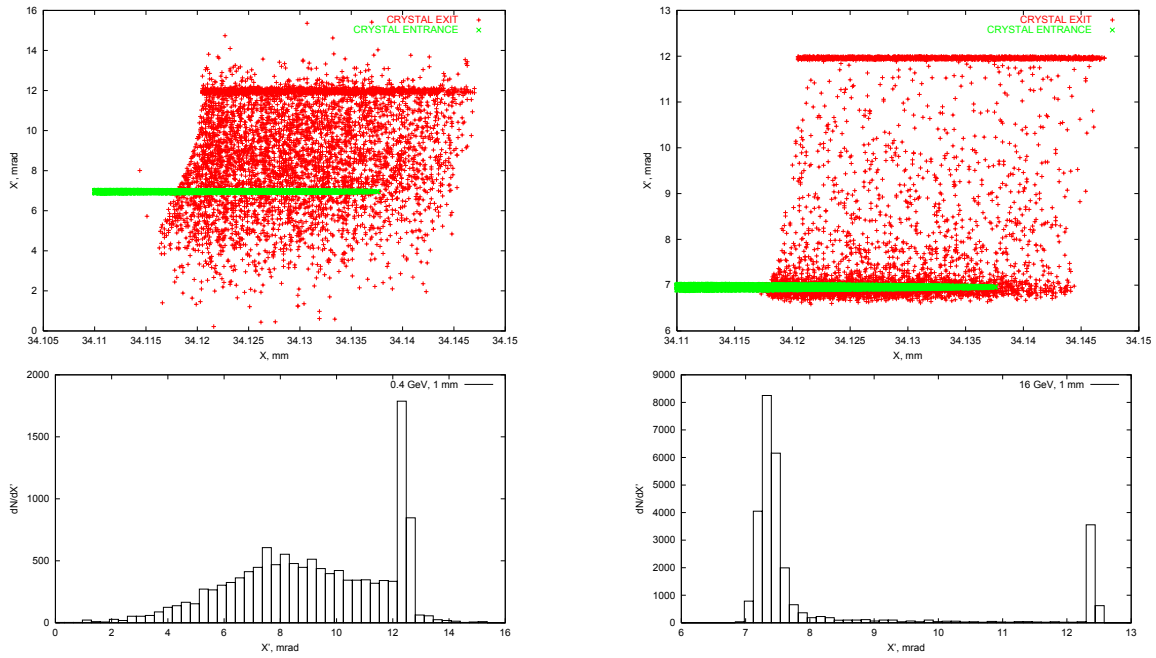

Figure 9.15. Horizontal phase space at a 1-mm crystal entrance and exit (top) and angular distribution at the crystal exit (bottom) at injection (left) and at the top energy (right).

length.

Current technologies allow bending a 1-mm crystal by 1-2 mrad, with a hope to increase this angle to 5 mrad in the near future. This would reduce dechanneling and nuclear interactions in the crystal resulting in a higher channeling/collimation efficiency. We have tried such a crystal in our simulations. Fig. 9.15 gives beam distributions with a 1-mm silicon crystal bent by 5 mrad. Calculated channeling efficiency on the first pass is 15% at the top energy and 21% at injection. A factor of four increase at injection is encouraging. Unfortunately, at the top energy, many protons are not channeled by a short crystal (see Fig. 9.15).

Beam loss rates with such a crystal are compared in Fig. 9.16 and Table 9.6 with those using an amorphous primary collimator. The particle energy loss and multiple Coulomb scattering angle at injection in the 1 mm thick tungsten collimator are quite large (θ_{mcs} = 8 mrad) compared to the dechanneling angle in the silicon crystal (Fig. 9.15). Therefore the losses with the crystal are lower in the main secondary collimators, but they are higher in the supplementary collimators compared to the case with an amorphous tungsten primary collimator. At the top energy, a long tail of dechanneled particles results in about a factor of four higher losses in the utility section at crystal collimation.

Radiation damage to the crystal will limit its use in high-intensity beams. At high dose, the irradiated layers become amorphous. An experiment at the CERN SPS at 450 GeV has shown crystal efficiency reduction by 6% at 10^{18} particles per mm^2 [12, 13]. A limiting flux with the 800 GeV beam at Fermilab was found to be 10^{19} particles per mm^2 [14]. At lower energy the crystal is less sensitive to crystal lattice damage with an acceptable angu-

Table 9.6. Beam loss in the Proton Driver at collimation with a channeling crystal.

	Beam loss		
Collimation system	Utility section	Rest of the ring	Peak loss rate in the ring
	kW	kW	W/m
at the top energy, three supplementary - one-side, two others two-side			
with 3 mm channeling crystal three secondary at 2, 2 and 3 mm five supplementary at 5 mm	11.514	0.006	2.7
with 1 mm channeling crystal three secondary at 2, 2 and 3 mm five supplementary at 5 mm	11.520	0.000	0.0
with primary collimators three secondary at 2, 2 and 3 mm five supplementary at 5 mm	11.497	0.023	2.1
at the injection, three supplementary - one-side, two others two-side			
with 3 mm channeling crystal three secondary at 2, 2 and 3 mm five supplementary at 5 mm	2.879	0.001	0.8
with 1 mm channeling crystal three secondary at 2, 2 and 3 mm five supplementary at 5 mm	2.878	0.002	3.2
with primary collimators three secondary at 2, 2 and 3 mm five supplementary at 5 mm	2.880	0.000	0.0

lar distortion changing as $1/\sqrt{p\beta}$ [13]. Assuming a step size due to a space charge effect of 0.1 mm/turn, one gets a beam size on the crystal of 20 mm$\times$0.1 mm. The proton flux through the crystal is then 10^{17} p/mm^2/hr at 3.3×10^{12} protons lost per accelerator cycle. Assuming radiation hardness of the crystal at 16 GeV of 7×10^{19}p/mm^2, the crystal lifetime is estimated as 800 hours. In a rapid cycling machine RF capture loss can be the main component to be collimated. Step size in this process is of the order of few mm/turn. With that, the proton flux through the crystal is $5\cdot10^{15}$ p/mm^2/hr. This gives 1.5 years for the crystal lifetime.

9.5. Sensitivity Analysis

Optimally aligned primary collimators are placed at the beam edge. The secondary and supplementary collimators are positioned with a small offset with respect to the primary ones. This provides beam halo interaction with primary collimators before interacting with secondary ones. Closed orbit deviation during the cycle and from cycle to cycle can change these conditions if a secondary collimator offset is too small. In a worst case, once the closed orbit has no displacement at the primary collimators, but displacement at the secondary and supplementary ones is large, beam can interact first with the secondary collimators. This

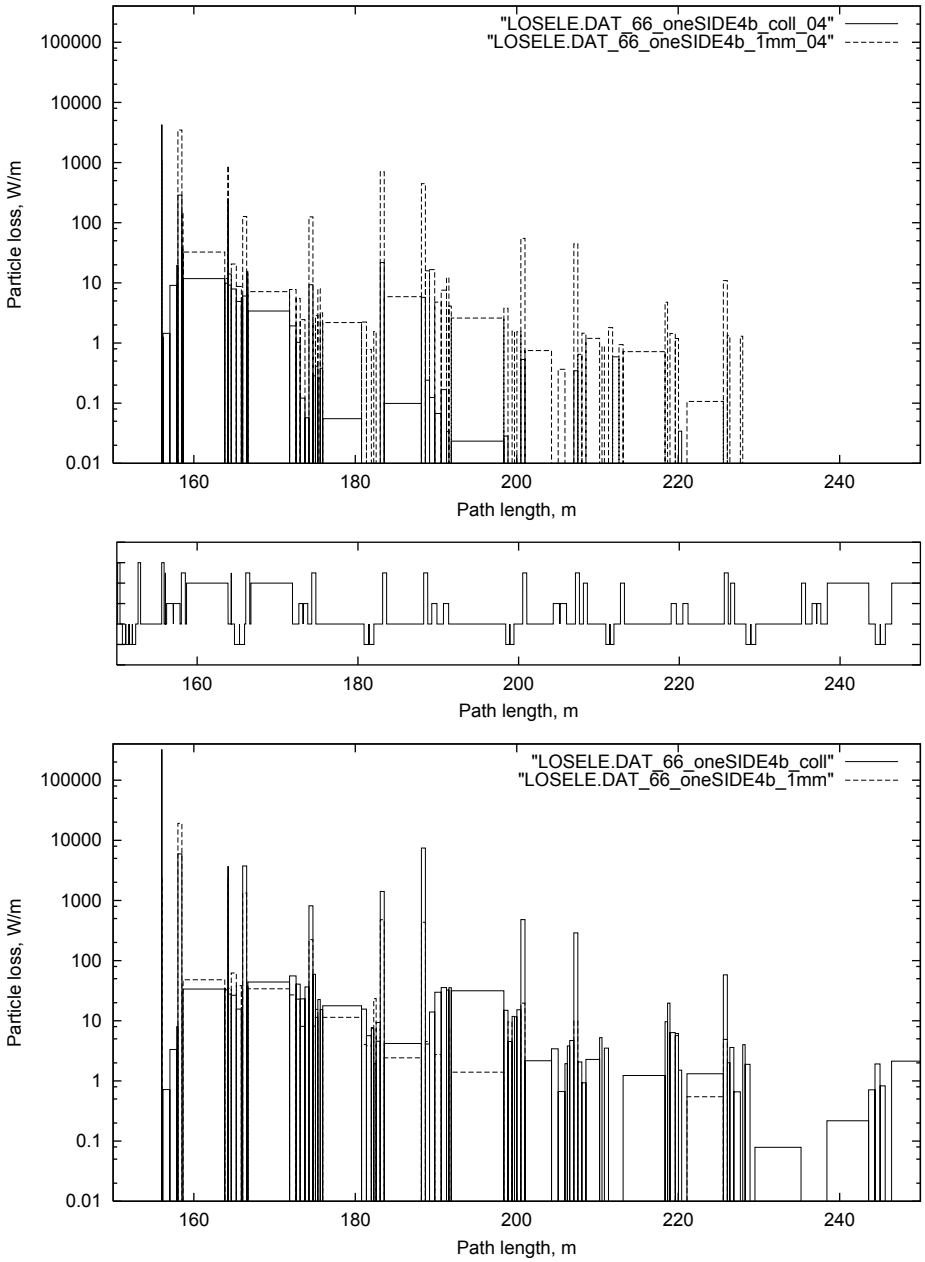

Figure 9.16. Beam loss in the utility section at injection (top) and at the top energy (bottom) for the systems with a 1-mm tungsten primary collimator (solid line) and with a 1 mm silicon crystal (dashed line).

can cause collimator overheating and eff ciency degradation. As shown in Table 9.7, positioning of the secondary collimators farther from the beam by 2 mm (from 1 mm to 3 mm) causes beam loss to increase in the ring by 13%, but this allows closed orbit deviation at the locations of collimators up to ± 3 mm without additional heating of secondary collimators.

In our simulations two types of closed orbit are used (Fig. 9.18): (A) closed orbit has

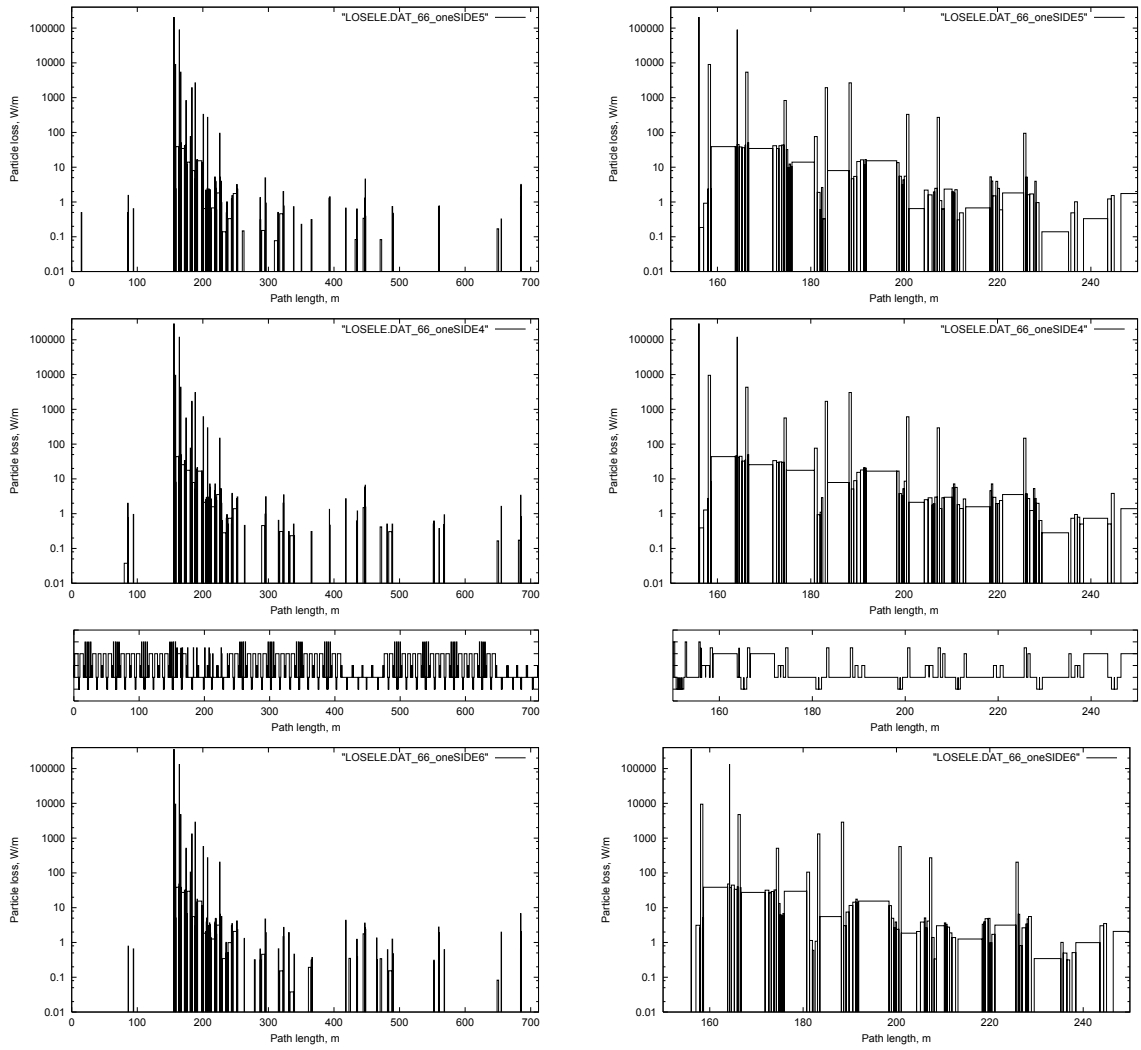

Figure 9.17. Beam loss at the top accelerator energy with 3 secondary and 5 supplementary collimators. Top: secondary collimators are at 1 mm offset and supplementary at 3 mm offset with respect to the primary ones. Middle: secondary are at 2 mm and supplementary at 5 mm. Bottom: secondary at 3 mm and supplementary at 7 mm.

maximum in the primary collimators, and (B) closed orbit has maximum in the secondary and supplementary collimators, and zero in the primary ones. Variations of both orbits were done in the range of ± 4 mm. Beam loss distributions for different closed orbit conf gurations in the system with secondary collimators at 2 mm, and supplementary ones at 5 mm from the beam are presented in Table 9.8. At orbit deviation of ± 4 mm, the number of protons lost outside the collimation region increases from 0.4% to 1.5% and peak loss in the ring from 5 W/m to 50 W/m.

The betatron tune deviation causes a change of phase advance between collimators and the distance to the resonances. As the betatron amplitude of protons after interaction with the primary collimator is large, the second factor can degrade collimation eff ciency. Beam

Table 9.7. Beam loss at the top energy for different positions of secondary collimators with respect to the beam.

Collimators	Beam loss		
collimation system	Utility section	Rest of the ring	Peak loss rate in the ring
	kW	kW	W/m
primary three secondary at 1 mm f ve supplementary at 3 mm	11.497	0.023	9.5
primary three secondary at 2 mm f ve supplementary at 5 mm	11.469	0.050	5.4
primary three secondary at 3 mm f ve supplementary at 6 mm	11.457	0.062	10.6

losses in the machine at the top energy as a function of accelerator tune are presented in Table 9.9. Accelerator tune deviation mostly affects the value of peak loss in the machine.

Table 9.8. Beam loss at the top energy as a function of closed orbit deviation.

	Beam loss		
Maximum closed orbit deviation	Utility section	Rest of the ring	Peak loss rate in the ring
mm	kW	kW	W/m
closed orbit type A			
-4	11.442	0.078	19.2
-3	11.454	0.066	18.1
-2	11.465	0.055	12.3
-1	11.461	0.059	14.0
0	11.470	0.050	5.4
1	11.463	0.053	12.5
2	11.452	0.065	11.4
3	11.448	0.072	9.4
4	11.398	0.122	26.8
closed orbit type B			
-4	11.348	0.172	49.6
-2	11.436	0.084	14.8
0	11.470	0.050	5.4
2	11.454	0.066	10.9
4	11.466	0.054	16.7

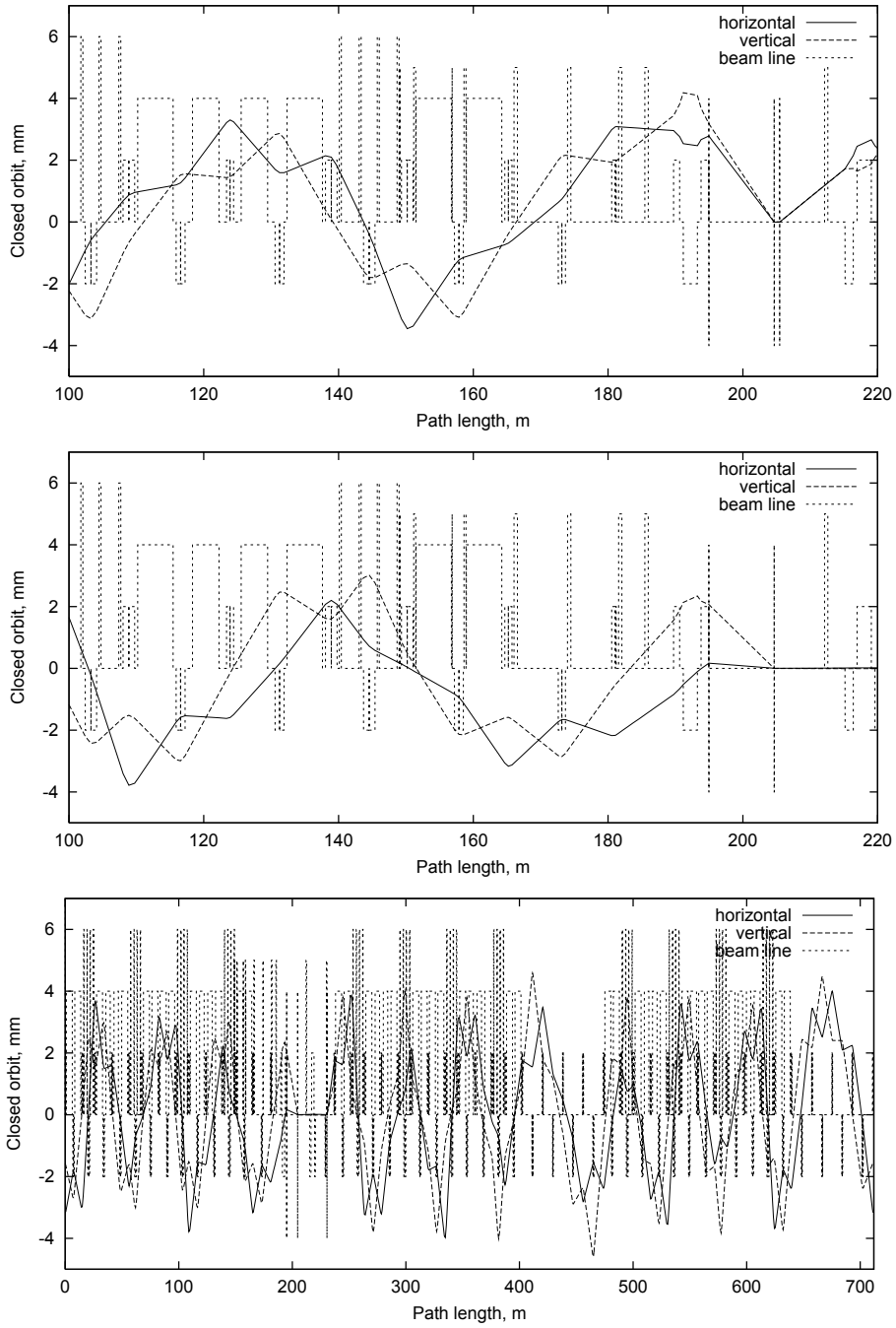

Figure 9.18. Closed orbit deviations at collimation system sensitivity analysis. Top: type A - orbit with maximum deviation in the primary collimators of -3 mm, middle and bottom: type B - orbit with zero deviations in the horizontal primary collimator.

9.6. Beam Accident

Consider a consequence to the machine components of an uncontrolled loss of a single pulse at 16 GeV for 3×10^{13} protons in Phase-I (1.2 MW) and 1×10^{14} protons in Phase-II (4 MW).

Table 9.9. Beam loss at the top energy as a function of accelerator tune.

	Beam loss		
tune	Utility section	Rest of the ring	Peak loss rate in the ring
	kW	kW	W/m
$\nu_x = 11.443,\ \nu_y = 11.351$	11.473	0.047	134.7
$\nu_x = 11.431,\ \nu_y = 11.369$	11.460	0.060	14.9
$\nu_x = 11.407,\ \nu_y = 11.407$	11.463	0.057	127.7
$\nu_x = 11.378,\ \nu_y = 11.416$	11.477	0.043	14.5
$\nu_x = 11.363,\ \nu_y = 11.421$	11.484	0.036	14.5

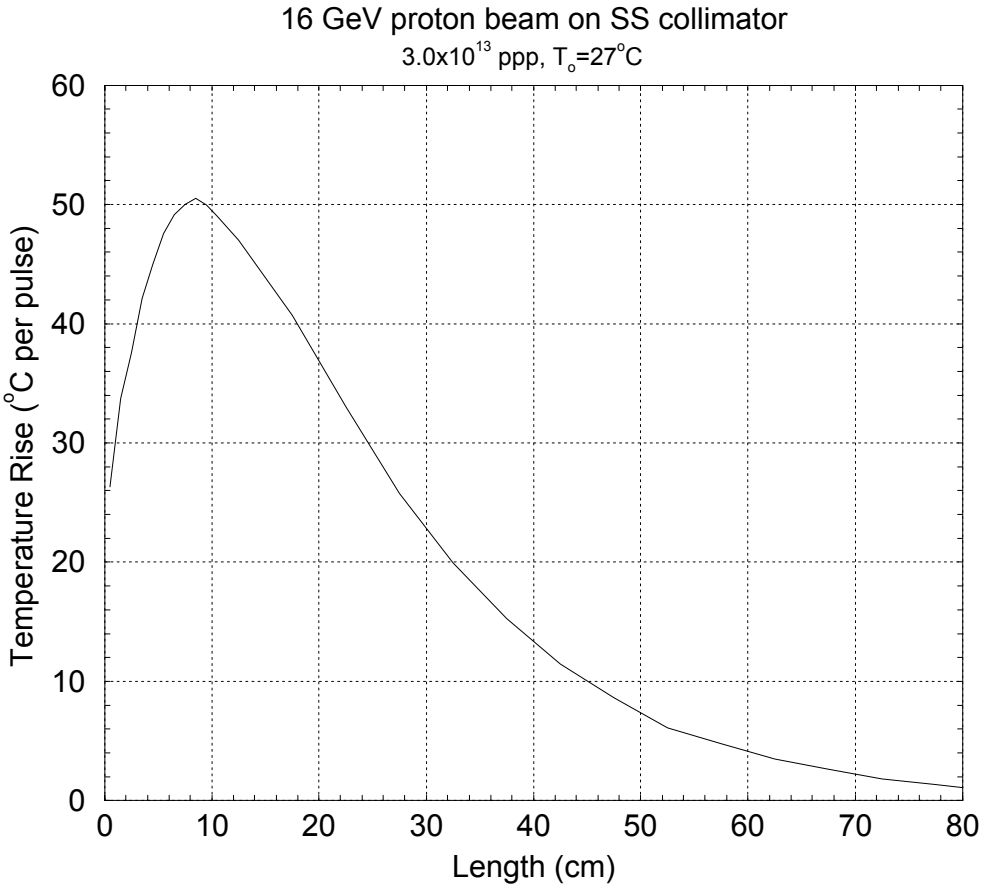

Figure 9.19. Instantaneous temperature rise in a secondary collimator jaw at beam axis *versus* jaw length.

A beam after painting is assumed to have a quasi-rectangular shape of a 7×5 mm half-size. This beam hits a beam pipe at a grazing angle or a jaw of a secondary collimator. Initial

temperature is assumed to be 27°*C*. Hadronic and electromagnetic showers are calculated with MARS14.

9.6.1. Beam pipe

Elliptical beam pipe dimensions are 5×9 inches with stainless steel walls 0.127 or 1.27 mm thick. Beam grazing angles are α=2, 5 and 10 mrad. Depending on the β-function, the maximum instantaneous temperature rise ranges from 33 to 38.5°*C* for a 0.127-mm beam pipe and from 41 to 48°*C* for a 1.27-mm beam pipe for the Phase-I beam. With Phase-II parameters, these numbers are roughly three times higher, but still quite acceptable. An accidental loss of successing pulses on a beam pipe exactly at the same location is unlikely; therefore one can conclude that this is not problem.

9.6.2. Collimator jaws

If a single 16-GeV pulse of 3×10^{13} protons hits normally at the center of a 3 cm thick and 80 cm long stainless steel or copper jaw of a secondary collimator, Fig. 9.19 shows the instantaneous temperature rise in the jaw immediately after the pulse at the beam axis as a function of the jaw length. One sees that ΔT_{max}=50°*C*. With Phase-II parameters, this value is roughly three times higher. This is still quite acceptable. With an appropriate cooling system, several such pulses on the same collimator could be allowed.

9.7. Collimators

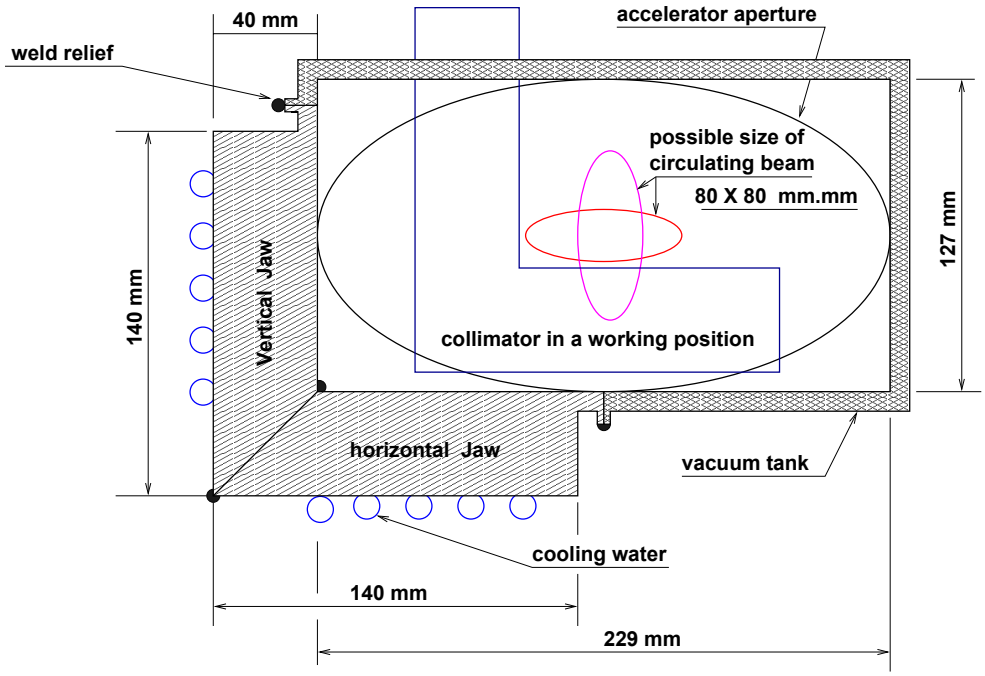

Figure 9.20. Secondary collimator cross section.

9.7.1. Requirements

The secondary collimators are chosen to be L-shaped stainless steel with L_x = 140 mm, L_y = 140 mm, thickness=40 mm, and length = 500 mm (Fig. 9.20). The primary collimators are chosen to be one-side jaw, tungsten with L_x = 140 mm, L_y = 140 mm, thickness=30 mm, and length=1 mm. These dimensions will accommodate the full beam size, after painting, and will accommodate maximum impact parameters. All collimators will be in a f xed position during the machine cycle, but motion control is required in order to adjust collimators to their optimum position.

9.7.2. Mechanical design

The mechanical design of the collimators and targets will be similar to those already built and installed in the Tevatron for Collider Run II [15, 16, 17]. Those collimators consist of 2 pieces of stainless steel, 0.5 m long, welded together in an ”L” conf guration. Machining and assembly tolerances of 25 μm are easily met for the collimator steel. The collimator assembly is welded inside a stainless steel box of outside dimensions approximately 230 mm x 130 mm and with bellows on each end. The box assembly is supported by a cradle which is moved independently in the vertical and horizontal directions by stepping motors. Full range of motion is 50 mm in steps as small as 25 μm if required and a maximum speed of 2.5 mm/sec. The collimator speed can be increased if a larger minimum step size is acceptable. Position readback is provided by linear differential voltage transformers, although investigation into the radiation hardness of these devices is required. Mechanical damage is prevented by limit switches on all degrees of motion. The entire assembly, including bellows, will occupy approximately 1 m of lattice space. The target assembly is identical to the collimator assembly except that the target ”L” blocks are only 0.1 m in length. The 1 mm thick machined tungsten targets are bolted to the stainless steel blocks. The blocks provide a good heat sink for energy dissipated in the tungsten. The entire assembly, including bellows, will occupy approximately 0.6 m of lattice space.

9.7.3. Controls

The motion controls for the collimators will be similar to the system already installed for the Tevatron Collider Run II collimators [15, 16], but without local loss monitor feedback. This system is also currently in use with other movable devices in the Fermilab accelerator complex. Up to 4 motors and 4 position readbacks will be controlled and monitored by a single MVME162 processor running VXWORKS in a VME crate in a nearby service building. Stepping motors and LVDT’s are interfaced to the CPU via commercial IP’s (Industrial Packs). The motor PS and motor controllers are also commercial hardware. A total of 3 ”stations” – VME crate, motor controller crate, and motor PS will be required for the entire system of 10 collimators.

9.7.4. Cooling

A total of 11.5 kW of DC power is expected to be dissipated in the collimators. 11.5 kW of power can be removed from a single collimator by circulating standard LCW (Low Conductivity Water) through cooling channels on the outside of the collimator box. A f ow of 2.2 gpm will remove 11.5 kW of power with a temperature rise of 20C. The requirement is that there is good thermal contact between the stainless steel "L" blocks and the welded box.

9.8. Conclusions

Detailed energy deposition studies performed in the machine elements give the tolerable beam loss in the Proton Driver. At the top energy in the arc for the proposed lattice, hands-on maintenance limits are 0.25 W/m in the open long beam pipes and 3 W/m in the magnets, while the ground-water limit is 1 W/m.

A 3-stage collimation system has been proposed based on detailed Monte-Carlo simulations at injection, top energy and at RF capture. The system consists of 1-mm thick tungsten primary collimators positioned at the horizontal and vertical edges of the beam after painting, followed by three secondary collimators with 2 mm offset with respect to the primary collimators and f ve supplementary collimators at 5 mm from the beam edge. Secondary and supplementary 0.5 m long stainless steel collimators are aligned with respect to the beam envelope after painting. Such a system allows localization of more than 99% of beam loss in a special 80 m long utility section. Beam loss in the rest of the machine is on average 0.2 W/m. Crystal collimation appears to not be eff cient in the Proton Driver because of the large divergence of halo distribution at the crystal entrance. Local shielding proposed in the hottest 30-m part of the utility section is described in Chapter 10. Overall, despite challenging parameters of the proposed new Proton Driver, beam loss and induced radiation effects can be controlled and reduced to allowable levels.

References

[1] A. I. Drozhdin, O. E. Krivosheev and N. V. Mokhov, "Beam Loss, Collimation and Shielding at the Fermilab Proton Driver", Fermilab-FN-693 (2000).

[2] O. E. Krivosheev and N. V. Mokhov, "Tolerable Beam Losses and Shielding", *Proc. of the 7th ICFA Mini-Workshop on High-Intensity, High-Brightness Hadron Beams "Beam Halo and Scraping"*, September 13-15, 1999, Lake Como, Wisconsin.

[3] A. I. Drozhdin, C. J. Johnstone and N. V. Mokhov, "16 GeV Proton Driver Beam Collimation System", *Proc. of the 7th ICFA Mini-Workshop on High-Intensity, High-Brightness Hadron Beams "Beam Halo and Scraping"*, September 13-15, 1999, Lake Como, Wisconsin.

[4] I. S. Baishev, A. I. Drozhdin and N. V. Mokhov, "STRUCT Program User's Reference Manual", SSCL–MAN–0034 (1994); http://www-ap.fnal.gov/∼drozhdin/.

[5] N. V. Mokhov, "The MARS Code System User's Guide", Fermilab-FN-628 (1995); N. V. Mokhov, S. I. Striganov, A. Van Ginneken, S. G. Mashnik, A. J. Sierk, and J. Ranft, "MARS Code Developments", Fermilab-Conf-98/379 (1998); N. V. Mokhov, "MARS Code Developments, Benchmarking and Applications", Fermilab-Conf-00/066 (2000). N. V. Mokhov and O. E. Krivosheev, "MARS Code Status", Fermilab-Conf-00/181 (2000). http://www-ap.fnal.gov/MARS/.

[6] A. I. Drozhdin and O. E. Krivosheev, "The Fermilab Proton Driver Beam Injection System Simulations", Fermilab–FN–694 (2000).

[7] "The NuMI Facility Technical Design Report", Fermilab (1998).

[8] A. I. Drozhdin, N. V. Mokhov et al., SSCL-Preprint-555 (1994).

[9] D. A. Edwards and M. J. Syphers, "An Introduction to the Physics of High Energy Accelerators", Wiley Series in Beam Physics and Accelerator Technology (1993).

[10] V. M. Biryukov, A. I. Drozhdin and N. V. Mokhov, "On Possible Use of Bent Crystal to Improve Tevatron Beam Scraping", *Proc. of the 1999 Particle Accelerator Conference*, New York, New York, March 29 - April 2, 1999, pp. 1234-1236; also Fermilab-Conf-99/072 (1999).

[11] V. M. Biryukov, "Crystal Channeling Simulation - CATCH 1.4 User's Guide", CERN SL/Note 93-74(AP) (1993).

[12] V. M. Biryukov, Yu. A. Chesnokov and V. I. Kotov, "Crystal Channeling and its Application at High Energy Accelerators", Berlin: Springer (1997).

[13] V. M. Biryukov, Private communication, IHEP (1999).

[14] C. T. Murphy, Private communication, Fermilab (1999).

[15] M. Church, "Proposed Tevatron Collimation System for Collider Run II", International Symposium on Near Beam Physics, ed. R Carrigan and N Mokhov, Fermilab, Batavia, IL, p. 134 (1997)

[16] M. Church, "Update on the Tevatron Collimator System for Collider Run II", in 7th ICFA Mini-Workshop on Beam Halo and Scraping, ed. W Chou and N Mokhov, Lake Como, WI, (1999)

[17] R. Reilly, Fermilab Assembly Drawing 1720.004-ME-326216 Rev. A (1998)

Chapter 10. Radiation Shielding and Activation

O. E. Krivosheev and N. V. Mokhov

10.1. Introduction

Radiation transport analysis, which includes accelerator and nuclear physics, shielding, activation, engineering, and safety analyses, is critical to almost all operations important to the design and construction of an intense high-energy accelerator facility like the proposed Proton Driver. As in similar projects of this type, such as the Spallation Neutron Source, these analyses are fundamentally important because of the impact on machine performance, conventional facility design, maintenance operations, and because the costs associated with incorporating the results of the radiation transport analysis can comprise a significan part of the total facility costs [1].

A very high beam power implies serious constraint on beam losses in the machine [2]. Only with a very efficien beam collimation system [3] can one reduce uncontrolled beam losses in the machine to an allowable level (see Chapter 9). The design strategy of the Proton Driver is that the beam losses are localized and controlled as much as possible via the dedicated beam collimation system described in Chapter 9. This way, the source term for the radiation analysis is a derivative of the collimation system performance with a high loss rate localized in the injection/collimation section and drastically lower uncontrolled beam loss rate in the rest of the lattice. As will be shown below, the main concerns are hands-on maintenance and ground-water activation. Massive local shielding is needed around the collimators. The entire complex must be well shielded to allow a non-controlled access to the outside surfaces under normal operation and accidental beam loss.

The radiation transport analysis of the Proton Driver can be subdivided into two major categories: (1) *Prompt radiation* and (2) *Residual radiation*. The firs drives shielding design and analysis to meet direct radiation criteria for non-controlled areas. It also determines beam-induced energy deposition effects in equipment: instantaneous and steady-state temperature rise, dynamic heat load to the cooling systems, dose accumulated in the machine components that causes material damage and limits component lifetime. The second category includes radio-activation of equipment (hands-on maintenance), ground and ground water, and air.

Thorough Monte Carlo calculations were performed for realistic assumptions and geometry under normal operation and accidental conditions. This allowed one to deduce the tolerable beam losses (see Chapter 9) and conduct shielding design and analysis in all aspects which impact on machine performance, conventional facility design and maintenance operations. Several issues—such as air and dirt activation—are left aside, because of the absence of corresponding input information at this stage and as it was estimated they are not critical factors in shielding design and analysis.

10.2. Regulatory Requirements

1. *Prompt radiation:* the criterion for dose rate in non-controlled areas on accessible outside surfaces of the shield is 0.05 mrem/hr at normal operation and 1 mrem/hr for the worst case due to accidents [4]. Currently, the Fermilab Radiological Control Manual (FRCM) [4] uses the phrase "credible accident". The ability to tolerate a one hour continuous maximum intensity loss was required in the past, but is no longer required under all conditions. In many cases, it is not even possible for a machine to do this. The FRCM [4] requires that the machine designers describe and justify what a possible credible worst case accident is, and design the shielding—or modify operation of the machine—accordingly [5].

2. *Hands-on maintenance:* residual dose rate of 100 mrem/hr at 30 cm from the component surface, after 100 day irradiation at 4 hrs after shutdown. Averaged over the components, the dose rate should be less than 10-20 mrem/hr. It is worth noting that the (100 days / 4 hrs / 30 cm) condition is practically equivalent to the (30 days / 1 day / 0 cm) one.

3. *Ground-water activation:* do not exceed radionuclide concentration limits $C_{i,reg}$ of 20 pCi/ml for ^{3}H and 0.4 pCi/ml for ^{22}Na in any nearby drinking water supplies. These limits mean that if water containing only one of the radionuclides at the limit was used by someone as their primary source of drinking water, that individual would receive an annual dose equivalent of 4 mrem.

Additionally, we assume the accumulated dose of 20 Mrad/yr or 400 Mrad over 20 years lifetime in the hot spots of machine components as a *radiation damage* limit for such materials as epoxy and cable insulation.

10.3. Ground-Water Activation

Ref. [4] define the concentration limits for the two long-lived isotopes that most easily leach and migrate to the ground water: ^{3}H (half-life time $\tau_{1/2}$=12.32 yr, β^{-} decay mode) and ^{22}Na ($\tau_{1/2}$=2.604 yr, β^{+} and γ decay modes). One needs to calculate creation and build-up of those nuclides. After irradiation over the time t, the concentration of a radionuclide i in the ground water in soil immediately outside the beam loss region is

$$C_i(\frac{pCi}{ml}) = \frac{1}{0.037} N_p S_{av} \frac{K_i L_i (1 - e^{-t/\tau_i})}{n}, \tag{10.1}$$

where N_p is the number of protons per second at the source, S_{av} is the star density above 50 MeV (stars/cm^3/proton) averaged over a volume surrounding the source out to an appropriate boundary (e. g., to 0.1% of the maximum star density at the entrance to the soil, that is a "99.9% star volume"), K_i is the radionuclide production yield (atoms/star), L_i is the leachability factor, n is the soil porosity, and τ_i is the mean lifetime of the radionuclide i, τ=$\tau_{1/2}/\ln 2$. The soil porosity n is the ratio of the volume of void in the soil (generally fille with water), to the volume of rock (unitless). $n = \rho w_i$, where w_i is the mass

of water per unit mass of soil that corresponds to the leaching fraction of the *i*th nuclide and ρ is the soil density. K_iL_i and w_i are site specifi parameters. For example, $K_{^3H}$ $L_{^3H}$ = 0.075 atoms/star, $K_{^{22}Na}$ $L_{^{22}Na}$ = 0.0035 atoms/star and n=0.30 for the glacial till of the Fermilab NuMI project [6].

The sum of the fractions of radionuclide contamination (relative to regulatory limits $C_{i,reg}$) must be less than one for all radionuclides [6, 7]:

$$C_{tot} = \sum_{i=1}^{N} \frac{R_i C_i}{C_{i,reg}} \leq 1, \tag{10.2}$$

where R_i is the reduction factor for the nuclide *i* due to vertical transport through the material surrounding the tunnel and horizontal transport in the aquifer. Usually, R_i is taken to be unity in such materials as dolomite, but $R_i < 1$ in glacial till and similar materials [7]. Using R_i=1 would therefore overestimate the result [5].

It is useful to know a MARS calculated hadron flu Φ_h^0 above a given threshold immediately outside the tunnel wall, which corresponds to C_{tot}=1. For the NuMI case, with a 120 GeV proton beam on a thin 1-m long graphite target in the center of a 2-m radius tunnel with 40-cm thick concrete walls, $\Phi_h^0(E > 30\ MeV)$=3640 $cm^{-2}s^{-1}$. That is rather close to $\Phi_h^0(E > 30\ MeV)$=4000 $cm^{-2}s^{-1}$ used in reference [6]. For the 16-GeV Proton Driver arcs, this flu outside a 40-cm thick concrete wall which is 1.6 m from a beam axis, is $\Phi_h^0(E > 30\ MeV)$=3450 $cm^{-2}s^{-1}$ and $\Phi_h^0(E > 20\ MeV)$=3850 $cm^{-2}s^{-1}$. The fraction of ^3H contamination is about 30%, while that of ^{22}Na is about 70%.

10.4. Radiation Analysis Methodology

10.4.1. Normal operation and beam accident

The shielding analysis for the beam transport lines, arcs and long straight sections is performed both for normal operation and for accidental beam loss. The simplest operational scenario is a 1 W/m beam loss rate distributed uniformly along the beam line. A realistic one is based on the beam loss distributions of Chapter 9 with the average rates in the arcs of about 0.2 W/m at the top energy and less than 0.05 W/m at injection. In all cases, beam loss and local shielding (see below) in the collimation region are determined from realistic distributions in the P20 straight section calculated in this study. With the long bare drifts in the arcs and P20 section components locally shielded to meet hands-on maintenance limits, the ground-water protection requirements (see Chapter 9) are fulfilled Certainly, the 4 MW Phase II of this project would require further consideration of radiation shielding issues. Prevention of ground-water flo in a vicinity of the tunnel wall is an additional possibility here. The shielding against prompt radiation is designed such that the dose rate on accessible outer surfaces of the shield is less than 0.05 mrem/hr in non-controlled areas.

For the worst case catastrophic *incredible* accident we assume a loss of the full 1.2 MW of beam at a single point, with the shielding reducing the dose on accessible outside surfaces of the shield to less than 1 mrem/hr in non-controlled areas. The new DOE regulations now

allow for credit to be taken for active shutdown measures, allowing one to address *credible* beam spill accidents with respect to the shield design [8]. In the current Proton Driver design, the "worst credible accident" approach is used, which would limit the amount of beam lost in such an accident to about 0.1% of that in the *incredible* case.

10.4.2. MARS modeling

The MARS code system [9] is used to perform all the calculations in this study. A new interface library has been developed—using ideas and the code of Ref. [10]—which allows one to read and build a complex machine geometry directly from the MAD lattice description. The call-back mechanism is used to achieve such a goal. The user describes the geometry components at $\vec{r} = \vec{0}$ and unrotated, their field materials and volumes as callable functions with well-define signature and registers them with the MAD interface code. Using information on the lattice description, MAD generates rotation matrices and translation vectors for the particular element together with glue elements. The call-back mechanism also allows one to register and call specifi geometry, fiel and initialization function for any non-standard element in the lattice. The dipole, quadrupole and sextupole fiel components from the MAD lattice description are transfered to the respective fiel functions in order to correlate the fiel with lattice bending angle. An example of the lattice model geometry generated is shown in Fig. 9.3. Using this MAD/MARS interface, the arc cells were built for the 16 GeV Proton Driver lattice. The beam lines include magnets, quadrupoles, bare beam pipes (drifts) and tunnel geometry. The magnetic field for the particular components were also implemented in the model. Typical cross-section views of the lattice elements in the calculation model are shown in Fig. 9.4.

To estimate tolerable beam loss, it is assumed that the beam loss rate is quasi-uniform along the arc region considered and that protons hit the beam-pipe under a grazing angle of 1 mrad horizontally inwards (see Chapter 9). The results are normalized to a beam loss of 1 W/m, which is equivalent to 3.9×10^8 protons/m/s for a 16 GeV machine.

In MARS calculations for shielding and activation analysis, more realistic beam loss distributions from Chapter 9 have been used as generated with a tracking code STRUCT [11]. Calculated are energy deposition in dipole and quadrupole coils, residual dose rates on contact to the lattice elements and shielding, and dose and particle flu distributions in the tunnel cross-section. The latter are averaged over the "99.9% volume" star density in soil to calculate the ground-water activation assuming a 20 yr irradiation time and the glacial till parameters with R_i=1, and dose distribution in soil to estimate shielding parameters.

10.4.3. Benchmarking and uncertainties

Reliable calculation of dose attenuation in the shielding to allowable levels is a non-trivial problem. Several techniques—such as biasing, mathematical expectation, exponential transformation and a combination of Monte Carlo with deterministic methods—are used to reach probability levels of $\sim10^{-10}$. The uncertainties of the radiation fiel predictions over such a dynamic range are not easy to quantify. The most direct way is benchmarking against experimental data and other reliable simulation codes.

There has been substantial progress with Monte-Carlo code developments and validation over the last several years. The current versions of the MARS [9], FLUKA [12, 13] and MCNPX [14] codes are obvious leaders. These days, if an expert uses the right code, energy deposition, particle fluxe and related values can be predicted with a 10% accuracy in a majority of cases. Residual dose rate calculation uncertainty is within a factor of two.

Recently, two code verification have been performed with independent calculation methodologies. The firs was for a simplifie model of the SNS Linac tunnel [15]. A section of the tunnel was modeled as a cylindrical shell of concrete 2.3 m in radius, 0.46 m thick and 30 m long. The tunnel was fille with air and surrounded by 9 m of earth berm for shielding. A 0.15 m diameter by 1 m cylinder of copper in the center of the geometry simulated the interaction of the 1 GeV proton beam with accelerator components. The ORNL, BNL and FNAL teams provided their results for this benchmarking. Fig. 10.1 shows dose attenuation in the earth berm predicted in six different approaches. The FNAL results obtained with the MARS code [9] closely match the ORNL ones obtained with the most recent version of the LANL MCNPX-CEM code [14] and are within a factor of two of the "recommended" MCNPX-BERTINI results.

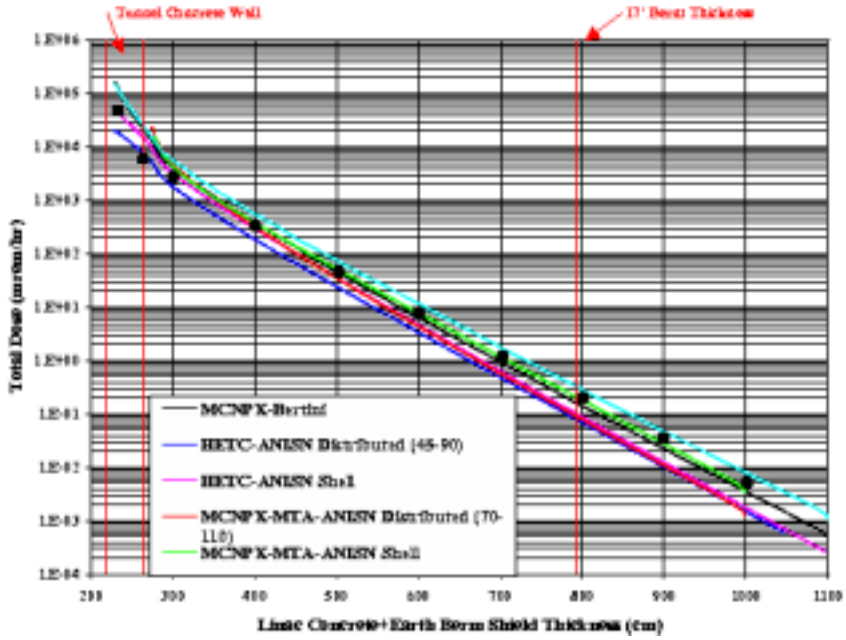

Figure 10.1. Dose attenuation in the ORNL SNS Linac earth berm [15] as calculated by ORNL group (lines) and with MARS14 (symbols).

Another recent benchmark [16] was performed for a 2-m long cylinder—representative of the forward shielding of the CMS detector at LHC—for a 10 GeV/c pencil proton beam hitting it. The absorber consisted radially of iron ($0 < r < 40$ cm), concrete ($40 < r < 100$ cm), borated polyethylene ($100 < r < 110$ cm) and air at $110 < r < 120$ cm. Fig. 10.2 shows almost perfect agreement of MARS14 and FLUKA [12] for energy-integrated neutron fluxes Both codes reproduce similarly the physics of interactions in different materials in the energy range spanning tens of GeV down to a fraction of an electronvolt.

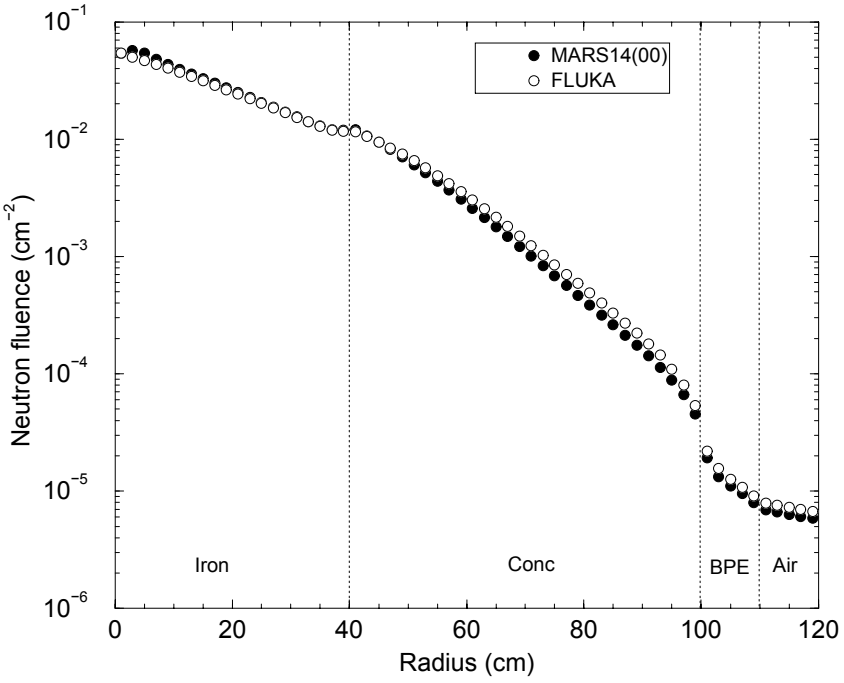

Figure 10.2. Total neutron f uence at $50 < z < 100$ cm in a 2-m composite cylinder irradiated by a 10 GeV/c pencil proton beam as calculated by MARS14 and FLUKA.

10.4.4. Tunnel shielding

The following approach to shielding design is used in this study. Both normal operation and accidental beam losses are considered at injection through the top energy. Realistic beam loss distributions of Chapter 9 are used as a source term for normal operation wherever they are available. A simplest operational scenario with a 1 W/m beam loss rate is assumed otherwise. Local shielding is provided around the components in all cases where hands-on maintenance limits on the component outer surface or radiation load to ground water around the tunnel walls in this region are exceeded. This equalizes (to some extent) the source term for the dirt shielding calculation around the entire machine. For accidental beam loss, both the worst case catastrophic *incredible* and *credible* accidents are considered: a point-like loss of 1.62×10^{18} protons for an hour (*incredible* accident) and 0.1% of that (*credible* accident). The maximum thickness from all cases considered is put into the design as the tunnel shielding in that part of the machine.

Dose on the outer shielding surface depends on the beam energy in a complex way. Assuming a quasi-local beam loss in the magnet, dose equivalent was calculated with MARS14 as a function of dirt thickness ($\rho = 2.24$ g/cm^3) outside the tunnel walls. Fig. 10.3 shows this dependence for a 400 MeV beam (injection), for two intermediate energies of 3 and 8 GeV, and for the top beam energy. Dose at high energies scales as E^{α}, where α is about 0.8, while $\alpha \geq 1$ at proton energies below about 1 GeV.

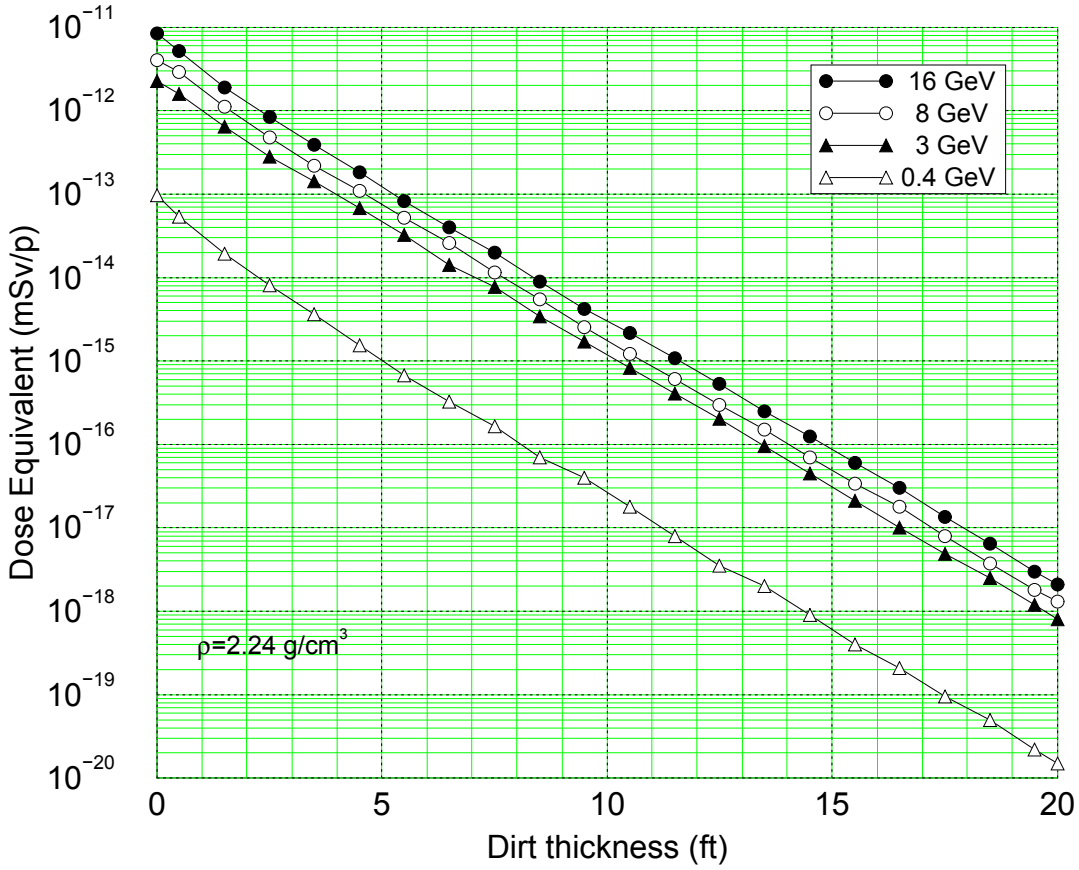

Figure 10.3. Prompt dose equivalent *vs* dirt thickness around the tunnel at a point-like loss of proton beams of different energies.

For the 16 GeV 15 Hz Proton Driver with 3×10^{13} circulating protons, the dose which corresponds to the 1 mrem limit for the worse case point-like loss of 1.62×10^{18} protons for an hour is D_0=6.18×10^{-24} Sv per proton (1 Sv = 100 Rem), requiring about 28 feet of the dirt shielding around the tunnel. With the accidental beam loss of 0.1% of the above—that can be def ned as a *credible* accident for this machine—the shield thickness at 16 GeV is reduced to 18.5 feet. In normal operation, the shielding required is noticeably thinner. With the uniformly distributed beam loss rate of 1 W/m in the magnets—which is equivalent to about 3.9×10^{8} p/m/s lost at 16 GeV—the dirt shielding thickness needed to reduce the dose to 0.05 mrem/hr is $\sim$14 feet. This thickness can be even smaller if one takes into account the lower average beam loss rates in some regions as calculated in Chapter 9.

10.5. Beam Transport Line Shielding

As Chapter 18 suggests, from the standpoint of machine reliability, a *credible* accident is def ned for beam transport lines as a point-like loss of the full beam continuing for one sec-

ond during a given one hour period of operations, resulting in N_A (p/sec) lost in a beam-line element. Lateral shielding of thickness t_A must provide attenuation of the dose at non-controlled areas on accessible outside surfaces of the shield to 1 mrem/hr.

For normal operation of the beam transport lines, we assume at this stage 0.1% loss over the line length, resulting in a uniform beam loss along a beam line at a N_O (p/m/sec) rate. Lateral shielding of thickness t_O must provide attenuation of the dose at non-controlled areas on accessible outside surfaces of the shield to 0.05 mrem/hr. Material of the lateral shielding outside the tunnel walls is assumed to be Fermilab wet dirt of density $\rho = 2.24$ g/cm^3.

10.5.1. Injection

Accidental 0.4-GeV beam loss of $N_A = 4.95 \times 10^{14}$ (p/sec) requires $t_A = 10.5$ feet of dirt. Operational 0.4-GeV beam loss of $N_O = 1.65 \times 10^9$ (p/m/sec) = 0.106 W/m along a 300-m long injection beam line requires $t_O = 9.5$ feet of dirt. Assuming a safety factor of 3, the thickness of dirt shielding above the 0.4-GeV injection beam line is 12 feet. Phase II (4 MW, 1 GeV) will require about 15.25 feet of dirt.

10.5.2. Extraction

Accidental 16-GeV beam loss of $N_A = 4.5 \times 10^{14}$ (p/sec) requires $t_A = 17$ feet of dirt. Operational 16-GeV beam loss of $N_O = 4.5 \times 10^8$ (p/m/sec) = 1.152 W/m along a 1000-m long extraction beam line requires $t_O = 14.5$ feet of dirt. Assuming a safety factor of 3, the thickness of dirt shielding above the 16-GeV extraction beam line is 18.5 feet. Phase II (4 MW) will require about 20 feet of dirt.

10.6. P10, P30 and P50 Arc Shielding

As described in Section 10.4.2, MARS14 simulations in the arcs are done first for longitudinally uniform 16-GeV beam loss and then for realistic beam loss distributions from Chapter 9. The full arc lattice in a rectangular tunnel embedded into wet Fermilab dirt is implemented into the MARS calculation model. The tunnel width is 16 feet, its height is 9 feet, the concrete walls are 15-inch thick, ceiling and floor are 30-inch thick. The lattice elements as modeled in MARS are described in Chapter 9. Fig. 10.4 shows a plan view of the arc tunnel with magnets as implemented into the model, while cross-sectional views are shown in Fig. 10.5. Cable trays are positioned at the ceiling in the left and right corners of the cross-sections shown.

10.6.1. Prompt radiation

Even with the beam lost uniformly along the arc lattice, there are pronounced peaks of radiation field around the long bare beam pipes. These could dominate the radiation environment near the beam line. Fig. 10.6 shows hadron flux distributions across the lattice elements, tunnel, its walls and first layers of the surrounding dirt. The flux and, as a result, all other radiation values are about a factor of ten higher on the long bare beam pipe compared to that on the magnet outer surfaces. At large distances from the lattice elements, at

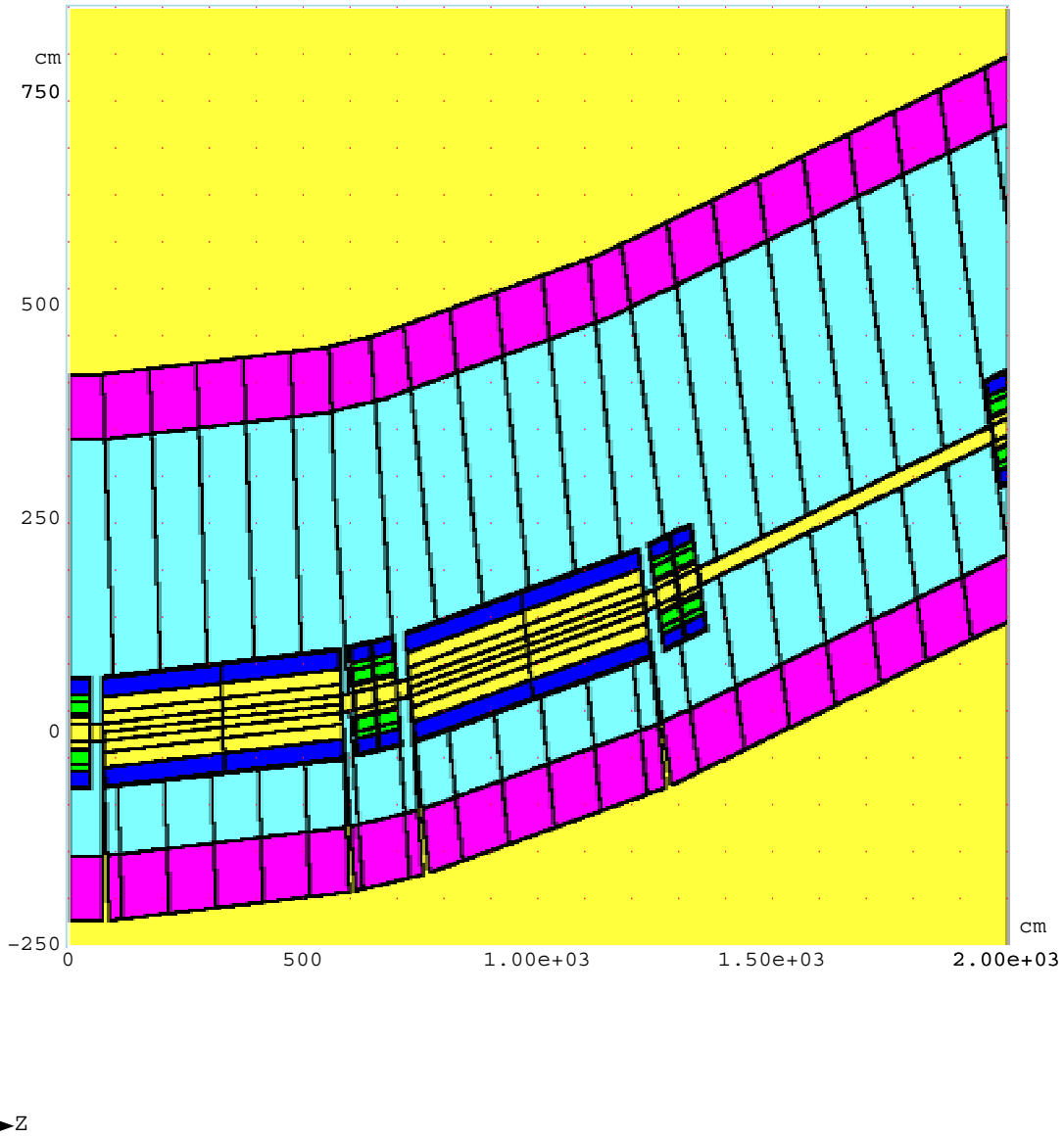

Figure 10.4. Plan view of the modeled arc.

tunnel walls, ceiling and floor, and in the surrounding dirt, the radiation levels are much more uniform longitudinally and transversely. In the model considered, the hadron flux immediately outside the tunnel walls near the peaks in the magnets is below the limit of $\Phi_h^0(E > 20\,MeV)$=3850 $cm^{-2}s^{-1}$. The flux outside of the inward tunnel wall and under the floor near the long bare beam pipe peaks is above the limit by a factor of 3 to 5, while it is right on the limit above the ceiling and outside the outward wall. This implies that either the beam loss rate on the long bare beam pipes should be kept below 0.2-0.3 W/m or these regions require local shielding.

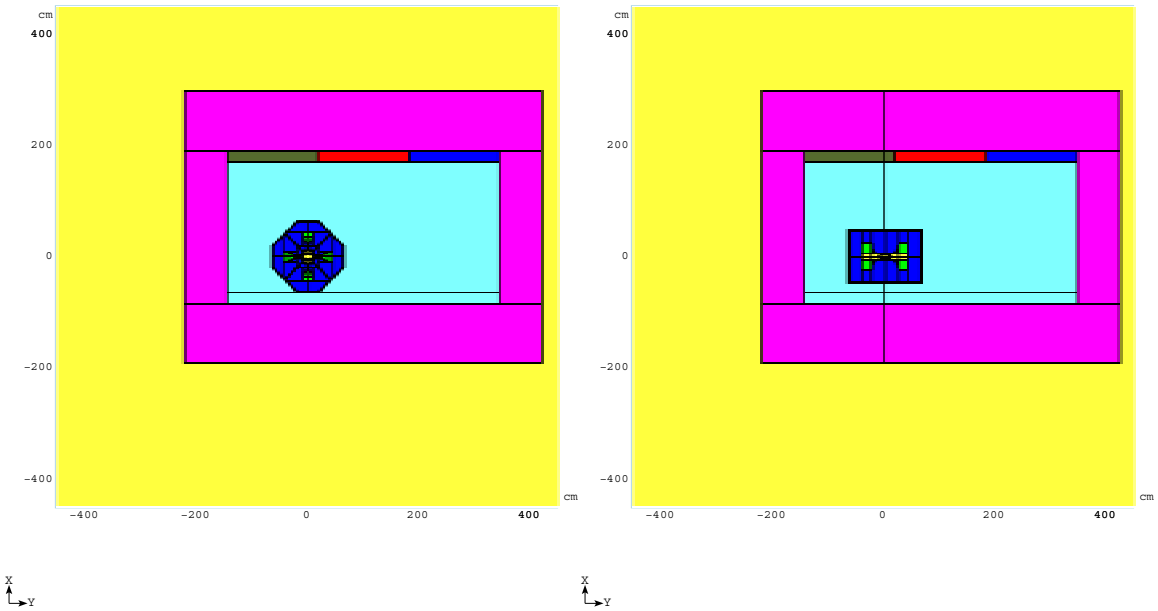

Figure 10.5. Cross-sectional views of the modeled arc at quadrupole (left) and dipole (right) locations.

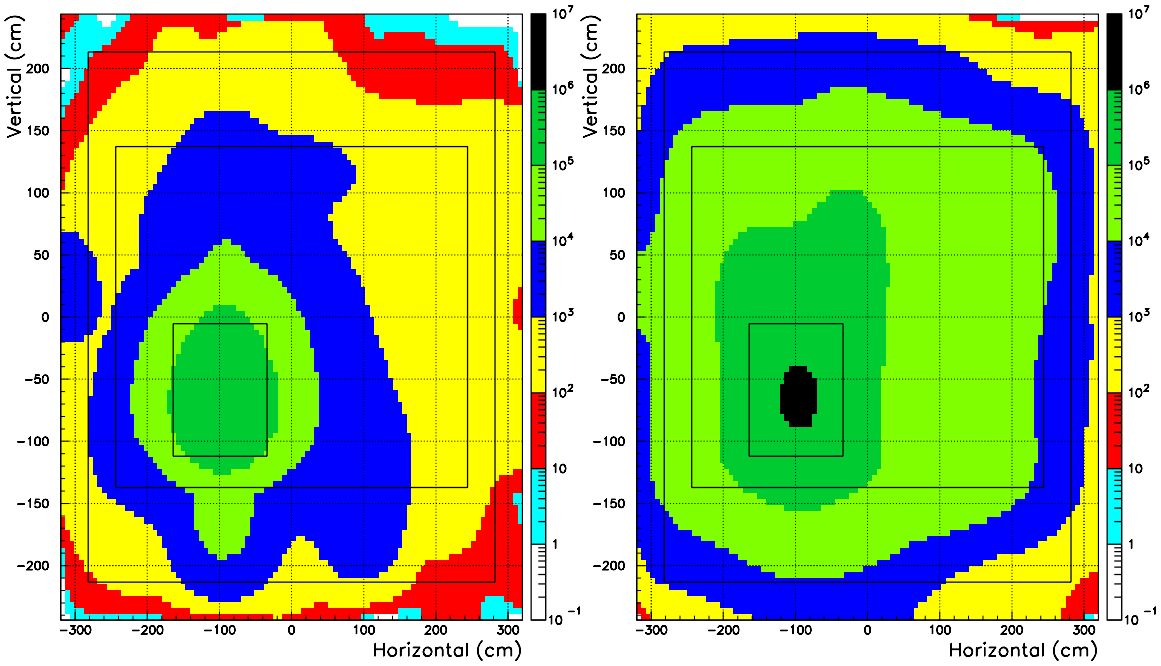

Figure 10.6. Hadron (E>20 MeV) isof uxes ($cm^{-2}s^{-1}$ at 1 W/m) in the arc tunnel cross-section at peak at a dipole magnet (left) and long drift (right).

Despite variation in realistic beam loss distribution along the lattice and remembering the fact that the shield thickness is driven by accidental beam loss which can take place in an arbitrary lattice location, a uniform shielding design along the arcs is suggested. With the worst case point-like accidental loss of 0.1% of the 1-hour beam intensity at 16 GeV—a *credible* accident for the arcs and long straight sections—the shield thickness required is 18.5 feet of Fermilab wet dirt. At normal operation, it is about 14 feet. Assuming a safety factor of 3, the thickness of dirt shielding above the arcs is 20 feet. Phase II (4 MW) will require about 21.5 feet of dirt.

Fig. 10.7 shows annual dose distributions in the same arc cross-sections at a dipole magnet and long drift peaks. The maximum dose accumulated in the coils is about 2 Mrad/yr at 1 W/m beam loss rate which is acceptable with use of appropriate materials for insulation. Care should be taken of cable insulation, possible oil and electronics in the tunnel. The maximum annual dose at cable locations at the ceiling is about 0.1-0.2 Mrad/yr above the magnet hot spots, and is about 0.3-0.5 Mrad/yr above the 6-m long bare beam pipes at 1 W/m beam loss rate.

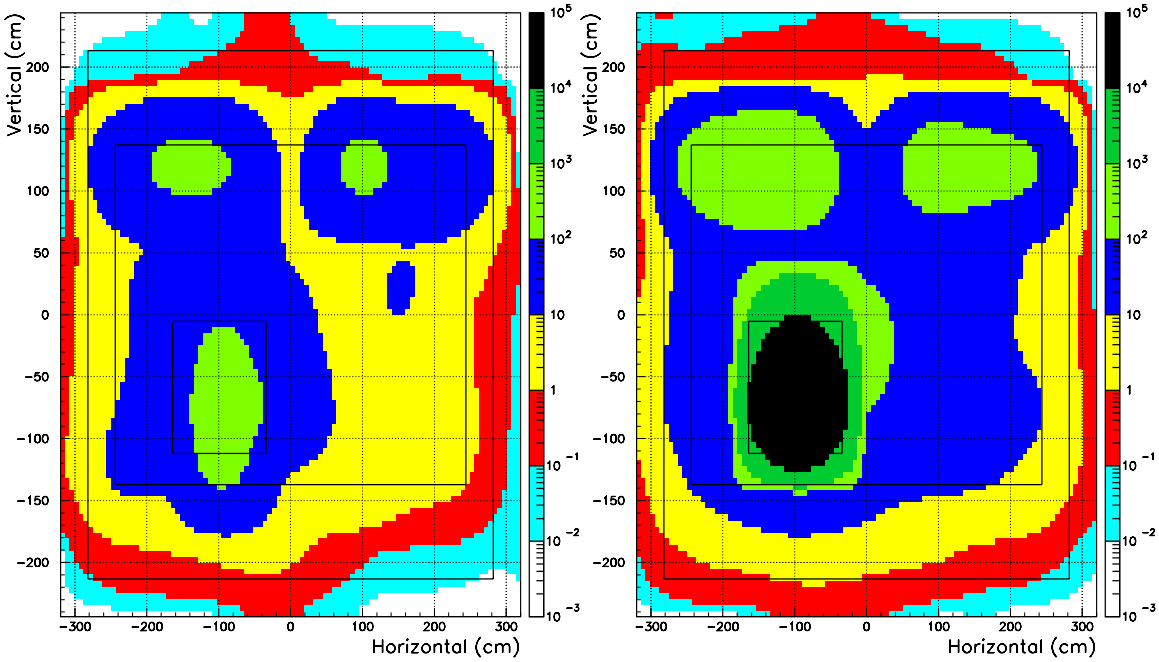

Figure 10.7. Isodose distributions (krad/yr at 1 W/m) in the arc tunnel cross-section at peak at a dipole magnet (left) and long drift (right).

10.6.2. Residual radiation

Calculated peak residual dose rates on contact are shown in Fig. 10.8 for 30 days of irradiation at 1 W/m uniform beam loss rate and 1 day of cooling. Remember that these conditions give results very close to 100 day irradiation and 4 hours cooling for the dose at 30 cm radial distance from the component surface. The dose near the bare beam pipes exceeds the design goal for hot regions of 100 mrem/hr, being noticeably lower near the magnets due to signif -

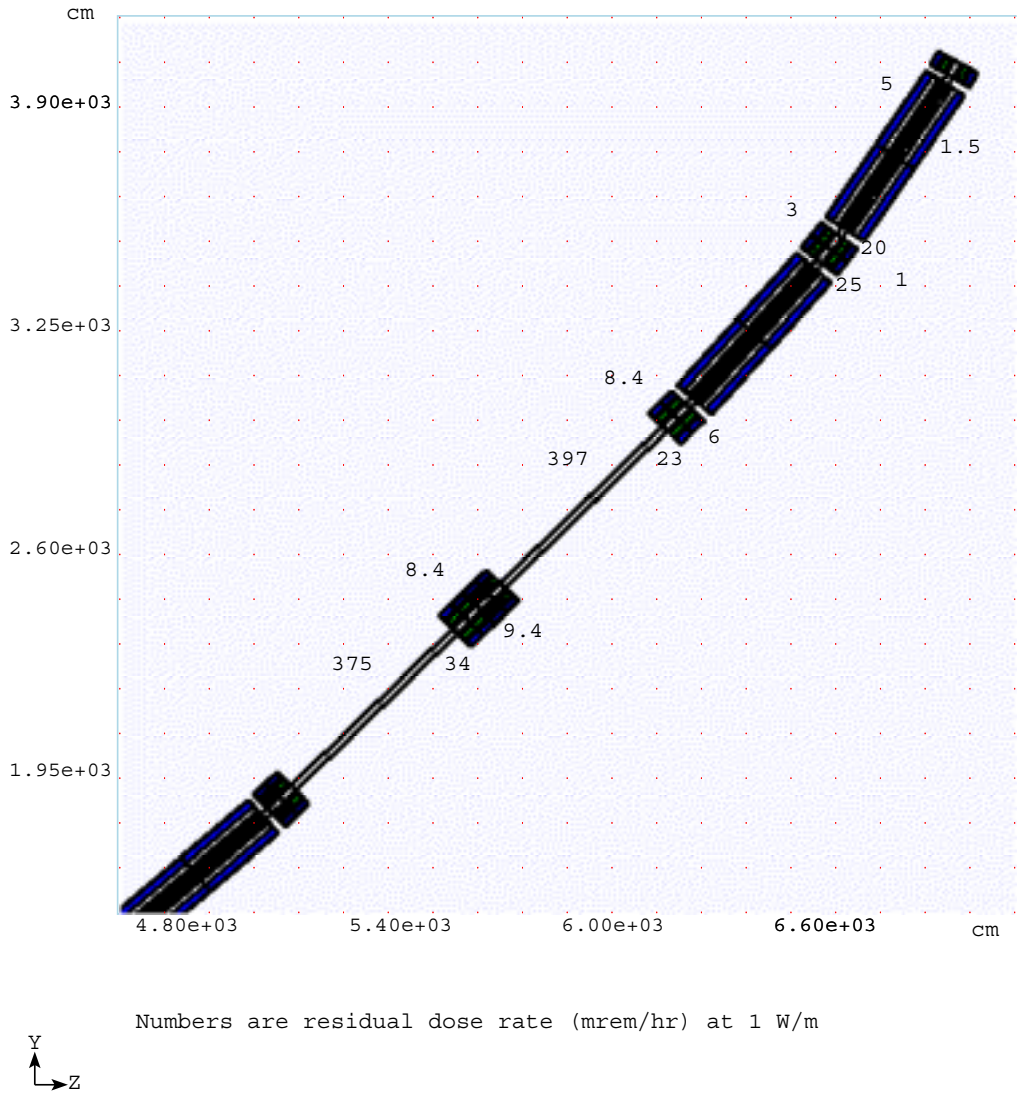

Figure 10.8. Peak residual dose rates (mrem/hr) on the outer surface of the arc elements at 1 W/m uniform beam loss rate at 16 GeV.

cant absorption of soft photons in the dipole and quadrupole materials. One sees that hands-on maintenance is a serious issue with about 3 W/m as a tolerable maximum beam loss rate in the lattice elements, except for the long bare beam pipes where one should decrease the loss rate to 0.25 W/m to reduce the dose to 100 mrem/hr. One needs further reduction to bring the dose down to a good practice value of about 10-20 mrem/hr. Alternatively, one can think of providing simple shielding around the bare beam pipes. For ground-water activation immediately outside the tunnel walls, the peak values are below the limit around the magnets, but are 2 to 3 times above the limit at 1 W/m beam loss rate on bare beam pipes.

At 16 GeV the determining factor is hands-on maintenance, with about 3 W/m as a tolerable maximum beam loss rate in the lattice elements, except for the open long beam pipes. There one should reduce the loss rate to 0.25 W/m to reduce the dose to 100 mrem/hr. One needs further reduction to bring the dose down to a good practice value of about 10-20 mrem/hr. Alternatively, one can think of providing simple shielding around the bare beam pipes.

10.7. P20 Long Straight Shielding

The P20 long straight section, with the injection system and with the collimation system intercepting about 99% of beam loss, is the hottest region in the machine. The beam loss distribution of Chapter 9 is used as a source term in the MARS14 simulations in this region. It is assumed that 10% of the intensity is intercepted at injection, and 1% at the top energy. The region considered includes all the components of the P20 long straight section (see Fig. 9.1) as shown in Fig. 10.9. The secondary copper collimators are 0.5-m long and 44×44 cm^2 transversely. They are the hottest spots, with beam loss rates of several kW/m.

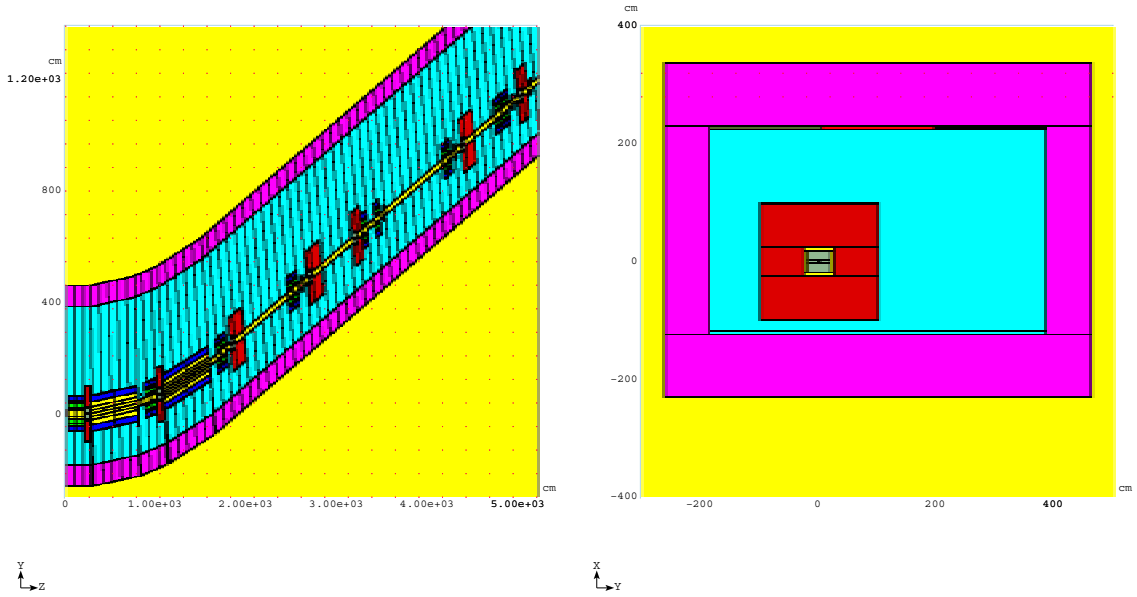

Figure 10.9. Longitudinal view of the collimation region (left) and cross-sectional view at the C1 collimator (right) with the proposed shielding as implemented into the MARS14 calculation model.

10.7.1. Prompt radiation

To meet the regulatory requirements for hands-on maintenance and ground-water activation, massive shielding is required in the P20 region. Calculations show that the optimal conf guration would include local shielding around collimators along with extended shielding over the entire region. Local steel shielding is 2.5 m long and extends to $|x,y|$=115 cm transversely around all secondary collimators, dipoles and quadrupoles downstream. To ac-

comodate this shielding, the P20 tunnel interior is enlarged by 90 cm horizontally and vertically. Hadron f ux distributions at the secondary collimator C2 and supplementary collimator SC3 (see Fig. 9.1) are shown in Fig. 10.10 and Fig. 10.11 (left). With such a shield, radiation levels outside the tunnel wall are very close to those in the arcs. Therefore, the same external shielding design both for normal operation and beam accident is applied. With a safety factor of 3, the thickness of dirt shielding above the P20 long straight section is 20 feet, increased to about 21.5 feet at Phase II (4 MW).

Fig. 10.11 (right) shows annual dose distribution in the P20 tunnel cross-section at the C2 collimator. The maximum dose accumulated in the collimator cores is several hundred Mrad/yr. The maximum annual dose at cable locations at the ceiling is about 50 krad/yr.

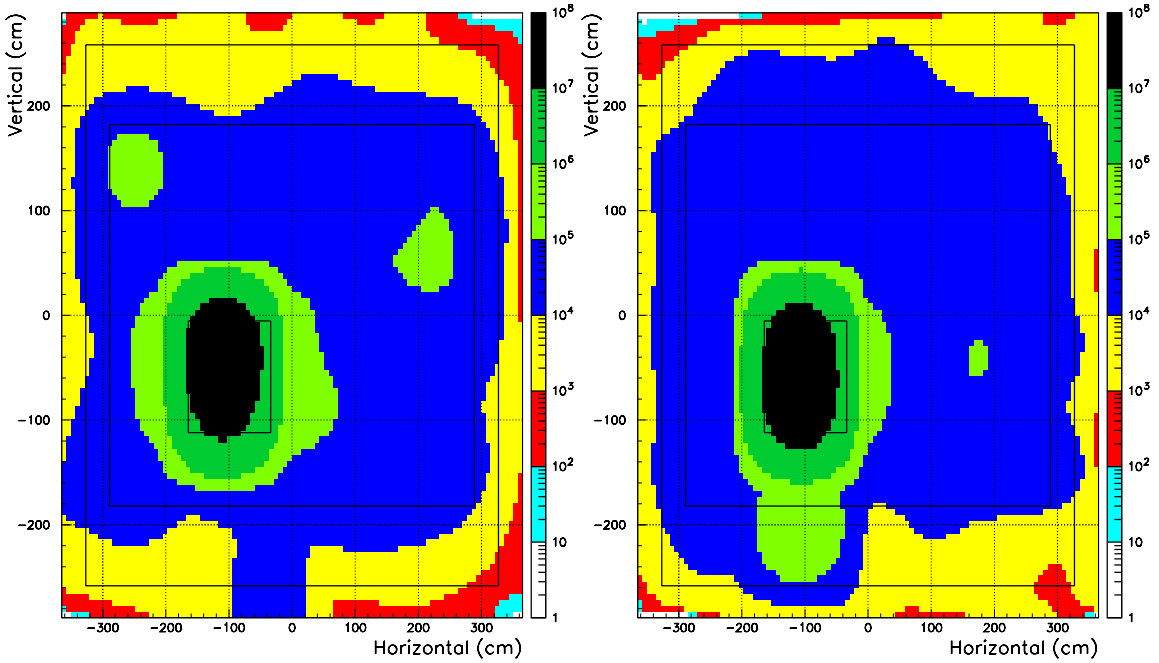

Figure 10.10. Hadron (E>20 MeV) isof ux ($cm^{-2}s^{-1}$) in the P20 tunnel cross-section at the collimators C2 (left) and SC3 (right).

10.7.2. Residual radiation

As shown in Fig. 10.10, the hadron f ux immediately outside the tunnel walls averaged over each side exceeds by about a factor of three the limit of $\Phi_h^0(E > 20\ MeV)$=3850 $cm^{-2}s^{-1}$, that corresponds to the ground water activation limit C_{tot}=1 in (10.2). This implies that the P20 tunnel wall thickness should be increased by about one foot, which may also be needed because of the large tunnel cross-section.

Residual dose rates on the outer surface of the proposed shielding do not exceed 20 mrem/hr after a 30 day irradiation and 1 day cooling. Taking into account all the current uncertainties, one can use the proposed conf guration as a baseline for further studies.

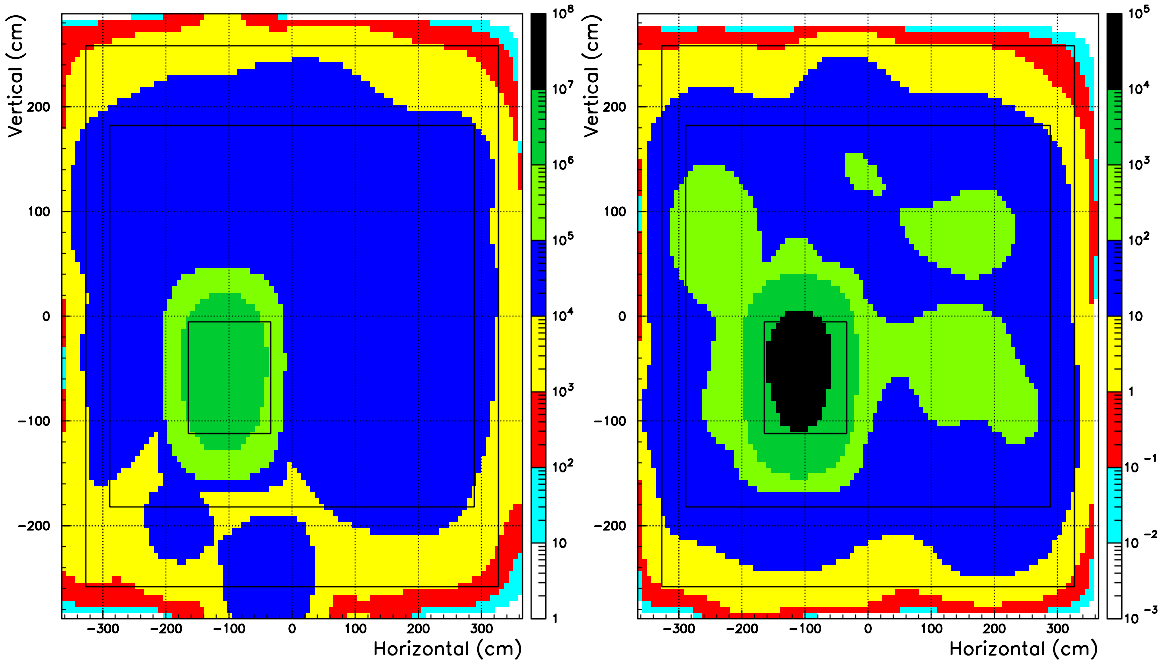

Figure 10.11. Hadron (E>20 MeV) isof ux ($cm^{-2}s^{-1}$) in the P20 tunnel cross-section two meters downstream of the collimator C3 (left) and isodose distribution (krad/yr) at the secondary collimator C2 (right).

It is interesting to note that the dose peaks are located about 2 m downstream of the collimators and the corresponding peaks in the beam loss distribution. These are a source of secondary particles irradiating the downstream quadrupoles. To provide adequate protection against low-energy neutrons at the hot spots, hydrogeneous liners (0.3 m thick concrete or polyethylene) inside and outside the steel shielding might be needed.

The ultimate shielding design will include material cost/volume minimization as well as civil construction, cooling and remote control. There are many engineering design issues in this region. The local shielding weight is about 12 ton/m. It occupies signif cant cross-sectional area and makes access to the region components a non-trivial task. Radiation levels inside it are extremely high preventing hands-on maintenance. Therefore the design should include a remotely operated crane to lift out the shielding and parts of the beam-line. The beam-line elements should be designed for fast remote maintenance. Remote operations are required for f ne tuning of the collimator jaws. Another problem is the heat buildup in the collimation system. The power intercepted by the collimators C1 and C2 is equal to about 3 and 4 kW, respectively. It is dissipated in the collimators themselves and along 2-3 meters in the downstream beam-line. A cooling system should be able to remove this power. Radiation damage to the cables, cooling water pipes, beam diagnostics elements and other sensitive components is a serious issue in this region and will be considered for the entire machine in the near future.

10.8. P40 and P60 Long Straight Shielding

Extraction from the Proton Driver will be one-turn fast extraction. In order to reduce the extraction loss in Stage 1, there will be a 7-bucket notch in a train of 126 bunches. Therefore, there will be little loss at the extraction septum. In Stage 2, this notch is not needed due to a large bunch spacing (132 ns). When the machine is well tuned, the extraction loss can be as low as the order of 10^{-4}, which has been achieved at the ISIS. As for the RF cavities with large apertures, our calculations show no noticeable beam loss in those regions.

The above implies that no local shielding is needed in the P40 and P60 long straight sections. At this stage, shielding design and radiation requirements in these regions are assumed the same as in the arcs.

References

[1] J. O. Johnson, "Radiation Transport Analyses for the U. S. Spallation Neutron Source (SNS)",in *Proc. of the Monte Carlo 2000 International Conference*, Lisbon, Portugal, October 23-26 (2000).

[2] O. E. Krivosheev and N. V. Mokhov, "Tolerable Beam Loss at High-Intensity Proton Machines", in *Proc. of the 7th ICFA Mini-Workshop on High-Intensity, High-Brightness Hadron Beams "Beam Halo and Scraping"*, Lake Como, Wisconsin, September 13-15, 1999, Fermilab-Conf-00/185, Fermilab-Conf-00/192 (2000).

[3] A. I. Drozhdin, O. E. Krivosheev and N. V. Mokhov, "Beam Loss, Collimation and Shielding at the Fermilab Proton Driver", Fermilab-FN-693 (2000).

[4] "Fermilab Radiological Control Manual", Article 236, http://www-esh.fnal.gov/FRCM/.

[5] J. D. Cossairt, Private communication (2000).

[6] N. Grossman et al., "Ref nement of Groundwater Protection for the NuMI Project", Fermilab-TM-2103 (2000).

[7] J. D. Cossairt, A. J. Elwyn, P. Kesich, A. Malensek, N. V. Mokhov, and A. Wehmann, "The Concentration Model Revisited", Fermilab-EP-Note-17 (1999).

[8] J. O. Johnson, Private communication, ORNL (2000).

[9] N. V. Mokhov, "The MARS Code System User's Guide", Fermilab-FN-628 (1995); N. V. Mokhov, S. I. Striganov, A. Van Ginneken, S. G. Mashnik, A. J. Sierk, and J. Ranft, "MARS Code Developments", Fermilab-Conf-98/379 (1998); N. V. Mokhov, "MARS Code Developments, Benchmarking and Applications", Fermilab-Conf-00/066 (2000). N. V. Mokhov and O. E. Krivosheev, "MARS Code Status", Fermilab-Conf-00/181 (2000). http://www-ap.fnal.gov/MARS/.

[10] D. N. Mokhov, O. E. Krivosheev, E. McCrory et al, "MAD parsing and conversion code", Fermilab-TM-2115 (2000).

[11] I. S. Baishev, A. I. Drozhdin and N. V. Mokhov, "STRUCT Program User's Reference Manual", SSCL–MAN–0034 (1994); http://www-ap.fnal.gov/∼drozhdin/STRUCT/STR2.html.

[12] P. A. Aarnio *et al*, CERN TIS-RP/168 (1986) and CERN TIS-RP/190 (1987). A. Fassø*et al*, *Proc. IV Int. Conf. on Calorimetry in High Energy Physics*, La Biodola, Sept 20-25, 1993, Ed. A. Menzione and A. Scribano, World Scientif c, p. 493 (1993). P. Aarnio and M. Huhtinen, *Proc. MC93, Int. Conf. on Monte Carlo Simulation in High Energy and Nuclear Physics*, p 1, ed. P. Dragowitsch, S. Linn and M. Burbank, World Scientif c (1994). A. Fassø*at al*, *Proc. Specialists' Meeting on Shielding Aspects of Accelerators, Targets and Irradiation Facilities*, Arlington, Texas, April 28-29, 1994. NEA/OECD doc., p. 287 (1995).

[13] A. Fassø, A. Ferrari, J. Ranft, P.R. Sala, "New developments in FLUKA modelling hadronic and EM interactions", *Proc. 3rd Workshop on Simulating Accelerator Radiation Environments*, KEK, Tsukuba, Japan, 7-9 May 1997, Ed. H. Hirayama, KEK Proceedings 97-5, p. 32-43. A. Ferrari, and P.R. Sala, "The Physics of High Energy Reactions", *Proc. the Workshop on Nuclear Reaction Data and Nuclear Reactors Physics, Design and Safety*, International Centre for Theoretical Physics, Miramare-Trieste, Italy, 15 April-17 May 1996, edited by A. Gandini and G. Reffo, World Scientif c, p. 424 (1998).

[14] http://mcnpx.lanl.gov.

[15] J. O. Johnson et al., "The Independent Verif cation and Validation of the ORNL SNS Linac Earth Berm Shielding Analysis", ORNL-SNS/TSR-177 (2000).

[16] M. Huhtinen and N. V. Mokhov, "A Cross-comparison of MARS and FLUKA Simulation Codes", Fermilab-FN-697 (2000).

Chapter 11. Injection

C. Ankenbrandt, A. Drozhdin, C. Johnstone, O. Krivosheev, J. Lackey, C. Prior

11.1. Introduction

There are three 63.921 m long straight sections in the ring. One of them with 17 m of preceding arc, called together "utility section", is used for beam injection and collimation [1]. Two other long straight sections are used for RF cavities and extraction. The Proton Driver beta functions and dispersion along the utility section are shown in Fig. 11.1.

Table 11.1. Proton Driver parameters.

Kinetic energy at injection	0.4 GeV
Injected beam normalized transverse emittance	3 mm.mrad
Normalized transverse emittance after painting	60 mm.mrad
Painting injection duration	90 μs (27 turns)
Total intensity at injection	3.3×10^{13}
Horizontal betatron tune	11.43
Vertical betatron tune	12.38
Horizontal β at the foil	22.895 m
Horizontal α at the foil	-0.256
Horizontal dispersion at the foil	0.013 m
Vertical β at the foil	9.231 m
Vertical α at the foil	0.002
Horizontal beam size at injection in the foil	σ_x= 3.35 mm
Vertical beam size at injection in the foil	σ_y= 2.13 mm

The beam halo collimation system [2] is used to localize proton losses in a specially shielded short section of the utility section, and so to reduce irradiation the rest of the ring to an acceptable level. It consists of two primary and several secondary collimators located in drift spaces in the firs 50 m of the utility section.

Painting injection is required to realize uniform density distributions of the beam in the transverse plane for space charge effect reduction. This preserves emittance at injection. Table 11.1 represents the Proton Driver parameters [3] that are relevant the painting system design.

11.2. Painting Injection Scheme

Painting injection is performed by using two sets of fast horizontal and vertical magnets (kickers). The proton orbit is moved in the horizontal plane at the beginning of injection by 52 mm to the thin graphite stripping foil to accept the firs portion of protons generated by H^- in the foil (Fig. 11.2). Four 0.5 m long kicker magnets are used to produce orbit

displacement (Fig. 11.3). The maximum fiel of the kicker magnets is 0.21 kG. The horizontal kick at the beginning of beam painting is shown in Fig. 11.4. Gradual reduction of kicker strength permits "painting" the injected beam across the accelerator aperture with the required emittance. Vertical kicker magnets located in the injection line (not shown here) provide injected beam angle sweeping during injection time, starting from maximum at the beginning of injection and going to zero at the end of painting process. Horizontal and vertical kickers produce particle betatron amplitude variation during injection. This results in a uniform distribution of the circulating beam after painting. Painting starts from the central region of phase space in the horizontal plane and from the border of it in the vertical plane, and goes to the border of the beam in the horizontal plane and to to the center in the vertical plane. This produces a so called "uncorrelated beam" with elliptical cross section,thereby eliminating particles that have maximum amplitudes in both planes simultaneously.

A septum-magnet located upstream of the foil (Fig. 11.3) is used to separate the proton and H^- beams at the quadrupole upstream of the foil by 700 mm. This allows the H^- beam to pass outside the quadrupole body. The beam dump located behind the stripping foil is used for H^o interception. Injection kickers cause negligible perturbation of the β functions and dispersion at injection (Fig. 11.4). Horizontal dispersion in the foil at injection is equal to -0.013 m.

Multi-turn particle tracking through the accelerator is done with the STRUCT [4] code. A stripping foil made of 300 μg/cm^2 (1.5 μm) thick graphite has the shape of so-called corner foil, where two edges of the square foil are supported and the other two edges are free. The foil size is 2.6 cm × 3.8 cm.

The dependence of kicker-magnets strength on time is chosen to get uniform distribution of the beam after painting both in horizontal and vertical planes. An optimal waveform of bump-magnets [5] was simulated in the STRUCT code as presented below:

- in the horizontal plane

$$B = B_o \left[0.4873 + 0.5127 \left(1 - \sqrt{\frac{2\,N}{27} - \left(\frac{N}{27}\right)^2} \right) \right] \qquad N < 27 \tag{11.1}$$

$$B = B_o \left[0.4873 - \frac{N - 27}{12.3127} \right] \qquad N > 27 \tag{11.2}$$

- in the vertical plane

$$Y' = Y'_o \sqrt{2\frac{27 - N}{27} - \left(\frac{27 - N}{27}\right)^2} \qquad Y'_o = 1.835\ mrad \tag{11.3}$$

Here N is the turn number from beginning of painting.

Horizontal phase plane of injected beam in the foil is shown in Fig. 11.5. Emittance of injected beam at 95% is equal to 3 mm·mrad.

Painting lasts during 27 turns, and after painting the circulating beam moves out of the foil during 6 turns. In the simulations the horizontal bump amplitude at the foil is 52 mm =

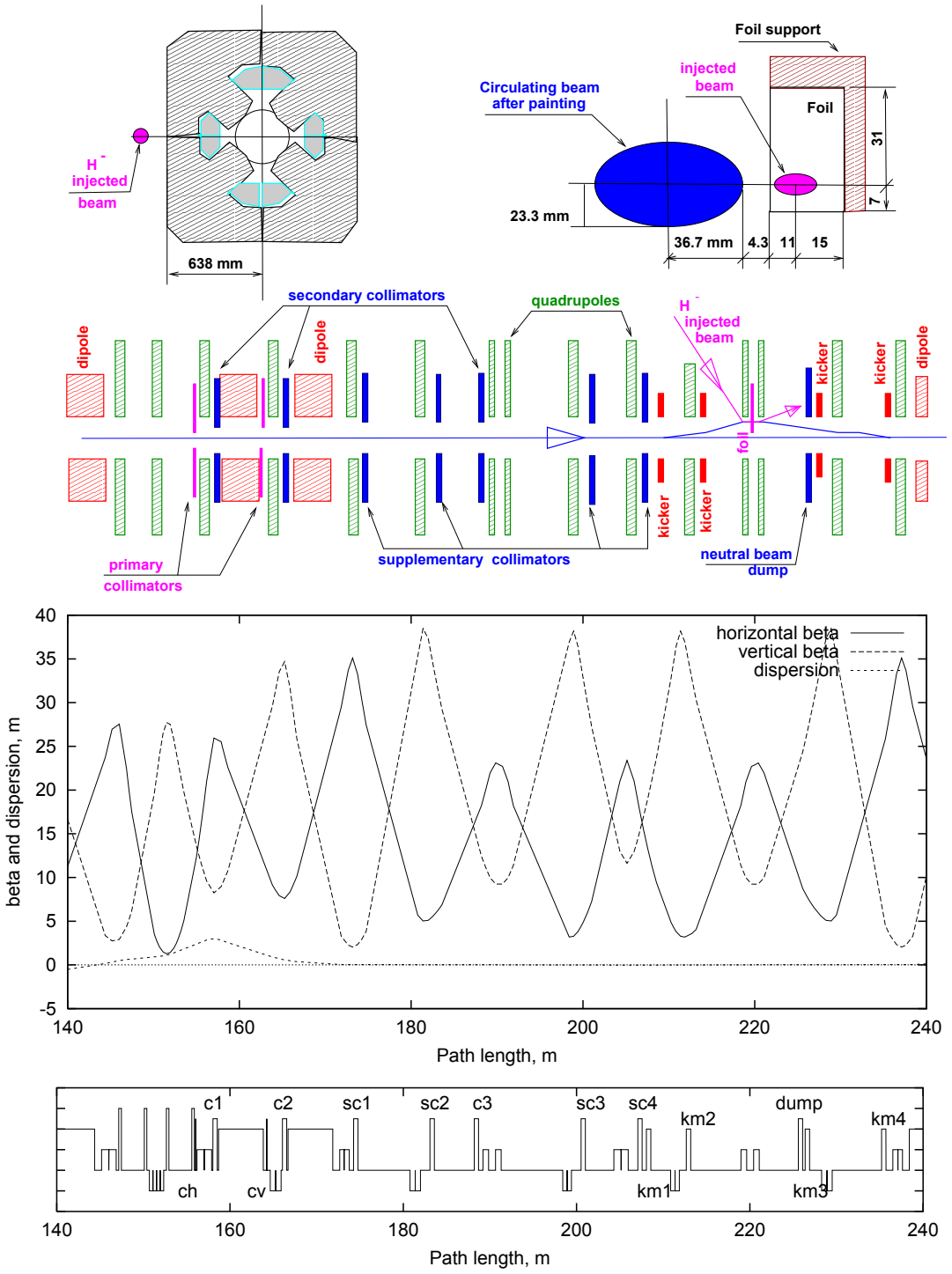

Figure 11.1. Beam collimation and beam painting systems (top) and beta functions and dispersion in the utility section (bottom).

26.7 mm (painting) + 25.3 mm (removing from the foil) (Fig. 11.2). Vertical angle variation is 1.835 mrad. Horizontal and vertical phase plane of circulating beam in the foil at 6-th, 28-st, and 33-d turns from the beginning of beam painting are presented in Fig. 11.6.

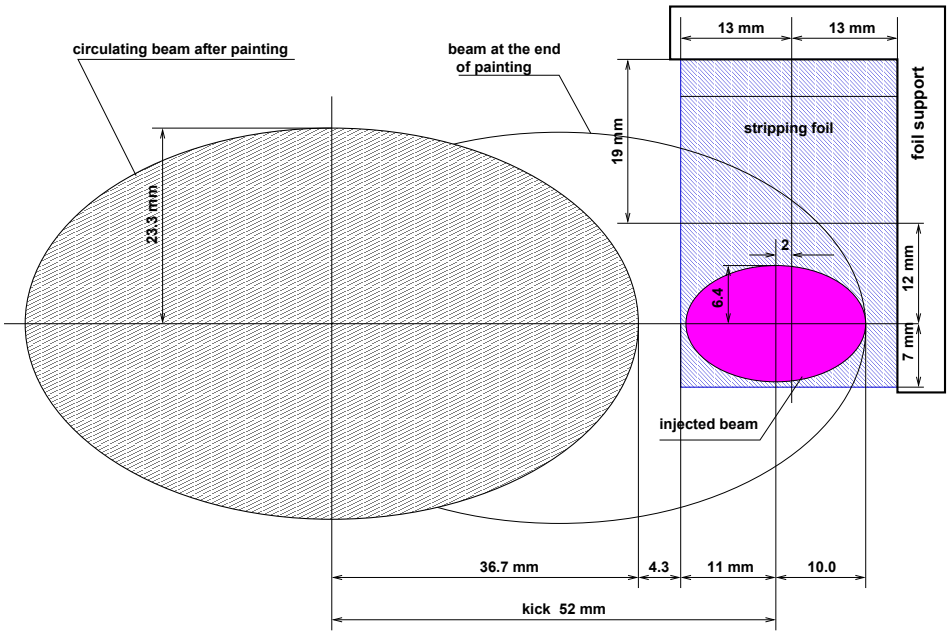

Figure 11.2. Injected and circulating beams location in the foil at painting.

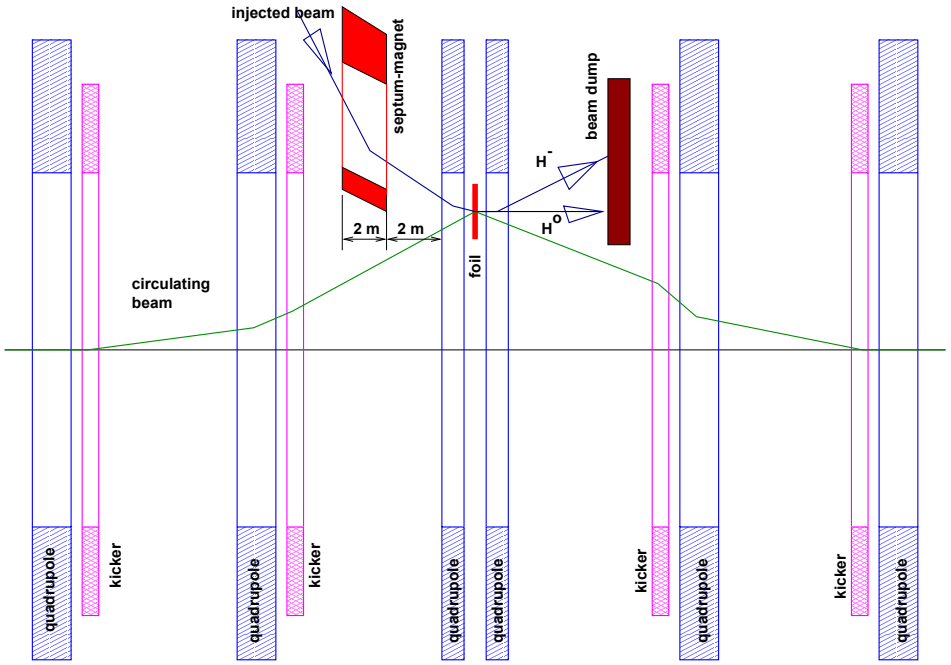

Figure 11.3. Painting injection scheme.

Horizontal kicker-magnet strength and vertical angle of the beam in the foil during injection are presented in the top of Fig. 11.7. Particle transverse population and particle density distribution after painting at the foil location are shown in the middle and at the bottom of Fig. 11.7. Injected beam at the foil and circulating beam after painting in a horizontal phase plane are shown in Fig. 11.7.

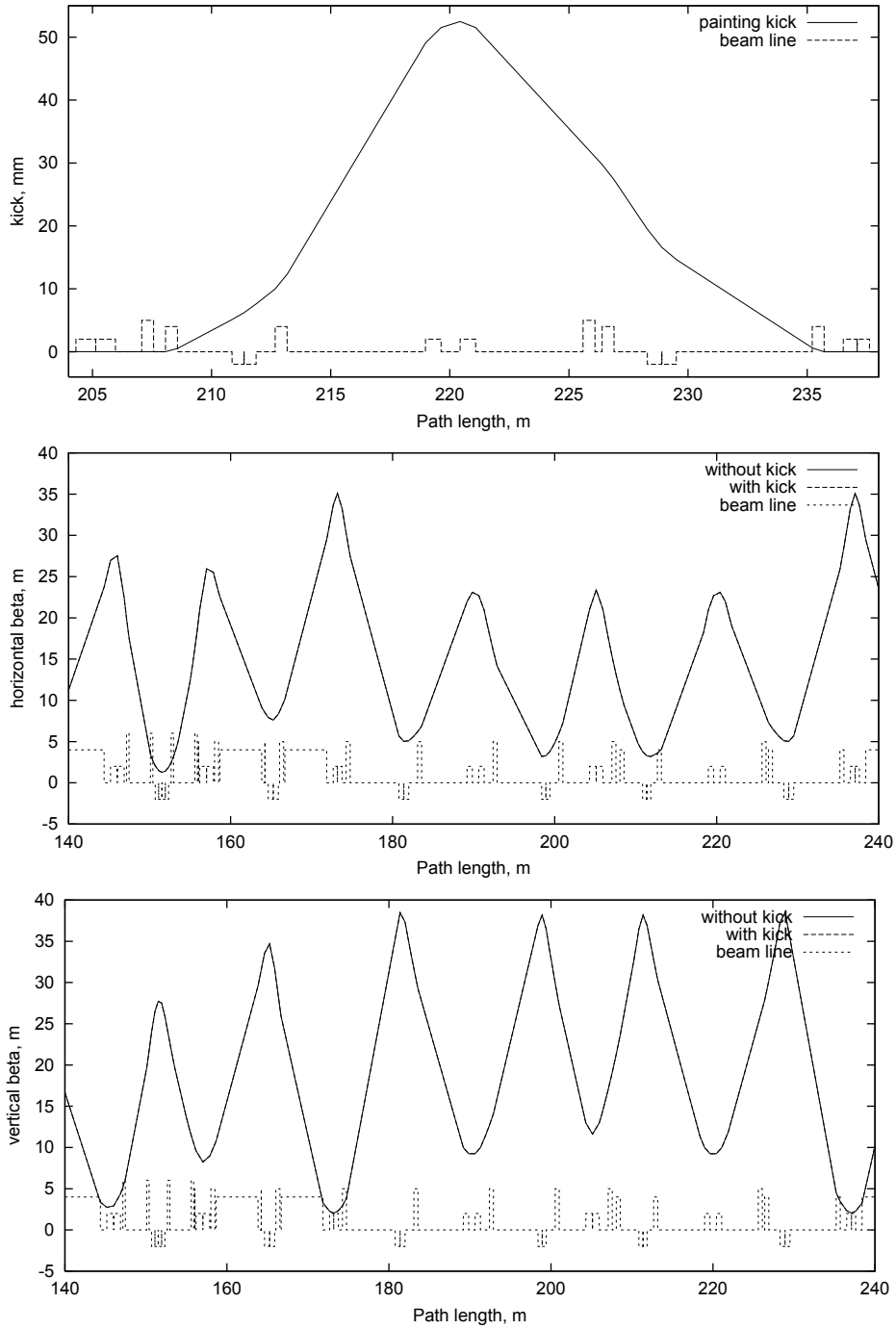

Figure 11.4. Horizontal kick for beam painting (top). Horizontal (middle) and vertical (bottom) beta functions with and without painting bump and kick.

Average number of hits upon the stripping foil for each particle is as low as 1.98. This effects low-level nuclear interactions and multiple Coulomb scattering in the foil at injection, and because of this causes low-level particle loss at injection.

The circulating protons pass several times through the foil and some of them can be lost

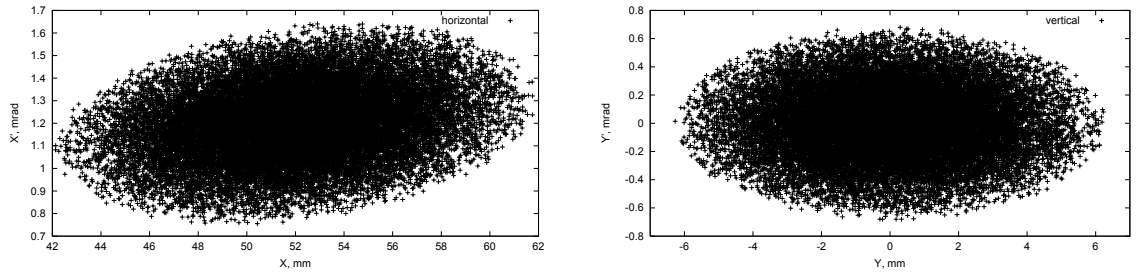

Figure 11.5. Horizontal (left) and vertical (right) phase plane in the foil at injection.

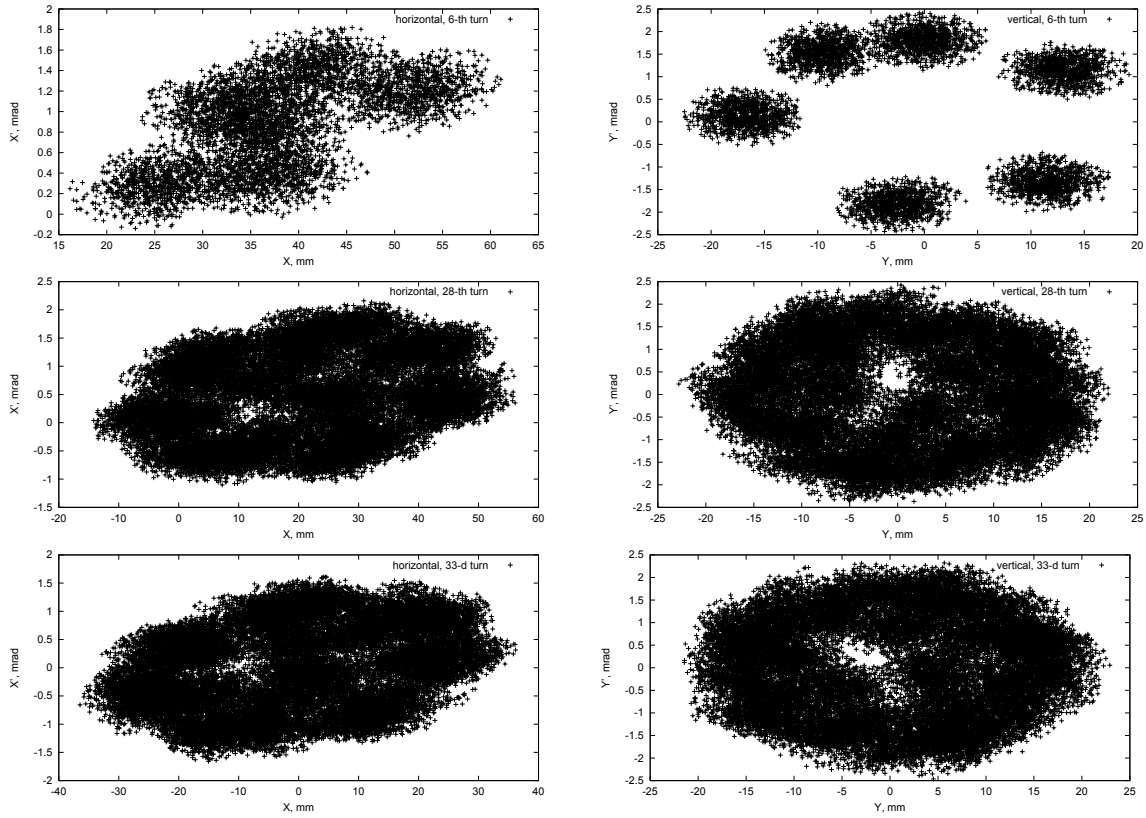

Figure 11.6. Horizontal (left) and vertical (right) phase plane in the foil at 6-th (top), 28-th (middle), and 33-d (bottom) turn from the beginning of beam painting.

because of scattering in the foil. Multiple Coulomb scattering is very small because of small foil thickness. Particle energy loss in the foil at one pass is $2.4 \cdot 10^{-6}$ of initial energy. The rate of nuclear interactions in the foil during the total process is $1.0 \cdot 10^{-5}$ of the injected intensity. The emittance of the circulating beam in the horizontal plane is small in the beginning of painting and it gradually reaches maximum only at the end of painting. Therefore particle horizontal amplitude, in average, is suff ciently less compared to the accelerator aperture. Particles can be lost only during the f rst few turns after injection, and only in the region of injection kick maximum where the beam is close to accelerator aperture. At every next turn after particles are injected, they move away from the aperture restriction because of fast reduction of painting kick amplitude. Simulations shown that the rate of particle loss

in the accelerator at interaction with foil is as low as $7.4 \cdot 10^{-5}$ of the injected intensity.

11.3. Stripping Foil

We developed and used an analytical approach for calculating the foil temperature after painting injection and after many passes of proton beam through the foil. In this section, we describe the method of calculation of the foil temperature after it reaches a quasi-steady state.

Standard notation is applied below, namely:

- c - the speed of light,
- $\hbar$ - the Planck constant,
- k - the Boltzmann constant,
- $m_e c^2$ - the electron rest mass,
- r_e - the electron classical radius,
- N_a - the Avogadro number,
- $\sigma_{SB} = \pi^2 k^4 / 60 \hbar^3 c^2$ is the Stefan-Boltzmann constant,
- M and E are proton mass and energy,
- γ - the Lorentz-factor,
- β - the proton speed in the units of c,
- N - the number of particles injected per turn,
- σ_x and σ_y are r.m.s. for Gaussian distribution of injected beam at the foil,
- A, Z and I are the mass, charge and ionization potential of target material,
- ρ and c_p are the material density and the specif c heat,
- κ and ε are the material thermal conductivity and the emissivity.

11.3.1. Deposited Energy

We consider that contributions from nuclear reactions are negligible. The only energy deposition, and therefore heating source, would be the ionization energy loss in the foil. The density of energy deposited during one injection pulse is:

$$S(\vec{r},t) = \frac{N}{2\pi\sigma^2} \cdot |\frac{dE}{dz}| \cdot e^{-r^2/2\sigma^2} \cdot \delta(t) \tag{11.4}$$

where $\delta(t)$ is Dirac's delta-function. It is properly normalized, so that the total energy deposition is

$$S_{total} = \int_V d^3\vec{r} \int dt\, S(\vec{r},t) = N \cdot |\frac{dE}{dz}| \cdot \Delta z$$

where Δz is the foil thickness. From "Review of Particle Properties" [6] the ionization energy loss - the main energy deposition source in the case of thin foil - can be written as the Bethe-Bloch equation:

$$-\frac{dE}{dz} = K \cdot \frac{Z}{A} \cdot \frac{1}{\beta^2} [\frac{1}{2} \log \frac{2 m_e c^2 \beta^2 \gamma^2 T_{max}}{I^2} - \beta^2 - \frac{1}{2}\delta] \tag{11.5}$$

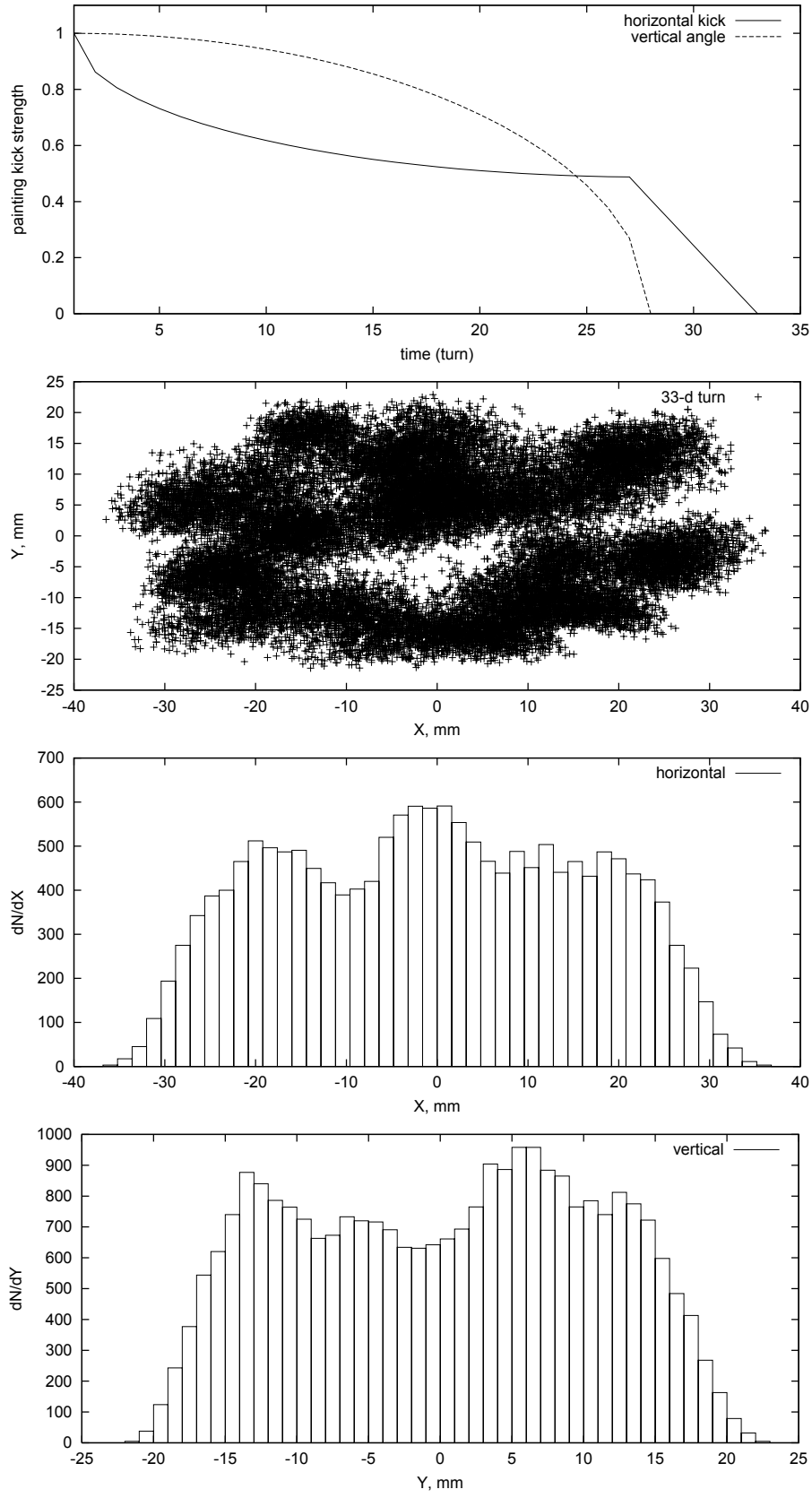

Figure 11.7. Horizontal kicker strength and vertical angle of the beam at injection in the foil (top). Particle transverse population (middle) and particle density distribution in the foil (bottom) at 33-d turn from the beginning of beam painting.

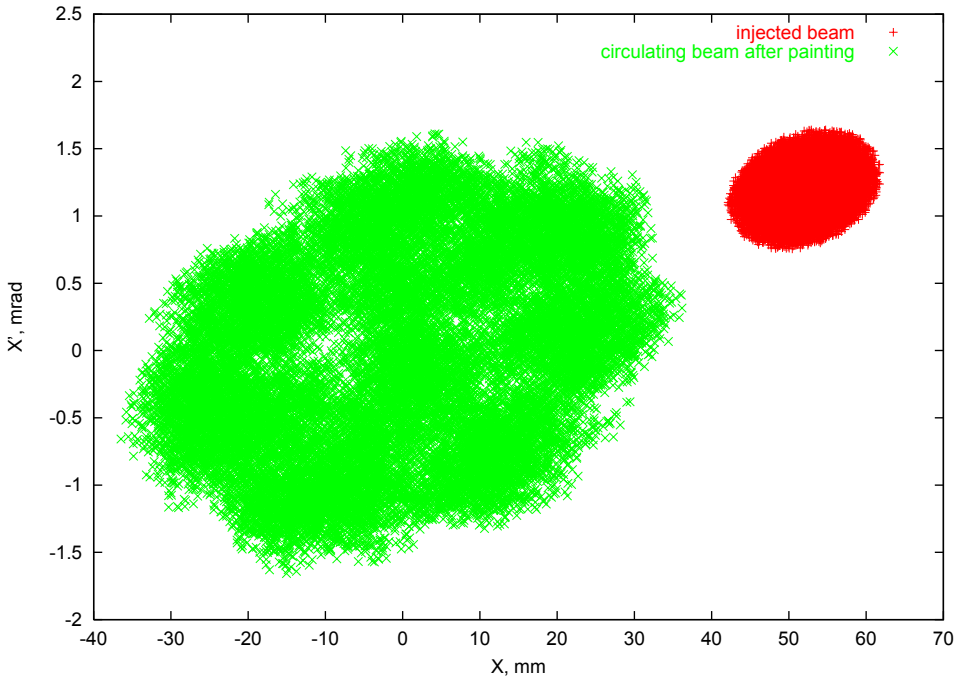

Figure 11.8. Injected beam at the foil and circulating beam after painting.

where $K = 4\pi N_a r_e^2 m_e c^2 = 0.307075 \ \frac{MeV \cdot cm^2}{g}$. T_{max} is the maximum energy transfer in one collision, and for foils it is smaller than the kinematically allowed maximum energy transfer

$$T_{max} = \frac{2m_e c^2 \beta^2 \gamma^2}{1 + 2\gamma m_e / M + (m_e/M)^2}.$$

and δ is density correction, calculated according to the Sternheimer approximation.

11.3.2. Beam Painting and Foil Heating

Because the foil thickness is quite small, we consider the heat propagation from heated area to the edges, where it could be collected and moved away, quite small, so we concentrated our efforts on the heat loss due to emission.

Heat Emission

Another way to dissipate heat after the injection pulse is by radiation. The energy emission of the black body is proportional to the temperature to the fourth power, according to the Stefan-Boltzmann law:

$$Q = \sigma_{SB} \cdot T^4.$$

The Stefan-Boltzmann law is approximately true for the foil if we include the material emissivity ε. Therefore, the heat propagation equation with emission as the only mechanism to cool the foil is

$$\frac{\partial T}{\partial t} = \frac{S(\vec{r},t)}{\rho c_p} - \frac{\varepsilon \sigma_{SB}}{\Delta z \rho c_p} \cdot (T^4 - T_0^4), \tag{11.6}$$

We will solve (11.6) in two steps. First consider the time interval from zero to very small ε. Emission did not change the temperature, therefore the only variable will be the source term and after integration over t from zero to ε we have:

$$T_\varepsilon = T_0 + \frac{1}{\rho c_p}\frac{N}{2\pi\sigma^2}|\frac{dE}{dz}|e^{-r^2/2\sigma^2}. \tag{11.7}$$

Then we solve the equation

$$\frac{\partial T}{\partial t} = -\frac{\varepsilon\sigma_{SB}}{\Delta z\rho c_p}\cdot(T^4 - T_0^4), \tag{11.8}$$

starting from time ε and using T_ε (11.7) as initial value. Integration of (11.8) gives us the equation for $T(t)$ dependence:

$$-\frac{\varepsilon\sigma_{SB}}{\Delta z\rho c_p}(t-\varepsilon) = \frac{1}{2T_0^3}[\arctan\frac{T_\varepsilon}{T_0} - \arctan\frac{T}{T_0}] + \frac{1}{4T_0^3}[\log\frac{T-T_0}{T_\varepsilon - T_0} - \log\frac{T+T_0}{T_\varepsilon + T_0}]. \tag{11.9}$$

In order to solve (11.6) it is obvious we have to obtain the limit $\varepsilon \to 0$. Such limit only removes ε from the right part of equation (11.8). For clarify, we provide the explicit dependence in the next equation

$$t = \frac{\Delta z\rho c_p}{2T_0^3\varepsilon\sigma_{SB}}[\arctan\frac{T_0(T(\vec{r},t) - T_\varepsilon(\vec{r}))}{T_0^2 + T_\varepsilon(\vec{r})T(\vec{r},t)} + \frac{1}{2}\log\frac{(T_\varepsilon(\vec{r}) - T_0)\cdot(T(\vec{r},t) + T_0)}{(T_\varepsilon(\vec{r}) + T_0)\cdot(T(\vec{r},t) - T_0)}]. \tag{11.10}$$

But it is probably impossible to get an explicit dependence $T(\vec{r},t)$ trying to reverse (11.9). Therefore numerical solution is required.

To f nd a temperature behavior at injection when pulses follow each other with τ seconds between them, is easy to write down the recursive procedures for the temperature at a given time

$$\begin{aligned}
T_{j\tau} &= T_{\varepsilon+(j-1)\tau}\cdot\sqrt[3]{\frac{\Delta z\rho c_p}{3\varepsilon\sigma_{SB}T^3_{\varepsilon+(j-1)\tau}\cdot\tau + \Delta z\rho c_p}},\\
T_{j\tau+\varepsilon} &= T_{j\tau} + \frac{N}{2\pi\sigma^2\rho c_p}|\frac{dE}{dz}|\exp(-\vec{r}^2/2\sigma^2),\\
T(j\tau < t < (j+1)\tau) &= T_{j\tau+\varepsilon}\cdot\sqrt[3]{\frac{\Delta z\rho c_p}{3\varepsilon\sigma_{SB}T^3_{j\tau+\varepsilon}\cdot t + \Delta z\rho c_p}}.
\end{aligned}$$

The same scheme can be written for $T(t)$ dependence when T_0 is not equal to 0, but from (11.10) it is obvious that $T_{j\tau}$ and $T(j\tau < t < (j+1)\tau)$ can be obtained only numerically.

Foil Temperature Rise

We consider the temperature rise due to multiple passage of protons through the foil to be instantaneous. Now we have to derive the expression which describes the particle and heat

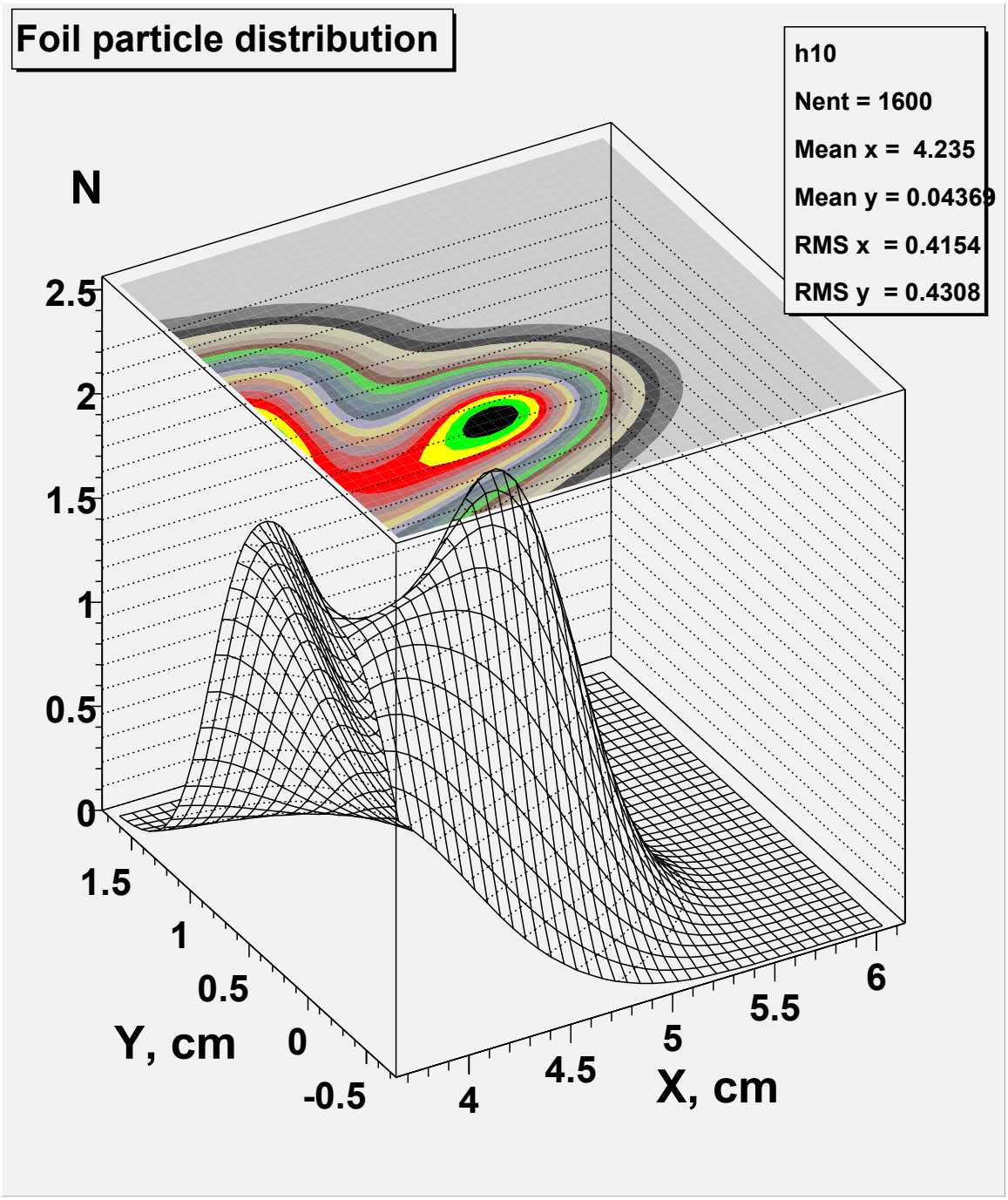

Figure 11.9. Proton hits distribution upon the stripping foil at painting injection.

distribution on the foil during the painting cycle. The following notation is used: x_n^k and y_n^k are the center of injected bunch. Index k is the turn index while n denotes the injection index. There are some conditions on k and n, namely $0 \le n \le N_c = 27$ and $n \le k \le N_c + N_f$, where N_f is the number of turns for beam removal from the foil at the end of injection. The

circulating orbit position resulting from equations (11.1, 11.2) is given by:

$$\begin{aligned} x_k^o &= x_0\{p_0 + p_1 \cdot [1 - \sqrt{\frac{2k}{N_c} - (\frac{k}{N_c})^2}]\} \quad N \le 27 \\ x_k^o &= x_0 \cdot p_0\{1 - \frac{k - N_c}{N_f}\} \quad N > 27 \\ y_k^o &= 0 \end{aligned}$$

where p_0 and p_1 denote orbit position at the end of painting and amplitude of the closed orbit bump during the painting process. Obviously, $p_0 + p_1 \equiv 1$. As was mentioned, painting starts from the center of the beam in the horizontal plane and from large amplitude in the vertical plane, producing an elliptical cross section for the circulating beam. The beam is injected in the ellipse with transverse amplitudes (11.3) of

$$\begin{aligned} x_n^e &= p_1 \cdot x_0 \cdot \sqrt{\frac{2n}{N_c} - (\frac{n}{N_c})^2} \\ y_n^e &= y_0 \sqrt{2 \cdot \frac{N_c - n}{N_c} - (\frac{N_c - n}{N_c})^2} \end{aligned}$$

We now can write down the expression for x_n^k and y_n^k. Knowing the horizontal and vertical tunes ν_x and ν_y

$$\begin{aligned} x_n^k &= x_k^o + x_n^e \cdot \cos[2\pi\nu_x(k-n)] \\ y_n^k &= y_k^o + y_n^e \cdot \cos[2\pi\nu_y(k-n) - \pi/2] \end{aligned}$$

and if we def ne N_i as number of particles injected in one cycle, the proton density $S_N(\vec{r},t)$ will be

$$S_N(\vec{r},t) = \frac{N_i}{2\pi\sigma_x\sigma_y} \sum_{n=0}^{N_c} \sum_{k=n}^{N_c+N_f} e^{-(x-x_n^k)^2/2\sigma_x^2 - (y-y_n^k)^2/2\sigma_y^2}$$

and for a foil with left lower corner (x_{ll}, y_{ll}) and upper right corner (x_{ur}, y_{ur}) we can get the average number of collisions as the result of integration

$$< N_{col} >= \frac{1}{N_c \cdot N_i} \int_{x_{ll}}^{x_{ur}} dx \int_{y_{ll}}^{y_{ur}} dy\, S_N(\vec{r},t)$$

Integrating this one can get

$$\begin{aligned} < N_{col} > &= \sum_{n=0}^{N_c} \sum_{k=n}^{N_c+N_f} [erf(\frac{x_{ur} - x_n^k}{\sqrt{2}\sigma_x}) + erf(\frac{x_n^k - x_{ll}}{\sqrt{2}\sigma_x})] \cdot \\ &\quad [erf(\frac{y_{ur} - y_n^k}{\sqrt{2}\sigma_y}) + erf(\frac{y_n^k - y_{ll}}{\sqrt{2}\sigma_y})]/4N_c \end{aligned}$$

Next a very similar expression gives us the total energy deposited in the foil:

$$\begin{aligned} E_{tot} &= \frac{\Delta z}{4N_c} \sum_{n=0}^{N_c} \sum_{k=n}^{N_c} [|\frac{dE_p}{dz}| + 2|\frac{dE_e}{dz}|\delta_{n,k}][erf(\frac{x_{ur} - x_n^k}{\sqrt{2}\sigma_x}) + \\ &\quad erf(\frac{x_n^k - x_{ll}}{\sqrt{2}\sigma_x})][erf(\frac{y_{ur} - y_n^k}{\sqrt{2}\sigma_y}) + erf(\frac{y_n^k - y_{ll}}{\sqrt{2}\sigma_y})] \end{aligned}$$

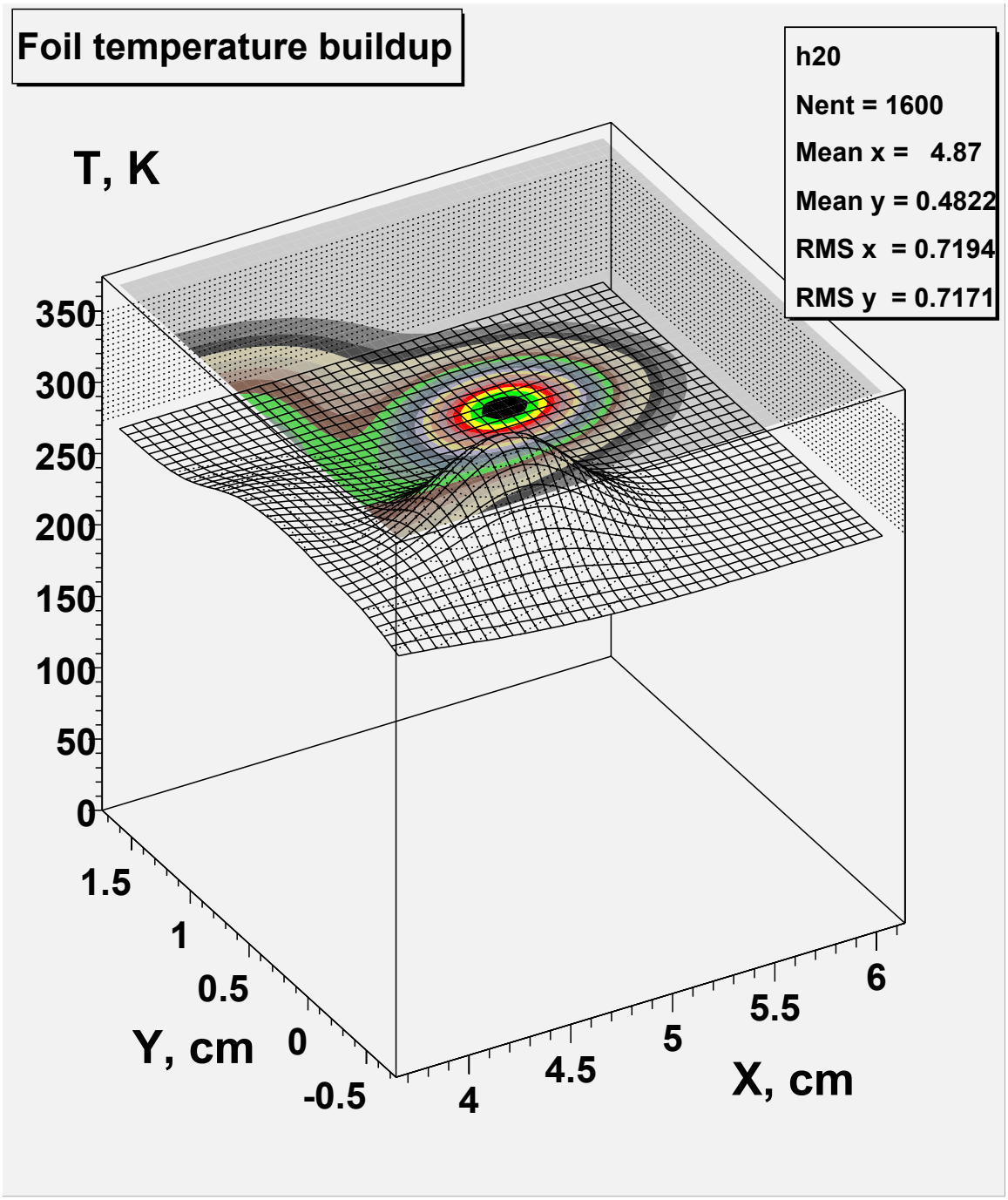

Figure 11.10. Stripping foil temperature buildup after one cycle of particles injected into the proton driver.

If we have both heat emission and heat transfer the equations become more complicated. Combining heat transfer and emission together, one can get

$$\frac{\partial T}{\partial t} = a(\vec{\nabla}^2 T) + \frac{S(\vec{r},t)}{\rho c_p} - \frac{\varepsilon \sigma_{SB}}{\Delta z \rho c_p} \cdot (T^4 - T_0^4), \qquad (11.11)$$

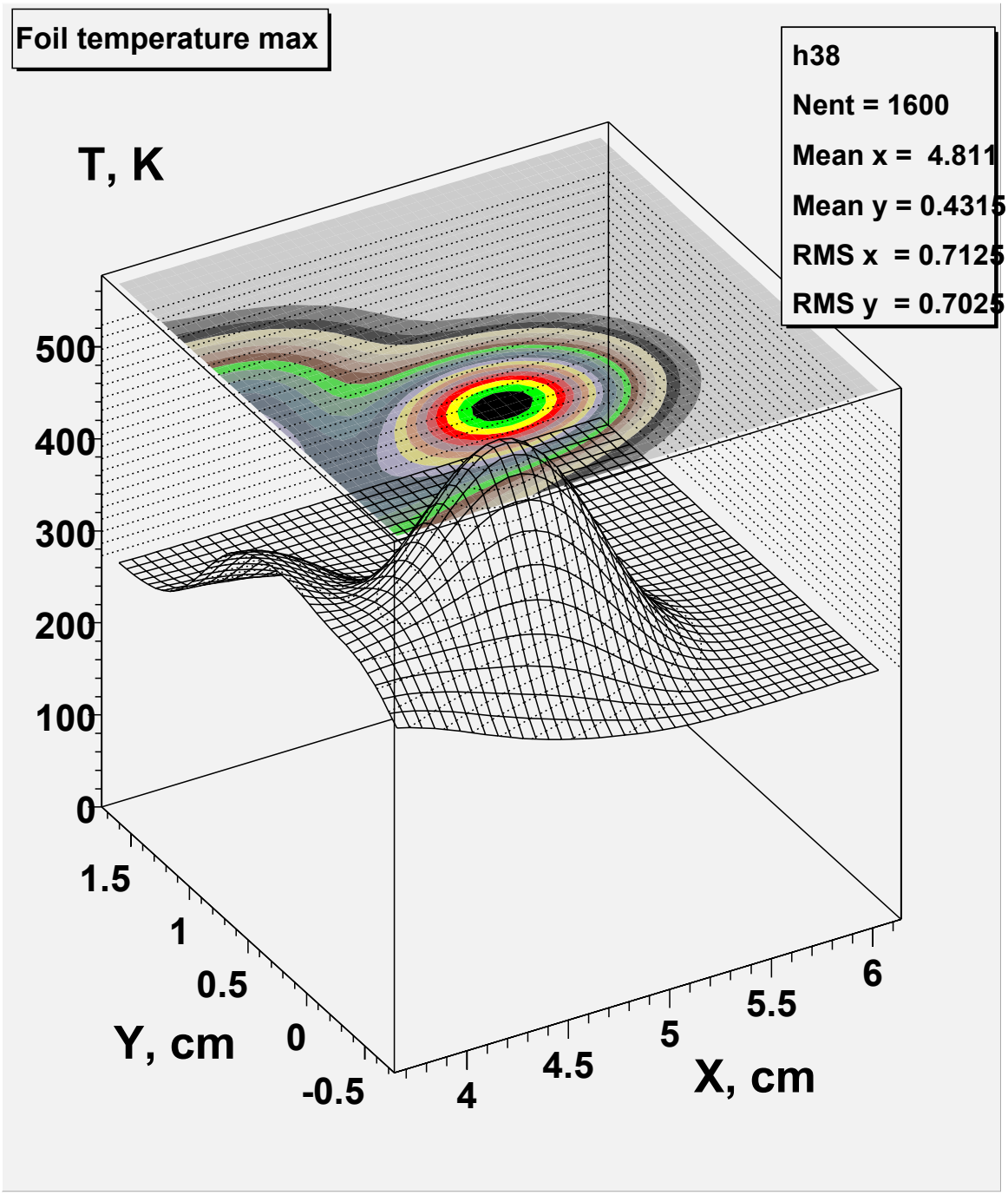

Figure 11.11. Steady state maximum temperature distribution in the stripping foil at painting injection to the proton driver.

The only way to solve such an equation is numerically, using a code such as ANSYS [7]. Because we estimate the heating and cooling of the foil using only emission, then our calculation should be viewed as conservative. We put a full ANSYS calculations on hold for the time being.

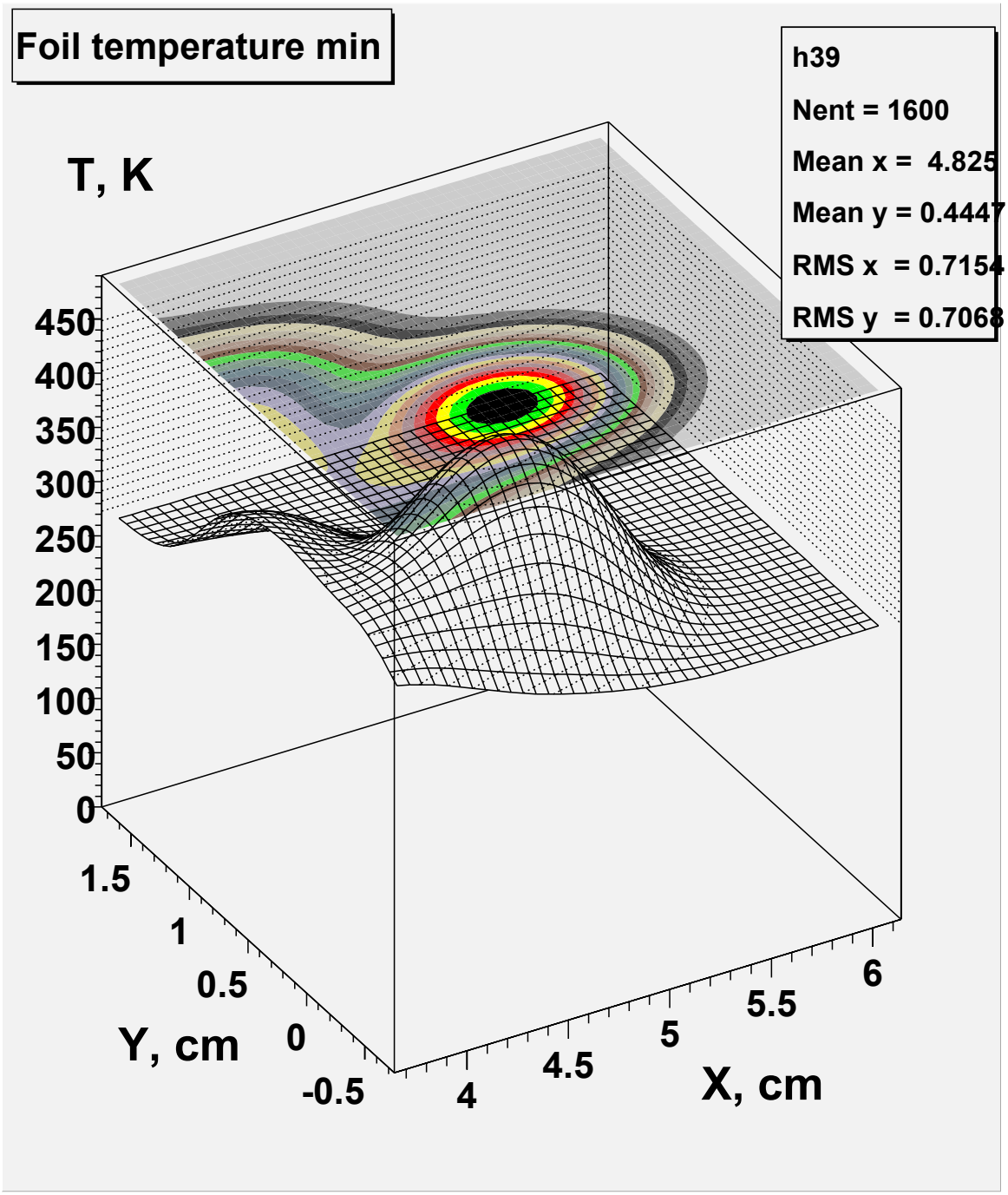

Figure 11.12. Steady state minimum temperature distribution in the stripping foil at painting injection to the proton driver.

11.3.3. Stripping Efficienc , Yield of Excited States $H^o(n)$ Atoms and Beam Dump

Most of injected H^- are stripped to protons in the foil and the rest into excited state of $H^o(n)$ atoms, where n is the principal quantum number of the excited state. Some excited states are f eld-stripped into protons on the way to the H^o dump. Those particles become a beam

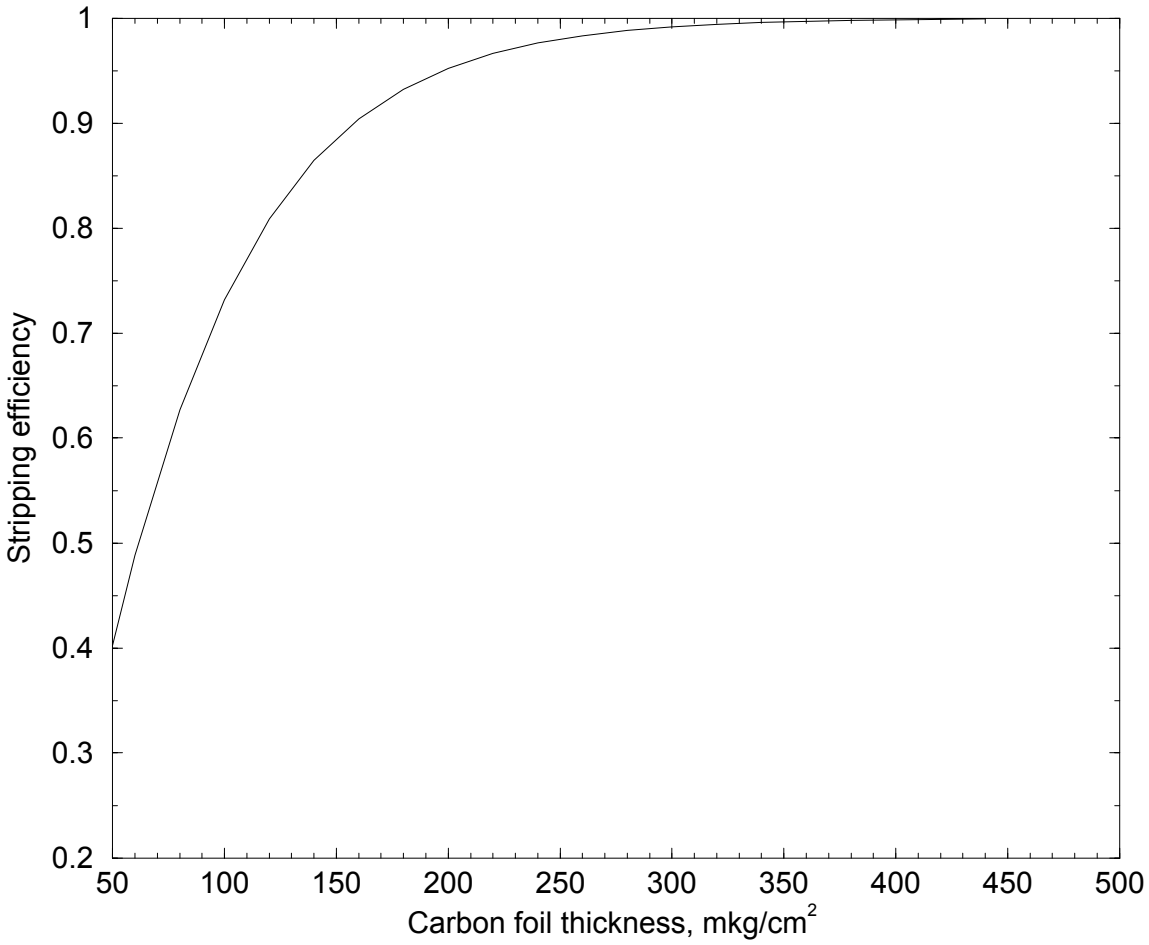

Figure 11.13. Carbon foil stripping eff ciency.

halo, and are lost somewhere else in the ring or are intercepted by the collimation system. Def ning σ_{if} as the cross-section for the process $H^i \rightarrow H^f + (f-i)e^-$ we can write the stripping eff ciency (Fig. 11.3):

$$N_+ = 1 - \frac{\sigma_{-10}\exp\{-\sigma_{01}x\} - (\sigma_{01}-\sigma_{-11})\exp\{-(\sigma_{-10}+\sigma_{-11})x\}}{\sigma_{-10}+\sigma_{-11}-\sigma_{01}}$$

The number of $H^o(n)$ atoms in a highly excited state ($n \geq n_{ex}$), assuming the yield of excited state is proportional to n^{-3}, can be written:

$$Y(n \geq n_{ex}) = (1-N_+)\cdot\frac{\sum_{n=n_{ex}}^{\infty} n^{-3}}{\sum_{n=1}^{\infty} n^{-3}} = (1-N_+)\cdot\frac{\psi'(n_{ex})}{\psi'(1)}$$

We can estimate the foil stripping eff ciency, the proton hit distribution and foil temperature after 400 MeV proton beam injection into the machine during 27 turns followed by beam removal from the foil during 6 turns.

The calculations are done with the following assumptions:

1. Electrons are stripped immediately and then pass through the foil independently;

2. Nuclear interactions in the foil are negligible; therefore the main energy deposition sources for a very thin foil are proton restricted ionization energy loss $-\frac{dE_p}{dz}\cdot\frac{\Delta z}{<\cos\theta_p>}\simeq -\frac{dE_p}{dz}\cdot\Delta z$ and electron energy loss during the stripping phase $-2\frac{dE_e}{dz}\cdot\frac{\Delta z}{<\cos\theta_e>}$. Here Δz is foil thickness and $<\cos\theta_p>\simeq 1$ and $<\cos\theta_e>$ are proton and electron angles at stripping.
3. At the kinetic energy of ≈ 218 keV for electrons accompanying this process, the range and $-\frac{dE_e}{dx}$ according to the ICRU37 are $580\cdot 10^2\frac{\mu g}{cm^2}$ and $2.4\frac{MeV\cdot cm^2}{g}$ respectively. Therefore we assume the electron contribution to the heating is approximately equal to -$2\frac{dE_e}{dx}\Delta s_e$.

For carbon foil parameters:

- density $\rho = 2.0\frac{g}{cm^3}$
- thickness $\Delta z = 300\frac{\mu g}{cm^2}$
- specif c heat $c_p = 0.165\frac{cal}{g\cdot K}$
- thermal conductivity $\kappa = 0.057\frac{cal}{cm\cdot K\cdot sec}$
- emissivity $\varepsilon = 0.80$,

The calculated stripping eff ciency is 99.2% and the estimated yield of excited states $H^o(n)$ atoms with $n \geq 5$ is equal to 0.016%. These atoms will be stripped into protons before they reach the dump and become a beam halo. The remaining excited atoms ($n \leq 4$) have a longer lifetime and they will go to the neutral beam dump.

The average number of proton hits on the foil (1.98) found from simulations is very close to that was calculated analytically (1.95).

The proton hit distribution calculated from the above formulas (Fig. 11.9) was used for foil temperature buildup and steady state temperature calculations.

Due to fairly large size of H^- beam at the foil, the small number of collisions and the small electron contribution, the temperature buildup in the foil per pulse is less than 100K (Fig. 11.10).

The heat emission cooling of the foil due to the Stefan-Boltzmann law

$$Q = \varepsilon\cdot\sigma_{SB}\cdot T^4$$

at this temperature is small. With only emission as a cooling mechanism the foil temperature reaches a steady state after about 10 pulses with maximum temperature of 540 K (Fig. 11.11) and minimum around 450 K (Fig. 11.12).

11.4. Septum and Kicker Magnets Parameters

Septum and kicker magnets parameters are presented in Table 11.2. The septum is curved to reduce the poletip width.

11.5. Stripping Foil Design

Table 11.2. Septum and kicker magnets parameters.

Element	Field	Current	Inductance	Length	Poletip width	Poletip gap	Turns number
Name	Gauss	Amps	μH	m	mm	mm	
septum-magnet	3180	11268	2.99	2	45	45	1
kicker-1	128	176.3	47.87	0.5	180	180	8
kicker-2	212	292.0	47.87	0.5	180	180	8
kicker-3	96	132.2	47.87	0.5	180	180	8
kicker-4	157	216.2	47.87	0.5	180	180	8

Carbon stripping foils of 300 $\mu g/cm^2$ have been in use in the Booster since the 400 MeV Linac upgrade. Foils of densities between 300 and 600 $\mu g/cm^2$ have been used. No foils have ever been lost because of beam damage. It should be pointed out however that the number of turns that the Booster uses is nominally 10 per beam cycle and the Proton Driver will use up to 27 per beam cycle. The Booster also typically operates at a reduced duty factor, something less than 1 Hz, whereas the Proton Driver will operate at 15 Hz continuously. The Booster operational repetition rate will change in the future with the Boone and NuMI experiments to as high as 10 Hz. It is possible that foil damage may become a factor and will have to be dealt with.

There are two basic concerns with the Proton Driver foils, heat dissipation and type of mount.

The stripping foil will reach temperatures of 540 K (513 F). This temperature may be of concern in the mounting of the foil. The Fermilab Booster foils are simply bonded to a thin copper support with super glue. There has never been any problem with this kind of mounting. However the Booster has never run beam at 15 Hz for sustained periods, so average temperature rise has never been a problem. If the foil actually reaches sustained temperatures this high, another mounting technique may have to be used. Keep in mind that even though the foil may get very hot at the beam location, the foil is exceeding is thin and the amount of heat that will be transmitted to the foil holder will be small. The metal holder will be capable of dissipating a large amount of heat relative to the foil so a simple glue bond may suff ce. This is not considered a serious matter however; there are many ways of mounting the foil.

The foil will have two free edges. See Fig. 11.2 for the foil dimensions. This is also of some concern. Carbon foils this thin have a tendency to curl up. If this proves to be the case then the foil may have to be mounted with only 1 free edge such as is done in the Booster. However this means the foil will be approximately twice as long. This is not a desirable thing to do since there would be more interactions of the circulating beam with the foil. On the other hand, if necessary, it can be done.

It is planned to test mount foils and try them out in the Booster. The Booster is an ideal test for any foil mounting technique. Changing foils in the Booster is not hard; typically the foils can be changed in about 4 hours with most of the time being for vacuum pump down. The only criterion is that the foil mount itself cannot be thick. The clearances on the

Booster foil changer are on the order of +/- 3 mm. Testing foils in the Booster allows not only various mounting techniques to be tried but measurements of foil temperature rise with beam could also be done.

11.6. Conclusions

A painting injection system, consisting of two sets of horizontal and vertical kicker magnets, produces the quasi-uniform density distribution of the circulating beam required for the beam space charge effect reduction and emittance preservation at injection.

The calculated stripping eff ciency is 99.2%, and the estimated yield of excited $H^o(n)$ atoms with $n \geq 5$ is 0.016%. These atoms contribute protons to the beam halo.

The temperature buildup during the injection pulse and steady state temperature of the foil are calculated from an analytical distribution of proton hits using ANSYS code. An instant temperature buildup, calculated with contributions of multiple collisions, ionization loss from protons and electrons accompanying the stripping process, is a little bit less than 100 K.

With only emission as a cooling mechanism the foil temperature reaches a steady state of $\sim$ 540 K after about 10 cycles of injection, that is, less than 1 second.

References

[1] A. Drozhdin, C Johnstone and N. Mokhov,'16 GeV Proton Driver Beam Collimation System', ICFA Mini-Workshop on High-Intensity, High-Brightness Hadron Beams "Beam Halo and Scraping", Lake Como, Wisconsin, September 1999.

[2] A. Drozhdin, O. Krivosheev, N. Mokhov, "Beam Loss, Collimation and Shielding at the Fermilab Proton Driver", Fermilab–FN–693 (2000).

[3] D. Ritson, 16 GeV Proton Driver Lattice, Private communications, December 1999.

[4] I. Baishev, A. Drozhdin, and N. Mokhov, 'STRUCT Program User's Reference Manual', SSCL–MAN–0034 (1994), http://www-ap.fnal.gov/∼drozhdin/

[5] 'JHF Accelerator Design Study Report', KEK Report 97-16, JHF-97-10, March 1998, p3-67 - 3-71..

[6] Particle Data Group, 1998.

[7] ANSYS v5.5 Manual, 1994.

Chapter 12. Extraction and Abort

Alexandr Drozhdin, Carol J. Johnstone, Jim Lackey and Shoroku Ohnuma

12.1. Introduction

This chapter outlines the 16 GeV extraction system. The extraction system is described in Section 12.2 and the required "notcher" in Section 12.3. In Section 12.4 are discussed the various issues related to an abort system.

The extraction system is designed to extract 100% of the beam in one turn. Design of a "slow" extraction system is not part of this study.

Although the design beam normalized emittance is 60 π mm-mrad, apertures of the extraction system elements are designed to maintain clearance for a maximum beam normalized emittance of 120 π mm-mrad at 400 MeV and at 16 GeV. An aperture this large at injection time insures that the collimation system will intercept circulating beam losses and prevent the various extraction elements from becoming radioactive. At 16 GeV an extraction channel aperture as large as reasonably possible is highly desirable since it reduces alignment tolerances and allows the extraction channel to accommodate to some amount of halo on the beam.

The layout of the extraction system in straight section P60 is shown in Figure 12.1.

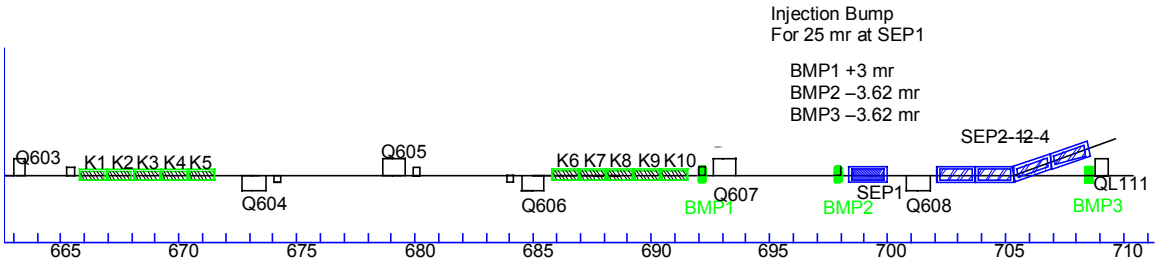

Figure 12.1. Proton Driver Extraction System Layout

12.2. Extraction system

12.2.1. Kickers

In the present lattice design the lattice functions at the kicker locations are not optimal for extraction. The net result is that the number of kicker magnets is larger than the number that a lattice optimized for extraction would require. The apertures of the kickers assume

the use of a ceramic beam tube with wall thickness ~5 mm. The kickers will be capacitively loaded ferrite transmission line magnets with a nominal impedance of 12.5 ohms. A current rise time of 125 ns is assumed, giving an effective fill time of ~168 ns.

There are two sets of kickers. The phase advance of the first set is ~240 degrees from Septum 1 and the second set is ~60 degrees. With these phase advances the first set of kickers has to give a negative kick to the beam so that 180 degrees later the kick angle becomes positive and adds to the positive kick of the second set. The horizontal beta function over the length of the kickers varies from near maximum to near minimum so the effective beta is the average for that location. The horizontal beta function at the location of Septum 1 is also quite small. Since kick amplitude at the septum x_2 is given by:

$$x_2 := \sqrt{\beta_1 \cdot \beta_2} \cdot \sin(\psi_{12}) \cdot x'_1$$

the effects of small betas and a 60-degree phase advance necessitate a larger number of kickers. There would be some gain in effective kicker strength if one changed the gap of the individual kicker magnets as the beta function changed, but that was not done in this design.

12.2.2. Septa

The design of the extraction system requires two septum magnets. The first septum (Septum 1) will of necessity be a "thin" septum design. Septum 1 will be a single turn pulsed magnet. The design assumes a maximum 10-mm septum thickness, believed to be sufficient to provide the required mechanical strength, cooling, and magnetic field shielding for the circulating beam. The design gap height is 30 mm and poletip width is 40 mm.

The gap height of 30 mm (1.181") is similar to the existing Booster extraction septum, and the 1.1 Tesla field is also about the same. A 1.5 meter, 15 Hertz extraction septum magnet with a 3-mm septum and nominal field of 1.0 Tesla for the Booster is under construction. It is expected that testing of the design will begin early in 2001. This new magnet is essentially the Septum 1 design. Figure 12.2 shows a cross section of this magnet.

The amplitude of the kicked beam at the upstream end of Septum 1 is given by $W_b + S_t + x_b$. W_b is the beam width, S_t the Septum thickness and x_b the injection bump. With $W_b = 20.28$ mm, $S_t = 10$ mm and $x_b = 1.5$ mm, $W_b + S_t + x_b = 31.78$ mm.

The extracted beam position at the upstream end of the second septum (Septum 2) is +165 mm (~6.5") outside the circulating beam orbit. This gives sufficient room to consider the use of a dc septum magnet or at least a multi-turn pulsed magnet. In this design it is assumed that Septum 2 will be 4 individual magnets. The gap height of the Septum 2 magnets is 30 mm and the poletip width is 75 mm.

The horizontal beam size at the downstream end of Quad Q608 is at ~137 mm (5.4") so a special vacuum pipe interface between Q608 and Septum 2 will be required.

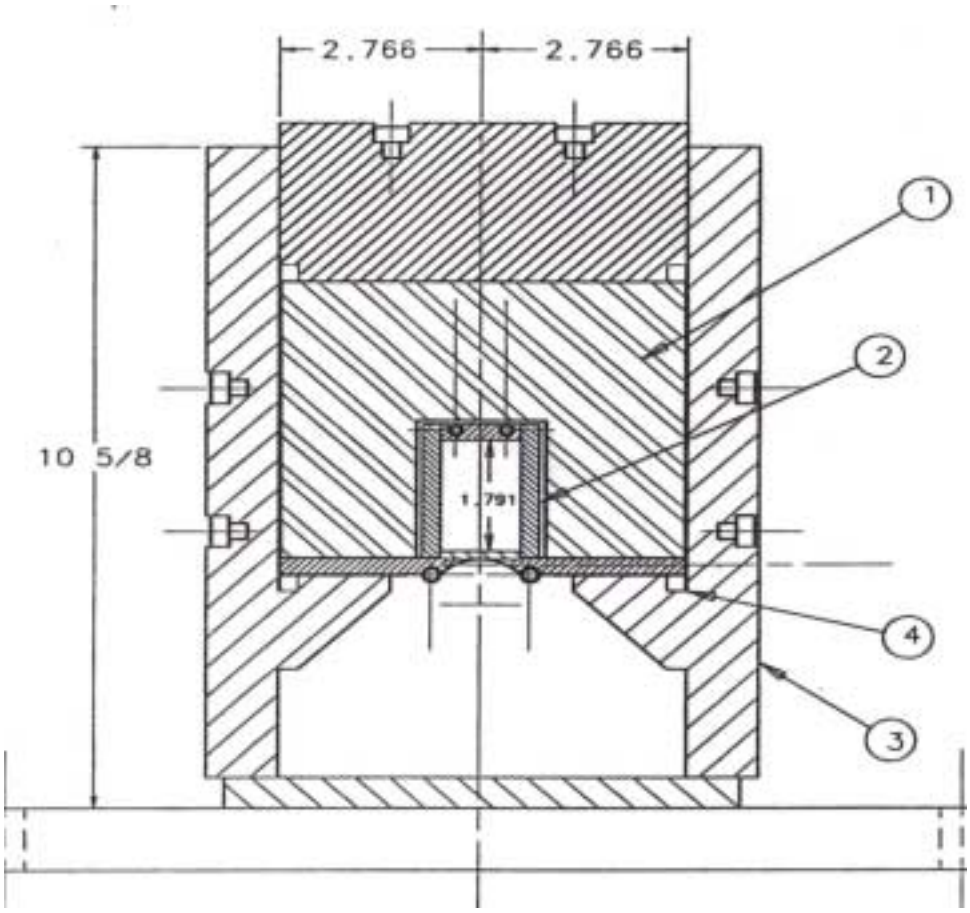

Figure 12.2. Booster Septum Cross Section

12.2.3. Local bump system (Injection Bump)

The extraction system design places the septum of Septum 1 at 10.14 mm outside the circulating beam. This placement minimizes the required extraction kicker strength. In order to maintain the nominal 120 π mm-mrad design aperture at injection, a local bump with an amplitude of ~23 mm at the upstream end of Septum 1 is required. The magnet strength required to accomplish this bump is not large, and it is expected that standard horizontal trim magnets will suffice. The first of these magnets is just upstream of Q607. The second and third magnets are installed just upstream of Septum 1 and QHL111 respectively. Table 12.1 lists the magnet parameters. Bump1, 2, and 3 are standard trim magnets and are dc powered; ramping is not required.

The amplitude of the bump at extraction is reduced by $1/(\beta\gamma)$ to about 1.5 mm. This residual bump amplitude adds to the effective thickness of Septum 1 and must be compensated for with the extraction kickers. Without this local bump, the septum would

have to be placed at the 120 π mm-mrad aperture, and the kickers would have to kick ~96 mm instead of 31 mm.

Table 12.1. Magnet Parameters

Name	Number	Field (kG)	Inductance (μH)	Length (m)	Current
Kickers	10	0.225	1.419	1.0	2.45 kA
Septum 1	1	10.93	2.77	1.65	32.47 kA
Septum 2	4	13.049	$2.33 \times N^2$	1.35	40.23 kA-turns
Bump 1	1	+0.320		0.3	
Bump 2	1	–0.383		0.3	
Bump 3	1	–0.383		0.3	

12.3. Notcher system

Because the extraction kicker magnet fill time is 168 ns, a notch (gap) in the beam will be needed to prevent high losses on Septum 1. This is accomplished operationally by kicking out a few beam bunches at low energy. In the Fermilab Booster such a system has been operational for some time. The notch in the Booster is created using a very short (60 ns), 28 kV pulse through a standard extraction kicker magnet. This dumps the 400 MeV beam into the gradient magnets just downstream of the kicker but causes high local losses.

A different method of notch creation has been tried in the Booster and appears to work very well. The technique is to use a very weak kicker, repetitively pulsed to excite the beam (in the notch) at its tune frequency until all of the beam in the notch has been scraped out of the machine. In the case of the Booster, the kicker is pulsed about 85 times every 4^{th} turn since the horizontal tune is near the quarter integer. The pulse modulator is operated at 3 kV. Since the fractional part of the tune in both planes of the Proton Driver is near 0.4 the kicker would be pulsed every 5^{th} turn. The beam could be kicked in either plane. The idea is to cause the beam amplitude to blow up relatively slowly and allow the collimation system to absorb the excited beam. This technique is being studied in the Booster and is not yet operational. A major advantage of this system is that all the system components with the exception of the magnet are commercially available and are much cheaper than conventional high voltage thyratron devices.

Methods for notch creation external to the Proton Driver are also under study. Clearly, the preferred method would be that the notched beam be dumped external to the Proton Driver. However, even if a notch is created externally, a notcher internal to the Proton Driver is still required. The beam in a notch created externally is subject to debunching (the notch refills partially) during the adiabatic capture process and the internal notcher would be needed to "clean up" the notch.

Another example of cogging is where the Proton Driver is used in the multi-batch mode to fill the Main Injector. In this scenario a notch "cogging" scheme is needed in order to synchronize the notch in each successive batch with the extraction kickers and at the same time place the beam azimuthally correctly onto the Main Injector circumference. This cogging technique is similar to the cogging techniques used in the Main Injector and Tevatron to insure that the proton and anti-proton bunches collide at the proper place in the Tevatron, i.e., at the detectors. If a notch is created externally to the Proton Driver then the notch could potentially have to be cogged as much as half the machine circumference. This is possible, but the radial position excursions of the horizontal orbit would be large and would certainly be detrimental to the effectiveness of the collimation system. A more practical scheme is to wait until the beam is in the machine and then determine where on the circumference to create the notch to minimize the amount of cogging required. Such a system has been tested on the Booster but is not operational.

12.3.1. Fast kicker

The kicker magnet for the notcher system can be very weak compared to the extraction kickers, and will have a fill time considerably shorter than that of the extraction kickers. This scheme is still under study, and a design is not complete.

12.3.2. Beam dump

If the beam is absorbed by the collimation system, a special beam dump will not be required.

12.4. Abort system

It is not certain that an abort system is required or possible. The ideal abort system cleanly extracts the beam from the machine at all energies and transports it to an external beam dump. Such a system would be very difficult and prohibitively expensive to build. The reason is that all the magnets (kickers and septa) would have to track the machine energy. The apertures of the septa would have to be large enough to accommodate at least the 60 π mm-mrad injected beam. Assuming there are loss mechanisms, the beam likely will have a halo or emittance larger than 60 π mm-mrad, which would increase the required apertures even more. Further and most importantly, there really is no place in the lattice to install such a system. Therefore the abort system would have to be the operational extraction system.

Even a system that aborts the beam internally in the machine is potentially very hard to design. The reason is that different loss mechanisms have different growth rates. Detecting the different loss events in time to do something about them can be very difficult. For example, in the Booster, if the rf systems trip at ~1 GeV (this does happen and is easy to detect), the beam falls out in about 10 μs. This would be equivalent to about 3 revolutions in the Proton Driver. Reacting fast enough to properly dump the beam is questionable at best. Only some kind of fast kicker system could react fast

enough to dump the beam in such an event. If such an event occurred in the Proton Driver without an abort system, the beam would simply spiral inward and one would expect that it would mostly be intercepted by the collimation system. The case of a high energy fast loss is of interest because it could be very hard on the collimation system. How well the collimation system works with the various fast loss scenarios needs further study.

There will be further study on an abort system that can safely dump the beam for at least some of the many beam loss scenarios.

12.4.1. Pulsed bumps

If one were to attempt to build an abort system, it likely would be built around a set of relatively fast pulsed magnets. These magnets would be arranged to form a local bump centered on a beam absorber/dump. The amplitude of the pulse would not be modulated with energy; rather it would be fixed and the pulse width would be tailored so that the pulse rise time is fitted to the loss times of the various beam loss mechanisms. At low energy the beam would hit the dump very quickly since it is being bumped at the highest rate of rise of the pulse. At high energy the beam would not hit the dump until the pulse reached full amplitude. For an rf loss mechanism such as described above this scheme would work well, but if some sort of high energy fast loss (fast with respect to the pulse rise time) occurred this system would not work.

12.4.2. Abort Beam dump

The design of such a beam dump has not been undertaken. More study is required.

Chapter 13. H^- Source and Linac Improvements

L. Allen, W. Chou, V. Dudnikov, M. Ferguson, E. McCrory, A. Moretti, M. Popovic, Z. Qian, C. Schmidt, M. Shea, D. Sun, R. Tomlin, R. Webber and D. Young

13.1. Introduction

The present Linac configuration consists of two 750-keV Cockcroft-Walton preaccelerators connected to a Drift-Tube Linac (DTL) through a Low Energy Beam Transport (LEBT) system. The LEBT contains an rf buncher that enables about 70 percent of the dc beam pulse to be captured in the rf bucket of the Linac. The Drift-Tube Linac accelerates the beam to 116 MeV where it is transferred through a transition section into a Side-Coupled Linac (SCL). The SCL accelerates the beam to 400 MeV.

The Fermilab Linac achieved its first 200-MeV proton beam in 1970. Shortly thereafter it ran consistently at a 15-Hz repetition rate providing 100 mA of beam current at the optimum pulse length required for injection into the Booster. In 1976 the Linac began supplying protons for the Neutron Therapy Facility, and the beam pulse length was increased to about 60 μs.

In 1978 the Linac was converted to H^- operation with an additional Cockcroft-Walton preaccelerator to provide redundancy when H^- ion-source changes became necessary. Stripper-injection into the Booster Accelerator resulted in improved injection efficiency and permitted the beam pulse length to be adjusted to achieve maximum injected intensity. The reduced beam intensity in the Linac resulted in a higher quality beam and less beam loss along the Linac.

To reduce the beam emittance degradation in the Booster due to tune spread caused by space charge and small errors in the magnetic guide field, it was decided to increase the energy of the Linac. After the replacement of the last four Linac drift-tube tanks with more efficient side-coupled cavities operating at a higher gradient, the energy of the Linac was increased to 400 MeV. In 1993, 400-MeV beam was achieved. Presently the Linac produces an output intensity of about 47 mA with a 30 μs pulse length resulting in an intensity of 8.5×10^{12} protons per pulse. To achieve the required 3×10^{13} protons per pulse desired in the Proton Driver, beam current and pulse length must be increased.

In 1999 an experiment was performed to determine the high current capability of the side-coupled Linac structure that accelerates the beam from 116 to 400 MeV. [1] The ion-source, preaccelerator and drift-tube Linac sections were restored to the proton mode of acceleration. It was determined that a beam of 86 mA at a pulse length of 90 μs could be accelerated to 400 MeV thereby confirming the capability of the side-coupled structure to accelerate beams of the required magnitude. However, at the highest beam intensities difficulties arose with increased beam loss. An improvement in the beam quality at the highest intensities would be necessary to minimize the beam loss and the induced radioactivity in the accelerator components.

Table 13.1 shows a consistent set of measurements of the beam emittance as a function of energy along the Linac at a beam intensity of 30 mA. (At the nominal 47 mA intensity the emittances would be somewhat larger.) The data show that considerable emittance growth occurs below 10 MeV. This dilution has been studied and it is generally due to: i) non-linear space charge forces in the beam in the LEBT, ii) coupling of the betatron and longitudinal motion, iii) phase space mismatch to the input of Tank 1, and iv) quadrupole misalignments in Tank 1. Considerable effort has been expended in the last thirty years in the accelerator field in understanding the problems of emittance dilution and in producing H^- beams of higher brightness. It is proposed to improve the system below 10 MeV by rebuilding this section, taking full advantage of the latest technology.

Table 13.1. Emittance for H^- Beams

	Preacc Out	Linac In	Tank1 Out	Linac Out
Energy (MeV)	0.75	0.75	10	400
Intensity (mA)	54	49	33	30
Emittance / π (mm-mrad, 95%, norm.)	1.3	2.6	5.2	7.8

It is expected that by improving the Linac front end to achieve a brighter beam of greater intensity and smaller emittance, it will be possible to retune the rest of the Linac above 10 MeV to transmit the beam without increasing beam loss along the Linac. This improvement will have little impact on the passive shielding of the Linac. In fact, since the areas adjacent to the Linac enclosure are protected by interlocked detectors, increasing intensity even at a continuous 15 Hz rate would not present problems with regards to prompt radiation fields outside of the Linac enclosure. Thus it is expected that the Linac can deliver the requested intensity without increasing beam loss that would compromise the shielding or the maintenance of components in the Linac.

The possibility of increasing the Linac pulse length or the Linac repetition rate to achieve the desired intensity in the Proton Driver has been considered. The beam pulse length is primarily limited in the Side Coupled Linac to 90 μs by the cooling in the accelerating cavities and by increased sparking at longer pulse lengths. A redesign of the accelerating cavities and the klystron rf systems would be required to overcome this limit. To increase the repetition rate above 15 Hz would require the entire Linac to be rebuilt.

13.2. General Description of Linac Low Energy Improvements

It is proposed that the entire low energy end of the Linac be replaced incorporating the latest technology and new possibilities. This redesigned low energy section is based on two RFQ's [2] and a new Tank 1. With a new H^- source a more intense brighter beam is

possible, reducing losses and producing a better beam for the Booster. The proposed system is shown in the isometric sketch in Figure 13.1.

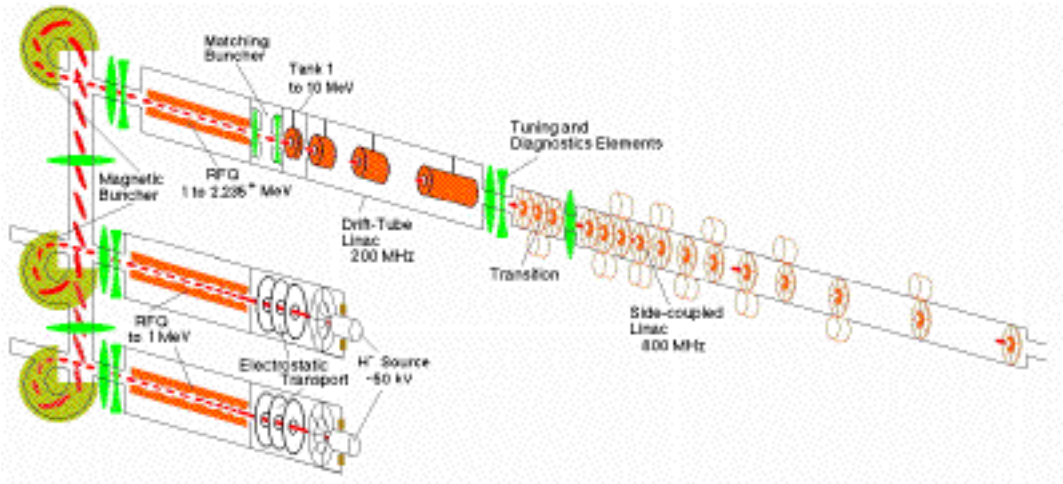

Figure 13.1. Sketch of the proposed low-energy improvements

13.2.1. Ion Source

Replacing the Cockcroft-Walton with an RFQ opens the possibility of improving the present H^- Magnetron ion source or considering other H^- sources to achieve the desired beam intensity and quality. Development of negative ion sources for accelerators has been reviewed by Peters [3-5] and in the book by Zhang.[6] First versions of the Surface-Plasma Sources (SPS) developed for charge-exchange injection of protons have operated at an intensity of approximately 50 mA in pulses of 0.05 - 1 ms with a repetition rate up to 50 Hz. H^- beam parameters of these SPS sources have been sufficient for normal operation of high-energy accelerator systems for the last twenty-five years without significant modernization of the ion sources. For the Proton Driver Project an increase in beam intensity and brightness is required. It is completely feasible to upgrade the SPS source for the required intensity, duty factor and beam quality without sacrificing the reliability and availability from its proven past performance.

The Fermilab Magnetron SPS has been operated since 1978. It produces a peak current of H^- ions, as measured at 750 keV, of 65 mA with an extraction voltage of 20 kV at a pulse length of 0.075 ms. 70 mA is possible at an extraction voltage of 25 kV. The emittance (brightness) of the source can be improved by optimizing the discharge geometry, gas injection extractor and plasma overneutralization. It is deemed possible to achieve a current of 85 mA of H^- beam with a reduction of the emittance by a factor of two, to 0.5 π mm-mrad (90%, norm.).

To significantly improve the brightness it is necessary to eliminate discharge noise. Development of noiseless Semi-Planotron sources and their adoption for injection into the RFQ will permit a beam of up to 110 mA of H^- with an emittance of 0.7 π mm-mrad (90%, norm.). For producing a beam of the highest brightness it is possible to use a

Surface-Plasma source with a Penning discharge, also known as the Dudnikov-type source. Fig. 13.2 demonstrates the production of a noiseless discharge by the small addition of N_2. A transition from a noiseless discharge to a noisy mode of operation decreased the brightness by 10 times or more.

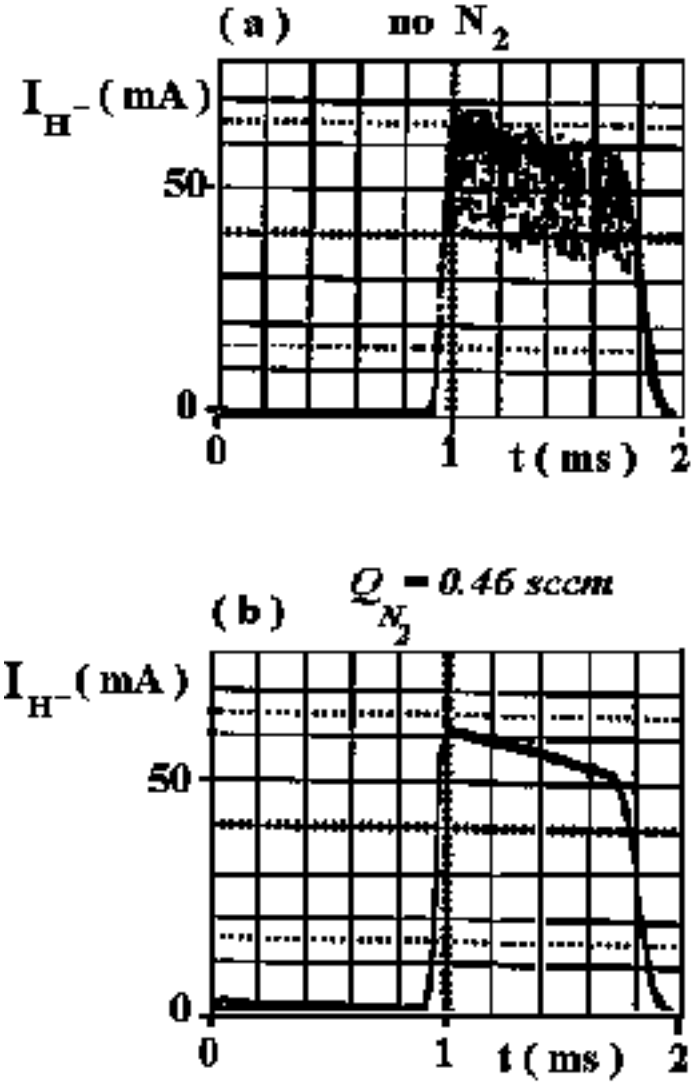

Figure 13.2. Production of noiseless discharge by a small admixture of nitrogen

The DESY rf type volume source is a possible alternative. It uses an rf coil outside a ceramic plasma chamber. Because of size it is not reasonable to fit this or many other types of H^- sources into the present pre-accelerator. The DESY ion source is reputed to have higher brightness, higher reliability and easier maintenance. A source of this type was run without cesium for 2800 hrs producing 40 mA with a duty factor of 0.05% and a pulse length of 100 μsec without any observed degradation in performance. A small injection of cesium and adjustment in the extraction system could well give the desired intensity of 115 mA. A 50 keV extraction voltage from the ion source is proposed for extracting sufficient current from the source and allowing for a short electrostatic

focusing structure. This closely couples the source to the following RFQ. The increased energy of the H^- ions allows easier injection and greater transmission through the RFQ.

13.2.2. Radio-Frequency Quadrupole Accelerator (RFQ) and Medium Energy Beam Transport (MEBT)

A 201-MHz RFQ with an energy from 50 keV to 2.23 MeV could be proposed for the Linac pre-accelerator. However, there are good reasons to consider dividing the RFQ into two sections. Until recently dividing an RFQ into a number of sections was considered unreasonable due to the difficulty of matching the beam between the sections. In the PET Project [7] the difficulty was overcome by using a magnetic five-dimensional phase-space imaging system. In this system all particles take the same time to pass through the transport line, independent of energy or transverse size and angle, so the transverse and longitudinal motions are uncoupled at the entrance to the second RFQ section. It is proposed to use a similar system. This will be referred to as the double alpha system or the medium energy transport system (MEBT). An R&D program is proposed to insure the calculated performance of this system can be achieved.

13.2.3. RFQ-2

It is proposed to separate the RFQ so that the first section will have an input energy of 50 keV and an output energy of 1 MeV. This RFQ will be followed by the double alpha transport line consisting of two 270^o bending magnets and five quadrupoles. The isochronous line will transport the beam to a second RFQ. The second RFQ will accelerate the beam from 1 MeV to 2.235 MeV or higher. The question of the output energy of the first RFQ will be studied in greater detail as system design progresses.

Although the question of dividing the RFQ into two sections rather than a full length RFQ will be studied in more detail as design studies are undertaken, some of the virtues of a split RFQ are the following:

i) It is highly desirable to have a second ion source for standby operation. This is even more urgent when high intensity beams from a cesiated ion source are required. The second source could be a replica of the first source. It would include a second low energy RFQ section and the first part of an isochronous line to feed into the second part of the isochronous system with the addition of 4 quadrupoles and one additional 270^o bending magnet. (See Fig. 13.1).

ii) A single section RFQ operating at 201 MHz is long. This exacerbates the difficulty of achieving the required tolerances and results in a small separation of the dipole modes without the addition of coupling devices. Detailed design studies are required to assess the extra complication resulting from the extra length. The extra complication results in an increased cost for the structure.

iii) The double alpha system allows beam diagnostic and beam chopping devices to be added at an intermediate energy.

iv) The double alpha system can be tuned to accommodate different beam intensities.

v) The first short section of the RFQ can be readily replaced if contamination (cesium) or sparking cause difficulties or require vane replacement.

vi) A long RFQ requires a larger rf system to excite the structure. There is an advantage in designing a shorter length that can be powered by the same size rf system that is currently being used in the other Linac systems.

13.2.4. Matching Section

The beam from the RFQ must be matched to the DTL acceptance for the design current in all three planes. There are at least two ways to match the beam to the DTL. The first consists of three quadrupoles and one rf gap or buncher. The virtue of this arrangement is that the elements are tunable which is desirable to accommodate a range of beam intensities. It also allows space for the insertion of beam diagnostic equipment. A second method requires four more RFQ cells at the end of the RFQ and a half-length quadrupole in the DTL. It may be desirable to use a combination of these two methods.

13.2.5. Chopper

Separating the sections of the RFQ with the double alpha MEBT allows the insertion of a chopper in the system. The electrostatic Einzel lens following the source extraction gap can be segmented and excited with a pulsed voltage to deflect a portion of the beam pulse from the acceptance of the first RFQ. However, further chopping of the beam pulse will be required to: a) create a 7-bucket notch at the injection revolution frequency (300 kHz) for reducing beam loss at extraction, b) for antiproton production to create a 42-bucket gap at the injection revolution frequency in order to fit the bunch train to the circumference of the Accumulator (both for Stage 1 at $h = 126$), and c) reduce injection losses in the Booster by chopping 30% of the Linac beam at the injection rf frequency (5.4 MHz) for rf capture (Stage 2 at $h = 18$). Choppers that have been considered are:

(a) An rf cavity type using a Finemet wound core [8,9] placed close to the second RFQ section. Since the RFQ has a small energy acceptance, a $\pm 10\%$ energy error in a beam before it enters the RFQ can effectively cut the transmission efficiency down to zero. A prototype chopper with power supply has been designed and built. It is now installed in the transport line before the Linac at the HIMAC (Japan) for testing and is part of the US-Japan collaboration.

(b) Deflecting electrodes. If the last Einzel lens in the LEBT is segmented and a pulsed voltage is used to excite a pair of the segments, the beam from the source can be deflected enough to fall outside of the acceptance of the RFQ. LBL has designed and built a prototype chopper for the SNS using this technique. [10]

(c) Using strip deflecting electrodes. Deflecting electrodes excited by a traveling wave and positioned before the RFQ can be used as a chopper. This is a conventional design and is being used in the transport line before the linacs at BNL and LANL.

(d) Laser beam. Laser beam chopping of H^- beams has been demonstrated at Fermilab. [24] It works by flooding the beam with photons energetic enough to strip the first electron from the H^- ion. The neutral beam then falls out as the ion beam is guided in subsequent magnetic fields. At 1 MeV, a commercial 1064 nm Nd:Yag laser with photon energy 1.16 eV will photodissociate one electron (bonding energy 0.74 eV) from H^-.

13.2.6. The New 10-MeV Drift-Tube Tank

By raising the energy into the first tank of the Linac from 0.75 MeV to 2.235 MeV, the first 18 drift tubes which have a 2-cm bore diameter and quadrupole lengths of 1 inch and 1 1/4 inch will be eliminated. The new DTL then starts with drift tubes having a 2.5-cm bore and a quadrupole length of 1.75 inches. Thus the problem of misalignments will be significantly mitigated and the cell transit time improved to give a better acceleration rate. The capability of the structure to accelerate higher intensity and better quality beams will be enhanced.

A new Tank 1 will accelerate the beam to 10 MeV and match to the present Tank 2. This tank will be shorter than the present Tank 1 by ≥ 1.44 m and should incorporate a better drift tube alignment mechanism. It is optional whether a stabilized structure will be used because of the short length of the tank. Copper plating is common today and can probably be utilized. The old power supplies and rf system can remain in use.

13.2.7. Parameters and Performance Goals of this Configuration

Table 13.2 gives the expected goals for the low energy Linac improvements. In addition to providing a chopped beam of 3.3×10^{13} protons per pulse required for injection into the Proton Driver, the design beam emittance will be smaller by at least a factor of two. This will allow running at these higher intensities without additional beam loss.

Table 13.2. Parameters and goals for the performance of the new configuration of components for the low energy end of the Linac.

	Ion Source	LEBT/ Chopper	RFQ-1	MEBT	RFQ-2	Matching Section	DTL	CCL
Type	H^-	Electrostatic	Vane	Double Alpha 540°	Vane	3 Quads 1Buncher	Drift-Tube	Coupled-Cavity
Output Energy (MeV)	0.05	0.05	1	1	2.23	2.23	116	400
Output Current (mA)	115	115	102	102	97	93	86	86
Output Chopped Current (mA)	115	80	72	72	68	65	60	60
EMITTANCE (π mm-mrad) (95%)		1.2	2	2.3	2.6		2.8	3
FREQUENCY (MHz)			201		201		201	805
Pulse Length (μs)	90		90		90		90	90

Other virtues of this new configuration are worthy of note:

i) H^- ion sources have been built and operated that approximate the brightness required in this proposal. Replacing the Cockcroft-Walton preaccelerators with radio frequency quadrupole structures will allow these sources to be used in this new configuration. Separating the RFQ sections will allow a spare source to be quickly brought on-line to provide the same redundancy that exists in the present system.

ii) Using RFQ technology for the Linac preaccelerator will eliminate the Cockcroft-Walton systems. DC accelerators require a special technology, unlike that used in the Linac itself. The RFQ systems are similar to those used in the Linac. Thus operation and maintenance will be simplified.

iii) The cost of these low energy improvements is modest when compared to the improvement goals.

iv) The physical space required for the proposed system will be considerably less than that used in the present Cockcroft-Walton system.

v) Improvements in the quality of the beam in the Linac allow studies to be conducted in systems downstream from the Linac to ascertain possible causes for beam deterioration. Although it is hard to predict what improvements in these downstream components are possible to prevent emittance dilution and beam loss, experience has shown that the dividends can be appreciable.

13.3. Description of the Ion Source and LEBT

13.3.1. General Remarks

High-brightness, intense H^- beams can be generated in Surface-Plasma Sources (SPS) by the interaction of a plasma with a surface to transfer electrons from an electrode to reflected or desorbed atoms, thus forming negative ions. The efficiency of negative-ion formation depends very much on surface properties, mainly the work-function. To enhance negative ion formation in the SPS, elements with a low ionization energy, such as the alkaline elements, are used. Most efficient of these is cesium. Still the work-function and catalytic properties of the surface for negative-ion formation depend very much on many parameters such as surface-cesium concentration, surface temperature and admixtures of other compounds, such as oxides, halides, nitrides, etc. Small changes in the surface condition dramatically change the efficiency of negative ion formation. It is a fine art to optimize the surface and plasma condition for high efficiency of negative ion formation. This condition is a strong reason for the variation in efficiency of negative ion production under apparently similar conditions. Small changes in the surface condition can increase or decrease the intensity of a negative ion beam by large factors. It is easier to have stable operation with relatively modest beam parameters such as I ~ 30 - 40 mA, J ~ 0.5 - 1 A/cm^2, Ti ~ 5 - 10 eV. Present day experience permits better optimization for long stable production of high-brightness, high-intensity beams of negative ions (I ~ 0.1 - 0.15 A, B ~ J/Ti > 1 A/cm^2 eV, N > 10^8 - 10^9 pulses).

13.3.2. Negative Ion Source for Charge-Exchange Injection

The first versions of the Surface-Plasma Sources developed for charge-exchange injection of protons had an operating intensity of about 50 mA with pulse widths of 0.05 - 1 ms and a repetition rate up to 50 Hz. H^- beam parameters of these sources were sufficient for normal operation of large proton accelerator complexes during the past 25 years without significant modernization of the ion sources. Now, new accelerator projects need an increase of the ion-beam intensity and brightness. Some upgrading of existing SPS could achieve the necessary increase of intensity, duty factor and beam quality without degradation of reliability.

The Fermilab Magnetron SPS pulse length could be increased significantly with a new discharge pulser and adjusted parameters. It is useful for stable operation to have a

discharge power supply as a current source with a high impedance (Z = 5-10 Ohm, now Z = 1 Ohm) and a corresponding higher voltage. Optimization of the discharge electrode configuration should help increase the intensity up to 0.1 A without increasing the discharge power above acceptable levels. Gas delivery optimization should allow a longer pulse and higher intensity without an increase of the gas loading.

An optimized extraction system with a suppression electrode should improve the beam intensity, beam quality and beam space-charge neutralization with low gas pressure. A suppression of the positive ion extraction to the accelerating gap should suppress cathode and anode sputtering by accelerated positive ions, a main reason for the short ion-source lifetime. Improved cathode and anode cooling is necessary for increased discharge pulse length and intensity. The semi-Planotron version of the SPS would be better for operation at a higher duty factor.

From previous experience it is possible to have a reliable SPS with the following parameters: peak current after the extraction bending magnet of 0.12-0.15 A with a pulse duration of 1 ms, and a repetition rate of 15 Hz. A possible SPS with these parameters was tested in a relatively long run, although the adaptation of this source for extended operation in the Linac environment will need some effort. For ion source optimization and testing it will be necessary to resume operation of the ion source test stand and to upgrade the equipment. For prototyping of the equipment it will be possible to use previous developments from ANL, BINP, UMD, BNL, ISIS, and DESY.

Of interest is the rf ion source from DESY. It would be possible to test this source type using an rf proton source from NEC as a prototype. Relatively simple modifications could be made for testing this possibility.

13.3.3. Lifetime of Negative Ion Sources

1. The lifetime of ion sources with a cold electrode discharge is limited by electrode (cathode) sputtering and the formation of flakes. The flakes can create a short circuit of the discharge electrodes, close the emission aperture, or initiate a discharge instability and arcing. Deposition also changes the surface properties and efficiency of ion formation. Sputtering rates increase with energy of the bombarding ions (increase of discharge voltage), and with increase of the ion mass and charge. Different materials could have a very different sputtering rate.

2. A small admixture of cesium or other substances with a low ionization potential could be used to decrease voltage and significantly reduce the sputtering rate. These admixtures are used as catalysts of negative ion formation in the surface-plasma interaction in the Surface-Plasma Sources (SPS). In this application cesium is used as a thin (fraction of a monolayer) film on the surface to lower the work function from 4 eV to 1.6 eV. This increases the probability of secondary negative ion emission up to hundreds of times. It also decreases the number of sputtered atoms on the electrodes per emitted negative ion by many orders of magnitude.

3. Presently the SPS lifetime is limited through the sputtering of the cathode or anode due to back accelerated high-energy positive ions and flake formation from this deposit. The intensity of back accelerated positive ions could be suppressed using a 3-electrode extraction system with a suppression electrode, which reflects positive ions from the ion beam and improves the space charge neutralization. This improves the beam quality and stability of the ion source operation.

4. Optimized cesium film recycling (deposition-desorption) could be used for shielding of electrodes from the sputtering and can reduce the sputtering to a very low level. Cesium in a SPS acts as an oil in an engine increasing the operational lifetime. "Cold Start" of a discharge without cesium for a few minutes could be more destructive than many hours of low voltage operation. Emission current density of H^- up to $J \sim 1$ A/cm^2 has been observed in discharges without cesium. A fingerprint with a trace of Na or K could increase the efficiency of H^- production significantly. The power density in a discharge without cesium is very high and the sputtering rate is much higher.

13.3.4. Low Energy Beam Transport (LEBT)

An ion beam from a compact SPS has a very high current density ($J \sim 1$ - 3 A/cm$^{2)}$ and perveance. For transport of these beams it is necessary to use a deep space-charge neutralization (compensation) or very strong continuous focusing by electrostatic forces as in the RFQ.

Partial compensation of space charge with magnetic focusing and noisy operation will create a strong variation of focusing and lead to an increase of emittance by ellipse oscillation. Still, this mode of transport is used in almost all injectors, and until recently it was acceptable. Space charge compensation by ions has some differences from the compensation by electrons. Ion oscillation in the potential of the beam is more coherent and can be a reason for very strong and fast beam-ion instability. Beam-ion instabilities have been observed recently in the electron beam of the Advanced Light Source (LBL) with increased residual gas density. In low energy negative ion beams this instability was observed many years ago (1976). Development of this instability along a 15 keV H^- beam at 70 mA is shown in Fig. 13.3. Coherent oscillations of positive ions in the beam potential excite quadrupole and dipole oscillations of the H^- beam and develop a decompensation and emittance growth.

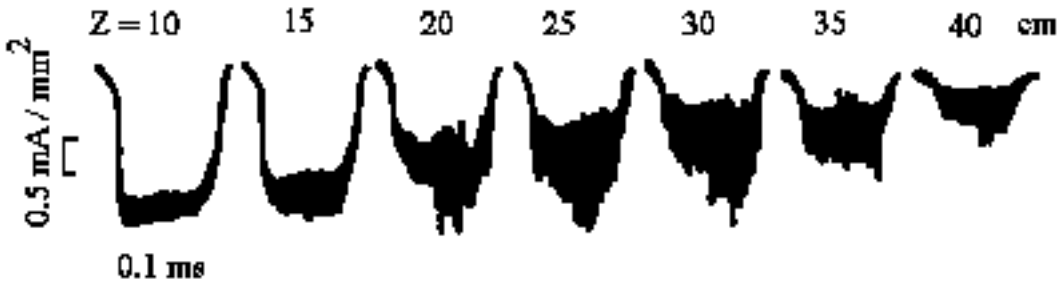

Figure 13.3. Beam current density evolution, p= 6×10^{-4} Torr

To eliminate this problem many versions of an electrostatic focusing-transport (ELEBT) have been proposed. Now under development is an ELEBT for SNS. The ELEBT developed at LBL [10] is shown in Fig. 13.4. Transport of a H^- beam of 65-keV energy with an intensity up to 42 mA has been demonstrated. Significant R&D for the development of an electrostatic LEBT operating at higher intensity is necessary.

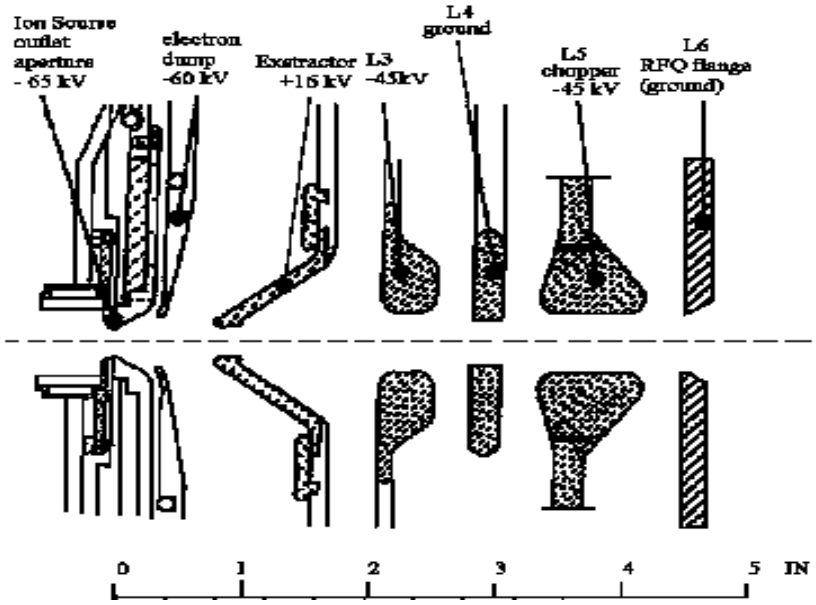

Figure 13.4. Cross section of the LEBT electrodes with ion source outlet aperture, electron dump, and RFQ endwall (LBL, for SNS)

The beam-ion instability could be damped by over-neutralization of the beam, changing the sign of the beam potential by an increase of the ion density in the beam. With increased ion and electron density, a stable beam transport could be reached with additional focusing by reversed space charge. This solution could be used for a short transport with acceptable levels of ion loss by stripping. This may be convenient because it is possible to locate a second (spare) ion source in front of one RFQ. Ion beam pulses from this ion source could be long enough for reaching a deep over-neutralization.

A good solution could be a LEBT with a fast beam over-neutralization by streams of noiseless plasma from a separate plasma source. With magnetic focusing, beams from two SPS could be steered to the entry of the RFQ. Close-coupled systems have been tested in ion implantation. Good neutralization decreases the beam emittance by approximately half.

13.4. Description of the Radio Frequency Quadrupole (RFQ) Structure

Using the design code PARMTEQ, RFQ's have been designed to accelerate a high intensity, low emittance beam to the entrance of Linac Tank 1. In the two section RFQ design, i.e. two RFQ's separated by the double alpha MEBT, the first RFQ is a "normal" design which accepts a 50 keV dc beam from the ion source, bunches it, and accelerates the beam to 1 MeV. The second RFQ accelerates the beam from 1 MeV to 2.23 MeV. The design allows a beam intensity of 115 mA to be accelerated with a transmission efficiency of better than 90%. To include the effect of possible emittance growth between the two RFQ's, the input emittance of the second RFQ is 20% larger than the emittance out of the first RFQ.

Table 13.3 shows the parameters of the first RFQ and Table 13.4 shows the parameters of the second RFQ. Note that in Table 13.4 the input emittance is 20% larger than the output emittance after the first section RFQ. Figure 13.5 shows the transmission as a function of input beam current for the first RFQ.

A one-section RFQ has been designed to transmit a 115 mA beam from 50 keV to 2.23 MeV. The transmission efficiency at this intensity is 98.8%. Table 13.5 shows the parameters of this RFQ.

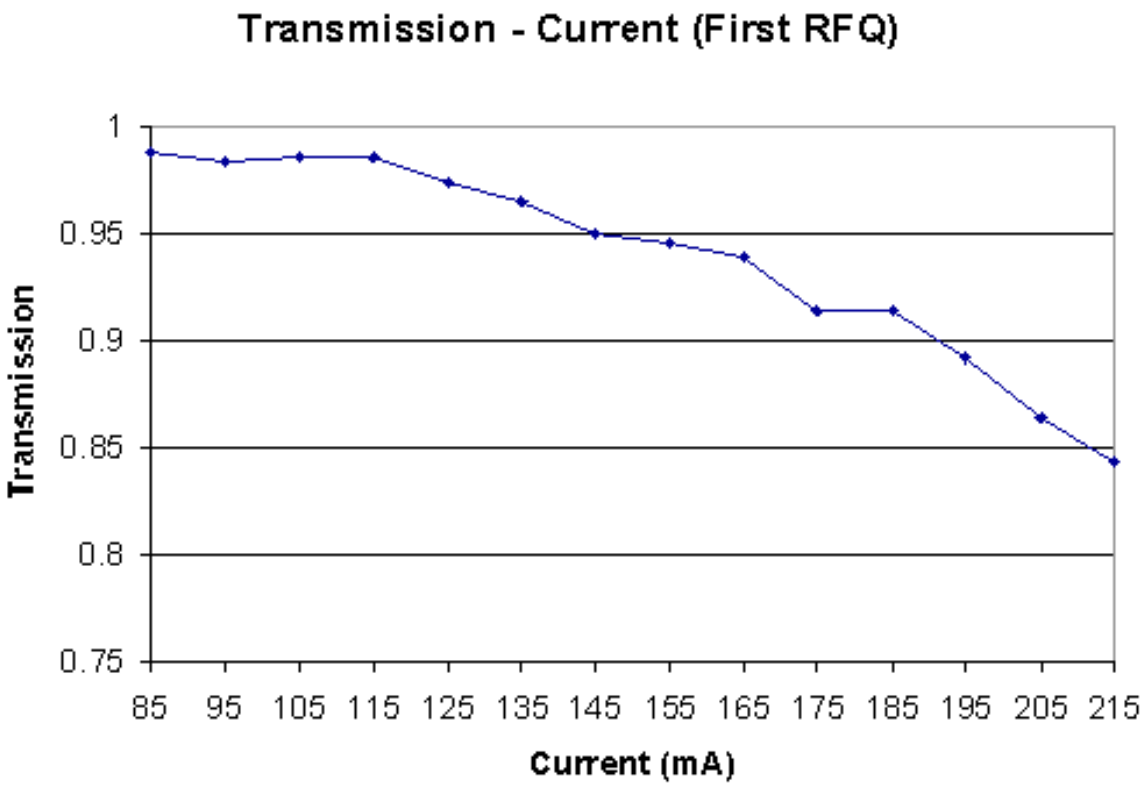

Figure 13.5. Transmission as a function of input beam current for the first RFQ

Table 13.3. First Section RFQ Parameters

Type	Conventional Four-Vane	
Frequency	201.25	MHz
Input Energy	50	keV
Output Energy	1.0	MeV
Input Current	115	mA
Aperture (r_o)(constant aperture design)	0.6	cm
Modulation	1.70	
Intervane Voltage	130	kV
Maximum E Field (2.06 Kilpatrick)	30.33	MV/m
Duty Factor (90 μsec, 15 Hz)	0.135	%
Peak Power	~313	kW
Length	~196.8	cm
Transmission	98.6	%
Input Emittance (X,Y), (normalized, rms)	0.25	π mm-mrad
Input Emittance (X,Y), (normalized, 5 rms)	1.25	π mm-mrad
Output Emittance (X), (normalized, rms)	0.377	π mm-mrad
Output Emittance (Y), (normalized, rms)	0.402	π mm-mrad
Output Emittance (X), (normalized, 5 rms)	1.885	π mm-mrad
Output Emittance (Y), (normalized, 5 rms)	2.010	π mm-mrad

Table 13.4. Second Section RFQ Parameters

Type (accelerator section only)	Conventional Four-Vane	
Frequency	201,25	MHz
Input Energy	1.0	MeV
Output Energy	2.23	MeV
Input Current	115	mA
Aperture (r_O), (constant aperture design)	0.6	cm
Modulation	1.70	
Intervane Voltage	127	kV
Maximum E Field (2.01 Kilpatrick)	29.63	MV/m
Duty Factor (90 μs, 15 Hz)	0.135	%
Peak Power	~294	kW
Length	~138.5	cm
Transmission	100	%
Input Emittance (X), (normalized, rms)	0.462	π mm-mrad
Input Emittance (Y), (normalized, rms)	0.489	π mm-mrad
Output Emittance (X), (normalized, rms)	0.525	π mm-mrad
Output Emittance (Y), (normalized, rms)	0.513	π mm-mrad
Output Emittance (X), (normalized, 5 rms)	2.625	π mm-mrad
Output Emittance (Y), (normalized, 5 rms)	2.565	π mm-mrad

Table 13.5. Single Section RFQ Parameters

Type	Conventional Four-Vane	
Frequency	201.25	MHz
Input Energy	50	keV
Output Energy	2.23	MeV
Input Current	115	mA
Aperture (r_O), (constant aperture design)	0.6	cm
Modulation	1.70	m
Intervane Voltage	129.3	kV
Maximum E Field (2.05 Kilpatrick)	30.17	MV/m
Duty Factor (90 μs, 15 Hz)	.135	%
Peak Power	~607	kW
Length	~341.27	cm
Transmission	98.8	%
Input Emittance (X), (normalized, rms)	0.25	π-mm-mrad
Input Emittance (Y), (normalized, rms)	0.25	π-mm-mrad
Output Emittance (X), (normalized, rms)	0.393	π-mm-mrad
Output Emittance (Y), (normalized, rms)	0.389	π-mm-mrad
Output Emittance (X), (normalized, 5 rms)	1.965	π-mm-mrad
Output Emittance (Y), (normalized, 5 rms)	1.945	π-mm-mrad

13.5. The Double Alpha Phase Space Imaging System (MEBT)

This section describes the design [23] of the double alpha phase-space imaging system or MEBT which transforms the beam from the match-point at the output of the first RFQ to the match point into the second RFQ. The design code TRACE 3D [22] was used. Table 13.6 shows the input parameters used in the computation. Table 13.7 shows the output beam parameters at the input match point to the second RFQ. Figure 13.6 shows the MEBT elements: two alpha dipoles and five quadrupoles. This arrangement is similar to that used in the PET project. The apertures of the dipole magnets have been increased a small amount over the PET magnets, but the edge angles have not been altered.

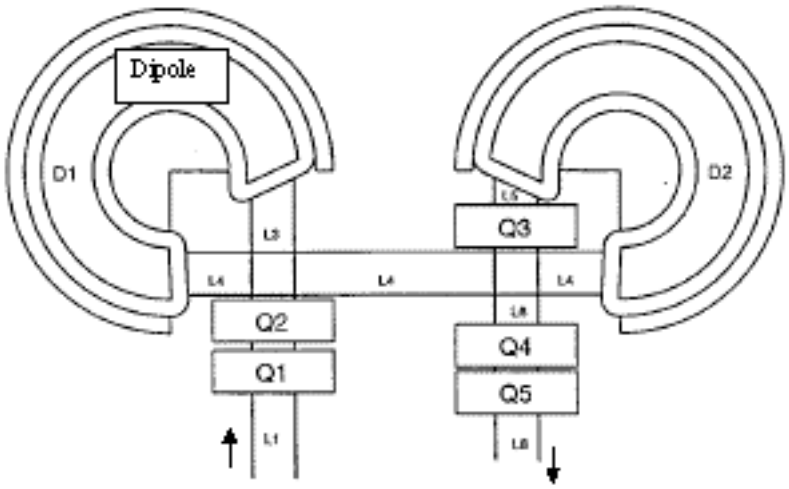

Figure 13.6. MEBT elements consisting of the two alpha dipoles and the five quadrupoles

Fig. 13.7 shows a good match into the second RFQ for a beam intensity of 80 mA. The small emittance mismatch is well within the acceptance of the RFQ, where an emittance growth of 20% has been allowed. Although this calculation demonstrates the feasibility of using such a system, as the PET project also demonstrated, an R&D effort will be required to validate the calculations and to derive the parameters for a physical design.

Table 13.6. 1.0 MeV RFQ Output

	α	β	ε	ε_n	
x	2.2788	0.1401	40.6163 π	0.5950 π	mm-mrad
y	-1.4541	0.0894	43.3576 π	0.6352 π	mm-mrad
z	0.1592	1.6562	739.582		deg-KeV

Table 13.7. 2.23 MeV RFQ Input

	α	β	ε	ε_n	
x	2.2456	0.1363	49.981 π	0.7322 π	mm-mrad
y	-1.412	0.0859	52.9293 π	0.7754 π	mm-mrad
z	0.1766	1.6606	885.1896		deg-KeV

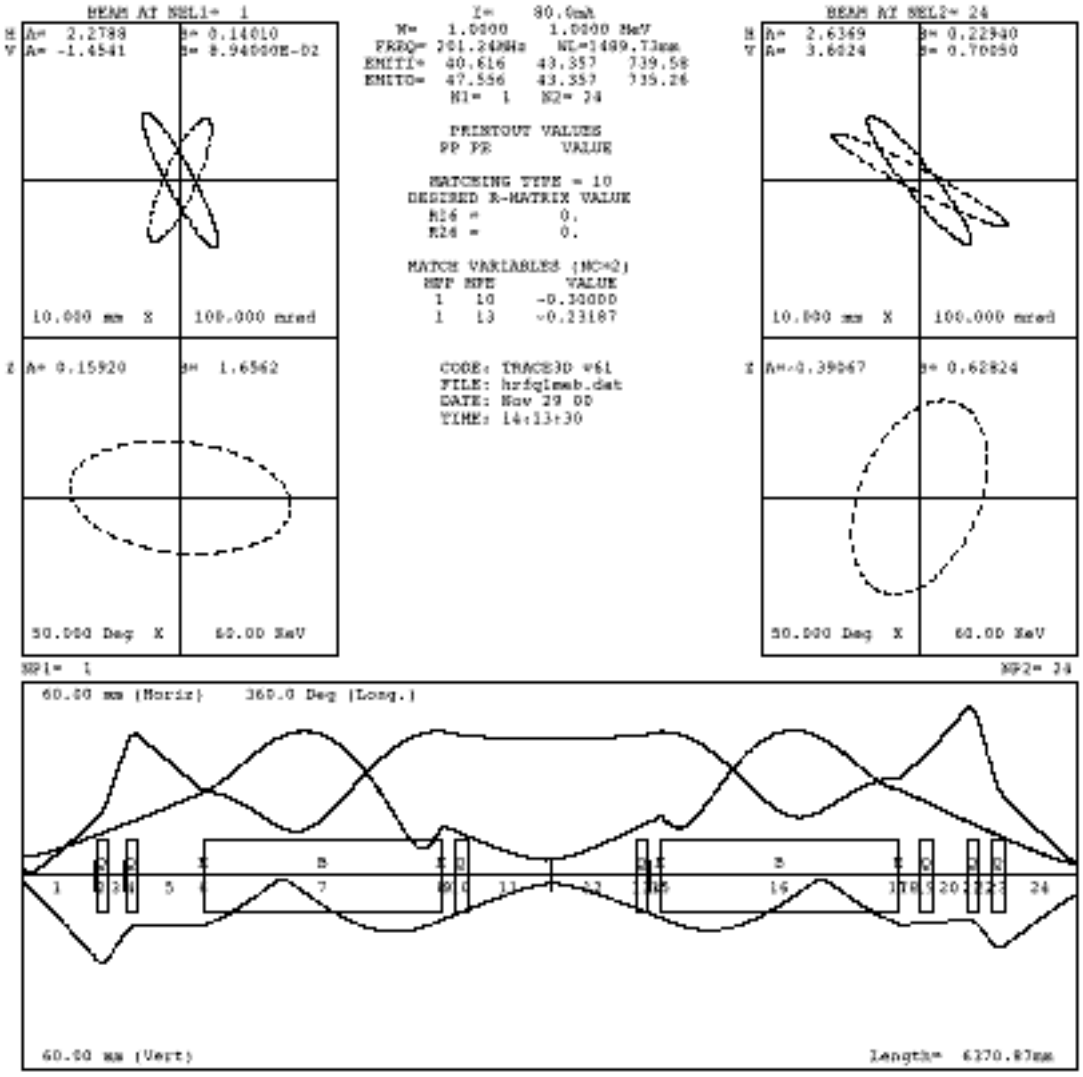

Figure 13.7. Trace calculation showing match to RFQ-2 for a beam intensity of 80 mA

13.6. Chopper

A beam chopper is necessary in the Proton Driver to reduce beam losses during injection from the Linac into the Booster and for creating a gap in the beam bunch train so that extraction loss due to kicker rise-time can be eliminated. Chopping of the beam is most conveniently done in the low energy part of the Linac system where the beam can be lost without causing induced radioactivity in the accelerator components. In this study various schemes have been investigated for providing the required chopping of the beam pulse.

The rf chopper will be used for creating 42-bucket gaps in Stage 1 and also for 30% beam chopping in Stage 2. Compared with the conventional traveling wave deflectors, its advantages are: i) simplicity, ii) fast rise- and fall-times (about 20 ns), and iii) short physical length (less than 10 cm). Laser chopping could be used to create the short extraction gap. It has very fast rise- and fall-time (several ns).

The rf chopper is similar to a beam transformer. It is based on the fact that the RFQ has a small energy window. A ±10% energy error in a beam at the entrance to an RFQ can effectively reduce the transmission efficiency to zero. The chopper consists of a pulsed power supply and a cavity. The cavity is loaded with Finemet-wound cores that serve as a beam transformer. The gap rf voltage is a waveform of square pulses with an amplitude of ±2.5 kV, or ±5% of the RFQ-1 injection energy of 50 keV. The spacing between two neighboring squares is equal to the chopped beam length. The extraction energy of the H^- ion source will be adjusted to 47.5 keV. After the chopper, the beam energy jumps between 50 keV and 45 keV. The beam portion with 45 keV is at the wrong energy for acceptance into the RFQ and will be chopped.

A prototype chopper cavity loaded with three 1 in. thick Finemet cores and driven with a power supply using a HTS 81-09 high-voltage transistor switch was built and installed in the LEBT before the RFQ in the Linac at the HIMAC in Japan. The preliminary results from the beam tests were encouraging. The Linac beam was successfully chopped and the beam with correct energy was captured in the rf bucket during injection into the synchrotron. Two issues need to be studied in greater detail: i) the tolerable voltage variation during the waveform peak, and ii) the effect of the low-energy (45 keV) H^- ion bombardment on the RFQ.

For laser chopping a 1.1 μs notch is to be created in a one-meter interaction region between the MEBT magnets. The one-meter notch is repeated 27 times by recirculating the laser pulse through the H^- beam as it streams into the interaction region. The laser pulse is routed to an external 20-meter delay line and reinjected when the interaction region refills with ions. The external cavity is a bowtie cavity with enough gain to make up for propagation losses. Judicious use of large aperture Q-switches, time of flight for clearing Q-switch rise times, and beam splitters will be used to shuttle the laser pulse in and out of the interaction region. Thus a 99% 1.1 μs notch will be created. H^0 beam will scatter on the MEBT magnet rather than the RFQ.

A 2.2 μs bow-tie cavity delay line will be required to accommodate multi-turn operation. It too requires some gain. The laser pulse is switched out of the 20-meter delay line to this one between turns.

13.7. The New 10-MeV Drift-Tube Cavity

The present 10-MeV drift-tube cavity was constructed at Fermilab as a prototype in 1968-69. The copper-clad steel for the tank walls was obtained from surplus materials at Lawrence Livermore Laboratory, and the welding was performed to develop the technique required for making copper-to-steel joints. Drift-tube fabrication as well as the drift-tube quadrupole alignment mechanism was experimental. The alignment of the drift tubes was unsatisfactory and failed to allow the required six-dimensional tolerances to be achieved. Alignment eventually depended upon controlled bending of the drift-tube support stems. Although the cavity accelerated beam to 10 MeV, beam quality was sacrificed by the poor quadrupole alignment. An attempt to realign the drift tubes after the tank was moved to its permanent building failed to improve the alignment. It was expected that a new tank could later be constructed to replace the prototype.

Considerable experience has been acquired since 1970 in the construction of drift-tube accelerating cavities. Copper plating of prefabricated tanks is the usual preferred fabrication technique. Better fabrication of drift tubes with cooling and quadrupole placement is available. Drift-tube alignment mechanisms have been improved. Stabilized rf structures allow better power transfer in the cavities, i.e. post couplers have been used in the higher-energy cavities of the drift-tube Linac, but the early construction of the 10-MeV cavity prevented their use in it. New types of rf structures for the acceleration of particles up to 10 MeV have been developed and are being promoted in the accelerator community. These issues will be studied before a final design is proposed.

Raising the input energy to the 10-MeV cavity allows a better phase-space match to be made to the drift-tube focusing system. In addition, it eliminates the first 18 drift tubes that contain quadrupoles with 2 cm. bore diameters and lengths of 1 and 1 1/4 inch. These quadrupoles were the most difficult to align and their fields were questionable. The accelerating gaps between these first drift tubes are short and the transit-time factor low, making acceleration inefficient. A new tank will be at least 1.4 m shorter than the present cavity and would start with drift tubes having a larger bore diameter and longer quadrupoles. The sparking problems associated with the low-energy drift tubes in the cavity would be ameliorated.

13.8. Linac Controls and Diagnostics

The Front End computers will run the same software used for the existing Linac. Data from these computers can be requested by consoles in the Main Control Room. The new additions to the Linac also operate at 15 Hz, and data will be collected synchronously with the 15 Hz repetition rate so that correlated readings from the entire Linac will be available.

The proposed low-energy Linac improvements are similar to the PET project done at Fermilab several years ago. The equipment to be controlled includes the ion source, two sections of RFQ Linac, the double alpha magnets, a new 10-Mev drift-tube Linac tank, the beam transport lines between these elements, and the beam instrumentation.

Although control system equipment tends to change rapidly over time, this write-up assumes that the control system will be built using today's technology and devices. The Front End computers consist of a single board computer, the Motorola MVME2400, mounted in VME bus crates, VXI crates, or IRM chassis. The IRM, Internet Rack Monitor, is a stand-alone chassis containing the computer and both analog and digital I/O. Additional I/O is added using commercially available VME bus boards and industrial PLC's, Programmable Logic Controllers. Table 13.8 is a list of the control system equipment and the devices controlled by each.

Table 13.8. Control Equipment for Linac additions

Chassis	Equipment	Comments
IRM-0	Ion Source	Ion Source potential, Fiber optic isolation
IRM-1	RFQ-1	Mounted in RF System Rack
IRM-2	RFQ-2	Mounted in RF System Rack
IRM-3	Power Supplies, PLC's	Transport and Alpha Magnets, Vacuum
IRM-4	Beam Instrumentation 1	See Table 13.9
IRM-5	Beam Instrumentation 2	See Table 13.9
VXI Crate	Phase control, cavity tuning	RF related signals and processing
IRM-6	Emittance Probes	May be needed only for commissioning

A variety of Beam instrumentation equipment will be needed to commission and monitor the operation of the RFQ part of the Linac. Table 13.9 is a list of needed devices.

Table 13.9. Beam Diagnostics Equipment

Quantity	Device
4	Emittance Probes, 32 channel, 2 horizontal and 2 vertical
4	Single wire Scanner beam Profile probes
5	BPM, Beam Position Monitors
4	Beam Current Toroids
1	Beam Phase Monitor Probe
4	Horizontal Trim Magnets
4	Vertical Trim Magnets.
4	Ion Profile Monitors, 2 Horizontal & 2 Vertical
1	Bunch Length Monitor

13.9. Retuning the Linac for Brighter Beam

After installing the new Tank 1, the five tanks of the drift-tube Linac will contain 191 quadrupoles excited from 118 power supplies, with most power supplies driving two quadrupoles. The transition section contains six quadrupoles, and the side-coupled Linac contains 28 quadrupoles. The quadrupoles will have been set from calculations assuming desired beam parameters, but little tuning will have been done to optimize the quadrupole settings for measured beam parameters due to the complexity of the focusing system. Measuring properties of this initial beam will allow a second calculation to better tune the focusing system. In addition, the matching between the cavities and the different Linac structures will be studied. By matching the output from each structure to the acceptance of the next structure, it is possible to eliminate emittance growth along the Linac as well as beam loss.

Currently the quadrupoles are tuned using a beam-loss criterion. The tuning should also include beam quality as one of the criteria.

13.10. Shielding Considerations

The 1991 Linac Shielding Assessment [11] is the current reference document governing radiation protection in the areas adjacent to the Linac enclosure at the low energy end (Tanks 1-5). The 1993 Linac Shielding Assessment1 [12] is the current reference document governing radiation protection in the areas adjacent to the Linac enclosure at the high-energy end (beyond Tank 5). The nature of the Linac operation and the complex shielding arrangements associated with the Linac enclosure make standard shielding calculation methods very difficult and somewhat unreliable.[13] Extensive radiation tests were performed prior to the completion of both the 1991 and 1993 Linac Shielding Assessments. [12,14,15] The results of the radiation tests performed for these shielding assessments show that relatively high dose rates could be achieved in very short periods of time; however, the dose delivered per pulse was relatively small and very manageable. (<<1 mR/pulse for locations outside of the Linac enclosure) [12,14,15]

Chapter 2 Articles 236 and 237 of the Fermilab Radiological Control Manual (FRCM) outline the posting requirements for beam-on radiation conditions for operating accelerators.[18] However, the posting requirements associated with Linac operation are governed only by Article 236. This is because it is highly unlikely that excessive beam loss could be sustained for a full hour in the Linac accelerator. [19] Table 13.10 is copied from the FRCM for the shielding requirements.

Table 13.10. (From the FRCM) Control of Accelerator/Beamline Areas for Prompt Radiation Under Normal Operating Conditions (refer to Article 236.2(b)(1))

Dose Rate (DR) Under Normal Operating Conditions	Controls
DR < 0.05 mrem/hr	No precautions needed.
0.05 < DR < 0.25 mrem/hr	Signs (CAUTION - Controlled Area). No occupancy limits imposed.
0.25 < DR < 5 mrem/hr	Signs (CAUTION - Controlled Area) and minimal occupancy.
5 < DR < 100 mrem/hr	Signs (CAUTION - Radiation Area) and rigid barriers (at least 4' high) with locked gates. For beam-on radiation, access restricted to authorized personnel.
100 < DR < 500 mrem/hr	Signs (DANGER - High Radiation Area) and 8 ft. high rigid barriers with interlocked gates or doors and visible flashing lights warning of the hazard. Rigid barriers with no gates or doors are a permitted alternate. No beam-on access permitted.
DR $\geq$ 500 mrem/hr	Prior approval of SRSO required.

Currently the areas adjacent to the Linac enclosure are posted as in Table 13.11.

Table 13.11. Posting of areas adjacent to the Linac enclosure

Adjacent Area	**Current Posting**
Upstream end (750 KeV) between the Linac enclosure and the Pre-Accelerator enclosure	Radiation Area
Linac Upper and Lower Level Galleries	Controlled Area
Downstream end located inside the Booster enclosure	Radiation Area
Outdoor berms and Utility Access area	Not posted

In order to comply with the limits established in Chapter 2 of the Fermilab Radiological Control Manual, interlocked radiation detectors are utilized throughout the Linac area. These interlocked detectors are positioned throughout the Linac enclosure and surrounding areas based on information provided in the 1991 and 1993 Linac Shielding Assessments. The information provided in these assessments shows that the detectors are positioned in the optimum locations to inhibit beam in the event of a multiple pulse beam loss scenario.

Prompt radiation levels outside of the Linac enclosure due to beam loss will increase approximately linearly as a function of increased intensity. Since the dose delivered per pulse is relatively small and very manageable to begin with, increasing the intensity by a factor of 5 would have very little impact. Since areas adjacent to the Linac enclosure are ultimately protected by interlocked detectors and not passive shielding, increasing intensity by any reasonable factor would not present problems with regards to prompt radiation fields outside of the enclosure.[16] The existing interlocked detector arrangement is adequate for an increase in intensity by a factor of 5.

Increasing Linac intensity without a concurrent upgrade of Linac control and diagnostic equipment will likely result in an increased number of interlocked radiation detector trips. Although upgrading Linac controls and diagnostics is planned (Section 13.8), it may still become necessary to upgrade the existing radiation detector cards from the somewhat over-reactive "rate" style card to the equally safe, yet more tolerant "integrating" style card. Other alternatives include the addition of more passive shielding to the Linac enclosure or imposing more restrictive occupancy limitations on the areas adjacent to the Linac enclosure and changing the radiological postings in accordance with the Fermilab Radiological Control Manual.

The radiation hazards associated with the operation of new rf producing equipment can be very significant. [17] The X-Ray production of the new H^- Source, RFQ's and associated power drivers will be addressed by a combination of enclosure interlocks, commissioning of equipment and periodic radiation surveys depending on their installed location.

Residual radiation levels and radiation damage to materials within the Linac enclosure are a function of beam intensity, beam loss and time of exposure. Work on activated components, regardless of the magnitude of activation, is handled in accordance with the procedures established by the Fermilab Radiological Control Manual. Minimizing beam loss and time of exposure are being addressed by upgrading the controls and diagnostics of this machine (Sec. 13.8).

13.11. Short Range Plans: The R & D Program

Although the technology for the low-energy Linac improvements have been generally accepted in the accelerator community and preliminary computational work done to verify the design parameters, the expertise for constructing a final system will have to be developed at Fermilab. An R & D program will be required to develop the hardware and verify its performance. The specific areas where R & D work will be required are:

1. Ion Source development and the electrostatic LEBT
2. The RFQ
3. The double alpha phase-space imaging system
4. The rf cavity with Finemet cores for beam chopping

5. Laser Beam chopping

13.11.1. Ion Source and Electrostatic LEBT

A short (one year) H^- source R&D program is proposed. The goal is to produce two new sources: (1) an improved magnetron, which would increase the H^- beam brightness by a factor of two; and (2) a noiseless semi-Planotron, which would increase the H^- current to 110 mA with high brightness.

1. Motivation:

   At the recent Proton Driver review, the committee recommended that the ion source *"should be an area of highest R&D priority"* for the ion source/Linac part of the Proton Driver Project. However, due to limited resources, we plan to reach the goal of an ion source required by the Proton Driver in several steps. This proposal represents the first step. It is a fairly short program (one year) and requires moderate investment. This effort may have an immediate impact on the improvement of the present Linac and Booster performance. These new sources can be mounted on the Cockcroft-Walton and provide an H^- beam with higher intensity and better quality *(i.e.,* a brighter beam).

2. R&D goals:

   (a) Improvement of the magnetron:
   The emittance (brightness) of the present magnetron can be improved by optimizing the discharge geometry, gas injection, extraction and plasma over-neutralization. The goal is to attain 85 mA of H^- with an emittance of 0.5 π mm-mrad (90% normalized, a factor of 2 smaller than the present beam emittance).

   (b) Development of a noiseless semi-planatron:
   The goal is to obtain up to 110 mA of H^- with an emittance of 0.7 π mm-mrad (90% normalized). This new source can be adapted for installation on the Cockcroft-Walton as a replacement of the magnetron.

As a future improvement of the H^- beam quality for the existing Linac and Proton Driver (after finishing the short R&D program), we propose to develop a H^- source giving a very high brightness, a Penning geometry Surface-Plasma Source, known as a Dudnikov type H^- source (DTS). Features of this source are: a noiseless discharge and beam formation, very high beam brightness, and the possibility of adapting it to the existing injector or the RFQ. The R&D goals are:

(a) Production of a H^- beam with an intensity of 120 mA and brightness 30-50 % better than the Semi-Planotron source.

(b) Adaptation of the DTS to the existing injector.

(c) Develop a source housing and a beam formation, transport, and focusing system for the RFQ.

It may be possible in this design to incorporate an optimized combination of the features of the DTS developed at BINP, ISIS, LANL, UMD, and INR. Developments at LBL and FU could be used in the LEBT. Suppression of fast ion instability is important for production of H^- beams with high brightness.

Space charge neutralization of H^- beams in the double-alpha line will be studied. Space-charge neutralization (compensation) by residual gas ionization is efficient for dc ion beams if an electron trap is created along the beam. For pulsed ion beams and for beams with intensity modulation, a higher gas density is needed for neutralization so beam loss by charge exchange or stripping of negative ions can be significant. Space charge neutralization by ions could result in fast ion instability. Over-neutralization is necessary for damping this instability. Space charge neutralization needs to have a plasma with a density close to the beam density, $n_p = n_b = 10^8 - 10^9$ cm^{-3}. But the gas density for production of this plasma by beam interaction with the gas should be much higher, $N_g = 10^{11} - 3 \times 10^{12}$ cm^{-3}. The corresponding level of gas ionization is very low. A plasma with a density $n_p = n_b = 10^8 - 10^9$ cm^{-3} could be produced with a very low gas density by plasma generation with a pulsed plasma gun where 50% of the injected gas could be ionized. The technology used for positive ion-beam neutralization could be used for negative beam neutralization (compensation) and over-compensation.

13.11.2. The RFQ

An RFQ using contoured circular rods exists at Fermilab and was provided by A. Schempp (IAP-Goethe University). [20] It is tuned to 201.5 MHz and has an input energy of 30 keV and an output energy of 750 keV with a transmission efficiency of 96 % at a beam current of 30 mA. It can be used to accelerate the H^- beam from the ion source and LEBT (a solenoid magnet exists from the PET Project that can initially serve as a LEBT) This will validate RFQ computations, assist in the characterization of the ion source output, and provide an input beam to the double-alpha magnet MEBT. This RFQ will also provide engineering and sparking level information.

13.11.3. The double alpha phase space imaging system

In the PET Project the RFQs were separated by two 270^o bending magnets and five quadrupoles to form a five dimensional phase-space imaging system to match the beam from one RFQ to the next RFQ. The system was used to match a 1-MeV beam of single

charged $^3He^+$ beam from a 200-MHz RFQ to a 400-MHz RFQ after passing through a stripper to form a double-charged $^3He^{++}$ beam. The success of this system constituted a proof-of-principle experiment to ascertain the validity of separating sections of RFQ.

A TRACE3D [21] study was done to see if this equipment could be used for a 750-keV H^- beam from the Schempp RFQ. The result indicated that with minor changes in the magnet excitation currents this same equipment could be used to match the beam into the acceptance of the 10-MeV Linac tank. An H^- beam with a peak current of 65 mA will allow space charge effects to be investigated in this type of MEBT. It also will allow parameters to be investigated to verify computational codes and to acquire information preliminary to a final design of a system to upgrade the low-energy section of the Linac.

13.11.4. The rf cavity with Finemet cores for beam chopping

A prototype rf cavity with Finemet cores and a bipolar HTS 81-09 high voltage transistor switch in the power supply was built and installed on the Linac at the HIMAC in Japan. The preliminary results from the beam tests were encouraging, but additional issues need to be studied, such as:

a. Tolerable voltage variation during the peak of the waveform,

b. The effect of low-energy H^- ions bombarding the RFQ.

These issues with additional information necessary for a final design of such a chopper could be investigated in the proposed R&D program.

13.11.5. Laser Beam Chopping

The laser beam chopping scheme requires modification of the MEBT magnets to get the laser beam between them. This should be modeled in the design of these magnets. The scheme requires a commercial 15 Hz 500 mJ ND:YAG laser, two delay lines with large bore Q-switching, and two 15 Hz low-gain (disk) optical power amplifiers. For safety and pointing considerations, the entire system would be enclosed in rough vacuum.

References

[1] M. Popovic, et. al. "High Current Proton Tests of the Fermilab Linac", Linac 2000, Aug. 21-25, 2000, SLAC, Monterey

[2] Wangler, Thomas P. "Principles of RF Linear Accelerators", New York, John Wiley & Sons, 1998. ISBN 0-471-16814-9

[3] J. Peters, LINAC 99

[4] J. Peters, "Negative Ion Sources for High Energy Accelerators", Rev. Sci. Instrum., 71(2), 1069 (2000)

[5] J. Peters, EPAC, 2000

[6] Zhang, HuaShun, "Ion Sources", Science Press and Springer, 1999. ISBN 3-504-65747-9 (Springer)

[7] Krohn, Link, Bida, Young, Larson, and Pasquinelli, "A He^3 RFQ for PET Isotope Production", 215th Am. Chem. Society Meeting, Mar. 29-Ap. 2, 1998, Dallas, TX

[8] Chou, W., et.al., KEK Report 98-10 (Sept. 1998)

[9] Chou, W., et.al., Fermilab-Conf-99/102 (1999); also PAC'99 Proceedings

[10] J. Staples, et.al., "The SNS Front End Accelerator Systems", PAC'99 Proceedings

[11] Radiation Shielding Assessment of the Linac Enclosure, by Schmidt, Kroc, Allen and McCrory dated Apr 26, 1991

[12] Radiation Shielding Assessment of the Linac High Energy Enclosure Following the 1993 Upgrade Installation and Low Intensity Commissioning, by Schmidt and Kroc dated Sep 21, 1993

[13] Memo entitled "Shielding Criteria to define the "red line" in Linac Shielding Assessments", by Gerry Dugan dated Feb 14, 1991

[14] Radiation Studies of the Linac Enclosure, by Schmidt, Kroc, Allen, McCrory and Noble dated Mar 6, 1991, Revised Apr 22, 1991

[15] Radiation Studies of the Linac Enclosure, by Schmidt, Kroc, Allen, McCrory dated Apr 25, 1991

[16] Memo entitled "Re: ES&H Review of the Linac Shielding Assessment", by C. Schmidt

[17] X-Ray Production, Measurement, & Shielding of Test Cavities, by Kroc and Leveling from APARS Review: The Linac Upgrade March 21 and 22, 1990

[18] Fermilab Radiological Control Manual

[19] Memo entitled "Ropes and Signs Along Linac Lower Utility Gallery", by C. Schmidt dated March 20, 2000

[20] A. Schempp, et.al., "A RFQ Concept Using Circular Rods", 1981 Linear Accelerator Conference

[21] M. Popovic, "Double Alpha MEBT for H^- Beams" Fermilab Report, unpublished, July, 2000

[22] K. R. Crandall and D. P. Rusthoi, Trace 3-d Documentation, LA-UR-97-886

[23] D. J. Larson, et. al., "Ion Optical Design of the BRF-FNAL-SAIC PET Accelerator", presented at the Particle Accelerator Conference, Vancouver, BC, May 1997

[24] A. Tomlin, "Laser Stripping of Relativistic H^- Ions with Practical Considerations", FERMILAB-TM-1957

Chapter 14. Beam Transport Lines

Carol J. Johnstone, Jim Lackey and Fred Mills

14.1. Introduction

The function of the injection-transfer line is to cleanly extract beam from the upstream end of the present 400 MeV transfer line, transport it, and provide the necessary matching at injection into the Proton Driver. There are several constraints on the design of this line. One of the most important is to allow normal operation of the present Booster. Thus extraction to the new line cannot disturb the existing 400-MeV lines, nor the two beam dumps. Also the extraction system must be able to operate at 15 Hz in order to select single Linac pulses, pulses not required for the Booster program.

The length of the approximately 1000-ft line is primarily dictated by allowing space for addition of a future 600 MeV Linac placed at the present Booster elevation. Since the Proton Driver will be at the Main Injector elevation, two vertical drops are required in this line--before and after a 450-ft straight section reserved for this future high-energy Linac. However, the most important considerations in the optics design and layout of the line come from the large number of fixed points and direction-specific trajectories that have been imposed on the line. Furthermore, the geometry of the line must be achieved with bends near 7 kG, or less, to keep losses from H^- magnetic stripping under 10^{-3}.

The extraction line, designed for 16 GeV protons, extracts beam using kickers and a series of septa and transports it to an intersection point with the current MI-8, (8 GeV transfer line to the Main Injector.) The layout and optics of the remainder of the MI-8 line serve to provide the basis for the remaining transport and matching required for injection into the Main Injector. Since all three straight sections are essentially identical, extraction must utilize the same optics as injection, whether optimal or not. Because of the unbroken FODO structure and absence of a long straight section, beam must be kicked off-center through ring quadrupoles and into a string of strong septum magnets in order to extract beam past downstream Proton Driver magnets. The relevant parameters describing extraction will be given along with the optics and magnets in the transfer line.

14.2. Injection Transfer Line

The injection transfer line to the Proton Driver consists of individual sections which:

a) extract and direct 400 MeV beam
b) perform an initial vertical translation to the present Booster Synchrotron level
c) perform dispersion suppression
d) support a long straight for a future energy upgrade
e) perform a second vertical translation to Main Injector elevation, and, finally
f) match and inject into the Proton Driver.

14.2.1. Extraction to the Injection Transfer Line

Extraction of the 400 MeV beam must be accomplished by integrating extraction elements into the existing operating lines. Two beamlines currently handle beam exiting the 400 MeV Linac. One line, called the transfer line, transports the central, stable portion of the Linac beam pulse down a chute (an elevation drop) to the Booster. The other, diagnostic line, diverts the remainder of the Linac beam through a spectrometer magnet and into a high-intensity beam dump. When the spectrometer is off, beam is transferred to a straight-ahead low-intensity dump. Momentum analysis and some monitoring of the beam are performed in the diagnostic line.

In order not to disrupt existing lines or move beam dumps, extracted beam needs to be directed along the existing Linac Upgrade Ramp. This is suitable without further civil construction as an enclosure for a primary beamline (see Figure 14.1). Where the enclosure ends, the beamline is directed along an open concrete pit, which will require modification to make it into a beamline enclosure.

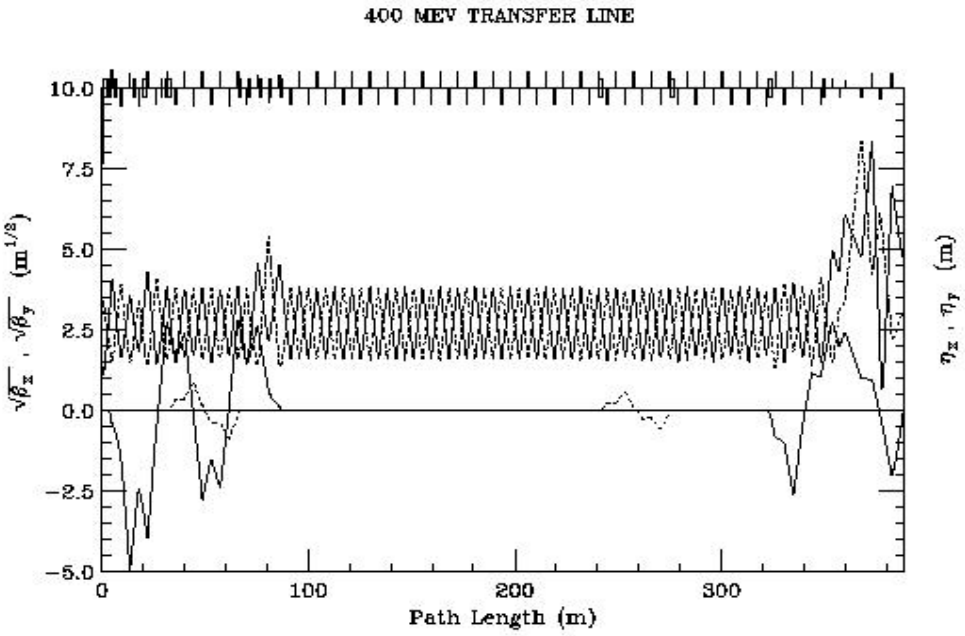

Figure 14.1. Lattice Functions for 400-MeV Injection Transfer Line

Two available drift spaces just upstream of the Linac Upgrade Ramp are potential locations for a pulsed extraction system. The drift upstream of the chopper was eliminated because of the large excursion, or dipole strength, required to clear the chopper tank (although beam could be kicked slightly across the chopper plates). The 2.1-m drift downstream of the chopper was then selected and a dipole length and strength chosen accordingly to cleanly bypass the quadrupole, QB2, in the existing transfer line.

On any 15 Hz clock cycle for which beam is to be delivered to the Proton Driver, the pulsed dipole will deflect the Linac beam horizontally from its normal trajectory and into the new line. When the dipole is not triggered, beam will pass undisturbed to the Booster or beam dump. The only drawback to placing the entire burden on a single pulsed dipole downstream of the chopper is that it has to be operated near or above 7 kG in order to steer beam properly along the Linac Upgrade Ramp. (The dipole needs to be lengthened by about a tenth of a meter to bring the field down to 7 kG.)

In current operation, the electrostatic beam chopper separates a selected (usually the central) part of the Linac beam pulse from its rising and trailing edges to send to the Booster. The edge pulses are sent down a diagnostic line through a spectrometer magnet to a high-intensity dump. The effect of this chopper on the new transfer line remains to be studied to preserve both its role and the function of the present diagnostic line.

Where the ramp straightens, it has a 45° angle relative to the Linac. (Since the bearing of the Linac is almost directly due project-south, the beam in Proton Driver injection transfer line will be headed project-southwest). The pulsed extraction dipole provides approximately 17° of the required bend. Three more dipoles add the remaining 28°. Two remaining steering dipoles are used to align the beam accurately down the ensuing vertical drop, which is immediately followed by dispersion suppression and the lengthy "linac" insert straight.

Because of the length of the line, and, in particular, the long "linac" insert, a regular 90° FODO structure was chosen for the basic optics. This also facilitates construction of achromats for the vertical drops. Since permanent magnets offer an economical opportunity for the long "linac" insert, the cell characteristics of the Linac were chosen to be compatible with permanent magnet quadrupoles whose pole tip fields were less than 2-kG. It was then observed that over half of the entire line could be implemented with permanent magnets with a length equal to that of the pulsed quadrupoles in the line (the quadrupole design in the existing transfer line), and an intervening drift of approximately 4-m. This also conveniently allows permanent magnets to replace electromagnetic quadrupoles where tuneability is not required. In addition, 4-m was found to be an optimal choice. It allows adequate space for insertion of bend elements and matches relatively smoothly to the shorter Linac FODO period. As a consequence, many quadrupoles outside of the "linac" insert can be replaced by a permanent magnet and an air core trim quadrupole when variations about the central gradient are small.

14.2.2. Vertical drops, dispersion suppression, and the linac insert

The vertical drop starts at the end of the Linac Upgrade enclosure to avoid any civil construction near the existing beam dumps. In the periodic structure imposed, a vertical achromat is achieved without modifying the cell structure or optical functions. With the magnet and drift lengths used, the length from center to center of the vertical bends is about 34 m, giving a total vertical descent of 4.1-m (13.5-ft.) This drop takes beam from the existing Linac floor elevation of 736-ft to the Booster floor elevation of 722.5-ft above sea level. The vertical bend magnet is assumed to be the kind used in the existing

vertical chute. The descent to Main Injector level is less, only 9-ft, but because of the identical periodic optics, both vertical achromats are essentially identical with the exception of the vertical bend angle.

In anticipation of a possible 600 MeV Linac, conventional dispersion suppressor cells were included in the geometry of the line in order to prepare a dispersion-free Linac insert and ease future implementation. The length allows 450-ft for a linac, although there is sufficient space for a 600-ft linac, a change readily achieved by moving the second vertical drop downstream an integer number of periods. Because no changes in optics are required in this straight, the entire insert can be completely constructed out of permanent magnet quadrupoles. In addition, there are sufficient unused cells to permit a debuncher to be placed optimally in this section of the line.

14.2.3. Matching and Injection into the Proton Driver

Presently there is a length of 60 m and 15 quadrupoles in which to match optically and geometrically to the Proton Driver at injection. There is not complete freedom in this range, as a bend is located at approximately the center of this final matching section, with a stronger bend at the beginning of the section.

In addition to aiming and angling the beam properly through the injection septum, it must also be directed onto the foil to sub-millimeter accuracy through an off-center ring quadrupole. Geometrically the matching section is very constrained. Beam enters the injection septum ~205 mrad relative to the closed orbit. After traversing both the septum and the off-center ring quadrupole, the injected beam crosses the foil at a 1.2 mrad angle and a 5.2-cm offset relative to the closed orbit. The entire injection line has been completed and closed in site coordinates from the Linac to the Proton Driver foil position to a fraction of a millimeter. Until detailed injection studies can be performed, the transfer line optics are simply matched to the Proton Driver optics, with $\beta_x = 22.861$, $\alpha_x = -0.256$, $\beta_y = 9.212$, and $\alpha_x = 0.0004$. There is residual ring dispersion across the injection straight, and, although the transfer line dispersion at the foil is also approximately zero, it has not been matched exactly to the ring's residual dispersion as this may change.

It has been planned that vertical phase space painting will be controlled in the transfer line. Since we are painting in y', a kicker needs to be installed 180° in vertical phase upstream of the foil. In effect, the kicker is located in a 3.5-m straight about 34-m away from the injection point. Figure 14.1 displays the lattice functions through the entire 400 MeV injection transfer line and Table 14.1 lists the required magnets and their basic optical parameters. Designs and drawings exist for all magnets except for the injection and extraction septa and a few dipoles. However, the different dipoles can most likely be reduced to two or three different types.

Table 14.1. Magnets and their parameters for the 400-MeV injection transfer line

Description	Type	Number	Length (m)	Pole tip strength (kG)
Quadrupoles				
Extraction	perm. mag. / trim quad	7 7	0.2985	1.5 0.4
Vert. Drops	perm. mag.	2 x 9	0.2985	1.5
Mat./Disp. Sup.	Loma Linda	5	0.2985	1.0-2.0
Long straights	perm. mag.	44	0.2985	1.5
Final Match	Loma Linda	15	0.2985	0.6-2.0
Dipoles				
Extraction Dipole	new	1	1.3160	7.6
Horizontal Bend Dipoles	Cooling Ring Steering Disp. Sup. Final Bends	3 2 2 3	1.3086 0.4 1.0 1.0	3.5-4.1 3.5 3.2 4.9
Vertical Bend Dipoles	Chute Bends	4	1.162	2.2-3.3
Injection Septum	new	1	2.0	3.15

14.3. Extraction Transfer Line

The extraction transfer line extracts 16 GeV beam from the Proton Driver, transports it over about 900-m, and prepares it for injection into the Main Injector. Because of limitations in the optics and the phase advances in the Proton Driver straight section, a number of septum magnets are required to complete the extraction process. The bearing of the extraction straight was deliberately sited to be due project-east. After direction control and dispersion suppression, the line bends along an arc carefully designed to interface with the optics and direction of the existing MI8 line; thereby using existing enclosures and power and water supplies for the final transport and injection match to the Main Injector. The entire line is based on 90° FODO cells with 10-m drifts and permanent magnet quadrupoles. The Proton Driver and Main Injector are based on similar 90° FODO cells and this choice therefore provides continuity between the two rings and makes for an ideal match.

Clearly the permanent magnet version of the MI-8 line cannot support 16 GeV beam with the same optics. Therefore, the original electromagnetic design of the MI-8 line has been resurrected in order to support higher energy beam. The electromagnetic version uses B2 dipoles and 3Q52 quadrupole magnets scavenged from the old Main Ring and, therefore, new magnets are not required.

14.3.1. Extraction from the Proton Driver

The extraction system is relatively complicated. Kickers first displace beam in the FODO-based straight through four ring quadrupoles before beam has sufficient offset from the central ring trajectory to enter the field region of a septum. The first septum is not strong enough to extract beam completely and it must traverse a horizontally defocusing quadrupole and a string of four more septum magnets before finally bypassing the ring elements. A list of the extraction kicks and offsets used in the design is given in Table 14.2. Final adjustments were made to the bend angles specified to arrive at the exact distances given. Magnetic parameters given for the septa reflect field changes.

Table 14.2. Extraction separations and kick relative to central ring orbit

Magnet	Offset, x (mm)	Angle relative to extraction straight (mrad)
Upstream		
QH604	-7.211	-2.323
QH605	-28.162	-3.687
QH606	-9.327	3.824
QH607	29.109	6.043
SM607	33.475	-1.206
QH608	85.643	27.677
SM608	165.123	38.748
Downstream		
SM608	710.709	159.5

14.3.2. Upstream section of the 16 GeV extraction line

After extraction is completed, bend dipoles opposite in field to that of the septum magnets are used to reorient the direction of the upstream section of the transfer line to project-east again. Since the extraction system generates a strong dispersion wave at the beginning of the line, the dipoles in this reverse-bend section are interspersed in the FODO structure to cancel the dispersion and ease the match into the periodic arc structure.

14.3.3. Match into existing MI-8 line

A softly bending arc with a radius of curvature about 163-m merges the new extraction line with the present MI8 line before cell #814 at site coordinates 30439.2043-m easting and 30148.2215-m westing. The arc is designed with conventional dispersion suppression cells at either end and the match occurs at an approximate zero dispersion point in the MI-8 line. (The point chosen occurs just after the vertical drop in elevation from the Booster to the Main Injector level.) The lattice from the point of extraction to intersection with the MI8 line is plotted in Figure 14.2. From there the beam and optics follow the lattice given in Figure 14.3, but starting at 172.4 m in the figure. A table of the required magnets follows with the quadrupole radial aperture assumed to be 4.5 cm.

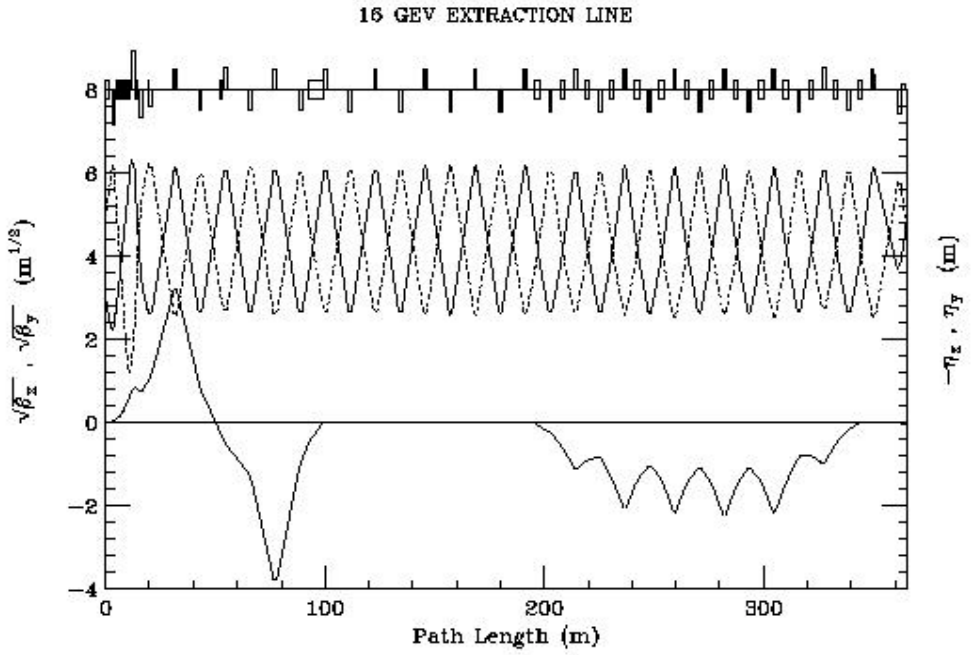

Figure 14.2. Upstream section of the extraction line

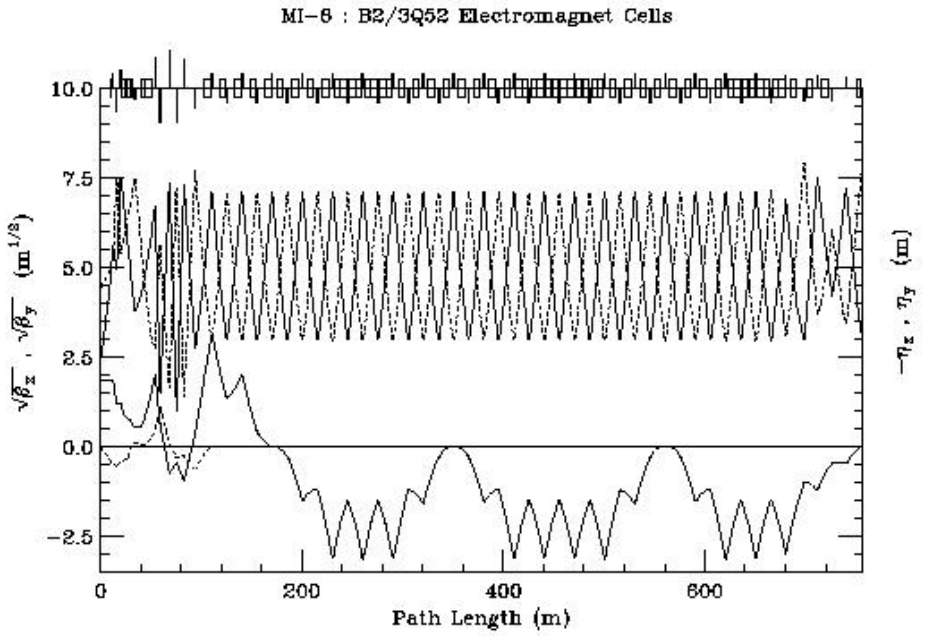

Figure 14.3. Downstream section of the extraction line located in the MI-8 enclosure

Table 14.3. Magnets in the downstream section of the extraction line

Description	Type	Number	Length (m)	Pole tip strength (kG)
Quadrupoles				
Upstream matching	electromagnetic	33	1.4	1.9-4.3
Upstream transport	perm. mag.	15	1.4	2.3
Arc	perm. mag.	14	1.4	2.3
MI8 match	perm. mag./ air-core trim	3	1.4	1.7-2.7
Dipoles				
Extraction Septa	new			
SM607		1	1.65	8
SM608		4	1.35	14
Horizontal				
Bend Dipoles	Rev. Bends	1	0.7610	1.2
		1	0.8384	1.2
		1	6.4634	1.2
	Arc	6	3.0	1.32
	Disp. Sup.	8	3.0	0.66

Chapter 15. Beam Instrumentation

Jim Crisp, Victor Terekhov, Bob Webber

15.1. Introduction

The Proton Driver (PD) will produce 3×10^{13} protons 15 times per second. The extraction energy will be 12 GeV for Stage 1 and 16 GeV for Stage 2 operation. The 1.2 MW average beam power demands reliable instrumentation for commissioning and operation. Challenges for instrumentation include high beam intensity, fast repetition rate, short bunches, rapidly sweeping rf, high vacuum, and radiation environments. This study focuses on established techniques used in instruments with a proven reputation. Basic engineering issues rather than scientific novelties are emphasized. Operational experience of beam diagnostics in the FNAL Booster is exploited. A summary of Proton Driver and associated beam line instrumentation is provided in Table 15.1.

15.2. Beam Properties and Special Requirements

Instrumentation must cope with the following beam properties:

1. In the 400 MeV Injection Line:
   H^- beam is modulated at 201.25 MHz and contains 3.4×10^{13} ions in a 90 μs pulse repeated at 15 Hz. The beam will be chopped at 7.5 MHz in Stage 2 operation.

2. In the Synchrotron:
   Proton beam momentum changes from 400 MeV to 16 GeV with rotation periods changing from 3.3 to 2.4 μs. The 3×10^{13} protons will be divided into 126 - 53 MHz 12 GeV bunches in Stage 1 and 18 - 7.5 MHz 16 GeV bunches in Stage 2 operation. Normalized transverse emittance is 60 π mm-mrad. Beam losses must not exceed 10% at injection or 1% at extraction.

3. In the 12 (or 16) GeV Extraction Line:
   Single turn (2.4 μs) fast extracted beam of 3×10^{13} protons divided into 18 (or 126) bunches with an rms bunch length (σ) of 1 ns.

4. A pilot beam with 20 times lower intensity will be used to verify injection, acceleration and extraction efficiency. Instrumentation will require sufficient dynamic range to insure pilot beam measurements are consistent with those at operational intensities.

5. One important role of the instrumentation will be to provide information to an equipment protection system. This system must respond quickly to limit damage from losses of the 1.2 MW contained in the beam.

6. Because of large beam intensities and rapid pulse rates, equipment located in the tunnel could receive up to 50 Mrads through the 20-year life expectancy of the Proton Driver. Electronics located in the tunnel should be kept to a minimum to avoid failures and minimize personnel exposure.

7. The expected vacuum in the Proton Driver ring is 1×10^{-7} Torr. Devices exposed to vacuum may require baking at up to 150°C.

15.3. 400 MeV Injection Line

One Beam Position Monitor (BPM) and Beam Loss Monitor (BLM) will be installed at each of the 89 quads in the 400 MeV line. Beam Profile Monitors (BPrM) will be installed at every other quadrupole and one Beam Current Transformer (BCT) will be placed at each end of the Line.

15.3.1. BPM's

BPM's will be placed inside the poles of each quadrupole to measure position in the focusing plane. A shorted stripline design will be used to measure the 201.25 MHz frequency content of the beam. Each electrode will subtend 90 degrees of arc. Considering the beam velocity, the optimum stripline length is 310 mm resulting in an assembly length less than 400 mm. The outside diameter will be 2 or 3 cm larger than the clear aperture. A 60 mA beam will produce 1.5 volts at the BPM output. The signals will be transmitted through phase matched ½″ Heliax cables to AM/PM conversion receivers. The dynamic range of the receivers is sufficient to accommodate the anticipated 26 db range in beam intensity. The bandwidth of the position output must be sufficient to track the 7.5 MHz chop rate. A 12-bit digitizer sampling at 7.5 MHz throughout the 90 μsec spill should be adequate. Triggering can be performed by either beam synch clock events or pulses derived from the chopper power supply trigger. Position error from the BPM, cables, and electronics should be less than ±0.5 mm.

As an alternative, processing could be performed at double the Linac frequency (402.5 MHz). This allows shorter electrode length and reduces interference from the 201.25 MHz Linac rf system. Although the signal level is slightly lower, the approach was proven effective at BNL [1].

15.3.2. BLM's

For best sensitivity to beam loss, monitors will be placed downstream of each quad. Sealed, argon-filled, glass ionization tubes [2] will be used. They have been used for years at several laboratories: FNAL, BNL, LANL, and others. Argon filled chambers have faster time response (with electron collection), and larger dynamic range than the cheaper air filled type. Typically, they have 1 or 2 μsec response for electrons, 70 nano-Coulombs/Rad sensitivity, and are linear up to thousands of Rad/s. Such features are attractive for monitoring beam losses with one turn time resolution. Faster processing for a few monitors located near the injection area would be useful.

Loss monitor signals will be transmitted through coaxial cables to the equipment gallery. There are three signal-processing options presently used at Fermilab: linear amplifier, integrator with S&H, and logarithmic amplifier. An additional method to consider is digital integration based on monolithic synchronous V/F converters. This approach provides a four-decade dynamic range without gain change. The fast monitors should have programmable thresholds to provide alarm signals for the Equipment Protection System.

15.3.3. BCT's

Two BCT's will monitor beam line intensity, transfer line efficiency, and injection efficiency for each injected turn. The 3.4×10^{13} total intensity must be measured to 0.2% accuracy to verify that beam loss does not exceed the limit. This requires a time constant of more than 50 ms (low frequency cut-off less than 3 Hz). A 20 MHz high frequency response would resolve the time structure of the 7.5 MHz chopped beam. The sensitivity will be 1 V/A into 50 Ω. These bandwidth and accuracy requirements demand special attention.

15.3.4. BPrM's

Secondary Emission grids, slow wire scanners, and Ionization Profile Monitors (IPM) are used to measure the transverse profiles. The first two are a well established and accepted means of accurately measuring profiles of single pass proton beams. However, these devices will suffer from several problems with the high average current H^- ion beam: parasitic ion stripping, extreme heating, and declining secondary emission efficiency after exposure to 10^{19} particles. IPM's are non-destructive, do not suffer from these problems, and are used at FNAL [4, 5] and BNL [6] to continuously measure circulating beam.

Movable secondary emission grids at FNAL consist of 48 horizontal and 48 vertical 0.003″ diameter gold plated tungsten wires. At full Proton Driver beam intensity, these wires would reach 1600°C. Carbon wires would reach 850°C and Beryllium wires 300°C. Springs would be required to maintain wire tension at these temperatures. Thin walled, 0.5 mm diameter capillary tubes are commercially available and would exhibit lower temperature because of their larger surface area. The tubes are sufficiently stiff to be free extended from one end to avoid thermal expansion problems. Wire grids have a little less mass and less ion stripping, however. Grids based on either design should be used at reduced beam power for limited periods of time. Single plane monitors without collector foils are expected to strip about 2% of the ions. No more than two monitors should be placed in the beam at once.

About 100 picoCoulombs per 10^{12} ions will be collected on the center wire. Rapid multiple profiles with one turn resolution should be possible. Shielded multiconductor twisted pair cable will be used to transport collected charge to gated integrators located in the equipment gallery. Multiwire scanners at Fermilab have 96 parallel integrators followed by S&H circuits multiplexed into two fast 16-bit digitizers. Both horizontal and vertical profiles are measured using 48 wires each. Gain of 1, 10, or 100 can be selected

remotely. Care should be exercised in the selection of cable to avoid problems with transient signals.

Single wire scanners will be used to measure profiles near the injection region. Carbon or Beryllium wires with 20 μm diameter would minimize beam blow-up from Coulomb scattering and could be used at intensities up to 10^{13} ions. The charge induced on the wire by secondary emission will be collected and the wire stepped to the next position after each beam injection. The desired profile resolution will determine the number of injection cycles required. Actuator triggering can be done from beam synchronized clock events. A useful watchdog tool for equipment protection could be implemented by monitoring the wire signal while it is parked at the periphery of the beam.

Only IPM's can be used to continuously monitor profiles at full beam intensity. This information may prove a useful input to the equipment protection system. HOT microchannel plates 100×80 mm in size with 10^4 charge gain are commercially available. About 2×10^5 ion pairs will be produced from 3×10^{13} beam particles passing through the expected geometry and vacuum. The charge collected from the MCP with 48 strips spaced 1.5 mm apart is comparable to that from secondary emission grids. The same cables, electronics, and applications programs can be used. The maximum lifetime charge obtainable from an MCP is 0.1 Coulombs/cm^2, equivalent to 8 years of continuous running.

A transverse electric field of 500 V/cm will direct positive ions to the surface of the first plate. The field can be made uniform with five equally spaced electrodes connected to voltage dividing resistors. One horizontal and one vertical IPM are recommended for the 400 MeV injection line.

15.4. Synchrotron

Many important phenomena in accelerator physics occur within or near the beam revolution period. Instrumentation for fast cycling high intensity machines should be capable of making measurements on turn-by-turn and, if possible, bunch-by-bunch basis. Assume one BPM and BLM for each of the approximately 100 quadrupoles. Tunes of 11.4 will provide just over 4 BPM's per betatron wavelength in each plane. Three IPM`s will be used to measure profiles on a turn-by-turn basis. One IPM per plane at low dispersion locations and one horizontal IPM at a high dispersion location will allow measurement and correction for momentum spread. Two BCT's with different frequency ranges will be used in the ring. A fast transformer will measure injection efficiency with turn-by-turn resolution. This transformer should resolve chopped beam and provide bunch-by-bunch extraction efficiency in Stage 2 operation. A slow transformer will measure intensity and acceleration losses with higher resolution. Tune measurement systems, a wide-band wall current monitor, and large bandwidth horizontal and vertical striplines should also be installed.

Diagnostic equipment such as a vector signal analyzer, network analyzer, and fast digital oscilloscope should be permanently installed and interfaced to the controls system. Installing certain instrumentation such as the Resistive Wall Monitor (RWM) and large bandwidth striplines near the low level rf system would provide a central location and facilitate sharing resources.

15.4.1. BPM's

Single plane BPM's will be nestled under the coil at the upstream end of each quad. The BPM will be mechanically indexed to the quadrupole to insure the location of the electrical center is known to better than 0.2 mm. Elliptically shaped, diagonally split, electrostatic pick-ups will provide both good linearity and low beam impedance. Electrodes will be made of stainless steel tubes 5 inch × 9 inch in cross section, 100 mm long, and 1 mm wall thickness. The electrodes are separated from the concentric outer tube with high-density alumina spacers. The electrode-to-ground capacitance is 160 ± 5 pF with 3.0 ± 0.1 mm spacers. Threaded plugs could be used to balance the capacitance. The 50 Ω output impedance and the 160 pF capacitance will differentiate the signals below 20 MHz. This will attenuate the 7.5 MHz signal for Stage 2 operation but should reduce the effect of losses on the plate and low frequency noise. A guard strip between electrodes could reduce the inter-electrode capacitance to 2 pF. An inter-electrode 4 kΩ compensating resistor will make the response independent of frequency. A built-in calibration ring could be used to simulate a centered beam. The total assembly would be 200 mm long and require three ceramic coaxial feed-throughs. The materials will withstand a 300° C bakeout. Low cost, 50 Ω, standard polyethylene cables can satisfy radiation requirements.

The BPM system could provide turn-by-turn position information for all 100 BPM's on each of the 15,000 turns. Bunch-by-bunch measurements for Stage 2 operation may prove useful. The closed orbit would be determined by averaging several turns. Electronics based on the log-ratio technique is preferred for its ability to accommodate various rf running modes and beam structures. Calibration and software correction should be used to achieve required accuracy over the entire dynamic range. Experience with log-ratio processing has been gained at FNAL [7]. A new technique for wide band, time normalization [8] could be considered for bunch-by-bunch measurements. In this approach, both electrode signals are combined with different delays and the beam position information is converted into a pulse width. This method uses inexpensive fast ADC's. Critical time adjustment is the main limitation. Further study will be required.

The Beam Synch Clock, locked to the Low Level rf system, will be used to trigger the BPM's. The data acquisition system will be based on VME or VXI. Anticipated accuracy of the position measurement is better than 1 mm on a single turn.

A Beam Line Tuner will measure turn-by-turn position at one horizontal and one vertical location and calculate betatron amplitudes and phases at injection. This data will be used to correct subsequent injections to correct slow repeatable errors in the 400 MeV Line. The Beam Line Tuner may require stand-alone position systems.

15.4.2. BLM's

The basic functions of the BLM system should be to minimize uncontrolled losses by providing data for tuning and disabling injection after high losses have occurred. About 110 monitors will be used: one downstream of each quadrupole and a few more at the injection, extraction, and collimation areas. Time response of 100 μs will be sufficient. Monitors located in the injection and extraction areas may benefit from faster detectors and should be read with one turn time resolution. The beam synch clock should be used to sample the BLM's. The BLM hardware would be similar to that used for the 400 MeV Line. Losses in the ring will vary over a large range and would benefit from fast logarithmic integrators. Inexpensive 8-bit ADC's should be adequate. Programmable comparators could produce an input to the equipment protection system. These comparators should not rely on software, as their reliability is critical.

15.4.3. BCT's

Bergoz [3] offers tape wound toroidal cores of high permeability amorphous alloy. A core with dimensions $245 \times 295 \times 22$ mm^3 would fit around the 9" beam pipe and provide: 0.1 ms time constant (1.5 kHz), sensitivity of 1 V/A into 50 Ω, and 15 ns rise time (10 MHz). The 2 Amp average beam current in the ring would produce a magnetic flux density of 0.3 Tesla at the inner surface of the core. Because the saturation value is 0.5 Tesla, the relative permeability of the core should be less than 10^5. Possible noise sources include: 60 Hz line, 15 Hz magnet power supply, rf systems, fast kicker magnets, and the beam image current. To reduce these effects, careful attention to grounding and shielding will be necessary. To reduce rf noise, the shield of the twinax cable should be connected to tunnel ground through a 20 nF capacitor.

Processing electronics for the fast BCT has challenging requirements: large dynamic range, necessity of base line restoration, variation of beam structure, and fast data flux. Two, gated, "ping-pong" integrators followed by fast 12-bit ADC's with S&H amplifiers will be used to measure turn-by-turn intensity. Variable gain, base line restoration, and an automatic calibration system will be required to measure turn-by-turn intensities to 0.2%. Again, triggering will require the beam synch clock. Delivered data includes turn-by-turn: intensity, injection efficiency, and extraction efficiency. Experience using 14-bit ADC's for fast intensity measurement has been gained at BNL [9]. This promising approach warrants further study.

The average circulating beam current could be obtained by numerically correcting the low frequency content of the fast BCT; however, the required resolution of 10^{-4} would not be realized. A DC Current Transformer (DCCT) is the best device for measuring beam intensity, or current, of circulating beam [10]. Commercially available DCCT's have 1 μA resolution, 15 μA noise, 50 μA long term drift, and 4 kHz bandwidth [3]. An 18-bit A/D converter would provide 8 μA resolution (1.6×10^8 particles at injection) with a 2 Amp range (3.0×10^{13} at extraction). To verify efficiency before full power operation a minimum of 1.6×10^{12} is required to obtain 10^{-4} resolution. The signal should be digitized at 1 kHz or faster. Data processing must account for the changing

beam velocity as it is accelerated. The assembled detector will require 0.3 m and should be placed as close to the equipment gallery as possible.

15.4.4. IPM

The PD ring IPM's will be similar to those already in use at FNAL [4, 5]. Care will be required when locating and using the monitors. Tunnel locations should be chosen to minimize micro channel plate (MCP) damage from radiation and X-rays. Measuring turn-by-turn profiles at the output currents used by the 400 MeV line IPM's would quickly deplete the MCP's. Profile measurements should be done sparingly and plate voltage must be switched off immediately after the measurement. Because of faster drift times, turn-by-turn measurements may benefit from electron collection rather than the heavier ions. In this case, a magnetic field of 0.1 Tesla parallel to the electric field is necessary to reduce profile spreading caused by beam space charge. Simple Helmholtz coils could produce this field, but their influence on the proton beam must be removed with balanced corrector magnets before and after the IPM. The corrector magnets and the IPM will occupy 2 m of beam pipe. The IPM itself is 0.3 m in length.

The vertical IPM should be placed at DLS13, between quads Q1F and Q2D, where vertical beta is 31.2 m and dispersion is zero. One horizontal IPM will be placed at DLS23, where horizontal beta is 35 m and dispersion is also zero. The second horizontal IPM, used to measure momentum spread, will be placed at DR113, where dispersion is 2.68 m and horizontal beta is 24.47 m. Separate horizontal and vertical designs are necessary because of the aspect ratio of the PD beam pipe. The collector arrays will consist of 64 strips with 1.0 mm spacing for vertical and 1.5 mm for the horizontal IPM. Electronic design and data handling could be similar to IPM's developed for the FNAL Booster [5].

15.4.5. Resistive Wall Current Monitor

To observe the evolution of bunch shape and phase through the acceleration cycle, a wide-band Resistive Wall Monitor (RWM) will be installed. The low frequency limit is about 3 kHz and is determined by the permeability and size of the core and the gap impedance. The gap impedance is well controlled to more than 5 GHz. The beam's electric field lines spread with an angle estimated by $1/\gamma$. This has the effect of limiting the RWM bandwidth to 1.9 GHz with 400 MeV beam. The microwave cut off frequency for the $5" \times 9"$ beam pipe is estimated to be 650 MHz. Above this frequency, microwave energy generated when the beam passes discontinuities will propagate through the beam pipe and contaminate the RWM signal. The elliptical shape of the beam pipe would cause "tails" on the RWM signal. A smooth transition from the elliptical pipe to the round RWM is recommended. Microwave absorber should be used in these transitions to attenuate spurious signals traveling along the beam pipe. Good quality cable such as 7/8" heliax should be used but kept as short as possible to minimize dispersion. A commercially available digitizer interfaced with the controls system will be used to perform general longitudinal measurements. The RWM signal will be used by the Sampled Bunch Display and by the Fast Bunch Integrator to automatically track bunch intensities and shapes [11].

The RWM should be located near the Low Level rf System to allow its use for the phase lock loop. This will insure the availability of an accurate low noise clock for measuring bunch-by-bunch intensities. The RWM would be useful for monitoring rf capture at injection as well as bunch compression at the extraction energy.

15.4.6. Fast Striplines

Two, one meter long, shorted, 50 Ω stripline BPM's should be installed for general-purpose diagnostics. The bandwidth will be limited by spreading of the beam's electric field and complicated above the 660 MHz cut off frequency of the beam pipe. The elliptical shape of the beam pipe suggests separate geometries for horizontal and vertical detectors. For 30° wide plates, horizontal plates should have a radius of 35 mm and vertical plates a radius of 205 mm to stiffen the plates and match the contour of the surrounding beam pipe. The striplines will be placed into a 9.5 inch × 5.5 inch elliptic stainless steel tube. Machinable ceramic such as Macor would be used for insulators because of its good electrical and vacuum properties. Type N vacuum feedthroughs will be used. Good quality cable such as 1/2 inch Heliax will transport the signal to hybrids located in the equipment gallery to produce sum and difference signals.

The striplines will be mounted in a 1.2 m section of beam pipe, as close to the equipment gallery as possible. It would be advantageous to have one region with circular beam pipe to install the wide band striplines and the RWM. Smooth transitions from the elliptical pipe to the round pipe could be used at both ends.

15.4.7. Tune Measurement

Tune measurements for both planes will be based on forced excitation of coherent transverse oscillations by a small angle kicker. An electrostatic pickup one-quarter betatron wavelength downstream of the kicker will monitor these oscillations. The tune system should work with a few tenths of a millimeter kick to avoid emittance growth. The Δ signal of the PU should have 250 kHz bandwidth centered between rotation harmonics. Considering the change in rotation frequency in the PD, using one of the lower rotation harmonics may be desirable. An FFT of 256 samples taken once per turn will provide 0.004 tune resolution. The amplitude of the FFT could be fed back to the kickers to limit emittance growth. The horizontal and vertical kickers will be one-meter long 50 Ω striplines.

15.4.8. Transverse Dampers

Transverse bunch-by-bunch active damping systems will be used to damp injection oscillations and coherent instabilities. Complete knowledge of the transverse impedance of the accelerator would be required to design a damper system with confidence. Without this, only a general approach can be considered [12, 13]. The dampers will consist of four basic parts: the stripline pick-ups, processing electronics, power amplifiers, and stripline kickers. Two important features are a 90° betatron phase advance between the

pick-up and kicker locations and a time delay through the processing electronics which matches the beam flight time. The betatron phase advance will depend on the tune of the machine. Arbitrary tunes can be accommodated by combining the output from two pickups 90° apart with the ratio required to simulate the ideal position. This ratio can be dynamically programmed to track the tune. To accommodate the 3.3 to 2.4 μs change in rotation period, the processing electronics must incorporate a compensating variable delay. Much of the energy in the pick-up signals is not associated with correctable transverse motion. To obtain the required damping gain without overdriving the amplifiers, notch filters designed to remove energy at the rotation harmonics are required. Digital filters clocked in synch with the accelerating rf are used to form the notch filters. One feature of this approach is that the notches and the delay automatically track the revolution period. An additional phase correction may be required to account for the frequency dependent phase shift from pickup and kicker cables. A damper gain of 200 V/mm, one-meter long stripline kickers, and 1.5 kW amplifiers are consistent with other damper systems. All of the coupled bunch modes are represented within a bandwidth of one half of the rf frequency. Solid state amplifiers with sufficient power, bandwidth, and gain are economical, commercially available, and easy to work with.

The wide band striplines, tune measurement kickers, damper pick-ups, and damper kickers are similar and could benefit from a single design. Their lengths could be adjusted as needed.

15.5. 16 GeV Extraction Line

As in the 400 MeV line, one BPM and BLM will be installed at each of the 65 quads in the 12/16 GeV line. Beam Profile Monitors (BPrM) will be installed at every other quadrupole and one Beam Current Transformer (BCT) will be placed at each end of the Line. BLM's and BPrM's will be similar to the 400 MeV line. BCT's and BPM's would be similar to those used in the PD ring.

Upstream of each extraction magnet and at the exit window, four BPM's will measure radial position during extraction. Two bi-plane movable beam profile monitors will be mounted upstream of the first septum and at the exit window. Three BLM`s will be placed downstream of each extraction magnet and one close to the exit window.

The four extraction BPM's and the upstream BCT should be able to resolve changes during the 2.4 μs extraction turn. Other devices would be sampled once per extraction.

15.6. Equipment Protection System

Personnel protection and radiation limits will be enforced by a separate and independent system not discussed here.

The purpose of the Equipment Protection System (EPS) is to protect equipment and provide a safe means of increasing beam intensity while starting up the accelerator. The EPS will monitor selected devices and signals and inhibit subsequent injections or abort the beam when they are out of tolerance. Beam could be aborted by steering it into the

collimator over several turns. Excessive beam loss, poor efficiency, bad vacuum, insufficient rf voltage, and key equipment status will likely be monitored. Indications of excessive coherent transverse oscillations from the damper or failures in the timing system may also be used. The EPS should be cast in hardware and consist of a permit loop with general purpose input chassis at key locations in the equipment galleries. The EPS system should respond in less than 100 μs. Hardware limits should be remotely controllable in a fashion easy to monitor and maintain.

Given the large power that can be delivered by the beam at high repetition rates, a hardware enforced, low intensity, low repetition rate mode of operation would be useful for turning the machine on or recovering from a trip. Different limits on loss and efficiency could be enforced while in this mode.

The controls system at FNAL has the ability to set alarms and limits on any device within the database. The value can be displayed in red, and/or alarmed and displayed on the alarm screen, and/or used to inhibit subsequent beam injection. This software system may take a few 15 Hz cycles to operate.

References

[1] T.Shea, J.Brodowski, R.Witcover, "Beam Position Monitoring in the AGS Linac to Booster Transfer Line", PAC`91, p.1428 (1991).

[2] R.Shafer, et al., "The Tevatron Beam Position and Beam Loss Monitor System", Proc. 12th Int. Conf. on HEA, p.609 (1983).

[3] http://www.bergoz.com

[4] J.Zagel, at al., "Fermilab Main Ring Ion Profile Monitor System", PAC`97, p.2166 (1997).

[5] J.Zagel, D.Chen, and J.Crisp, "Fermilab Booster Ion Profile Monitor System Using LabVIEW," AIP Conf. Proc.333, p.384.

[6] R.Connoly, et al., "A Prototype Ionization Profile Monitor for RHIC", PAC`97, 152 (2997).

[7] G.Aiello, M.Mills, R.Gonzalez, "Test Results of the SSC Log-Ratio Beam Position Monitor Electronics", PAC`93, p.2322 (1993).

[8] D.Cocq, G. Wismara, "From Narrow to Wide Band Normalization for Orbit and Trajectory Measurements," CERN SL-98- 063 BI.

[9] M.Kesselman, et al., "SNS Project-Wide Beam Current Monitors," EPAC`00, p.1750 (2000).

[10] K.Unser, "A Toroidal DC Beam Transformer with high Resolution", CERN-ISR-OP/81-14.

[11] J.Utterback, G.Vogel, "Fast Bunch Integrator. A System for Measuring Bunch Intensities in Fermilab`s Main Ring", Proc. ICALEPCS95, p.628 (1995).

[12] J.Crisp, et al., "A programmable High Power Beam Damper for the Tevatron", PAC85, p.2147 (1985).

[13] J.M.Steimel Jr. and D.McGinnis, "Damping in the Fermilab Booster", PAC93, p.2100 (1993).

Table 15.1. Instrumentation Summary

DEVICE/POSITION	QUAN-TITY	FEATURES	PROCESSING PARAMETERS, ACCURACY
400 MeV Line			
Position Monitors	89	Single plane stripline electrodes, L = 0.3 m	Integrated over injection, ± 0.5 mm
Intensity Monitors	2	BCT, 3Hz-20 MHz, 1 V/A, Integrating	Injection turn resolution, 0.1%
Profile Monitors	44	Movable single-plane grids, 48Be wires, 0.5 - 1.0 - 1.5 mm apart	Integrated over injection
	6	Slow single wire scanners, 3H+3V	0.5 mm resolution
	2	Ioniz. type, 1H+1V, MCP Ampl., 48 strips, 1.5 mm apart	Integrated over injection
Loss Monitors	89	Argon-filled Ion chambers, V = 0.11 cc	Integrated over injection
16 GeV Synchrotron			
Position Monitors	50H + 50V	Single plane elliptic electrostatic PU, at each quad, 100 mm length	Turn-by-turn measurements, ± 1.0 mm
Intensity Monitors	1	Fast BCT, 1.5 kHz-20 MHz, 5 V/A, 245 mm ID	Turn-by-turn measurements, 0.1% error
	1	DCCT, 245 mm ID	Resolution 10 μA, 500 Hz drift 5μA/24 h
Profile Monitors	2H + 1V	Ionization type, MCP Amplifier, 64 strips, 1 mm apart, L = 3 m	turn-by-turn time resolution
Loss Monitors	110	Argon-filled Ion chambers, V = 0.11 cc	Time resolution 0.1 ms
Wall Current Monitor	1	100 kHz – 0.6 GHz	1 GHz digital scope - based processing
Fast Striplines	2	1 m long, 50 Ω	Wide band diagnostics use
Tune Measurement	1H + 1V	Single plane elliptic electrostatic PU, 100 mm length, FEE	Resolution of 0.01 tune units, kick of a few tenths of a mm
Transverse Dampers	1H + 1V	Stripline, 1m long	Bunch-by-bunch active damping
12/16 GeV Line			
Position Monitors	4H	Single plane elliptic electrostatic PU`s	Bunch-by-bunch resolution, ±0.5 mm
	65	Single plane electrostatic PU`s	Integrated over spill, ±0.5 mm
Intensity Monitors	2	Fast BCT, 5 V/A	Bunch-by-bunch resolution, 0.1%
Profile Monitors	2	Movable bi – plane grids, 48H+48V wires, 1mm apart	Integrated over spill
	34	Movable single plane grids, 48wires, 1 mm apart	Integrated over spill
Loss Monitors	69	Argon-filled Ion chambers, V = 0.11cc	Integrated over spill

Chapter 16. Control System

Jim Crisp, Sharon Lackey, Mike Shea and Bob Webber

16.1. Overall Architecture of Fermilab Controls

The overall architecture of Fermilab control systems follows the standard design shown in Figure 16.1. Individual Front End Computers that control accelerator hardware are networked to each other, to console computers, and to various Servers using a Local Area Network. The network connections contain 10 MHz, 100 MHz, and 1 GHz Ethernet segments and switches and routers as needed, so that Control Room Consoles may access data for all the accelerators. Fermilab device naming convention is a single letter that designates the machine where the device is located, a colon, and a 6-character device name. Accordingly, Proton Driver devices will be of the form **P:devnam**, where the P: indicates that devices reside in the Proton Driver.

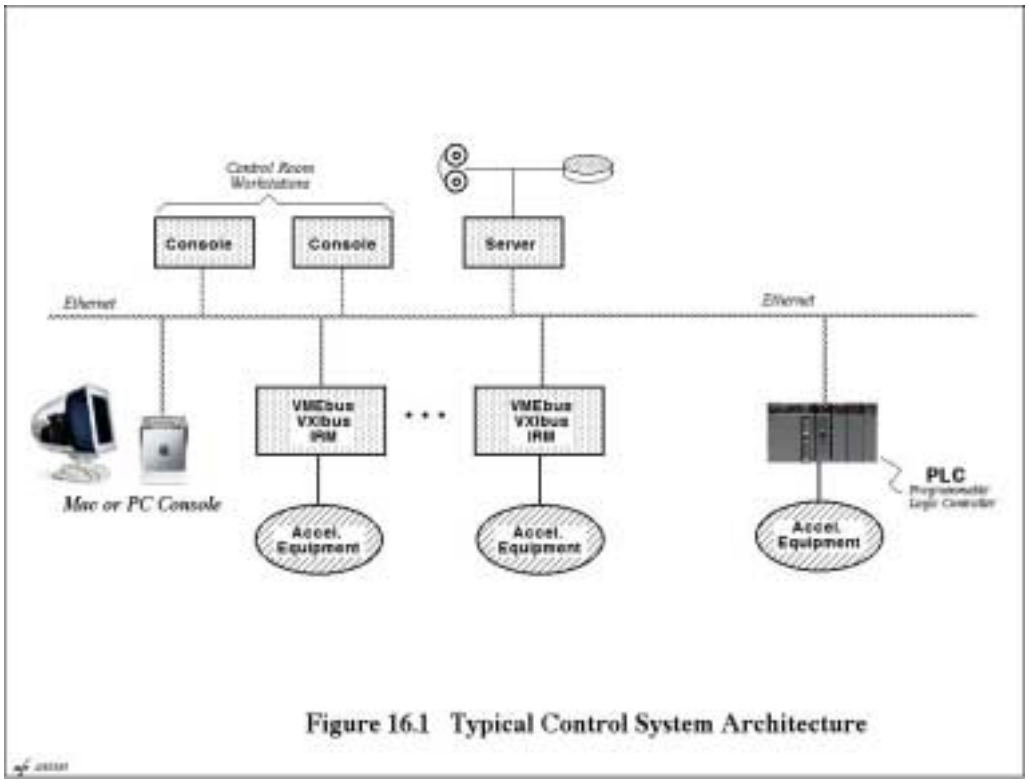

Figure 16.1 Typical Control System Architecture

To the Fermilab Control System, the Proton Driver must appear as one more accelerator in the complex. It will be operated from the Main Control Room, and data from the Proton Driver will be presented on console displays along with data from other Fermilab accelerators. Therefore, the Control System for the Proton Driver will be very similar to control systems for other machines and will use much of the same hardware and software. Although control system hardware changes rapidly, the description in this report assumes that the Proton Driver control system will be built using today's technology and products.

16.1.1. Compatibility with existing Controls

The Proton Driver controls will be organized in the same way as control systems for the other Fermilab accelerators. Parameter information will be stored in the central database, displays will be handled by the same console computers, Front End computers will connect to the accelerator hardware and requested data from the Front End computers will be sent to the console computers as needed.

16.1.2. 15 Hz Considerations

The Proton Driver is a 15 Hz machine, and data acquisition must operate synchronously at that repetition rate. Because the existing Linac control system Front End computers operate synchronously at 15 Hz, that design will be used throughout the Proton Driver. Each 15^{th} of a second, analog and digital data is read from the hardware by the Front End and made available to remote requestors. Analog data is scanned to find readings that are in alarm, that is, readings that differ from the nominal value by more than a selected tolerance. Similarly, digital readings that are not in the nominal state are considered to be in alarm. Parameters that are newly in alarm are reported to the central computers each cycle. Each parameter can be set to cause a Beam Inhibit when it is found to be in alarm.

The beam inhibit function will be useful to limit the amount of beam loss during commissioning and later in operation. When a beam inhibit occurs, it will be latched for a time that can be set by the operator. This will allow the operator to shorten the inhibit time when the machine is operating at lower current levels or at the reduced repetition rates often used during commissioning.

16.1.3. Front End Computers

The Front End computers are based on a Motorola VMEbus-based single board computer, MVME2400. VxWorks is used as the real-time operating system, the operating system that is the Fermilab standard for Front End computers. Linac Front End computers include all the software needed to control a 15 Hz machine. Each cycle, the signals from equipment attached to the system are read and stored in a local database. Remote computers may request data from the Front End computers to be returned at selected intervals up to and including 15 Hz. Because the data are read once per cycle and kept in a local database, multiple remote hosts that request the same data get exactly the same values. The local database for each Front End includes the name of the channel and the data necessary to convert the raw reading into engineering units. Also, each channel may be monitored, in which case the nominal value and tolerance are also stored locally. Fixed data, including the most recent settings, are stored in the non-volatile memory. At power-on time, the local station knows the most recent settings and can restore these settings, both analog and digital, to the hardware.

Each Front End controls different equipment and typically has different tasks to perform, such as closed loop regulation of special devices. To accommodate these

differences, Front Ends allow for small, separately compiled programs, called Local Applications, to be downloaded and stored in the non-volatile RAM. These programs can be triggered to run each 15^{th} of a second. Such programs are used in the Linac to regulate rf gradients and to control the gas flow in the ion source.

16.1.4. Network

Ethernet is the network used for all Fermilab accelerators. Each VMEbus CPU card includes a 10/100 MHz Ethernet port. Category 5 cabling will connect each CPU to a separate port on a local Ethernet switch. The uplink from individual switches will be concentrated in another 100 MHz switch that has a 1 GHz uplink connection that will connect to a router in the Computer room by way of a single-mode fiber.

16.2. Data Acquisition Hardware

Wherever possible, the Proton Driver will use some of the same data acquisition hardware used in other Fermilab accelerators. A variety of hardware exists and can be replicated as needed for various parts of the Proton Driver.

16.2.1. Internet Rack monitor

For many locations an Internet Rack Monitor, IRM, will be used. This device includes a short VMEbus card cage, the MVME2400 CPU card, a 64 channel A-D, 8 D-A outputs, and eight bytes of digital I/O, all contained in a 3U chassis. This forms a stand alone Front End that attaches to the network using the Ethernet port provided on the CPU card. Additional digitizers, D-As, and VMEbus cards may be added as needed.

16.2.2 Hot-link Rack Monitor, HRM

A recently developed digitizer system allows for 64 analog inputs, each sampled and digitized at a 10 kHz rate. The HRM is a self-powered remote chassis that connects to a PMC receiver card in a VME bus Front End computer. Communication between the PMC card and the HRM chassis uses a high-speed serial connection, Hot-link, with a serial bit rate that can be selected as 160 or 320 MHz. Individual HRM registers, such as digital I/O and D-A registers appear as PCI memory locations to the VME bus host computer. The analog subsystem autonomously reads all 64 channels at 100 μs intervals, and sends the results to the PMC interface card, where analog data is stored in a circular buffer memory. Two megabytes of RAM are used for the buffer, enough to hold 16K sets of readings for all 64 channels. Old data is overwritten by new data after 1.6 seconds. Remote hosts may request data about any group of channels to make fast time plots at sample rates of 10 kHz or slower. This is fast enough to examine power supplies for ripple and to examine the envelope of rf and beam related parameters during the 38 ms acceleration cycle, for example.

The HRM can also accommodate one daughter board designed for some special purpose. An example daughter board is an 8-channel quick digitizer that can record signals at digitizing rates up to 10 MHz. These can be used to make snapshot recordings of signals such as BPM and Beam Toroids in the transport lines and Linac related signals. Up to 16k samples per channel are recorded. The digitize trigger can be set at regular intervals or can be provided externally to synchronize the digitizer to external events such as the beam revolution period. The HRM system also includes 8 analog D-A output signals that can be used as analog reference voltages for power supplies. Additional analog outputs can be provided by installing commercially available modules in VME bus crates. VME bus cards, Industry Pack or PMC mezzanine modules are typically used for this purpose.

16.2.3. Digital I/O

Eight bytes of digital I/O are included in each digitizer system. These can be configured by the byte as either input or output and used for digital control outputs and digital status inputs. As with the analog output signals, mezzanine modules or VMEbus cards may be used to expand the amount of digital I/O.

16.2.4. Programmable Logic Controllers

Programmable Logic Controllers, PLCs, provide a cost-effective method for interfacing to some types of external hardware. These devices have been used at Fermilab to control equipment such as power supplies and ion sources. A variety of commercial analog and digital interface modules are available. The PLCs are nodes on the control system Ethernet network and can be programmed and monitored over the network.

PLCs are particularly useful for controlling stand-alone systems and high availability systems that are best configured to be independent of the control system's Front End computer. Programming of the PLCs can often be done by the group that is responsible for a given system. Simple shared-memory protocol between the PLC and the Controls Front End computer allows control and monitoring of the PLC-based systems by storing settings and reading values within the PLC's memory space.

16.2.5. Power Supply Controls

It is assumed that the power supply - controls interface is the same as the Fermilab standard that provides for ON-OFF-RESET commands using isolated relay contacts, one byte of digital status readback, analog readback signals for both power supply current and voltage, and an analog input. For a programmable power supply, an appropriate waveform would be provided to the analog command input. For power supplies that require 15 Hz waveforms, the program voltage will be generated from a 1-2k word memory that is sequentially output through a digital to analog converter. Calculation of the waveform data will be done in an upper level computer and downloaded to the Front End computers as needed. The waveform generators will be packaged with 8 channels

contained on a single VME bus board. Multiple Waveform Generator boards will be installed in Front End computers.

Digital control of the power supplies requires commands for ON, OFF, and RESET using momentary relay contact closures or openings. A 2-byte digital I/O connector from an IRM or an HRM will connect to a power supply interface fanout chassis. This chassis can accommodate 16 power supplies. Two such chassis can be attached to an IRM, the limit being the 64 analog channels available.

16.2.6. Event Clock, TCLK

Event timing for accelerators is distributed within the Fermilab complex using TCLK, a system that has 8-bit events encoded on a 10 MHz pulse train. Fanout chassis provide clock signals to equipment where timing information is needed, and the clock signal is decoded internally in equipment using programmable gate array logic. Most pulsed devices can be triggered by pulses programmed to appear at a time that is set as a delay following a selectable event. The minimum time resolution is 100 nanoseconds.

16.2.7. Beam Sync Clock

In addition to the event timers that use TCLK, there is a need for a Beam Sync clock. This clock will be generated by the Low Level RF system, and it would be used by the beam instrumentation systems to trigger the digitizer cycles to acquire turn-by-turn data from the circulating beam.

16.3. Linac Controls

Modifications to the Linac will require a modest increase in the Linac control system to accommodate the new ion source, the RFQ, and the associated beam instrumentation. This part of the project resembles the PET project that was done at Fermilab a few years ago. One IRM will be located at Ion Source potential, connected to the ground based Ethernet switch using a fiber optic Ethernet link. Other IRMs will be used for the RFQ, the LEBT, RF systems, instrumentation, and the first drift tube Linac tank. Details of the Controls and beam instrumentation for the Linac improvement can be found in Chapter 13, Section 13.8.

16.4. Controls for the 400 MeV Transport Line

Controls for the 400 MeV line include the control and monitoring of the beamline power supplies have not yet been done. Data acquisition from the beam instrumentation is listed in Chapter 15.

16.5. Synchrotron Controls

16.5.1 Ring Magnet Power Supply

Control of the ring magnet power supply will be similar to the technique used in the Main Injector. An embedded processor will try to match the requested field using the measured transfer functions, and a learning mode will help improve the accuracy. This system will be structured as a controls coprocessor inserted in the VMEbus crate containing the magnet regulator system. Using shared memory communication, the Controls processor will provide the ring magnet controller with the requested amplitude and phase of the 15 Hz and the 30 Hz components of the field.

16.5.2. Correction Element Controls

Each correction element will be driven by an analog waveform that is input to each correction element power supply. A multi-channel waveform generator will be designed for this purpose. It will be a VMEbus card that controls eight correction elements. Each channel will have a 1 k word buffer that will be played out each 15 Hz cycle. The digital waveform can be modified from the control room and downloaded to the appropriate correction element.

16.5.3. Sextupole correction

Control of the sextupole magnets will be the same as that used for other correction elements in the ring. There are 2 sextupole current busses each powered by a separate programmable power supply.

16.6. RF Controls

16.6.1. Low Level RF

The Low Level RF system, LLRF, will be configured as a VXI crate that contains its own processor board. Connection to the control system will be made using an additional Controls processor board, mounted in the VXI crate, that has shared-memory access to the Low Level settings and readings. The Controls processor functions as a normal Front End to provide communication with the central control system. LLRF data read by the Controls processor and settings sent to the Low Level system will appear the same as communications with any other Front End. The addition of the Controls processor completely separates the control system functions from the Low Level functions performed by the LLRF processor. This technique has been used in the klystron area of the existing Linac.

16.6.2. High Level RF

The control system connection to the High Level rf systems, HLRF, will be made using an Internet Rack Monitor. This type of interface is used in the existing Booster HLRF systems. For Stage 1, much of the Booster HLRF systems can be reused.

16.7. Water System Controls

The LCW system will be controlled by PLCs as needed. These PLCs will be connected to Ethernet. A Front End computer will control their operation. This configuration isolates the water system from power interruptions to its Front End computer.

16.8. Vacuum Controls

Vacuum controls for the Proton Driver will be the same as those used in other accelerators at Fermilab. Although these vacuum systems use proprietary hardware, both hardware and software exist and can be replicated for the Proton Driver. The hardware consists of a card cage, called a CIA crate that connects to the Front End using Arcnet. Existing cards for this system include digitizers to read parameters such as ion pump currents, Pirani gauges, and ion gauges, and cards that handle the logic to control the opening of sector valves. The Front End software for this system also exists.

16.9. Diagnostics Interface

Signals from beam instruments will be processed to present signal levels on the order of a few volts so the standard Controls A-Ds can be used. Signals that are slowly varying can be digitized directly; faster pulses will require sample-and-hold amplifiers. If the shape of pulsed signals is needed, A-D inputs with sampling rates up to 10 MHz are available. Very fast signals, such as wall current monitors, will need to be digitized in a fast digital oscilloscope.

16.10 Commercial Instrument Interface

16.10.1 IEEE-488

In some cases, commercial instruments need to be connected to the control system. Older instruments that use IEEE-488 will be connected using a device like the National Instruments ENET module. This device receives Ethernet messages and outputs them as IEEE-488 commands.

16.10.2 Ethernet

Recently, commercial instruments have become available that use Ethernet as the connection to external systems. If there is a choice, Ethernet is preferred over IEEE-488.

16.11 Software

Much of the existing Fermilab control system software is directly usable for the Proton Driver. The standard control room parameter pages and plotting packages can be used without modification. However, some new programs specific to the Proton Driver will be needed.

16.11.1. Front End Software

Additional local applications will be needed to perform regulation of the RFQ gradient, the ion source operating characteristics, and so forth, but most of the core functions of the Front End software will be needed and can be used without modification.

16.11.2 Console Application programs

A few new application programs will be needed to control and display information about Proton Driver systems. These include applications for the RFQ, transport line tuning, rf systems, injection and extraction.

16.12 Beam Permits, Beam Inhibit, e-Berm

Personnel safety for the Proton Driver will be overseen by the Fermilab ES&H Department. For operator aid and convenience, the control system's ability to inhibit beam will be used. This capability can help limit the amount of beam lost, particularly during the commissioning period.

16.13. R&D Program

During the R& D phase of the Proton Driver program, two VME bus cards should be developed: an 8-channel waveform generator and an 8-channel quick digitizer.

Although the IRM and the HRM support 8 channels of 10 MHz digitizers, some locations in the ring will need many more channels. If the digitizer is built as a VME bus card, many more channels can be accommodated in a single VME bus crate.

Similarly, many correction element waveforms will be needed at specific points in the ring. Given an 8-channel waveform generator card, a VME bus crate can contain all the waveform generators needed at these locations.

In addition to these, a power supply interface fanout chassis could be designed and built during the R&D phase of the project.

Chapter 17. Civil Construction

Russ Alber, Tom Lackowski, Jeff Sims

17.1. Introduction

This Chapter outlines the conventional facilities required to house and support the proposed 16 GeV, 1 MW rapid cycling Proton Driver. Enclosures to house injection and extraction lines are also required. An enclosure from the existing 400 MeV Linac will be required to inject beam into the Proton Driver. In addition, an enclosure is necessary to carry the 16 GeV extraction line from the Proton Driver to the Main Injector.

The project is separated into two distinct phases. Phase I includes construction of the machine as outlined above. In Phase II the beam power is upgraded to 4 MW as required by the Muon Collider. This report only addresses facilities required in Phase I.

The existing 400 MeV Linac will be reused with technical upgrades at the beginning of the Linac. A future (Phase II) Linac expansion will be required to increase the linac beam energy by 600 MeV and a Pre-Booster to increase the injection energy to 3 GeV.

17.2. Overview of Civil Construction

Civil Construction, for the Proton Driver includes all below-grade beamline enclosures. All above-grade buildings, roads, parking, primary utilities, and primary services to accommodate the equipment for the operation of the Proton Driver on the Fermilab site are also included.

The cost estimate for the civil construction has grouped elements in a logical sequence as well as by facility function or type of construction work involved. While the cost estimate organization presents a reasonable construction scenario, it probably will not be identical with the actual subcontract packages, nor is the final schedule of construction inflexible.

17.2.1. Site Construction

17.2.1.1. Wetland Mitigation - all required compensatory floodplain construction.

17.2.1.2. Site Work and Utilities - Survey monuments, temporary power, construction access roads, tree protection, stream diversion, power and communication duct banks, 13.8kV power feeders, and underground utilities including industrial cold water (ICW), primary cooling ponds, domestic water, sanitary sewer, chilled water supply and return, and final paving of all roads and hardstand areas.

17.2.1.3. Landscaping - includes construction yard removal, signage, site landscaping, and soil erosion control.

17.2.2. Facilities Construction

17.2.2.1. Proton Driver Enclosure - Conventional below grade cast-in-place enclosure constructed to house the Proton Driver.

17.2.2.2. Injection Enclosure - Conventional pre-cast enclosure constructed to house the Injection beamline to the new Proton Driver enclosure. *A portion of this work must be accomplished during Booster beam off conditions.*

17.2.2.3. Extraction Enclosure - Conventional pre-cast enclosure constructed to house the Extraction beamline from the new Proton Driver to the Main Injector enclosure. *A portion of this work must be accomplished during Main Injector beam off conditions.*

17.2.2.4. Proton Driver Service Gallery - An above grade service building used to house support equipment for the Proton Driver Enclosure.

17.2.2.5. Utility Support Building - An above grade utility building used to house equipment for process cooling equipment for the Proton Driver Enclosure.

17.2.3. EDI&A

17.2.3.1. EDI&A - Consists of all Engineering, Design, Inspection, and Administration costs associated with the construction aspects of the project.

17.3. Detailed Facilities Descriptions

Construction of the Proton Driver Enclosure, Extraction Enclosure, Injection Enclosure and above grade service buildings is similar to previously utilized and proven construction methods at Fermilab. Construction of all below-grade enclosures consists of conventional open cut type construction techniques. The architectural style of the new buildings reflects, and is harmonious with, existing adjacent buildings. Currently, the layout has been optimized for the accelerator. Future layouts will consider existing topography, watersheds, vegetation, natural habitat, and wetlands. All these aspects will be thoroughly addressed in the Environmental Assessment for the project.

Safety provisions for radiation, fire protection and conventional safety are included in this report. Energy-efficient construction techniques will be incorporated into all new structures. Quality assurance provisions will be part of all project phases including conceptual, preliminary, and final design, construction, and construction management.

17.3.1. Site Construction

17.3.1.1. Wetlands Mitigation

Detailed and specific definitions of the wetland area, floodplain and storm water management, archaeological concerns and ecological resources will be identified by environmental consultants resulting in the preparation, submittal and approval of a Floodplain/Wetland Assessment Report and an Environmental Assessment. All required permits will be obtained prior the start of construction. See Chapter 18 for environmental considerations.

After the environmental consultants report, modifications may be made on the location of roads, utilities or siting of structures to minimize the impact on the environment while still retaining the ability to construct in a cost effective manner.

17.3.1.2. Site Work and Utilities

Site Drainage will be controlled by ditches and culverts while preserving the existing watershed characteristics both during construction and subsequent operation. Permanent stream relocation of a portion of Indian Creek may be required.

Minor road construction is anticipated for this project. Existing Kautz Road adjacent to the antiproton complex will be out of service for the length of time required to construct the Injection Enclosure. A temporary road will need to be installed to facilitate adequate traffic flow. Parking lots will be required at the Proton Driver Support Buildings.

Power, communications, and chilled water supply and return will tie in to existing systems at the intersection of Main Injector Road and Kautz Road. These utilities will extend up to the Site.

Industrial Cold Water (ICW) will tie into existing utilities at the corner of Kautz and Giese Roads. Primary cooling water will be taken from surrounding existing ponds and one proposed new 20 acre cooling pond.

Sanitary Service (SAN) and Domestic Water (DW) will tie into existing utilities at the intersection of Kautz and Giese Roads.

Natural gas will tie into an existing gas line running along Giese road.

Excess and unsuitable spoil from the construction of the underground enclosures and caverns will be stockpiled on the Fermilab site in an appropriate manner. This material will then be used as nonstructural backfill for future projects.

17.3.1.3. Landscaping

Construction yards will be removed after completion of the construction phase of the project. All disturbed areas will be returned to a natural state or landscaped in a similar manner as found at other Fermilab experimental facilities. Erosion control will be maintained during all phases of construction.

17.3.2. Facilities Construction

17.3.2.1. Proton Driver Enclosure

The Proton Driver Enclosure is a cast in place enclosure 16-ft wide and 9-ft tall with approximately 24.5-ft of equivalent earth radiation shielding (26-ft at all buildings). See attached sketches for location and dimensions.

17.3.2.2. Injection Enclosure

The Injection Enclosure is a conventional below grade 10-ft wide by 8-ft tall precast concrete enclosure with a depth profile as shown in Figure 17.2. This enclosure will house the beamline components necessary to transport the 400 MeV beamline from the existing Linac to the Proton Driver Enclosure.

17.3.2.3. Extraction Enclosure

The Extraction Enclosure is a conventional below grade 10-ft wide by 8-ft tall precast concrete enclosure under approximately 24.5-ft of equivalent earth radiation shielding. This enclosure will house the beamline components necessary to transport the 16 GeV beamline from the Proton Driver to the Main Injector. The existing 8 GeV transport line enclosure will be utilized to continue the 16 GeV beamline to the existing Main Injector.

17.3.2.4. Proton Driver Service Gallery

The proposed Proton Driver Service Gallery will consist of three above grade metal frame and wall panel buildings that house the equipment necessary to supply power, instrument and control the beamline components housed in the Proton Driver enclosure located below and adjacent to the service buildings. The four figures, 17.1 - 4, show building locations and dimensions. Total area of building(s) is approximately 108,000 sq-ft.

17.3.2.5. Utility Support Building

The Utility Support Building will be located in the center of the Proton Driver Service Gallery Campus. The above grade metal frame and wall panel building will house the equipment required for heat rejection and electrical distribution including chillers, pumps, and transformers. Total area of building is approximately 53,000 sq-ft.

17.4. Requirements and Assessments

17.4.1. Safeguards and Security

Security issues related to the design of the facilities will be compatible with the current operating procedures found at other experimental sites and other components of the Fermilab Accelerator complex.

All above grade structures will be accessible to authorized personnel during beam on conditions. The below grade beamline enclosure will not be occupied during beam on conditions and will be interlocked in accordance with Fermilab operating procedures. Access will be allowed in these areas only during beam off conditions either as controlled access or supervised access depending on the beam shutdown conditions.

17.4.2. Energy Conservation

All elements of this project will be reviewed for energy conservation features that can be effectively incorporated into the overall facility design. Energy conservation techniques and high efficiency equipment will be utilized wherever appropriate to minimize the total energy consumption of the buildings.

Design of mechanical and electrical systems, as well as architectural elements, conform to the requirements of the Fermilab Necessary and Sufficient Standards and the Fermilab Environmental, Safety and Health Manual (FESHM).

17.4.3. Health and Safety

17.4.3.1. Life Safety

Exiting for the facilities will be provided in accordance with NFPA 101 Life Safety Code to assure adequate egress in the event of an emergency. The buildings will also be provided with fire detection and suppression systems appropriate for the intended use of the buildings.

17.4.3.2. Safety Analysis Report

An in depth, internal safety analysis review will be conducted for this facility construction project prior to its operation. Based on this analysis, Fermilab will prepare a Preliminary Safety Analysis Document (PSAD), per draft DOE Order 5480.ACC (titled "Safety of Accelerator Facilities"), or a Safety Analysis Report (SAR), per DOE order 4700.1. The facility will not be operated until either a Safety Analysis Document (SAD), or a SAR is prepared and approved.

17.4.4. Environmental Protection

The overall environmental impact of this project is being evaluated and reviewed as required to conform to all applicable portions of the National Environmental Policy Act (NEPA). To initiate this evaluation, an Environmental Notification Form (CH 560) will be written for this project.

17.4.5. Decontamination and Decommissioning

Decontamination and Decommissioning procedures are an important part of Fermilab environment, safety and health policies. These policies are described in Chapter 8070 of the Fermilab Environment, Safety and Health Manual.

17.4.6. Quality Assurance

All aspects of this project will be periodically reviewed with regard to Quality Assurance issues from Conceptual Design through Title III completion. This review process will be completed in accordance with the applicable portions of the Fermilab Institutional Quality Assurance Program (FIQAP). The following elements will be included from the Fermilab Quality Assurance Program for the design and construction effort:

- An identification of staff assigned to this project with clear definition of responsibility levels and limit of authority as well as delineated lines of communication for exchange of information.

- Requirements for control of design criteria and criteria changes and recording of standards and codes used in the development of the criteria.

- Periodic review of the design process, drawings and specifications to insure compliance with accepted design criteria.

- Identification of underground utilities and facility interface points prior to the commencement of any construction in affected areas.

- Conformance to procedures regarding project updating and compliance with the approved construction schedule.

- Conformance to procedures regarding the review and approval of shop drawings, samples test results and other required submittals.

- Conformance to procedures for site inspection by Fermilab personnel to record construction progress and adherence to the approved contract documents.

- Verification of project completion, satisfactory system start-up and final project acceptance.

17.4.7. Telecommunications

The existing Fermilab telephone communications network will be extended to provide normal telecommunication support to the new addition. Operations at this facility will not require enhanced systems.

17.4.8. Handicapped Provisions

The applicable requirements of the Americans with Disabilities Act (ADA) and the Americans with Disabilities Act Accessibility Guidelines (ADAAG) will be incorporated into the design of this project. Compliance with the ADA will be based upon an evaluation of the job descriptions and required tasks for the personnel assigned to work in these buildings. Those areas of the facility that will require accessibility as well as the established routes to those areas will be designed in full compliance to the existing statute.

17.4.9. Emergency Shelter Provisions

Provision for protection of users of the facilities, in the event of a tornado or other extreme weather conditions, will be taken into consideration. Guidelines established by the Federal Emergency Management Agency (FEMA) in publications TR-83A and TR-83B and referenced in Section 0111-2.5, DOE 6430.1A, will be used to select a safe area within each facility, for the protection of the building occupants. These protected areas will be identified by directional signage and will also serve a dual-purpose space with regard to protection during a national emergency in accordance with the direction given in Section 0110-10, DOE 6430.1A.

17.5. Estimated Schedule for Civil Construction

The following schedule is predicated on the assumption that a funding profile to match the construction needs will be established and maintained. This schedule has been developed without consideration to the accelerator operation schedule. Work requiring accelerator beam off conditions is assumed to be accomplished during normal scheduled accelerator shutdowns.

	DURATION
Conceptual Design Complete	TØ - 0.25 yrs
Start Title I	TØ
Complete and submit Environmental Assessment	TØ + 0.25 yrs

Approved Finding of No Significant Impact	TØ + 0.50 yrs
Submit ACOE 404 Permit Application	TØ + 0.50 yrs
Title I Complete, Approval to start Title II	TØ + 1.00 yrs
Obtain ACOE 404 Permit	TØ + 1.50 yrs
Approval to Start Title III (Start Construction)	TØ + 1.75 yrs
Underground Enclosures Complete	TØ + 2.50 yrs
Above Grade Buildings Complete	TØ + 3.25 yrs
Civil Construction Complete	TØ +3.40 yrs
Shielding Assessment Approved - Project Complete	TØ +3.50 yrs

17.6. Cost Estimate Model

A cost estimate for the civil construction part of the project is included in Table A.1. Unit costs are in FY 2000 dollars. Site work and underground enclosures are based on ratios of past projects and buildings are based on square-foot costs. At this stage, the uncertainty in the cost estimate is ±40 percent. At the project definition stage of development, there will be a bottom-up cost estimate with an associated contingency of 25 to 30 percent. Further development of a conceptual design and baseline report will include a contingency of 20 to 25 percent.

17.6.1. Basis For Design

The following information is used in the formulation of this report:

1. Beamline optics program output

2. Design sketches, Figures. 2.1, 2.2 and Figures 17.1-4. It is assumed that all construction will be done using competitive bid fixed priced contracts.

3. Meetings with the Proton Driver Project Group

4. Previous projects and designs

Following are additional comments and explanations for the cost estimate appearing in Appendix A (Table A.1).

Geotechnical investigation, environmental, and material testing costs are estimated for all phases of work. Administration of testing services is included in the EDIA costs.

The cost of the Shielding Assessment Documentation is included in engineering, design, inspection, and administration.

Escalation has not been included in the cost summary and is to be added by the reviewer.

Overhead and Profit by the subcontractor is taken as 20%. This accounts for some upswing in the construction industry over the next several years.

Engineering, Design, Inspection and Administration (EDIA) are consistent with the DOE and Fermilab guidelines. Costs include A/E administration, design data input, project review and project administration.

The total EDIA applied to the project is 21% as shown in Table 17.1.

Table 17.1. Breakdown by the various phases of design

	Fermilab Engineering	Consulting A&E	Percent of total construction
PDR and CDR	3.0%	1.0%	4.0%
Title II	1.0%	10.6%	11.6%
Title III	2.4%	3.0%	5.4%
TOTAL	6.4%	14.6%	21.0%

The cost estimate is based on conventional underground excavation and soil support techniques. The costs have been developed without the completed geotechnical report, which was not available at the time of this estimate.

The cost for utilities, power and process systems for experimental equipment have been restricted to the secondary distribution only with the primary distribution costed elsewhere. Process water (CLCW and LCW) is estimated elsewhere as well. HVAC, utilities and conventional power for building systems have been included in the estimate.

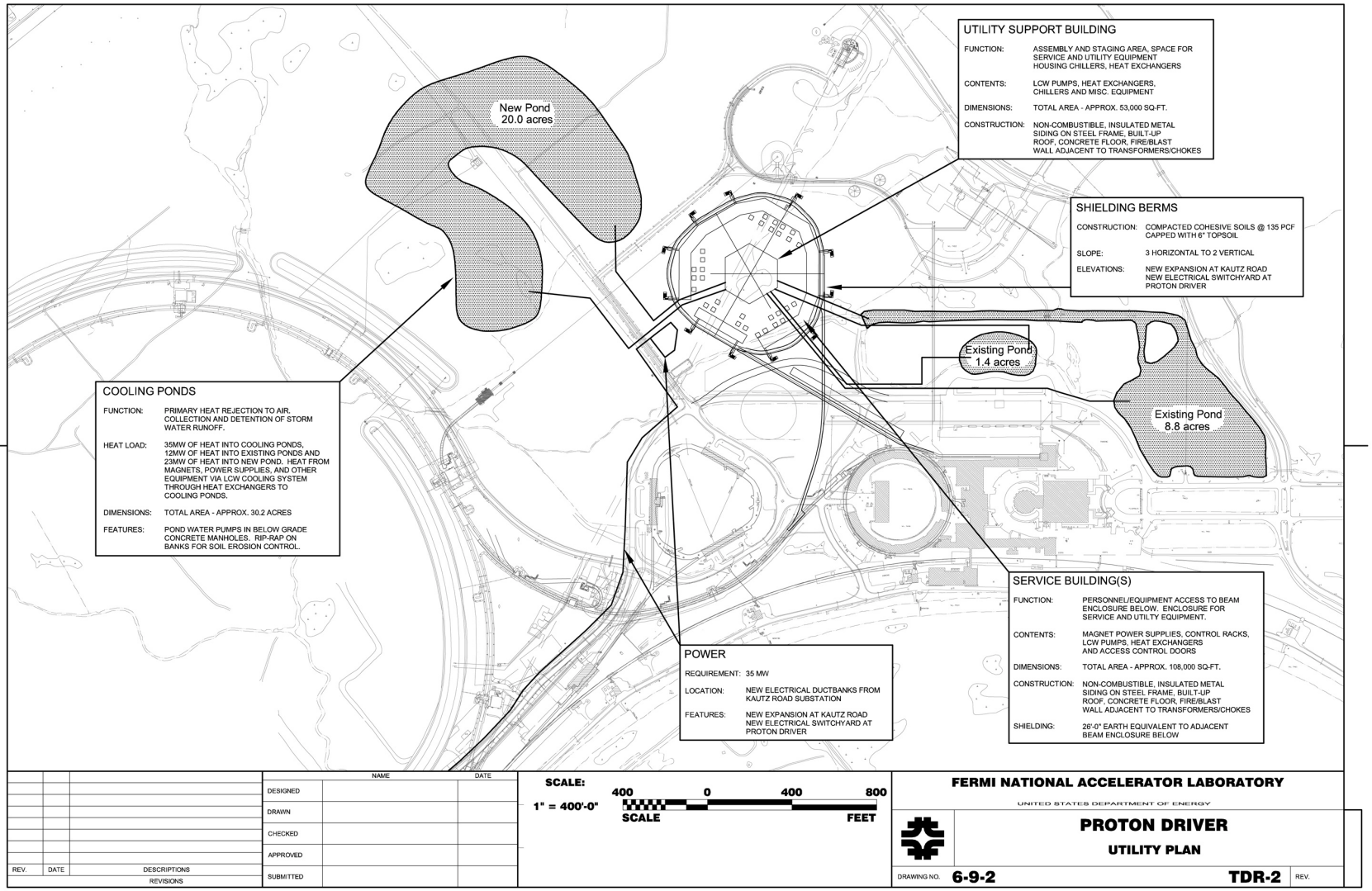

Figure 17.1. Proton Driver Utility

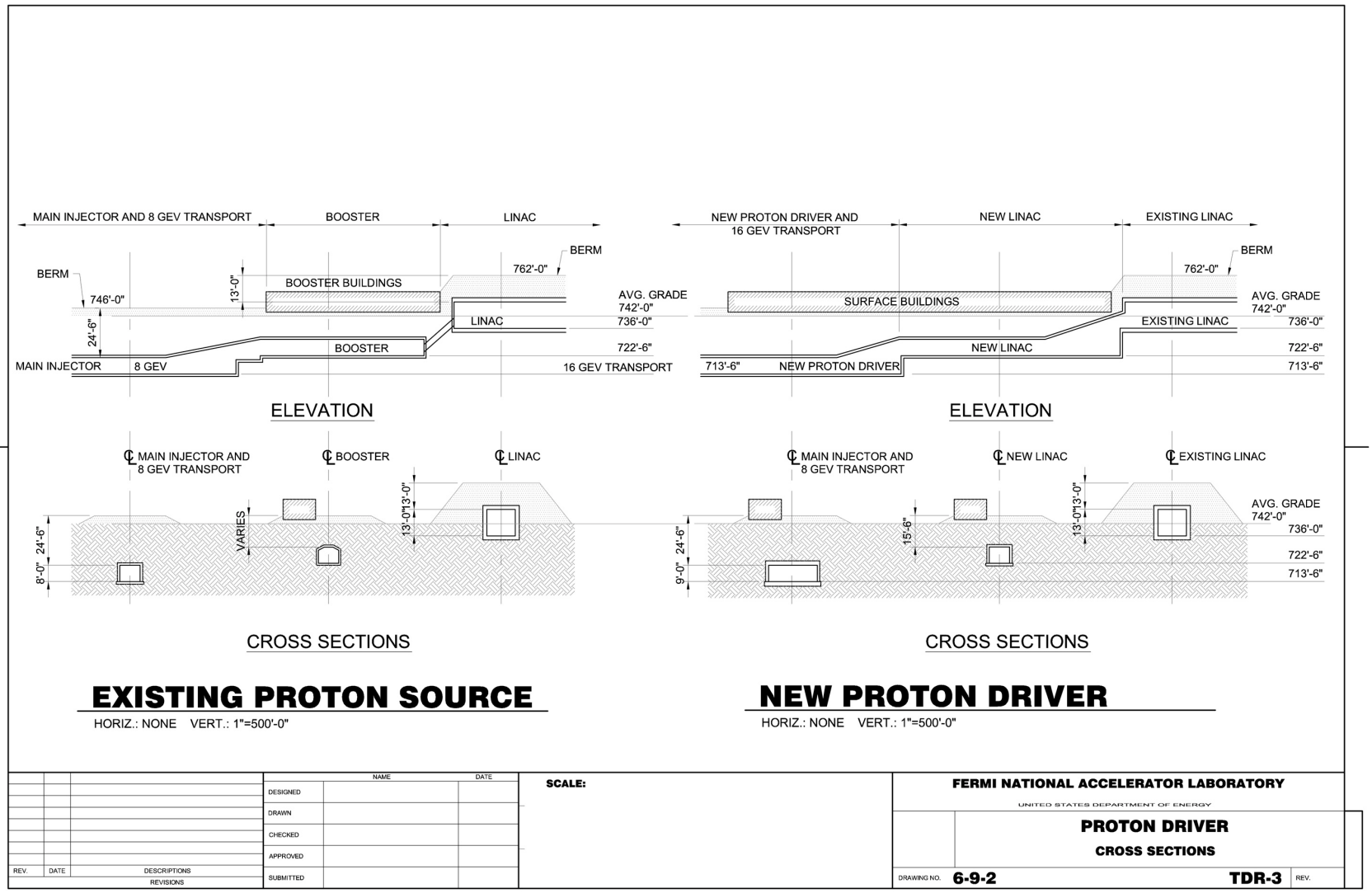

Figure 17.2. Proton Driver Elevation

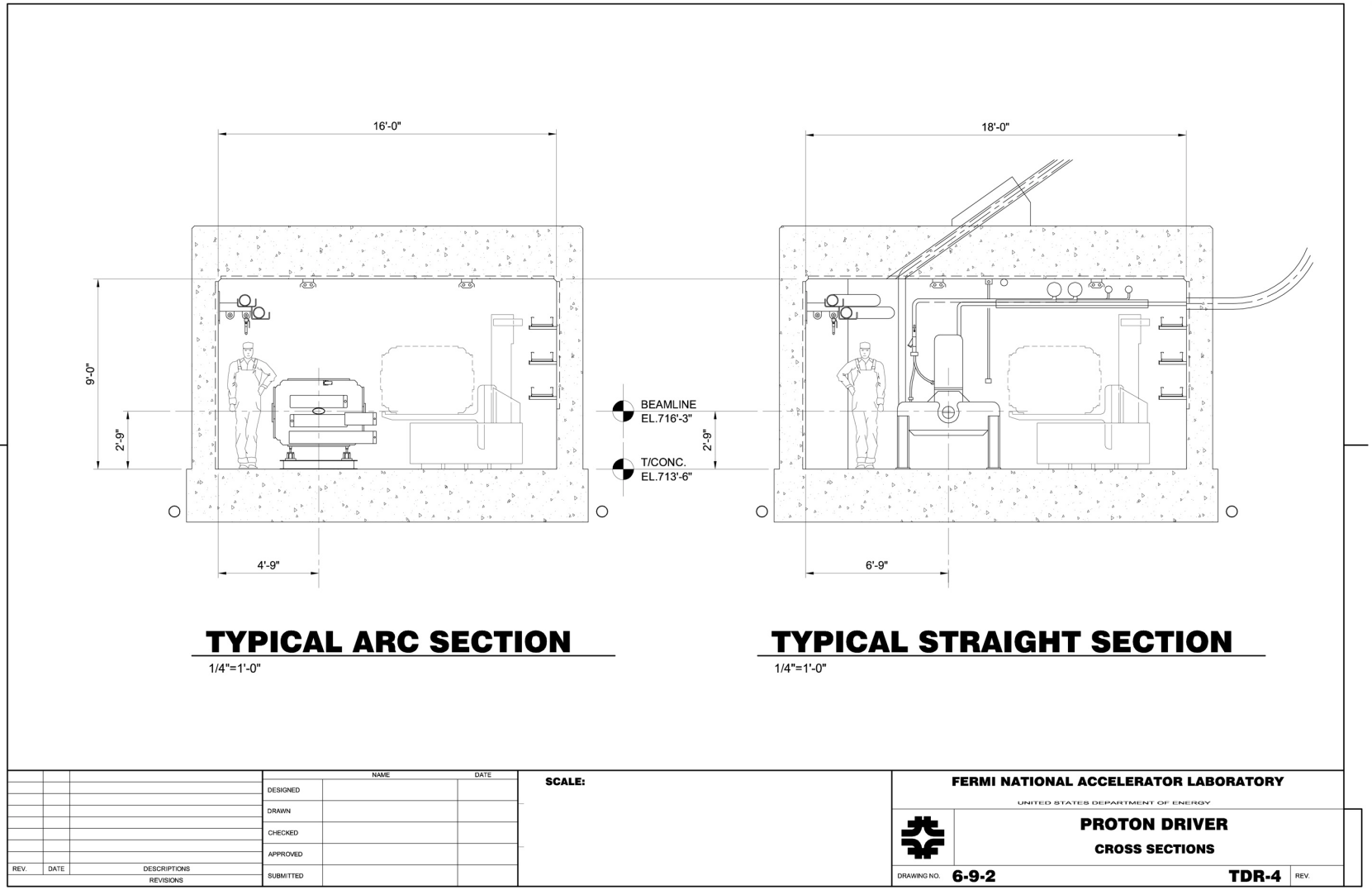

Figure 17.3. Proton Driver Enclosure Cross Sections

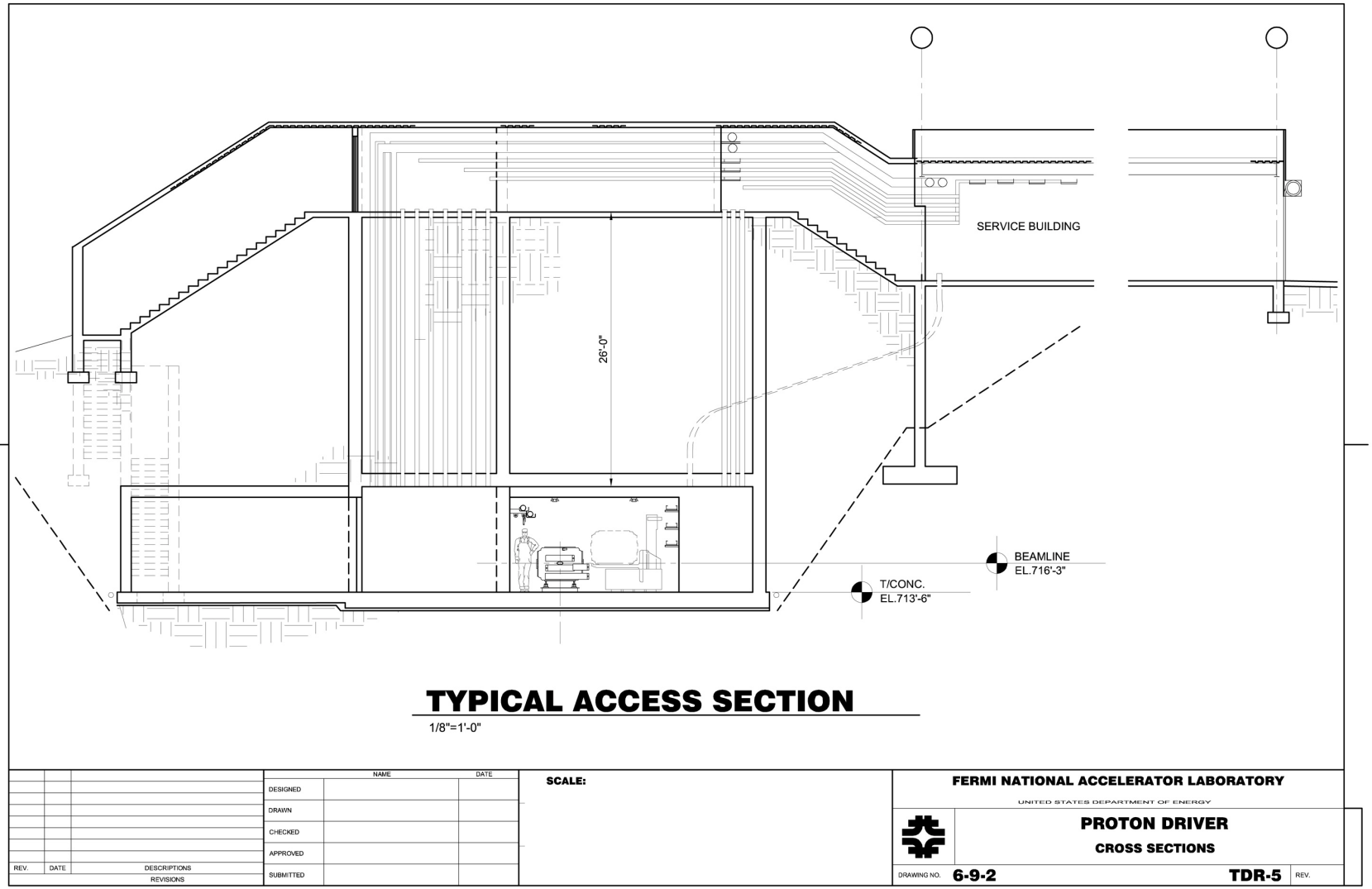

Figure 17.4. Proton Driver Access Section

Chapter 18. Environment, Safety, and Health Considerations

D. Cossairt, K. Vaziri, and R. Walton

18.1 Introduction

The Proton Driver presents a number of challenges in the general area of environment, safety, and health. This chapter identifies these challenges and makes a preliminary assessment of how they might be addressed and of their potential impact on the project. While many of these issues are very similar to those that have been encountered and solved during the construction and operation of other facilities at Fermilab and elsewhere, others are quite novel. The novel ones will require particular attention as the project proceeds to assure their timely resolution in a cost-effective manner that meets the approval of the Department of Energy and the public. It is concluded here that with adequate planning in the design stages, these problems can be addressed in a manner that merits the support of the Laboratory, the Department of Energy, and the public. Future R&D needs are identified and summarized at the end of the chapter.

18.2 Overall View of Procedural/Regulatory Matters

The actual design, construction, and operation of the Proton Driver will have to meet a number of procedural/regulatory milestones in the area of environment, safety, and health to assure its success. The devotion of early attention to these issues is likely the best way to enhance public support of the project. These requirements are currently provided in Fermilab's Work Smart Standards in Environment, Safety, and Health [1]. The list of Work Smart Standards is reviewed annually.

18.2.1 Safety and Health Procedural/Regulatory Matters

The Laboratory will be required to prepare an assessment of the environment, safety, and health issues associated with this project in the form of a Safety Assessment Document (SAD). Given the size and scope of this project, the preparation of a Preliminary Safety Assessment Document (PSAD) will likely occur first. The purpose of the PSAD is to identify the relevant ES&H issues at an early stage and propose how they might be mitigated. The SAD, then, documents the resolution of the issues. It is quite possible that DOE will review these safety documents by utilizing an external review team. Just prior to facility operation, a readiness review will be conducted in similar fashion. PSAD/SAD activities generally begin after funds are released. Early planning will expedite this task. DOE is presently "self-regulating" in the areas of industrial safety and occupational radiation protection. Developments in these areas are being monitored closely to identify new requirements or procedures that might apply to new projects such as the Proton Driver. Fire safety/Life Safety Code considerations, particularly those concerning egress conditions should be especially carefully thought out prior to Title I design.

18.2.2 Environmental Protection Procedural/Regulatory Matters

All new DOE projects are subject to the National Environmental Policy Act (NEPA). Initially, the project will be analyzed to determine the appropriate level of review. For a project of this scope, DOE will require an Environmental Assessment (EA). The required analysis is broad in scope and includes societal impacts, such as traffic and noise, along with the standard environmental protection topics. Also included would be investigation of archaeological and historic preservation sites located within the footprint. DOE will choose the methods used to involve the public. The conclusion of the environmental assessment process is either a Finding of No Significant Impact (FONSI) or the need to prepare an Environmental Impact Statement (EIS). The possibility of a determination by DOE that an EIS would be necessary should not be dismissed. The requirement to proceed with the preparation of an EIS may well hinge on how the Proton Driver is connected with other actual or anticipated sources such as a neutrino source or a muon collider. If the Proton Driver project becomes formally connected with some larger project that clearly requires an EIS, then the environmental review of the Proton Driver would likely need to be included in that EIS. The environmental impacts associated with the proposed project could also bear importantly on the level of NEPA review. The completion of the EIS results in the issue of a formal notice called a Record of Decision (ROD). To set the time scale, the process of preparing an EA from the beginning to the publication of the FONSI could be anticipated to take from one year to 18 months. Two or three years are likely needed, at a minimum, to complete an EIS. The NEPA process is generally considered to be arduous, but one that can be followed to a successful conclusion. This task must be completed prior to expenditure of project funds or any "detailed design."

A significant part of the NEPA process, regardless of the level of the final review (i.e., EA or EIS), consists of an analysis of alternatives to this proposal, identifying the environmental impacts of all of them and demonstrating that the proposed project either has the least impact or that the impacts are justified by other considerations. Potential "hypothetical" alternatives must include the "no action" alternative, i.e., "making do" with the present Linac and Booster. Other obvious alternatives that should be considered are upgrading the Booster in its current location and placing the Proton Driver in a different location on the Fermilab site or elsewhere. Alternative locations may have a substantial effect on the analysis of impacts. For example, locating the project in non-wetland areas (e.g., south of Giese Road, or west of the NuMI access road) may warrant serious consideration if it results in the alleviation of important environmental problems. Furthermore, any decontamination or decommissioning of portions of the accelerator complex that might be replaced by the Proton Driver (e.g., the 8 GeV Booster) should be included in the environmental analysis.

Other procedural requirements apply in the arena of environmental protection in the form of environmental permits that will be needed. Some of these apply during the construction stages, others apply to operations, and some apply to both stages. Topics covered by such permits include storm water discharges, discharges of cooling water,

wetlands mitigation, releases of air pollutants for both non-radioactive pollutants and for radionuclides, and construction in any floodplains. Some of these topics are covered by existing environmental permits issued to DOE and the Laboratory. However, the operating conditions of the Proton Driver will likely result in the need to modify these permits. A prominent example is the need to secure a permit under the National Emissions Standards for Hazards Air Pollutants (NESHAPS) to construct a new source of airborne radionuclide emissions [2]. The lead-time required for submittal of these permits is typically 180 days or longer. The above permits all come with lists of "terms and conditions", all of which are enforceable by the regulating agencies and will need to be properly assured during both construction of the facility and its subsequent operations. Specifically, requirements for periodic monitoring, maintenance, inspection and reporting commonly arise. It is particularly important that these issues be carefully considered and realistically planned for early in the project and included in the preparation of cost estimates for the bidding process. This early attention is needed to avoid major funding and compliance problems later, where they can, under some scenarios, delay the completion of construction.

18.2.3 Wetlands Impact

The wetland impacts would be major for this project as it is currently envisioned. At this early stage, it is estimated that the extent of the construction area is roughly 20 acres, nearly all of which would be in jurisdictional wetlands (i.e., wetlands of a size of regulatory importance). That means that an individual permit from the U.S. Army Corps of Engineers (CoE) must be obtained before the commencement of construction. For a project of this size, the permitting process is likely to take a minimum of one year from the date of submittal. The permit would certainly require the replacement of the wetland acreage lost. The CoE typically wants replacement wetlands to be "in kind", that is, of the same type as that lost. Unfortunately, the wetland in the location presently preferred is forested, which is essentially impossible to replace. Therefore, the CoE is likely to require a higher ratio of replaced to lost acres than the typical 1.5:1. A replacement ratio of 2:1 or even 3:1 should be anticipated, resulting in the necessity to create up to 60 acres of new wetland. The process of choosing a place on site for such a large expanse of wetland should be done carefully, since the new wetland becomes essentially untouchable for development in the future. At the time of this writing, replacement wetland typically costs about $50,000 per acre to build and manage. Created wetland acreage must be monitored as a condition of the permit, typically for a period of five years, and failure to meet performance criteria would necessitate remediation. Obviously efforts that can be made to reduce the size of the impacted wetlands can pay considerable dividends in terms of overall project cost and perhaps even in complexity of construction.

Additional wetland and/or floodplain impacts may result from siting of a new twenty acre cooling pond. Siting such a pond in a wetland or floodplain would constitute “fill” as defined in regulations, and would add to the permit burden.

18.3 Environment, Safety, and Health Considerations During Construction

18.3.1 Occupational Safety During Construction of the Facility

These facilities all would be located within the glacial till strata at a distance below the surface of less than 33 ft (10 meters). At this level construction is likely to proceed by the standard "cut and fill" method. The Occupational Safety and Health Administration's (OSHA) regulations on the construction activities will be followed. Industrial radiography operations and any other work conducted using radioactive sources must be performed in compliance with State of Illinois requirements. Other routine radiological issues that might arise will be handled according to the *Fermilab Radiological Control Manual* (FRCM). There are no new occupational safety issues identified with this work. However, should alternative methods of construction such as underground tunneling be chosen, perhaps in order to minimize the size of impacted wetlands, further review may be necessary.

18.3.2 Environmental Protection During the Construction of the Facility

Erosion control measures similar to those employed elsewhere must be employed in accordance with good engineering practice and Federal and State regulations. Dust and runoff from any spoil piles must be kept under control. A National Pollutant Discharge Elimination System (NPDES) storm water permit for construction will be needed. This will include specific erosion and sedimentation controls that must be followed during the construction period. The usual precautions to prevent pollution from spills of regulated chemicals from the construction equipment will need to be taken. Noise from construction activities is not expected to be significantly more intense than that associated with normal civil construction activities in the vicinity of Fermilab. It is important to demonstrate adequate care for floodplains due to significant local public concerns about flood prevention. Also, due to the fact that Indian Creek runs through the proposed site, it is very likely that the construction would qualify as a "Class III" dam, a condition that would require a permit from the State of Illinois.

18.4. Environment, Safety and Health Considerations During Operation

18.4.1. Occupational Safety Hazards During Operations

The occupational safety hazards encountered at all other large particle accelerator facilities, including the present complex at Fermilab, will be found in this facility:

- The project will use high current electrical circuits in the magnets on a large scale.
- Radio frequency (RF) generation and distribution equipment will be used extensively.

- Large amounts of cables in cable trays, with associated fire protection implications, will be installed.
- Long tunnels will be present with corresponding egress and fire protection issues that need to be addressed.
- There will be movements and alignment of large, heavy components.
- There will be significant amounts of cooling water present.

These have been successfully addressed in the past by the application of well-known technologies and safety practices that should be applied to this facility.

The incorporation of unusual materials in accelerator components or as target materials could pose industrial hygiene issues that will need proper evaluation and mitigation.

18.4.2. Ionizing Radiation Safety During Operation of the Proton Driver

The major issues related to ionizing radiation have been discussed in detail in Chapters 9 and 10 of this report. The discussion here is based upon the latest (at the time of this writing) statement of the parameters of the Proton Driver [3] and on extensive Monte Carlo calculations that have already been carried out [4,5]. The latter calculations were specifically performed to establish and control allowable beam losses and to understand their consequences. The discussions of this chapter are based on the machine parameters for Phase II Proton Driver as they appear in Table 1 of Ref. [3]. This choice was made in consideration of the finality of the civil construction. It is crucial to recognize that radiological issues pertaining to future target stations are not within the scope of this report. Preliminary discussions of the significant impacts of an example of such a target station have been provided in the Neutrino Factory Feasibility Study [6].

18.4.2.1 Prompt Radiation Shielding

The Proton Driver will require massive amounts of hadron shielding similar in scale and type to that of other proton accelerators in this energy and intensity regime. It is clear that suitable combinations of steel, concrete, and earth shielding can meet the standard criteria for above ground shielding at Fermilab. Figure 6 of Ref. 4 provides useful results of calculations of the dose equivalent due to a quasi-local loss of protons on a magnet centered in a 2 m radius tunnel comprised of 0.3-m concrete walls as a function of the radial thickness of earth of standard density typically found at Fermilab ($\rho = 2.24$ g cm^{-3}). These were done for the various energy stages. Likewise, presently available civil construction conceptual drawings show the lateral shielding thicknesses selected in a preliminary manner.

From the standpoint of machine reliability, it is inconceivable for a catastrophic loss of the full beam to continue for more than about one second during a given one hour period of operations. Likewise, as stated in Ref. 4, the maximum credible uncontrolled loss of beam on a steady state basis would most certainly be less than 0.1%. Results for

the presently-envisioned lateral shields are given in Table 18.1. The maximum dose equivalent rate external to the shield due to the quasi-local loss of the beam of duration one second is given along with the dose equivalent rate outside of the shield expected at a quasi-local 0.1 % steady-state loss of beam.

Table 18.1. Dose Equivalent Rates External to Lateral Shielding

Maximum Energy/Machine	Preliminary Design Lateral Shield (feet)	Normalized Dose Equivalent Rate Outside Shield[a,b] (mSv proton^{-1})	Maximum Dose Equivalent Rate Outside Shield[c] (mrem s^{-1})	Dose Equivalent Rate Outside Shield at 0.1 % Steady Loss (mrem hr^{-1})
400 MeV Linac	13.0	2.7×10^{-18}	0.14	0.50
1000 MeV Linac	15.5	8.3×10^{-18}	1.25	4.5
3 GeV Pre-Booster	24.5	2.9×10^{-20}	0.0044	0.016
16 GeV Booster	24.5	7.3×10^{-20}	0.011	0.040

[a]This result is read directly from Fig. 6 of Ref. 4 or determined from extrapolations from those results. The extrapolation is reliable since the plotted results are nearly perfectly fit by the exponential function.

[b]The 1000 MeV value was determined, conservatively, by scaling the 3 GeV value as $E^{0.8}$.

[c]The values in this column were determined using the values of beam delivery provided in Table 1 of Ref. 3. For the 400 MeV 15 Hz Linac, this was 3.4×10^{13} protons/pulse for Phase I and 1×10^{14} protons/pulse in Phase II.

Regulatory [7] and DOE [8] requirements pertain to radiation fields present on a DOE site. While Ref. [7] primarily concerns exposures to occupational workers and Ref. [8] pertains primarily to members of the public, these two standards, both incorporated into Ref. 1, are consistent in that the annual radiation dose equivalent must be kept below 100 mrem in locations where members of the public or employees who have not been specifically trained as "radiation workers" could be present. Fermilab has adopted policies that are intended to achieve this condition [9]. If the dose equivalent in an hour resulting from the maximum credible accidental beam loss can be constrained to be less than 1 mrem and if the dose equivalent due to normal operating conditions can be shown to result in a dose equivalent of less than 0.05 mrem hr^{-1}, the affected area needs no further controls, the desired condition for an accelerator such as the Proton Driver. Examining the above results, it is clear that even for the 0.1% beam loss, a level that may be larger than typical operating conditions, the planned lateral shield dimensions for the 3 and 16 GeV synchrotrons are adequate to meet the conditions on dose equivalent. However, for the 400 MeV (Phase I) and the 1000 MeV (Phase II) Linacs these conditions are not met at this fractional rate of beam loss. Since the 400 MeV Linac is constrained by its being housed in the present Linac enclosure, the loss of beam in it must be limited to less than 0.01% since it would be difficult to add the equivalent of 3.1 ft of lateral earth shielding needed to allow for a 0.1 % loss. In particular, the limits on dose equivalent rate must be met in the Linac Gallery due to its high occupancy, an occupancy that presumably would continue during Phase I operations. For the 1000 MeV Linac, based upon the extrapolations of the results of Fig. 6 of Ref. 4, it is recommended that its

lateral shielding be increased to 21.6 ft to achieve a consistent level of protection. An alternative would be to provide assurance that *localized* steady-state beam losses under normal operational conditions can be kept below 0.001 %. The control of beam loss in the Linacs as it trades off with lateral shielding requirements clearly needs to be better understood.

Radiation fields due to muons must be considered. At 16 GeV, the range of the muons of maximum energy is less than 100 ft of earth. Due to their forward-peaking, any muons produced by stray beam loss should be ranged-out in the soil shield and hence are of no consequence.

Thus, the shielding against the prompt radiation hazards is well understood and can be addressed by conventional means. An especially welcome result is the elimination of the quite troublesome shielding problem associated with the present 8 GeV Booster and certain work places of high occupancy. However, the present conceptual drawings show various support structures, presumably occupied during operations, as being located nearly directly above the planned beam enclosures and protected by the minimum value of lateral earth shielding. While initial shielding estimates may determine that these locations are adequately shielded, they should not be placed directly over the beam enclosures. Experience at nearly all accelerators, including the present Fermilab Booster, is that future upgrades nearly always are compromised or made more costly by such "occupied structures" being located above or beside the accelerator enclosure. Instead, they should be kept at the same elevation but relocated horizontally away from being directly over the accelerator enclosures. It is suggested that this be done in a way that results in at least 3 ft of additional shielding in order to provide approximately an order of magnitude of additional attenuation in radiation levels at relatively low cost. Otherwise, operational difficulties are likely to arise due to the need to control radiation exposures in work places much more stringently than those required to control those in "uncontrolled" areas, where one has options such as fencing available as fallback positions.

18.4.3.2 Residual Radioactivity of Components

References [4] and [5] have documented initial studies of the residual activation problem. The result of this work has been the identification of a scheme for using collimation to limit the beam loss to a well-shielded collimation system while achieving an average loss of about 0.3 W m^{-1} elsewhere. The resulting radiation levels at contact with the beam pipe in unshielded portions of the 16 GeV lattice should be less than approximately 130 mrem h^{-1} while those at contact with magnets should be less than about 10 mrem h^{-1}. It turns out that at 16 GeV, a beam loss of 0.3 W m^{-1} averaged over the circumference of 711.32 m corresponds to a total fractional loss of beam of only 5.5 x 10^{-3} per cent, a challenging level to achieve. For the 16 GeV Booster, these levels are acceptable from the standpoint of the control of occupational radiation exposure during routine maintenance activities. However, the prompt radiation levels are sufficient to require continuous attention to beam loss during operations and careful planning of maintenance activities in order to keep occupational radiation exposures as low as reasonably

achievable, in compliance with the requirements of Ref. 7. Engineered-in design features which provide for easier access and replacement of equipment will help in easing the radiological operational issues. Proper selection of materials for the buildings and equipment will also help to reduce the residual activation.

18.4.3.3 Airborne Radioactivity

Airborne radioactivity levels will largely be encountered either in areas where collimators are employed to limit beam loss (see Sect. 18.4.3.2) or at the target stations that are not within the scope of this report. The design of the collimation system will include a calculation of the airborne radioactivity released, to support the permitting requirements outlined in Section 18.2.2 and to assure compliance with regulations governing airborne radionuclide releases set forth in Ref. [2]. An early assessment of this issue will allow the inclusion of mitigation into the design of the facility.

18.4.3.4 Radioactivity in Soil and Groundwater

The results of Refs. [4] and [5] considered soil activation due to losses of beam in the various acceleration stages. For all stages considered, it was demonstrated that the control of residual activity to the levels described in Section 18.4.3.2 will achieve acceptable levels of soil activation. As the design proceeds, this issue will warrant continued attention. In particular, a hydrogeological survey in the vicinity of the planned facility should be conducted to better refine the parameters relevant to groundwater activation prior to the finalization of the design.

18.4.4 Non-Radiological Environmental Protection Issues During Operations

Efforts should be made to prevent the creation of regulatory mixed wastes and to control spills. Surface water discharges must be managed in accordance with Laboratory policies and any State and Federal environmental permits that are in place. Depending on previous analyses of radioactivation of soil/groundwater, monitoring wells may be in place, requiring a sampling and maintenance schedule. These considerations are quite similar to those encountered at other Fermilab facilities located in the glacial till.

The cooling water requirements for the Proton Driver are significant. These requirements should be examined to determine if the impact on Fermilab's industrial cooling water (ICW) system requires modifications to the Laboratory's current National Pollutant Discharge Elimination System (NPDES) permit under which these systems are operated. Any chemical additives to these systems must be approved within the framework of existing permits.

18.5 Summary

The Proton Driver provides a number of challenges in the area of environment, safety, and health. Many of these have been encountered, and effectively addressed, at Fermilab

and other accelerators. Some of the problems are common to technological advancements in other accelerators worldwide. For these, collaborative efforts should continue to develop and improve the solutions that are needed. This project raises a few new issues that must be addressed. Continued attention to these issues is anticipated as the project proceeds.

18.6 Need for Work on Environmental and Safety Issues

A. The Fire Safety/ Life Safety Code considerations need to be carefully addressed prior to Title I design (Section 18.2.1).

B. The needed environmental permit applications should be developed and submitted at the earliest possible stage (Sections 18.2, and 18.3.2). Specific time requirements for each permit application process are available from the ES&H section, but all permits must be assumed to take at least 180 days.

C. The alternatives to be studied as part of the NEPA process must be identified (Section 18.2.2).

D. Archaeological/historic sites within the footprint project will need to be surveyed (Section 18.2.2).

E. The potential size/type of impacted wetlands and floodplains should be further investigated before the "footprint" of the project becomes completely defined by other constraints (Section 18.2.3). Modifications to the footprint should be considered that would minimize the impacted areas.

F. The cost of environmental compliance, maintenance, monitoring and oversight must be included explicitly in early planning/budgeting processes. This is especially true for projects of this magnitude, where such costs could be several million dollars, and the efforts needed extend for years beyond actual construction. Significant funds may also be necessary to complete studies for preliminary environmental work (e.g., wetland delineations, wildlife surveys, groundwater investigations) prior to project funding *per se* (Sections 18.2.2, 18.2.3, and 18.3.2).

G. The trade-off between control of beam loss in the Linac with additional lateral shielding needs to be better understood (Section 18.4.3.1).

H. The support structures should be located so that they are not above any part of the accelerator enclosures and are shielded by more than "the minimum" amounts of lateral shielding to allow for uncertainties in shielding calculations and to accommodate future upgrades (Section 18.4.3.1).

I. Calculations of airborne radionuclide releases are needed concerning the beam collimation system to establish permitting requirements and demonstrate that operations will be within established regulatory requirements (Section 18.4.3.3).

J. A hydrogeological survey in the vicinity of the planned facility should be conducted to better refine the parameters relevant to groundwater activation prior to the finalization of the design (Section 18.4.3.4).

References

[1] "Fermilab Work Smart Standards Set," Fermi National Accelerator Laboratory, http://www-lib.fnal.gov/library/protect/worksmart.html, November 15, 1999.

[2] United States Code of Federal Regulations, Title 40, Part 61, Subpart H, "National Emissions Standard for Hazardous Air Pollutants (NESHAP) for the Emission of Radionuclides other than Radon from Department of Energy Facilities," 1989.

[3] W. Chou, "Proton Driver", FERMILAB-Conf-00/180, August 2000.

[4] O. E. Krivosheev and N. V. Mokhov, "Tolerable Beam Loss at High-Intensity Proton Machines," FERMILAB-Conf-00/192, August 2000.

[5] A. I. Drozhdin, C. J. Johnstone, and N. V. Mokhov, "Beam Collimation System for a 16 GeV Proton Driver," FERMILAB-Conf-00/194, August 2000.

[6] N. Holtkamp and D. Finley, editors, "FNAL Feasibility Study on a Neutrino Source Based on a Muon Storage Ring," FERMILAB-Pub-00/108-E, June 2000, (http://www.fnal.gov/projects/muon_collider/nu/study/report/machine_report/). The ES&H material has been expanded by J. D. Cossairt in "Environment, Safety, and Health Considerations for a Neutrino Source Based on a Muon Storage Ring," FERMILAB-TM-2112, May 2000.

[7] Code of Federal Regulations, 10 CFR 835, "Occupational Radiation Protection," current version.

[8] DOE Order 5400.5, "Radiation Protection of the Public and the Environment," January 1993.

[9] *Fermilab Radiological Control Manual*, Article 236.

Chapter 19. R&D Program

W. Chou

19.1. Introduction

The R&D required to build the Proton Driver has been discussed in some detail in the last section of each relevant chapter. This Chapter is a brief summary of these items. For each item, the reader is referred to the original section for more information. The components of the R&D program are divided into three categories:

- Category A includes those items that are not only needed by the Proton Driver but will also be useful for improving the performance of the present proton source. Therefore, they have the highest priority.
- Category B is the R&D work that is critical to the Proton Driver and is currently underway.
- Category C lists other R&D items that are necessary to the Proton Driver but may have to wait until more resources can be made available.

There is a US-Japan Accord for joint R&D on high intensity proton facilities. A number of the R&D items are part of this collaboration.

19.2. Category A

- High intensity high brightness H^- source development. Develop three different types of sources: an improved magnetron, a noiseless planatron and a Dudnikov Type Source (DTS). The goal is to increase the beam intensity by a factor of two and the brightness by a factor of four. This would help the present Linac and Booster in high intensity operations. (Section 13.11.1)
- Linac front-end improvement. Reassemble hardware left from the PET project (solenoid, 200 MHz RFQ, double alpha magnet and several quadrupoles) and retune it for the H^- operation. A charge neutralization experiment for reducing the space charge effect would also be carried out. If additional resources can be devoted to this item, the solenoid will be replaced by an Einzel lens and new rods will replace the existing ones in the RFQ (Sections 13.11.2 and 13.11.3)
- Booster 53 MHz rf cavity modification. Enlarge the central pipe aperture from 2-1/4" to 5" and increase the voltage per cavity from 55 kV to 66 kV. These modifications would also benefit the present Booster. (Section 5.4.1)
- Finemet 7.5 MHz rf cavity development. As part of the US-Japan Accord, a cavity using Finemet cores from Japan has been constructed at Fermilab. It has been installed in the Main Injector for a 132 ns bunch spacing coalescing experiment. Seven 53 MHz bunches in the Main Injector have been successfully coalesced to form a single 7.5 MHz bunch by using one Finemet cavity. This cavity is 0.5 m long and provides more than 12 kV accelerating voltage. The 132 ns bunch spacing is a critical parameter of Tevatron Run IIb.

- Beam loading compensation system development. This system also helps the Main Injector operation. In particular, when the slip-stacking scheme is implemented, this system would play a crucial rule. (Section 5.4.2)
- Inductive insert study in the present Booster. From the experience at the PSR at Los Alamos National Laboratory and simulations on the Proton Driver as well as on the Booster, it is expected that inductive inserts would effectively reduce the potential well distortion due to space charge and thus reduce beam losses at high intensity. The proposal is to install several ferrite modules at two long straight sections (about 10-m long total) in the Booster. (Section 5.4.4)
- Booster magnet study. This has two parts. One is to install metallic strips and/or a metallic liner in the magnet and measure the coupling impedance. The goal is to reduce the impedance from the laminations seen by the beam. The other is to carry out dynamic measurements of the magnetic field during the cycle. Both would be useful to the present Booster. (Section 6.2)

19.3. Category B

- Stranded conductor coil study. This type of coil is necessary for the Proton Driver magnets. Fermilab has no experience with these coils and there are no U.S. vendors that have this product. However, there are two Japanese companies (Hitachi and Toshiba) that can manufacture the coils made of stranded conductor (copper or aluminum) with a cooling pipe (stainless steel) in the center. We are expecting to receive samples from Toshiba soon. (Section 6.7) (Section 6.6)
- Material outgassing rate test. Because the magnets are canned, the outgassing rate of the laminations and coils will determine the vacuum. In particular, the outgassing rate of the coil made of stranded conductor must be measured carefully. (Section 8.6)
- Chopper development. This is also part of the US-Japan Accord. A new type of chopper based on modulating the energy of the beam from the ion source has been designed and built by a KEK-Fermilab team and installed on the Linac at the HIMAC in Chiba, Japan. The beam test was successful but further improvement is needed and this study should continue. (Section 13.11.4)
- High gradient, low frequency rf system for burst mode operation. Develop an rf cavity with 0.5 - 1 MV/m average accelerating voltage at 7.5 MHz. This cavity would be important for bunch compression operation at the end of the cycle of the Proton Driver. This is part of a US-Japan collaboration. (Section 5.1.3)

19.4. Category C

- Prototyping of a large aperture dipole and quadrupole. The challenges are: high voltage to ground stranded conductor coil and vacuum. (Sections 6.7 and 7.8).
- Prototyping of a complete resonant cell of the dual resonance power supply, and investigation of high power IGBT technology. (Section 7.8)
- Prototyping of a quadrupole tracking error correction system. (Section 7.8)
- Vacuum chamber made of fiber-reinforced epoxy with a continuous metal foil lining. (Section 8.6)

- Laser beam chopping. (Section 13.11.5)
- Two VME bus cards, an 8-channel waveform generator and an 8-channel quick digitizer. (Section 16.13)
- Fast rise- and fall-time kicker. (Section 12.2.1)
- Active feedback systems. (Section 15.4.8)
- TRIUMF rf cavity study. This is a backup as well as a future improvement of the modified Booster cavity. (Section 5.4.3)
- Long pulse test of the Linac klystron. Although this is not mentioned in Chapter 13, it would provide a useful technical contingency in case the H^- source cannot meet its design goal of 115 mA. The bottleneck for the Linac beam pulse length is the klystron stations in the Side-Coupled Linac (SCL) section. If the test shows a 200 μs pulse can be achieved reliably, then the required H^- beam intensity could be reduced by a factor of two.

Appendix A. Cost Estimate

R. Alber, T. Anderson, M. Ball, M. Champion, W. Chou, J. Crisp, A. Drozhdin,
D. Harding, C. Jach, J. Lackey, J. Leibfritz, N. Mokhov, J. Reid, M. Shea, J. Steimel,
D. Wildman, D. Young

A.1. Introduction

A cost estimate for each technical system as well as for civil construction has been carried out. A WBS was not done at this stage of the project but will be produced when it is required.

The cost estimate is for Phase I only. It includes a 16 GeV synchrotron, a 400 MeV transport line, a 12/16 GeV transport line, improvements in the present H^- source and Linac, and civil construction. We present an "unloaded" cost estimate, a cost estimate in which G&A and contingency are not included. These items can be added later following guidelines to be provided by the Fermilab Director and the DOE.

All the figures are in FY 2000 U. S. dollars. No inflation is included.

A.2. Two-Stage Cost Estimate

The cost estimate for Stage 1 is given in Table A.1. Every technical system shown is capable of working in Stage 2 except the rf system and the power supplies.

In Stage 1, the rf is a 53 MHz system, which would reuse a large portion of the existing Booster rf components, thus reducing the cost. The power supplies would employ chokes and capacitors that are limited to 12 GeV operation. Because these chokes and capacitors are major cost items and their costs are proportional to the total stored energy, the savings in power supplies in Stage 1 compared to what will be required in Stage 2 are significant.

In Stage 2, a new 7.5 MHz rf system would replace the 53 MHz rf system, and the chokes and capacitors would be upgraded for 16 GeV operation. The cost estimate is **K$ 44,694** for the rf system and **K$ 21,057** for the power supplies, respectively. Therefore, the additional cost for Stage 2 would be **K$ 65,751**.

Table A.1. Proton Driver Stage 1 Cost Estimate (in thousand US dollars K$)

1	**Technical Systems**			**184,893**
1.1	16 GeV Synchrotron		173,551	
1.1.1	Magnets	53,982		
1.1.2	Power supplies	52,095		
1.1.3	RF	11,051		
1.1.4	Vacuum	9,222		
1.1.5	Collimators	325		
1.1.6	Injection system	1,039		
1.1.7	Extraction system	3,542		
1.1.8	Instrumentation	2,553		
1.1.9	Controls	2,214		
1.1.10	Utilities	10,615		
1.1.11	Installation	1,696		
1.1.12	ED&I	25,217		
1.2	400 MeV Transport Line		2,110	
1.2.1	Magnets	1,443		
1.2.2	Power supplies	361		
1.2.3	ED&I	307		
1.3	12/16 GeV Transport Line		3,718	
1.3.1	Magnets	2,542		
1.3.2	Power supplies	636		
1.3.3	ED&I	540		
1.4	Ion Source and Linac Improvements		5,514	
1.4.1	Negative ion source	480		
1.4.2	LEBT	225		
1.4.3	RFQ	1,850		
1.4.4	MEBT	255		
1.4.5	Chopper	100		
1.4.6	New drift tube Tank #1	1,500		
1.4.7	Instrumentation and controls	135		
1.4.8	Building modification	250		
1.4.9	ED&I	719		
2	**Civil construction**			**54,184**
2.1	16 GeV Synchrotron		25,600	
2.1.1	Enclosure	8,600		
2.1.2	Service buildings	10,200		
2.1.3	Utility support building	6,800		
2.2	400 MeV Transport Line		1,800	
2.3	12/16 GeV Transport Line		2,200	
2.4	Site work		6,300	
2.5	Subcontractors OH&P		7,180	
2.6	ED&I		7,324	
2.7	Environmental controls and permits		3,780	
3	**Project Management**			**3,000**
	TOTAL			**242,077**

Note: Items 1.1.4, 1.1.8, 1.1.9, 1.1.10 and 1.1.11 include the costs for the synchrotron as well as for the two transport lines.

Appendix B. Cost and Performance as a Function of Energy

C. M. Ankenbrandt and R. P. Johnson

Summary

Alternative Proton Drivers (PD) with different maximum energy, magnet aperture, and injection strategies are examined. It is found that lower energy designs with smaller ring circumference can provide construction and operation cost savings. Using the cost of the machine components as shown in Appendix A, the cost of each alternative PD is derived by using scaling laws. The most important scaling law is that the cost of magnets and magnet resonant power supply systems should scale as the stored magnetic energy in the accelerator. The next most important scaling factor is the RF power, effectively the number of RF cavities, which increases with ring circumference and with energy swing. The reduced circumference of a lower energy ring allows Stage 1 MI injection requirements to be met with the present Linac and H^- source by virtue of more batches. A less expensive method to achieve the Stage 2 power on target for a lower energy machine would be to improve the H^- source and raise the injection Linac energy. Other performance and construction issues are discussed and costs for alternative proton drivers of 8, 12, and 16 GeV are derived.

B.1. Introduction

In this Appendix, plausible alternative energy Proton Drivers (PD) are described that should have performance equal to the 16 GeV machine described in the main body of the report. That is, for Stage 1 (MI Operation) at least 1.2×10^{14} protons must be injected into the MI. In Stage 2 (Neutrino Factory) there should be 1 MW of beam power. In all cases, the calculated Laslett tune shift should be the same or less than that in the baseline Proton Driver (bPD).

Using a simple spreadsheet, three studies are described which demonstrate the consequences of certain parameters choices.

In the first study, machines of 8, 12, and 16 GeV maximum kinetic energy (T_{max}) with 40π mm-mrad transverse acceptance are modeled to show how their costs compare to each other and to the 16 GeV 60π baseline design. These energies are chosen because 8 GeV is considered the lowest energy compatible with present Booster functionality, 16 GeV allows a comparison between two different transverse acceptances, and 12 GeV, besides being midway between the other two, is the actual Stage 1 energy of the bPD. The 8, 12, and 16 rings with 40π acceptance have, respectively, circumferences of ¾, 1, and 1.5 times that of the present Fermilab Booster.

The strength of the comparison is that general cost scaling arguments can be used to get rather good relative values for components. Two of the most important scaling parameters turn out to be stored energy in magnet and power supply systems and rf power. These are found to dominate the cost comparisons. Machines of lower energy,

smaller circumference, and smaller transverse acceptance are therefore favored, providing they can satisfy the Stage 1 MI intensity and Stage 2 beam power requirements. Where needed, these requirements are accomplished by increasing the Linac energy and H^- source capabilities. Costs for the needed injector improvements are estimated and included in the comparisons.

The second study is a comparison of operating costs for the 40π model machines at 8, 12, and 16 GeV and the 60π baseline PD.

The third study is to compare the costs for an 8 GeV machine of Fermilab Booster circumference as a function of B_{max}, the maximum dipole field. The study indicates that the cost savings for a lower B_{max} can offset the increased rf and conventional construction costs associated with a larger circumference.

B.2. Important Parameters

B.2.1. Laslett space charge tune shift

The Laslett incoherent space charge tune shift or spread,

$$\Delta\nu = \frac{3 f_T r_P}{2B} \frac{N_P}{\beta\gamma^2 \varepsilon_N} \tag{B.1}$$

is used as the touchstone in all the accelerator models discussed below and allows the parameters of the machines to be varied in a consistent manner. Here B and f_T, the bunching and transverse form factors, and Δν are defined to be the same as used for the baseline PD design. The number of protons (N_P), the beam normalized transverse emittance (ε_N), and the injection energy (which determine the Lorentz parameters of β and γ), are the variables used to equalize performance parameters of MI intensity (Stage 1) and beam power (Stage 2) for each design. The relativistic Lorentz factor βγ for 400 MeV kinetic energy is 1.02 so the geometrical acceptance, ε_G, is very nearly the same as the normalized emittance, $\varepsilon_N = \beta\gamma\varepsilon_G$.

B.2.2. Circumference

One important parameter, which is not in the Laslett tune shift formula, is the machine radius or circumference. The maximum number of protons that can be stored in a ring limited by the Laslett tune shift is independent of the circumference of the ring. This fact can be used in the design of the 8 and 12 GeV machines, which can have a smaller circumference than the 16 GeV baseline machine. With more batches (PD beam acceleration cycles) to load the MI, each batch can have fewer protons, allowing the transverse acceptance to be smaller with the same Laslett tune shift.

Of course, fewer batches means that the MI can be loaded faster, which in the case of the 4-batch injection of the baseline PD implies a 7% increase in protons per hour for MI operation compared to the 6-batch injection from a ring of Booster circumference. On

the other hand, a ring with circumference larger than that of the present Booster cannot efficiently create and store antiprotons in the Booster-sized Antiproton Accumulator. One third of the batch destined to hit the antiproton production target from the baseline PD should be without beam in this case, and if there were three other batches, this would lead to an 8% decrease in protons/hr from the MI.

Synchrotrons of smaller circumference will also have a smaller transverse beam size and require less magnet aperture since each transverse beta function scales as the square root of the radius.

Fewer rf cavities are needed as the circumference is reduced, since the beam passes through the cavities more often. Fewer cavities are needed, as well, if the machine energy is reduced such that the maximum dE/dt is lowered. Approximately, then, a ring of half the energy and half the circumference will require a quarter as many rf cavities.

Since the fraction of the circumference occupied by rf in a smaller, lower-energy machine is also reduced, the fraction of the ring used for other things can be increased. This means, for example, that a larger packing fraction (total bending magnet length/circumference), or more complex lattice design is easier to accomplish. As discussed below in the third study, a larger packing fraction can be used to reduce costs by reducing the B_{max} and lowering the stored energy in the magnet and power supply systems. A lower B_{max} also has the virtue that magnet saturation and induced dipole and quadrupole tracking problems are reduced.

B.2.3. Injection Energy and Intensity

For the alternative Proton Drivers in this Appendix, the choice has been made to rely on upgrading the existing H^- source and the Linac to provide more protons for Stage 2 beam power or to provide more energy to reduce the Laslett tune shift at injection by increasing $\beta^2 \gamma^3$. This choice has the virtue of lowering costs for the Proton Driver itself by reducing both the required beam energy and magnet apertures. However, the costs for the Linac and source improvements, unlike the costs for the ring components, cannot be scaled from the baseline design.

Considerations of Linac front-end improvements have been made in the main body of this report. Replacement of the Cockcroft-Walton pre-accelerators by RFQs, modifications to the initial drift tube structures of the 200 MHz Linac, and improved H^- sources are included in the PD project. These improvements are included in each model in this appendix at a cost of $5.5M, even though improvements are not needed in all models.

Absolute costs for additional Linac and source improvements needed for some models have been included in the studies below by using estimates based on past experience. The Fermilab Linac energy upgrade done in 1992 cost about $2M for each 40 MeV module. In the studies below we have assumed an inflation-adjusted cost of $2.67M per 40 MeV. This might be somewhat conservative in that one might expect 50 MeV from a module built today. A combination of pulse length and beam current

improvements is needed for the H^- source to provide all that is required for the cases in the studies. Where more than 3×10^{13} protons are needed from the Linac, a rather arbitrary figure of $2M for a source improvement program has been added. It is assumed that the source can be improved to provide the required number of protons within the present Linac pulse length of ~100 μs such that improvements to the Linac pulse forming networks will not be needed.

An additional benefit from increased injection energy is higher injection velocity. This reduces the frequency range of the rf system and perhaps, therefore, the cost of the Finemet system. While $\Delta f/f = 2(f_{ext} - f_{inj})/(f_{ext} + f_{inj}) = 33\%$ for the bPD, it is only $\Delta f/f = 13\%$ for the 8 GeV model with $T_{Linac} = 0.73$ GeV. While it is not clear that this reduced frequency swing would eliminate the need for the bPD 7.5 MHz rf tuners (roughly a $10M item), it would surely help if ferrite systems of a more conventional sort were chosen because of power considerations.

B.2.4. Apertures

The magnet good-field aperture usually defines the machine acceptance at the injection energy. In the 16 GeV baseline Proton Driver design, the aperture is such that a beam of $\varepsilon_N = 60\pi$ mm-mr is accepted. This is larger than the 40π acceptance that the MI was designed to have at 8 GeV. While this may have some consequences for MI extraction and beam transport, there is no problem with injection into the MI from the bPD at 12 GeV since the 60 π beam emittance will be reduced by the adiabatic damping factor $\beta\gamma$.

One reason the bPD must have a 60π acceptance is that it has a circumference that allows only 4 batches to be stacked in the MI. With only 4 batches, it is necessary to have at least 3×10^{13} protons per batch to reach the 1.2×10^{14} MI requirement. Thus the normalized emittance was increased from 40π to 60π to keep the Laslett tune shift fixed as the needed intensity increased from 2×10^{13} to 3×10^{13}.

However, by reducing the PD circumference to that of the present Booster (C_B), one can inject 6 batches each with 2/3 the number of protons into the MI and provide the same total intensity with $\varepsilon_N = 40\pi$ and the same Laslett tune shift as in the baseline PD. To reduce the circumference T_{max} must also be lowered.

To satisfy the Stage 2 requirement of 1 MW on target with a machine with lower top energy it is necessary to inject more protons. Larger N_P increases the Laslett tune shift unless the normalized emittance can be increased the same fraction. The algorithm used in the spreadsheet studies is to increase the Linac energy so that $\beta^2\gamma^3$ makes up for the increase in protons.

A major advantage in using a smaller magnet aperture is the reduced cost for the magnet and power supply systems. The costs of magnets, chokes, and capacitors in the resonant system are proportional to the stored energy in the ring magnets,

$$\text{Stored Energy} = k \sum_{magnets} (B_{max}^2 \, L \, A_T) \qquad \text{(B.2)}$$

where B_{max} is the maximum magnetic field, L the effective length, and A_T is the transverse aperture of each magnet. A_T depends on a combination of the acceptance requirements for the needed beam emittance and the momentum acceptance. For injection, only a few mm of momentum acceptance are needed and the geometric aperture is primarily determined by ε_G. At extraction energies, large momentum acceptance is needed to allow short bunches to be formed. In this case, the horizontal emittance is damped by the $\beta\gamma$ adiabatic damping factor such that when the momentum excursion is added, the total beam size fits within the acceptance determined by the injection requirements.

An assumption in the baseline PD design is that the present Booster 53 MHz rf cavities will be used to provide Stage 1 acceleration for MI use. While the reuse of these cavities reduces Stage 1 costs, it does limit the 16 GeV ring to operation at 12 GeV and it also precludes simultaneous operation of the PD and Booster. Perhaps a more significant problem is that the 2.25" diameter aperture of these cavities is thought to limit the ~ 20π acceptance of the present 8 GeV Booster. The PD design acceptance and circumference determine the amount the cavity bore will have to be increased. Tests of a modified Booster cavity with a 5" diameter bore suitable for the baseline 16 GeV PD with 60π emittance are now underway. Although no problems are envisioned with this upgrade, it might be facilitated by using an rf cavity bore diameter of 3.8", which an 8 GeV 40π ring with present Booster circumference would require.

B.3. First study: Cost as a function of T_{max}

To study the cost drivers for the two construction stages, hypothetical Proton Drivers of 8, 12 and 16 GeV maximum kinetic energy (T_{max}) have been modeled. A magnet with fixed geometric transverse acceptance of 40π mm-mrad is used. This acceptance was chosen because it is the design acceptance of the MI, it seems adequate to satisfy the performance requirements, and using a single number for all three energies simplifies the comparison of other variables. Another variable, which is held constant for the first two studies, is the maximum dipole field of 15 kG used in the baseline design. Note that while the kinetic energy is traditionally used for the description of machines at Fermilab, the momentum is the true scaling variable, where $P_{max} = \Sigma_{dipoles}(BL)$. The ratio of momenta for the nominal 16 and 8 GeV rings is 1.9.

The variables to be used to satisfy the performance requirements for the three different energies are then the machine circumference and the Linac and H^- source parameters of number of protons and injection energy. The circumference is chosen to maximize the number of batches to be injected into the MI while keeping the packing fraction reasonable. For the three energies of 8, 12, and 16 GeV, circumferences of 3/4, 1, and 1.5 C_B, respectively, seem reasonable, where $C_B = 2\pi \times 75$ m is the circumference of the present Fermilab Booster. The Linac parameters are more debatable in that considerable source development will be needed to achieve Stage 2 for the 8 GeV case, although Stage 1 for that energy serves the MI well because of the larger number of

batches that can be injected. Increasing the Linac energy seems rather straightforward, and space for this has been allocated in the bPD design.

It is important to note that the 16 GeV Proton Driver considered in this part of the Appendix is not the same as the baseline PD, which has an acceptance of 60π. Note also that the costs of the Stage 1 baseline PD in the spreadsheet include only the power supply system needed to power the ring to 12 GeV.

The costs used in the baseline PD are used to scale costs and performance for these machines. The cost of a machine is assumed to be made up of things proportional to: 1) stored energy (magnets and power supplies, ½ utilities), 2) rf volts per turn (cavities and their supplies), 3) tunnel length (conventional construction, vacuum system, ½ utilities, project management) and 4) to things which do not scale (Linac Front-end improvements). When required, increased Linac energy (taken to be ~$2.7M/40MeV module) and H^- source development ($2M) are also included.

Table B.1 is the spreadsheet for the three-energy study. Figure B.1 shows the scaled costs for the model machines on the spreadsheet for Stage 1 (lower curve) and Stages 1 and 2 combined (upper curve). The points on the smooth curves are for the 40π models at 8, 12, and 16 GeV with circumference ¾, 1, and 1.5 C_B, respectively. The extra points at 16 GeV correspond to the baseline 60π Proton Driver. The Stage 2 cost for the bPD is higher than the 16 GeV model because of its larger acceptance. The Stage 1 cost for the bPD is shown at 16 GeV, though its magnet power supplies and reused Booster 53 MHz rf system limit it to 12 GeV. All models have the same calculated Laslett tune shift as the bPD. Stage 2 models provide 1 MW beam power. Stage 1 models inject 1.2×10^{14} into the MI, except the 8 GeV case, which provides 1.6×10^{14}. Costs do not include G & A or contingency.

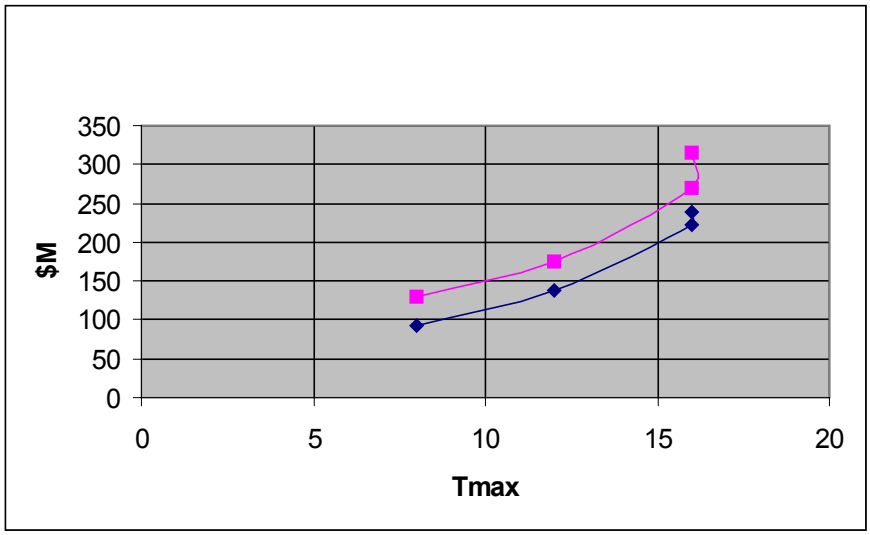

Figure B.1. T_{max} vs. Cost.

B.4. Second Study: Comparison of Operating Costs.

Here we use values estimated for the baseline PD and scale them to other machines. The magnet power supply system should require wall power proportional to the stored energy of the magnet system. The 20 MW estimated for the baseline PD magnet system seems to scale with the measured 2.5 MW of the present Booster GMPS system which has about one tenth the stored magnetic energy as the baseline PD.

The rf operating costs should scale as the number of cavities or rf Volts per turn and by the duty factor. Twenty Booster cavities operating to accelerate beam at 15 Hz require 7 MW of wall power. For Stage 1 operation with only the MI being serviced the duty factor is small. For example, with two prepulses and a PD cycle for each of the 6 batches injected into the 1.86s MI cycle, the duty factor is 8/28 = 28%, giving 2 MW of rf power. For Stage 2 operation, the 7.5 MHz rf system of the baseline PD is estimated to need 20 MW.

Figure B.2 shows the sum of the estimated annual Magnet and rf power cost needed to operate the machines discussed in Study 1. The corresponding numbers are found in the last row of Table B.1 in the spreadsheet

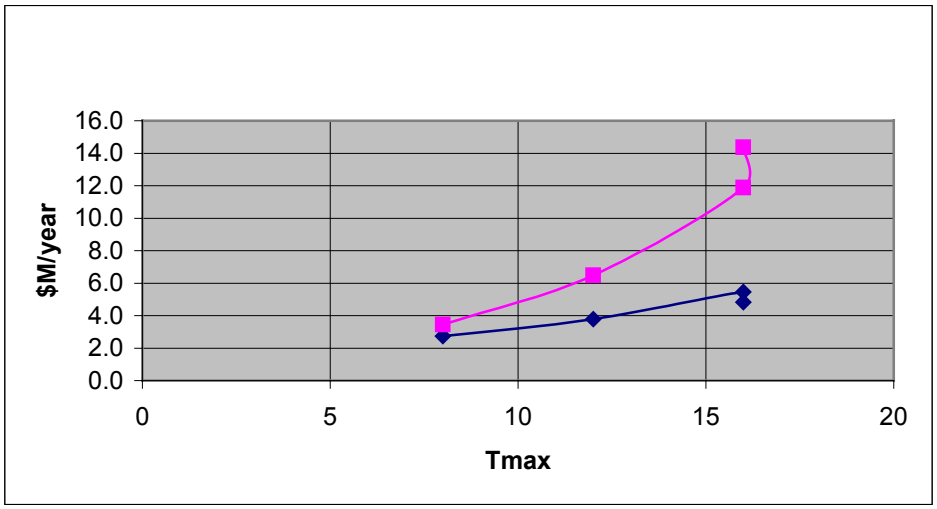

Figure B.2. Operating Expenses. The scaled annual operating power expenses for the model machines on the spreadsheet are shown for Stage 1 (lower curve) and Stage 2 (upper curve). The machine is assumed to run 80% of the time with the present electricity rate of $0.05 per kW-h. The points on the smooth curves are for the 40π designs. The extra points at 16 GeV correspond to the baseline 60π baseline Proton Driver, although the Stage 1 value actually operates at 12 GeV.

B.5. Third Study: Cost as a function of B_{max}

Another study of interest involves a tradeoff between B_{max} and the machine circumference. In this example, the 8 GeV case from the previous study is modified by

increasing its circumference to that of the present Fermilab Booster. The reduced packing fraction from this ring enlargement allows longer magnets and a lower B_{max}, even though this reduces the number of batches that can be injected into the MI and also increases the cost of rf. Since B_{max} affects costs of magnets and power supplies quadratically, one should still win by lowering B_{max} although at a reduced, but acceptable, level of performance.

An additional motivation for this study at 8 GeV is the issue of compatibility of the new Proton Driver with existing Booster functions. For normal Tevatron Collider operations, special 8 GeV Booster beam cycles are interleaved with other cycles in order to tune up the parameters for the transfers between the 8 GeV Antiproton Accumulator and the MI. To supply such cycles with a higher-energy machine will require extracting on the ramp or using the PD in a dedicated 8 GeV mode.

Table B.2 is the spreadsheet for the 8 GeV B_{max} study. Figure B.3 shows the scaled costs for Stage 1 (lower curve) and for the combined Stages 1 and 2 (upper curve) for the three choices of B_{max}. Indeed, lowering B_{max} does compensate for higher rf and construction costs. For a real design with these parameters, however, complications of a lattice that avoids transition may require a smaller packing fraction.

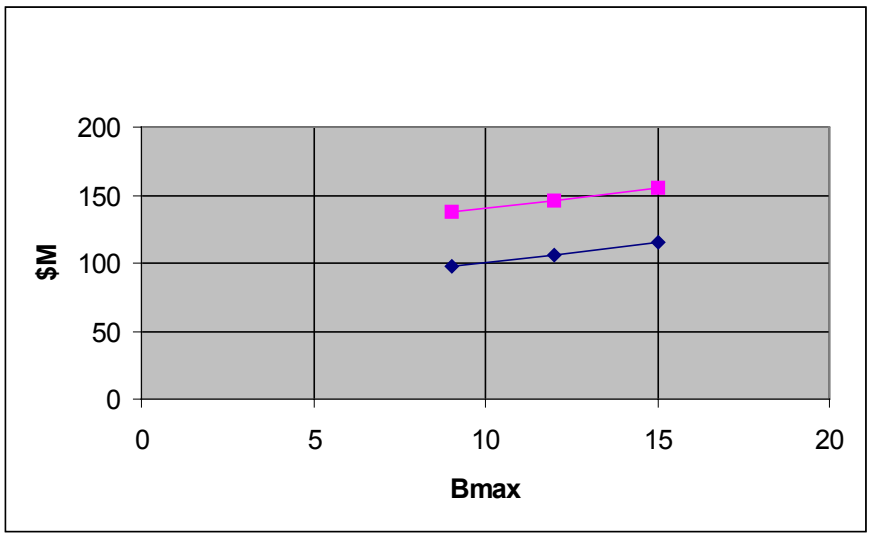

Figure B.3. B_{max} vs. Cost. The construction cost for an 8 GeV PD with Booster circumference is shown as a function of the maximum field of the dipoles. Compare these costs with the 8 GeV model with $C = 3/4\ C_B$ of Figure B.1. The smaller stored energy costs for lower B_{max} can offset the higher rf and conventional construction costs of a larger circumference. The packing fractions for the 9, 12, and 15 kG cases are 0.44, 0.33, 0.26, respectively. At B_{max} = 10 kG the cost is roughly the same as the smaller circumference machine at 15 kG. In this model, the packing fraction is 0.4 at 10 kG, compared to the bPD, 0.33, while the Stage 2 rf has one third as many cavities as the bPD in a ring with 2/3 the circumference. That is, since the fraction of the circumference occupied by rf is less in the smaller, lower energy ring, the magnetic packing fraction can be larger.

Table B.1. Construction and Operation Costs versus T_{max}

Machine		baseline PD		3/4CB, 8 GeV		CB, 12 GeV		1.5CB, 16 GeV	
stage		1	1&2	1	1&2	1	1&2	1	1&2
T_{max}	GeV	12	16	8	8	12	12	16	16
C	/CB	1.5	1.5	0.75	0.75	1	1	1.5	1.5
N	E13	3.0	3.0	2.0	5.2	2.0	3.5	3.0	2.6
T_{linac}	GeV	0.4	0.4	0.4	0.73	0.4	0.572	0.523	0.475
Acceptance	π mm-mr	60	60	40	40	40	40	40	40
N Emit	π mm-mr	61	61	41	59	41	50	48	45
batches		4	4	8	8	6	6	4	4
N MI	E14	1.2	1.2	1.6	4.2	1.2	2.1	1.2	1
Power	MW	0.86	1.15	0.38	1.00	0.58	1.00	1.15	1.00
Laslett tune	spread/bPD	1.00	1.00	1.00	1.00	1.00	1.00	1.00	1.00
B_{max}	kG	11.45	15	15	15	15	15	15	15
L_{mag}	m	236	236	124	124	180	180	236	236
E_{stored}	/bPD	0.582	1.000	0.248	0.248	0.415	0.415	0.667	0.667
rf factor	/bPD		1.000	0.244	0.233	0.496	0.488	0.992	0.995
packing fraction			0.334	0.351	0.351	0.382	0.382	0.334	0.334
Costs separated by scaling factors									
~E_{stored}	$Mags	69.4	69.4	17.2	17.2	28.8	28.8	46.2	46.2
~E_{stored}	$PS	61.0	85.6	21.2	21.2	35.5	35.5	57.1	57.1
~rf factor	$RF	12.9	65.2	3.1	15.2	6.4	31.9	12.8	64.9
~C	$Civil	86.5	86.5	43.2	43.2	57.7	57.7	86.5	86.5
~T_{linac}-.4	$$E_{linac}$$	0.0	0.0	0.0	23.9	0.0	13.4	10.2	7.0
constant	$LFE	8.7	8.7	8.7	8.7	8.7	8.7	8.7	8.7
Total Cost	**$M**	238	315	93	129	137	176	221	270
Operating Power MW		13.8	41.0	7.8	9.9	10.8	18.5	15.6	33.9
$M/Year	**@5¢/kW-h**	6.0	18.0	3.4	4.3	4.7	8.1	6.8	14.8

Table B.1 is the spreadsheet used to calculate the costs of alternative Proton Drivers. Columns show the parameters and costs for the baseline Proton Driver (bPD) and for 3 other model machines at 8, 12, and 16 GeV but with smaller transverse acceptance and different circumference, C. Each model has a column for Stage 1 and a column for Stages 1 and 2 combined. Rows are the maximum kinetic energy (T_{max},), the machine circumference (C) in units of the Booster circumference (CB), the number of protons in the ring (N_P), the injection energy (T_{linac}), the number of protons injected into the MI (N_P MI), and the MW on target. Three entries are normalized to the same parameter defined by the bPD: the Laslett tune shift, the energy stored in the ring magnets (E_{stored}), and the rf volts/turn (rf factor). The packing fraction is the ratio of the effective lengths of all the dipoles in the ring (L_{mag}) divided by the circumference. The costs of the bPD from Appendix A are separated according to how they should scale and then entered appropriately. The rows are labeled to indicate proportional to energy stored in the dipoles (~E_{stored}), proportional to volts/turn (~rf factor), proportional to circumference (~C), proportional to added Linac energy (~T_{linac}-0.4), or a constant addition. The entries

for the model machines on these rows come from multiplying the bPD costs by the scaling factors.

Table B.2. Costs of an 8 GeV Booster-sized Ring as a function of B_{max}

Machine		**bPD, 3/2 CB, 16 GeV**				**C = CB, 8 GeV**			
stage		1	1&2	1	1&2	1	1&2	1	1&2
T_{max}	GeV	12	16	8	8	8	8	8	8
C	/CB	1.5	1.5	1	1	1	1	1	1
N	E13	3.0	3.0	2.0	5.2	2.0	5.2	2.0	5.2
T_{linac}	GeV	0.4	0.4	0.4	0.73	0.4	0.73	0.4	0.73
Accept	π mm-mr	60	60	40	40	40	40	40	40
N Emit	π mm-mr	61	61	41	59	41	59	41	59
batches		4	4	6	6	6	6	6	6
N MI	E14	1.2	1.2	1.2	3.1	1.2	3.1	1.2	3.1
Power	MW	0.86	1.15	0.38	1.00	0.38	1.00	0.38	1.00
Laslett tune spread/bPD				1.00	1.00	1.00	1.00	1.00	1.00
B_{max}	kG	11.45	15	**9**	**9**	**12**	**12**	**15**	**15**
L_{mag}	m	236	236	207	207	155	155	124	124
Estore	/bPD	0.582	1.000	0.172	0.172	0.229	0.229	0.286	0.286
rf factor	/bPD		1.000	0.325	0.311	0.325	0.311	0.325	0.311
packing fraction			0.334	0.439	0.439	0.329	0.329	0.263	0.263
Costs separated by scaling factors									
~E_{store}	$Mags	69.4	69.4	11.9	11.9	15.9	15.9	19.8	19.8
~E_{store}	$PS	61.0	85.6	14.69	14.69	19.59	19.59	24.49	24.49
~rf factor	$RF	12.9	65.2	4.2	20.3	4.2	20.3	4.2	20.3
~C	$Civil	86.5	86.5	57.7	57.7	57.7	57.7	57.7	57.7
~T_{linac}-.4	$Elinac	0.0	0.0	0.0	24.0	0.0	24.0	0.0	24.0
constant	$LFE	8.7	8.7	8.7	8.7	8.7	8.7	8.7	8.7
Total cost	$M	238	315	97	137	106	146	115	155
Operating	MW	13.3	41.0	5.16	9.82	6.36	11.02	7.56	12.22

Table B.2 is the spreadsheet used to calculate the costs of model Proton Drivers at 8 GeV with Booster circumference but different maximum dipole fields. The columns show the parameters and costs for the baseline Proton Driver (bPD) and for model machines with 9, 12 and 15 kG B_{max}. All definitions are the same as in Table B.1.

Appendix C. Upgrade to 4 Megawatts (Phase II)

Chuck Ankenbrandt

A note from the author: This appendix describes an upgrade path to a facility having a beam power of 4 MW to support a muon collider. This upgrade is called Phase II of the Proton Driver and is based upon a 1 GeV linac and a 3 GeV Pre-Booster. As I began to think about how to write this appendix, I realized that I had written a similar document, "Design Concepts for Fermilab Proton Source Rings", for the 1997 Fermilab Proton Source Summer Study. (That document appeared in Fermilab Technical Memo TM-2021, "A Development Plan for the Fermilab Proton Source", edited by Steve Holmes.) It would have been expedient to simply edit my original document to reflect the design changes that have occurred in the intervening three years. However, after further thought I decided instead that it would be more informative, more interesting, perhaps even more educational for student readers (albeit perhaps also more self-indulgent) to produce this appendix by annotating that document to indicate how our thinking has evolved and where design changes have been made since it was written. Accordingly, the text of that document is reproduced here in normal typeface, and my notes about subsequent design developments appear in italics.

Design Concepts for Fermilab Proton Source Rings

Chuck Ankenbrandt
August 4, 1997

C.1. Introduction

The Fermilab physics programs of the future need a reliable, high-performance proton source. A straightforward approach to meet the diverse and demanding needs of those programs is described. In particular, the considerations that led to the choice of first-iteration values for major parameters for the synchrotron rings are presented.

The perfect proton source for Fermilab would be able to deliver beams having the ideal beam parameters for all possible future physics programs. Among the possibilities presently envisioned are beams for the Tevatron collider and for the VLHC, for antiproton production, for fixed-target physics based on the Main Injector, for experiments such as miniBOONE that use beam from the source directly, and for muon production for a muon collider.

The muon collider makes such severe demands on the proton source that it tends to dominate design considerations. Over the last few years, various approaches to meet those needs have been explored. Within the last year a simple approach has been developed that not only satisfies the requirements of the muon collider but also can be adjusted, by appropriate parameter choices, to match the needs of the rest of the future program.

The main body of this design study report describes a facility intended to support the Phase I applications. (Note that a neutrino factory based on a muon storage ring was apparently not yet on my radar screen in 1997.) The muon collider originally drove the development of the concepts described in this appendix and would presumably be the main customer of the Phase II upgrades.

C.2. The Muon Collider Requirements

Two short (σ = 2 nsec) bunches each containing 5×10^{13} protons at an energy around 16 GeV and a repetition rate of 5 Hz would meet the needs of a high-performance muon collider. (The proton source requirements are about the same over the whole range of final muon collider energies that have been considered, from 50×50 GeV up to 2×2 TeV.) These specifications deserve some elaboration.

Subsequently the muon collider designers requested four proton bunches in order to reduce beam loading effects during muon acceleration and beam-beam effects in the collider. Accordingly, the present scenario envisages 4 bunches each containing 2.5×10^{13} protons.

A kinetic energy of 8 GeV rather than a higher energy would seem a natural choice for a proton source at Fermilab; 8 GeV is the energy of the present Booster and antiproton source as well as the design injection energy of the Main Injector. However, the performance of the Main Injector is likely to benefit from raising its injection energy. Not only would space-charge effects be alleviated, but the available normalized aperture would roughly double, scaling with momentum, and the injection field quality would improve. (The ultimate benefit would derive from raising the injection energy above the Main Injector transition energy of about 20 GeV, or alternatively lowering the transition energy.) Furthermore, the dependence of pion production on proton energy is thought to be such that almost twice as many protons would be needed at 8 GeV as at 16 GeV. (There are significant uncertainties in the pion production cross sections in normalization, distributions, and energy dependence. There are disagreements amongst the hadroproduction model programs, and the data are insufficient to resolve the discrepancies. There is an experiment in progress at the Brookhaven AGS intended to shed light on the situation.)

The present design has an output kinetic energy of 16 GeV; that value results from constraining the circumference of the second ring to match that of the existing Booster. There are two main advantages of this choice. First, the second ring could occupy the same tunnel as the relocated Booster; secondly, the beam batch length from the second ring would match that of the present Booster, which would be ideal for antiproton production. Note, however, that the existing Booster magnets can not go beyond about 10 GeV.

The design choices described in these two paragraphs have evolved considerably, but the issues discussed remain controversial. First of all, more work on measuring and

modeling pion production and muon capture has clarified the situation considerably, confirming the rough scaling with beam power implied above. (Deviations from the scaling rule of thumb favor lower beam energies, particularly for carbon targets.) Regarding the choice of accelerator parameters, the lattice designers were unable to achieve all the desired features of the lattice, including separate function and transition avoidance, in a 16-GeV machine having the same circumference as the Booster. The decision was made to increase the circumference to 1.5 times that of the Booster rather than lowering the maximum energy from 16 GeV. However, the purported benefits of increasing the energy of injection into the Main Injector seem marginal at best unless it is possible to get above transition in the Main Injector, which would be very expensive at 15 Hz. While it is true that the Main Injector would presumably accept a beam of larger normalized emittances at a higher injection energy, its extraction components and high-energy beam transport lines would not necessarily accommodate such larger normalized emittances without significant modifications. Arguments involving compatibility with existing machines on site favor preserving the output energy and bunch structure of the existing Booster. If the energy of the Phase-1 machine is lowered to 8 GeV, then an alternative upgrade scenario (to 4 MW of beam power for a muon collider) involving a second ring at 30 GeV suggests itself. That would serve the additional purpose of getting above Main Injector transition energy. Ultimately the choice may depend on whether potential future high energy physics programs that would directly use the output of the new facility will require beam energies greater than 8 GeV.

The proton bunch structure for the muon collider is specified at the pion production target; it might be achieved by combining several bunches at the target via chicanes. However, the present design adopts the straightforward approach of accelerating only two bunches. Regarding the bunch length, an rms value of 1 nsec is preferable, especially if it is desired to enhance the natural muon polarization, but the muon collider designers are willing to settle for 2 nsec. It is worth noting that the combination of high bunch intensities and short bunch lengths makes it difficult to avoid space-charge problems in the rings.

It might be wise to keep in mind the possibility of combining bunches at the production target, but the present design maintains the straightforward approach of accelerating the four bunches now required. An rms bunch length of 2 or 3 nsec would probably still suffice, but the present design aims for the more extreme value of 1 nsec. Shorter bunch lengths are preferred not only by those who would like to preserve the possibility of achieving higher muon polarizations for a neutrino factory or a muon collider, but also by those who would like to justify the choice of a higher beam energy for the proton driver. They argue that for a given longitudinal emittance, shorter bunches imply larger momentum spreads, and that for a given absolute momentum spread, the fractional momentum spread is larger at lower beam energy. However, even for beam energies as low as 8 GeV, the required dynamic aperture to contain the fractional momentum spread is not excessive.

The present design adopts the 15-Hz repetition rate of the existing proton source at Fermilab. The factor of three over the muon collider specification of 5 Hz can be

regarded either as a safety factor or as enabling operation of other physics programs at the same time as the muon collider.

The muon collider now needs the full repetition rate of 15 Hz to achieve its design luminosity because the process of production, capture, cooling, and acceleration of muons is less efficient than originally envisaged.

C.3. Synchrotron Design Concepts for Muon Production

The present plan for achieving the muon collider performance specifications calls for two rapid-cycling synchrotrons in series, each of which accelerates two bunches at a time. Table 1 presents output of a spreadsheet containing major parameters of the two rings. The strategy for achieving the required short bunches at the target while alleviating space-charge effects in the rings is to start with two relatively long bunches occupying most of the circumference of a small ring, and to do a bunch-narrowing rotation in longitudinal phase space just before extraction from each stage. In order to simplify matching of the bucket contour in the second ring to the rotated bunch distribution emerging from the first ring, the rf frequency in the second ring is chosen to be a multiple of that of the first ring. The rf frequency ratio, herein sometimes called the compression ratio, is chosen to be four in the present design.

After this was written, ESME simulations showed that it was possible to achieve the desired short rms bunch length of about 1 nsec with a single bunch rotation at extraction from the second ring, that is, without any rotation coming out of the first ring. Accordingly, the design now calls for the same rf frequency in the two rings.

The Laslett incoherent space-charge tune shift limits the beam brightness at low energy. The limitation on beam intensity can be raised by increasing the injection energy and by making the transverse emittances larger. Of course physical and dynamic apertures must be large enough to accommodate the large emittances. A useful approximation for the space-charge tune shift $\Delta\nu_{sc}$ at the center of a round Gaussian beam is

$$\Delta\nu_{sc} = -\frac{3r_p N_{tot}}{2\varepsilon_n \beta\gamma^2 B}$$

In this expression $r_p = 1.535\text{x}10^{-18}$ m is the electromagnetic "radius" of the proton, N_{tot} is the total number of protons in the ring, ε_n is the 95% normalized transverse emittance, β and γ are the usual Lorentz kinematical factors, and B is the bunching factor, defined as the ratio of the average beam current to the peak current. Note that B is always less than or equal to one.

Both rings have peak dipole fields of 1.3 T in order to keep the ring circumferences relatively small while still allowing straightforward design of the conventional magnets. The magnet design is discussed elsewhere.

Even though the circumference of the larger ring was increased 50%, it was still necessary to raise the peak dipole field to 1.5 T.

Both rings employ separated-function lattices with flexible momentum compaction in order to raise transition above the extraction energy. This not only avoids accelerating through transition but also provides other advantages. Intense beams are not subject to certain instabilities such as the negative-mass instability below transition and empirically seem less susceptible to other instabilities such as microwave instability. Also, the negative natural chromaticity is beneficial for stabilizing the beam below transition, thereby perhaps obviating the need for sextupole correctors, especially in the first ring. Having transition not too far above extraction also provides substantial bucket area in which to accomplish beam-shortening rf manipulations. In the present design the transition energy is chosen to make the synchrotron frequency in the final stationary bucket high enough to accomplish the bunch rotation in less than about half a millisecond.

Careful design of the beam pipes for both rings is required in order to manage eddy-current effects. Two approaches are under consideration. One is a thin metal pipe with water cooling and eddy-current coil corrections integrated on the pipe as in the AGS Booster. The other is ceramic beam pipe with some sort of interior cage to carry beam image currents as in ISIS.

The present design calls for external vacuum skins for both rings as in the existing Fermilab Booster. However, unlike the Booster, some kind of conductive liner will be provided to carry beam image currents.

The first ring operates at a harmonic number h=2. This allows the two bunches to be formed directly and accelerated with efficient use of the whole circumference in order to keep the bunching factor large. An important paradoxical implication of the tune shift formula is that the tune shift for a given total number of particles is independent of the ring circumference; that is, a small ring will accommodate just as many particles as a large ring, other factors being equal. Space-charge effects are alleviated by a high injection energy (1 GeV kinetic) and large normalized transverse 95% emittances (200 π mm-mrad). (Large magnet apertures of order 15 cm are necessary to accommodate these emittances.) This produces a Laslett incoherent space-charge tune shift of 0.4 for a bunching factor of 0.25.

Of course the first ring now accelerates four bunches with the harmonic number h=4. The discussion of beam parameters required to make the space-charge tune shift tolerable uses the formula given above for Gaussian beams. The main body of this report assumes that injection painting can produce more favorable transverse and longitudinal form factors, resulting in a reduction of the tune shift by about a factor of two. That same factor of two could be used in this appendix to reduce the transverse emittances and/or the injection energy from the linac. The observation that both rings will require similar physical apertures is still true; the 200π beam emittance of the small ring is compensated by the higher injection energy and smaller circumference, implying smaller beta functions. Hence magnet and rf cavity apertures can be similar if not identical.

The transfer energy of 4.5 GeV between the two rings is chosen to equalize the space-charge tune shift in the two rings. In the tune shift formula, there are two factors of γ. Roughly speaking, one factor of γ is used to make up for the larger circumference of the second ring; the other factor of γ is used to compensate for the shorter bunch length resulting from the bunch rotation. Both effects reduce the bunching factor in the second ring. (The bunching factor of 0.25 in Table 1 is the "bucket bunching factor"; it uses the average beam current over one rf wavelength rather than over the whole ring.)

Eliminating the bunch rotation upon extraction from the first ring makes the bunch longer when it is injected into the second ring. That means that a transfer energy of 3 GeV is high enough to equalize the space-charge tune shifts in the two rings, so the energy of the first ring was lowered to that value. At that energy it may not be necessary to employ flexible momentum compaction in order to avoid going through transition.

The design of the required 1-GeV linac is discussed elsewhere; here only a brief overview is given. H^- injection is used. It is assumed that the injected beam will be chopped and injected into pre-existing buckets to achieve high capture efficiency; the detailed optimization of this process is just beginning. (In simulations, adiabatic capture does not work well at the low rf frequencies considered here.) A debuncher is included to allow injection of small momentum spread, should this prove beneficial for creation of relatively small longitudinal emittance at injection into the first ring. The specified bunch rotations at extraction from each ring are expected to create momentum spreads of order 1% with longitudinal emittances of order 1 eV-sec per bunch. Such spreads would contribute a few centimeters in quadrature to the beam size for a short period before extraction from each machine. This is thought to be tolerable, given the large apertures required in any case.

As the first sentence implies, an energy upgrade to 1 GeV and an intensity upgrade to 10^{14} protons per cycle are described in TM-2021. The site layout depicted on the cover of this proton driver design study provides space for a 600-MeV "afterburner" downstream of the existing 400-MeV linac as well as for matching the 400-MeV beam into it and debunching downstream of it. The above paragraph implicitly contains another interesting design idea, namely that the horizontal aperture required for the bunch rotation at extraction time should not exceed what is required to contain the injected beam.

The detailed design of the rf systems is discussed elsewhere. Only an overview of some of the design choices is presented here. The magnet/power supply circuit for each ring is a 15-Hz resonant system like that of the existing Booster, with dipoles and quadrupoles electrically in series. (Of course this implies that the second ring can accelerate only one batch of two bunches at a time from the first ring in muon production mode.) Adding about 15% of second harmonic to the magnet ramp reduces the required peak accelerating voltage by about 25%, which is probably worth doing, especially for the second ring with its large voltage requirement. Table 1 shows a few rf parameters such as accelerating voltages (in the absence of second harmonic) and rf frequencies. One of the

advantages of a two-ring system is that the two rings divide the work of accelerating the beam. The rf system of the first ring is relatively modest because of its small circumference and small energy gain.

Table 1 is not reproduced here because the numbers are mostly obsolete. However the ideas expressed in this paragraph are still pertinent. Both rings would probably have Finemet cavities operating around 5 MHz to 7.5 MHz. The rf systems in the second ring would have to be modified to accommodate the higher beam power and beam loading of Phase II.

ESME simulations of longitudinal motion are underway; results to date have conformed qualitatively with expectations. In particular, the simulated rms bunch length at output of the second stage is consistent with a simple back-of-the-envelope estimate of 2 nsec, as desired. Accelerator studies at the Fermilab Booster and the Brookhaven AGS have begun to test bunch-narrowing concepts. Further work is in order, both experimental and computational, to optimize the bunch-shortening strategy. Also, longitudinal space-charge effects are important in these simulations; significant but tolerable emittance growth is predicted. High injection energies help to alleviate these longitudinal effects, which result from space-charge voltages having the same $1/\beta\gamma^2$ kinematic dependence as the transverse tune shifts. Incorporation of tunable inductive inserts in the rings is under consideration to compensate the space-charge voltages below transition. An experimental program is underway in collaboration with Los Alamos to study the effects of inductive inserts on the beam in the PSR.

Inductive inserts were installed in the PSR and provided the intended benefits. The accelerator studies at the Fermilab Booster and the Brookhaven AGS demonstrated the expected bunch-shortening. However, further study of bunch-shortening strategies is in order for the particular parameters of the second ring.

C.4. Meeting the Needs of the Rest of the Program

Within the general framework of multiple rings in series with bunch rotations before extraction from each stage, there is considerable flexibility in the choice of parameters (including the number of rings!). The parameters can be chosen in order to match the output beam to the needs of the rest of the physics program.

The present design starts with the choice of the circumference of the second ring to match that of the existing Booster. The output energy of about 16 GeV then results from an assumed dipole packing fraction of 0.575 and from the estimation that a dipole field of 1.3 T is about the highest reasonable choice that is consistent with straightforward design of magnets having thin silicon steel laminations. Driving such magnets into saturation would cause significant heating of the magnet yoke as well as potential problems with tracking of the dipoles and quadrupoles.

The issues limiting the maximum magnetic field were examined and found to allow a somewhat higher value of 1.5 T. Nevertheless, the circumference of the second ring had

to be increased to 1.5 times that of the existing Booster in order to reach 16 GeV. The packing fraction of 0.575 (like that of the existing Booster) could not be achieved for a separated-function lattice with flexible momentum compaction and zero-dispersion straight sections.

The harmonic numbers of the two rings (2 and 21) and their respective circumferences are chosen in such a way that the bucket spacing in both is an integral multiple of the canonical Fermilab bucket spacing of 5.645 m. In particular, the circumference of the first ring is 8/21 times that of the second ring. Thus the bucket spacing in the second ring is four times, and that of the first ring is sixteen times, that of the Tevatron and Main Injector. The bunch structure resulting from either machine will then fall into buckets of any of the existing Fermilab rings. Thus the existing rf systems in downstream machines need not be replaced.

There are numerological constraints on the choices of circumferences and harmonic numbers to preserve compatibility between the two rings and with existing rings on site. The circumference of the small ring is chosen to be one-third that of the large ring, or in other words, half that of the existing Booster. That implies that the large ring should run at h=12 to match the bunch spacing of the small ring. Since the rf systems of the large ring must provide a large frequency swing anyway to accommodate injection at 400 MeV, it should also be possible to run them at h=12, instead of h=18, when the injection energy is 3 GeV.

An important design idea results from the realization that the Main Injector is grossly mismatched to the capabilities of the first ring. The Main Injector is incapable of handling the bunch intensities of 5×10^{13} that the muon collider requires, and the fill time would be excessive at the rate of two bunches every 66.6 msec. The normalized emittance of 200 π mm-mrad from the first ring, or 240 π mm-mrad from the second ring, also greatly exceeds the normalized acceptance of the Main Injector, which is specified as 40 π mm-mrad at 8 GeV and hence would be about 80 π mm-mrad at 16 GeV.

The mismatch between the first ring and the Main Injector can be circumvented by the simple expedient of bypassing the first ring when filling the Main Injector. All 21 buckets of the second ring would instead be filled directly from the linac using H^- injection. The Main Injector could then be filled with one or more Booster-length batches just as presently planned. However, since the rf bucket length of the second ring is four times that of the Main Injector, every fourth bucket of the Main Injector would contain beam.

The idea of bypassing the first ring is obviously incorporated in the main body of the design presented here since the first ring does not exist in Phase 1. Other changes are obvious; for example, there are 18 buckets in the second ring instead of 21, and every seventh Main Injector bucket would be filled.

It is worth noting that the first ring could be omitted if the muon collider does not materialize. However, if the first ring exists and the muon collider is not running, the

output of the first ring could be used directly to support low-energy physics programs while the second ring is used to feed the Main Injector.

The capabilities of the second ring at an injection energy of 1 GeV are well-matched to those of the Main Injector, as can be seen by the following scaling. A normalized acceptance of 240 π mm-mrad at 4.5 GeV scales with momentum to 76 π mm-mrad at 1 GeV, closely matching the 80 π mm-mrad acceptance of the Main Injector at 16 GeV. The bunch intensity of 5×10^{13} at the space-charge limit at 4.5 GeV scales as $\beta^2\gamma^3$ to 1.8×10^{12} per bunch, or 3.75×10^{13} per Booster-length batch, or 2.25×10^{14} per six Booster-length batches, at 1 GeV. This is 7.5 times the Main Injector design intensity. According to Weiren Chou, the Main Injector seems capable, with upgrades, of accelerating five times its design intensity. However, Chou's calculations were done for an injection energy of 8 GeV and with adjacent buckets filled, and they ought to be redone for the present case.

Redoing this scaling for the present parameters is left as an exercise for the reader.

The strategy of sometimes bypassing the first ring has several ramifications. It suggests a layout that has both rings tangent to the line from the linac as in Figure 1. The first ring should have a long straight section that supports both H^- injection and 4.5 GeV extraction. The second ring needs a long straight section that supports H^- injection at 1 GeV and proton injection at 4.5 GeV. Scaling from the Fermilab Booster implies that H^- injection at 1 GeV requires about a 12-meter straight section. This suggests a racetrack configuration for both rings.

Figure 1 is not reproduced here; the same features are contained in the picture on the cover of this report. Of course the shape of the second ring is now triangular, and the transfer energy is now 3 GeV rather than 4.5 GeV.

If it is desired to interleave cycles, some of which go into the first ring and some directly into the second, on a short time scale, then the linac must be capable of asynchronous operation. This requires further study.

The main parameters of Phase II, i.e., an upgrade to 4 MW from Phase I, are listed in Table C.1. As a comparison, the parameters of the present proton source and Proton Driver Phase I are also listed.

Table C.1. Proton Driver Parameters of Present, Phase I and Phase II

Parameters	Present	Phase I (MI, ν-Fact)	Phase II (μ-Coll)
Linac (operating at 15 Hz)			
Kinetic energy (MeV)	400	400	1000
Peak current (mA)	40	60	80
Pulse length (μs)	25	90	200
H^- per pulse	6.3×10^{12}	3.4×10^{13}	1×10^{14}
Average beam current (μA)	15	81	240
Beam power (kW)	6	32	240
Pre-Booster (operating at 15 Hz)			
Extraction kinetic energy (GeV)			3
Protons per bunch			$2{,}5 \times 10^{13}$
Number of bunches			4
Total number of protons			1×10^{14}
Normalized transverse emittance (mm-mrad)			200 π
Longitudinal emittance (eV-s)			2
RF frequency (MHz)			7.5
Average beam current (μA)			240
Target beam power (MW)			720
Booster (operating at 15 Hz)			
Extraction kinetic energy (GeV)	8	16	16
Protons per bunch	6×10^{10}	1.7×10^{12}	2.5×10^{13}
Number of bunches	84	18	4
Total number of protons	5×10^{12}	3×10^{13}	1×10^{14}
Normalized transverse emittance (mm-mrad)	15 π	60 π	200 π
Longitudinal emittance (eV-s)	0.1	0.4	2
RF frequency (MHz)	53	7.5	7.5
Extracted bunch length σ_l (ns)	0.2	1	1
Average beam current (μA)	12	72	240
Target beam power (MW)	0.1	1.2	4

Appendix D. Intensity Upgrade of the Main Injector

W. Chou, J. Griffin, I. Kourbanis

D.1. Main Injector Modes of Operation

The Main Injector needs to provide beam for Collider operations, neutrino experiments (NuMI) and slow spill to the 120 GeV switchyard. In Stage 1, the Proton Driver will provide a total of 3×10^{13} p/cycle in 119 rf buckets at 53 MHz. The MI is filled with 4 Proton Driver batches (588/126 = 4.66) resulting in a total intensity of 12×10^{13}. The first 84 bunches with a total intensity 2.1×10^{13} will be used for stacking, resulting in a 4.2x intensity increase. The rest of the 360 bunches can be used for NuMI, or for NuMI and the 120 GeV switchyard. The total beam intensity available for NuMI will then vary from 6.5×10^{13} (NuMI + KAMI + Meson slow spill) to 10×10^{13} (NuMI + stacking).

For collider operations we need to produce 99 proton bunches with 2.7×10^{11} p/bunch and transverse emittance of 20π mm-mrad spaced 132 ns apart (7 buckets at 53 MHz). Due to the smaller transverse emittance required, the total Proton Driver intensity will be around 1×10^{13} p/cycle or 8.5×10^{10} p/bunch. Three bunches at a time will be injected from the Proton Driver to the MI for a total of 4 - 9 batches at the required 132 ns spacing. Then the batches will be accelerated to 150 GeV and coalesced before they are injected into the Tevatron. Since the antiprotons required for the collider come from the Accumulator and Recycler Rings at a fixed 8 GeV energy, protons in the MI will have to be decelerated from 12 to 8 GeV for tuning the antiproton transfer lines.

In Stage 2 the Proton Driver will provide 3×10^{13} p/cycle in 18 rf buckets at 7.5 MHz. In this case we plan to fill the MI with four Proton Driver batches resulting in 72 bunches at 53 MHz with 1.7×10^{12} p/bunch. Out of the 72 bunches 12 will be used for stacking and 60 for NuMI and switchyard. The total intensity available for each user will be the same as in Stage 1.

The bunch intensity in Stage 2 will be too high for collider operations while the bunch spacing is ideal (we assume 99 on 99 with 132 ns spacing). The Proton Driver intensity will have to be reduced by a factor of 6. Then 9 of the 18 Proton Driver bunches will be injected into the MI and accelerated to 150 GeV. In this case no coalescing will be required.

D.2. Crossing Transition in the MI with High Intensity Bunches

D.2.1. ESME Simulations

In all the MI operation scenarios outlined above, bunches with intensities 4 - 28 times larger than the MI design intensities are accelerated through transition. For this reason we

performed a series of ESME [1] simulations of MI transition crossing. Below we outline the general parameters of the ESME simulations:

1. We considered parabolic bunches with 20,000 macroparticles.
2. Each 53 MHz bucket was divided into 64 bins.
3. Only space charge was considered.
4. We considered a magnetic field ramp closely representing the current MI PS ramps.
5. Transition was crossed with a *dp/dt* of 150 GeV/sec.
6. The effect of a γ_t jump was simulated. The γ_t jump considered was a first order bipolar jump that maintained a clearance of

$$|\gamma - \gamma_t| \geq 0.8 \cong 2\,(d\gamma/dt)\,T_{nonlinear} \qquad \text{(D.1)}$$

except for 0.5 ms. Transition is crossed at $d(\gamma - \gamma_t)/dt = 4000\ s^{-1}$, twenty times faster than without a jump. A plot of the γ_t jump is shown in Figure D.1.

7. The effect of an inductive insert [2] was simulated. The insert considered was a pure inductor with $|Z/n| = 2.6\ \Omega$ up to 1.06 GHz. The value of the inductance was chosen so that the space charge force is cancelled at transition. A plot of the inductor impedance vs. frequency is shown in Figure D.2.

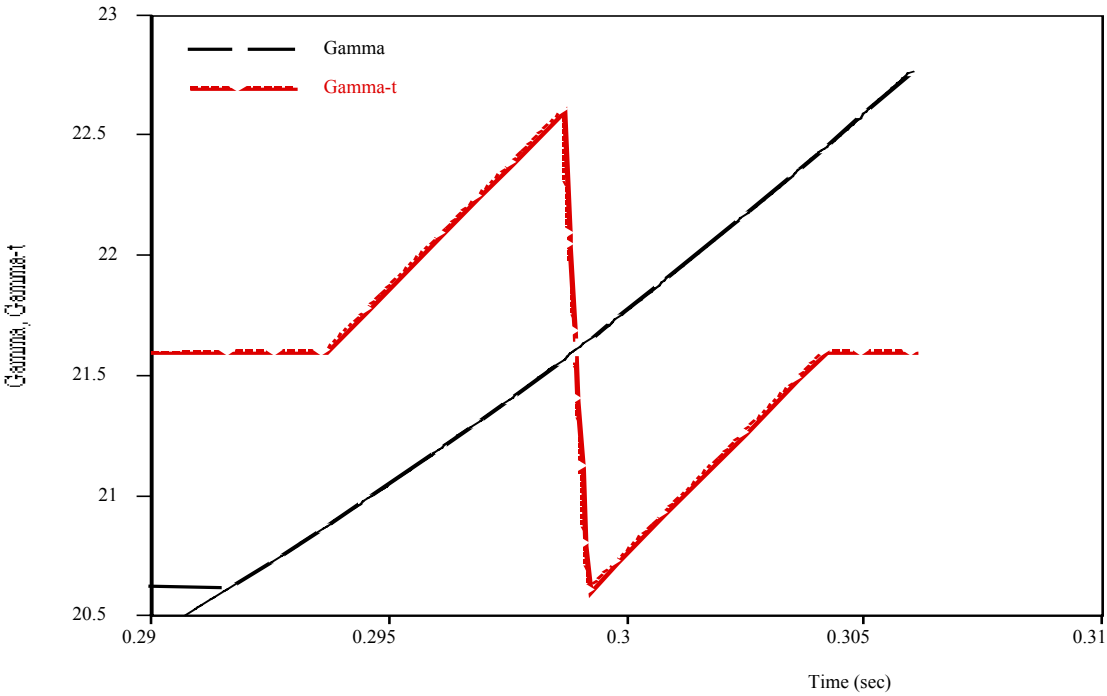

Figure D.1. Main Injector γ_t jump used in the ESME simulations

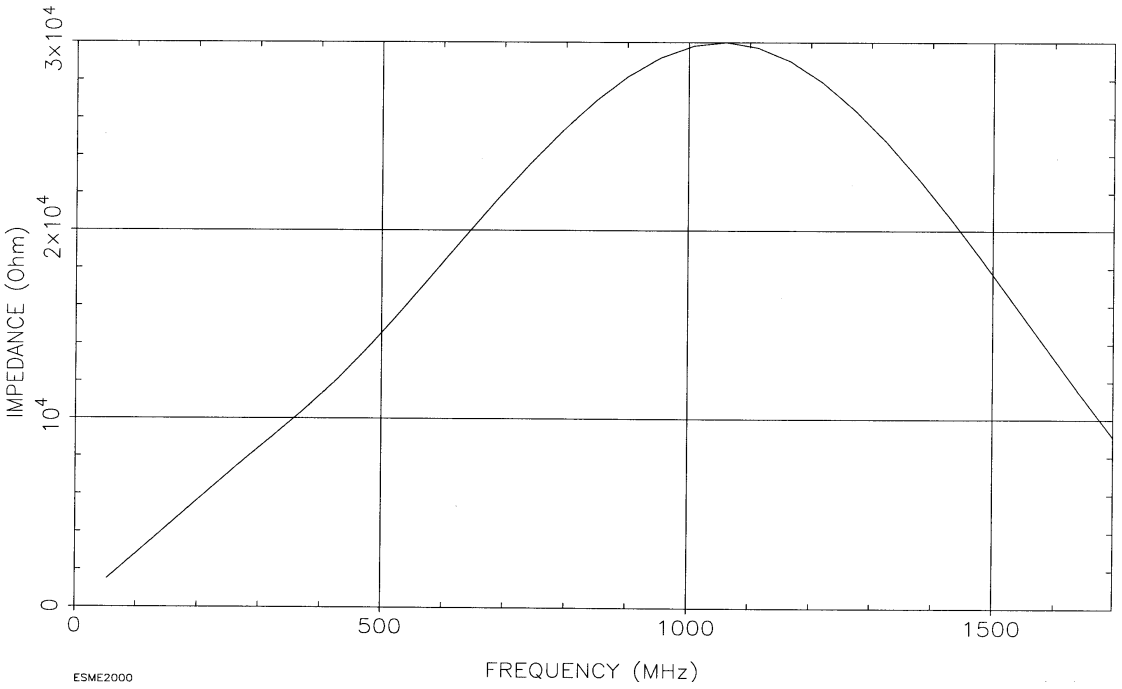

Figure D.2. Impedance vs. frequency for the inductor used in the ESME simulations

D.2.2. Simulation results for Stage 1

In this case a single parabolic bunch with longitudinal emittance of 0.2 eV-s (95%) and charge of 2.5×10^{11} p was accelerated through transition in the MI. Only normal transition crossing and crossing transition with a γ_t jump were studied. No particle loss was observed in either case, but the longitudinal emittance blowup was reduced from 300% to 5% with use of the γ_t jump.

D.2.3. Simulation results for Stage 2

In this case we used as input the actual bunch distribution from the ESME simulations of the Proton Driver. The bunch longitudinal emittance was 0.4 eV-s and the charge 1.7×10^{12} ppb. Normal transition crossing, transition crossing with a γ_t jump and transition crossing with an inductive insert were studied. The simulation results are outlined below.

1. With normal transition crossing beam breakup and 20% beam loss was observed (Figure D.3).
2. In the case of transition crossing with a γ_t jump there was no particle loss but an emittance blowup of 70% was observed (Figure D.4).
3. In the case of transition crossing with an inductive insert, 1% particle loss was observed (Figure D.5).
4. In the case where both the γ_t jump and the inductive insert were used during transition crossing, only 12% emittance blowup was observed (Figure D.6).

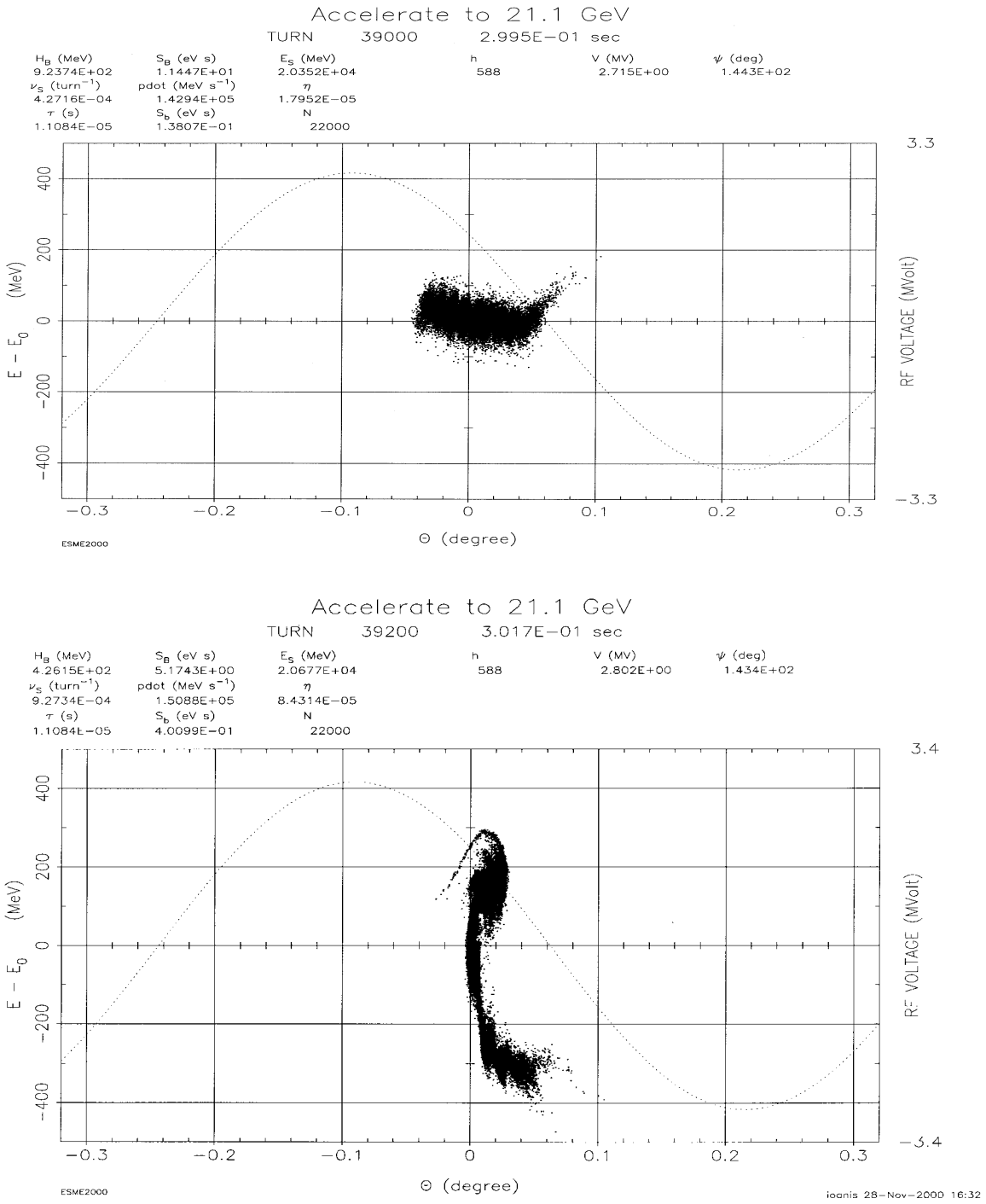

Figure D.3. Beam distributions at transition and 200 Turns after transition for normal transition crossing

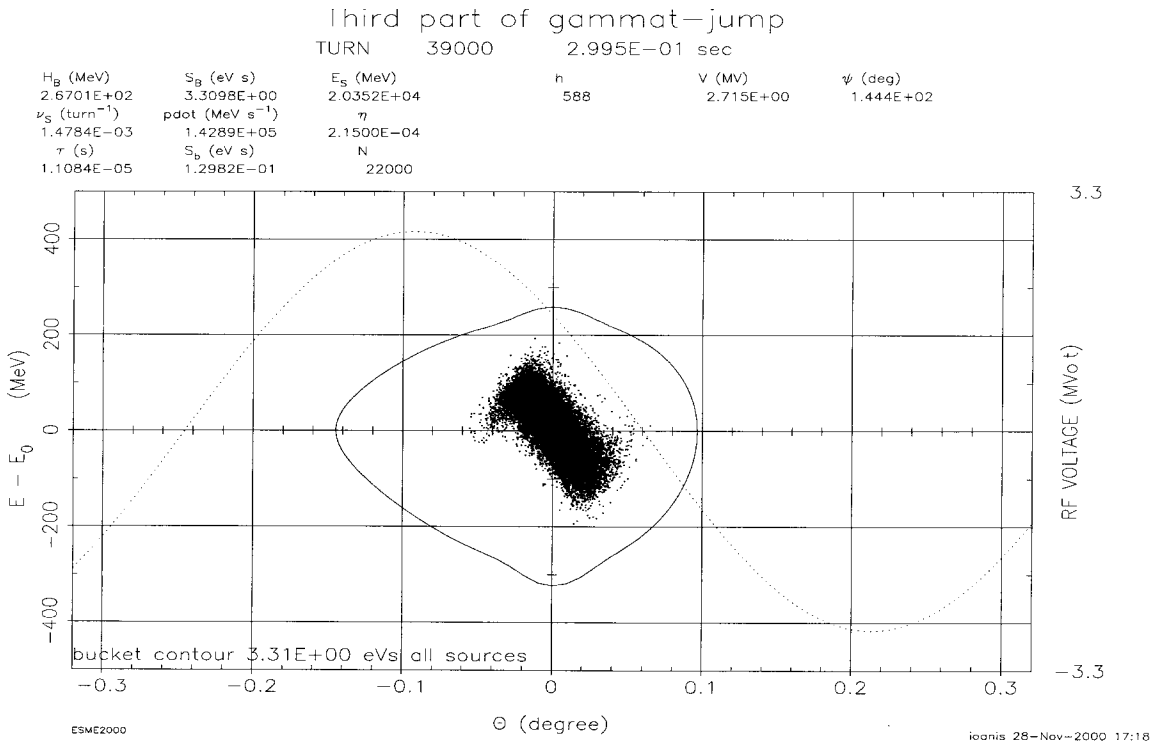

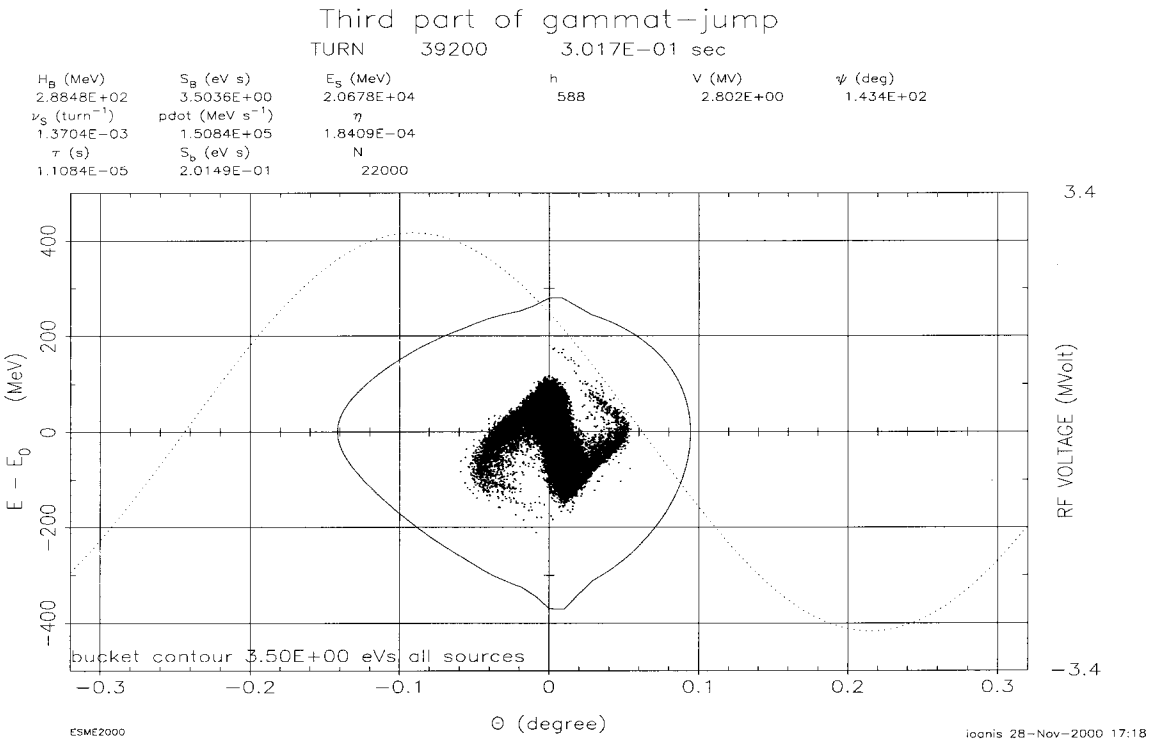

Figure D.4. Beam distributions at transition and 200 Turns after transition in the case of transition crossing with a γ_t jump

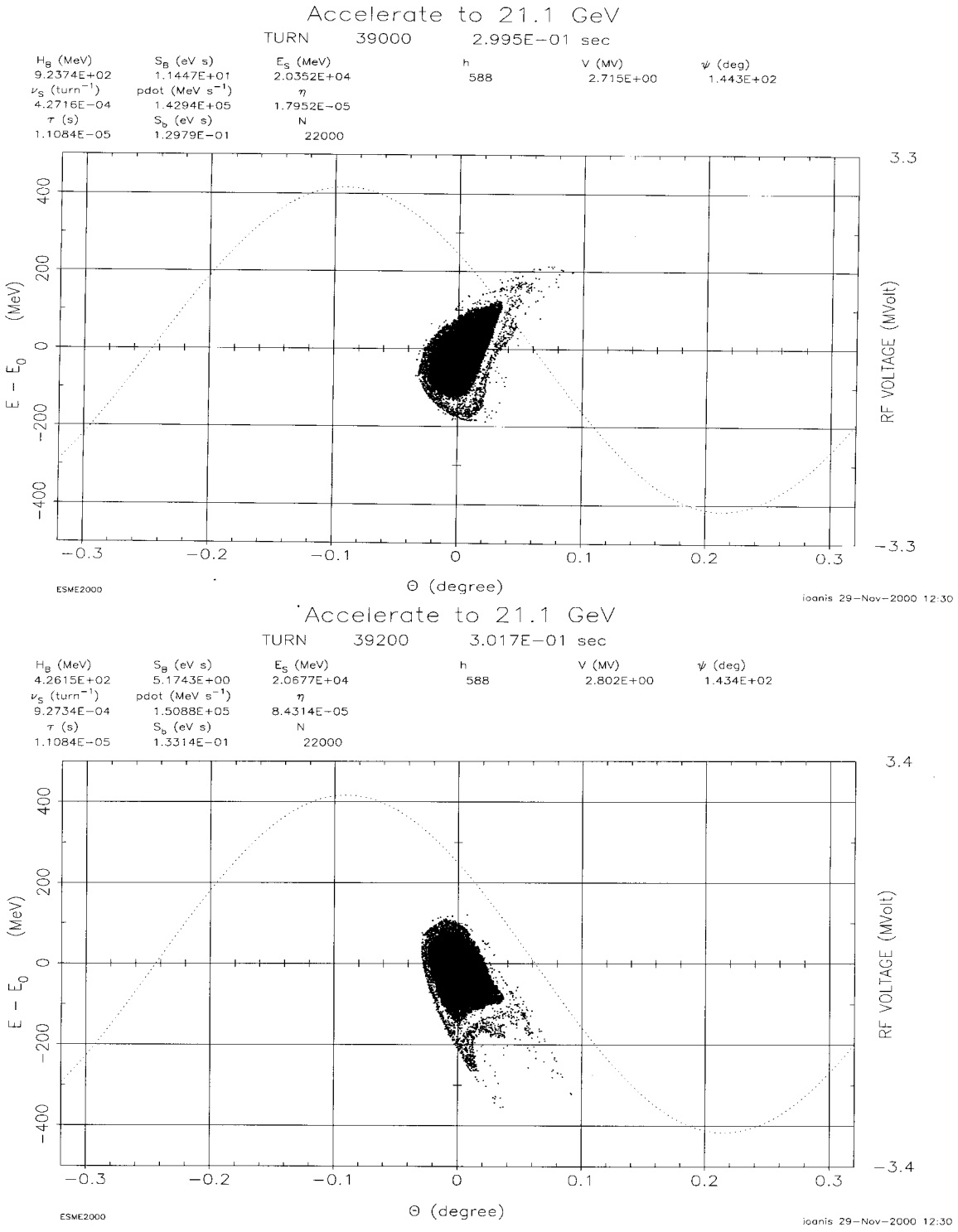

Figure D.5. Beam distributions at transition and 200 Turns after transition in the case of transition crossing with an inductive insert

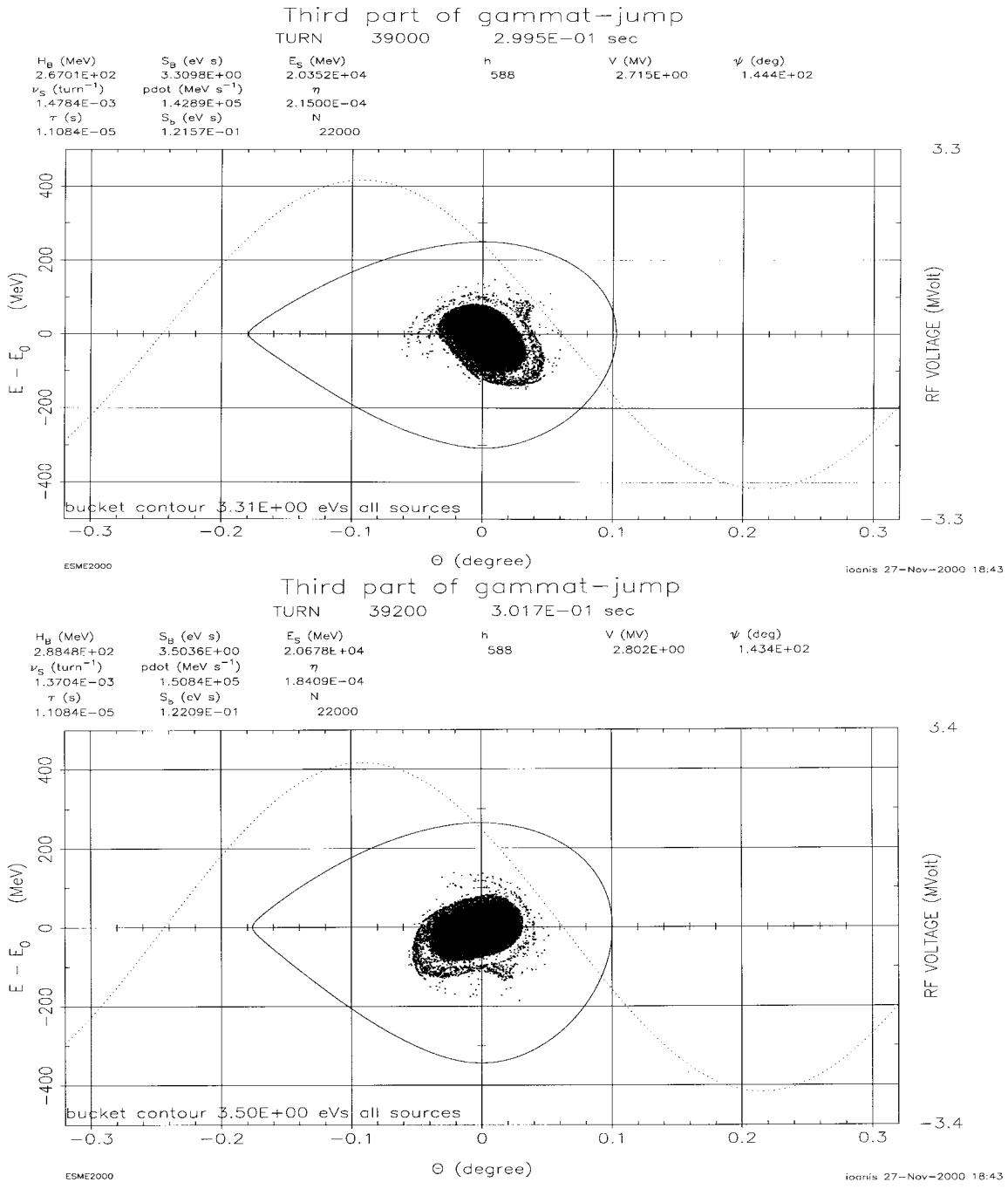

Figure D.6. Beam distribution at transition and 200 Turns after transition in the case of transition crossing with both a γ_t jump and an inductive insert

D.3. Necessary Upgrades in the Main Injector

D.3.1. RF Voltage and Power Requirements

For MI acceleration at 240 GeV/s (current maximum *dp/dt*) the required accelerating voltage $V \times \sin(\phi_s)$ is:

$$V \sin\phi_s = F_\infty^{-1} \frac{d(pc)}{dt} = \frac{240\times10^9}{90.314\times10^3} \frac{GeV/s}{s^{-1}} = 2.66\times10^6 Volts \qquad \text{(D.2)}$$

The rf power required by the beam is:

$$P = eV \sin\phi_s \frac{\beta c}{2\pi R} = 3.84\times10^{-8} W/proton \qquad \text{(D.3)}$$

The total rf power required to accelerate the maximum intensity of 12×10^{13} protons in the MI is then 4.61 MW. The total rf power available is 3.6 MW. If however, we reduce the maximum acceleration to 180 GeV/s the existing rf power is enough to accelerate the full intensity. In all the transition crossing simulations that follow, a maximum acceleration rate of 180 GeV/s has been assumed.

Since the MI cavities can develop 4.3 MV per turn, $\Gamma = \sin(\phi_s) = 0.62$ and the corresponding moving bucket factor $\alpha(\Gamma) = 0.231$. At $\gamma = \sqrt{3}\ \gamma_t$, where bucket area is minimum with constant ramp rate, the corresponding bucket area is 1.87 eV-s.

D.3.2. γ_t -jump System

As was shown from the MI transition crossing simulations, a γ_t-jump is required for higher intensity bunches. A conceptual design of a first order γ_t-jump system has been published [3]. The system consists of 8 sets (triplets) of pulsed quadrupoles that provide a jump of $\Delta\gamma_t$ from –1 to +1 within 0.5 ms. Each triplet has two quadrupoles in the arc and one of twice integrated strength in the straight section, with a phase advance of π between each quad. This design was chosen to keep the perturbation to the original lattice localized.

In order to find space to install the eight triplets, four (out of a total of 54) horizontal sextupoles and four (out of a total of 62) octupoles will have to be removed.

D.3.3. Inductive Insert

An inductive insert has been shown to reduce the effect of space charge at transition and prevent beam breakup and instabilities. The inductive insert used in the simulations was a perfect inductor (no real part) so more simulations are needed using a realistic inductor.

Since the inductive insert is going to be used to compensate the space charge around transition, a microwave ferrite needs to be used. It is estimated that about 1 - 2 meters of ferrite will be needed.

D.3.4. Dynamic and physical aperture

The normalized transverse emittance of the beam out of the Proton Driver is going to be 60π. Since the MI acceptance is 40π at 8 GeV there is no problem in accepting the larger beam at 12 or 16 GeV.

However, there are certain areas in the MI where the physical aperture is noticeably small, in particular, in the MI-52 region. It is conceivable that this area would be a radiation hot spot due to large particle losses. Possible solutions include the use of large quadrupoles, local shielding and careful beam shielding.

D.3.5. Beam acceptance of MI Beamlines

Both NUMI and Switchyard lines have enough vertical aperture to accommodate the larger emittance beam from the Proton Driver. However there are expected to be horizontal aperture limitations for emittances larger that 40π. In the case of NuMI some (up to six) small aperture dipoles will need to be replaced.

D.3.6. Passive and active dampers for beam instabilities

The impedance budget and the thresholds for microwave and mode coupling instability in the MI have been calculated [4,5]. It is expected that in Stage 2, where the bunch intensity will be increased by a factor of 28 compared to the MI design intensity, we will exceed the microwave and mode coupling instability thresholds at 120 and 150 GeV. A possible solution will be a controlled blowup of the longitudinal emittance after transition.

Since the total intensity in the MI will increase by a factor of 4, coupled bunch instabilities driven by the higher order modes of the rf cavities will become an issue. In particular the two narrow-band passive dampers for the modes at 128 and 225 MHz may have to be supplemented by active dampers.

D.3.7. Stopband correction

In Stage 1 the total intensity in the MI will be increased by a factor of four while the injection energy will increase from 8 to 12 GeV and the transverse normalized emittance from 40π to 60π. Because of this the space charge Laslett tune shift will remain the same.

In Stage 2 the average current remains the same while the peak current is increased by a factor of seven. In this case the Laslett tune shift can become as large as –0.4 and some sort of stopband correction will be required.

References

[1] J. MacLachlan and J.F. Ostiguy, "User's Guide to ESME 2000."

[2] A.M. Sessler and V.G. Vaccaro, CERN Report CERN 68-1, 1968.

[3] W. Chou et al., "Design of a γ_t-Jump System for Fermilab Main Injector," Proc. of the 1997 PAC, p.994 (1997).

[4] M.A. Martens and K.Y. Ng, "Impedance and Instability Threshold Estimates in the Main Injector," FERMILAB –TM-1880, March 1994.

[5] W. Chou, "Intensity Limitations in Fermilab Main Injector," Proc. of the 1997 PAC p. 991 (1997).